Lipid-polymer hybrid nanoparticles as an anti-infective delivery system

Valeria Carini

A thesis submitted in partial fulfilment of the requirements of

Liverpool John Moores University for the degree of Doctor of Philosophy

March 2025

Declaration

The work presented in this thesis was carried out at the Byrom Street City Campus of Liverpool John Moores unless otherwise stated. The work is the original work of the author.

While registered as a candidate for the degree of Doctor of Philosophy, for which submission is now made, the author has not been registered as a candidate for any other award. This thesis has not been submitted in whole, or in part, for any other degree.

James Parsons Building

Byrom Street City Campus

Liverpool John Moores University

3 Byrom Street

L3 3AF

Liverpool

UK

To my family,

who gave me the confidence to embark on this journey,

to the incredible women, mamma and nonna,

who instilled in me their unyielding spirit and determination to help me continue it,

and to the family I built along the way,

whose unwavering support helped me find my inner strength to finish it.

Acknowledgements

In completing this PhD, I recognize that this achievement is far more than the culmination of years of rigorous academic work; it is the embodiment of a deeply personal victory. For much of my life, I was told that I wasn't 'smart enough' to pursue my dreams, that my aspirations were beyond my reach. These doubts could have been discouraging, but instead, they motivated me to push harder, to prove to myself and others that I could achieve whatever I set my mind to.

Throughout these years, I've learned that success is not defined by the absence of setbacks but by the ability to rise after each one. As the lyrics from Imagine Dragons' *"Believer"* say, *'I'm the one at the sail, I'm the master of my sea,'* I took control of my journey, navigating through challenges with resilience and strength. This PhD stands as proof that we are capable of shaping our own destiny, no matter the doubts or obstacles along the way.

First and foremost, I would like to thank my supervisors.

Dr. Sarah Gordon, you have been my unwavering support since 2018, guiding me with patience and wisdom throughout this entire journey. Your dedication and mentorship have been invaluable, and I am profoundly grateful for the time, effort, and consideration you have devoted to my progress. I sincerely valued the flexibility of your availability for meetings at any hour, even during your periods of leave, and your prompt and thorough responses to emails at all times of the day and night, exemplifying your steadfast commitment and support.

Dr. Imran Saleem, I want to express my deepest gratitude for your unwavering support since I first arrived at LJMU in 2016. From the very beginning, you've been there to offer guidance and encouragement, and your insights and advice have been crucial in helping me navigate the challenges of this PhD. Your belief in me has been a constant source of motivation.

Dr. Katie Evans and Dr. Jo Foulkes, you both played a pivotal role in my development, especially when I was just beginning my journey in the microbiology field. Your insightful advice and willingness to guide me, even in the face of countless questions, have been invaluable. Your expertise and patience provided me with the confidence and knowledge I needed to navigate the challenges I encountered. The time, dedication, and mentorship you both offered have been integral to my growth, and I am profoundly grateful for your guidance and encouragement throughout this journey.

Beyond my supervisory team, there have been countless others whose support and contributions have made this journey possible.

To **Mamma and Babbo**, your love and support have been my anchor, even from afar. Moving away from home to follow my dreams was one of the hardest decisions I've ever made, but it was your belief in me that gave me the strength to pursue this path. Mamma, we've always joked '*che so la figlia de ba'* because of how much you see him in me. But as the years go by, I realize that I've taken much more from you than I ever thought. Your resilience, your wisdom, and your ability to find strength in every situation have shaped me in ways I am only now beginning to understand. Babbo, your quiet wisdom and steady support have always been a guiding light for me. Together, you both have taught me the value of hard work, determination, and unconditional love. I've never been good at telling you how much I love you, but with these words, I want to dedicate the song "*Padremadre*" by Cesare Cremonini to you. Every time I hear it, it brings tears to my eyes and makes me think of you both, of everything we've shared, and everything you've done for me. Though the distance has often been difficult, I always felt your presence with me. This accomplishment is as much yours as it is mine, and I am eternally grateful for the sacrifices you both made so that I could chase my dreams. I love you, more than words can express.

To my brother **Riccardo**, sharing a birthday with you has always made our bond even more special. Being born exactly three years apart, we've grown up celebrating our lives together. I can't help but laugh when I think back to how jealous we were of each other as kids, forced to share one birthday cake and one present between us. Now that I live

in England, the one thing I wish for more than anything is to be able to celebrate that day together again. Thank you for your endless support, for pushing me to aim higher, and for always reminding me that no challenge is too great to overcome. You are my alter ego, the indelible mark on my skin, the person without whom I wouldn't be who I am today—flaws and all. I will always carry you with me, even when we are far apart, and I'll continue to protect you for the rest of my days, because deep down, you will always be the little one of the family.

To **Max**, my partner, my *poco loco* and the one who made everything brighter when the days felt impossibly long. Despite the miles between us and my hectic work schedule, you never once made me feel guilty for the time we couldn't spend together. Instead, you supported me without hesitation, always understanding and encouraging me to keep going and reminding me that love is not measured by moments spent together, but by the strength shared through them. We bonded over COVID, and since then, you've been my constant support, always there to lift me up. You have this way of knowing when I need you the most, answering my calls before I even speak, with Archie always by your side. You learned about my work, my struggles, even about nanocarrier delivery systems, just to be part of my world. You made me laugh when stress got too heavy, held me up when I felt like breaking, and taught me that loving someone means loving every part of their journey, even when it takes them away from you. Your love has been my safety net, my reason to keep pushing, my reminder that even after the hardest day, I am never alone. And *"when I stop, and see you here, I remember who all this was for*"… and my promise to you is that "*from now on what's waited 'til tomorrow starts tonight"* — #Vietnam2025? Thank you for your endless love, warmth, and for being the person I can always count on, no matter what.

To **Giulia and Vera**, my Liverpool family, you turned a new city into home and made every challenge worth it. If I managed to finish this PhD without hitting my head against the wall (too hard), it's only thanks to you! You have endured my breakdowns, existential crises, disappearances, paranoia, and endless monologues at all hours of the day and night. You have been my anti-panic hotline, my on-demand distraction service, and my 24/7 emotional emergency support. And through it all, you both stood by me, keeping me sane. I will never thank you enough!

To my lifelong friends, **Nicoletta and Gaia**, distance has never diminished our bond. Gaia - I still think about that song you sent me when I firstly moved to Liverpool. It felt like you were there with me, wrapping me in your words and making the whole thing less scary. You've always known how to make me feel understood, even from afar. It was a reminder that I wasn't facing everything on my own, and your love and support have been with me every step of the way. Thank you for being the kind of friend who's always there, even when we're apart.

Nicoletta - from Erasmus adventures to our wild Liverpool nights and scooter rides in Baltimore, our friendship has been a constant source of joy and laughter. Even though we are now thousands of kilometers apart, the connection we share remains as strong as ever, and I am so thankful for your endless support, laughter, and understanding.

To **Paolo, Michele, David, John, Lalli, Seba, and Giummi**—my Liverpool crew. We started this journey together, and even though we're now spread across the globe, we make time every year to reunite in places like Faro, Marrakech, Athens, and Budapest... where next? Thanks to you, I learned happiness isn't a distant dream—it's right there in Liverpool… and I am speaking about The Blue Angel!

To **Linda**, thank you for always being there, ready to welcome me with a beer every time I came back to Liverpool. We've already planned out all the courses we'll take once I move back, and I can't wait to start that chapter together. Despite our playful way of throwing insults at each other, you know how much you mean to me and I have always appreciated your support. Thank you for every laugh, every chat, and every moment you stood by my side. You've been a true friend, I'm so grateful to have you in my life.

To **Athina**, my dear friend and colleague, who was my rock throughout our time in Chippenham. From road trips to salsa classes and late-night talks, you've been there through it all. Though you've now moved back to Greece to start an exciting new chapter, I'll always cherish the memories we've shared. No distance will ever diminish our friendship, and I couldn't be prouder of all you've accomplished. To the dream **VR993 team**, my Chippenham family, you became my home away from home. The

community we built made the long days lighter and the challenges easier to face. I will always be thankful for the sense of belonging and support you all provided.

To **Fede, Dino, Sonia, Tucci, Anto', Vale, and Giu**, even though we only see each other once a year, you always make me feel like no time has passed and that distance is just a number. Every time I hear *"Oh ma quando 'rtorni giù? Dobbiamo organizzare un ape!"*, it's like a reminder that *Castello* will always be home, no matter how far I live.

To those who were once an important part of my life but have since moved onto different life paths, I look back on the time we spent together, under the protection of the *Busdignao*, with a smile. The adventures we shared, both big and small, remain precious memories that I carry with me. Though we've taken different directions, I hold onto those times fondly, knowing they played a meaningful role in my journey.

Finally, to every obstacle, moment of doubt, and sleepless night—you have shaped me more than I ever imagined. Each setback, each hard day taught me that real growth comes from facing challenges straight on. This is a symbol of my journey, a testament to how I found strength I didn't know I had. It taught me to trust myself, lean on those who stood by me, and face the unknown without fear. Most of all, this journey is proof of how powerful love and support can be. Without my family, my friends, and Max, this road would have been so much harder. Their faith in me, their encouragement on the hardest days, reminded me that with determination and the unwavering love of those who stand by us, anything can be achieved. I end this chapter stronger, more grateful, and full of hope for what comes next, knowing that no matter what, I'm ready.

This is just the beginning, and I look forward to taking all the lessons learned on this journey into the next exciting chapter of my life.

"…Si tú no estás aquí
Aquí a mi lado
De nada vale ya
Lo que sé y mi doctorado"

Abstract

Antimicrobial resistance poses a significant global health challenge, highlighting the urgent need for innovative drug delivery systems that enhance the efficacy of existing antibiotics and new antimicrobial agents. This thesis investigates the development, optimization, and evaluation of lipid-polymer hybrid nanoparticles (LPHNPs) as a dual-delivery platform for cefotaxime (CTX), a β-lactam antibiotic, and RN7IN6, a synthetic antimicrobial peptide (AMP). The overarching goal was to create an advanced co-delivery system to improve treatment outcomes against Gram-positive and Gram-negative pathogens.

Initial investigations focused on chitosan nanoparticles (CS NPs) and POPE:POPG:CL liposomes as separate systems, with the aim of combining them to form the core and lipid shell of LPHNPs, respectively. Methodologically, microfluidic mixing was employed for the precise and scalable synthesis of CS NPs, POPE:POPG:CL liposomes, and LPHNPs. Various formulation parameters were systematically optimized to ensure desirable physicochemical properties such as particle size, polydispersity index (PDI), and Z-potential. High-performance liquid chromatography (HPLC) was used for drug quantification, while antimicrobial efficacy was assessed using minimum inhibitory concentration (MIC) and time-kill assays against clinically relevant bacterial strains.

Two types of CS, being chitosan hydrochloride (CHCL) and chitosan low molecular weight (CHT), were explored for CTX encapsulation within NPs. Despite the similarity in physicochemical and antibacterial properties of both CTX encapsulating CS NPs, CHCL-based NPs were chosen due to the CHCL aqueous solubility, enabling more efficient production and streamlined formulation for LPHNP development. The optimized CHCL NPs achieved a high CTX loaded concentration while maintaining small and uniform particle characteristics. Meanwhile, bacteriomimetic POPE:POPG:CL liposomes, designed to mimic bacterial membranes, were evaluated for the incorporation of a novel AMP being RN7IN6. Results revealed that while free RN7IN6 demonstrated potent antimicrobial activity against various bacterial strains, its adsorption onto liposome surface presented challenges such as aggregation, instability, and reproducibility issues.

Consequently, RN7IN6 was incorporated within the lipid bilayer to address these limitations. Although RN7IN6-loaded formulations demonstrated limited peptide release and no significant antimicrobial activity against *Staphylococcus aureus* and *Escherichia coli*, the POPE:POPG:CL system might be promising as the lipid shell of LPHNPs to enhance interaction with bacteria.

Encapsulation within LPHNPs was driven by the synergistic potential observed between CTX and RN7IN6, forming the foundation for developing a co-loaded delivery system. The resulting CTX and RN7IN6 co-loaded LPHNPs demonstrated superior antibacterial activity compared to free and encapsulated CTX, as evidenced by the inhibition of *E. coli* bacterial growth. Similarly, for *S. aureus*, the encapsulation of RN7IN6 within LPHNPs alongside CTX demonstrated increased antimicrobial activity compared to CTX-only loaded LPHNPs.

The development of CTX and RN7IN6 co-loaded LPHNPs showcases the advantages of using hybrid nanocarriers to overcome the limitations of traditional antimicrobial therapies. These findings emphasize the potential of LPHNPs not only to deliver dual-drug formulations effectively but also to enhance synergistic antibacterial effects. However, further refinement is necessary to understand the contribution of RN7IN6 to the overall antimicrobial activity of the co-loaded LPHNPs. Moreover, future studies should focus on investigating the mechanisms underlying the interaction between LPHNPs and bacterial cell membranes, optimizing release kinetics by tuning the lipid composition of LPHNPs lipid shell, and assessing the potential for these nanocarriers to combat a broader spectrum of multidrug-resistant pathogens.

List of abbreviations

aa	amino acid
ACN	acetonitrile
AE%	adsorption efficiency %
AI	artificial intelligence
AMEs	aminoglycoside-modifying enzymes
AMP	antimicrobial peptide
AMR	antimicrobial resistance
ANOVA	analysis of variance
ATP	adenosine triphosphate
AUC	area under the curve
Arg	arginine
BCA	bicinchoninic acid assay
Boc	t-butyloxycarbonyl
CD	circular dichroism
CFU	colony forming unit
CHCL	chitosan hydrochloride
CHT	low molecular weight chitosan
CIP5	ciprofloxacin disc
CL	cardiolipin
CLSI	Clinical and Laboratory Standards Institute
CN10	gentamicin disc
CR%	cumulative release %
CRISPR	clustered regularly interspaced short palindromic repeats
CS	chitosan
CTX	cefotaxime
DIC	N,N’-diisopropylcarbodiimide
DLS	dynamic light scattering
DMF	N,N-dimethylformamide

DNA	deoxyribonucleic acid
DoE	design of experiment
DOPE	mPEG2000 - 1,2-distearoyl-sn-glycero-3-phosphoethanolamine-N-[methoxy(polyethylene glycol)-2000
DOTAP	dioleoyl-3-trimethylammonium propane
DPPC	dipalmitoylphosphatidylcholine
DSPE-PEG-2000	1,2-distearoyl-sn-glycero-3-phosphoethanolamine-N-[methoxy (polyethylene glycol)-2000]
EE%	encapsulation efficiency %
EDTA	ethylenediaminetetraacetic acid
EMA	European Medicine Agency
EPS	extracellular polymeric substances
ESBLs	extended-spectrum β-lactamases
ESKAPE	*Enterococcus faecium, Staphylococcus aureus, Klebsiella pneumoniae, Acinetobacter baumannii, Pseudomonas aeruginosa, and Enterobacter spp*
EUCAST	European Committee on Antimicrobial Susceptibility Testing
FA	formic acid
FDA	Food and Drug Administration
FIC	fractional inhibitory concentration
FICI	fractional inhibitory concentration indices
FRAP	fluorescence recovery after photobleaching
FRR	flow rate ratio
ICH	International Council for Harmonization of Technical Requirements for Pharmaceuticals for Human Use
IM	inner membrane
LC-MS	liquid chromatography mass spectrometry
LLOD	Lower limit of detection
LLOQ	lower limit of quantification
LPS	lipopolysaccharide
LPHNPs	lipid-polymer hybrid nanoparticles

LUVs	large unilamellar vesicles
MBC	minimum bactericidal concentration
MBLs	metallo-β-lactamases
MeOH	methanol
MHA	Mueller Hinton agar
MHB2	Mueller Hinton Broth 2
MIC	minimum inhibitory concentration
MLV	multilamellar vesicles
MMF	microfluidic mixing technique
MPS	mononuclear phagocyte system
MRSA	methicillin-resistant *S. aureus*
Mw	molecular weight
MWCO	molecular weight cut off
NA	nutrient agar
NPs	nanoparticles
Oa-TOF	orthogonal acceleration- time of flight
OD	optical density
OM	outer membrane
OVAT	one-variable-at-a-time
Pbf	2,2,4,6,7-pentamethyldihydrobenzofuran-5-sulfonyl
PBS	phosphate buffered saline
PC	phosphatidylcholine
PCL	polycaprolactone
PDI	polydispersity index
PE	phosphatidylethanolamine
PG	phosphatidylglycerol
PI	phosphatidylinositol
PLA	poly lactic acid
PLGA	poly lactic-co-glycolic acid

PLGA-PLH-PEG	poly(dl-lactide-co-glycolide-b-ethylene glycol-b-dl-lactide-co-glycolide)
PMF	proton motive force
POPE	1-palmitoyl-2-oleoyl-sn-glycero-3-phosphoethanolamine
POPG	1-palmitoyl-2-oleoyl-sn-glycero-3-phospho-(1'-rac-glycerol)
QToF	quadrupole time-of-flight
RDS	relative standard deviation
REMA	resazurin microtitre plate assay
RND	resistance–nodulation–division
ROS	reactive oxygen species
RP-HPLC	reversed-phase high-performance liquid chromatography
Rt	retention time
SD	standard deviation
SHM	staggered herringbone mixer
Solutol® HS 15	polyethylene glycol-15-hydroxy stearate
SPPS	solid phase peptide synthesis
SUV	small unilamellar vesicles
TFA	trifluoroacetic acid
TFE	trifluoroethanol
TFR	total flow rate
TIPS	triisopropylsilane
Tm	phase transition temperature
TPGS	d-α-tocopherol polyethylene glycol 1000 succinate
TPP	tripolyphosphate
Trp	tryptophan
UC	ultracentrifugation
UF	ultrafiltration
WHO	World Health Organization
Z-Potential	zeta potential

Table of content

List of Figures

List of Tables

List of Publications and Awards

Publications:

- Kaneko K., Osman N., **Carini V**., Scagnetti G., Saleem I. Overview of the Advantages and Disadvantages of Different Mucosal Sites for the Delivery of Nanoparticles. In: Muttil P., Kunda N. (eds) Mucosal Delivery of Drugs and Biologics in Nanoparticles. AAPS Advances in the Pharmaceutical Sciences Series, vol 41. Springer, Cham, 2020.

- Osman N., Kaneko K., **Carini V.**, Saleem I. Carriers for the targeted delivery of aerosolized macromolecules for pulmonary pathologies. Expert Opinion on Drug Delivery.15(8):821-34. 2018

Oral/Poster Presentations:

- ***Carini V.**, Evans K., Foulkes J., Saleem I., Gordon S.*
  Antimicrobial-loaded Lipid-Polymer Hybrid Nanoparticles. *Controlled Release Society Annual meeting and Exposition, 2022*

- ***Carini V.**, Evans K., Foulkes J., Saleem I., Gordon S.*
  Biomimetic liposomes for AMP delivery: formulation and surface loading via microfluidic mixing. *Controlled Release Society Annual meeting, 2021*

- ***Carini V.**, Evans K., Foulkes J., Saleem I., Gordon S.*
  When 2+2=5. The breakthrough of using Lipid-Polymer Hybrid Nanoparticles as anti-infective Delivery Systems. Research Festival Day, 2021

- ***Carini V.**, Evans K., Foulkes J., Saleem I., Gordon S.*
  Biomimetic carriers and cargos for anti-infective therapy. Controlled Release Society Annual meeting and Exposition, 2020

- ***Carini V.**, Evans K., Foulkes J., Saleem I., Gordon S.*

Biomimetic liposomes as delivery systems for antimicrobial peptides. United Kingdom & Ireland Controlled Release Society Conference, 2020.

- ***Carini V.**, Evans K., Foulkes J., Saleem I., Gordon S.*
  Lipid-polymer Hybrid Nanoparticles: A new Strategy to address the challenge of antibiotic-resistant infections. STEM for Britain, House of Parliament, 2019

- ***Carini V.**, Evans K., Foulkes J., Scagnetti G., Saleem I., Gordon S.*
  Preparation and optimization of cefotaxime-loaded chitosan nanoparticles using a microfluidic mixing technique. United Kingdom & Ireland Controlled Release Society Conference, 2019.

- ***Carini V.**, Evans K., Foulkes J., Scagnetti G., Saleem I., Gordon S.*
  Cefotaxime-loaded chitosan nanoparticles to overcome antibiotic-resistance. Formula X, 2019

- ***Carini V.**, Evans K., Foulkes J., Saleem I., Gordon S.*
  Lipid-Polymer Nanoparticles: a new strategy for delivering anti-infectives across the bacterial envelope, LJMU Research & Innovation Celebration Day, 2019

- ***Carini V**., Esenturk I., Scagnetti G., Saleem I.*
  Preparation and optimization of chitosan nanoparticles through microfluidic mixing technology. United Kingdom & Ireland Controlled Release Society Conference, 2018.

- ***Carini V.**, Pekoz A., Hutcheon G., Saleem I., Mohamed A.*
  Dry powder intended for pulmonary delivery: Comparison between PGA-co-PDL and chitosan Nano Composite Microparticles. Drug Delivery to the Lungs, 2016.

Awards and Fundings

- **Student Excellence Award sponsored by DAM Health** (£5000) to attend an international conference or to undertake training and development opportunities.

- **3-Minute-Thesis competition –** Liverpool John Moores University winner, entered UK quarter finals competition in 2021

- ***Carini V.**, Evans K., Foulkes J., Saleem I., Gordon S.*
  When 2+2=5. The breakthrough of using Lipid-Polymer Hybrid Nanoparticles as anti-infective Delivery Systems. Research Festival Day, 2021 – LJMU Poster Competition Winner

- ***Carini V.**, Evans K., Foulkes J., Saleem I., Gordon S.*
  Biomimetic carriers and cargos for anti-infective therapy. Controlled Release Society Annual meeting and Exposition, 2020 – Best Poster Award

- **United Kingdom & Ireland Controlled Release Society Travel Prize 2020** (£1000) to attend the CRS Conference in Las Vegas, US in June/July 2020.

- **3-Minute-Thesis competition** – School of Pharmacy and Biomolecular Sciences winner in 2020

- ***Carini V.**, Evans K., Foulkes J., Saleem I., Gordon S.*
  Lipid-Polymer Nanoparticles: a new strategy for delivering anti infectives across the bacterial envelope, LJMU Research & Innovation Celebration Day **–** School of Pharmacy and Biomolecular Sciences winner in 2019

1. General Introduction

1.1. Overview of Antimicrobial Resistance

Antimicrobial resistance (AMR) poses an increasingly urgent threat to global public health, driven by the adaptive capabilities of microorganisms to withstand the effects of antimicrobial agents. The misuse and overuse of antibiotics in both human medicine and agriculture have accelerated the emergence and dissemination of resistant bacterial strains, compromising the effectiveness of available treatments [1-4]. Although AMR encompasses resistance in bacteria, fungi, viruses, and parasites, this section will focus specifically on antibacterial resistance.

Historically, antibiotics have played a pivotal role in combating bacterial infections, significantly reducing morbidity and mortality worldwide. However, the evolutionary response of bacteria to the selective pressures exerted by these drugs has led to the development of resistance mechanisms that render once-effective treatments, ineffective [1, 2, 5]. Mechanisms such as enzymatic degradation of antibiotics, modification of drug targets, upregulation of efflux pumps that expel drugs from bacterial cells, and alterations in membrane permeability collectively contribute to the multidrug-resistant phenotype observed in many pathogens [5]. For instance, the formation of biofilms, a protective matrix that bacteria create on surfaces, further complicates treatment by limiting drug diffusion and fostering environments that promote resistance [6, 7]. The clinical implications of AMR are profound, manifesting in treatment failures, prolonged hospital stays, increased healthcare costs, and elevated mortality rates [1, 2, 4]. Certain bacterial pathogens, such as methicillin-resistant *Staphylococcus aureus* (MRSA) and extensively drug-resistant Gram-negative bacteria, pose challenges due to their ability to resist multiple classes of antibiotics [2, 8, 9]. Pathogens like *P. aeruginosa* exhibit biofilm formation, which enhances their resistance and persistence in chronic infections [10]. The persistence and spread of these resistant strains underscore the critical need for enhanced infection control measures, judicious antibiotic prescribing practices, and the development of new antimicrobial agents, as well as innovative drug delivery systems to enhance the pharmacokinetics,

bioavailability, and targeted delivery of existing antimicrobials [4]. These advanced delivery strategies could help overcome current barriers such as poor tissue penetration and off-target effects, including damage to healthy tissues or disruption of beneficial microbiota, improving therapeutic outcomes and minimizing the risk of further resistance development. Global efforts to address AMR encompass a multifaceted approach involving surveillance, antimicrobial stewardship, and research into new treatment modalities [11-15]. Collaborative initiatives by international organizations and national health agencies aim to mitigate the impact of AMR through policy development, public awareness campaigns, and research funding directed towards novel antimicrobial agents and alternative treatment approaches [4]. Therefore, combating antimicrobial resistance requires concerted action across multiple fronts, including healthcare, agriculture, and regulatory frameworks. By fostering global collaboration and innovation, it is possible to mitigate the spread of resistance, preserve the effectiveness of existing antibiotics, and ensure sustainable strategies for future infectious disease management [16]. Addressing the complex interplay of biological, socioeconomic, and environmental factors driving AMR will be crucial in safeguarding public health and maintaining effective treatment options for generations to come.

1.2. Impact of Antibiotic Resistance

1.2.1. Impact of AMR on Global Health and Economy

AMR is significantly increasing morbidity, mortality, and healthcare costs. Resistant infections lead to higher rates of severe health complications and mortality compared to non-resistant infections. Globally, approximately 700,000 deaths annually are attributed to drug-resistant infections, with projections estimating this number could reach 10 million by 2050 if no effective measures are implemented [4, 17]. In the United States alone, around 23,000 deaths each year are due to AMR, with similar figures in the European Union [4]. The economic burden of AMR is extreme, encompassing not only direct medication costs but also the expenses associated with prolonged hospital stays, additional diagnostic tests, and the use of more expensive and toxic drugs [18]. In the United States, antibiotic resistance contributes an estimated $20 billion annually in healthcare costs, alongside $35 billion in lost productivity [19]. According to the latest national surveillance data, an estimated 58,224 people in England experienced an antibiotic-resistant infection in 2022, representing a 4% increase from 2021 (55,792 cases) [20]. Deaths due to severe antibiotic-resistant infections also rose during this period, from 2,110 in 2021 to 2,202 in 2022 [20]. Although antibiotic use in England declined between 2014 and 2020, with significant reductions in 2020 due to the COVID-19 pandemic, the latest data indicates a reversal of this trend. In 2022, antibiotic use increased across most healthcare settings, with total prescribing rising by 8.4% compared to 2021, though still below pre-pandemic levels in 2019 [20].

Globally, AMR could result in a 1% decrease in gross domestic product, potentially leading to economic losses of up to $100 trillion by 2050 [4]. AMR also poses significant threats to modern medicine. Indeed, critical medical interventions, including surgeries, cancer chemotherapy, and the management of chronic diseases, rely heavily on effective antibiotics for infection control [18]. Resistant infections complicate these procedures, increasing the risk of treatment failure and patient mortality. For instance, cancer treatments such as chemotherapy become challenging, as AMR can lead to higher rates of infection-related complications, further complicating patient outcomes [21, 22]. In organ transplantation, resistant infections significantly elevate the risk of transplant failure and mortality [23]. The ramifications of AMR extend to broader public

health challenges, including its impact on infectious diseases like tuberculosis, HIV, and malaria. Hence, the consequences of AMR are far-reaching, threatening global health, economic stability, and the efficacy of essential medical practices. Compounding the challenges of AMR, biofilm-associated infections, such as those on prosthetic implants or catheters, are particularly resistant to treatment, leading to recurrent infections and prolonged hospital stays [24]. These biofilms not only resist antibiotics but also create a difficult-to-eradicate reservoir for persistent infections [25]. Comprehensive strategies, including robust surveillance, judicious antibiotic use, and global cooperation, are imperative to mitigate the adverse impacts of AMR on society and healthcare systems worldwide.

1.2.2. Global Priority Pathogens and the Fight Against AMR

In 2024, the World Health Organization (WHO) published an updated comprehensive list of critical, high and medium priority pathogens, as shown in Figure 1-1, that demand urgent research and development for new treatments due to their significant impact on public health and increasing resistance to available antibiotics [26]. This update builds on previous lists published in 2017 [27] and highlights the ongoing need for research and development of new treatments for these pathogens. The WHO's prioritization of these bacteria is based on criteria such as mortality rates, burden, resistance levels, transmissibility, preventability, and treatability of infections [28]. Within this broad list, the so-called ESKAPE (*Enterococcus faecium*, *Staphylococcus aureus*, *Klebsiella pneumoniae*, *Acinetobacter baumannii*, *P. aeruginosa*, and *Enterobacter* species) pathogens [29] were designated “critical priority” [27]. Among this list, *A. baumannii* and *P. aeruginosa,* both carbapenem-resistant, are particularly notorious for their multidrug-resistant profiles and ability to cause severe infections, particularly in healthcare settings due to their limited treatment options and high fatal burden [30]. These pathogens have developed resistance mechanisms against multiple antibiotics, limiting treatment options and posing a serious threat to patients, especially those with compromised immune systems. Pathogens like *P. aeruginosa*, known for biofilm formation, further complicate treatment of chronic infections such as those seen in

cystic fibrosis, where biofilms contribute to persistent inflammation and lung damage [31].

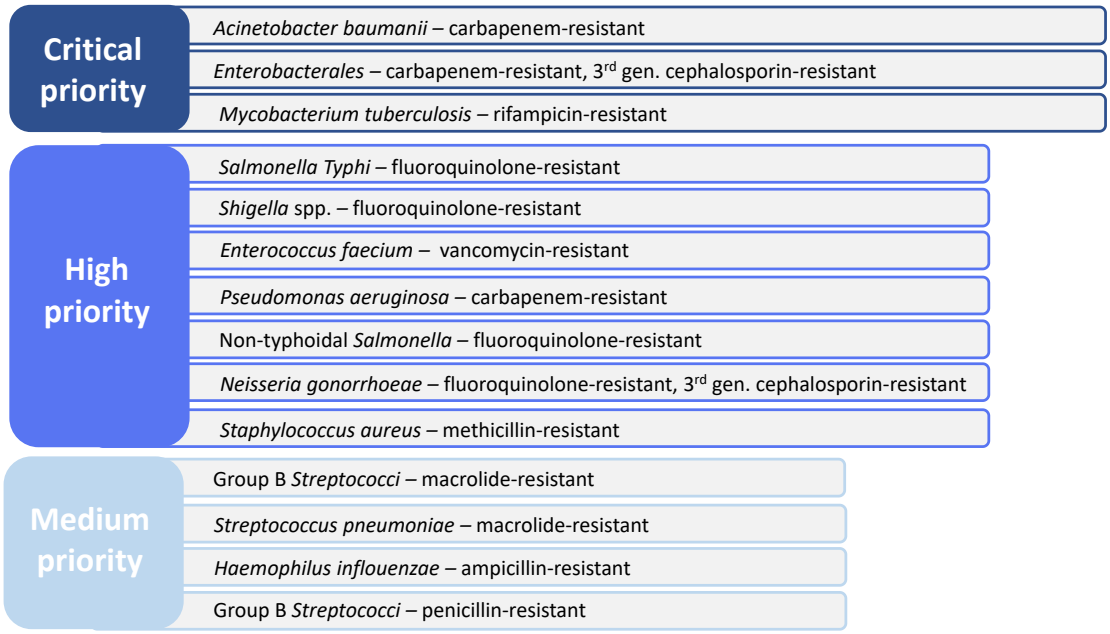

Figure 1-1: List of priority pathogens given by WHO in 2024 [26, 27].

S. aureus, including MRSA, and *Enterococcus faecium*, resistant to vancomycin, are classified as high priority pathogens. MRSA infections are challenging to treat due to resistance to β-lactam antibiotics like methicillin, requiring alternative therapies that are often limited. Vancomycin-resistant *Enterococcus faecium* continues to pose challenges, particularly due to the spread of clonal complex 17, which complicates infection control strategies [26, 32]. Enterobacterales, including strains resistant to carbapenems and third-generation cephalosporins, are listed as critical priority pathogens, as these antibiotics are often considered the last line of defense against multidrug-resistant Gram-negative bacteria [33]. The primary cause of resistance to third generation cephalosporins in *Enterobacteriaceae* strains is attributed to the production of MLBs enzymes, which significantly impact the effectiveness of these antibiotics [34]. Indeed, the 2024 update highlights the growing burden of third-generation cephalosporin-resistant Enterobacterales, especially in low- and middle-income countries, as a critical issue that needs targeted public health measures [26]. In light of these challenges, addressing the spread and impact of these high-priority pathogens requires a

multifaceted approach that includes not only the development of new treatments but also robust strategies for infection control and prevention.

The first significant initiative is the WHO global action plan on AMR, initially adopted during the 68th session of the World Health Assembly in May 2015 [35]. This plan underscores the importance of international collaboration and coordinated action in tackling AMR and remains essential in light of the 2024 WHO bacterial priority pathogen list update. By focusing on enhancing surveillance through initiatives like the Global Antimicrobial Resistance Surveillance System (GLASS), the WHO aims to monitor resistance trends and inform global strategies to mitigate AMR [36, 37]. The strategies to combat AMR include enhancing awareness and understanding through education and communication, strengthening knowledge through surveillance and research, reducing infections via improved sanitation and hygiene, optimizing the use of antimicrobial agents in human and animal health, and developing sustainable investment for new treatments [38]. The 2024 update calls for regional adaptations to these strategies, emphasizing that the burden of AMR varies significantly by geographical region and that tailored solutions are needed [26]. Moreover, in 2024, the UK launched its updated National Action Plan on AMR (2024-2029), continuing the effort to reduce antibiotic resistance [39]. The plan emphasizes infection prevention and control, reducing unnecessary use of antibiotics, and enhancing surveillance of resistant infections. It also outlines goals for reducing antibiotic use in healthcare settings and animal agriculture, with a renewed focus on developing novel antibiotics, vaccines, and diagnostics through public and private partnerships.

In addition to enhanced surveillance, these efforts involve establishing professional education on AMR, integrating AMR topics into school curricula, promoting vaccination, and implementing regulatory frameworks for antimicrobial use [38]. Furthermore, there is an emphasis on international collaboration for research and development of new antibiotics, diagnostics, and vaccines, along with public-private partnerships to drive innovation and ensure equitable access [38]. Therefore, the WHO stresses the need for sustained investment in the development of novel antibiotics and alternatives, particularly to address critical resistance mechanisms and emerging threats [26].

Economic strategies focus on assessing investment needs and securing financing for national action plans, supported by global coordination and investment mechanisms through several organizations [38].

1.3. How Evolution Drives AMR

AMR is primarily driven by evolutionary mechanisms that allow microorganisms to adapt and survive in the presence of antimicrobial agents. This process is shaped by various genetic and environmental factors, which collectively enhance the ability of microorganisms to withstand antimicrobial treatments. Key evolutionary drivers include natural selection, genetic mutations, and horizontal gene transfer, all of which facilitate the development and spread of resistance. Additionally, human activities such as the overuse and misuse of antibiotics in medicine and agriculture, combined with environmental factors, significantly contribute to the acceleration of AMR.

Table 1-1 summarizes these key factors, mechanisms, and their impacts on AMR development and dissemination. By understanding the interplay between these elements, researchers and healthcare professionals can better predict resistance patterns and design strategies to combat this global threat.

Table 1-1: Key factors driving AMR including evolutionary mechanisms (natural selection, genetic mutations, and horizontal gene transfer) and human factors (antibiotic misuse, agricultural practices, and environmental contamination), along with strategies to mitigate resistance.

AMR Aspect	Key Evolutionary or Contributing Factor	Mechanism or Cause of Resistance	Impact on AMR Development and Spread	Supporting Evidence or Example	References
Evolutionary Mechanisms in AMR	**Natural Selection**	Microbial survival under antimicrobial pressure	Resistant microorganisms survive and reproduce, spreading resistance genes within microbial populations	Resistant bacterial strains outcompete susceptible strains under antibiotic treatment, leading to more resistant populations	[40-42]
	Genetic Mutations	Random genetic changes affecting drug targets	Alterations in proteins reduce antibiotic binding and efficacy	Mutations in ribosomal proteins prevent effective antibiotic binding, neutralizing drug effects	[9, 43]
	Horizontal Gene Transfer (HGT)	Exchange of genetic material between microorganisms	Acceleration of the spread of resistance across bacterial species, contributing to AMR	Bacteria transfer resistance genes via transformation, transduction, or conjugation	[44-49]
	Mobile Genetic Elements	Plasmids, transposons, and bacteriophages carrying resistance genes	Facilitates the rapid spread of multiple resistance genes across different bacterial species	Plasmids and bacteriophages carry multiple resistance genes, aiding in the swift dissemination of AMR traits	[46, 49]
Adaptation and Dissemination of AMR	**Evolutionary Dynamics in AMR Development**	Interaction between microbes and antimicrobials over time	Microbial populations evolve under selective pressure, driving AMR through genetic adaptation	Real-time studies reveal how microorganisms evolve resistance to antibiotics, shaping AMR landscapes	[50]
	Experimental Evolution Studies	Monitoring microbial adaptation under	Reveals specific genetic changes leading to AMR in response to antimicrobial treatments	ESBL-producing bacteria demonstrate evolution of resistance to β-lactam antibiotics, offering insights into real-time adaptation mechanisms	[45, 51]

AMR Aspect	Key Evolutionary or Contributing Factor	Mechanism or Cause of Resistance	Impact on AMR Development and Spread	Supporting Evidence or Example	References
		controlled conditions			
Strategic Approaches to Mitigating AMR	**Collateral Sensitivity**	Resistance to one drug increases susceptibility to another	Exploiting evolutionary trade-offs between drugs may offer novel strategies for targeting resistant bacteria	Designing therapeutic regimens that take advantage of collateral sensitivity can slow resistance development	[52]
	Interplay of Evolutionary Forces	Combined effects of mutation, selection, and gene transfer	The convergence of genetic mutations, selection pressures, and HGT accelerates bacterial adaptation to antibiotics, contributing to widespread AMR	Bacteria rapidly acquire and spread resistance traits through this multifactorial evolutionary process	[52, 53]
Human and Agricultural Contributions	**Antibiotic Misuse in Human Medicine**	Over-prescription or inappropriate antibiotic use	Misuse, such as prescribing antibiotics for viral infections, accelerates resistance by exposing bacteria unnecessarily to antimicrobials	Misuse of antibiotics in human health care, especially in viral infections, selects for resistant strains	[54-57]
	Antibiotic Use in Agriculture	Use of antibiotics in livestock and crops	Selective pressure in agricultural settings leads to the survival of resistant bacteria, which can spread to humans via the food chain	Resistant bacteria in livestock can be transmitted to humans through contaminated food, raising AMR risks	[58]
Environmental and Healthcare Factors	**Environmental Dissemination of AMR**	Improper disposal of antibiotics and contamination of wastewater	Antibiotic residues in the environment allow resistant bacteria to thrive and spread through environmental compartments (e.g., soil, water bodies, air), exacerbating AMR	Hospital wastewater containing resistant bacteria contributes to the environmental spread of AMR	[55, 59, 60]

AMR Aspect	Key Evolutionary or Contributing Factor	Mechanism or Cause of Resistance	Impact on AMR Development and Spread	Supporting Evidence or Example	References
	Infection Control in Healthcare Settings	Poor hygiene and sanitation practices in hospitals	Inadequate infection control facilitates the spread of resistant infections among patients and healthcare workers	Resistant bacteria can thrive in healthcare settings due to poor hand hygiene and improper sterilization of medical equipment	[61, 62]
Interconnectedness of AMR Sources	**Human-Animal-Environment Interaction in AMR**	Cross-species transmission of resistant bacteria	AMR is interconnected across human health, animal health, and environmental systems, necessitating a holistic approach to its mitigation	Bacteria from animals and the environment can be transmitted to humans, while human activity can further contaminate environments and contribute to AMR spread	[58, 59, 62]
Mitigation Strategies	**Integrated Strategies to Combat AMR**	Reducing misuse in medicine and agriculture, improving infection control and waste management	A concerted effort across human health, agriculture, and environmental sectors is required to effectively mitigate AMR by reducing selective pressure and preventing bacterial transmission	Reducing antibiotic prescriptions, promoting responsible use in agriculture, and improving infection prevention and waste disposal can mitigate the spread of AMR	[63, 64]

1.4. Resistance Mechanisms

Antimicrobial resistance, a pervasive challenge in modern healthcare, is particularly acute in Gram-negative bacteria due to their complex cell envelope structure and diverse resistance mechanisms. These bacteria are notorious for their ability to develop resistance to multiple antibiotics through different mechanisms that confer resistance to multiple classes of antibiotics. Gram-negative bacteria have developed sophisticated strategies to withstand antibiotics, primarily categorized into three main groups of resistance mechanisms: enzymatic inactivation or modulation of antibiotics (such as β-lactamases and aminoglycoside modifying enzymes), reduced drug accumulation (via efflux pumps and decreased permeability) and alteration of drug targets (such as mutations in penicillin-binding proteins) [65].

1.4.1. Bacterial Cell Envelope and its Role in Antimicrobial Resistance

Bacterial resistance is heavily influenced by the structure of the bacterial cell envelope, which varies between Gram-positive and Gram-negative bacteria. Gram-positive bacteria exhibit a thick peptidoglycan layer around their plasma membrane (Figure 1-2), resulting in a purple/blue coloration when stained [66]. Conversely, Gram-negative bacteria possess a thinner peptidoglycan layer external to their plasma membrane, and an extra outer membrane (Figure 1-2) [66], resulting in a pink/red coloration when stained. The peptidoglycan layer in bacterial cell walls is crucial for permitting the diffusion of molecules. This layer, composed of alternating N-acetylglucosamine and N-acetylmuramic acid saccharide groups cross-linked by pentapeptide chains, forms a meshlike structure that provides structural support to the cell [67] and provides permeability for small molecules while maintaining a protective barrier [68]. The composition of bacterial cell membranes primarily comprises phosphatidylglycerol (PG), phosphatidylethanolamine (PE), and cardiolipin (CL), supplemented with small quantities of phosphatidylcholine (PC) and phosphatidylinositol (PI) [69]. However, the distribution of these phospholipids varies significantly between Gram-positive and Gram-negative bacteria, with Gram-positive bacteria notably lacking PE in their

membranes. This differential composition impacts the biophysical properties, contributing to variations in permeability and susceptibility to antimicrobial agents.

PG, CL, and PI all carry a negative charge at physiological pH, with additional negatively charged lipoteichoic acids and lipopolysaccharides in Gram-positive and Gram-negative membranes, respectively, enhancing the anionic character of bacterial membranes [70]. External structures like flagella aid in directional movement, while pili serve to anchor bacteria to surfaces and facilitate DNA transfer [71]. These adaptations, while essential for survival and propagation, also contribute to the complexity of addressing bacterial infections.

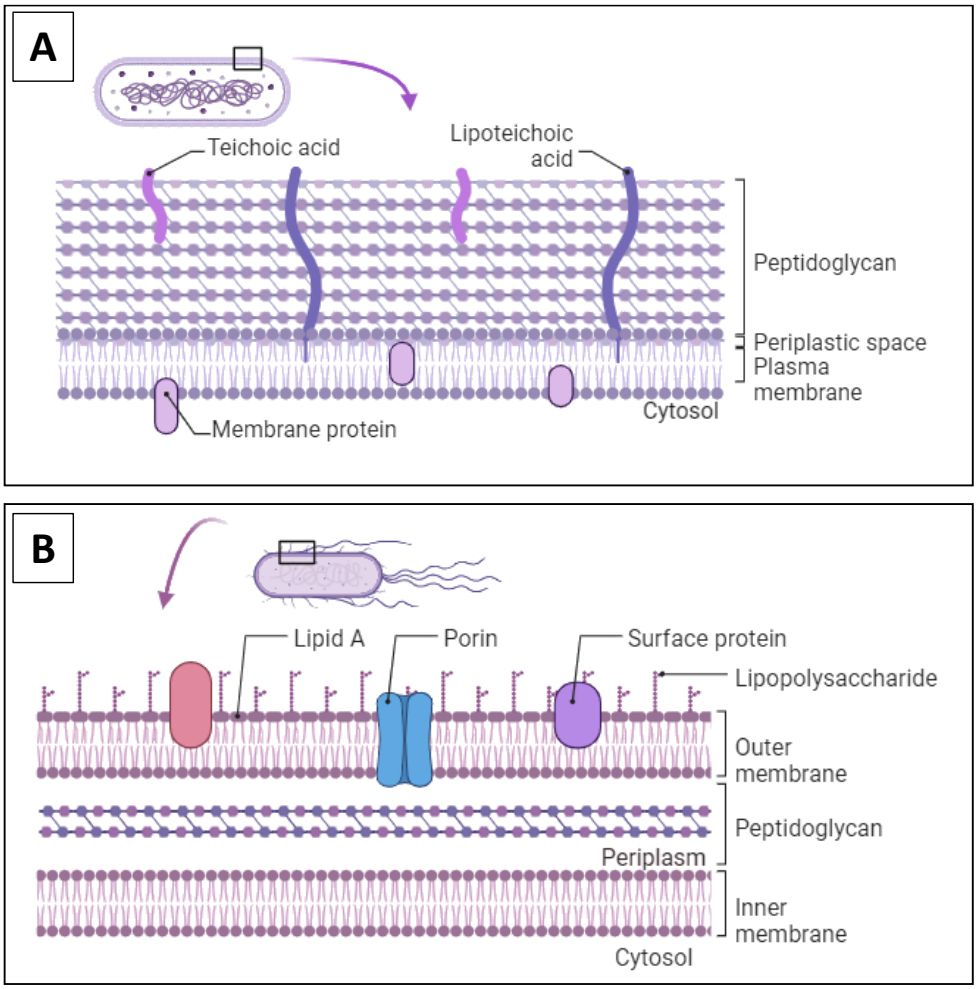

Figure 1-2: Schematic structure of Gram-positive (A) and Gram-negative (B) cell envelopes. Gram-positive cell envelopes consist of a single lipid plasma membrane and a thick peptidoglycan layer that is interconnected with teichoic and lipoteichoic acids. In contrast, Gram-negative bacteria have an inner and outer cell membrane, as well as a thin layer of peptidoglycan in the periplasmic space between the inner and outer membrane. The outer membrane of Gram-negative bacteria is lined with a layer of lipopolysaccharide. Created with BioRender.com.

Gram-negative bacteria possess a sophisticated cell envelope structure comprising two distinct permeability barriers: the outer membrane (OM) and the inner membrane (IM). The following section will focus specifically on the details of the Gram-negative cell envelope, highlighting its complexity and resistance mechanisms. The OM, a defining feature of these bacteria, is a lipid bilayer characterized by its outer leaflet composed mainly of lipopolysaccharide (LPS) [72]. LPS, in turn, consists of Lipid A, a core oligosaccharide, and an O-antigenic polysaccharide side chain [72] (Figure 1-3 A). Lipid A attaches LPS to the outer membrane by anchoring it through a glucosamine backbone, adorned with fatty acids and often phosphorylated. Integral to the OM are proteins such as porins, which act as transmembrane channels facilitating the selective passage of hydrophilic molecules into the periplasmic space [72].

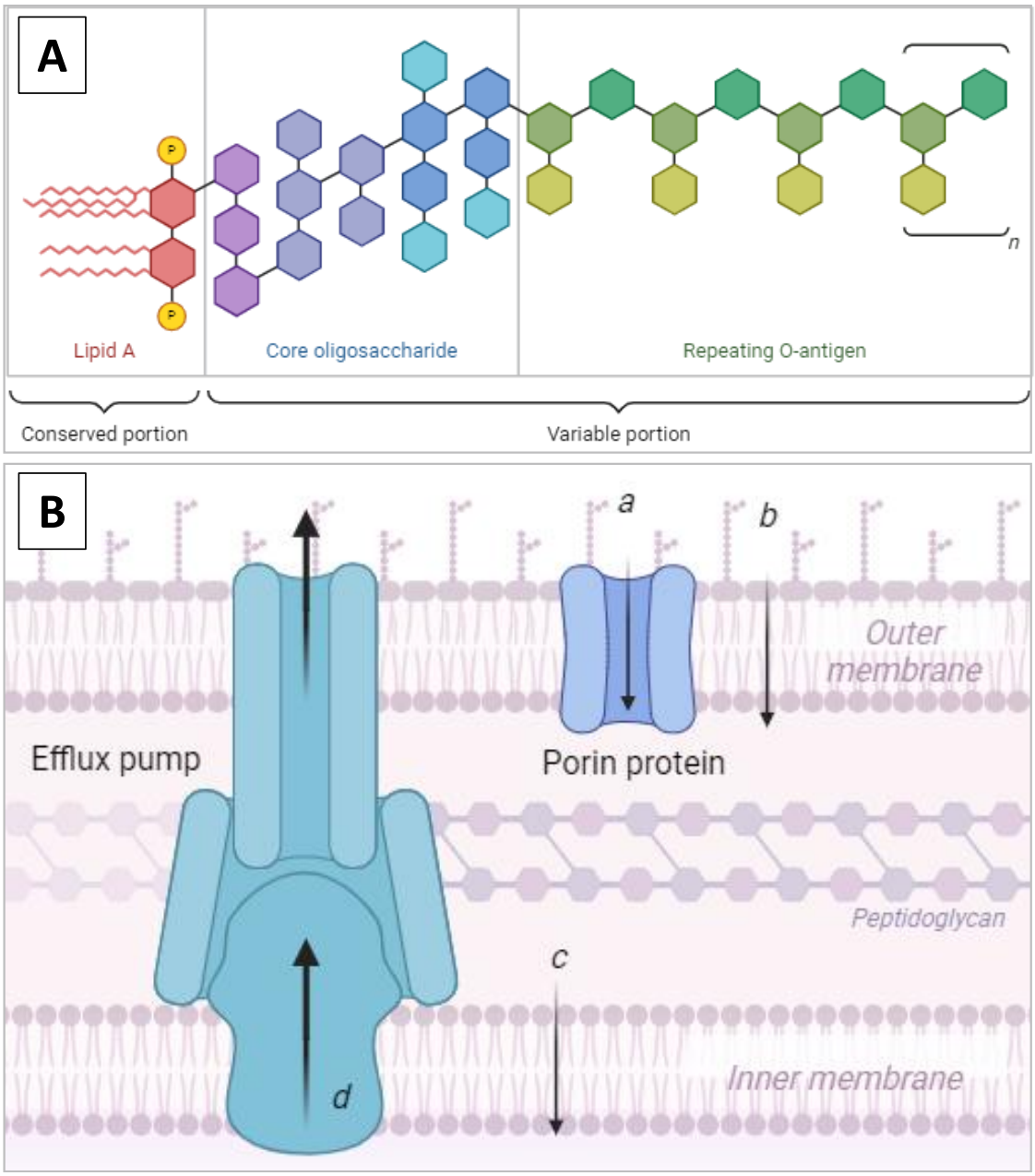

Figure 1-3: Structural characteristics of lipopolysaccharide from Gram-negative bacteria (A) and different ways by which a substance can be transported across the membranes (B). The general structure of LPS is comprised of three distinct regions: hydrophobic lipid A, core polysaccharide, and O-antigen (repeats of polysaccharide chain, where n can be up to 40). The backbone of lipid A is bisphosphorylated diglucosamine, which is substituted with six acyl chains that are connected by ester or amide linkage. Hydrophilic components and nutrients can pass through porins (a), and hydrophobic molecules diffuse through the OM and/or IM (b and c respectively). Drugs can be recognized as foreign molecules by the efflux pumps and can be transported out of the membranes (d). Created with BioRender.com.

This selective permeability enables Gram-negative bacteria to protect against hydrophobic compounds [72], including antimicrobial agents, while ensuring sufficient uptake of essential nutrients vital for survival and growth. However, some antibiotics, particularly hydrophilic ones, can cross the outer membrane via porin channels, allowing them to penetrate the periplasmic space and interact with their bacterial targets. Between the OM and the IM, the peptidoglycan layer provides additional structural support and flexibility to the cell envelope. Proteins embedded within the IM play pivotal roles in cellular processes such as energy metabolism, lipid synthesis, protein secretion, and transport of molecules across the membrane [72]. Efflux pumps located within the cell envelope contribute significantly to bacterial survival by actively expelling toxic compounds, including antimicrobial agents, from the bacterial cell. These efflux pumps (Figure 1-3 B) are typically composed of a transporter protein embedded in the IM, a membrane-fusion protein in the periplasmic space, and an outer membrane protein channel (Figure 1-3 B a), collectively ensuring effective detoxification and resistance mechanisms [73].

The characteristics of the bacterial cell envelope, particularly in Gram-negative bacteria, provide the foundational basis for understanding specific resistance mechanisms. These mechanisms, which allow the bacteria to withstand antimicrobial treatment, are discussed in the following sections.

1.4.2. Enzyme-Mediated Antibiotic Resistance

Antibiotic resistance in Gram-negative bacteria is largely driven by enzymes such as β-lactamases and aminoglycoside-modifying enzymes. β-lactamases hydrolyze the β-lactam ring in antibiotics like penicillins, cephalosporins, carbapenems, and monobactams, rendering them ineffective. These enzymes are classified into four main groups: Class A (e.g., *Klebsiella pneumoniae* carbapenemase, KPC), Class B (metallo-β-lactamases, MBLs, e.g., New Delhi metallo-β-lactamase, NDM), Class C (AmpC cephalosporinases), and Class D (e.g., oxacillinase-48), each with distinct substrate specificities.

Aminoglycoside-modifying enzymes chemically alter aminoglycosides, such as kanamycin and tobramycin, reducing their binding to bacterial ribosomes. These enzymes include acetyltransferases, phosphotransferases, and nucleotidyltransferases, each functioning through different modification mechanisms. The specific classes of enzymes, their mechanisms of action, and the antibiotics they affect are detailed in Table 1-2.

Table 1-2: Enzymatic mechanisms of antibiotic resistance in Gram-negative bacteria.

Resistance Mechanism	**Enzymes Involved**	**Function/Mechanism of Action**	**Antibiotics Affected**	**Key Points**	**References**
β-lactamase-mediated Resistance	β-lactamases (Class A, B, C, D)	Hydrolyze the β-lactam ring in β-lactam antibiotics, rendering them ineffective	Penicillins, cephalosporins, carbapenems, monobactams	Classified into four classes (A-D); notable examples include *K. pneumoniae* carbapenemase, New Delhi metallo-β-lactamase, and oxacillinase-48. Horizontal gene transfer promotes spread	[74-76]
	Class A (e.g., *K. pneumoniae* carbapenemase)	Hydrolyze β-lactam antibiotics including penicillins and carbapenems	Broad range of β-lactams	*K. pneumoniae* carbapenemase is a major carbapenemase in Gram-negative bacteria	[77]
	Class B (metallo-β-lactamases, e.g., New Delhi metallo-β-lactamase)	Metallo-β-lactamases hydrolyze carbapenems and other β-lactams	Carbapenems, cephalosporins	Metallo-β-lactamases are a significant threat due to their ability to hydrolyze carbapenems	[76, 78, 79]
	Class C (AmpC cephalosporinases)	Cephalosporinases hydrolyze cephalosporins, especially third-generation cephalosporins	Cephalosporins	Common in Gram-negative pathogens, contributing to multidrug resistance	[77, 79]
	Class D (e.g., oxacillinase-48)	Hydrolyze oxacillin and other β-lactam antibiotics, including carbapenems	Oxacillin, carbapenems	Oxacillinase-48 is a growing concern because it confers resistance to carbapenems	[77, 80]
Aminoglycoside-modifying Enzymes	Acetyltransferases, phosphotransferases, nucleotidyltransferases	Chemically modify aminoglycosides by adding acetyl, phosphate, or nucleotide groups, preventing binding to the ribosome	Kanamycin, neomycin, tobramycin	Aminoglycoside-modifying enzymes inhibit their function in protein synthesis by altering ribosomal binding	[81-84]

Resistance Mechanism	Enzymes Involved	Function/Mechanism of Action	Antibiotics Affected	Key Points	References
	Acetyltransferases	Transfer acetyl groups to aminoglycosides, reducing antibiotic binding efficiency	Kanamycin, tobramycin	Modifies the 2-deoxystreptamine nucleus or sugar groups	[82, 83]
	Phosphotransferases	Phosphorylate aminoglycosides, disrupting their interaction with ribosomes	Neomycin, kanamycin	Alter the charge distribution, hindering binding to ribosomal targets	[82]
	Nucleotidyltransferases	Add nucleotide groups to aminoglycosides, reducing their efficacy	Tobramycin, neomycin	Modify hydroxyl groups on aminoglycosides, reducing their antimicrobial activity	[82, 84]

1.4.3. Efflux Systems and Outer Membrane Dynamics

In addition to enzymatic inactivation or modulation of antibiotics, efflux pumps and porins represent another major mechanism of antibiotic resistance in Gram-negative bacteria [4]. Multidrug-resistant Gram-negative bacteria employ mechanisms to limit antibiotic influx by altering the OM permeability and increasing efflux. Efflux pumps, located in both the IM and OM of Gram-negative bacteria, play a vital role in antibiotic resistance by expelling antibiotics and other toxins from the cell, reducing intracellular antibiotic levels and enabling bacterial survival under high antibiotic concentrations (Figure 1-3 B) [82].

These pumps belong to six families — (1) small multidrug resistance, (2) the major facilitator superfamily, (3) resistance–nodulation–division (RND), (4) the adenosine triphosphate (ATP)-binding cassette, (5) multidrug and toxic compound extrusion, and (6) proteobacterial antimicrobial compound efflux family — capable of effluxing diverse antibiotic classes and are widespread across bacterial species, contributing significantly to antibiotic resistance [84]. They operate using ATP or the proton motive force (PMF) as energy sources, with the RND family predominating in Gram-negative bacteria and playing a crucial role in resistance to antibiotics like tetracyclines, fluoroquinolones, aminoglycosides, and penicillins [85]. For instance, the AcrAB-TolC efflux system in *Enterobacteriaceae* exemplifies this mechanism, expelling various antibiotics, including β-lactams, fluoroquinolones, and tetracyclines, thus reducing intracellular drug concentrations [86]. These pumps are encoded by multidrug efflux pump genes (e.g., acrAB, mexAB-oprM, adeABC), whose expression is often upregulated in response to antibiotic exposure or environmental stressors [87]. For instance, efflux pumps such as MexAB-OprM and MexEF-OprN, play a significant role in antibiotic resistance development in *P. aeruginosa* [88]. The β-barrel assembly machinery complex, a crucial multiprotein system in Gram-negative bacteria, facilitates the insertion of porins (Figure 1-2 B) into the OM. Regulator proteins like CpxR and OmpR, along with small noncoding RNAs such as micF, micA, and micC, modulate porin gene expression in response to environmental stimuli. Two-component signaling systems, such as EnvZ-OmpR, detect changes in osmolarity and the presence of antimicrobial drugs, triggering OM remodeling [89]. For instance, Lipid A undergoes structural changes such as acylation,

deacylation, and the addition of positively charged groups like 4-amino-4-deoxy-L-arabinose [90]. These modifications increase membrane rigidity, reduce permeability to hydrophobic antibiotics, and neutralize the negative charge of the membrane [90], thereby decreasing the binding efficiency of cationic compounds such as antimicrobial peptides (see later). Enzymes like PagP, LpxR, and LpxT are involved in this remodeling process [90], which ultimately strengthens bacterial defense against antibiotic penetration and is crucial for bacterial survival and resistance.

1.4.4. Modifications of Drug Target Sites

Modifications of antibiotic targets in Gram-negative bacteria play a crucial role in the development of multidrug resistance. One such example is the alteration of Lipid A, a component of LPS located in OM of these bacteria. Lipid A-modifying enzymes facilitate modifications such as addition of positively charged groups like N-Ara4N and phosphoethanolamine, along with acylation, deacylation of fatty acyl chains, and hydroxylation [91, 92]. Consequently, antibiotics such as polymyxins, which rely on electrostatic interactions to disrupt bacterial membranes, become less effective. This adaptation enables Gram-negative pathogens to evade antimicrobial mechanisms and survive antibiotic treatment, contributing to their increased viability [93]. Another example of target modification is 16S ribosomal RNA (rRNA) methylation, observed particularly in Gram-negative pathogens like *Acinetobacter baumannii* and *P. aeruginosa* [94]. This mechanism, mediated by enzymes such as RmtB and RmtA, confers resistance specifically to aminoglycoside antibiotics which inhibit bacterial protein synthesis by binding to the bacterial ribosome [95]. These enzymes, often encoded on mobile genetic elements like transposons within transferable plasmids, facilitate rapid dissemination through horizontal gene transfer. This process significantly contributes to the spread of multidrug-resistant strains by co-localizing with other resistance determinants, such as ESBLs and MBLs, further complicating treatment strategies against multi drug-resistant (MDR) Gram-negative pathogens.

Therefore, the multifaceted nature of antibiotic resistance in Gram-negative bacteria underscores the urgent need for coordinated efforts to restore the effectiveness of

existing antibiotics through the development of novel antimicrobial strategies as well as to discover new antibiotic classes, targeting of bacterial resistance mechanisms, and optimizing combination therapies while developing new therapeutic agents.

1.5. Innovative Approaches to Combat Antimicrobial Resistance

The escalating global crisis of antibiotic resistance demands urgent exploration of novel therapeutic approaches beyond conventional antibiotics, given that current treatments are increasingly compromised by bacterial resistance mechanisms, as highlighted in recent studies and reviews [18, 36, 65, 82, 84, 94, 96-98].

Antimicrobial peptides (AMPs) are a promising tool in combating antimicrobial resistance due to their broad-spectrum activity and rapid bactericidal effects. Found naturally in various organisms, these peptides or small proteins (10-100 amino acids) interact with microbial membranes, leading to cell death. AMPs have a low propensity for resistance development and are effective against multidrug-resistant pathogens like *P. aeruginosa* [99-101]. Their mechanisms include membrane disruption, inhibition of intracellular processes, and strong anti-biofilm activity, making them particularly useful in chronic infections where biofilms form and conventional antibiotics struggle to penetrate [102-104]. AMPs also show potential when used in combination with traditional antibiotics, enhancing drug efficacy and delaying resistance development [105, 106].

Alternative antimicrobial strategies offer promising avenues beyond traditional antibiotics to combat resistant infections. Phage therapy utilizes bacteriophages to target specific pathogens [107-109], while fecal microbiota transplantation restores microbiome balance, particularly effective in *C. difficile* infections [110]. Quorum sensing inhibitors disrupt bacterial communication, reducing virulence without exerting selective pressure [111]. AI-driven drug discovery has expedited the development of novel antibiotics, such as teixobactin and halicin [112, 113], that target resistant pathogens such as *S. aureus* and MDR Gram-negative bacteria. Advanced gene-editing tools like CRISPR-Cas and RNA silencing techniques offer precise genetic disruption in bacteria [114-118], highlighting a shift towards targeted approaches despite regulatory and translational challenges that slow clinical application [119].

1.5.1. Multidrug Approaches Against Antimicrobial Resistant Infections

Combination therapy, involving the simultaneous use of multiple anti-infective agents and conventional antibiotics, has emerged as a promising strategy to combat antimicrobial resistance [120]. It leverages synergistic interactions between anti-infectives with different mechanisms of action to enhance bacterial growth inhibition efficacy and mitigate resistance development [121, 122]. Research has shown that combining anti-infective agents can lead to synergistic effects, where the combined effect is greater than the sum of individual effects, making it a promising strategy in the fight against resistance [123]. This approach utilizes the complementary modes of action of individual anti-infectives, targeting combinations of essential bacterial processes such as cell wall synthesis, protein synthesis inhibition, or nucleic acid metabolism [110, 124]. As a prime example, established tuberculosis treatment employs a multidrug regimen including isoniazid, rifampicin, ethambutol, and pyrazinamide, each targeting different metabolic pathways essential for *Mycobacterium tuberculosis* survival [125]. While this combination involves conventional antibiotics, it demonstrates the principle of synergy that is also being explored with novel anti-infective agents in combination with older drugs, as seen in treatments against multidrug-resistant pathogens [125].

The rationale behind combinational therapy lies in its ability to mitigate the emergence of resistance by minimizing the likelihood of bacteria acquiring mutations that confer simultaneous resistance to multiple anti-infectives [124]. At a chemical level, synergistic interactions are mediated through cooperative molecular actions, leading to enhanced bactericidal activity compared to single-agent therapy [124]. This pharmacodynamic synergy enhances the efficacy of treatment regimens, thereby improving clinical outcomes and providing a robust strategy to combat antimicrobial resistance. A key focus of current research is the particular use of novel AMPs in combination with conventional antibiotics. AMPs, which disrupt bacterial membranes, offer a mechanism that complements the actions of many traditional antibiotics. Studies have shown that AMP-antibiotic combinations can result in synergistic effects against multidrug-resistant pathogens. These combinations will be explored in detail in later sections (see section 1.5.2.3).

Beyond AMPs, another innovative approach involves combining polymyxins (a class of lipopeptides) with conventional antibiotics. For example, colistin combined with carbapenems has been shown to be effective against carbapenem-resistant *K. pneumoniae*. Polymyxins disrupt the bacterial outer membrane, allowing carbapenems to inhibit cell wall synthesis more effectively. This combination has proven particularly valuable in clinical settings where carbapenem-resistant *K. pneumoniae* infections pose a significant challenge [126]. Furthermore, combination therapy addresses the challenge of toxicity and antagonism by balancing pharmacokinetic and pharmacodynamic interactions [127]. Pharmacodynamic interactions can be synergistic, enhancing drug effects against pathogens, or antagonistic, potentially reducing bactericidal activity [128]. For instance, the combination of β-lactam antibiotics with aminoglycosides exemplifies this principle. β-lactams, which inhibit cell wall synthesis, facilitate the increased intracellular uptake of aminoglycosides, which in turn inhibit protein synthesis by binding to the 30S ribosomal unit. This potentiated effect has been clinically validated, particularly in treating severe Gram-negative bacterial infections, yielding superior bactericidal activity compared to the monotherapy [129]. Another successful example of combination therapy is the use of vancomycin with rifampicin for MRSA infections. Vancomycin disrupts cell wall synthesis, while rifampicin inhibits RNA polymerase, together producing a robust antibacterial effect that effectively clears infections refractory to monotherapy [130]. In addition to this, the combination of antibiotics with natural antimicrobial products or plant extracts is another area of active research. Evidence suggests that such combinations can lead to synergistic interactions that enhance the antimicrobial effects of conventional antibiotics. For instance, Cheesman *et al.* highlighted the potential of synergistic combinations of plant extracts with antibiotics as a viable strategy to combat antibiotic resistance [131]

1.5.2. Key Players in Combating Pathogens: Antimicrobial Peptides

AMPs are valuable in combating AMR due to their broad-spectrum activity, low propensity for resistance development, and rapid bactericidal effects against bacteria, as well as fungi, and even some viral species [100]. AMPs are a diverse group of molecules found in various organisms, ranging from bacteria to humans, that play a

crucial role in defense against pathogens. These peptides exhibit potent antibacterial properties and are characterized by specific physiochemical features. AMPs typically have a net positive charge ranging from +2 to +9 [99]. They often possess cationic (implied by having a positive net charge) and/or amphipathic characteristics, allowing them to interact with microbial membranes [99]. These peptides represent a promising class of antimicrobial agents, particularly effective against multidrug-resistant pathogens like *P. aeruginosa* [101] and have shown the ability to enhance antibiotic activity against resistant bacteria and slow down the evolution of resistance, making them a potential solution to AMR challenges [132].

AMPs are classified into five distinct families based on their secondary structural components. The first family, linear α-helix peptides, consists of peptides with a predominantly α-helical structure characterized by helix-stabilizing residues such as alanine, leucine, and lysine, with a prominent example being Magainin-2 derived from *Xenopus laevis,* a species of African clawed frog [133, 134]. The second family, β-sheet peptides, comprises peptides with at least one pair of β-strands stabilized by disulfide bonds [135], exemplified by bovine lactoferrin and human defensins [136]. The third family includes peptides with both α-helix and β-sheet structures, which are found in various organisms, including humans and plants, and are often stabilized by multiple disulfide bonds [137]. The fourth family, peptides without α-helix or β-sheet structures, features extended linear structures typically enriched with glycine, proline, tryptophan, or histidine [138]. The fifth family, topologically complex AMPs, encompasses peptides with cyclic or complex topologies, stabilized by disulfide bonds or thioether bridges [139]. The classification of AMPs into distinct structural families is crucial as it facilitates the understanding of their diverse mechanisms of action and activity profiles [102, 140]. Each structural class, whether linear α-helix, β-sheet, mixed α-helix/β-sheet, non-helical/β-sheet or topologically complex, correlates with specific modes of microbial membrane disruption, immune modulation, and intracellular targeting.

1.5.2.1. The Multifaced Mechanism of Action of Antimicrobial Peptides

As mentioned above AMPs primarily function by disrupting bacterial cell membranes, the exact mechanism of which can be classified according to the barrel-stave, carpet,

aggregate channel, and toroidal pore models as shown in Figure 1-4 [141]. In the barrel-stave model, peptides enter the hydrophobic core region of the bacterial cell membrane arranging themselves into a barrel-like structure which is perpendicular to the bacterial cell membrane surface [142], thereby disrupting membrane integrity. Alternatively, in the carpet model, peptides cover the membrane surface, causing membrane disintegration without pore formation [104]. Moreover, in the aggregate channel model, AMPs can interact with outer membrane LPS or peptidoglycans, forming micellar complexes that disrupt the membrane structural components. These complexes can compete with divalent metal ions, such as Mg^{2+} and Ca^{2+}, which are essential for maintaining membrane integrity, leading to the aggregation of surrounding bacterial cells. This aggregation prevents the release of endotoxins and disrupts the organization of macromolecules on the membrane surface, further compromising bacterial defenses [143]. In the toroidal pore model, after binding to the membrane, the peptides insert themselves into the lipid bilayer, but unlike the barrel-stave model, the lipids themselves bend inward along with the peptides to form continuous pores [144]. The toroidal process integrates the lipid head groups within the pore, which contrasts with the barrel-stave model, where only the peptides line the pore without involving lipids. The toroidal pore disrupts the membrane's hydrophobic center, leading to the leakage of intracellular contents and cell death, and differs from the barrel-stave model by involving the lipid molecules in pore formation, creating a more dynamic and less rigid structure.

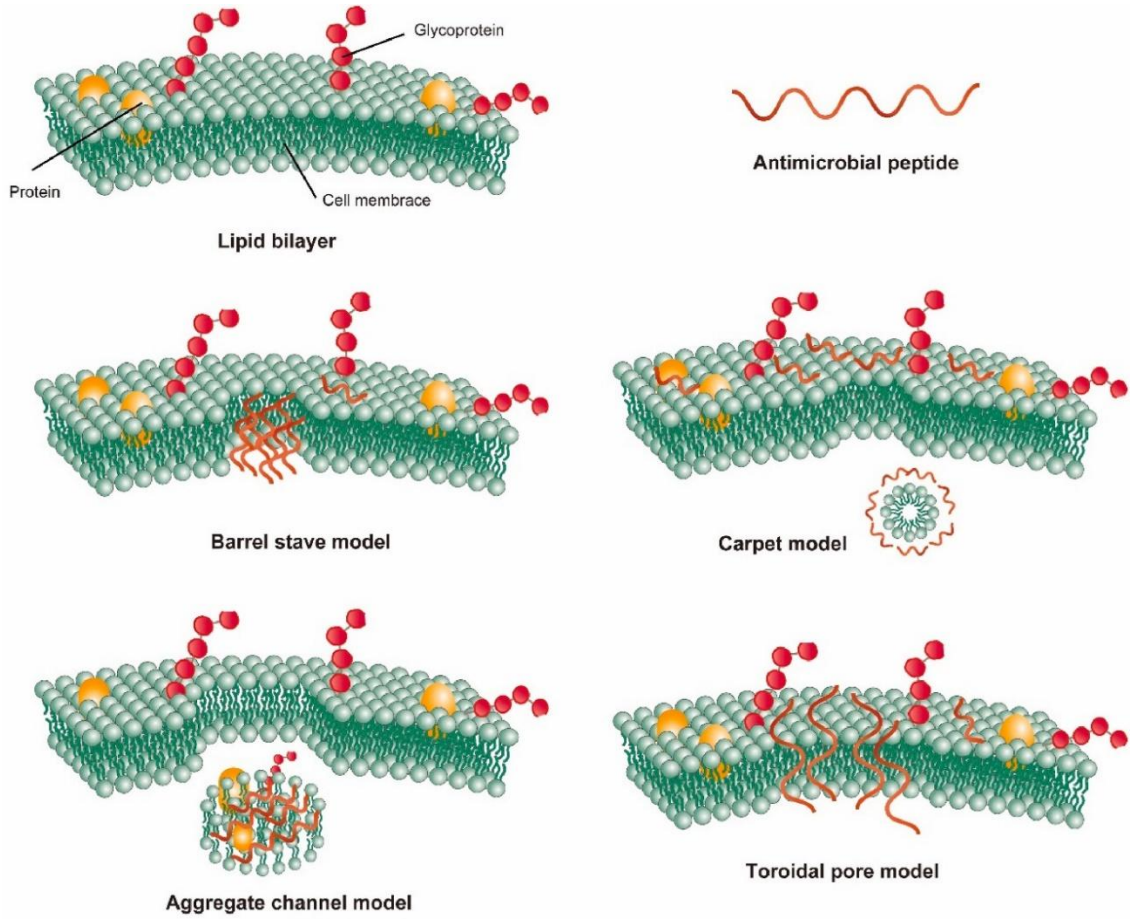

Figure 1-4: Different models of antimicrobial peptides membrane disturbance [103]. Image reproduced with permission of the rights holder, Elsevier.

Beyond membrane disruption, AMPs can target bacterial cell walls by inhibiting the synthesis of critical components like lipid II, a precursor in peptidoglycan formation. For example, gallidermin and the lipopeptide Tridecaptin A1 bind to lipid II, which compromises the structural integrity of the cell wall, leading to increased permeability and vulnerability to osmotic stress by affecting the PMF and cellular metabolism [103]. Some AMPs like magainin peptides also directly interact with peptidoglycan chains or outer membrane components in Gram-negative bacteria [145], altering the cell envelope structure and function.

Moreover, AMPs can penetrate bacterial cells and interfere with intracellular processes. They can inhibit the synthesis of DNA, RNA, and proteins, crucial for bacterial replication and function [146]. Buforin II, Bac5 and Bac7, for instance, penetrate the bacterial cell membrane and bind to or inhibit DNA and RNA synthesis leading to metabolic

imbalances and physiological dysfunction within the cell [147, 148]. Furthermore, upon entering bacterial cells, some AMPs may directly bind to enzymes to block electron transfer and inhibit ATP production, leading to the accumulation of toxic molecules and eventually bacterial cell death [149]. AMPs are also capable of exhibiting anti-biofilm activity by preventing bacterial adhesion to surfaces, interfering with biofilm formation signalling molecules, and degrading the extracellular matrix [150]. LL-37 inhibits *P. aeruginosa* biofilm formation by downregulating genes involved in biofilm formation [151] and by decreasing bacterial surface adhesion [152].

1.5.2.2. Clinical Progress of AMPs

Peptides with potent antimicrobial properties have garnered significant attention as therapeutic strategies against bacterial infections, with several already successfully making their way to the market. Bacitracin, a cyclic polypeptide derived from *Bacillus subtilis*, targets Gram-positive bacteria, notably Staphylococci and Streptococci, and is approved for treatment of topical infections [153]. Polymyxins (colistin and polymyxin B) exhibit efficacy against Gram-negative bacteria particularly against multidrug-resistant strains such as *P. aeruginosa* and *A. baumannii*. They are primarily used as a last-line treatment for severe infections like pneumonia, bloodstream infections, and urinary tract infections due to the historical concerns over nephrotoxicity [154]. Similarly, vancomycin, a glycopeptide, remains pivotal against MRSA since its approval in 1958. Its derivatives - dalbavancin, oritavancin, and telavancin - also offer enhanced potency against vancomycin-resistant bacteria [155]. Daptomycin, a lipopeptide effective against Gram-positive organisms, was approved by the Food and Drug Administration (FDA) in 2003, focusing on *Staphylococcus* and *Enterococcus* infections [156]. Gramicidin, though limited to topical use due to toxicity concerns, remains valuable against Gram-positive bacteria and fungi [155]. Given the success and ongoing expansion of marketed AMPs in combating bacterial infections, researchers are now focusing on developing novel AMPs with enhanced efficacy and reduced toxicity profiles to address the inherent challenges associated with the clinical translation of AMPs. These challenges often arise from issues such as limited bioavailability, proteolytic degradation, and unintended cytotoxicity toward host cells, all of which can hinder their therapeutic potential.

Table 1-3: AMPs undergoing clinical trials for various infections - a summary of selected AMPs that are currently in different stages of clinical trials, detailing their source, targeted medical conditions and clinical trial phase.

Peptide Name	Source	Target Bacteria	Clinical/Experimental Use	Reference
Murepavadin (POL7080)	Peptidomimetic derived from protegrin 1	Gram-negative (*P. aeruginosa*)	Phase I/II clinical trial for cystic fibrosis infections	[157, 158]
Pexiganan (MSI-78)	Analog of magainin from *Xenopus laevis*	Gram-positive and Gram-negative bacteria	Topical treatment for diabetic foot ulcers (Phase III)	[158, 159]
Omiganan (MBI-226)	Synthetic analog of indolicidin	Gram-positive and Gram-negative (and fungi)	Topical treatment for catheter infections and acne (Phase III)	[158, 160]
LTX-109	Synthetic antimicrobial peptidomimetic	Gram-positive skin infections (S. *aureus*)	Nasal colonization by *S. aureus*, impetigo (Phase II)	[160]
Iseganan (IB-367)	Derived from protegrin 1 (porcine)	Gram-negative and Gram-positive (and fungi)	Oral mucositis prevention in cancer patients (Phase III)	[160, 161]
Brilacidin	Synthetic defensin mimetic	Oral infections, skin infections caused by sensitive and resistant *S. aureus*	Treatment of serious skin infections, oral mucositis (Phase II)	[159]
C16G2	Synthetic peptide	*Streptococcus mutans*	Prevention of dental caries (Phase II)	[159]
LL-37	Human cathelicidin	Gram-negative	Broad-spectrum activity, wound healing (Phase I/II)	[161]
Tachyplesin III	Derived from horseshoe crab hemocytes	*P. aeruginosa*, *A. baumannii*	Gram-negative lung infections, sepsis (Phase I/II)	[160]

Next-generation AMPs, such as omiganan and pexiganan, are being developed to improve bioavailability, resist proteolytic degradation, and reduce cytotoxicity, offering potential solutions to emerging antimicrobial resistance challenges [157-159, 162].

Several AMPs currently in clinical trials demonstrate efficacy against a broad spectrum of pathogens (Table 1-3). For instance, murepavadin (POL7080), a peptidomimetic AMP has shown potent activity against *P. aeruginosa*, including MDR strains; although, its systemic administration has led to renal toxicity issues, limiting its use [157]. However, a formulation for inhalation remains under investigation in Phase 1 clinical trials, highlighting its potential for cystic fibrosis patients [157]. Similarly, pexiganan, an analog of magainin, has progressed through phase 3 trials for treating diabetic foot ulcers infected with Gram-negative and Gram-positive bacteria [159, 160, 162]. However, concerns over hemolytic toxicity at higher concentrations remain a challenge [163]. Other AMPs, such as omiganan and LL-37, have demonstrated topical efficacy in clinical settings for infections and wound healing, though further investigation is needed to refine their safety and efficacy profiles [164]. Moreover, the advent of synthetic and bioengineered AMPs offers promise in overcoming specific challenges posed by resistant pathogens. For instance, IB-367, a synthetic analog of protegrin, has exhibited synergistic effects with conventional antibiotics like polymixins and imipenem against *P. aeruginosa* and *Escherchia coli* in dermal wound models [161].

Despite their therapeutic potential, challenges such as hemolytic toxicity, inadequate pharmacokinetic profiles, and high development costs have hindered the clinical progression of many AMPs. Strategies to enhance AMP stability, optimize delivery mechanisms, and mitigate adverse effects are essential to harness their full therapeutic potential [165]. Furthermore, ongoing research into AMP combinations with conventional antibiotics aims to potentiate their efficacy and broaden their spectrum against resistant pathogens as discussed in more details in the following section.

1.5.2.3. AMPs Boost Antibiotic Performance

The use of AMPs in combination with traditional antibiotics has emerged as a promising approach to treat drug-resistant infections. The distinct mechanism of action from that of conventional antibiotics forms the basis for their potential synergy, offering new avenues to combat resistant pathogens. This combination can lead to a variety of beneficial outcomes, such as enhanced bactericidal effects, reduced therapeutic doses, and shortened treatment durations [106]. One of the primary mechanisms through which AMPs enhance antibiotic efficacy is by altering bacterial membrane permeability as discussed in section 1.5.2.1. This increased permeability facilitates the uptake of antibiotics into bacterial cells, allowing them to reach intracellular targets more effectively (Figure 1-5 A, [166, 167]). Further, it has been shown that some antibiotics promote the binding of AMPs to bacterial membranes (Figure 1-5 B). For instance, gentamicin has been shown to enhance the activity of AMPs, such as LL-37, by promoting increased membrane disruption. Gentamicin works synergistically with LL-37 to increase membrane permeability, allowing both the AMP and antibiotic to act more effectively, particularly against Gram-negative bacteria [166]. Furthermore, AMPs can act as bacterial efflux pump inhibitors, thereby increasing the intracellular concentration and efficacy of antibiotics including macrolides such as azithromycin, clarithromycin, and telithromycin, as well as other antibiotics classes like tetracyclines, rifampcins, and quinolones (Figure 1-5 C [168]). As an example, a D-amino acid-containing AMP, such as the synthetic peptide D-11,was shown to increase intracellular accumulation of azithromycin by inhibiting the activity of efflux pumps, impairing the respiration chain and promoting the production of reactive oxygen species (ROS), ultimately resulting in cell death [168]. In addition to these mechanisms, AMP-antibiotic combinations can induce the formation of hydroxyl radicals, leading to oxidative damage of bacterial DNA, lipids, and proteins (Figure 1-5 D). For example, the combination of arenicin-1 with ampicillin has been shown to induce oxidative stress by depleting NADH [169]; while, by inhibiting the transcription of the vanRS two-component system, SLAP-P1 can restore the activity of vancomycin against resistant bacteria [170].

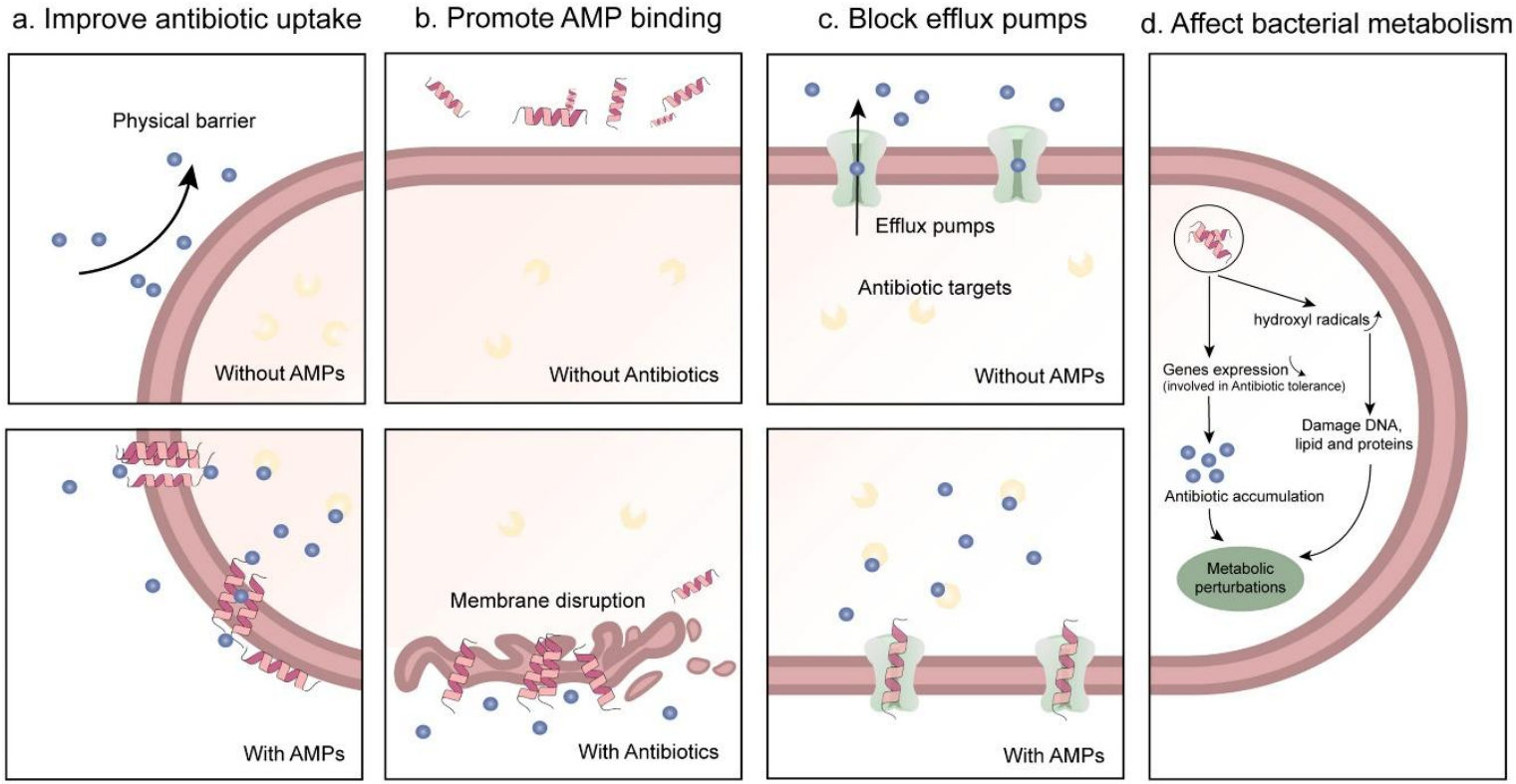

Figure 1-5: Mechanisms of synergy between antibiotics and AMPs. (a) Antibiotic uptake is enhanced by AMPs. The permeability of the bacterial membrane is increased when AMPs interact with it, allowing antibiotics to more easily enter the cell and bind to intracellular targets. (b) The binding of AMPs to bacterial membranes is facilitated by certain antibiotics, which in turn enhances membrane permeability and induces membrane rupture. (c) AMPs obstruct efflux pumps, Leading to an increase intracellular concentration of antibiotics, and an enhanced efficacy. (d) The metabolic activity of bacteria is influenced by AMPs, which in turn can enhance the synergistic activity of antibiotics and AMPs. Reproduced with permission from [171].

However, the potential of AMP-antibiotic combinations goes beyond laboratory studies, showing significant promise in animal models and clinical settings. In murine models of infection, combinations of AMP and conventional antibiotics have shown improved survival rates and enhanced clearance of infections compared to antibiotic monotherapy [172, 173]. For example, the proline-rich AMP A3-APO, when combined with imipenem, improved the survival rates of mice infected with MDR bacteria from 40% to 80%, demonstrating a potent synergistic effect [172]. Similarly, Jindal *et al.* demonstrated that the *in vivo* antibacterial efficacy of RN7-IN8 (derived from indolicidin and ranalexin) was higher when combined with ceftriaxone, with 100% of infected rodents surviving for up to seven days post-infection [173].

One of the critical advantages of AMP-antibiotic synergy is its potential to reduce the development of resistance. By lowering the dosage of individual drugs required for effective treatment, these combinations can diminish the selection pressure for resistant strains. Combining AMPs with antibiotics has been shown to delay bacterial drug resistance, providing a viable option for preventing resistance induction [105]. Furthermore, the multi-targeted action of AMPs, which demands that bacteria undergo multiple changes in their membranes, cell walls, and metabolic processes to resist their effects, reduces the likelihood of bacteria developing resistance to these peptides [174]. Therefore, the synergistic use of AMPs and traditional antibiotics offers a promising strategy to combat drug-resistant infections, providing enhanced therapeutic outcomes, reducing the development of resistance, and ultimately improving treatment outcomes.

1.5.2.4. Toxicity and Stability of AMPs: Impediments to Clinical Utility

The transition from promising laboratory results to clinical applications of AMPs is often impeded by several challenges related to their toxicity, stability, and degradation.

The toxicity of AMPs presents a substantial hurdle for their clinical application because their cationic and amphipathic nature can also disrupt mammalian cell membranes, leading to cytotoxic effects [175]. For example, melittin, derived from bee venom, exhibits potent antimicrobial activity but also causes significant hemolysis and cytotoxicity to human cells [176, 177]. Additionally, systemic administration of AMPs may result in off-target effects and adverse immune responses, including inflammation

and cytokine release [178]. These toxicities necessitate careful modulation of AMP sequences to enhance selectivity for microbial cells while minimizing detrimental impacts on host tissues. Stability is another critical issue limiting the therapeutic potential of AMPs as they are often susceptible to proteolytic degradation by endogenous enzymes, both at the site of infection and within the systemic circulation [179]. For instance, the peptide LL-37, derived from human cathelicidin, has shown rapid degradation in human serum, which significantly reduces its therapeutic efficacy [180]. Proteases present in bodily fluids such as blood and mucus can rapidly degrade AMPs, reducing their bioavailability and efficacy [181]. However, structural modifications, such as cyclization, incorporation of non-natural amino acids, or conjugation with polymers, have been explored to enhance the proteolytic stability of AMPs [182]. For example, the incorporation of D-amino acids has shown increased stability against proteolytic degradation by human and microbial proteinases, which exclusively recognize L-amino acids [175, 183, 184].

Furthermore, terminal modifications, including N-terminal acetylation and C-terminal amidation, enhance AMP stability and bioavailability [185, 186]. Cyclization and stapling techniques, such as the formation of disulfide bridges stabilize AMP structures and improve their pharmacokinetic properties [183, 187, 188]. Cyclic peptides, particularly those stabilized by disulfide bridges, exhibit greater resistance to enzymatic degradation and increased antimicrobial efficacy [183, 187, 188]. For instance, the cyclic AMP ZY4, isolated from *Bungarus fasciatus* snake venom, showed enhanced activity against *P. aeruginosa* and *A. baumannii* [189]. However, despite these advancements, the clinical application of AMPs still faces challenges like optimizing delivery mechanisms, ensuring targeted action, and preventing resistance. Additionally, chemical modifications to improve stability and reduce toxicity can affect key determinants of AMP function like charge and hydrophobicity [190, 191] hence affecting AMP activity. Indeed, the main challenge in AMP delivery is represented by balancing stability and efficacy due to the complex structure-activity relationships of AMPs [192]. Strategies like incorporating AMPs into drug delivery vehicles can address issues of stability and proteolytic degradation [193]. By improving AMP bioavailability, permeation across barriers, and

protection against degradation, nanotechnology can effectively address key limitations of AMPs [194].

1.6. Nanotechnology in Antibiotic Delivery

1.6.1. The Role of Nanotechnology in Transforming Antibiotic Therapy

The term "nanotechnology" has been in use since the mid-1970s, representing a convergence of technologies from diverse fields like physics, materials sciences, electronics, and chemistry, although lacking a precise definition [195]. Kim *et al.* define nanotechnology as the deliberate design, characterization, manufacture, and use of materials, structures, devices, and systems by controlling their size and shape within the nanoscale range (1 to 100 nm) [196]. However, a broader size range up to 1000 nm is also frequently specified in the literature, accommodating a wider array of nanomaterials and systems, including those used in drug delivery applications. This technology led to revolutionary applications across various fields, including medicine, environmental monitoring, and materials science. The unique properties of nanomaterials make them especially suitable for therapeutic and diagnostic applications, fueling the rapid growth of nanomedicine over the past two decades [197]. Nanotechnology-based drug delivery systems (often referred to as nanocarriers), offer promising avenues for drug delivery and improved therapeutic outcomes [198] across various fields, including antibiotic therapy, because such systems can lead to sustained release of therapeutic agents, including antibiotics, as well as enhanced effectiveness *in vivo* by improving bioavailability and targeting specific sites of infection [199]. Additionally, nanotechnology is capable of facilitating the protection and targeted delivery of antibiotics, enhancing their bioavailability and therapeutic effects [200]. Finally, these advanced delivery systems may play a crucial role in protecting and transporting antibiotics to specific targets in the body, ensuring optimal drug penetration and treatment efficacy while minimizing systemic side effects [201].

1.6.1.1. Nanocarriers for Enhanced Solubility and Targeted Antibiotic Delivery

Nanotechnology plays a crucial role in enhancing the solubility of various drugs including antibiotics, through various mechanisms that leverage the unique physicochemical properties of nanocarriers. The encapsulation process alters the surface characteristics of the drug, increasing its apparent solubility in aqueous environments. Nanocarriers enhance drug solubility by forming colloidal structures that encapsulate hydrophobic

drugs within their cores while presenting hydrophilic surfaces to the aqueous environment. This general mechanism applies to various nanocarriers, including micelles and liposomes, improving the apparent solubility of poorly soluble drugs [202]. Indeed, nanocarriers can increase aqueous solubility by providing a hydrophilic outer shell that interfaces with the aqueous environment while protecting the hydrophobic core, where the drug is sequestered. The high surface area to volume ratio of nanocarriers allows for improved drug dispersion, leading to enhanced dissolution rates as per the Noyes-Whitney equation [203]. Moreover, the encapsulation within nanocarriers can also inhibit drug crystallization, maintaining the drug in an amorphous or molecularly dispersed state, which is more soluble than its crystalline counterpart [204].

Furthermore, nanotechnology has revolutionized drug delivery by offering targeted delivery systems that can enhance treatment efficacy while minimizing side effects. Through the use of nanocarriers, therapeutic agents can be precisely delivered to specific sites in the body, allowing for improved drug concentration at the target location and reducing systemic exposure [205]. Strategies for antibiotic targeted delivery have been significantly advanced through nanotechnology-based drug delivery carriers, which have been developed to deliver antibiotics effectively into host cells, enhancing the intracellular antibacterial activity of antibiotics [206]. By utilizing nanocarriers that respond to the infection microenvironment, specific bacterial cells can be targeted, increasing drug concentration at the site of infection and reducing adverse effects on normal tissues [207]. Targeting by microenvironmental excitation leverages the unique microenvironmental changes caused by bacterial colonization such as pH changes and enzymatic activity at the site of infection, to design intelligent drug delivery systems [208, 209]. For instance, pH-sensitive polymers, used for example to fabricate poly(dl-lactide-co-glycolide-b-ethylene glycol-b-dl-lactide-co-glycolide) (PLGA-PLH-PEG) nanoparticles (NPs) [208], and polyelectrolyte multilayer coatings [210], respond to acidic conditions created by bacterial metabolism, enhancing nanocarrier adhesion to bacterial cells and drug release. Enzyme-responsive carriers, such as dextrin-colistin conjugates and phospholipase A2-sensitive liposomes, exploit bacterial secretion of hydrolases and phospholipases to trigger drug release [211]. Additionally, exotoxin-

triggered systems, like chitosan-modified gold NPs [212] and mesoporous silica NPs [213], utilize bacterial toxins to induce nanocarrier structural changes and therefore drug release at the infection site, ensuring targeted and efficient antimicrobial therapy. In addition to custom-made formulations that respond to the bacterial microenvironment, formulations can be tailored to target bacterial cells themselves as well as infected host cells. Various approaches utilize specific bacterial triggers such as carbohydrates, LPS and proteins to design targeted drug delivery systems. For example, molecularly imprinted NPs synthesized using *P. aeruginosa* amphiphilic LPS as a template exhibit high specificity in binding to their target bacterial cells. This is because the NPs are designed with cavities that are precisely shaped to fit the LPS molecules, allowing for strong and selective interactions [214]. Furthermore, formulations utilizing mannosylated nanogels effectively target macrophages via mannose receptors, facilitating the delivery of antimicrobial drugs to intracellular pathogens like *S. aureus* and *M. tuberculosis* [215]. Indeed, microbial enzymes and endolysosomal enzymes can activate the nanogel, thereby causing the drug to be released [216]. These advanced delivery systems not only enhance drug bioavailability and therapeutic efficacy but also minimize off-target effects, underscoring their role in combating drug-resistant bacterial strains and persistent infections.

1.6.1.2. Nanocarriers: Sustained and Controlled Antibiotic Delivery

Nanocarriers play a crucial role in enhancing the efficacy of antibiotic delivery for combating bacterial infections. By regulating drug release kinetics, nanocarriers ensure sustained therapeutic levels necessary to overcome bacterial resistance mechanisms and address persistent infections [217]. Traditional drug delivery methods such as intravenous or oral administration often lead to significant fluctuations in drug concentration, necessitating frequent doses [218]. Unlike conventional non-nanocarrier antibiotics, which often require frequent dosing to achieve therapeutic levels that may fluctuate, some nanocarrier systems may provide a controlled and steady release of antibiotics at the target site. Indeed, nanocarriers maintain therapeutic drug concentrations at the infection site for extended periods, reducing the frequency of dosing and enhancing patient compliance [219]. Moreover, controlled release systems can address the rapid clearance and degradation *in vivo* of antibiotics [220]. For

instance, nanocarriers made from PLGA, can encapsulate antibiotics like ciprofloxacin for sustained and controlled release, improving drug effectiveness [221, 222]. This sustained delivery minimizes the peaks and troughs in drug concentration, thereby lowering the risk of toxicity and side effects associated with high doses while ensuring continuous antibacterial activity [223, 224]. In the quest for effective drug delivery systems, researchers have explored various approaches, including the development of nanostructures, polymer-based systems, and stimuli-responsive carriers to achieve controlled and sustained drug release, optimizing dosage, efficacy, and safety [225, 226] by providing precise control over drug delivery [227]. Additionally, the use of stimuli-responsive nanocarriers further allows for on-demand drug release in response to environmental triggers like pH, temperature, or light, providing precision in drug delivery [228].

1.6.1.3. Challenges and Strategies in Overcoming Biological Barriers

The efficient delivery of therapeutics to bacterial infection sites is substantially impeded by the presence of numerous barriers, which can be broadly classified into three categories: physiological, microenvironmental, and cellular. The altered physicochemical characteristics of biological tissues at the site of infection are the primary physiological barriers [229]. However, the diffusion of NPs is often improved due to their nanoscale size, which facilitates enhanced penetration through tissues, including areas with altered microvascular permeability, which can occur during a bacterial infection, in addition to the disruption of tight junctions between endothelial cells. On the other side, the exacerbation of inflammatory responses results in increased clearance rates, as phagocytic cells, such as macrophages, actively engulf NPs due to their foreign appearance [230, 231].

The microenvironment that surrounds an infection site presents supplementary obstacles. The formation of dense, viscous mucus layers is often a protective response to bacterial infections and can serve as a physical barrier that impedes direct nanocarrier transport, entrapping therapeutic agents and reducing their bioavailability at the infection site [232]. A biofilm matrix, if present, also has the potential to entrap therapeutic agents, thereby decreasing their effective concentration and penetration

within the biofilm itself [233]. Furthermore, cellular uptake presents another layer of complexity in delivering therapeutics to infected tissues. Once nanocarriers reach the target cells at the infection site, various cellular barriers, such as receptor-mediated endocytosis and competition from natural cellular uptake mechanisms, which varies between Gram-positive and Gram-negative bacteria, can reduce the efficiency of therapeutic delivery [234]. The composition and charge of the nanocarriers critically influence their interaction with cell membranes; for instance, certain types of cationic nanocarriers have been shown to selectively target microbial membranes and be readily internalized due to strong electrostatic interactions with negatively charged microbial cell surfaces, leading to inhibition of bacterial growth [235, 236]. However, this effect is not consistently observed across all nanocarrier systems and can vary depending on the specific composition, charge density of the nanocarrier, and the microbial strain involved. Therefore, addressing these multifaceted biological barriers through sophisticated NP design and engineering is crucial for improving the precision and effectiveness of therapeutic delivery to bacterial infection sites, ultimately enhancing patient outcomes.

To overcome cellular uptake barriers when delivering nanocarriers to infected tissues, several strategies can be employed. Engineered interfaces on nanocarriers can enhance their interaction with target cells, addressing the challenges posed by the cellular membrane, which includes a negatively charged phospholipid bilayer and various surface transporters [237]. Additionally, designing drug delivery systems to achieve more efficient drug uptake can involve leveraging the unique properties of smart nanoparticle systems, that facilitate bacterial internalization [238]. In addition to this, optimizing particle characteristics—such as hydrophobicity/hydrophilicity, charge, and mechanical properties such as rigidity or fluidity —can significantly influence cellular adsorption and internal trafficking [239], tailoring them to specific cellular environments. Collectively, these approaches promote better biodistribution and efficacy of nanotherapeutics in the context of targeting bacterial infections.

1.6.2. Overview of Advanced Nanocarrier Strategies for Infection Treatment

Nanocarriers represent advanced strategies for enhancing the treatment of infections through improved drug delivery and therapeutic efficacy as detailed in sections above. Commonly used systems, in this respect, can be categorized into metal-based, inorganic non-metallic, polymeric, lipid-based, lipid-coated, and endogenous nanocarriers, each offering distinct advantages in combating infections.

Metal-based nanocarriers, including iron oxide, gold, and silver NPs, are particularly significant in infection therapy due to their stability and versatile properties [240]. Iron oxide NPs facilitate magnetic targeting and controlled drug release, enhancing therapeutic precision [241]. Gold NPs utilize their photothermal properties for targeted infection treatment, leading to efficient heat generation upon exposure to specific light wavelengths [242]. By utilizing pH-responsive polymers, such as triblock copolymers, gold NPs can form core-shell structures or clusters with tunable properties [243] allowing for controlled responses to changes in pH or temperature. Silver NPs offer broad-spectrum antimicrobial effects [244, 245] and have been found to exhibit synergistic interactions with antibiotics, enhancing their antimicrobial action [246].

Inorganic non-metallic nanocarriers, such as carbon-based and silica-based systems, are renowned for their high stability and drug-loading capacities. For instance, carbon-based nanomaterials like carbon nanotubes composed of graphene possess exceptional antimicrobial activity against various pathogenic strains, making them suitable for tissue engineering, drug delivery, and infection control applications [247]. Similarly, hollow carbon nitride spheres enable high drug loading capacity and possess multiple porous channels and improved surface area, making them suitable for various uses including drug delivery [248]. Graphitic carbon nitride functions as a visible light-responsive photocatalyst and represents a promising research hotspot for antibiotic-free treatment due to exceptional features, such as facile synthesis, high stability, and low toxicity [249]. Silica-based nanocarriers, including mesoporous silica NPs, offer tunable surface chemistry and effective drug delivery. For instance, studies have shown the synergistic antibacterial effects of mesoporous silica NPs loaded with chlorhexidine and silver against both Gram-positive *S. aureus* and Gram-negative *Escherichia coli* [250].

Furthermore, inorganic non-metallic nanocarriers have also been explored for their potential in enhancing the treatment of drug-resistant bacterial infections. By being loaded with various agents like photothermal agents, photosensitizers, sonosensitizers, gas-generating molecules, and glucose oxidase, nanocarriers offer a multifaceted approach to combatting infections [251].

In addition to these, polymeric nanocarriers represent a significant advancement due to their biocompatibility, biodegradability, and ability to encapsulate a wide range of active antimicrobial compounds. These nanocarriers, made from polymers such as PLGA and chitosan (CS), may provide controlled drug release and enhanced stability, allowing for precise delivery of antimicrobial agents at infection sites [252]. Their customizable structures, including nanospheres and nanocapsules, further enable efficient targeting and sustained therapeutic effects and thus represent a viable treatment option for bacterial infections [253, 254], as discussed in more details in 1.6.2.1.

Lipid-based nanocarriers, such as liposomes, solid lipid NPs, and nanostructured lipid carriers, are highly effective due to their biocompatibility and versatile drug loading capabilities [255-259]. Liposomes, with their phospholipid bilayers, enhance drug delivery by mimicking cellular membranes, thus facilitating interaction with target cells. Indeed, liposomes can facilitate the delivery of high concentrations of drug contents into bacteria by fusing with their membranes, enhancing drug uptake and potentially bypassing bacterial defenses such as limited membrane permeability [260]. For instance, it has been demonstrated that liposomes loaded with the photosensitizer temoporfin can significantly enhance drug delivery to both MRSA and *P. aeruginosa*, bypassing bacterial defenses and improving photodynamic inactivation efficiency by releasing high concentrations of the drug directly into the bacterial cells [260]. Additionally, solid-lipid NPs provide stability and controlled drug release and therefore the incorporation of antibiotics into solid-lipid NPs has been explored as a strategy to combat antibiotic resistance and enhance antibacterial efficacy [255, 259]. Similarly, nanostructured lipid carriers combine solid and liquid lipids to encapsulate both hydrophilic and hydrophobic drugs effectively [261] and are therefore a versatile method for delivering antimicrobial agents [257].

By integrating the biocompatibility and drug-loading efficiency of lipid-based nanocarriers with the unique properties of metal-based, inorganic non-metallic, or polymeric NPs, lipid-coated NPs offer a multifaceted approach to infection treatment. These hybrid systems enhance the stability, targeting capabilities, and controlled release properties of encapsulated drugs, thus maximizing therapeutic efficacy. Such lipid-coated nanocarriers, whether incorporating metal NPs such as gold or silver or polymeric NPs like PLGA or CS, offer a range of advantages including improved biocompatibility compared to uncoated metal or polymeric NPs, as the lipid layer enhances interaction with biological systems and reduces immunogenicity. Increased stability is achieved compared to uncoated nanoparticle systems due to the protective lipid shell, which reduces aggregation and premature drug release. Although controlled release and targeted delivery are possible with the individual components, the hybrid system allows for more precise modulation of these characteristics by integrating the structural benefits of NPs with the functional versatility of lipid coatings, improving drug-loading efficiency and therapeutic performance [262]. These hybrid NPs address some limitations seen in traditional nanocarriers, such as poor loading of hydrophilic bioactive compounds and uncontrolled drug release, by combining the advantages of both polymeric and lipid-based nanocarriers [263]. Lipid-coated metal NPs, such as those made from gold or silver, improve biocompatibility and targeting while enabling targeting bacterial infections. By utilizing lipid coatings on PLGA NPs, researchers have achieved improved bacterial biofilm penetration and antibacterial properties, showcasing the potential of this approach in addressing bacterial infections [264, 265]. Moreover, this approach can combine and deliver various therapeutic modalities for more effective treatments and the enhancement of antibacterial activity of antibiotics [266]. Therefore, the use of lipid-coated nanocarriers, whether in the form of lipid-polymer hybrid nanoparticles (LPHNPs), which consist of a polymeric core surrounded by a lipid layer, or lipid-enveloped hybrid NPs, where a lipid bilayer fully encapsulates a core that can be polymeric or made of other materials, presents a promising avenue for drug delivery applications [267].

Endogenous nanocarriers are naturally occurring vesicles derived from biological sources, offering a high degree of biocompatibility and inherent targeting abilities due to their origin. These nanocarriers include extracellular vesicles and cell membrane-derived vesicles, which are increasingly recognized for their role in therapeutic delivery. Extracellular vesicles, including exosomes and microvesicles, are increasingly valued in antibacterial therapy due to their biocompatibility and targeted delivery capabilities. Bacterial extracellular vesicles, for example, have been loaded with gentamicin to target *Burkholderia cepacia* [268], enhancing drug delivery and protection. Similarly, OM vesicles from *K. pneumoniae* showed protective effects in sepsis models by reducing bacterial loads and improving survival [268]. Additionally, exosomes from immune and stem cells play a key role in antibacterial applications [269].

In conclusion, the diverse range of nanocarriers currently employed for infection therapy, including metal-based, inorganic non-metallic, polymeric, lipid-based, lipid-coated, and endogenous nanocarriers, offers innovative solutions for enhancing infection treatment through improved drug delivery and therapeutic efficacy. By utilizing their unique properties, these nanocarriers pave the way for more precise, effective, and targeted infection therapies. The following sections will delve deeper into the particular potential of polymeric NPs, liposomes, and lipid-coated systems, as these nanocarrier categories have demonstrated exceptional promise in infection treatment due to their biocompatibility, versatility in drug loading, and ability to overcome traditional drug delivery limitations. Their unique structural and functional properties make them particularly effective in targeting infections and enhancing therapeutic outcomes.

1.6.2.1. Biodegradable Polymeric NPs

Polymeric NPs are capable of encapsulating or adsorbing active compounds and offer advantages over metallic NPs due to their higher capability of chemical modification, biocompatibility, biodegradability, and potential for drug loading [270]. They are versatile in design, allowing precise control over their architectures and assembly, making them valuable in nanomedicine [270]. The structure of NPs can vary, including nanospheres or nanocapsules (see Figure 1-6) based on their structural design [253].

Nanospheres are solid spherical particles composed of a polymer matrix in which the drug is either dispersed throughout or adsorbed onto the surface, ideal for controlled release and protection of sensitive drugs. In contrast, nanocapsules have a core-shell structure with the drug encapsulated within a liquid or solid core that is surrounded by a thin polymeric shell.

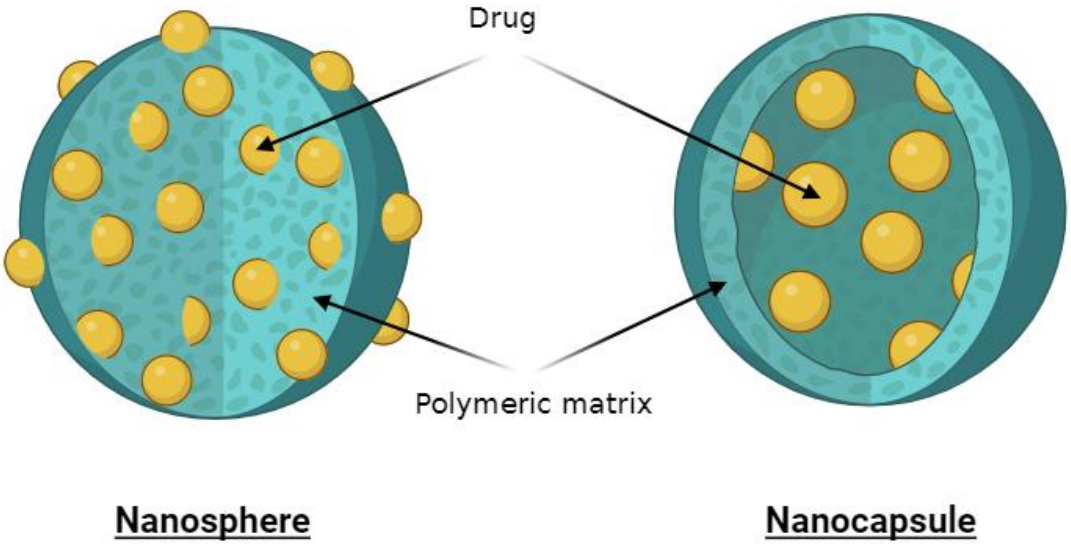

Figure 1-6: Structural comparison of nanospheres and nanocapsules. Nanospheres are uniform spherical particles with a homogeneous material composition throughout, with the drug distributed within the particle matrix. In nanocapsules, the drug is specifically encapsulated within the core, surrounded by a polymeric protective shell, allowing for targeted delivery and enhanced control over drug release. Created with BioRender.com.

Polymeric NPs, particularly those derived from polymers like PLGA, polycaprolactone (PCL), Polylactic acid (PLA) and CS have revolutionized antimicrobial drug delivery. These nanosystems excel in enhancing drug efficacy, increasing local drug concentration, minimizing toxicity, and combating antimicrobial resistance. Using biodegradable and biocompatible polymers is crucial in drug delivery systems because they ensure that NPs are safely broken down and absorbed by the body, minimizing long-term toxicity and reducing the risk of accumulation in tissues [252]. Furthermore, their biocompatibility ensures that the NPs do not provoke immune responses or cause inflammation [271], enhancing patient safety and tolerability. This approach is essential for developing effective and safe antimicrobial treatments, especially for chronic or recurring infections [252]. The practical applications of polymeric NPs in antimicrobial drug delivery are

numerous and varied. Researchers have leveraged the unique properties of these NPs to develop innovative solutions for combating microbial infections. Several recent studies highlight the successful use of polymeric NPs in enhancing antimicrobial efficacy and overcoming drug resistance. For instance, Da Costa *et al*. developed rifampicin-loaded PLA NPs functionalized with poly-L-lysine, demonstrating enhanced antimicrobial activity against both planktonic bacteria and biofilm growth [272]. Similarly, Deepika *et al.* synthesized PEG–PLGA NPs for co-delivery of rutin, a natural compound, and benzamide, showcasing effective antimicrobial properties [273]. Similarly, PCL has been utilized for its sustained release properties, such as in the study conducted by Srisang *et al.*, who prepared chlorhexidine-loaded PCL nanospheres for coating urinary catheters. This approach proved effective in combating common uropathogens responsible for urinary tract infections [274]. Moreover, CS NPs, with their positively charged surfaces capable of interacting with microbial cell membranes, can alter permeability and enhance antimicrobial effects [275]. They have been employed in various studies due to their low toxicity and biodegradability and have demonstrated antimicrobial effects against a wide range of bacteria, including *P. aeruginosa*, MRSA, *E. coli* and various oral microorganisms [254, 276].

NPs employ passive and active targeting strategies for enhanced antimicrobial delivery. Passive targeting exploits the enhanced permeability and retention effect, allowing NPs to accumulate in infection sites through increased vascular permeability [277], with properties like hydrophobicity enhancing interactions with biofilms, such as in *P. aeruginosa* infections [278]. Active targeting, in contrast, involves functionalization with ligands for specific cellular interactions [279], such as the use of *S. aureus*-specific aptamers in teicoplanin-loaded PLGA NPs, enabling precise targeting [280]. Biomolecules like antifolates and AMPs further refine targeting by exploiting microbial metabolism or enhancing uptake [281, 282], with recent AMP-functionalized NPs demonstrating targeted delivery to inflammation sites and bacterial cells in sepsis models [283]. These approaches underscore the potential of NPs to provide localized, receptor-mediated antimicrobial effects.

1.6.2.1.1. Physiochemical Characteristics of NPs

The physicochemical characteristics of NPs, including size, shape, and surface charge, play a pivotal role in their antibacterial efficacy, significantly influencing their interactions with bacterial cells and their subsequent antibacterial effects. Size is a critical determinant; smaller NPs generally exhibit enhanced antibacterial properties due to their increased surface area-to-mass ratio, which promotes more frequent and effective contact with bacterial surfaces [284]. Indeed, Applerot *et al.* showed that when particles dimensions were reduced from the micro to the nanoscale, antibacterial effects improved [285]. This enhanced efficacy was attributed to their ability to generate higher quantities of ROS, which induce oxidative stress within bacterial cells, ultimately leading to cell death [285].

The shape of NPs also significantly affects their antibacterial performance. Spherical NPs are the most common shape, however the bacterial interactions of several different shapes including rods, triangles, cubes, pyramids, and sheets have been investigated [286]. Rod-shaped and wire-shaped NPs, for example, have demonstrated a more efficient bacterial penetration and interaction compared to spherical NPs [287, 288]. This is due to the higher aspect ratio and specific crystal facets of these NPs, which can facilitate more effective binding and entry into bacterial cells [289]. Research has demonstrated that truncated triangular silver nanoplates, with their unique lattice planes, exhibit superior biocidal activity against *E. coli* compared to spherical and rod-shaped silver NPs [289]. Similarly, flower-shaped NPs have shown enhanced antibacterial activity against *S. aureus* compared to their spherical counterparts [290]. Although non-spherical nanoparticle shapes have been shown to enhance bacterial interaction through increased surface area and facet-specific binding, their reproducible formulation presents significant challenges, including control over shape consistency and scaling up the manufacturing process.

Surface charge is another crucial physicochemical parameter influencing nanoparticle-bacterial cell interactions. Positively charged NPs tend to adhere more strongly to the negatively charged bacterial surfaces, leading to membrane destabilization, disruption, and cell wall hydrolysis [291]. This electrostatic attraction enhances the ability of NPs to

breach bacterial cell membranes and alter cellular functions. Indeed, Ivask *et al.* showed that positively charged NPs bound more firmly to bacterial surfaces and cause greater membrane damage compared to their negatively charged counterparts [292]. Additionally, modifications such as the incorporation of hydrophilic and cationic polymers into nanoparticle formulations can further enhance antibacterial efficacy by increasing the charge density and improving bacterial membrane disruption [293].

1.6.2.2. Liposomal Strategies for Anti-Infective Delivery: Prospects and Challenges

Liposomes are spherical vesicles primarily composed of a single or multiple phospholipid bilayers. Unilamellar vesicles are further categorized by size: small, large and giant based on their size ranging from approximately 25 to 100 nm, 100 to 400 nm and >1 μm, respectively [294]. Liposomes are capable of encapsulating both hydrophilic substances in their aqueous core and in the interbilayer spaces in case of multilamellar liposomes, as well as lipophilic/hydrophobic substances within the lipid bilayer (Figure 1-7). These structural features make liposomes highly advantageous for drug delivery applications. For instance, amikacin, a hydrophilic drug, is encapsulated in the aqueous core of Aricayce®, a liposomal formulation composed of dipalmitoylphosphatidylcholine (DPPC) and cholesterol used for the treatment of Mycobacterium avium complex lung disease, while Amphotericin B, a hydrophobic drug, is incorporated into the lipid bilayer of Ambisome®, a liposomal antifungal therapy [295]. Moreover, liposomes can enhance the circulation time and targeted delivery of encapsulated drugs, leading to reduced toxicity and improved therapeutic efficacy. In the case of ciprofloxacin, liposomal encapsulation not only prolongs its presence in the bloodstream but also enhances its accumulation at infection sites, offering superior antibacterial efficacy compared to the free drug [296]. Finally, liposomes can be engineered for targeted delivery by modifying their surface with ligands such as antibodies, peptides or small molecules that bind to specific cell receptors (Figure 1-7), thus improving therapeutic outcomes and minimizing off-target effects [297, 298].

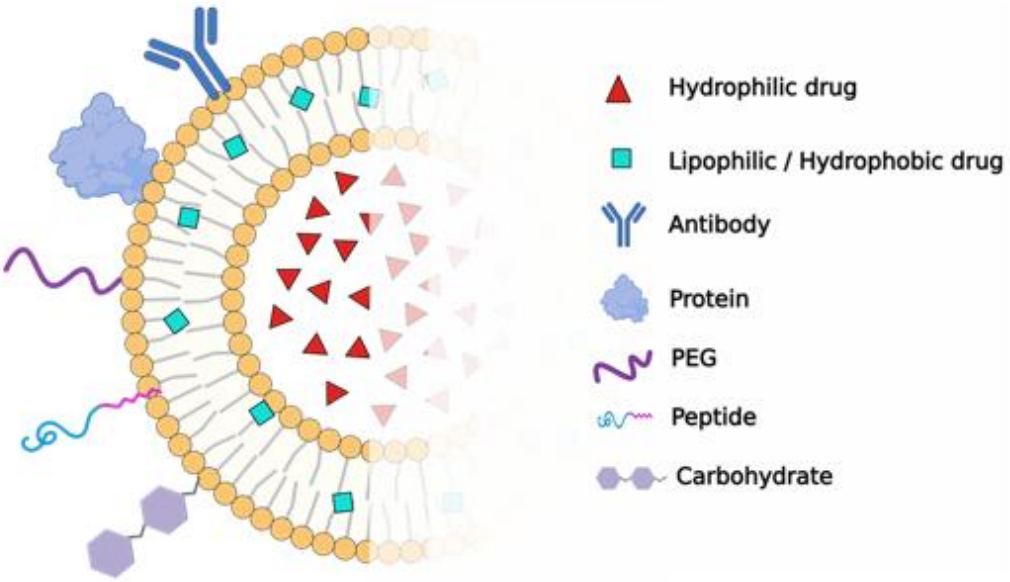

Figure 1-7: Schematic representation of different types of liposomes and their various functions. A traditional liposome is made up of a lipid bilayer with an aqueous core, and the surface can be anionic, cationic, or neutral. Lipophilic/hydrophobic and hydrophilic drugs can be entrapped in the lipid bilayer and the aqueous core, respectively. Liposome properties and behavior can be changed by adding a hydrophilic polymer coating, such as PEG, to the liposome surface. Ligand-targeted liposomes can be made by conjugating various ligands, such as antibodies, peptides, carbohydrates and proteins to the liposome surface, or to the end of the connected PEG chains. Created with BioRender.com.

A particularly innovative application of liposomes is the use of fusogenic liposomes in antimicrobial therapy, which has shown significant promise in combating bacterial infections and addressing antibiotic resistance. These specialized liposomes, capable of fusing with bacterial cell membranes, provide a novel pathway to enhance the antibacterial properties of antibiotics especially against resistant strains. For example, fusogenic liposomes composed of DPPC and dioleoylphosphatidylethanolamine (DOPE) have enhanced the delivery of antibiotics like tobramycin to biofilms formed by mucoid pulmonary *P. aeruginosa* [299]. Additionally, incorporating vancomycin into fusogenic liposomes has broadened its spectrum of action against Gram-negative bacteria and the same effect was not observed when non-fusogenic liposomes or free antibiotic were employed [299]. Furthermore, fusogenic liposomes have been shown to improve the cytosolic delivery to bacteria of compounds including AMPs, by promoting fusion with bacterial cellular membranes and bypassing endocytic pathways [300]. This fusion

capability is primarily attributed to the unique lipid composition of fusogenic liposomes, which typically includes lipids such as the cationic 1,2-dioleoyl-3-trimethylammonium-propane (DOTAP), as well as DOPE [301]. Lipids like DOPE confer a high degree of membrane fluidity and curvature stress, facilitating the merging process [301]. When fusogenic liposomes approach bacterial membranes, the lipid bilayers of the liposomes and bacteria interact, leading to the destabilization of the lipid bilayers at the point of contact driven by electrostatic interactions [302]. The process often involves the formation of hemifusion intermediates, where the outer leaflets of the liposomal and bacterial membranes merge, followed by the complete fusion of both bilayers [302] (Figure 1-8). Through this mechanism, fusogenic liposomes can effectively deliver encapsulated antibiotics or AMPs into bacterial cells, bypassing traditional resistance mechanisms such as efflux pumps and permeability barriers, and thus enhancing the bactericidal efficacy of the therapeutic agents [302].

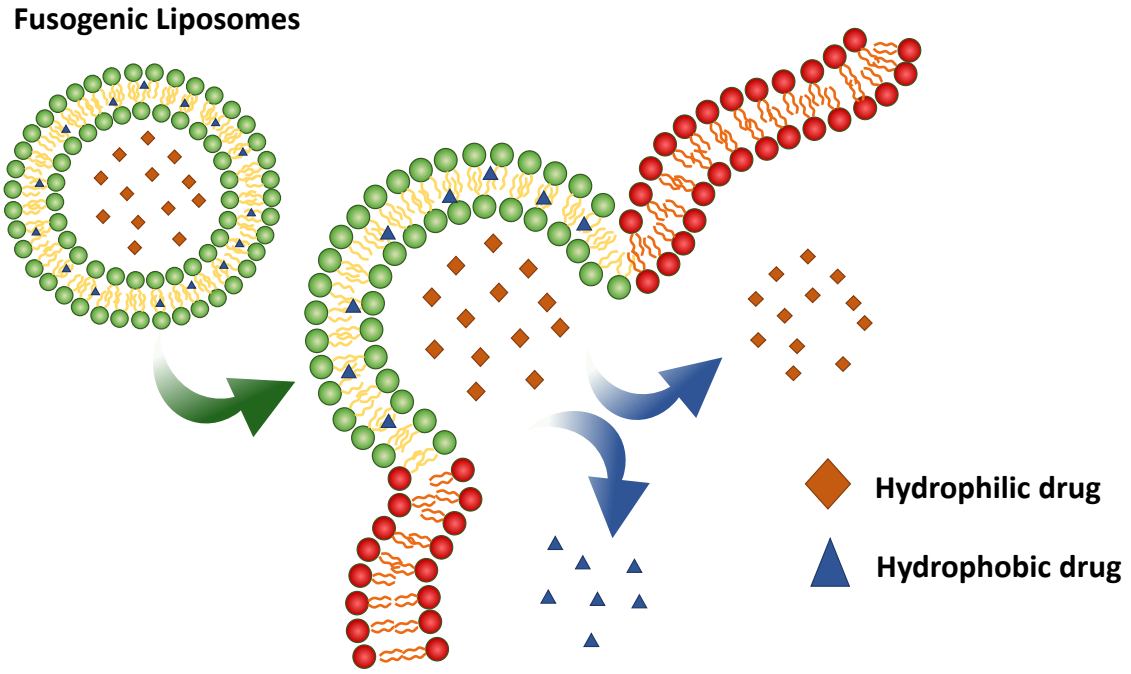

Figure 1-8: Schematic representation of the mode of action of fusogenic liposomes. Fusogenic liposomes merge with encountered membranes through headgroup dehydration, facilitating attachment and membrane fusion. Fusogenic lipids promote lipid mixing and the formation of fusion intermediates, leading to the formation of fusion pore and compartment mixing.

Another option that has shown promise in enhancing therapeutic efficacy is through the use of biomimetic liposomes, which are liposomal systems designed to mimic biological membranes, such as those of bacterial cells, in order to enhance interaction with target bacterial cells. Due to their ability to mimic natural biological systems, biomimetic liposomes may show an enhanced interaction with target cells and an improved antibacterial efficacy [303]. One notable example is the enhanced ability of such systems to adhere to and penetrate bacterial biofilms. In this respect, liposomes engineered to contain LPS or outer membrane proteins like OprF porins of *P. aeruginosa* can effectively interact with bacterial cells and biofilms, improving the delivery of antimicrobial agents [304]. Similarly, Drost *et al*. showed that liposomes mimicking the lipid composition of *S. aureus* and *S. pneumoniae* encapsulating a hydrophobic antibiotic demonstrated superior inhibition of energy-coupling factor transporters and growth against *B. subtilis* compared to the free drug [305]. Additionally, the bacteriomimetic liposomes outperformed phosphatidylcholine-based liposomes in both encapsulation efficiency and antibacterial activity, highlighting the advantages of using a lipid composition that mimics bacterial membranes for drug delivery [305].

Despite these advantages, liposomes face significant limitations to their use, chiefly with respect to their stability. They are prone to physical and chemical instability, leading to aggregation, fusion, and drug leakage. Also, phospholipid oxidation and hydrolysis can occur due to enzymes like phospholipase A2, resulting in the formation of lysophospholipids, impacting the surface charge and Z-Potential of liposomes [306]. Furthermore, high production costs and challenges in large-scale manufacturing further hinder their clinical application [307]. The processes involved in their preparation, purification, and characterization require advanced technologies and stringent quality control, contributing to these high costs. Cationic liposomes pose additional challenges due to their potential cytotoxicity, further increased by the presence of residual organic solvents used during liposomes preparation [307]. Furthermore, rapid clearance by the mononuclear phagocyte system (MPS) reduces the circulation time of liposomes following their systemic administration, necessitating frequent administration [294]; strategies like PEGylation employed to evade this natural defense system [308] can also affect drug release and targeting efficiency. Future research aims to overcome these

limitations through several approaches. The development of stimuli-responsive liposomes that release their payload in response to specific triggers like pH, temperature, or light is promising [309]. These systems enhance stability and target-specific drug release, improving therapeutic efficacy while minimizing off-target effects and reducing the need for frequent administration. Moreover, improving the scalability and cost-effectiveness of liposome production is also a critical focus, with techniques like microfluidics and continuous manufacturing being investigated to streamline the production process and ensure consistent quality [310].

1.6.2.3. Lipid-Coated Nanocarrier Systems in Antimicrobial Therapy

Lipid-coated or lipid-shell systems have advanced the field of antimicrobial therapy, by combining the structural and functional benefits of NPs and liposomes to effectively enhance the delivery and efficacy of therapeutic agents against bacterial infections. These systems typically consist of a nanoparticle core made from biodegradable materials like PLGA, mesoporous silica, or metallic NPs such as gold or silver, encapsulated within a lipid monolayer or bilayer [311]. The lipid component can consist of a single lipid such as DOTAP, or more complex combinations, including phospholipid-cholesterol mixtures, or formulations that mimic bacterial membrane compositions to enhance biocompatibility and reduce immunogenicity [311, 312]. For example, vancomycin-loaded lipid-coated NPs, composed of a PLGA core and DOTAP lipid shell, have shown exceptional efficacy against methicillin-resistant *S. aureus* in comparison to free vancomycin or vancomycin-loaded PLGA NPs, effectively eradicating biofilm cells typically resistant to standard treatments [313]. Furthermore, the core-shell structure of these systems offers several advantages. The nanoparticle core provides a high structural stability and enables the encapsulation of significant amounts of therapeutic agents, while the lipid shell facilitates biocompatibility, prolonged duration of circulation and immune evasion; it may also enable controlled drug release, although this is not always achieved [314]. Moreover, the presence of the core-shell structure provides distinct compartments for dual encapsulation, enabling the separate co-delivery of hydrophilic and hydrophobic/lipophilic drugs [315], thereby facilitating combination therapy where e.g. traditional antibiotics can be readily combined with novel antimicrobial compounds within a single delivery system.

An innovative application of lipid-coated systems involves the use of bacteria-derived lipids. These lipid coatings, derived from various bacterial membrane components, including both the outer and inner membranes of Gram-negative bacteria, offer unique advantages as they enhance target specificity, allowing coated NPs to interact more effectively with bacterial cells and biofilms due to their natural affinity for bacterial membranes [316]. This facilitates the bacterial fusion and subsequent delivery of encapsulated drugs. Moreover, bacteria-derived lipid coatings provide immunomodulatory benefits by mimicking bacterial membrane components, enabling these coatings to prolong circulation time, and enhancing therapeutic delivery to infection sites. For instance, Wu *et al.* carried out a study where rifampicin-loaded mesoporous silica NPs were coated with outer membrane vesicles from *E. coli* to target Gram-negative bacterial infections [316]. The outer membrane vesicle coating significantly enhanced the uptake and antibacterial efficacy of rifampicin against *E. coli* [316]. Additionally, the coated system achieved a complete bacterial eradication, improved survival rates in infected mice, and leveraged the immunogenic properties of outer membrane vesicles for a stronger immune response [316]. Moreover, bacterial outer membrane vesicle-coated NPs allow for the delivery system to efficiently penetrate bacterial cells, as bacteria recognize outer membrane vesicles as homologous structures, facilitating their uptake and interaction. This leads to enhanced antibacterial activity, particularly in cases where nanoparticle penetration is typically challenging [316].

Therefore, lipid-coated and lipid-shell systems offer a multifaceted approach to antimicrobial delivery by combining the stability and high drug-loading capacity of NPs with the biocompatibility and targeting capabilities of liposomes. The use of bacteria-derived lipids enhances targeting specificity toward bacterial cells by mimicking their membranes, improving interaction and immune response.

1.6.3. Nanocarrier Therapies: Translating Research to Market

Nanocarriers have revolutionized the treatment of bacterial infections, with several European Medicines Agency (EMA) -approved and FDA-approved products and ongoing

clinical trials showcasing their effectiveness. Among the FDA-approved products used for anti-infective applications, Arikayce® stands out as a liposomal formulation specifically designed for treating non-tuberculous mycobacterial lung disease caused by *Mycobacterium avium* complex. Arikayce® Kit consists of amikacin encapsulated in relatively small liposomes (~ 300 nm in diameter [317]) composed of phospholipids DPPC and cholesterol [318]. This product utilizes a nebulizer for drug delivery to the lungs, enhancing therapeutic efficacy while minimizing systemic side effects.

Additionally, AmBisome®, a liposomal formulation of Amphotericin B, was approved by the FDA in 1997 due to its lower incidence of nephrotoxicity compared to earlier formulations [319]. AmBisome® consists of amphotericin B intercalated with phospholipids and sterol alpha tocopherol in small unilamellar liposomes, providing a nanocarrier system with enhanced stability and targeted drug delivery. Its liposomal structure improves pharmacokinetics and reduces drug toxicity, making it more effective in treating invasive fungal infections [320]. The design of AmBisome® as a liposomal formulation serves as a model for optimizing nanocarrier systems for antibacterial agents, where targeted delivery and reduced toxicity are critical for therapeutic success [321].

Despite the limited number of marketed nanocarrier-based products for infection treatment, ongoing clinical trials are exploring a diverse range of nanocarrier systems with promising antibacterial applications. For instance, NPs such as silver nanoparticles (AgNP), titanium dioxide (TiO_2), and CS are being tested for their effectiveness against various bacterial strains and infections in clinical settings (Table 1-4). These trials include innovative approaches like integrating AgNPs into dental materials or CS NPs into an antibiotic paste to enhance antibacterial properties. For instance, in clinical trial NCT05079802, CS nanoparticles are hypothesized to exhibit superior antimicrobial activity compared to bulk or non-nanoparticle CS, due to their smaller size and enhanced surface interaction with microbial cells. It is expected that when incorporated into antibiotic pastes, CS NPs may enhance the penetration of the paste into dentin tubules, improving bacterial eradication and offering better biofilm penetration. This is hypothesized to increase the overall efficacy of the antimicrobial treatment in

comparison to other vehicles such as propylene glycol, pending confirmation by the clinical trial results.

Table 1-4: Antibacterial NPs and their applications via clinical trial-based study.

NPs	Bacteria strain/ disease	Intervention	Status	Refs.
AgNP and CS	*E. faecalis*	Bioceramic sealer	Phase 4	NCT04481945
Iron Oxide NPs	Root canal biofilm disinfection	Ferumoxytol/H_2O_2		NCT06110494
TiO_2 and CS	*S. mutans*	–	Phase 3	NCT04365270
AgNP	*Serratia marcescens*	Alcohol-based hand gel		NCT00659204
Nano silver fluoride	*S. mutans*	CS and fluoride		NCT03186261
Nano CS	infections associated with non-vital primary molars with root resorption	Antibiotic paste		NCT05079802
nano calcium hydroxide	Primary endodontic treatment	Hydrogel		NCT06196515
Chlorhexidine Hexametaphosphate NPs	Peri-implantitis prevention	Coated orthodontic miniscrews		NCT06124235

Despite the significant promise nanocarriers hold in enhancing antimicrobial therapies, several challenges impede their successful translation from the lab to the market. Key issues include the lack of consistent site-specific targeting, which, despite advancements in active targeting methods such as ligand-receptor binding, can still lead to reduced bioavailability and effectiveness, especially in complex or resistant infections. While some nanocarriers demonstrate improved targeting capabilities, these effects are often model-dependent and not universally reproducible. Additionally, the difficulty in scaling up production from the lab to commercial levels remains a significant hurdle for the widespread clinical application of these systems [226, 322]. Furthermore, limited knowledge about the interaction of nanocarriers with biofilms and the inherent instability of certain antimicrobial agents, such as β-lactam antibiotics that are susceptible to hydrolysis by bacterial enzymes like β-lactamases, pose additional hurdles [322]. Moreover, the absence of standardized protocols for testing the efficacy of novel antimicrobial nanocarriers remains a critical barrier [323]. Overcoming these challenges is essential to unlock the full potential of nanocarriers in treating bacterial infections and successfully bringing these innovative solutions to the market.

1.6.4. Transforming Nanocarrier Production: The Role of Microfluidic Mixing

Microfluidic technology has emerged as a transformative method for the manufacturing of nanocarriers, offering substantial advantages over traditional techniques (solvent evaporation, nanoprecipitation, emulsification, thin-film hydration) in terms of precision, scalability, and efficiency [324]. This advanced technology not only enhances the control over particle size and composition but also addresses key challenges associated with the translation of nanocarrier products from research to market. By using microfluidic systems, researchers can achieve highly reproducible and scalable production processes [324], which are crucial for meeting regulatory standards and commercial requirements. As a result, microfluidic technology holds significant promise for bridging the gap between laboratory innovations and their practical applications in clinical settings. The core advantage of microfluidic technology lies in its ability to precisely control the formation of nanocarriers. Through the manipulation of fluid flows within micrometer-sized channels, researchers can finely tune parameters such as flow rates and mixing ratios to produce NPs with uniform size distributions and controlled compositions [325]. This level of precision is particularly important for ensuring the consistency and reliability of nanocarriers, which are critical factors for their effectiveness and safety in drug delivery applications. For example, microfluidic devices have enabled the production of liposomes with controlled and reproducible characteristics, which enhances their performance in drug delivery applications and reduces variability compared to conventional methods [326].

Microfluidic manufacturing processes involve the careful design and operation of microchannel systems, which are typically constrained within chip-based structures that provide precise control over fluid flow and mixing, allowing for accurate manipulation of fluids and consistent production of nanocarriers under controlled conditions [327]. Staggered herringbone mixers (SHM) (Figure 1-9), as developed by Stroock *et al.* [328] are among the most common micromixing structures that facilitate efficient and homogeneous mixing by inducing chaotic advection, which is a key mechanism in many microfluidic mixers [328]. While chaotic advection is often utilized to enhance mixing, it is not the sole mechanism in all microfluidic mixers, as other designs may rely on diffusion or laminar flow manipulation to achieve efficient mixing, depending on the

fluid properties and device configuration [329]. Various micromixing strategies exist beyond SHMs, such as serpentine channels [330], T-junctions [331] and toroidal structure [332] designs, offering different advantages depending on the application. The scalability and reproducibility provided by microfluidic systems is enabled by the precise control of flow dynamics, reagent mixing, and nanocarrier formation parameters, allowing for consistent, high-quality production of nanocarriers. These systems can be integrated into parallelized or continuous manufacturing processes, significantly increasing throughput without compromising the reproducibility or uniformity of the nanocarriers. This versatility facilitates the transition of these innovative nanocarrier technologies from the research phase to commercial production, meeting the demands of both regulatory bodies and market needs [327].

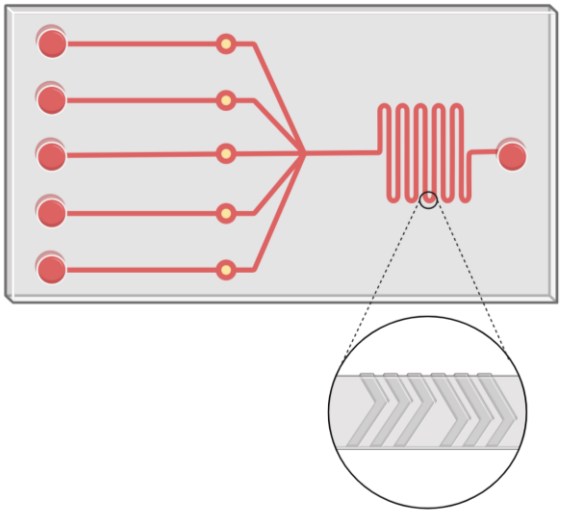

Figure 1-9: Schematic representation of the SHM design, which consists of grooved patterns that induce chaotic advection, disrupting laminar flow. This promotes enhanced mixing and uniform particle distribution, making it suitable for microfluidic applications. Created with BioRender.com.

One notable example of this scalability in action is the NanoAssemblr™ Benchtop platform by Precision Nanosystems (Figure 1-10 A). The microfluidic chip of the NanoAssemblr™ Benchtop (Figure 1-10 B) is Y-shaped, with two inlet ports and micro-channels that converge (Figure 1-10 C). This system has given rise to the NanoAssemblr™ Ignite and a new, related platform range offering even more precise control over particle characteristics, allowing for both clinical and commercial-scale nanoparticle production.

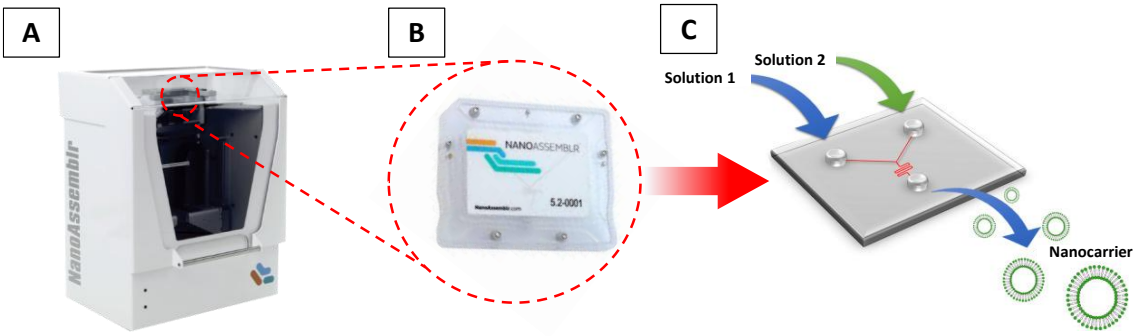

Figure 1-10: (A) Image of the previously commercially available NanoAssemblr™ Benchtop (Precision Nanosystems, Canada) and (B) its cartridge that (C) uses microfluidic channels to enable the self-assembly of components into nanocarriers.

SHM structures remain commonly employed in other microfluidic mixing setups, in which the liquid, typically consisting of precursor solutions for nanocarrier formation, is flowed continuously through micro-channels and forms nanocarriers by the chaotic mixing principle, aided by the presence of the staggered herringbone structures. This process facilitates precise control over nanocarrier size and morphology, highlighting the potential of microfluidic technology to advance the translation of nanomedicine into clinical and market applications [326].

The applications of microfluidic-manufactured nanocarriers extend across various areas of drug delivery and personalized medicine. Microfluidic technology has been successfully employed to produce delivery systems for the encapsulation of a range of therapeutic agents, including oligonucleotides [333], proteins, peptides [334] and small molecules [335], and more recently, lipid nanoparticles (LNPs) used in mRNA vaccines for COVID-19, such as those developed by Pfizer-BioNTech, demonstrating the scalability and versatility of microfluidics in drug delivery applications [336]. For instance, microfluidics has been instrumental in creating CS NPs embedded with essential oils, which enhance antibacterial effects through precise encapsulation and controlled release mechanisms [337]. Similarly, core-shell carriers developed via microfluidic techniques allow for precise fine-tuning of particle size and properties, enabling long-lasting antibacterial performance through controlled release mechanisms, as demonstrated in the work of Chen *et al.* and Feng *et al.* [338, 339]. This fine control over

formulation ensures more effective targeting and prolonged efficacy in antibacterial applications. Another example includes the synthesis of biocompatible sodium alginate-silk fibroin microspheres using microfluidic techniques, which demonstrate potent antibacterial properties and versatility in infected wound repair [340]. Moreover, this advanced technique has facilitated the production of antibacterial silver nanoparticle–CS composites, demonstrating superior efficacy against *E. coli* and *S. aureus* [341]. These examples illustrate the versatility and precision of microfluidic technology in advancing nanocarrier-based antibacterial therapies.

1.7. Nanocarriers and Antimicrobial Testing Challenges

1.7.1. Evaluating the Antimicrobial Activity of Nanocarriers

Assessing antimicrobial activity is crucial for developing effective treatment strategies and combating infectious diseases. Reliable and standardized methods are essential to ensure reproducibility and comparability of results. This standardization is not only important for clinical decision-making but is also a regulatory requirement for the approval of new antimicrobial agents. Regulatory bodies, such as the FDA and EMA, mandate the use of standardized methods to assess antimicrobial efficacy to ensure the validity and reliability of the submitted data. For example, standardized techniques from the Clinical and Laboratory Standards Institute (CLSI) and the European Committee on Antimicrobial Susceptibility Testing (EUCAST) are pivotal in providing consistent data, which facilitates accurate evaluation and comparison across different studies and settings. However, despite their widespread use, both CLSI and EUCAST methods have been found to have limitations and challenges [342]. One key limitation of the CLSI and EUCAST standardized methods is the discrepancy in the minimum inhibitory concentration (MIC) values they produce for various antimicrobial agents, despite the same method being employed [342]. Studies have shown that there can be differences in MIC values when using the CLSI and EUCAST methods [343], with the EUCAST method reported to consistently yield MICs that are 1- to 2-fold higher compared to the CLSI method [344]. Moreover, the absence of established clinical breakpoints (which refer to the specific concentrations of an antimicrobial agent that define whether a particular microorganism is susceptible, intermediate, or resistant to the treatment) can pose challenges in interpreting susceptibility results accurately and standardizing treatment approaches across different settings [345]. Another critical aspect to consider is the impact of methodological differences between CLSI and EUCAST on susceptibility testing outcomes. Variations in inoculum size, incubation conditions, and other technical factors can contribute to differences in MIC values obtained using these methods [346]. These discrepancies underscore the importance of understanding the nuances of each method and considering these factors when interpreting susceptibility results. Furthermore, methodological variations among laboratories might exacerbate these issues. Different laboratories may use varying testing protocols, such as disc diffusion (see below) versus automated systems, leading to differing susceptibility profiles.

Variability in test condition, such as pH, temperature, and inoculum size, can significantly impact the results [347]. For instance, changes in pH can alter the ionization of antimicrobial agents, influencing their effectiveness [348]. Therefore, establishing clear, universally accepted criteria is essential to guide clinical decisions.

Within the next sections of this chapter, various antimicrobial susceptibility testing methodologies utilized for the assessment of nanocarriers will be examined, each of which provides unique insights into drug efficacy. The time-kill assay, well diffusion assay, and broth microdilution assay will be discussed, with emphasis on their respective strengths, limitations, and the critical importance of adhering to standardization guidelines. Furthermore, a comparative analysis will be presented, enabling the selection of the most appropriate method based on specific research requirements.

1.7.2. Diffusion Assays: Strengths and Limitations

Well and disc diffusion assays are fundamental techniques for evaluating the antimicrobial properties of various compounds, as well as of nanocarriers (Figure 1-11, [349, 350]). These assays are particularly useful in assessing the efficacy of nanocarriers against a wide range of microorganisms. Although they are primarily regarded as screening techniques due to their simplicity and ease of use, they can provide semi-quantitative data when measuring the zone of inhibition, which correlates with the antimicrobial activity of the tested compounds [351]. In the disc diffusion assay (Figure 1-11 A), paper discs, impregnated with test compounds, are placed on an agar plate inoculated with the target microorganism. Over time, the active agents diffuse out of the disc, inhibiting bacterial growth if the microorganism is susceptible to the antimicrobial agent in a zone surrounding the disc, with larger zones suggesting greater efficacy [352]. In contrast, the well diffusion assay (Figure 1-11 B) involves creating wells in an agar plate (Figure 1-11 C), into which the test antimicrobial sample is introduced. Similar to the disc diffusion method, the diffusion of the test substance results in a zone of bacterial growth inhibition around the well, reflecting the degree of its antimicrobial activity [353].

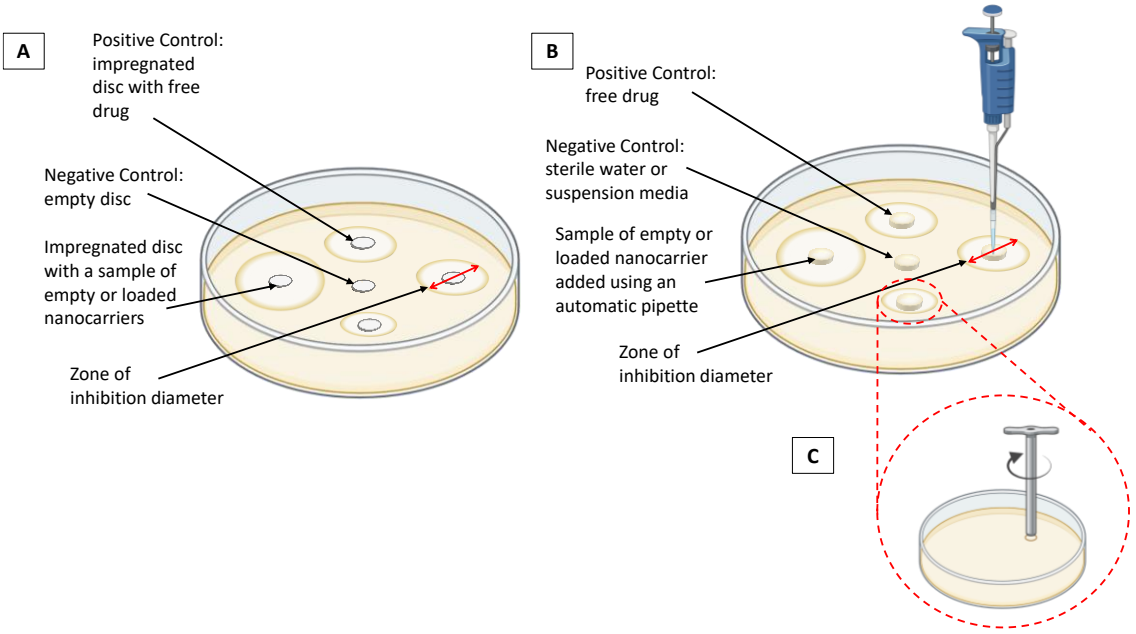

Figure 1-11: Schematic representation of disc diffusion assay (A) and agar well diffusion assay (B). Wells in the agar are created with a cork borer of specific diameter (C). Briefly, in both cases the agar plate is inoculated with the test microorganism. Subsequently, a disc containing an appropriate concentration of the sample is placed on top of the agar (A) or a solution of the sample is pipetted in the agar well (B). After incubation, the plate is examined for the presence of a clear zone of inhibition and the diameter of the zone of inhibition is measured.

One of the primary strengths of well and disc diffusion assays is their simplicity and cost-effectiveness. They do not require sophisticated equipment, making them accessible to a broad range of researchers. Additionally, these assays allow for the rapid screening of multiple samples, enabling comparative studies of different formulations at the same time. This feature is particularly advantageous in the early stages of research when assessing the basic antimicrobial potential of newly synthesized nanocarriers.

However, despite these advantages, the effectiveness of well and disc diffusion assays can be influenced by various factors related to the physical properties of nanocarriers, which may affect the reliability of the results. The physical properties of nanocarriers, such as size, shape, surface charge, concentration, temperature, pH, and the viscosity of the medium significantly influence their diffusion through the agar and, consequently, the size of formed inhibition zones [354]. This variability can lead to inconsistent results, making it difficult to draw definitive conclusions about the antimicrobial efficacy of the

nanocarriers being tested. Additionally, these inconsistencies can complicate direct comparisons between nanocarrier-associated drugs and their free drug counterparts, as the methods may not accurately reflect differences in how the active compounds are delivered or interact with microorganisms in each form. For instance, smaller nanocarriers typically diffuse more readily, potentially leading to larger zones of inhibition. This diffusion effect can be controlled by testing of empty nanocarriers to account for the physicochemical properties of the carrier itself. Additionally, conducting comparative studies where the antimicrobial agent is tested in the absence of the nanocarrier helps isolate its intrinsic activity, providing a clearer understanding of the carrier's influence on the overall efficacy. In addition to this, the interaction between nanocarriers and the agar matrix can sometimes impede diffusion, particularly if the nanocarriers aggregate or adhere to the matrix [355, 356], reducing the reliability of the assay. Indeed, the large size and low diffusivity of nanocarriers compared to small molecule anti-infectives hinder their ability to diffuse uniformly through the utilized agar matrix, which can result in inconsistent or underestimated antibacterial activity [355]. Similarly, certain nanocarriers, particularly those that are hydrophobic or have a high molecular weight, may not diffuse efficiently through the agar medium [354]. This can result in smaller or non-existent inhibition zones, potentially underestimating the antimicrobial activity of the nanocarriers [357].

Therefore, while well and disc diffusion assays are valuable tools for the preliminary screening of antimicrobial activity of nanocarriers, they have limitations that must be carefully considered. These assays provide essential insights but should be complemented with other methods to fully evaluate the efficacy and mechanisms of action of these advanced materials.

1.7.3. Broth Microdilution vs. Resazurin assay

The broth microdilution and resazurin assays are pivotal in evaluating the antimicrobial activity of antimicrobial drugs and nanocarriers. The broth microdilution assay is the gold standard quantitative method used to determine the MIC of antimicrobial drugs or formulations [355]. This assay involves serial dilutions of the test sample within a growth

medium, typically in a 96-well microtiter plate, followed by the inoculation of a standardized microbial suspension (Figure 1-12 A). After incubation, the lowest concentration of the compound/nanocarrier that inhibits visible microbial growth is recorded as the MIC value [355]. Although the broth microdilution assay follows standard protocols and is relatively straightforward, it does have some limitations when used with nanocarriers.

Nanocarrier dispersions often exhibit baseline turbidity, which can complicate the interpretation of results, as it becomes difficult to distinguish between microbial growth and the inherent optical properties of the nanocarriers (Figure 1-13). For instance, turbidity measurements, as an indicator of microbial growth, pose another challenge since nanocarriers can interfere with optical density readings, either through intrinsic optical activity or by causing colloidal instability, particularly when nanocarriers precipitate or aggregate in the medium [355]. This makes it difficult to accurately assess bacterial growth, as nanocarrier-induced changes in turbidity may not correlate with bacterial viability (Figure 1-13). Indeed, determining the MIC and the minimum bactericidal concentration (MBC) is problematic due to the inherent turbidity of the formulation dispersions and their potential instability in culture media (depending on the physicochemical properties of the nanocarriers and the composition of the media). Moreover, nanocarriers may precipitate over time or undergo changes in their surface chemistry due to interactions with the components of the culture medium, such as proteins and counterions, or due to pH fluctuations. These alterations can result in protein corona formation around nanocarriers or shifts in nanocarrier surface charge, leading to inconsistent bacterial exposure and inaccurate measurements of inhibitory or bactericidal concentrations [358].

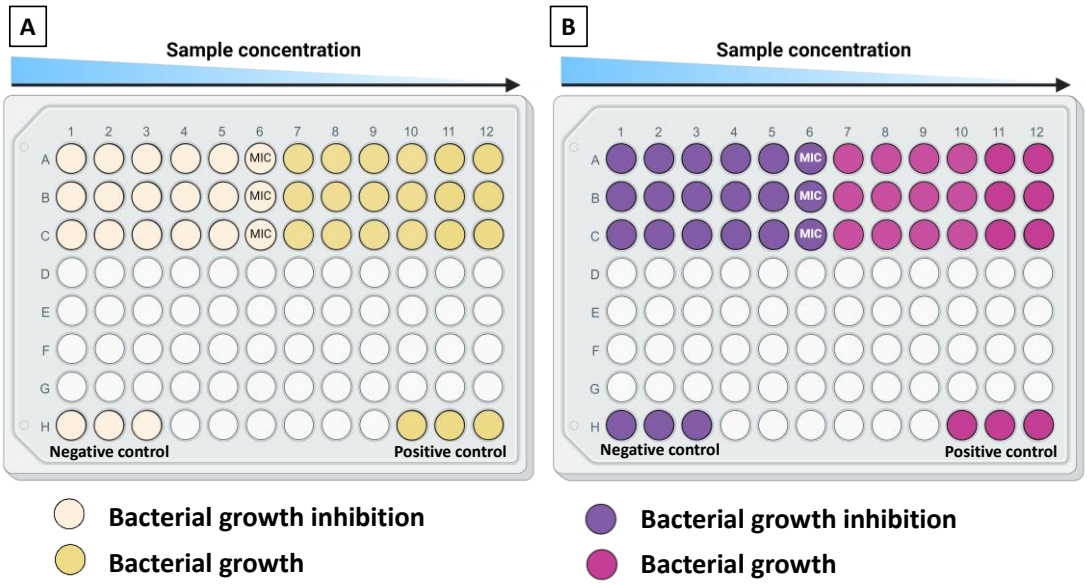

Figure 1-12: Schematic representation of broth microdilution assay (A) and resazurin assay (B) using a 96-well plate. Wells show a gradient of antimicrobial concentration from left (high) to right (low). In the case of the broth microdilution assay, yellow indicates microbial growth, while clear wells indicate inhibition (A). With respect to the resazurin assay, pink indicates viable cells (resazurin reduced to resorufin), while purple indicates non-viable cells (B). The MIC value is determined as the lowest concentration of the test antimicrobial resulting in no growth (A) or purple rather than pink color (B). Created with BioRender.com.

To address some of these challenges, the resazurin assay is often used as an alternative to the traditional broth microdilution assay. Resazurin, a blue non-fluorescent dye, is reduced to pink resorufin by metabolically active cells [359], providing a colorimetric readout of cell viability (Figure 1-12 B). This test gives a clear indication of the presence or absence of viable microorganisms by monitoring metabolic activity and microbial viability [351] - as such it is important to note that this is an assay that measures cell viability, rather than direct inhibition of bacterial growth. This assay offers a more sensitive assessment of microbial viability, making it particularly useful for evaluating the antimicrobial activity of nanocarriers where turbidity of nanocarrier dispersions may interfere with the readout of a traditional broth microdilution assay. However, the resazurin assay also has limitations. It is particularly suited to aerobic or microaerophilic microorganisms due to its dependence on oxygen consumption, which may limit its applicability to anaerobic pathogens [351]. Additionally, certain nanocarriers can interact with resazurin, either by directly reducing the dye or by interfering with the

fluorescence measurement, leading to potential false positives or negatives [360]. Moreover, high bacterial concentrations or extended incubation times may result in over-reduction of resazurin, leading to a masking of any subtle nanocarrier effects – in this case by producing an excess of the reduced resorufin form, which leads to signal saturation and hinders the ability to detect incremental metabolic changes in the presence of nanocarriers, ultimately limiting the accuracy of the antimicrobial efficacy assessment [351]. Therefore, while both the broth microdilution and resazurin assays are valuable tools for assessing the antimicrobial efficacy of nanocarriers, they require careful adaptation and optimization to account for the unique properties of the nanocarriers to be assessed.

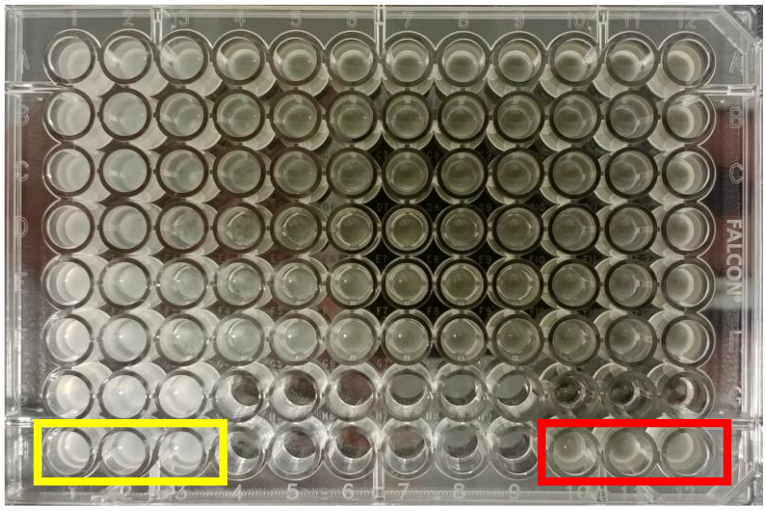

Figure 1-13: Example of formulation turbidity preventing the correct interpretation of broth microdilution assay against E. coli*. Turbid wells highlighted in yellow represent wells containing empty liposomes and broth, while turbid wells highlighted in red represent broth and bacteria inoculum. The turbidity in wells highlighted in yellow is given by the formulation while the turbidity in wells highlighted in red is given by bacterial growth.*

1.7.4. Time Kill Assays

The time kill assay measures the rate at which an antimicrobial agent or formulation causes a reduction in the population of a specific microorganism over time [361] and therefore gives a dynamic picture of how quickly a particular antimicrobial agent/nanocarrier can eliminate or inhibit the growth of pathogens over a specified period. Typically, the test involves incubating the microorganism of interest with the test

drug or formulation at various concentrations, and sampling at set time intervals to determine the number of surviving organisms. This number is then plotted as a function of time to create a time-kill curve. This curve provides insights into the kinetics of microbial killing, including whether the antimicrobial agent exerts a bactericidal (killing) or bacteriostatic (growth-inhibiting) effect [362]. Moreover, the time-kill assay allows researchers to assess the onset of action and the rate of microbial killing of a particular compound/formulation, as well as the potential for bacterial regrowth or resistance development over time [363]. However, the use of the time-kill assay with nanocarriers also comes with certain limitations. One significant challenge is the stability of nanocarriers during the assay. These may agglomerate or change in size, which can alter their antimicrobial activity due to an alteration in release kinetics and interactions with bacterial cells [364]. Indeed, changes in size can influence adhesion, uptake, and internalization by bacteria. Larger aggregates may hinder penetration, while smaller particles can enhance uptake, impacting overall antimicrobial efficacy. Moreover, the time-kill assay, while useful *in vitro*, may still not fully capture the complexity of antimicrobial activity *in vivo*, where factors like immune responses, tissue penetration, and pharmacokinetics play critical roles [351]. The static concentrations of nanocarriers used in the assay may not accurately reflect the dynamic conditions encountered in a living organism, potentially leading to discrepancies between *in vitro* and *in vivo* efficacy [351]. Moreover, time-kill assays can be time-consuming due to the need for continuous monitoring and sampling of bacterial or microbial cultures, over a period which can range from several hours to days. Hence, the time-kill assay is a powerful tool for assessing the antimicrobial activity of nanocarriers, providing valuable information on the kinetics of microbial killing. However, researchers must carefully consider the limitations related to nanoparticle stability, potential assay interference, and the differences between *in vitro* and *in vivo* environments when interpreting results.

1.7.5. Choosing the Right Antimicrobial Testing Method Based on Research Needs

The selection of an antimicrobial testing method is contingent on the specific data required for a given study. For instance, to elucidate the dynamics of microbial killing, such as the rate and extent of bactericidal activity over time, the time-kill assay is the most appropriate method. Indeed, this method is able to measure viable

microorganisms at defined intervals after the exposure to an antimicrobial agent, thereby providing detailed kinetic profiles. It is particularly advantageous for assessing whether the antimicrobial effect is time-dependent or concentration-dependent, making it indispensable for studies focusing on the temporal dynamics of microbial killing and the potential for bacterial regrowth. In contrast, for high-throughput screening of multiple antimicrobial agents/formulations, the disc diffusion or the well diffusion methods may be more appropriate as they demand less time and resources in comparison to the time-kill assay. These techniques allow the simultaneous evaluation of several agents against a specific microorganism or against multiple microorganisms. Although these methods do not provide precise quantification of antimicrobial efficacy, they are efficient for rapidly identifying agents with significant inhibitory effects, making them ideal for initial screening or when testing large numbers of compounds in the early stages of research. When precise quantification of antimicrobial potency is necessary, particularly for determining the MIC or the MBC, the broth microdilution method, often coupled with resazurin, is the method of choice. This technique involves exposing microorganisms to serial dilutions of an antimicrobial agent in a liquid medium, followed by the addition of resazurin as an indicator of cell viability. The broth microdilution assay is crucial in clinical microbiology and drug development, where accurate dosing information is essential. It is also valuable for comparing the relative efficacy of different antimicrobial agents against the same microorganism. Therefore, the selection of an antimicrobial testing method should be guided by the specific research objectives and must be carefully chosen based on the type of information required. Selecting the appropriate method ensures that the data obtained aligns with study goals, whether it be understanding antimicrobial kinetics, screening a large number of compounds, or determining specific dosage requirements.

1.8. Thesis Aim and Objectives

The overall aim of this thesis was to develop, optimize, and evaluate LPHNPs for the dual delivery of a conventional antibiotic, cefotaxime (CTX), and a novel antimicrobial peptide, RN7IN6. This was achieved by first developing and characterizing the polymer core (CS NPs) and the lipid shell (POPE:POPG:CL liposomes) individually, which were later combined to create the hybrid delivery system. The antibacterial efficacy of these nanocarriers was tested against a clinically relevant panel of Gram-positive and Gram-negative pathogens, including *P. aeruginosa*, *E. coli*, *K. pneumoniae*, and *S. aureus*.

This overall aim was realized through work detailed in Chapters 2-5 of the thesis, with the following objectives:

- **Chapter 2:** To develop CS-based nanoparticle formulations containing CTX (LPHNP cores) using microfluidic mixing and evaluate their antibacterial activity.
- **Chapter 3:** To establish and optimize the production of bacteria-relevant POPE:POPG:CL liposomes (LPHNP shells) via microfluidic mixing, and investigate the ability to surface adsorb nisin to these liposomes as a model peptide
- **Chapter 4:** To utilize POPE:POPG:CL liposomes developed in Chapter 3 as delivery systems for the synthesized antimicrobial peptide RN7IN6 and assess their antimicrobial efficacy.
- **Chapter 5:** To formulate and optimize lipid-polymer hybrid nanoparticles for the co-delivery CTX and RN7IN6 delivery, informed by findings of Chapters 2-4, and to investigate their physiochemical properties and antibacterial activity.

2. Development of CTX Loaded Nanoparticles and Antibacterial Activity

2.1. Introduction

As described in detail in Chapter 1, drug-resistant bacteria are a significant global health challenge, with increasing rates of antibiotic-resistant infections and related deaths [27]. The WHO in 2024 identified priority pathogens urgently requiring new antibiotics, categorized into critical, high, and medium priority [26]. Despite the urgent need for novel antibiotics, new discoveries have significantly declined since the mid-20th century, leading to increased healthcare costs, prolonged hospital stays, and heightened transmission risks [366-370]. The O'Neill Report has emphasized the importance of antibiotic stewardship, research investment, and innovative delivery systems to improve therapeutic efficacy and reduce resistance [4].

Nanotechnology offers a promising approach to address these challenges, with nanocarriers demonstrating antimicrobial activity and the potential ability to enhance drug delivery through targeted and/or sustained release mechanisms [371-374]. Polymeric nanoparticles have emerged as a promising approach for antibiotic delivery, offering several potential advantages such as sustained systemic delivery, improved targeting through both passive and active mechanisms [378] and improved drug stability. In this regard, CS nanoparticles have been investigated as carriers for antibiotic delivery, showing potential in acting as drug-delivery systems [379]. CS, which is a polymer naturally derived from crustaceans or fungi, provides interesting properties including biocompatibility, biodegradability and mucoadhesive properties [380]. Also, CS has been widely studied as an antimicrobial for healing of wounds and burn infections [381], for surgical use in hydrogel form [382] and for the delivery of antimicrobial drugs to the site of the infection, such as diabetic foot ulcers, chronic wounds, and post-surgical infections [383]. Given its properties, CS shows a broad range of application in food, cosmetic, agriculture, textile and paper industries, as well as biomedical and pharmaceutical applications [384-387]. However, CS is only soluble in weakly acidic environments and poorly soluble in water and most organic solvents, causing significant

limitations to its application [388]. Water-soluble CS derivatives can be obtained by chemical functionalization of hydroxyl (-OH^-) and positively charged amino groups (-NH_3^+) present in the CS backbone. Positively charged CS groups can interact through electrostatic interactions with negatively charged molecules such as tripolyphosphate (TPP), a known crosslinking agent [392], to form coacervates with a size in the nanometer range. This process, known as the ionotropic gelation method, was first described by Calvo *et. al* [393], and relies on the material transition from liquid to gel due to ionic interaction conditions at room temperature [394].

CS has a proven broad spectrum of antibacterial activity [399] against both Gram-positive and Gram-negative bacterial strains [400]. Previous studies have shown that CS NPs exhibited a higher antimicrobial activity when compared with CS in solution [401-404] suggesting the potential of CS NPs to be employed as a drug delivery system for infectious diseases. While the specific mechanism of action of CS NPs is yet to be fully understood, the most prevalent model of their antimicrobial action involves electrostatic interactions between positively charged amino groups of CS with the negatively charged bacterial membrane. The different mechanism of action between Gram-positive and Gram-negative bacteria can be attributed to the different components of the cell envelope. In addition to this, to explain the antibacterial activity of CS NPs three other models have been proposed including the chelation of metal ions present on the bacterial surface by amino groups of CS [412, 419, 420], CS binding to DNA/RNA followed by suppression of mRNA and protein generation as shown in Figure 2-1 [412, 421-423], and the formation of a thick polymer film on the surface of the bacterial cell which inhibits the exchange of nutrients [424, 425]. This film of CS in solution acts as a barrier, preventing the uptake of essential nutrients by the bacteria and ultimately leading to their inhibition.

Nanocarriers have been used in combination with antibiotics to achieve an effective antibiotic therapy along with protection of the antibiotic from degradative enzymes at the infection site [426, 427]. The potency of antibiotics can be enhanced by loading them within CS NPs. This has been shown to synergize the activity of CS NPs and antibiotics by

increasing the antibiotic concentration in target bacteria [428] and reducing antibiotic side effects [421, 429].

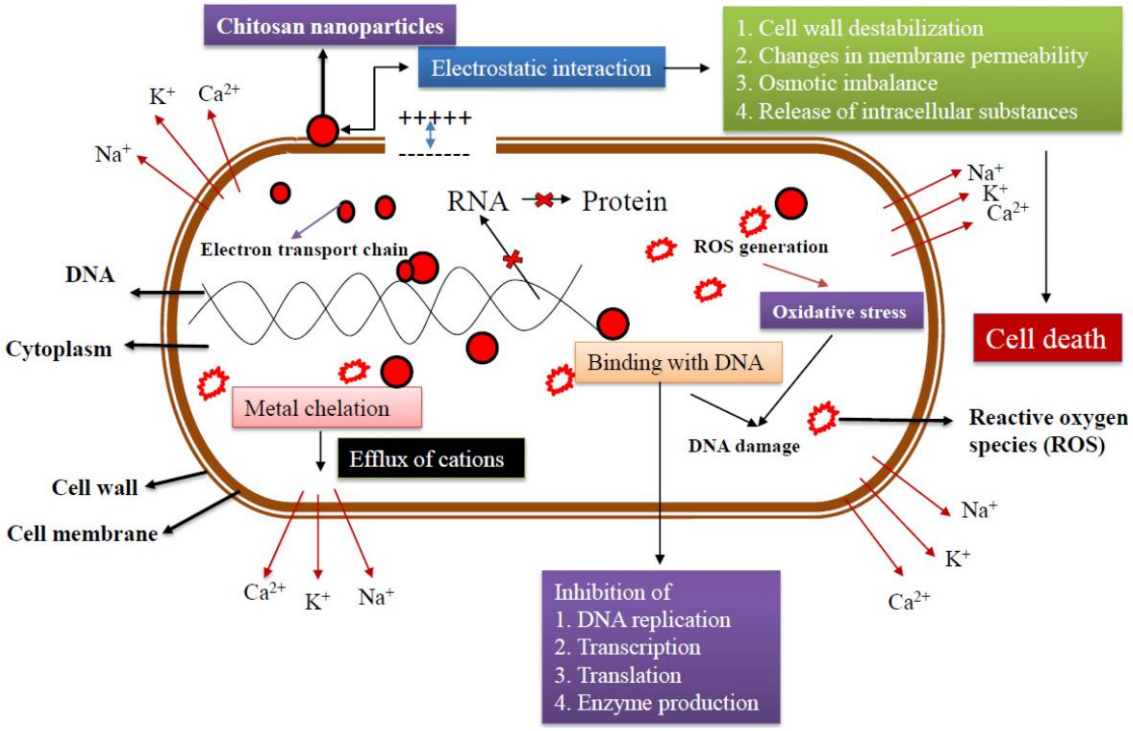

Figure 2-1: Antibacterial mechanisms of CS nanoparticles. Positively charged CS NPs interact with the negatively charged bacterial cell wall, leading to destabilization, increased membrane permeability, osmotic imbalance, and the release of intracellular contents. CS NPs induce oxidative stress through the generation of ROS, causing DNA, protein, and lipid damage. Additionally, the NPs chelate essential metals, disrupt the electron transport chain, and bind to DNA, inhibiting processes like replication, transcription, translation, and enzyme production. These effects collectively lead to bacterial cell death through ion efflux and oxidative damage. Reproduced with permission from [430].

Combining antibiotics with nanoparticles such as CS NPs represents a promising strategy to mitigate drug resistance mechanisms in bacteria, including enzymatic degradation by β-lactamases, reduced antibiotic entry due to porin deficiencies in Gram-negative bacteria, and alterations in antibiotic target sites [431, 432]. Indeed, CS NPs can facilitate increased antibiotic concentration at the site of action, potentially compensating for reduced binding affinity caused by mutations in bacterial target sites, thereby enhancing therapeutic effectiveness and combating resistance in these organisms.

In the present study, a third-generation cephalosporin, CTX, was selected on the basis of its broad-spectrum activity against both Gram-positive and Gram-negative bacteria.

The high water-solubility of CTX [436, 437], couple with the increasing prevalence of CTX-resistant bacterial strains, particularly among Enterobacteriaceae and other Gram-negative pathogens [438] makes it an ideal candidate for its incorporation within CS NPs. Additionally, the broad-spectrum efficacy of CTX against both Gram-positive and Gram-negative bacteria, together with its established clinical utility in treating severe infections such as meningitis and sepsis, underscores its relevance as a candidate cargo for enhanced delivery systems to overcome resistance mechanisms and improve therapeutic outcomes. To date, the encapsulation of a number of different classes of antibiotics within CS NPs has been investigated [439, 440]. However, the encapsulation of CTX within CS NPs manufactured via a microfluidic mixing technique has not been explored to date, which set the basis of the current study. In addition to this, the optimization of NPs manufactured with water-soluble CS derivatives via microfluidic mixing intended for antimicrobial delivery is yet to be fully investigated.

Hence, the work detailed in this chapter intended to provide a full investigation of parameters affecting the formulation of empty and CTX-loaded chitosan low molecular weight (CHT) and chitosan hydrochloride (CHCL) NPs, via a microfluidic mixing technique. Subsequently, the antibacterial activity of CTX-loaded CS NPs was compared to free CTX against a panel of both Gram-positive and Gram-negative clinically relevant bacteria.

2.2.Aim and Objectives

The aim of this chapter was to develop, manufacture via microfluidic mixing and evaluate the antibacterial activity of CHT and CHCL NP formulations for CTX delivery. This was achieved through the following objectives:

- Optimizing the formulation of CHT NPs and CHCL NPs with microfluidic mixing technology
- Investigating the capability of CS NPs to encapsulate CTX
- Developing and validating a suitable HPLC method allowing for indirect quantification of entrapped CTX within CS NPs
- Evaluating the antibacterial activity of CTX-loaded CS NPs in comparison to free CTX against clinically relevant bacteria.

2.3. Materials and Methods

2.3.1. Materials

CTX (as sodium salt, ≥95%) was bought from Enzo Life Sciences (Exter, UK) and Acros Organics (New Jersey, USA). CHCL (MW: 30-400 kDa, degree of deacetylation: 80-95%) was purchased from Heppe Medical Chitosan GmbH (Halle, Germany). Glacial acetic acid, acetonitrile and trifluoroacetic acid (TFA) were purchased from Fisher Scientific (New Hampshire, USA). Gentamicin discs (CN 10), ciprofloxacin discs (CIP 5) and phosphate buffered saline (PBS, pH 7.4) tablets were obtained from Oxoid Ltd (Basingstoke, UK). Centrisart® centrifugal ultrafiltration units (MWCO 300000 Da) were obtained from Sartorius (Goettingen, Germany). CHT (MW: 50-190 kDa, degree of deacetylation: 75-85%), Mueller Hinton Broth 2 (MHB2), Mueller Hinton Agar (MHA), Nutrient agar (NA), resazurin and TPP were purchased from Sigma-Aldrich (Missouri, USA). Formic acid (FA) and sodium hydroxide were purchased from VWR (Pennsylvania, USA).

2.3.2. Methods

2.3.2.1. Empty CS Nanoparticles Manufactured via Microfluidic Method

2.3.2.1.1. CS Nanoparticle Manufacture

CS NPs were manufactured by a microfluidic mixing method and ionotropic gelation [393]. CHT was dissolved in 1% acetic acid, while its water-soluble derivative, CHCL, was dissolved in purified water at desired concentrations (0.25 mg/mL, 0.5 mg/mL and 1 mg/mL as per Table 2-1) [441]. CHT and CHCL solutions were left under magnetic stirring (500 rpm) overnight. The following day, the pH of CS solutions was adjusted to 5 using either 0.1 M or 2 M NaOH as appropriate, according to previous studies performed within the research group. The resulting solutions were filtered through Whatman no. 40 filter paper (8 µm, supplied by Sigma-Aldrich Missouri, USA) to remove any impurities. TPP was used as a cross-linker and was dissolved in purified water at desired concentrations (0.25 mg/mL, 0.5 mg/mL and 1 mg/mL as per Table 2-1) [441].

CS NP formation was achieved using the Nanoassemblr® Benchtop instrument (Figure 2-2 A) (Precision Nanosystems Inc., Vancouver, Canada) equipped with a SHM cartridge (Figure 2-2 B).

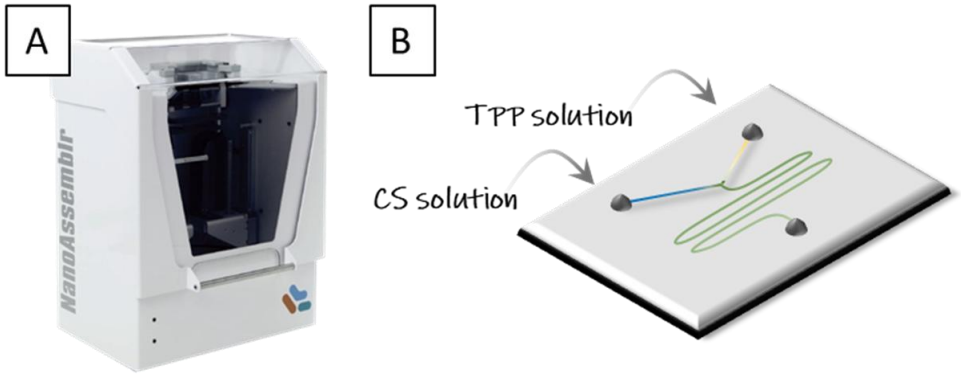

Figure 2-2: Nanoassemblr® Benchtop instrument (A) equipped with SHM cartridge with a Y-shaped microchannel architecture (B). In this setup, CS NPs are formed by the controlled mixing of CS and TPP solutions within the microchannels, where rapid mixing facilitates the ionic gelation process, resulting in the formation of nanoparticles.

Briefly, CS and TPP solutions were loaded into disposable and compatible syringes (BD Emerald 307731, 5 mL sterile disposable) and injected into separate inlets of the cartridge following specification of suitable process parameters – namely, total flow rate (TFR), flow rate ratio (FRR) (indicative of the volume ratio between the two inlet solutions), batch volume, end waste and initial waste volume. NPs formed spontaneously as a result of controlled mixing were collected from the outlet port of the SHM cartridge in a 15 mL-Falcon tube.

2.3.2.1.2. CS Nanoparticle Characterization

A Zetasizer Nano ZS (Malvern Instruments Ltd, UK) was employed to analyze the Z-average (mean diameter), polydispersity index (PDI) and Z-Potential of CS NPs . In each case, three measurements were conducted at 25 °C [442] on NP samples without dilution. An aliquot (1 mL) of the nanoparticle dispersion was transferred into a cuvette (DTS0012, 12mm square disposable polystyrene cuvette for Ns size and PDI, and DTS1070 disposable cuvettes for NPs Zeta-potential) and analysis was carried out.

2.3.2.1.3. Taguchi Design of Experiments

To evaluate the influence of formulation parameters on NP size and PDI and minimize the number of experiments to be conducted, a Taguchi Design of Experiment (DoE) approach was employed using Minitab® version 20 statistical software (Minitab, LLC). A Taguchi L18 orthogonal array design was constructed for CHT and CHCL NP formulations. Each DoE was composed of 4 variables (CS concentration, TPP concentration, TFR and FRR) set at 3 or 6 levels, as indicated in Table 2-1. The software output for the L18 orthogonal array provided a set of 18 formulations that were then prepared in triplicate for both CHT and CHCL.

The optimum conditions were set as a high signal to noise (S/N) ratio, which corresponds to minimum variance of the outcome and a better performance, with the target output parameters being the particle size and PDI [443]. The optimization of the particle size and PDI was performed using the Taguchi 'smaller-is-better' criterion to achieve a particle size and a PDI as small as possible [444].

Table 2-1: Set of 18 CS NP formulations resulting from Taguchi DoE L18 orthogonal array. Formulations A-R were prepared using both CHT and CHCL.

Formulation	FRR (CS:TPP)	TFR (mL/min)	CS concentration (mg/mL)	TPP concentration (mg/mL)
A	2 : 1	0.64	0.25	0.25
B	2 : 1	0.8	0.5	0.5
C	2 : 1	1	1	1
D	3 : 1	0.64	0.25	0.5
E	3 : 1	0.8	0.5	1
F	3 : 1	1	1	0.25
G	4 : 1	0.64	0.5	0.25
H	4 : 1	0.8	1	0.5
I	4 : 1	1	0.25	1
J	5 : 1	0.64	1	1
K	5 : 1	0.8	0.25	0.25
L	5 : 1	1	0.5	0.5
M	6 : 1	0.64	0.5	1
N	6 : 1	0.8	1	0.25
O	6 : 1	1	0.25	0.5
P	7 : 1	0.64	1	0.5
Q	7 : 1	0.8	0.25	1
R	7 : 1	1	0.5	0.25

2.3.2.1.4. FRR Investigation

To obtain a small NP size and PDI and increase the S/N ratio, a further investigation of FRR of polymer and cross-linker solution was carried out following preparation of formulations A-R detailed above. The best formulation, as determined following conduction of the DoE (Table 2-1), was chosen as a starting point to further investigate the impact of FRR. In this case, all parameters of the optimum formulation were fixed, while FRR was changed to values ranging from 1:1 to 8:1.

2.3.2.2. Development and Validation of an HPLC Method for the Quantification of CTX

2.3.2.2.1. Investigation of the Optimum Wavelength

A UV-Vis spectrophotometric scan (SPECTROstar Nano, BMG Labtech, Germany) between 220 nm and 1000 nm [445] was carried out to find a wavelength which allowed for CTX detection with minimal interference from all formulation components. For this purpose, the UV-Vis scan was performed for a CHT solution, as well as CHT NP centrifugal ultrafiltrate, liposomal centrifugal ultrafiltrate, 1% and 5% Triton X, 1% and 5% Triton X mixed with liposomes. Triton X and its mixture with liposomes were included in this wavelength investigation to ensure that future studies involving CTX-loaded LPHNPs, which are composed of a CS core surrounded by a lipid shell, would not experience interference in CTX detection. Although this chapter is focused solely on CS NPs, validating Triton X's compatibility at this stage ensures that when the lipid components are introduced in subsequent formulations, such as LPHNPs, the detection of CTX remains unaffected. This approach adds rigor by accounting for the anticipated composition of future LPHNP formulations.

CHCL solution was not included in the study as it was expected to give a similar UV absorption spectrum as CHT [446, 447].

2.3.2.2.2. HPLC Chromatographic System

An HPLC system (1200 series) from Agilent Technologies (Santa Clara, CA, USA), was used for the purpose of CTX quantification. The system was operated via ChemStation software and was equipped with a G1322A degasser, a G1312A binary pump, a G1316A thermostated column compartment, a G1329A autosampler and a G1314B variable wavelength detector. An Agilent Eclipse XDB-C18 column with dimensions of 4.6 × 150 mm and a particle size of 5 µm was employed (Agilent Technologies, USA). The column oven temperature was set at 30 °C with an injection volume of 5 µL. The final composition of the mobile phase was optimized to consist of 40:60 0.2% FA (A) in water and acetonitrile (B) at a flow rate of 1 mL/min (total run time 3.30 min), and a UV detection wavelength of 308 nm.

2.3.2.2.3. Method Linearity

Method linearity was established in accordance with ICH guidelines [448]. A standard curve was obtained by plotting mean peak area (n=3) against concentration for a series of known concentration CTX standards in purified water ranging from 1 µg/mL to 1000 µg/mL. The gradient, *y*-intercept and linearity of the curve were determined by linear regression analysis. Linearity was evaluated according to the determined regression value (R^2).

2.3.2.2.4. Precision, Accuracy and Limits

ICH guidelines were also followed for determination of reproducibility and intraday and interday repeatability, as specified measures of precision and accuracy [448]. Intraday repeatability was calculated using three different CTX concentrations analyzed on the same day. Three replicates were measured at three different timepoints on the same day for each sample, resulting in a total of 9 measurements of each sample at each concentration level. Inter-day variation was calculated by quantification of the freshly prepared CTX samples at 3 concentration levels in the analysis series on different days (at least 3 different days). For repeatability of injections, the relative standard deviation (RSD) was calculated for 3 different concentrations tested (n=5).

Moreover, the lower limit of detection (LLOD), expressed as the smallest amount of drug that can be detected but not quantified, was calculated using the standard deviation (SD) of the y intercept (s) and the slope (m) of the calibration curve as in Equation 2-1 [448]. The lower limit of quantification (LLOQ), which is the minimum amount of analyte in a sample that can be quantified with adequate precision and accuracy, was calculated using the SD of the y intercept (s) and the slope (m) of the calibration curve as in Equation 2-2 [448].

Equation 2-1

$$LLOD = 3.3\ x\ \ s/m$$

Equation 2-2

$$LLOQ = 10\ x\ \ s/m$$

2.3.2.2.5. Specificity and Robustness of the Method

The specificity of the analytical procedure, as defined in ICH guidelines [448], was demonstrated by performing injections of CHT solution, blank CHT NP centrifugal ultrafiltrate and CTX solution of concentration 100 µg/mL.

To evaluate the robustness of the system, which refers to the ability of the method to withstand small, intentional changes in parameters without significantly affecting the results, some variations were made in the method and samples were analyzed. The method was varied by changing flow rate (± 10%), detection wavelength (± 2 nm) and column compartment temperature (± 5 °C) during analysis [449]. Sample solutions of 3 different CTX concentrations were prepared and injected for every condition and the drug retention time (Rt) was determined.

2.3.2.2.6. Analyte Solution Stability

With the objective of assessing analyte solution storage stability, CTX solutions were prepared at 3 different concentrations (7.5 µg/mL, 100 µg/mL and 750 µg/mL) and stored at 5 ± 3 °C, 25 ± 2 °C and -18 ± 3 °C [448] for up to 96 hours (4 days). Samples were then analyzed in triplicate at specific time points (0, 4, 8, 24 and 96 hours) via HPLC. The stability of analyte solutions stored at different temperatures was evaluated via HPLC peak areas as per Equation 2-3.

Equation 2-3

$$ST\% = S_t/S_0\ x\ 100$$

Where ST% is the analyte stability percentage, S_t is the peak area obtained from HPLC analysis when analysis was carried out with a pause of duration t prior to the analysis and S_0 is the initial peak area, determined without introducing any extra pauses in the

analysis process. Freshly prepared calibration standards (at concentration levels corresponding to the stability study samples) were considered as containing 100% of the initial analyte content.

2.3.2.3. Microfluidic Manufacture of CTX-Loaded CS NPs

2.3.2.3.1. Synthesis, Optimization and Characterization

CTX-loaded CS NPs were manufactured via a microfluidic mixing technique as previously described in 2.3.2.1.1. Optimal parameters for unloaded CS NPs as identified from studies described in 2.3.2.1.3 and 2.3.2.1.4 were used as a starting point for optimization of CTX-loaded NPs. Employing optimized CS and TPP concentrations as well as FRR and TFR values allowed for investigation of the impact of varying CTX loading concentration on NP size, PDI, Z-Potential and EE%.

Based on the findings from previous studies (see 2.3.2.1), the CS and TPP concentrations, FRR, and TFR were chosen, and then the impact of increasing CTX concentrations on size, PDI, Z-Potential and EE% of NPs was investigated. Briefly, increasing concentrations of CTX ranging from 0.3 mg/mL to 3 mg/mL were added to either CS (CHCL or CHT) or TPP solutions [440, 450-455]. Subsequently, solutions were injected into separate inlets of the microfluidic cartridge. Formed NP were then recovered in a 15 mL Falcon tube and characterized as described in 2.3.2.1.2.

2.3.2.3.2. CTX Encapsulation Efficiency within CS NPs

CTX encapsulation efficiency (EE%) within CHT and CHCL NPs was indirectly calculated by quantification of unentrapped CTX amounts, using the optimized and validated HPLC method described in section 2.3.2.2. In this respect, two different purification methods were employed: ultrafiltration [456] and ultracentrifugation [457].

In the first case, a preliminary study to investigate the ability of free CTX to pass through a Sartorius Centrisart® I centrifugal ultrafiltration unit and be completely recovered in the ultrafiltrate was first performed. This was achieved by centrifuging 1 ml of CTX

solution (0.5 mg/mL to represent CTX concentration in NPs suspension) and by analyzing the ultrafiltrate at the HPLC. The preliminary study yielded a complete recovery of CTX in the ultrafiltrate. Subsequently, 1 mL of CTX-loaded NPs was loaded into each Centrisart® unit (Figure 2-3) and centrifuged (Eppendorf centrifuge 5804r, Germany) at 1188 x *g* and 25 °C for 30 min. After centrifugation, the concentrated CTX-loaded NP dispersion (yellow liquid in Figure 2-3) was collected and kept for further studies, while the liquid present in the ultrafiltrate compartment (purple liquid in Figure 2-3) was collected and analyzed via HPLC to quantify CTX EE% using Equation 2-4.

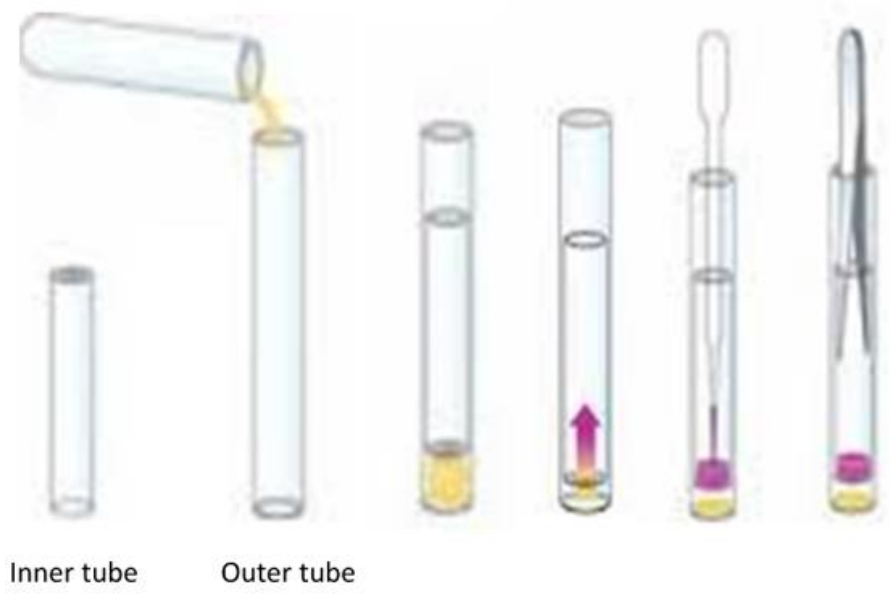

Figure 2-3: Separation of free CTX from CTX-loaded NPs using Centrisart® units. Each unit consists of 3 parts: an outer tube, an inner tube with a polysulfone membrane at the bottom, and a cap. The ultrafiltration of the sample (yellow liquid) takes place in the opposite direction to the centrifugal force. The sample to be centrifuged is placed in the outer tube, followed by careful insertion of the empty, inner tube. After ultrafiltration, the ultrafiltrate (purple liquid) is collected, the inner tube is removed, and the concentrated sample is recovered.

In the latter case, 3 mL of NPs were diluted with 2 mL of PBS and collected via ultracentrifugation (Beckman Coulter Optima XPN-80) using a 70.1 Ti rotor at 25 000 rpm for 30 min at 10 °C. After ultracentrifugation, the supernatant was collected and analyzed via HPLC for CTX content, while the pellet of CTX-containing NPs was resuspended in 3 mL of PBS and kept for further studies. Subsequently, CTX EE% within NPs was calculated using Equation 2-4 given below, where Wt represents the theoretical

amount of CTX added to formulation, Wu represent the amount of CTX present in the supernatant/ultrafiltrate quantified by HPLC.

Equation 2-4

$$CTX\ EE\% = \frac{Wt - Wu}{Wt}\ x\ 100$$

2.3.2.3.3. Statistical Analysis

All statistical analyses were performed using IBM SPSS statistical software (Version 26.0. Armonk, NY: IBM Corp). Multiple regression analysis, analysis of variance (ANOVA) and F-Test were used to build prediction models for nanoparticle size and PDI for data obtained from the study described in 2.3.2.1.3. One-way ANOVA with Tukey's post hoc test was employed to compare formulations obtained as described in 2.3.2.1.4, 2.3.2.3.2 and 2.3.2.3.2. A p value of <0.05 was taken as indicating statistical significance throughout the studies.

2.3.2.4. Antibacterial Activity Evaluation of Empty and CTX-loaded CS NPs

2.3.2.4.1. Bacterial Characterization and Cultures

Before use, all microorganisms employed in this study were identified by Gram staining morphology according to literature [458], and further confirmed using coagulase test for staphylococci, oxidase and catalase test.

Bacterial strains employed in the study were the following:

- *E. coli* NCTC 12241
- *S. aureus* NCTC 12981
- *P. aeruginosa* NCTC 12903
- *K. pneumoniae* NCTC 9633

MHA plates and MHB2 for microorganism sub-culturing and testing were prepared by dissolving 38 g and 21 g of base powder, respectively, in 1 L of distilled water in Duran bottles. Bottles were then sterilized for 15 minutes at 121 °C (Prestige Medical Classic Media Autoclave - 12L / LTE Touchclave-R TCR/160/V7 Top Loading Chamber Autoclave, Richmond Scientific, Chorley, UK). After autoclave sterilization, MHB was stored in Duran bottles until further use, while MHA was poured into 90 mm sterile agar plates and left to solidify overnight.

Coagulase Test:

To determine the presence of coagulase enzyme in bacterial samples, a coagulase test was conducted [459] using the following methodology. A drop of plasma sourced by Thermo Fisher Scientific (Massachusetts, US) was placed onto a clean glass microscopy slide. Using a sterile loop, several bacterial colonies from the MHA plate culture were carefully collected and thoroughly emulsified with plasma. The mixture was then observed for a few seconds. A positive coagulase reaction was indicated by the formation of clear suspension with visible aggregates, whereas a negative reaction was characterized by the mixture remaining creamy or milky in appearance.

Oxidase Test:

The oxidase test was performed to determine the presence of cytochrome c oxidase enzyme in selected Gram-negative bacteria, including *P. aeruginosa*, *E. coli*, and *K. pneumoniae* [460]. A small number of bacterial colonies were collected using a sterile loop and applied to a strip pre-soaked with the reagent mixture containing N,N-dimethyl-p-phenylenediamine and alpha-naphthol, sourced from Thermo Fisher Scientific (Massachusetts, US). The development of a purple color within a specified time frame indicated a positive oxidase reaction, confirming the presence of cytochrome c oxidase enzyme in the tested bacterial isolates.

Catalase Test:

A drop of 3% hydrogen peroxide (catalase reagent) was placed on a clean microscope slide. Using a capillary glass tube, a small amount of the hydrogen peroxide reagent was

drawn up. Subsequently, a bacterial colony was collected with the same capillary glass tube. The presence of catalase enzyme in the bacteria was determined by the appearance of bubbles within the capillary glass tube upon contact with the hydrogen peroxide [461]. The formation of bubbles indicated a positive catalase test, confirming the presence of catalase-producing bacteria.

2.3.2.4.2. Agar Well-diffusion Assay Optimization

The agar well-diffusion method was employed to compare antibacterial activity [462] of free CTX and CTX-loaded CHT and CHCL NPs. MHA plates were prepared as described in 2.3.2.4.1. The protocol employed in the testing was adapted from that detailed by Magaldi *et al.* [463]. The preparation of standardized bacterial suspension was achieved by the selection of a microorganism colony, from the MHA plate, followed by its suspension in 50 mL of MHB2, which was left to incubate in an orbital shaking incubator (SciQuip Incu-Shake MIDI Benchtop Shaking Incubator, Richmond Scientific, 250 rpm) set at 37 °C overnight. A 40 µL volume of the overnight culture was used to inoculate 150 mL of MHB2, which was left in an orbital shaking incubator (250 rpm) set at 37°C for 3 hours. Subsequently, the OD_{600} of bacterial suspensions was measured on a SpectroStar Nano microplate reader (BMG LABTECH) and adjusted to OD_{600} 0.05-0.1 (corresponding to $1x10^6$ CFU/mL, as determined from bacterial growth curves). The adjusted bacterial suspension was evenly swabbed over the sterile agar surface and 9 mm diameter reservoirs were cut into the agar plates with a sterile cork borer. CTX-loaded CHT and CHCL NPs, prepared as described in 2.3.2.3.1 with CTX dissolved in TPP solution, were ultracentrifuged (Beckman Optima XL, rotor 70.1 Ti, minimum radius 4.05 cm, max radius 8.20 cm) at 25000 rpm, for 30 minutes at 10 °C. The supernatant was analyzed by HPLC, as described in 2.3.2.2, and the pellet was resuspended in sterile water and adjusted to final CTX concentrations of 0.903 mg/mL, 0.101 mg/mL and 0.045 mg/mL. These concentrations represent the amount of CTX encapsulated within the formulations after purification, corresponding to three different initial CTX loading concentrations used during the formulation process. Free CTX solutions in sterile water were prepared at the same concentrations. Volumes of 25 µL of CTX-loaded CHT and CHCL NPs and free CTX solutions were introduced into allocated reservoirs (Figure 2-4) at the same time to avoid differences in diffusion between the first and last reservoirs.

In order to allow time for drug and NP diffusion into the agar medium, the plates were left for 2 hours at room temperature after which, they were incubated overnight at 37 °C. After 16 to 18 hours, each plate was visually evaluated to ensure that a semi-confluent lawn of bacterial growth had been achieved and that any formed zones of inhibition were uniformly circular. The diameters of formed zones of inhibition were then measured with a ruler positioned underneath the inverted plate (standard error of ± 0.5 mm). Inhibition zones with diameters of 9 mm or less were considered to indicate no antimicrobial activity.

Positive (gentamicin, 10 µg or ciprofloxacin, 5 µg sterile disc) and negative (25µL of sterile PBS) controls were additionally performed within each test plate (Figure 2-4).

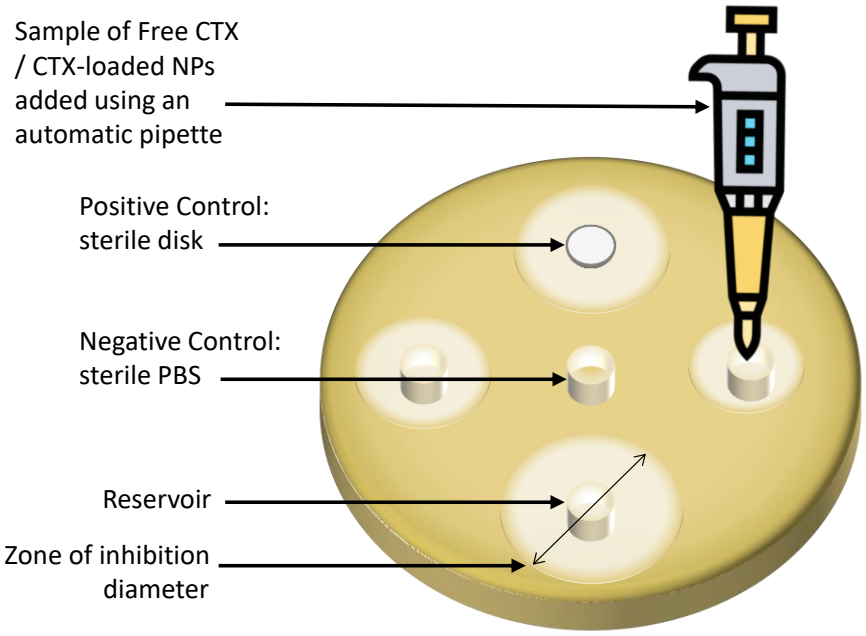

Figure 2-4: Schematic representation of agar well-diffusion assay employed to evaluate CTX-loaded CS NP antimicrobial activity compared to free CTX. Created with BioRender.com.

2.4. Results and Discussion

2.4.1. Empty CS NPs

Since its approval as GRAS (Generally Recognized as Safe) by the United States Food and Drug Administration (FDA), CS has been widely applied in the design and production of different nanocarriers that can be used in a broad range of applications including drug delivery [464, 465]. In particular, CS and its derivatives represents a major polymer of choice for formulation of NPs designed to deliver antibacterial drugs, because of their intrinsic antibacterial activity [430]. Thus, to achieve a synergistic antimicrobial effect, many researchers have used CS as a platform for antibiotic and AMP delivery [466-469]. One of the most preferred synthesis methods for CS NPs is the ionotropic gelation method [393], which is a straightforward process that does not involve high temperatures or the use of toxic solvents. Despite several advantages provided by this bottom-up production method there is a lack of control over the fabrication process, leading to high batch-to-batch variation in physicochemical NP properties as well as difficulties in process scale-up and clinical translation. In recent years, the automated microfluidic mixing technique has emerged as a useful tool for production of CS-based NP with tunable characteristics. This technology provides numerous advantages including improved formulation reproducibility by eliminating user variability, as well as a rapid, cost-effective manufacturing process. Recent studies have advanced the use of microfluidic techniques for synthesizing CS NPs aimed at antibiotic delivery. For instance, Greco *et al.* and Chiesa *et al.* both explored microfluidic platforms for precise control over CS NP synthesis, highlighting their potential in tailoring NPs for drug delivery applications, including antibiotics [325, 470]. Furthermore, bioconjugated CS NPs with AMPs showed improved antimicrobial efficacy [471]. These studies collectively underscore the growing role of microfluidics in advancing the effectiveness and versatility of CS NPs for antibiotic therapies. Currently, there are gaps and limitations in the understanding of microfluidic synthesis of CS NPs, particularly in systematically studying the impact of multiple mixing parameters and phase concentrations on CS NP physicochemical characteristics and drug EE%. While studies like those by Huanbutta *et al.* have explored aspects of microfluidic synthesis [472], there remains a need for comprehensive investigations that consider interactions between various parameters (such as TFR, FRR and concentrations of reactants) and their influence on NP properties.

Moreover, based on current literature, studies specifically focusing on the synthesis of CHCL NPs using microfluidic techniques appear limited in comparison to conventional methods [473, 474]. Therefore, a comprehensive study was performed in the current work with the objective of identifying key parameters that influence the physicochemical properties of microfluidic-produced CS NPs. To address this question, the production of empty CHT NPs and CHCL NPs was investigated using a systematic DoE approach as detailed in Table 2-1.

Table 2-2 displays NP size, PDI and Z-Potential for the set of 18 experiments performed for CHT NPs and CHCL NPs, indicating a size ranging from 60.87 ± 4.86 nm to 182.07 ± 32.72 nm, and from 89.15 ± 26.29 nm to 4290.67 ± 1295.92 nm respectively. The PDI was between 0.14 ± 0.02 and 0.61 ± 0.13 for CHT NPs and between 0.29 ± 0.04 and 0.62 ± 0.23 for CHCL NPs.

Table 2-2: CHT and CHCL NP size, PDI and Z-Potential of the 18 formulations prepared according to Taguchi L18 orthogonal array DoE. The results represent mean ± SD, n=3 independent batches. Formulations D (CHT NPs) and G (CHCL NPs) were identified as the best formulations based on experimental data, where 'BEST' formulation refers to the theoretical optimum formulation predicted by DoE (Design of Experiments) analysis.

	CHT NPs			CHCL NPs		
	Size ± SD (nm)	**PDI ± SD**	**Z-Potential ± SD (mV)**	**Size ± SD (nm)**	**PDI ± SD**	**Z-Potential ± SD (mV)**
A	60.87 ± 4.86	0.27 ± 0.05	7.78 ± 2.13	4023.67 ± 2182.36	0.35 ± 0.16	4.41 ± 0.81
B	69.29 ± 7.14	0.17 ± 0.03	9.91 ± 2.53	4290.67 ± 1295.92	0.42 ± 0.28	6.63 ± 2.65
C	90.97 ± 13.34	0.15 ± 0.01	9.08 ± 0.46	3006.00 ± 466.66	0.62 ± 0.23	1.07 ± 1.28
D	**70.24 ± 4.56**	**0.15 ± 0.01**	**9.25 ± 0.75**	381800 ± 532.25	0.45 ± 0.44	7.63 ± 3.04
E	96.31 ± 10.00	0.14 ± 0.02	9.62 ± 1.10	3752.67 ± 1260.42	0.52 ± 0.16	0.93 ± 0.47
F	120.10 ± 7.56	0.47 ± 0.06	16.25 ± 1.91	130.47 ± 14.84	0.36 ± 0.07	35.75 ± 0.78
G	123.25 ± 51.74	0.48 ± 0.07	14.15 ± 2.76	**105.96 ± 11.00**	**0.29 ± 0.04**	**31.30 ± 1.70**
H	134.90 ± 45.78	0.38 ± 0.01	17.55 ± 3.04	158.60 ± 7.83	0.36 ± 0.05	33.20 ± 3.54
I	95.79 ± 6.72	0.16 ± 0.02	7.23 ± 0.91	4022.33 ± 715.06	0.48 ± 0.08	3.28 ± 2.64
J	106.80 ± 8.07	0.25 ± 0.02	16.70 ± 0.42	215.10 ± 82.31	0.48 ± 0.15	32.45 ± 0.35
K	88.24 ± 10.67	0.40 ± 0.06	13.80 ± 1.13	102.50 ± 39.17	0.39 ± 0.10	13.00 ± 2.55
L	93.27 ± 11.72	0.42 ± 0.06	13.95 ± 2.05	109.52 ± 18.26	0.35 ± 0.06	25.95 ± 2.90
M	79.71 ± 4.38	0.22 ± 0.04	4.25 ± 5.18	220.47 ± 37.51	0.47 ± 0.04	24.95 ± 2.19
N	182.07 ± 32.72	0.61 ± 0.13	12.59 ± 4.68	148.71 ± 29.15	0.39 ± 0.06	33.90 ± 4.24
O	80.07 ± 18.24	0.42 ± 0.09	10.55 ± 4.03	89.15 ± 26.29	0.38 ± 0.05	21.40 ± 1.13
P	139.77 ± 8.99	0.50 ± 0.05	19.00 ± 1.98	198.83 ± 58.01	0.38 ± 0.04	35.60 ± 1.27
Q	64.64 ± 3.04	0.20 ± 0.03	7.22 ± 3.43	2360.33 ± 417.90	0.36 ± 0.16	8.47 ± 2.31
R	154.47 ± 42.20	0.54 ± 0.03	16.10 ± 1.41	126.39 ± 59.55	0.33 ± 0.03	10.14 ± 8.44
BEST	199.20 ± 8.50	0.23 ± 0.01	8.56 ± 1.21	128.9 ± 4.922	0.40 ± 0.05	29.66 ± 2.52

The analysis of the results by Minitab 16 Statistical Software® for CHT NPs and CHCL NPs are shown in Figure 2-5 as a rank, where rank 1 indicates the maximum influential factor on the output parameters (particle size and PDI) and rank 4 shows the minimum influencing factor. Accordingly, the parameter which most affects NP physicochemical characteristics was found to be CS concentration in the case of CHT NPs, and FRR for CHCL NPs.

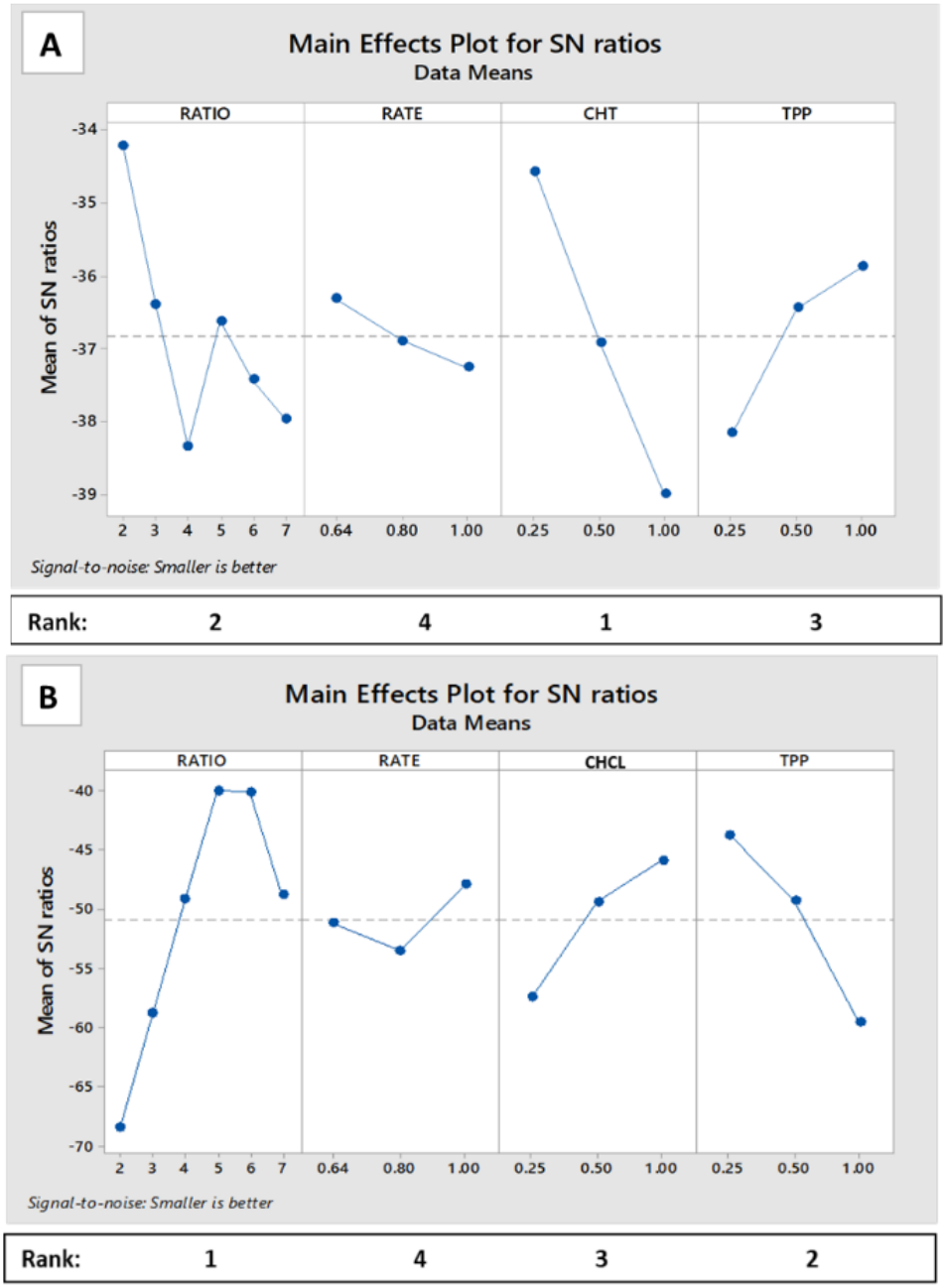

Figure 2-5: Mean signal-to-noise (S/N) graph for CHT (A) and CHCL (B) particle size and PDI response. Numerical values corresponding to experimental parameters denote parameter levels. The results represent mean ± SD, n=3 independent batches.

Multiple linear regression analysis for particle size and PDI was performed and indicated that all factors except TFR affected particle size with statistical significance, for both CHT NPs and CHCL NPs (Table 2-3).

Table 2-3: Regression analysis of NP size and PDI versus CHT NPs and CHCL NP preparation variables. In the table, the T-value indicates how strongly a parameter affects the response variable, with larger values showing a stronger effect. The p-value shows the likelihood that the result is due to chance, with p < 0.05 (*) meaning the effect is statistically significant. Coefficients represent the change in the response (e.g., particle size) for each unit change in the predictor, with positive values indicating a direct relationship and negative values an inverse one.

		Particle size				PDI			
	Predictor (Symbol)	**Coefficients**	**Coefficients St. Err.**	**T**	**p**	**Coefficients**	**Coefficients St. Err.**	**T**	**p**
CHT NPs	**Constant**	40.799	23.143	1.763	0.084	0.173	0.054	3.201	0.002*
	FRR (A)	7.511	2.074	3.622	0.001*	0.045	0.005	9.286	0.000*
	TFR (B)	23.959	24.049	0.996	0.324	0.135	0.056	2.408	0.020*
	CHT (C)	67.49	11.359	5.942	0.000*	0.166	0.026	6.256	0.000*
	TPP (D)	-39.638	11.359	-3.49	0.001*	-0.355	0.026	-13.405	0.000*
CHCL NPs	**Constant**	4453.579	1038.455	4.289	0.000*	0.296	0.128	2.318	0.025
	FRR (A)	-654.549	93.053	-7.034	0.000*	-0.017	0.011	-1.468	0.148
	TFR (B)	-671.255	1079.083	-0.572	0.57	0.044	0.133	0.33	0.743
	CHCL (C)	-2228.752	509.672	-4.373	0.000*	0.045	0.063	0.714	0.479
	TPP (D)	1945.29	509.672	3.817	0.000*	0.189	0.063	3.007	0.004*

In addition, the results of ANOVA and F-Test performed on the two obtained sets of data (Table 2-2) for both polymers, indicated that the fitted model predicted particle size with statistical significance (Table 2-4), as demonstrated by the low p-values ($p < 0.05$), which reflect the likelihood that the observed effects are not due to random chance.

Even though FRR was not the parameter with the highest rank for CHT NPs (Figure 2-5 A), the influence of FRR on CHT and CHCL NP size, PDI and Z-Potential was further investigated, as a change in FRR value results in molar ratio change between CS and TPP. Thus, by varying this parameter and changing the molar ratio between CHT and TPP, it was possible to indirectly modify the amount of polymer (which resulted in a rank of 1). FRR values were varied from FRR 1:1 to 7:1 while polymer concentration, TPP concentration and TFR were fixed according to formulations D (CHT NPs) and G (CHCL NPs) obtained from the Taguchi DoE (Table 2-2).

Table 2-4: ANOVA tables of fitted model for CHT NP and CHCL NP size and PDI. The table presents the ANOVA results, showing sources of variation, degrees of freedom, sum of squares, mean squares, F-statistic, and p-values for both CHT and CHCL NPs. The regression row reflects the influence of independent variables (e.g., FRR, TFR, CS and TPP concentration) on particle size and PDI. The low p-values ($p < 0.05$) indicate that the model significantly predicts particle size and PDI, meaning the observed effects are not due to random chance.

		Source	Degree of Freedom	Sum of Squares	Mean square	F	p
CHT NPs	*Particle size*	Regression	4	41719.423	10429.856	15.398	0.000*
		Residual error	49	33189.882	677.345		
		Total	53	74909.305			
	PDI	Regression	4	1.146	0.286	77.715	0.000*
		Residual error	49	0.181	0.004		
		Total	53	1.326			
CHCL NPs	*Particle size*	Regression	4	113870048.9	28497512.22	20.874	0.000*
		Residual error	49	66824721.97	1363769.836		
		Total	53	180694770.8			
	PDI	Regression	4	0.244	0.061	2.953	0.029
		Residual error	49	1.012	0.021		
		Total	53	1.256			

The results of the study, examining the impact of varying FRR on NP size and PDI for CHT NPs and CHCL NPs, showed in Figure 2-6 and Figure 2-7 for CHT NPs and CHCL NPs, respectively, revealed the same trend for both polymers employed in the study: that is, NP size decreases as FRR increases.

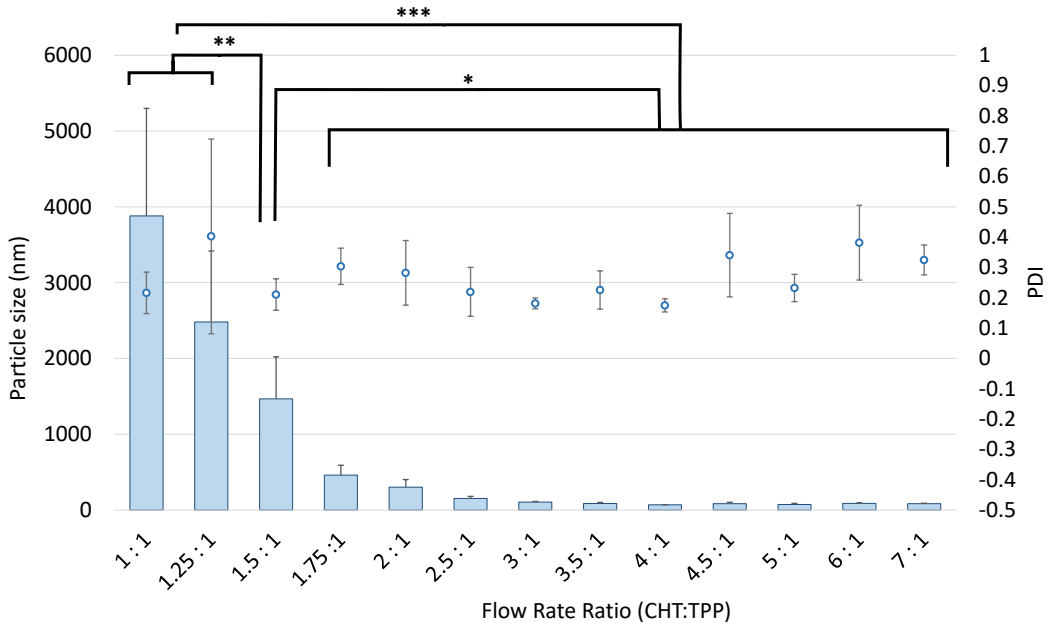

Figure 2-6: CHT NP size ± SD (nm) and PDI ± SD of formulations manufactured with different FRR ranging from 1:1 to 7:1. In addition, the chart shows the One-Way ANOVA/Tukey's comparison between the formulations with the output being NP size. The results represent mean ± SD, n=3 independent batches. NP PDI did not show any statistically significant differences. If a p-value is less than 0.05, it is flagged with one star (*). If a p-value is less than 0.01, it is flagged with 2 stars (**). If a p-value is less than 0.001, it is flagged with three stars (***).

Formulations manufactured with FRR between 1:1 and 1.5:1 for CHT NPs and FRR between 1:1 and 1.05:1 for CHCL NPs resulted in a size in the micrometer size range; this, together with the polydispersity of the NP populations and the high values of SD between the replicates, suggests that aggregation or clumping of NPs may have occurred for these formulations [475]. This phenomenon of aggregation and clustering can be attributed to the high value of CS:TPP mass ratio. The presence of a high number of TPP molecules allows the crosslinking not only to form single particles (intra-N bonds) but also to cross-link NPs to other NPs (extra-NP bonds) [476], leading to the formation

of aggregates. Furthermore, the high amount of TPP can cause the formation of H-linked CS and result in the formation of nanofibers [477].

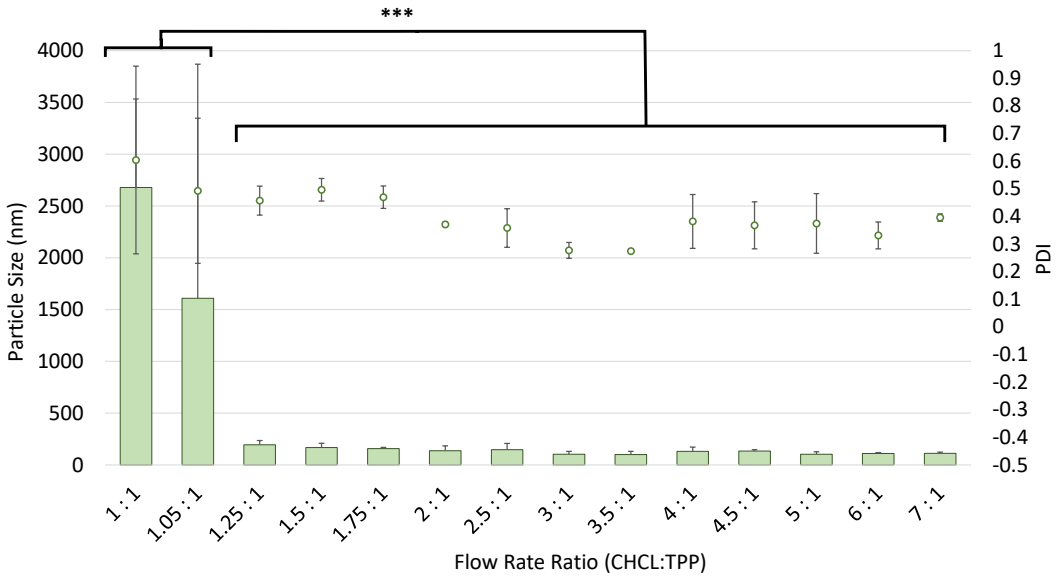

Figure 2-7: CHCL NP size ± SD (nm) and PDI ± SD of formulations manufactured with different FRR ranging from 1:1 to 7:1. In addition, the chart shows the One-Way ANOVA/Tukey's comparison between the formulations with the output being NPs size. The results represent mean ± SD, n=3 independent batches. NPs PDI did not show any statistical differences. If a p-value is less than 0.05, it is flagged with one star (*). If a p-value is less than 0.01, it is flagged with 2 stars (**). If a p-value is less than 0.001, it is flagged with three stars (***).

Formulations manufactured using FRR ranging from 1.75:1 to 7:1 for CHT NPs (Figure 2-6) showed a considerably smaller size compared to the formulations manufactured with FFR between 1:1 and 1.75:1. The same trend was also observed for CHCL NPs manufactured with FRR between 1.25:1 and 7:1 (Figure 2-7). In these cases, the molar ratios between polymer and cross-linker are much higher compared to other formulations, suggesting that the smaller number of TPP molecules present allows for the formation of stable and smaller particles. The smaller number of negative charges, provided by TPP, does not permit the extra-NP interactions that would lead to NP aggregation and bigger NP size outcomes [325]. Statistical analysis revealed that formulations manufactured with FRR values ranging from 1.75:1 to 7:1 for CHT NPs and from 1.25:1 to 7:1 for CHCL NPs did not show any significant difference in terms of size and PDI. However, a FRR value of 4:1 for CHT NPs and 3.5:1 for CHCL NPs was chosen

(Table 2-5) to investigate CTX encapsulation efficiency as a function of CTX loading concentration. Indeed, FRR values of 4:1 for CHT NPs and 3.5:1 for CHCL NPs were chosen as they provided the smallest and most stable nanoparticles without aggregation (Figure 2-6 and Figure 2-7). This parameter tuning minimized the occurrence of inter-particle bonding (extra-NP bonds) and aggregation, resulting in monodisperse particles with low PDI. Additionally, CS and TPP concentrations of 0.25 mg/mL and 0.5 mg/mL for CHT, and 0.5 mg/mL and 0.25 mg/mL for CHCL, were found to be suitable to manufacture NPs with small size and PDI in combination with TFR of 64 mL/min (Table 2-2). This decision was driven by the statistical analysis performed on the sets of formulation manufactured and based on experimental data obtained for the selected formulations.

Table 2-5: Optimized process parameters for CHT and CHCL NP formation, further employed to manufacture CTX-loaded NPs.

Parameters		CHT NPs	CHCL NPs
CS concentration (mg/mL)		0.25	0.5
TPP concentration (mg/mL)		0.5	0.25
FRR	**CS solution**	4	3.5
	TPP solution	1	1
TFR (mL/min)		0.64	0.64
Total volume (mL)		1.5	1.5
Initial Waste (mL)		0.045	0.045
Final Waste (mL)		0.05	0.05

2.4.2. Development and Validation of an HPLC Method for Detection and Quantification of CTX within Formulations

2.4.2.1. Investigation of the Optimum Wavelength

A UV-Vis spectrophotometric scan was carried out between 220 nm and 1000 nm to determine the absorbance of CTX and formulation components. The analysis of the results led to a determination of the optimal wavelength for CTX detection of 308 nm, in order to avoid interference from other formulation components analyzed (Figure 2-8). For wavelength values lower than 308 nm, liposomal components and Triton X at different percentages (relevant for later considerations in Chapters 3, 4 and 5) showed

a high absorbance impeding the specific detection of CTX; at wavelength values higher than 308 nm, CTX absorbance decreased even though other components showed an absorbance close to zero.

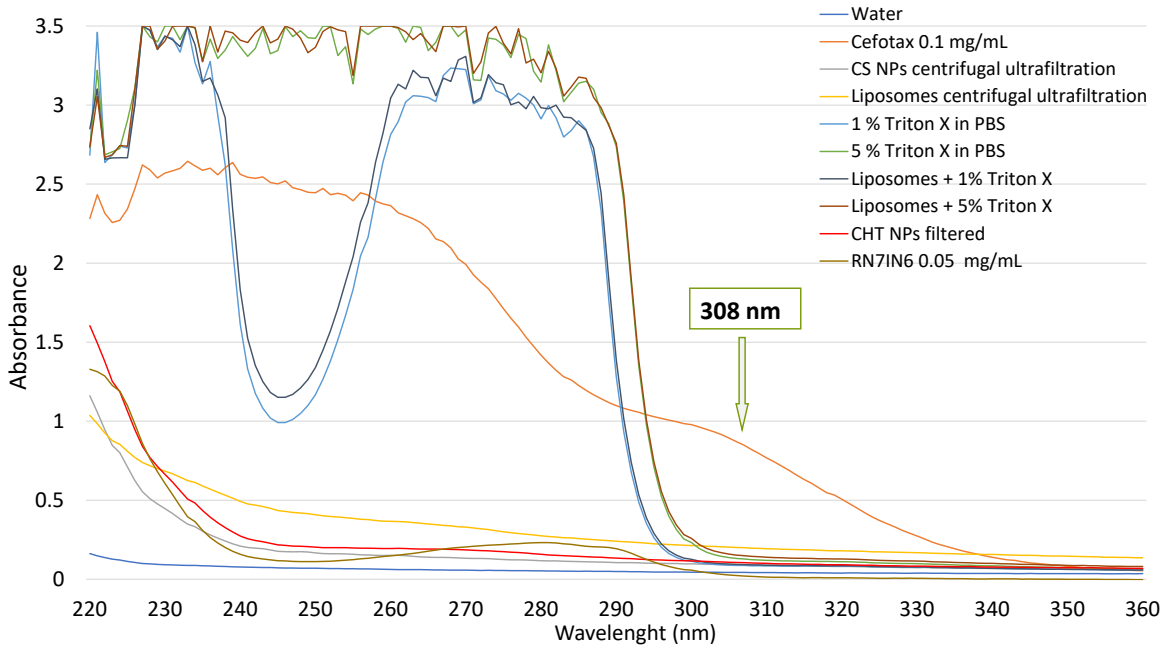

Figure 2-8: Investigation of UV absorption spectra of CTX and various formulation components. A wavelength of 308 nm, as indicated by the arrow, was chosen for CTX detection and analysis. Liposomal centrifugal ultrafiltration products, Triton X in PBS, the AMP RN7IN6 and liposomes and Triton X mixture were tested for future considerations in Chapters 3, 4 and 5.

2.4.2.2. CTX Range, Linearity and Limits

The peak area of CTX standard solutions measured via HPLC at a detection wavelength of 308 nm was directly related to CTX concentration over the concentration range of 1-1000 µg/mL (Figure 2-9) which covered the working concentration range of CTX-containing formulation samples. The calibration curve equation (displayed in Figure 2-9, where *y* represents the peak area and *x* the CTX concentration) resulting from the linear regression analysis ($R^2 = 1$) was further employed to determine the accuracy and relative SD of the analytical procedure.

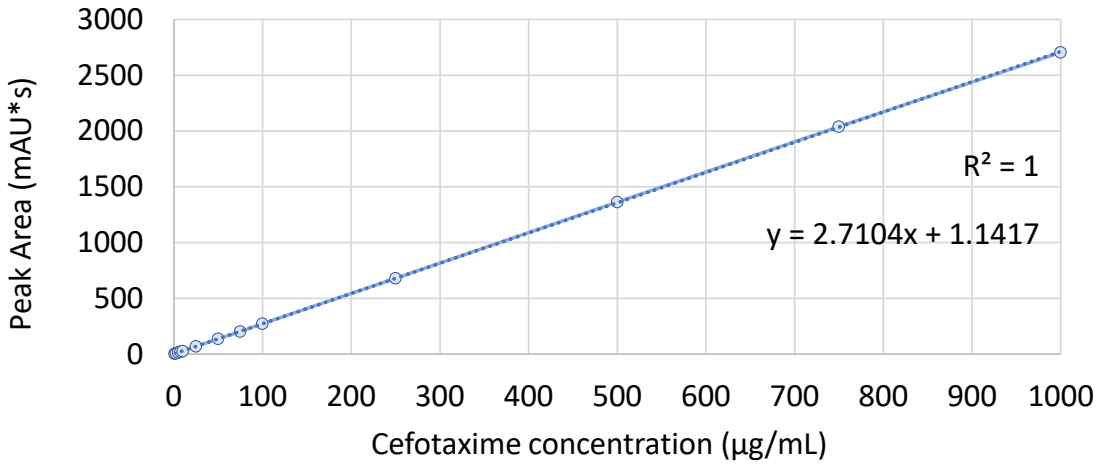

Figure 2-9: Standard curve of peak area as a function of CTX concentration, demonstrating a linear relationship for the investigated concentration range. Error bars represent SD from the mean (n=3).

2.4.2.3. Chromatographic Precision, Accuracy and Limits

The employed isocratic HPLC method was found to be precise for both intra-day and inter-day variability as indicated by RSD% values ≤1% (Table 2-6).

Table 2-6: Intraday (A) and interday (B) accuracy of the unweighted linear regression and RSD% applied to calibration standards in the range 7.5–750 µg/mL. The results represent mean ± SD, n=3 independent batches.

Spiked concentration of CTX (µg/mL)	**Calculated concentration of CTX (µg/mL) ± SD**	**Accuracy (%)**	**RSD (%)**
	Intraday repeatability (A)		
7.5	7.3 ± 0.03	97.69	0.36
100	102.2 ± 0.34	102.21	0.33
750	761.2 ± 0.25	101.49	0.03
	Interday repeatability (B)		
7.5	7.3 ± 0.02	97.53	0.34
100	102.6 ± 0.85	102.60	0.83
750	755.1 ± 5.82	100.69	0.77

For repeatability of injections (n=5), RSD was ≤2.0%, as detailed in ICH guidelines [448] and thus injections were accurate for all concentrations tested (Table 2-7), further underpinning the precision of the assay. The accuracy of the assay was found to be greater than 97.69% (Table 2-6).

Table 2-7: Injection repeatability for three different CTX concentrations. The results represent mean ± SD, n=5 independent batches.

Spiked concentration of CTX (µg/mL)	***Peak intensity ± SD***	***RSD (%)***
7.5	3.8 ± 0.0	0.0
100	49.6 ± 0.3	0.7
750	369.7 ± 2.0	0.5

LLOD and LLOQ parameters, which are particularly affected by small concentration changes and are thus variable, were calculated according to Equation 2-1 and Equation 2-2 and found to be 1.44 µg/mL and 4.37 µg/mL respectively, indicating that the method demonstrates sufficient sensitivity for detecting and quantifying low concentrations of the analyte.

2.4.2.4. Specificity and Robustness of the Method

There was no interference from formulation components at the Rt of the CTX analyte peak, and peak purity data revealed that there were no co-eluting peaks and no interference from impurities at the Rt of CTX (Rt = 1.365 min, Figure 2-10).

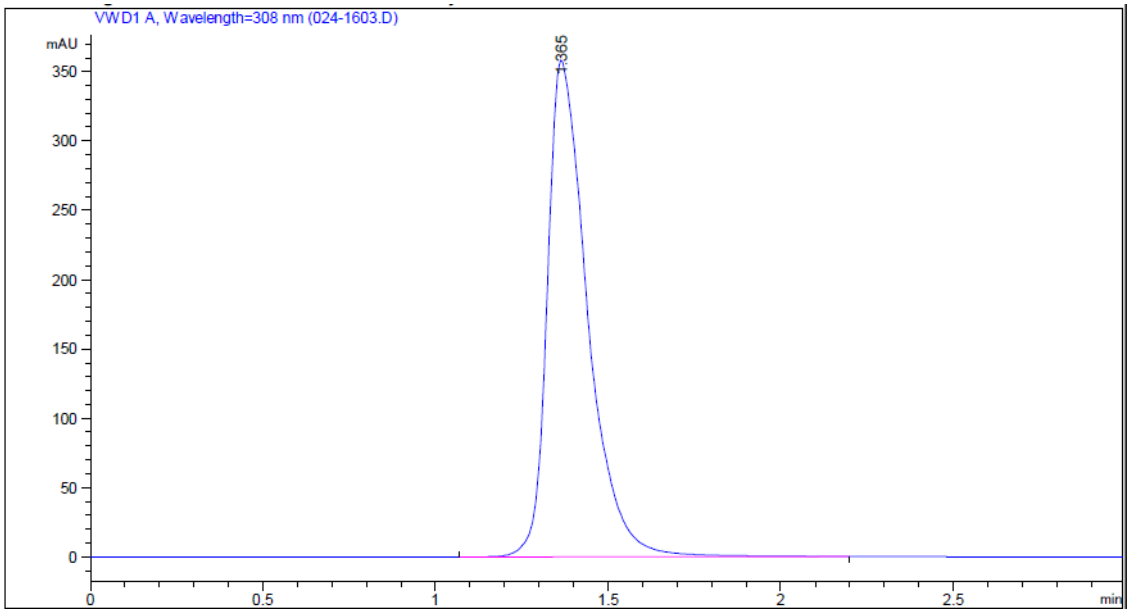

Figure 2-10: CTX HPLC chromatogram showing a distinct analyte peak at 1.365 min with no interference from formulation components or impurities, confirming the specificity of the method for CTX detection.

Robustness of the analytical procedure was certified by its capacity to remain unaffected by small but deliberate variations, with results summarized in Table 2-8. Findings showed that there were no significant changes in CTX Rt when method parameters were changed.

Table 2-8: Effect of varying method parameters on CTX Rt (min)

	Flow rate (mL/min)			Column temperature (°C)			Wavelength (nm)		
Parameters	**0.9**	**1**	**1.1**	**25**	**30**	**35**	**303**	**308**	**310**
CTX 7.5 µg/mL	1.522	1.372	1.249	1.370	1.372	1.370	1.372	1.372	1.370
CTX 100 µg/mL	1.521	1.373	1.248	1.371	1.373	1.370	1.372	1.373	1.372
CTX 750 µg/mL	1.522	1.371	1.248	1.371	1.371	1.371	1.372	1.371	1.372

2.4.2.5. CTX Solution Stability

Finally, the stability of CTX in analytical solutions was evaluated at different conditions as described in 2.3.2.2.6 up to 4 days. The freshly prepared calibration standards (at corresponding concentration levels to the stability study samples) were considered as containing 100% of the initial analyte content. Results revealed that the CTX solution remained stable within an acceptable range of ±5% from the initial concentration, which is commonly considered as an acceptable criterion in stability studies based on standard analytical practices [448] when stored for up to 96 hours in the fridge (5 °C), freezer (-18 °C) and at room temperature (25 °C, Table 2-9).

Table 2-9: CTX stability, expressed as percentage of initial concentration, at 25 ± 2 °C (A), 5 ± 3 °C (B), and -18 ± 3 °C (C) for up to 96 hours. Results represent the mean ± SD of three replicate measurements.

	Room Temperature 25 °C (A)				
CTX concentration (µg/mL)	**Storage time (h)**				
	0	**4**	**8**	**24**	**96**
7.5	100.00	102.98 ± 1.57	100.95 ± 3.12	94.85 ± 3.00	99.68 ± 0.45
100	100.00	98.00 ± 0.76	96.75 ± 0.78	95.80 ± 0.78	101.33 ± 1.18
750	100.00	100.89 ± 0.31	99.72 ± 0.17	98.80 ± 0.42	105.54 ± 0.95
	Fridge 5 °C (B)				
7.5	100.00	103.21 ± 1.64	100.35 ± 3.28	103.90 ± 2.09	105.46 ± 1.68
100	100.00	99.25 ± 0.97	103.96 ± 1.84	99.41 ± 0.54	103.50 ± 1.27
750	100.00	102.42 ± 0.74	107.73 ± 5.71	95.86 ± 0.27	98.42 ± 0.87
	Freezer -18 °C (C)				
7.5	100.00	99.49 ± 1.51	100.86 ± 0.24	99.66 ± 0.24	102.57 ± 2.10
100	100.00	100.90 ± 0.28	100.94 ±0.40	100.51 ± 0.05	100.56 ± 0.45
750	100.00	97.03 ± 0.27	99.14 ± 0.12	99.88 ± 0.07	100.35 ± 0.64

2.4.3. CTX-loaded CS NPs

Achieving high drug loading efficiency within CS NPs presents a challenge [478], particularly given the high water solubility of CTX, which increases the risk of drug leakage during encapsulation [479]. Such leakage can compromise the formulation's effectiveness, as well as drug stability issues like aggregation, sedimentation, or crystallization [480], which may reduce the shelf life and efficacy post-administration. The size and surface charge of nanoparticles also play a crucial role, impacting pharmacokinetics [481], cellular uptake, and targeted delivery. Consequently, optimizing both parameters is essential for effective and stable drug delivery.

To assess the impact of CTX loading on the physicochemical properties of CS NPs, varying CTX loading concentrations (0.3 mg/mL, 0.5 mg/mL, 0.7 mg/mL, 1 mg/mL, 2 mg/mL and 3 mg/mL) were incorporated within CHT NP and CHCL NP formulations. Other process and formulation variables for CTX-loaded CS NP manufacture, namely CS and TPP concentrations, TFR and FRR were established in 2.4.1 and are summarized above in Table 2-5. These optimized parameters were kept fixed while CTX loading

concentrations varied and thus, only the effect of one variable on loaded NP size, PDI, Z-Potential and EE% was examined in this study. Increasing concentration of CTX were added either to CS solutions or TPP solutions for both CHT and CHCL NPs production as shown in Figure 2-11.

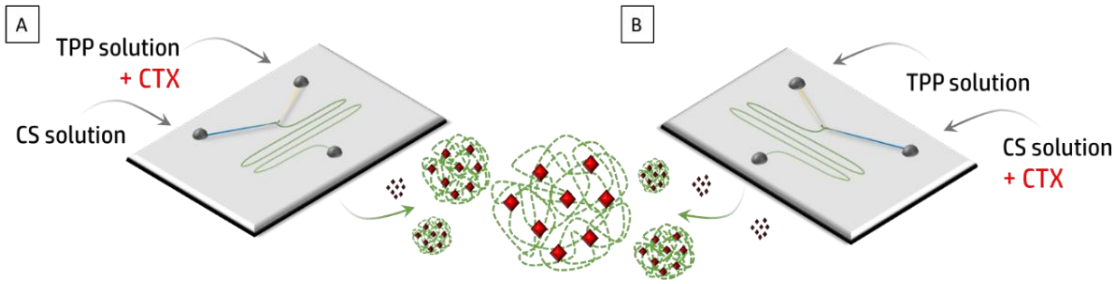

Figure 2-11: Schematic illustration of microfluidic manufacture of CTX-loaded CS NPs by adding increasing CTX loading concentrations to either TPP solution (A) or CS solution (B).

The loading of CTX within CHT NPs resulted in a similar size compared to empty CHT NPs, when different CTX loading concentrations were added to TPP solution (Figure 2-12A). A one-way ANOVA with Tukey's post-hoc comparison revealed no significant difference in NP size between empty and CTX-loaded CHT NPs produced in this manner ($p>0.005$). In contrast, when CTX-loaded CHT NPs were manufactured using 3 mg/mL of CTX added to CHT, NP size increased compared to the empty formulation ($p=0.002$ for 3 mg/mL of CTX in CHT solution and empty NPs (Figure 2-12A).

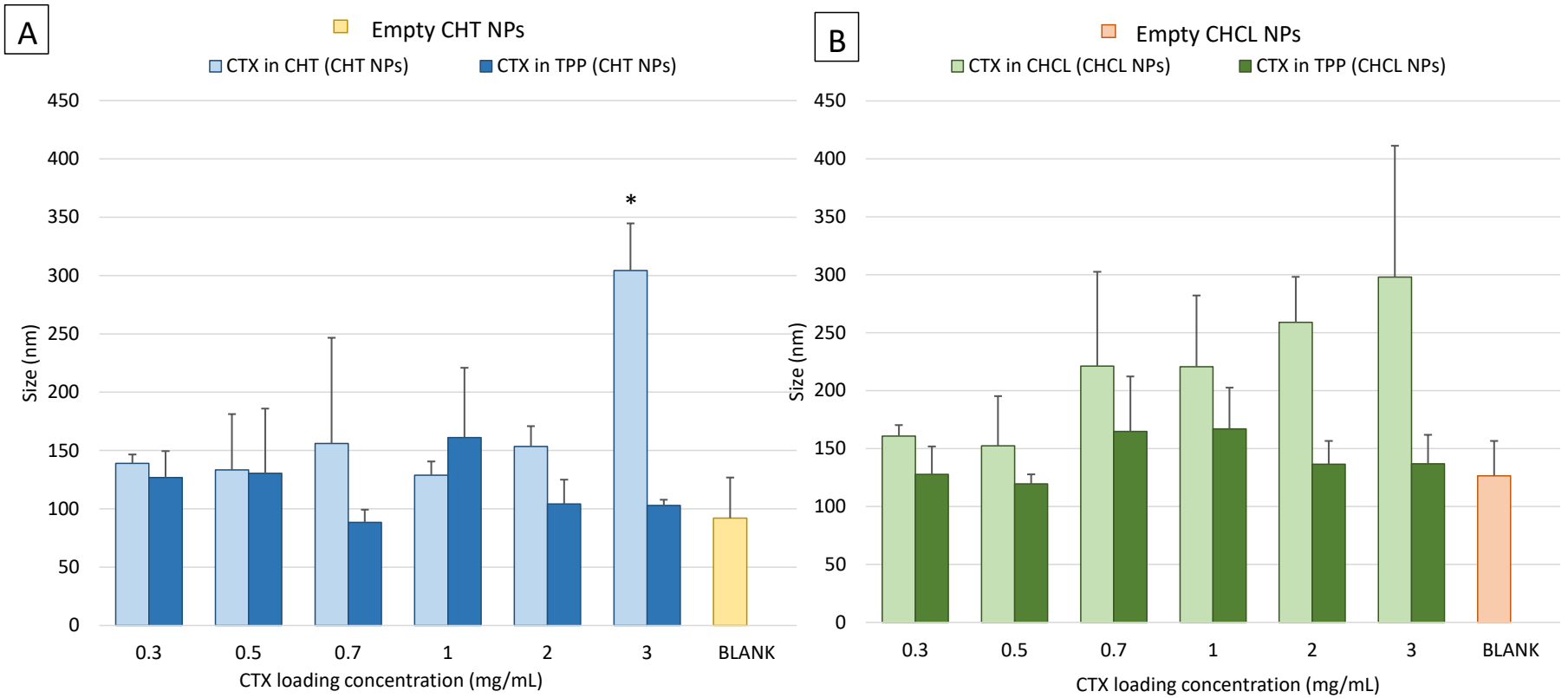

Figure 2-12: The effect of increasing CTX loading concentrations on CHT NP (A) and CHCL NP (B) size produced by microfluidic mixing at TFR 0.64 mL/min and FRR 4:1 (A) or FRR 3:5:1 (B) compared to empty CHT NPs (A) and CHCL NPs (B). The results represent mean ± SD, n=3 independent batches. CHT NPs manufactured with 3 mg/mL CTX loading concentration added to CHT solution showed a significantly different size from formulations manufactured with lower CTX loading concentrations added either to CHT or TPP solution, empty NPs and CTX-loaded formulation manufactured with 3 mg/mL CTX loading concentration added to TPP solution ($p<0.05$). Statistical analysis refers to CTX added either to CHT or CHCL solution.

Regarding CTX-loaded CHT NP PDI, the trend was similar to that obtained for NP size. As shown in Figure 2-13A, the PDI of loaded formulations produced by adding CTX to CHT solution was slightly higher than the PDI of formulations prepared by adding CTX to TPP solution ($p<0.001$ for NPs prepared by loading 3 mg/mL of CTX in CHT solution compared to 3 mg/mL of CTX in TPP solution) or blank CHT NPs ($p=0.001$ for NPs prepared by loading 3 mg/mL of CTX in CHT solution compared to empty NPs), indicating heterogeneous sample size distribution. When loaded NPs were produced by adding CTX to TPP solution, there was no significant difference in PDI between loaded and empty formulations ($p>0.005$).

With respect to CTX-loaded CHCL NPs, the one-way ANOVA with Tukey's post-hoc comparison performed to compare the effect of increasing CTX loading concentration on NP size showed that there was no significant difference between loaded and empty formulations, when CTX was either added to TPP or CHCL solutions (Figure 2-12B). Nevertheless, the trend was similar to that observed for CHT NPs, suggesting a higher mean NP size when CTX was added to CHCL rather than TPP solution. Moreover, in accordance with literature [482], the current study highlighted a trend showing higher NP size with increasing CTX loading concentration. When CTX is added directly to CHCL, the carbonyl group of CTX may interact with CHCL amino groups, decreasing the positively charged amino-groups available for ionic interaction with the negatively-charged TPP counter ions upon solution mixing [483]. Thus, increasing CTX-loading concentrations results in a reduction in CHCL and TPP interactions, leading to bigger NP size.

CTX was added to either the CS or TPP solutions because, despite limited direct information on the solubility of CTX in weak acids available in literature, CTX resulted to be highly soluble in both water and weakly acid solutions. In literature, the addition of drugs to CS solution has been widely investigated for the encapsulation of antibiotics, antifungal and anticancer drugs [440, 450-455], while the addition of drugs to TPP solution is mainly used for oligonucleotides [457].

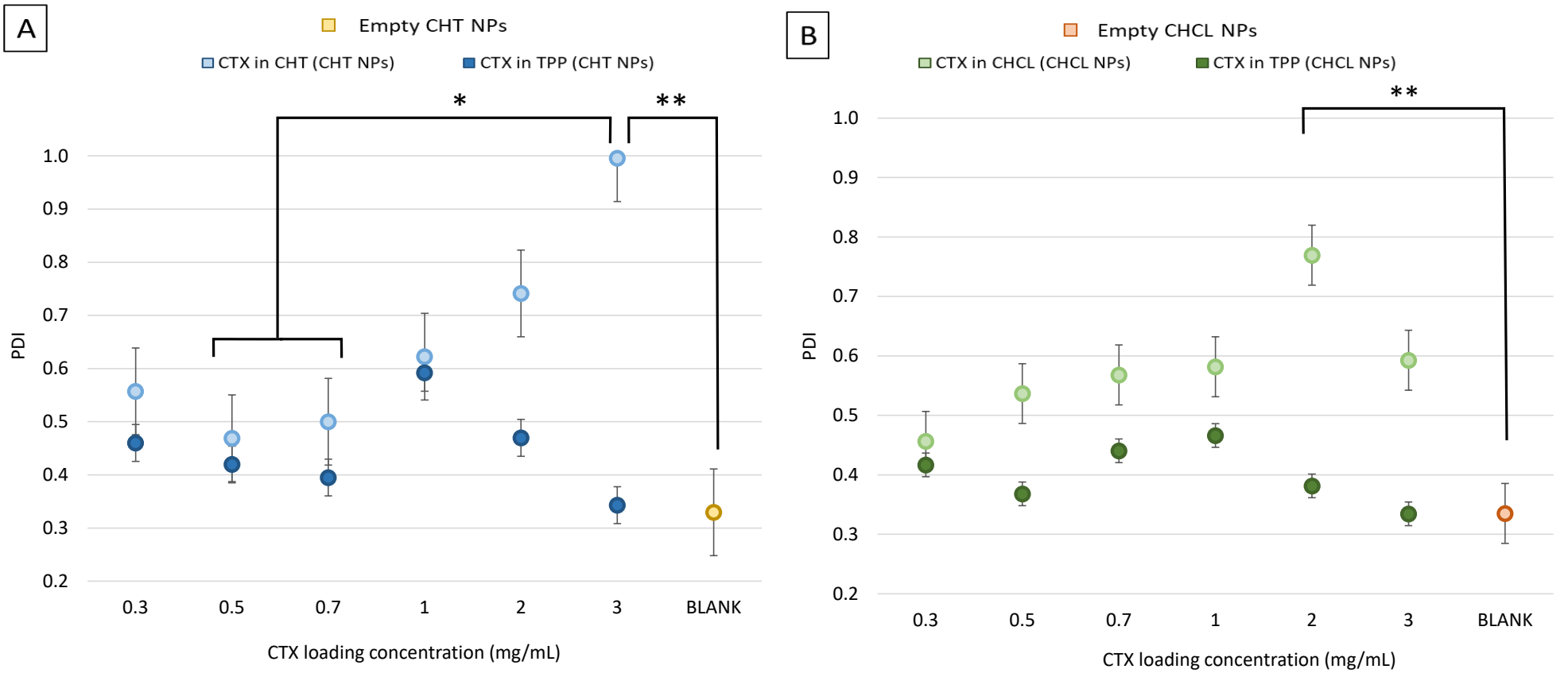

Figure 2-13: The effect of increasing CTX loading concentration on CHT NP (A) and CHCL NP (B) polydispersity index (PDI) produced by microfluidic mixing at TFR 0.64 mL/min and FRR 4:1 (A) or FRR 3:5:1 (B) compared to empty CHT NPs (A) and CHCL NPs (B). The results represent mean ± SD, n=3 independent batches. Statistical analysis refers to CTX added either to CHT or CHCL solution. CHT and CHCL NP PDI when CTX was added to TPP solution did not show statistical differences. If a p-value is less than 0.05, it is flagged with one star (*). If a p-value is less than 0.01, it is flagged with 2 stars (**).

Oligonucleotides are not stable in acid solutions and are negatively charged molecules, which can act to enhance complexation with CS through interaction of polyanionic oligonucleotides with positively charged CS [484]. However, as mentioned above, the addition of the antibiotic to either CS or TPP solution has never been systematically investigated to understand the impact on nanoparticle physiochemical characteristics in literature.

In general, higher PDI values were obtained when CTX was added to CHCL solution rather than TPP solution; however, only the formulation prepared with 2 mg/mL of CTX added to CHCL solution was significantly different from the formulation prepared by adding the same CTX-loading concentration to TPP solution ($p=0.003$) and from empty CHCL NPs ($p=0.001$, Figure 2-13).

The Z-Potential of CTX-loaded CHT NPs was found to be positive and in the range between 7.28±3.42-11.23±0.12 mV, with no significant differences between empty and loaded NPs ($p>0.005$, Figure 2-14 A). Similarly, there was no significant difference between the Z-Potential of CTX-loaded CHCL NPs and empty CHCL NPs. There was however a trend indicating a slight decrease in NP surface charge with increasing CTX-loading concentrations, ranging from 34.27±3.54 to 26.43±1.41 mV, prepared with 0.3 mg/mL and 3 mg/mL of CTX, respectively (Figure 2-14 B). Empty and CTX-loaded CHCL NPs showed a higher Z-Potential compared to CHT NPs ($p<0.005$ – Figure 2-14 B), indicating a more stable colloidal suspension system that prevents nanoparticle aggregation [485]. Previous studies highlighted that the Z-Potential of CS nanoparticles is a function of the polymer concentration [486], which is doubled, according to optimum parameters, for the preparation of CHCL NPs compared to CHT NPs. Hence, the higher Z-Potential of CHCL NPs compared to CHT NPs can be attributed to an initial higher polymer concentration.

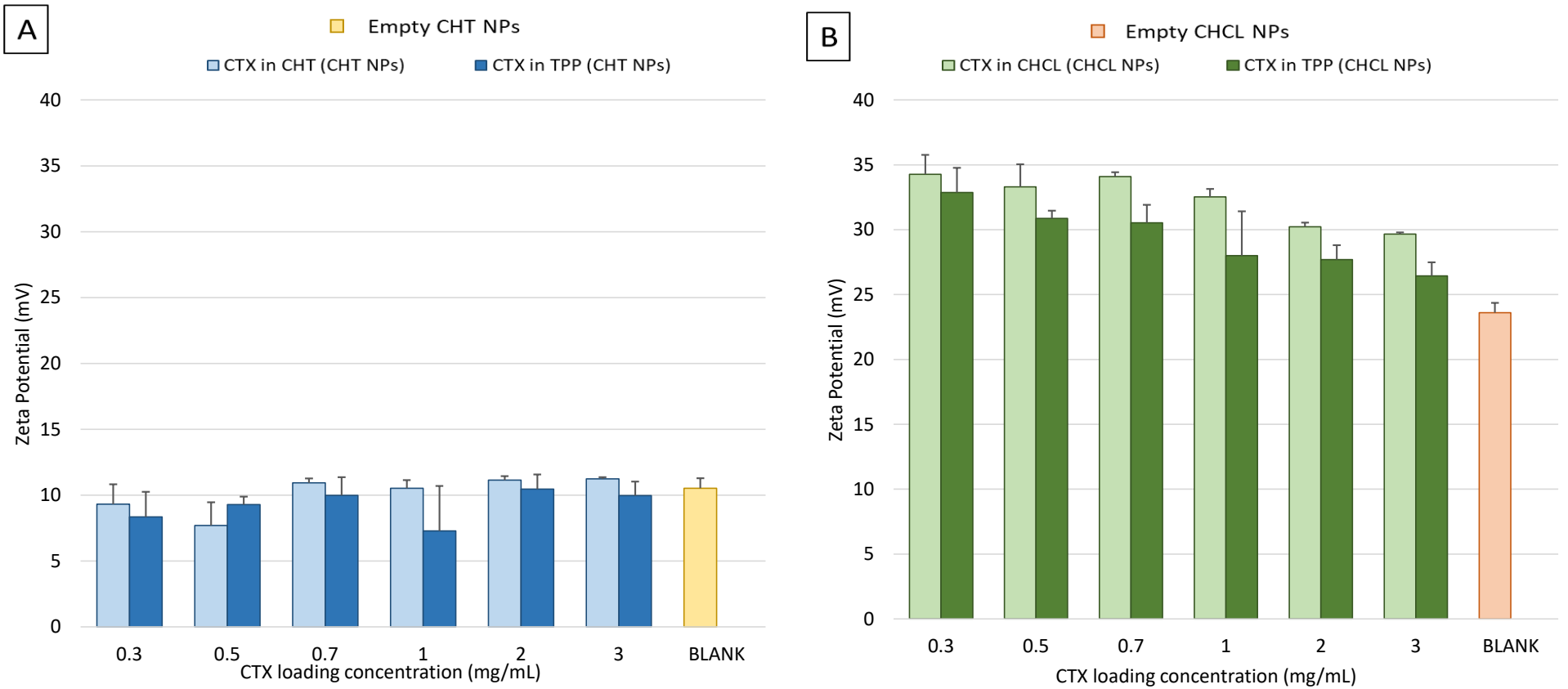

Figure 2-14: The effect of increasing CTX loading concentrations on CHT NP (A) and CHCL NP (B) Z-Potential produced by microfluidic mixing at TFR 0.64 mL/min and FRR 4:1 (A) or FRR 3:5:1 (B) compared to empty CHT NPs (A) and CHCL NPs (B). The results represent mean ± SD, n=3 independent batches.

The effect of CTX loading concentrations on NP EE% was also investigated by increasing the amount of initial CTX from 0.3 mg/mL to 3 mg/mL. Figure 2-15 A shows that, in the case of CHT NPs where CTX was added to TPP solution, as the initial CTX loading concentration increases the EE% increases from 14.8 ± 9.4% to 37.7 ± 1.6% ($p<0.005$). For CHCL NPs (Figure 2-15 B), the trend was similar as the lowest CTX loading concentration added to TPP resulted in a formulation with an EE% significantly lower than other formulations prepared with higher CTX loading concentrations. Despite the difference in CTX EE% observed, when 3 mg/mL of CTX was added to TPP solution for CHT and CHCL NP production, the size of formulations was comparable to empty formulations (Figure 2-12) as discussed earlier. The present findings of increases in EE% with increasing drug loading concentration are in accordance with previous studies carried out by Sobhani *at al.* where ciprofloxacin EE% within CS NPs was found to be increased slightly by increasing the amount of drug in polymer : drug ratios (W:W) from 1:0.125 to 1:0.5 [440]. On the other hand, the authors also noticed that further increase in polymer : drug ratio from 1:0.5 to 1:8 led to a decrease in drug EE% due to saturation of nanoparticle loading capacity [440]. Contrary to Sobhani *et al.*, in the present study a similar decrease in EE% at higher loading concentrations was not noted. This might indicate that the saturation capacity of NPs was not reached using a 3 mg/mL CTX loading concentration. The encapsulation efficiency of nanoparticles can be influenced by various factors, such as the size and composition of the nanoparticles, the method of preparation, and the properties of the drug encapsulated [487, 488]. Thus, depending on the NP physiochemical characteristics the relationship between loading concentration and encapsulation efficiency might vary [489].

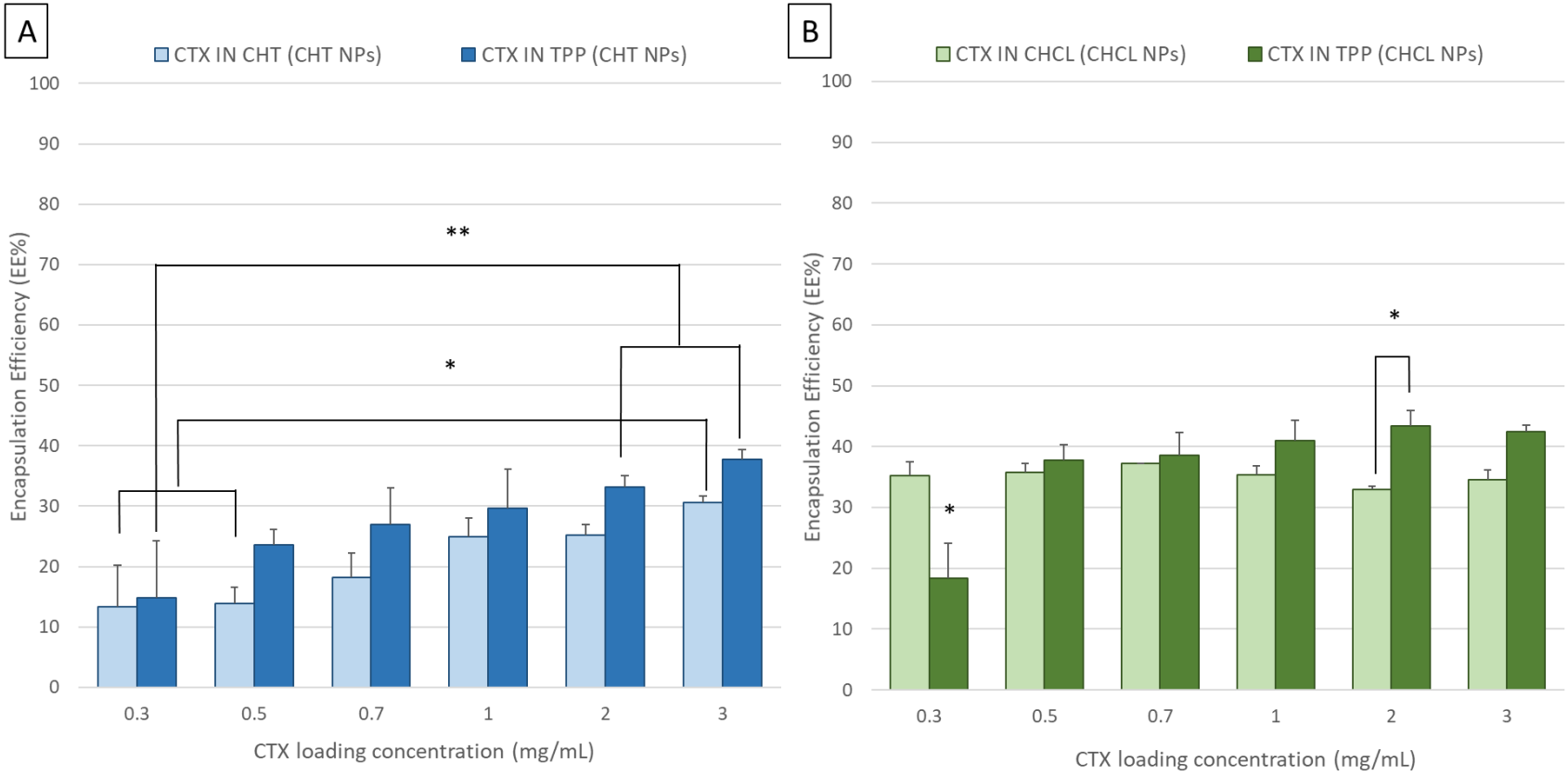

Figure 2-15: The effect of increasing CTX loading concentrations on CHT NP (A) and CHCL NP (B) encapsulation efficiency (EE%) produced by microfluidic mixing at TFR 0.64 mL/min and FRR 4:1 (A) or FRR 3:5:1 (B). EE% was indirectly calculated using a validated RP-HPLC method by quantification of unentrapped CTX following centrifugation using Centrisart® tubes. The results represent mean ± SD, n=3 independent batches. If a p-value is less than 0.05, it is flagged with one star (*). If a p-value is less than 0.01, it is flagged with 2 stars (**).

Figure 2-16 shows that, while CTX EE% showed a slight increase with increasing loading concentration, the amount of CTX (μg) encapsulated within CS NPs/mL of formulation increased in a statistically significant manner over the entire loading concentration range. Furthermore, the amount of drug encapsulated at CTX loading concentrations of 2 and 3 mg/mL was significantly higher for both CHT NPs and CHCL NPs when CTX was added to TPP solution rather than CS solution.

The study's findings reveal important distinctions between EE% and the total amount of CTX loaded within CS NPs at varying CTX loading concentrations. The data show a steady increase in EE% for CHT NPs without plateauing, even at higher CTX loading concentrations (Figure 2-15 A), suggesting that the nanoparticles have not reached their loading capacity. In contrast, CHCL NPs show a less pronounced increase in EE%, potentially indicating a nearing saturation point, despite no plateau was reached for the amount of CTX encapsulated within CHCL NPs (Figure 2-16 B). Notably, very little literature systematically explores the impact of adding drugs, particularly water-soluble antibiotics like CTX, to different phases (CS vs. TPP solution) during nanoparticle formation. This aspect of drug loading is often under-explored, despite its significant influence on encapsulation efficiency and NP properties. Therefore, the current study provides valuable insights into how this step affects both EE% and total drug loaded withing the formulation, highlighting the novelty and importance of investigating the drug addition strategy to optimize loaded NP-based drug delivery systems.

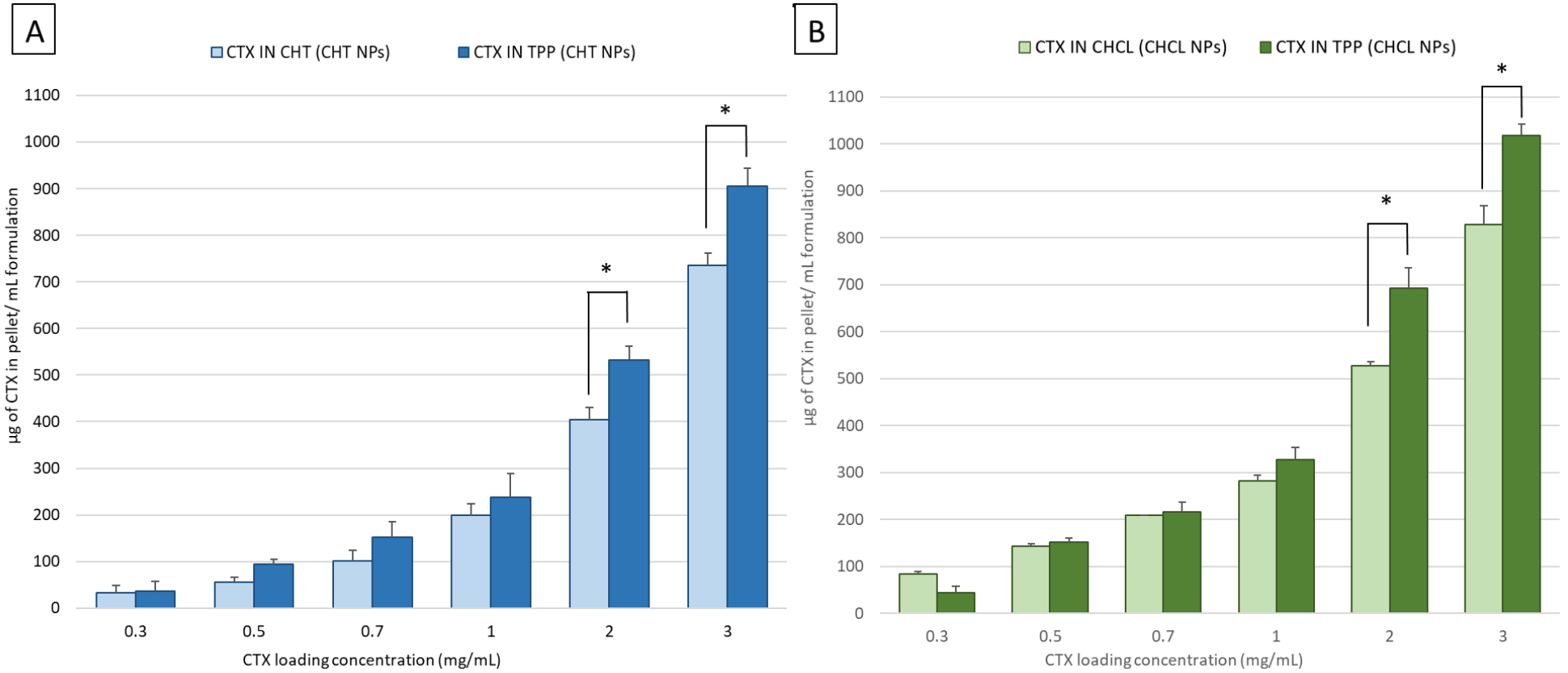

Figure 2-16: The amount of CTX successfully encapsulated within CHT NPs (A) and CHCL NPs (B) using increasing CTX loading concentrations. Amount of CTX successfully encapsulated was calculated by subtracting Wu, the amount of CTX present in the ultrafiltrate quantified by HPLC after centrifugation, from Wt, the calculated theoretical amount of CTX added to NPs during the manufacturing process. The results represent mean ± SD, n=3 independent batches. If a p-value is less than 0.05, it is flagged with one star (*). If a p-value is less than 0.01, it is flagged with 2 stars (**).

As a further study, the impact of – purifying NPs by ultracentrifugation, in contrast to ultrafiltration as employed in the studies detailed above, – on NP size, PDI and Z-Potential after resuspension of pelleted NPs in PBS was determined. This comparative study was conducted as the separation of nanoparticles using Centrisart® ultrafiltration units may be problematic, especially for high particle content formulations, due to impaction and clogging of the filter, leading to an incomplete ultrafiltration of the sample [490]. On the other hand, separation of NPs using ultracentrifugation, which is achieved by forcing particles to sediment into a pellet under high forces and long times, might be unable to sediment particles smaller than 100 nm [490] and subsequent redispersion of pelleted NPs can be challenging because the forces acting on the nanoparticles during ultracentrifugation can cause them to come into close proximity and form strong interactions, leading to irreversible aggregation [491]. Thus, to investigate, three different formulations for each CS type were manufactured using 0.3, 1 and 3 mg/mL of CTX loading concentration added to TPP solution and purified via ultracentrifugation at 25 000 rpm for 30 minutes at 10 °C (Figure 2-17). These concentrations were chosen to represent the lowest, mid-range, and highest drug loading concentrations previously investigated in our studies, providing a comprehensive view of the impact across a range of CTX loading concentrations. CTX was added to the TPP solution based on prior data showing that this approach resulted in more favorable outcomes in terms of NP size, PDI, Z-Potential and EE% compared to adding CTX to the CS solution.

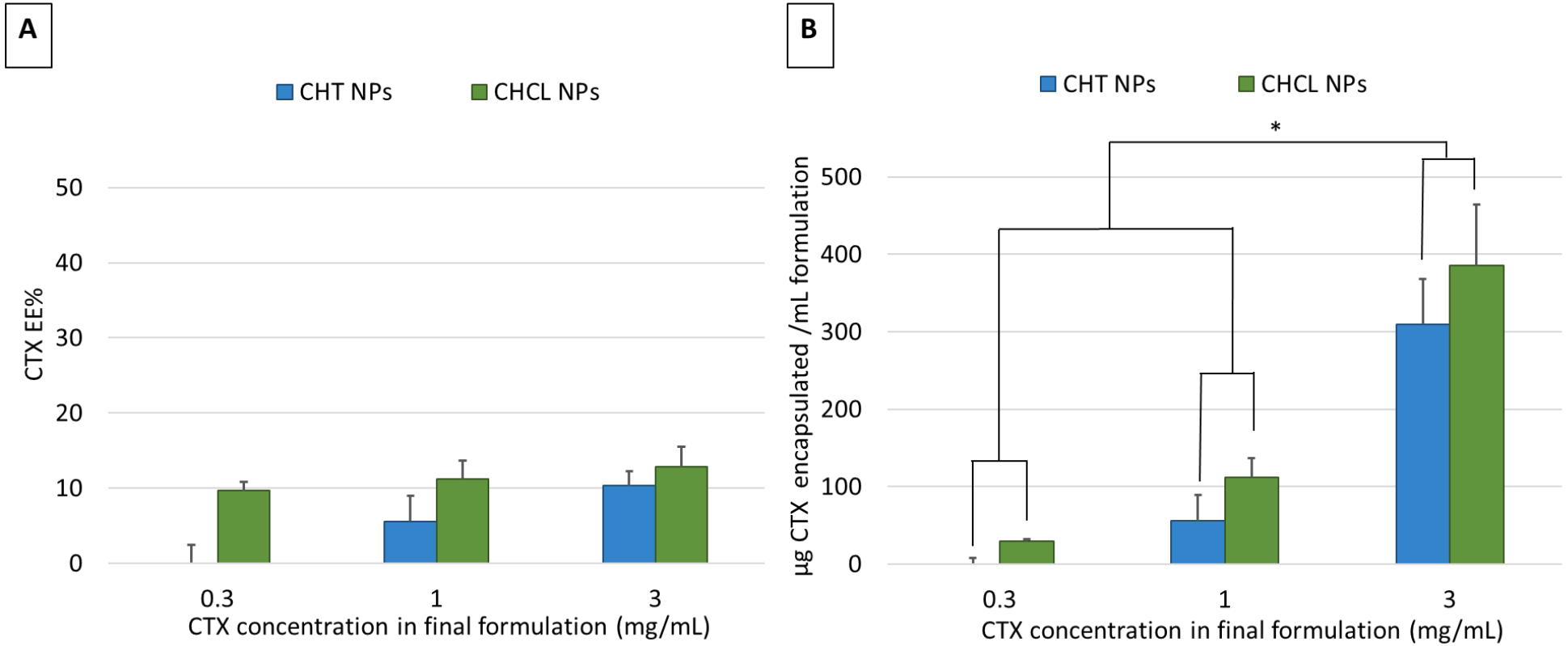

Figure 2-17: CTX EE% (A) and amount of CTX successfully encapsulated (B) within CHT and CHCL NPs produced by microfluidic mixing at TFR 0.64 mL/min and FRR 4:1 (CHT NPs) or FRR 3.5:1 (CHCL NPs). EE% and the amount of CTX encapsulated was indirectly calculated using a validated RP-HPLC method following ultracentrifugation and resuspension of NPs. The results represent mean ± SD, n=3 independent batches (, p<0.05).*

The results of this study, shown in Figure 2-17 A, revealed a much lower CTX EE% compared to the previous investigations where Centrisart® tubes were employed ($p<0.005$, Figure 2-15). The amount of CTX successfully encapsulated within formulations (Figure 2-17 B) was approximately half that calculated for the corresponding formulations when separated by centrifugal ultrafiltration (Figure 2-16). To further this investigation a direct comparison of empty and loaded NP size, PDI and Z-Potential immediately following microfluidic preparation, in contrast to following ultrafiltration or ultracentrifugation was also conducted. Each formulation was analyzed immediately after preparation and again after ultrafiltration with Centrisart® units or ultracentrifugation. Following purification, each formulation was diluted to 1 mL (ultrafiltration) or resuspended in the original formulation volume (ultracentrifugation). Figure 2-18 shows the results of the conducted study.

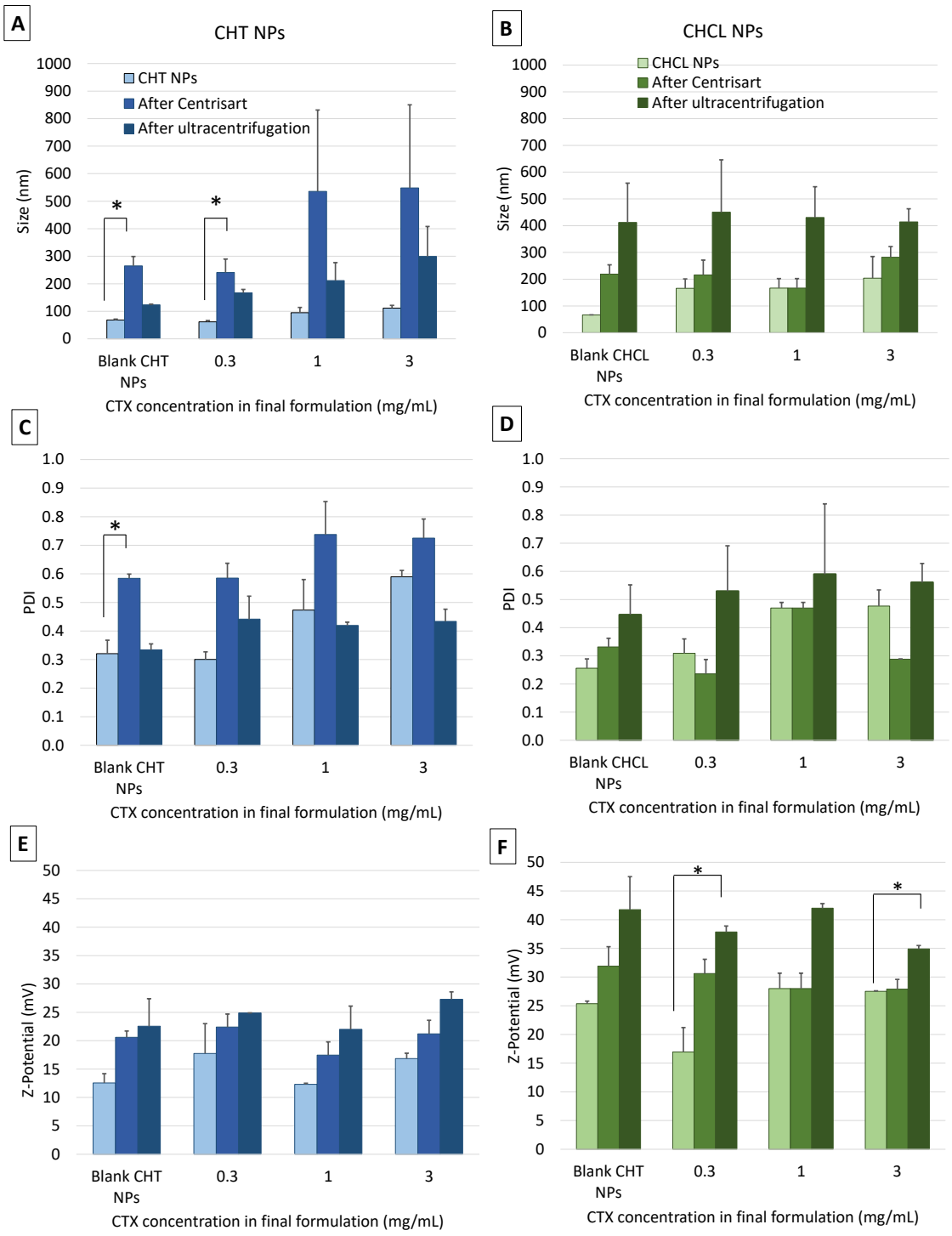

Figure 2-18: Size (A, B), PDI (C,D) and Z-Potential (E, F) of empty and loaded CHT NPs (blue shades) and CHCL NPs (green shades) straight after preparation, after centrifugal ultrafiltration and after ultracentrifugation. After purification, the pellet was diluted (ultrafiltration) or resuspended (ultracentrifugation) in the initial volume of the formulation prior to analysis. The results represent mean ± SD, n=3 independent batches (= p<0.05)*

A one-way ANOVA with Tukey's post-hoc analysis for each formulation revealed that there was no significant difference in size and PDI of each formulation immediately after production, and after purification using ultracentrifugation. In contrast, for CHT NPs, a statistically significant increase in particle size was found for empty and 0.3 mg/mL CTX-loaded NPs when particles were purified by centrifugal ultrafiltration. For higher CTX loading concentrations there was no significant difference in size, PDI and Z-Potential of NPs purified by ultrafiltration or ultracentrifugation, however, there was a trend showing an increase in particle size and PDI after centrifugation with Centrisart® units. On the other hand, for empty and CTX-loaded CHCL NPs the study highlighted a reversal in the trend observed for CHT NPs. While the one-way ANOVA statistical analysis didn't reveal any significant differences in particle size and PDI after either purification method, resuspended NPs at all loading concentrations tested showed a trend for increasing particle size and PDI after ultracentrifugation. Regarding the Z-Potential of CTX-loaded CHT NPs, the one-way ANOVA statistical analysis with Tukey's post-hoc analysis showed no significant difference in Z-Potential between formulations purified via ultrafiltration and ultracentrifugation. In contrast, for CTX-loaded CHCL formulations, there was a significant increase in Z-Potential for formulations loaded with 0.3 mg/mL and 3 mg/mL of CTX when purified via ultracentrifugation.

Ultrafiltration offers significant advantages for nanoparticle purification in drug delivery applications. By allowing separation based on size, ultrafiltration membranes with specific pore sizes retain particles larger than the pores while smaller particles pass through, facilitating efficient purification [492]. This method is also versatile and mild, as it does not require prolonged centrifugation or dilution of formulations [490]. Furthermore, ultrafiltration can separate nanoparticles from unbound drug molecules without dependence on the density of the particles [493], making it suitable for diverse nanoparticle-related applications. However, ultrafiltration is not without limitations. Drug-filter interactions can cause drug precipitation within the filter pores, potentially leading to an overestimation of encapsulation efficiency (EE%) when the drug in the ultrafiltrate compartment is analyzed. The presence of nanoparticles may obstruct the ultrafiltration membrane [492], hindering the flow of unentrapped drug, while particle loss may occur as nanoparticles adhere to the regenerated cellulose chains within the

membrane [494]. For these reasons, in this study, ultracentrifugation was preferred as a more reliable and robust method for separating free CTX from CS NPs and determining EE%. Ultracentrifugation, on the other hand, also presents limitations. It often requires prolonged centrifugation periods and careful handling to avoid particle aggregation and density-based losses as discussed in section 5.1.2. Despite the known limitations of both methods, ultrafiltration was chosen for its efficiency and the ability to maintain monodispersity of the nanoparticles in this study.

2.4.4. Antibacterial Activity Evaluation

2.4.4.1. Bacterial Strains Characterization

Characterizing bacterial strains is critical to verify their identity and relevance as clinical models, ensuring the study results are applicable to real-world infections and reflective of the behavior of targeted pathogens in clinical scenarios. Therefore, bacterial strains to be employed as part of a clinically relevant pathogen panel in this study and throughout the thesis were first characterized, with results summarized in Table 2-10. As expected, *K. pneumoniae, E. coli and P. aeruginosa* were found to be rod-shaped and Gram negative while *S. aureus* was coagulase positive, Gram positive, cocci-shaped and cells tended to be arranged in clusters. These characterizations align with known traits for each species, validating the panel selection for this study. Additionally, all strains were positive for catalase test and *P. aeruginosa* was further distinguished by its positive oxidase test (Table 2-10). This combination of tests confirmed the expected morphology and biochemical properties for each pathogen, ensuring that the strains used are representative of typical clinical isolates.

Table 2-10: Characterization of bacteria employed in the study

	P. aeruginosa	***S. aureus***	***E. coli***	***K. pneumoniae***
Gram stain test	Negative	Positive	Negative	Negative
Gram stain color	Red/Pink	Purple	Pink	Pink
Shape	Rods	Cocci	Rods	Rods
Coagulase test	-	Positive	-	-
Oxidase test	Positive	-	-	-
Catalase test	Positive	Positive	Positive	Positive

2.4.4.2. CTX-loaded CS NP antimicrobial activity

The antimicrobial properties of CS against a wide variety of bacteria have been reported in literature [495] and several studies have proved the antibacterial activity of CS NPs [404, 413, 416]; however, the reported effectiveness of CS as an antimicrobial agent is not consistent, varying depending on its physicochemical characteristics and the type of microorganism being targeted [496]. As a further complication, the poor water solubility of CS can lead to challenges in the formulation and administration of CS-based NPs – this can be overcome by derivatizing free amino groups of CS to obtain more water-soluble derivatives such as CHCL [497].

In this study, optimized CTX-loaded CS NPs were prepared with CTX loading concentrations of 0.3, 1, and 3 mg/mL for both CHCL and CHT formulations. These concentrations were selected to represent a range from low to high CTX loading levels, allowing a thorough assessment of antimicrobial activity across varying drug loading within the formulation. CTX was added specifically to the TPP solution, as previous findings indicated this approach yielded more favorable results in terms of particle size, PDI, and EE% compared to adding CTX to the chitosan solution. The antimicrobial properties of these CTX-loaded CHT and CHCL NPs were investigated alongside empty CHT and CHCL NPs against *E. coli*, *K. pneumoniae*, *P. aeruginosa* and *S. aureus* as a panel of clinically relevant Gram-negative and Gram-positive pathogens. An agar well diffusion assay was utilized in this first instance as this methodology has been previously employed to screen the antibacterial activity of antibiotic-loaded NPs [498, 499].

Alongside CTX-loaded CHT and CHCL NPs, as described in section 2.3.2.4.2, free CTX, PBS as negative control, and gentamicin (10 µg, CN10) or ciprofloxacin discs (5 µg , CIP5) as a positive control were tested. All inhibition zones produced were plotted according to their size as shown in Figure 2-19. A prominent zone of inhibition for free and encapsulated CTX was shown against *E. coli* and *K. pneumoniae*. The zone of inhibition was similar comparing free and encapsulated CTX at all three concentrations tested. Incorporating CTX into CS nanoparticles maintained its antimicrobial activity, showing that the formulation did not compromise the effectiveness of CTX. On the other hand, smaller zones of inhibition were shown for free CTX against *P. aeruginosa* and *S. aureus* which is in accordance with literature [500, 501]. The higher antibacterial activity observed against *E. coli* and *K. pneumoniae* compared to *S. aureus* aligns with literature reports on CTX-loaded nanoparticles, which have demonstrated enhanced efficacy against Gram-negative bacteria due to favorable electrostatic interactions between positively charged NPs and the negatively charged bacterial cell walls [502]. For *P. aeruginosa*, although electrostatic interactions between the CTX-loaded NPs and the bacterial cell surface might still occur, CTX itself exhibits limited intrinsic activity against this pathogen, as is reflected in the literature [503, 504]. This limitation is consistent across both free and nanoparticulate forms of CTX, explaining the relatively smaller zones of inhibition observed for both *P. aeruginosa* and *S. aureus* when compared to *E. coli* and *K. pneumoniae*.

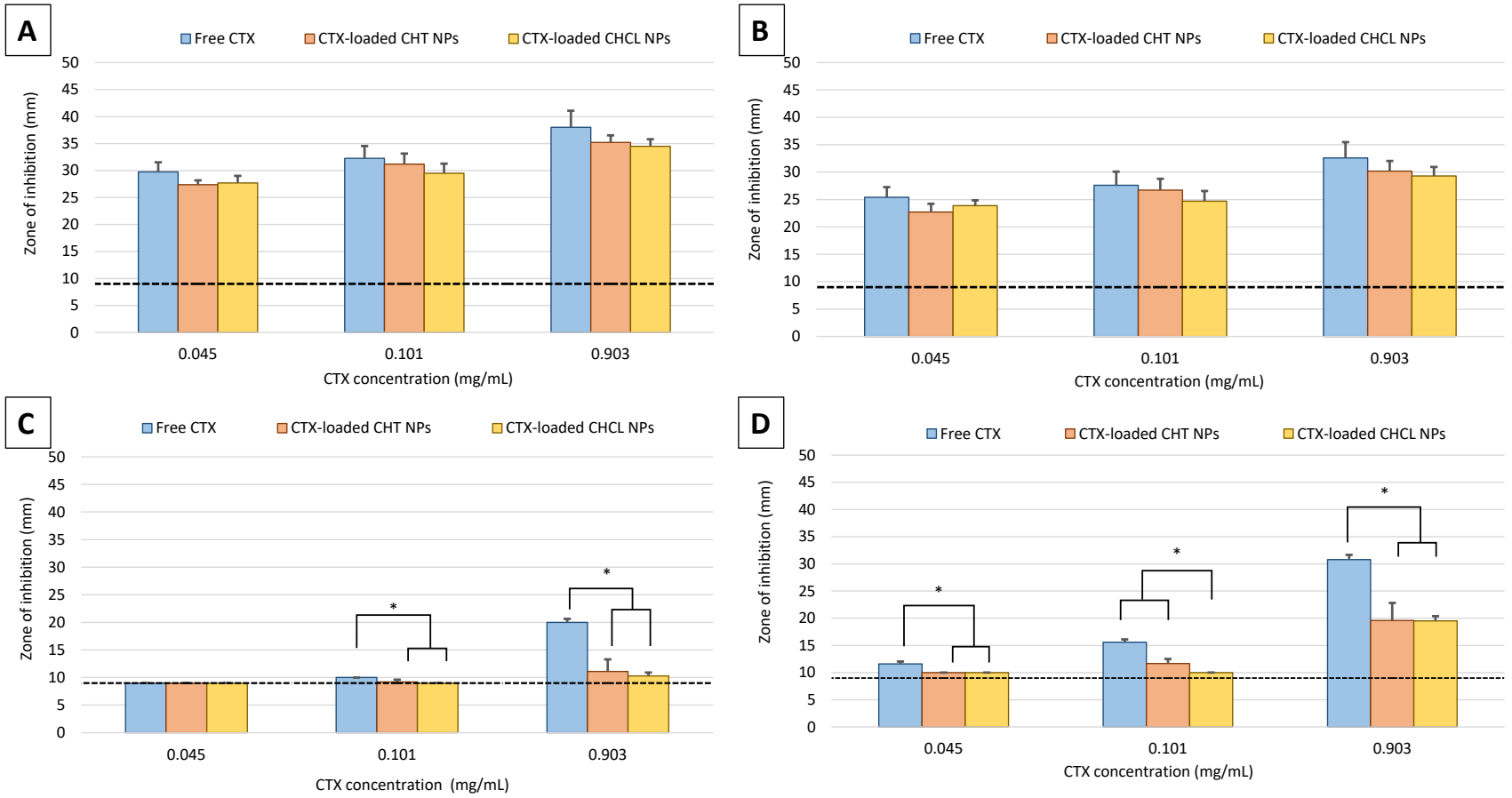

Figure 2-19: Distribution of zone diameters (mm) obtained by well diffusion with empty and CTX loaded NPs at different concentrations (0.045, 0.101 and 0.903 mg/mL) of CTX against E. coli (A), K. pneumoniae (B), P. aeruginosa (C) and S. aureus (D). The results represent mean ± SD, n=4 independent batches (, p<0.05). The dotted line in each figure represents the well diameter (9 mm).*

Moreover, for both *S. aureus* and *P. aeruginosa*, the zones of inhibition shown by CTX-loaded CHT and CHCL NPs at the highest concentration tested were significantly different (smaller) compared to free CTX ($p<0.05$).

Jamil *et al*. showed that the encapsulation of CTX within CS NPs provided effective control against multi-drug-resistant pathogens, outperforming free CTX, which showed no activity [505]. Several factors in the study by Jamil *et al.* could contribute to this increased efficacy: medium molecular weight chitosan was used, likely resulting in higher Z-potential values and smaller particle sizes compared to those in the current study. These physicochemical characteristics can strongly influence the antimicrobial activity of CS NPs, as noted earlier, where size, Z-potential, and molecular weight were all discussed as critical factors for interaction with bacterial cell walls. Moreover, Jamil *et al.* employed a microdilution assay that spanned 6 days [505], which differs significantly from the agar diffusion method used in this study. The prolonged assay time used by Jamil *et al.* could explain the inactivity of free CTX in those results, as CTX may degrade or lose efficacy over extended incubation periods. Additionally, only a single CTX concentration was assessed in the study performed by Jamil *et al.*, potentially missing any concentration-dependent effects that could influence antibacterial performance. These methodological and formulation differences underscore the variability in antibacterial efficacy of CS NPs depending on assay conditions and physicochemical properties, supporting the findings in this study on the role of these parameters in determining nanoparticle efficacy. Similar findings to those of Jamil *et al.* have been also confirmed by other studies carried out on CTX-loaded gold nanoparticles against bacteria resistant to CTX, where the conjugation of CTX to NPs resulted in bigger zones of inhibition as well as antimicrobial activity [498, 506, 507]. Gold NPs are able to penetrate into bacterial cell and cause the lysis of their membrane [507], while their significant payload is readily taken up by bacterial cells, escaping the degradation caused by bacteria [506].

Furthermore, interestingly, no zone of inhibition was obtained for the blank CHT or CHCL NPs (data not shown), despite the documented antimicrobial properties of CS [401-404]. The specific mechanism of CS NP antibacterial activity still remains to be fully

understood. The main role in the antibacterial activity of CS NPs is played by the electrostatic interaction between the positively charged amino groups of CS and anionic groups found on the bacterial cell surface. This causes the disruption of the cell membrane of Gram-positive and Gram-negative bacteria, an alteration in its permeability and also an inhibition of DNA replication followed by bacterial cell death [399, 508].

The antibacterial activity of CS NPs is also dependent on various factors including MW, degree of deacetylation, size, concentration and Z-Potential of NPs [509, 510]. In general, CS with higher degree of deacetylation (97.5%) are expected to have a higher Z-Potential. Hence, the higher positive charge density determines stronger electrostatic interactions and a greater antimicrobial activity [511]. Also, it has been shown that CS nanoparticles prepared from low molecular weight CS have been found to exhibit better inhibitory activity against various microorganisms compared to CS in solution form [512]. In addition to this, CS NPs show a pH-responsive drug release [513] and exhibit stronger inhibitory effects in more acidic conditions [514-516]. Thus, considering all these factors affecting the antimicrobial activity of CS NPs, the reasons for a noted inactivity of empty CS NPs might be multiple. The concentration of CS used in the manufacturing of NPs, along with a degree of deacetylation of 92.2%, contributed to the formation of NPs with a moderate charge density, which may influence the extent of electrostatic interactions between the positively charged amino groups of CS and the negatively charged bacterial cell membrane. Given that CS NPs have been shown to exhibit higher antimicrobial activity at lower pH values [517, 518] this delivery system could hold particular promise in treating biofilm-forming infections that thrive in more acidic environments [518, 519]. Interestingly, while previous studies on similar nanocarriers have reported intrinsic antimicrobial activity [505], the CS-based NPs in this study did not exhibit this property in the agar-based assay used. A likely explanation for this result is that the NPs may not diffuse optimally through the agar medium [520, 521] which could limit the direct interaction between NPs and bacterial cells in this specific setup. This observation suggests that the antimicrobial activity of CTX-loaded NPs may primarily result from the release of CTX rather than NP diffusion through the agar. Consequently, the assay may underestimate the full antimicrobial potential of these

NPs, as it primarily captures the effect of free CTX. These findings open up an interesting area for further investigation into the release kinetics of CTX from CS NPs, which will be explored in later chapters and compared to other delivery systems. Understanding these release kinetics more fully could provide valuable insights into how these NPs function in more complex infection environments, revealing their potential as versatile and effective drug delivery systems.

In addition to aforementioned considerations and comparison between free and NPs-encapsulated CTX, the two CS employed to manufacture CTX-loaded NPs were compared at all the CTX concentrations tested (Figure 2-19). Statistical analysis of well-diffusion assay data was performed to compare CTX-loaded NPs manufactured with both CHT and CHCL. However, no significant differences were found between NPs manufactured with both polymers, indicating comparable antimicrobial activity against *E. coli*, *K. pneumoniae*, *P. aeruginosa* and *S. aureus.* Despite limited literature available on CHCL NP antimicrobial activity, water-soluble derivatives of CS have previously demonstrated enhanced antimicrobial activity due to their permanent positive charge on nitrogen atoms side-bonded to the polymer backbone [522, 523]. Indeed, as discussed above, CS antimicrobial activity is linked to its positive charge, which drives its interaction with negatively charged bacterial cell membranes. Thus, in order to enhance the antimicrobial activity of CS, it is rational to increase its cationic character by introducing additional positively charged moieties [524] by preparing functional derivatives of CS, which is then linked to improved antimicrobial properties [525]. While the current study didn't observe any enhanced antimicrobial activity of CHCL-loaded NPs over CHT-loaded nanoparticles, the use of water-soluble derivatives of CS can still provide several advantages. The solubility of these derivatives in water is crucial for their potential applications in various fields, including medicine, pharmacy, and biotechnology [526]. For instance, water-soluble CS derivatives have been shown to enhance the dissolution of poorly water-soluble drugs, making them promising for pharmaceutical applications [527]. Thus, despite similar antimicrobial efficacy, CHCL NPs might provide additional advantages over CHT NPs in terms of drug delivery. However, it's also possible that the higher surface charge of CHCL NPs could impede their diffusion through the agar, potentially limiting their observed efficacy in this type of assay.

The antimicrobial activity results revealed that both CHT and CHCL NPs loaded with CTX exhibited comparable efficacy against the bacterial panel, confirming that both formulations maintained the antibacterial action of CTX. Given this similarity, the choice of formulation for further development into LPHNPs, discussed in Chapter 2, was based on other factors such as encapsulation efficiency and ease of production.

Among these considerations, the 3 mg/mL CTX loading concentration in TPP solution was favorable for both CHT and CHCL NPs, achieving the highest concentration of CTX loaded within CS NPs significantly affecting particle size or PDI. CTX-loaded CHCL NPs were selected over CHT NPs not only for a simplified production process—since CHCL is water-soluble and does not require additional preparation in weakly acidic conditions—but also for their higher Z-potential, which might facilitate stronger electrostatic interactions with negatively charged lipid components of the shell when the CHCL core is used in LPHNPs. In conclusion, 3 mg/mL CTX-loaded CHCL NPs was identified as the optimal formulation for further LPHNP development.

2.5. Conclusions

The present study aimed to develop, manufacture, and evaluate a CTX-loaded polymeric core structure, using CHT and CHCL NPs, as a foundation for LPHNPs with potential antimicrobial activity. A suitable HPLC method that allows for indirect quantification of unencapsulated CTX within CS NPs was developed and validated. Also, results revealed that microfluidic mixing technology is a promising approach to manufacture suitable CTX-loaded CS NPs in terms of size, PDI, Z-Potential and EE% by adjusting manufacturing parameters. Antimicrobial efficacy studies performed on promising CTX-loaded CHT and CHCL NPs indicated that the activity of encapsulated CTX was comparable to that of free CTX. However, these NPs, with their tunable properties such as size, charge, and EE%, provide a foundational core for the development of LPHNPs, which will be explored in Chapter 5. As core structures, CHT and CHCL NPs hold potential for encapsulating CTX when integrated into a more complex LPHNP system, which will serve as a delivery platform for combination delivery.

3. Bacteriomimetic Liposomes as a Platform for AMP Delivery

3.1.Introduction

3.1.1. AMP Delivery

As a result of the overuse and misuse of antibiotics, the so-called post-antibiotic era is rapidly approaching [528]. The efficacy of antibiotics is crucial for the success of various routine medical procedures and, according to WHO projections, antimicrobial resistant infections may be linked with a higher mortality rate than cancer by 2050 [27]. This situation has prompted the exploration of novel alternatives to combat bacterial infections. AMPs have been identified as a promising class of antimicrobials for combating microbial resistance [529]. As defined in Chapter 1, AMPs are generally short (10-50 amino acids) and amphiphilic molecules. They are widely expressed in various organisms, and represent a key component of the innate immune response [530]. Their mechanism of action is primarily governed by electrostatic interactions between the negatively charged bacterial membranes and cationic AMPs, leading to membrane disruption or intracellular interference [531]. Unlike conventional antibiotics, AMPs typically exhibit a lower propensity for resistance development due to their broad targeting mechanisms. Despite their promise, AMPs face challenges limiting clinical translation, primarily due to proteolytic degradation, short half-life, and cytotoxicity at high concentrations. Regulatory and economic barriers further hinder AMP clinical translation [532]. Peptide synthesis and purification remain costly and complex, requiring rigorous pharmaceutical standards [533].

AMPs often exhibit poor plasma stability due to rapid degradation by host and bacterial proteases, which limits their routes of administration [534, 535]. In contrast to the disadvantages of short half-lives and sensitivity to protease degradation, only low amounts of AMP are often needed to exert antimicrobial activity; however, achieving this concentration without having undesirable cytotoxic effects can be challenging. These challenges have hindered the full realization of the potential of AMP-based drugs in clinical applications [536] and only a limited number of AMPs have reached clinical use, primarily for Gram-positive infections as per Table 3-1.

Table 3-1: AMP currently approved by the FDA and their clinical applications. Each AMP includes its primary mechanism of action and therapeutic application, providing an overview of their specific roles in treating bacterial infections and the companies responsible for their manufacture.

Drug	Type	Medical Use	FDA-approval	Administration	Mode of action	Company	References
Bacitracin	Cyclic peptide	Minor skin injuries, pneumonia and empyema in infants	1984	Topical	Interference with cell wall and peptidoglycan synthesis	BACiiM / X-GEN Pharmaceuticals	[537]
Dalbavancin	Lipoglycopeptide	Bacterial skin and skin structure infection	2014	Intravenous	Disruption of cell wall synthesis	Dalvance / Allergan	[538]
Daptomycin	Lipoglycopeptide	Bacterial skin and skin structure infection	2003	Intravenous	Disruption of cell wall synthesis	Cubicin / Cubist pharmaceuticals	[537]
Oritavancin	Glycopeptide	Acute bacterial skin and skin structure infection	2014	Intravenous	Disruption of cell membrane functions, inhibition of protein, DNA and RNA synthesis	Orbactiv / The Medicines Company	[537]
Teicoplanin	Glycopeptide	Treatment of pseudomembraneous colitis and *C. difficile* diarrhea	1990	Intravenous and intramuscular	Disruption of cell wall synthesis	Targocis / Sanofi / Cipla	[537]
Telavancin	Lipoglycopeptide	Complicated bacterial skin and skin structure infection	2009	Intravenous	Interference with cell wall and peptidoglycan synthesis	Vibativ / Theravance Biopharma	[539]
Vancomycin	Glycopeptide	Complicated bacterial skin infections, endocarditis, bloodstream infections and meningitis caused by MRSA.	1954	Intravenous and oral	Disruption of cell wall synthesis	Alvanco / Human Pharmacia / Eli-Lilly	[540]

Although bacteria can develop resistance to AMPs via surface charge modifications, membrane restructuring, or protease production, resistance emerges more slowly than with traditional antibiotics due to their multiple modes of action [96, 541-543]. For this reason, AMPs continue to be explored for antimicrobial therapy, including through structural modifications and combination therapy with conventional antibiotics to enhance efficacy and minimize resistance development [544].

3.1.2. Liposomes for AMP Delivery

The utilization of nanocarrier systems for the delivery of AMPs has been proposed and investigated as a possible solution to address the delivery challenges and off-target effects associated with delivery of these peptides, as reported in previous studies [545]. This approach enhances the antibacterial efficacy of AMPs by improving their stability, reducing cytotoxicity, and modulating their release profile [546]. For instance, PLGA NPs encapsulating the AMP GIBIM-P5S9K demonstrated superior antimicrobial activity and reduced hemolytic toxicity compared to free peptide [547]. Encapsulation within nanocarriers protects AMPs from enzymatic degradation, increases their specificity towards bacterial cells, and enhances their uptake through bacterial membranes [548]. Additionally, nanocarriers can provide controlled release, prolonging peptide stability and bioavailability. For instance, pexiganan-loaded NPs exhibited prolonged gastric retention compared to the free peptide, enhancing its effectiveness against *H. pylori* infections [549].

3.1.2.1. Importance of Liposome Composition for AMP Delivery

Liposomes are versatile carriers as they can deliver both hydrophilic and lipophilic/hydrophobic cargos, which is helpful given that AMPs are diverse structures. Depending on their characteristics and intended application, an AMP can be incorporated within the aqueous core of liposomes, into the lipid bilayer or surface-adsorbed to liposomes. As discussed in 1.6.2.2, liposomes have shown promise for fusion with bacterial surfaces [550]. This property enhances AMP delivery by increasing bacterial membrane interaction and improving antimicrobial efficacy [551]. The selection of a lipid composition that is appropriate for delivering a specific AMP is crucial,

as it influences liposome size, surface charge, stability, and release kinetics. The fluidity of the lipid bilayer also modulates adsorption/fusion with bacterial membranes [299], a characteristic directly influenced by the degree of lipid unsaturation [552]. Lipids such as phosphatidylethanolamines (PE) and/or cholesterol hemisuccinate enhance bilayer fluidity, promote fusion with bacterial membranes and cause biological membrane destabilization [299, 553]. Recently, biomimetic approaches in drug delivery have gained attention for improving bacterial targeting and enhancing therapeutic efficacy. Among these, bacteriomimetic liposomes composed of PE, phosphatidylglycerol (PG), and cardiolipin (CL) mimic bacterial membrane structures [312]. Their incorporation into liposomes enhances encapsulation efficiency, improves membrane interaction, and facilitates targeted bacterial interactions, ultimately boosting antibacterial efficacy against MDR pathogens [305].

PE (Table 3-2), enhances membrane flexibility and fusogenicity, facilitating AMP release into bacterial cells [555]. 1-palmitoyl-2-oleoyl-sn-glycero-3-phosphoethanolamine (POPE), the main lipid component of the Gram-negative inner bacterial membrane [556], shares properties with 1,2-dioleoyl-sn-glycero-3-phosphoethanolamine (DOPE), widely used in the preparation of fusogenic liposomes [557], but has a lower spontaneous curvature.

PG (Table 3-2), contributes to bacterial targeting through electrostatic interactions with cationic AMPs, enhancing retention and delivery [558]. 1-palmitoyl-2-oleoyl-sn-glycero-3-phosphoglycerol (POPG), a PG analogue, increases bacterial affinity but requires careful optimization to prevent lipid phase separation [559].

CL (Table 3-2), also known as diphosphatidylglycerol, is a unique negatively charged phospholipid, composed of two PG molecules linked by a glycerol bridge [561]. In bacterial membranes, cardiolipin plays a crucial role in maintaining membrane integrity, functionality and stability [561]. Studies have demonstrated that cardiolipin segregates to specific monolayer leaflets of the liposomes, affecting their curvature and composition [564] as well increaseing membrane leakiness and contributing to liposome permeability [565].

Table 3-2: Bacterial-relevant lipids commonly employed to manufacture bacteriomimetic liposomes.

Lipids	Tm (°C)	Mw (g/mol)	Structure
POPE	+25 °C	717.996	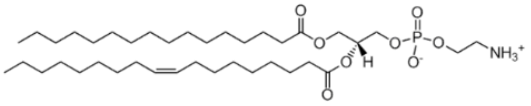
POPG	-2 °C	770.989	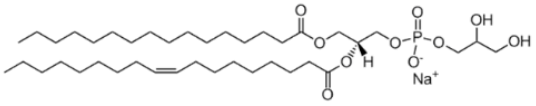
CL	~ -4 °C	1501.959	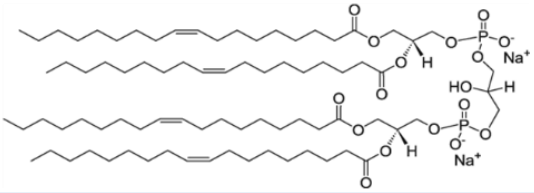

POPE, POPG and CL, the main components of the inner membrane of *E. coli* and *P. aeruginosa,* were investigated by Graef *et al.* in a system composed of a mixture of these phospholipids in the mass ratio 70:20:10 (%wt) [312], to develop an *in vitro* permeation model of the Gram-negative inner membrane. Their study suggested a more rigid bilayer compared to mammalian phospholipid-containing formulations. [312]. Moreover, the uptake and interaction of liposomes composed of POPE:POPG:CL have been previously investigated for mammalian cells revealing promising potential due to their effective cellular uptake and minimal cytotoxicity [566]. However, the interaction of this bilayer system with bacterial cells remains to be investigated.

3.1.2.2. AMPs Loading within Liposomes

A high drug loading of nanocarriers is preferred in order to minimize the quantity of excipient, achieve the desired concentration of therapeutic agents, decrease the volume of dosage, and reduce the treatment period. To achieve optimal encapsulation efficiency, it is imperative to select a suitable loading technique based on the distinct characteristics of the molecule being encapsulated [567]. Drugs can be incorporated within liposomes either in the aqueous core or in the lipid bilayer (see section 1.6.2.2), depending on their physicochemical properties. The common cationic and/or amphiphilic nature of AMPs allows for their ready incorporation into liposomes through various interactions, including electrostatic and hydrophobic interactions, enabling the

encapsulation of both hydrophilic and lipophilic molecules. For instance, anionic liposomes can adsorb cationic AMPs via electrostatic attraction, while amphiphilic AMPs may integrate into the bilayer [571]. Traditional AMP-loading methods, including thin-film hydration and passive adsorption, have been widely used, though they are associated with batch-to-batch variability due to inconsistent control over key formulation parameters [572-574]. In contrast, a microfluidic-based approach enables controlled mixing with high reproducibility, addressing these limitations by precisely regulating mixing and flow rates.

AMP incorporation within liposomes depends on several factors, including the physicochemical properties of the compound, such as hydrophobicity, solubility, and charge. Biswaro *et al.* [575] and Carmona-Ribeiro *et al*. [576] demonstrated how hydrophilic AMPs encapsulated within liposomes exhibited enhanced stability and antimicrobial efficacy. Amphiphilic AMPs can interact with both hydrophilic and hydrophobic liposomal compartments, improving encapsulation efficiency. A similar principle is observed with amphipathic drugs like Amphotericin B, which integrates into the liposome bilayer via ionic interactions with phospholipids [577]. Where bilayer incorporation is challenging, electrostatic adsorption to the liposomal surface offers an alternative, albeit with reduced stability. Traditional bulk loading methods often suffer from inconsistent AMP distribution and lower encapsulation efficiency.

As briefly mentioned in section 1.6.4 and demonstrated in sections 2.4.1 and 2.4.3 by the successful production of empty and antibiotic-loaded CS nanoparticles, microfluidics has the capability to generate nanocarriers in a time-efficient and easily scalable manner. Hence, microfluidic methodology to produce POPE:POPG:CL liposomes loaded with an AMP was assessed in this chapter. The surface adsorption of a model AMP, nisin, to these liposomes served as an initial formulation study using a commercially available AMP. While microfluidics has been widely employed in liposome production, its use in optimizing peptide surface adsorption remains underexplored. Both empty and model AMP-adsorbed formulations were tested in terms of size, PDI, Z-Potential, and adsorption efficiency (AE%).

3.2. Aim and Objectives

The aim of this chapter was to establish and optimize the production of POPE:POPG:CL liposome formulations by varying microfluidic process parameters and to achieve surface adsorption of nisin, as a model AMP, to pre-formed liposomes. These liposomes serve as the *shell* component of the LPHNPs described in Chapter 5, designed to enhance drug targeting and interaction with bacterial cells. Surface adsorption was selected over encapsulation to facilitate a faster release of the AMP upon bacterial contact, aligning with the overall thesis goal.

This aim was achieved through the following objectives:

- Optimizing the formulation of POPE:POPG:CL liposomes via microfluidic mixing technology by varying parameters including initial lipid concentration, TFR and FRR
- Optimizing the formulation of POPE:POPG:CL liposomes for nisin surface-adsorption via microfluidic mixing, by varying process parameters including initial nisin concentration, TFR and FRR

3.3. Materials and Methods

3.3.1. Materials

Gentamicin-impregnated discs (CN 10), ciprofloxacin-impregnated discs (CIP 5) and PBS, pH 7.4 tablets were obtained from Oxoid Ltd (Basingstoke, UK). MHB2, MHA, Nutrient agar (NA), dialysis tubing cellulose membrane (MWCO ~14kDa) and resazurin were purchased from Merck (New Jersey, USA). POPE, POPG and CL were purchased from Avanti Polar Lipids (Merck, Ney Jersey, USA)). Acetonitrile, nisin from *Lactococcus lactis* (potency: ≥900 IU/mg) and Micro BCA™ Protein Assay Kit were purchased from Thermo Fisher Scientific (Massachusetts, USA). N,N-dimethylformamide (DMF) was bought from Acros Organics (New Jersey, USA). Propan-1-ol was purchased from VWR (Pennsylvania, USA).

3.3.2. Methods

3.3.2.1. Empty POPE:POPG:CL Liposome Manufacturing and Characterization

Empty liposomes were manufactured using a microfluidic mixing technique employing a Nanoassemblr® Benchtop from Precision Nanosystems (Vancouver, Canada). Bacteriomimetic liposomes were formulated, composed of POPE, POPG and CL in a weight ratio of 70:20:10 (%wt) [312].

Biomimetic liposomes composed of POPE:POPG:CL were prepared using a staggered herringbone micromixer (SHM) and Nanoassemblr™ platform from Precision Nanosystems (Vancouver, Canada) as described in section 1.6.4. Lipids were dissolved in a mixture of 1-propanol and DMF (80:20 v/v) at the desired concentration and lipid solution was injected into the left inlet of the SHM (Figure 3-1), whereas the aqueous phase consisting of PBS (pH 7.4) was injected in the right inlet. The formed liposome dispersion was collected from the outlet port in a 15mL-Falcon tube.

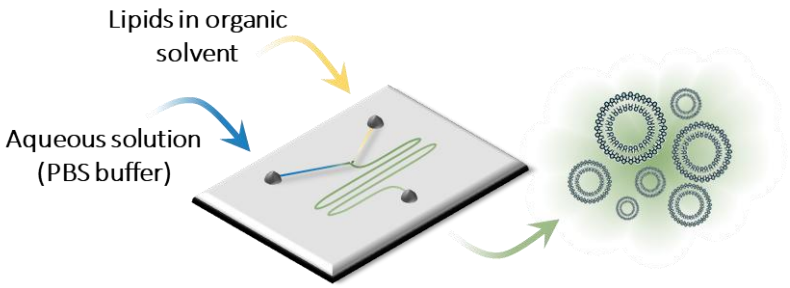

Figure 3-1: Schematic representation of employment of SHM for production of bacteriomimetic liposomes. Lipids in 1-propanol:DMF 80:20 (left inlet) and PBS buffer (right inlet) were injected into the cartridge as depicted, resulting in the spontaneous formation of l liposomes.

In order to evaluate the influence of formulation parameters on liposome size, PDI and Z-potential, an L9 orthogonal array Taguchi DoE was constructed using Minitab® 20 statistical software [444]. Subsequently, 9 liposomal formulations were prepared by varying initial lipid concentration (2, 4, 8 mg/mL), TFR (5, 10, 20 mL/min) and FRR between aqueous and organic phases (2:1, 3:1, 4:1) as shown in Table 3-3. In general, a total sample volume of 2 mL was prepared with start and end waste volumes fixed at 0.35 mL and 0.05 mL, respectively. Liposomes were characterized in terms of size, PDI and Z-Potential after dilution 1:10 with PBS as previously described by Forbes *et al.* [324], using a Zetasizer Nano ZS as described in section 2.3.2.1.2.

Table 3-3: Set of 9 formulations employed in accordance with Taguchi DoE to investigate the effect of initial lipid concentration, TFR and FRR on liposomal formulation size, PDI and Z-Potential.

Formulation	Initial lipid concentration (mg/mL)	TFR (mL/min)	FRR (PBS buffer : lipid solution
F1	2	5	2 : 1
F2	2	10	3 : 1
F3	2	20	4 : 1
F4	4	5	3 : 1
F5	4	10	4 : 1
F6	4	20	2 : 1
F7	8	5	4 : 1
F8	8	10	2 : 1
F9	8	20	3 : 1

The output of the Taguchi L9 orthogonal array was analyzed with Minitab® 20 statistical software (Minitab, LLC). The optimum conditions for empty liposome preparation were indicated by a high signal to noise (S/N) ratio, which corresponds to minimum variance of the outcome and a better performance, with the target output parameters being the particle size and PDI [443]. Optimization of the particle size, PDI and AE% was performed using the signal to noise (S/N) Taguchi 'smaller-is-better' criterion which consider both the variation of replicated measurements and the proximity of the average response to a specified target value.

3.3.2.1.1. Liposome Purification (Dialysis)

Dialysis tubing of MWCO ~ 14 kDa was employed for solvent removal from formed liposomes as previously described by Roces *et al.* [326]. Before use, dialysis membranes were pre-treated, as per the manufacturer instruction, in a solution of 1 mM ethylenediaminetetraacetic acid (EDTA) and 2% sodium bicarbonate for 2 hours at 80 °C in order to remove sulphites and glycine, then washed with deionised water and stored in 20% methanol for maximum 1 month in the fridge.

In order to establish optimal dialysis conditions for removal of residual solvents present in liposomal formulations, 1 mL of liposomes was dialyzed against 20, 100 and 200 mL of PBS buffer for 1, 2, 4, 6 and 24 hours [580] as shown in Figure 3-2. For the purpose, formulation F1 from Table 3-3 was employed due to its high organic solvent content (alongside F6 and F8). Following dialysis purification, liposomal formulation F1 was diluted 1:5 with PBS buffer and ultracentrifuged at 55000 rpm, 4 °C for 1 hour [581] (Optima XPN-80, rotor 70.1 Ti, minimum radius 4.05 cm, max radius 8.20 cm, Beckman Coulter Inc., Brea, California, USA). Residual solvent remaining in liposome formulations was then quantified as described below in section 3.3.2.1.2.

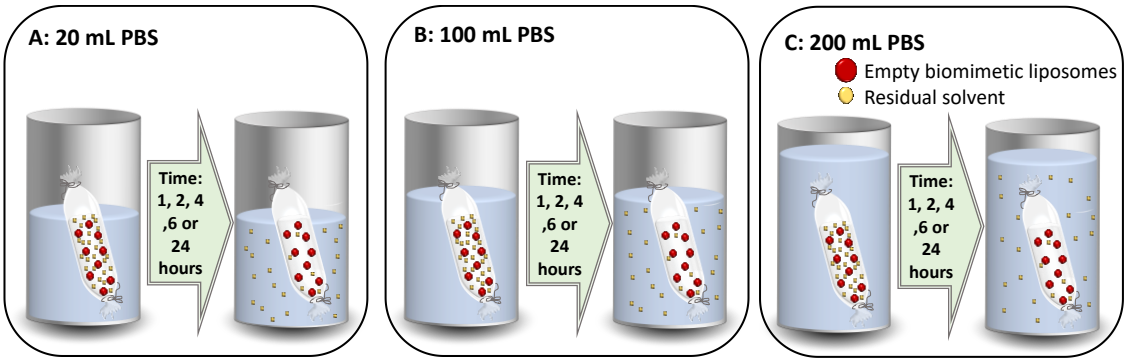

Figure 3-2: Schematic representation of dialysis process employed to purify liposomal formulations. Different volumes of outer media (PBS, 20 mL, 100 mL and 200 mL) and different dialysis times (1, 2, 4, 6 and 24 hours) were investigated.

3.3.2.1.2. Gas Chromatography (GC)

Quantification of the residual 1-propanol and DMF within the liposomal formulations after dialysis was performed by GC [582]. GC is a chromatography technique mainly used for quantitative analysis of the residual solvent within sample formulations. It can separate mixtures of volatile analytes. After ultracentrifugation of liposomes, the supernatant was analyzed for residual solvent content on an Agilent 6890N gas chromatograph equipped with an Agilent 7683B automatic liquid sampler and a DB-1 column (30 m × 0.25 mm i.d., J&W Scientific) with a programmed temperature gradient of 70-130 °C at 10 °C/min. Injector and detector temperatures were set at 250 °C. Residual solvent content in F1 following dialysis was calculated from constructed 1-propanol and DMF calibration curves. Residual solvent content in formulations was then compared to safe residual solvent content limits established by ICH guidelines [583].

3.3.2.2. Nisin Loading of POPE:POPG:CL Liposomes: Surface Adsorption

Surface-adsorption of nisin to empty POPE:POPG:CL liposomes was investigated in the current study via microfluidic mixing. Nisin was chosen to perform preliminary studies investigating the effect of AMP solution concentration, FRR of empty purified POPE:POPG:CL liposomes to AMP solution and TFR on loaded liposome physiochemical characteristics.

3.3.2.2.1. Microfluidic Preparation of Surface-adsorbed Nisin Liposomes

The microfluidic mixing setup described previously (see section 3.3.2.1) was employed for the manufacture of nisin-adsorbed POPE:POPG:CL liposomes. Briefly, following empty bacteriomimetic liposome preparation and purification, empty liposomes were injected into the left inlet of the SHM while nisin solution (in PBS) was injected into the right inlet as adapted from Balbino *et al.* [584]. In order to evaluate the influence of formulation parameters on liposome size, PDI and AE% and to minimize the number of experiments conducted, a Taguchi DoE was again employed using Minitab® 20 statistical software (Minitab, LLC). A Taguchi L9 orthogonal array design was constructed (3 variables set at 3 levels, see Table 3-4) and the software output provided a set of 9 formulations which were each prepared in triplicate. The output of the Taguchi L9 orthogonal array was analyzed Minitab® 20 statistical software (Minitab, LLC) as described in section 3.3.2.1.

Table 3-4: Parameters used to manufacture a set of 9 formulations resulting from a Taguchi DoE L9 orthogonal array, employed to optimize the production of nisin-adsorbed liposomes.

Formulation	**Initial nisin concentration (mg/mL)**	**TFR (mL/min)**	**FRR (liposomes : nisin solution)**
F11	1	5	1:1
F12	1	10	3:1
F13	1	20	5:1
F14	3	5	3:1
F15	3	10	5:1
F16	3	20	1:1
F17	5	5	5:1
F18	5	10	5:1
F19	5	20	3:1

3.3.2.2.2. Physiochemical Characterization of Nisin-adsorbed Liposomes

Nisin-adsorbed liposomes were characterized in terms of size, PDI and Z-Potential as described in section 2.3.2.1.2.

3.3.2.2.3. Nisin AE% – Micro BCA Assay

The efficiency of nisin adsorption to POPE:POPG:CL liposomes was indirectly calculated by quantification of unbound nisin, using the bicinchoninic acid (BCA) assay [585]. Following production, a 1 mL volume of nisin-adsorbed liposomes was loaded into Sartorius Centrisart® I centrifugal ultrafiltration units with a cut-off regenerated cellulose membrane of 300 kDa and centrifuged (Eppendorf centrifuge 5804r, Germany) for 30 minutes, at 1188 x g and 25 °C. After centrifugation, the ultrafiltrate (containing free nisin) was collected and analyzed via BCA assay according to the manufacturer's instructions. Briefly, a 125 µL volume of ultrafiltrate sample was pipetted into a 96-well plate and 150 µL of working reagent (reagent A:B:C 25:24:1) was added. The plate was incubated for 30 mins at 37 °C following which the absorbance was read at 562 nm using a SPECTROstar® Nano microplate reader (BMG LABTECH, Germany). Free nisin and subsequently liposome-adsorbed nisin were then quantified in reference to a nisin calibration curve, performed for each plate. Liposome-adsorbed nisin was expressed as an AE% which was calculated as per Equation 3-1, where Wt represents the theoretical total amount of nisin added to formulation during the manufacturing, and Wu represents the amount of nisin present in the ultrafiltrate quantified by BCA assay.

Equation 3-1

$$Nisin\ AE\% = \frac{Wt - Wu}{Wt}\ x\ 100$$

3.3.2.3.Statistical Analysis

All statistical analyses were performed using IBM SPSS statistic software (Version 28.0. Armonk, NY: IBM Corp). Multiple regression analysis, Analysis of Variance (ANOVA) and F-Test were used to build prediction models for liposome size and PDI for data obtained from the study described in 3.3.2.1 and 3.3.2.2.1. One-way ANOVA with Tukey's post hoc test was employed to compare empty (3.3.2.1) and nisin-adsorbed (3.3.2.2.1) liposome size, PDI and Z-Potential. A p value of <0.05 was taken as indicating statistical significance throughout the studies. An independent T-test was also run on empty (3.3.2.1) and nisin-adsorbed (3.3.2.2.1) liposome size, PDI and Z-Potential to determine if there was a significant difference in formulation physicochemical characteristics

before and after dialysis. A p value of <0.05 was taken as indicating statistical significance throughout the studies.

3.4. Results and discussion

3.4.1. Empty POPE:POPG:CL Liposomes

3.4.1.1. Empty Liposome Manufacturing and Characterization

To manufacture bacteriomimetic liposomes intended for AMP delivery, a microfluidic mixing technique was employed to facilitate the spontaneous formation of liposomes under laminar flow of lipid solution and PBS buffer. Given the novelty of using microfluidic technology for the preparation of liposomes consisting of the bacteriomimetic POPE, POPG and CL composition, it was essential to investigate which parameters had the greatest degree of influence on liposome size and PDI in particular, as preliminary analyses indicated that Z-potential remained consistent across formulations, irrespective of variations in lipid concentration, TFR, and FRR. Since chloroform, commonly employed in association with methanol to dissolve lipids for liposome preparation, was not compatible with the SHM chip or microfluidic system components, a preliminary study was necessary to evaluate lipid solubility in other organic solvents compatible with the SHM. Several solvents and solvent mixtures were assessed in this respect (data not shown) with a mixture of 1-propanol and DMF (80:20 v/v %) finally being employed due to its ability to efficiently dissolve the employed lipid mixture, as well as its compatibility with the SHM cartridge. Subsequently, an L9 orthogonal array mixed-design Taguchi DoE was constructed, performed, and analyzed by Minitab 16 Statistical Software. This design is employed to identify important process parameters required to more efficiently fine-tune desired nanocarrier outputs such as size, PDI, Z-potential or encapsulation efficiency, in comparison to traditional 'one factor at a time' methods. Following the optimization of the liposome purification method detailed in section 3.4.1.2, formulations F1 to F9 were prepared as described in 3.3.2.1 to understand critical parameters influencing particle size, PDI and Z-Potential.

The characteristics of F1-9 liposomes manufactured using microfluidic mixing are displayed in Figure 3-3. Further data on the size, PDI, and Z-potential of liposomes manufactured using the conventional thin-film hydration method can be found in Table S-1 (see Appendix). The formulations manufactured using microfluidic demonstrated an average particle size ranging from 89.22 nm (F5) to 509.40 nm (F8) , with only 3

formulations (F5, F7 and F9) having a size less than 100 nm. Concerning the PDI, most values were in the range 0.14-0.42, with more than half of the tested formulations displaying a PDI below <0.3, indicating a homogenous population of liposomes [586].

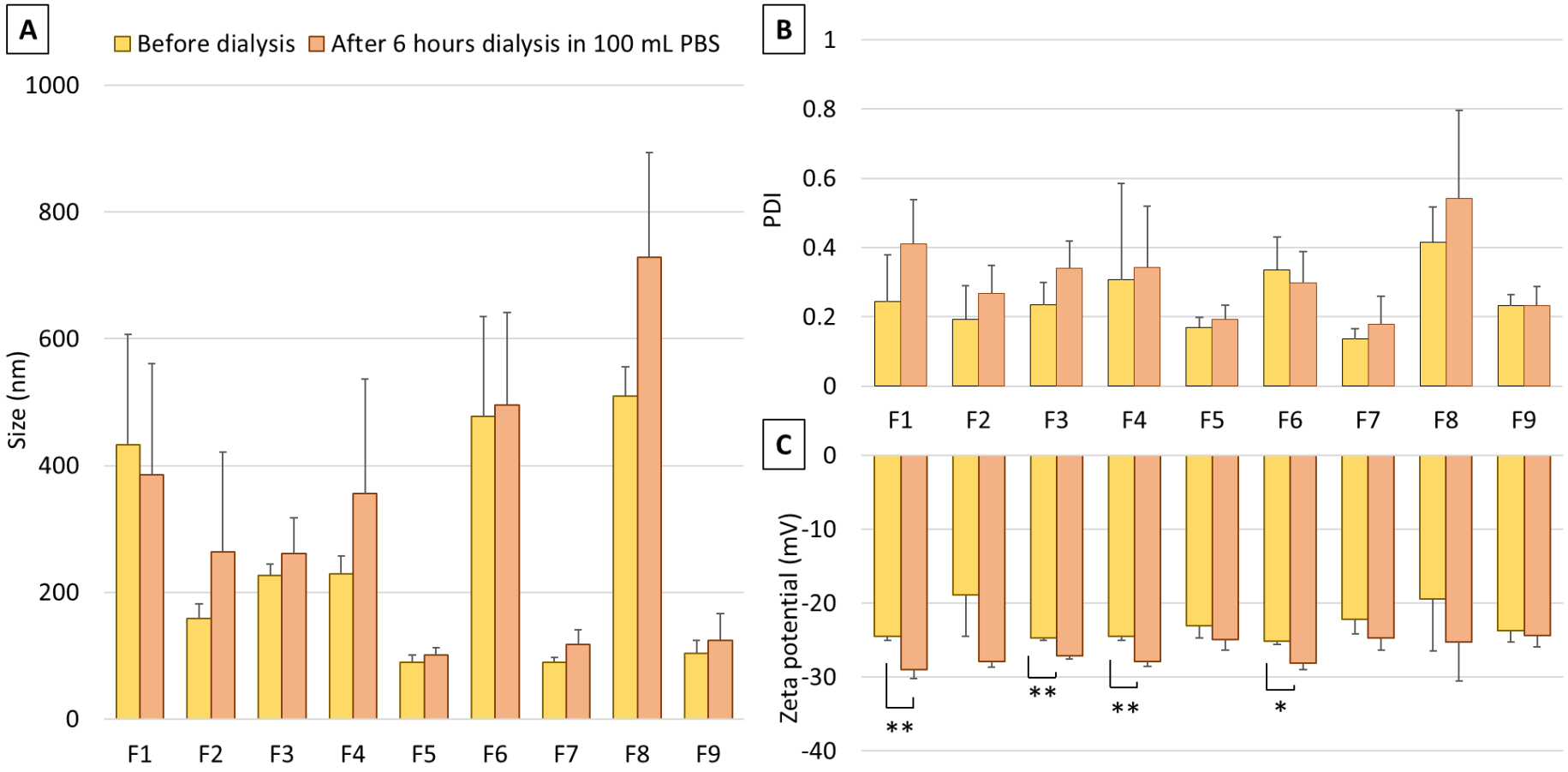

Figure 3-3: Size (A), PDI (B) and Z-Potential (C) of the 9 empty POPE:POPG:CL liposome formulations prepared according to Taguchi L9 orthogonal array DoE. The results represent mean ± SD, n=3 independent batches. Indications of statistical significance: if the two-tailed p-value is less than 0.05, it is flagged with one star (*). If the two-tailed p-value is less than 0.01, it is flagged with 2 stars (**).

To identify the optimal conditions for liposome production, the key factors influencing the size and PDI value both before and after purification by dialysis were analyzed. Thus, the collected data were analyzed by Minitab 16 Statistical Software®. With respect to before dialysis, according to the Taguchi DoE analysis with the “smaller-is-better” criterion (Figure 3-4 A) and the performance of multiple linear regression analysis (Table 3-5), only FRR significantly affected liposome size and PDI. The R^2 values for the regression analysis for liposome size and PDI were found to be 0.593 and 0.198, respectively. This result from the multiple linear regression indicates that the model applied can predict only 19.8% of the PDI output. The low R-squared value for PDI likely reflects the limited number of runs in the Taguchi L9 orthogonal matrix, which may not capture more complex relationships or interactions influencing PDI. The R-squared value is a measure of how well the model explains the variability in the data. In the context of Taguchi DoE, a low R-squared value for predictions indicates that the model does not adequately capture or explain the variation in the response variable based on the chosen factors and their levels.

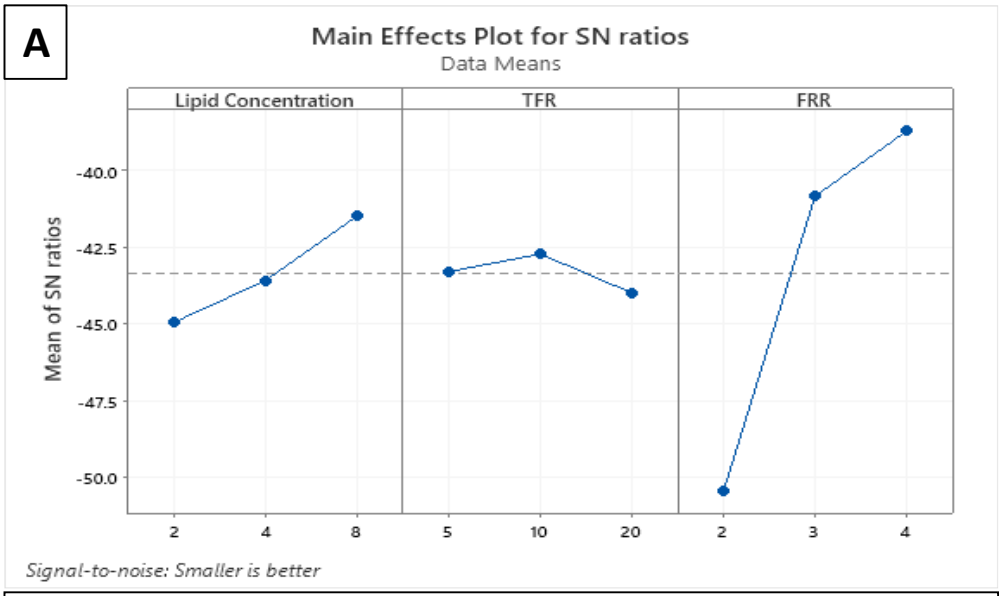

Rank:	2	3	1

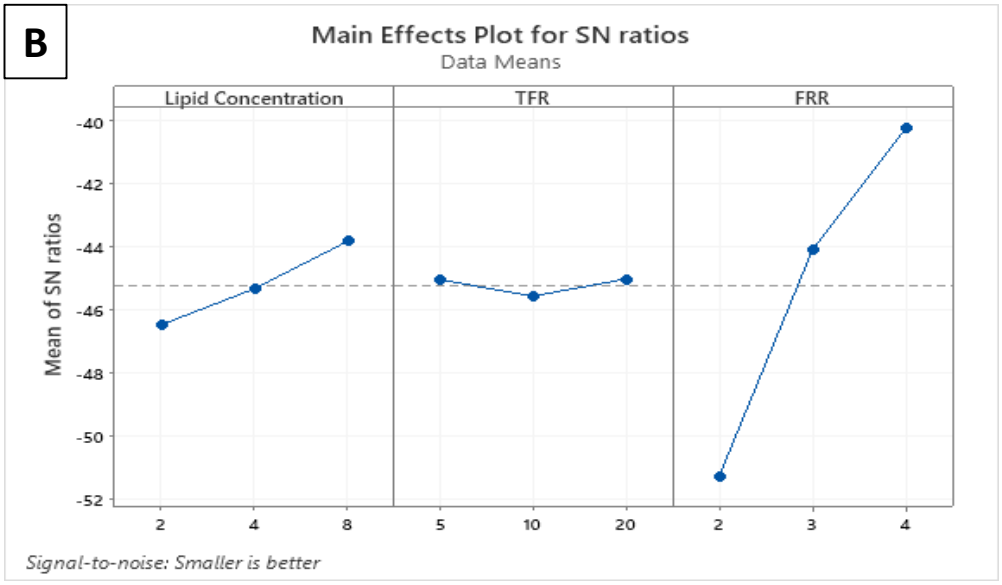

Rank:	2	3	1

Figure 3-4: Liposome size and PDI mean signal-to-noise (S/N) graph response before (A) and after (B) dialysis. The FRR has the most substantial impact (ranked 1), while lipid concentration and TFR show lesser effects, ranked 2 and 3, respectively.

Taguchi DoE assumes a linear relationship between factors and the response variable. If the true relationship is nonlinear, the model may not accurately capture the variations, resulting in a low R-squared value. Also, Taguchi experiments aim to minimize the effect of noise or variability, but it may not be possible to eliminate it entirely. If there is a significant amount of uncontrolled variation in the system, it can contribute to a low R-squared value.

Table 3-5: Regression analysis of liposome size and PDI before and after dialysis versus liposome preparation variables. This table presents the results of a regression analysis examining the impact of lipid concentration (A), TFR (B), and FRR (C) on liposome particle size and PDI before and after the dialysis purification step detailed in section 3.4.1.2. Coefficients, standard errors, t-values, and p-values for each predictor variable are shown to assess the significance of each factor. The constant values reflect baseline measurements of size and PDI in liposome preparations without predictor adjustments, while the asterisks (*) highlight statistically significant values ($p < 0.05$).

		Particle size				PDI			
	Predictor (Symbol)	**Coefficients**	**Coefficients St. Err.**	**T**	**p**	**Coefficients**	**Coefficients St. Err.**	**T**	**p**
Liposomes before dialysis	**Constant**	610.466	89.987	6.784	0.000 *	0.354	0.102	3.464	0.002*
	Lipid concentration (A)	-6.636	9.642	-0.688	0.498	0.005	0.011	0.455	0.654
	Total Flow Rate (B)	1.329	3.857	0.345	0.734	0.002	0.004	0.532	0.6
	Flow Rate Ratio (C)	-168.866	29.455	-5.733	0.000 *	-0.076	0.033	-2.277	0.032
Liposomes after dialysis	**Constant**	684.666	134.074	5.107	0.000 *	0.52	0.116	4.48	0.000 *
	Lipid concentration (A)	3.082	14.365	0.215	0.832	-0.002	0.012	-0.123	0.903
	Total Flow Rate (B)	-0.611	5.746	-0.106	0.916	-0.002	0.005	-0.367	0.717
	Flow Rate Ratio (C)	-188.618	43.886	-4.298	0.000 *	-0.09	0.038	-2.368	0.027

Despite the fact that the regression model was not a good fit for PDI ($F(3, 23) = 1.892$, $p = 0.159$, where $F(3,23)$ denotes the F-statistic with 3 degrees of freedom for the factors tested and 23 for the residual error), Table 3-6 shows that the independent variables predict liposomes size with statistical significance, as $F(3, 23) = 11.153$, $p = 0.000$, hence the regression model is a good fit of the data. This high F-statistic and a p-value well below 0.05 indicate that the model explains a significant portion of the variance in liposome size, confirming that the regression model fits the size data well.

Table 3-6: ANOVA tables of fitted model for liposomes size and PDI before and after dialysis. The ANOVA results for models assessed the influence of lipid concentration, TFR, and FRR on liposome size and PDI pre- and post-dialysis. Asterisks (*) indicate significance ($p < 0.05$).

		Source	Degree of Freedom	Sum of Squares	Mean square	F	p
Liposomes before dialysis	*Particle size*	Regression	3	522536.187	174178.729	11.153	0.000*
		Residual error	23	359192.089	15617.047		
		Total	6	881728.276			
	PDI	Regression	3	0.114	0.038	1.892	0.159
		Residual error	23	0.462	0.02		
		Total	6	0.577			
Liposomes after dialysis	*Particle size*	Regression	3	642371.697	214123.893	6.177	0.003 *
		Residual error	23	797351.137	34667.441		
		Total	6	1439722.815			
	PDI	Regression	3	0.15	0.05	1.919	0.155
		Residual error	23	0.598	0.026		
		Total	6	0.748			

A similar output was also obtained for formulation size and PDI after dialysis. After dialysis, the Taguchi DoE analysis with the 'smaller-is-better' criterion (Figure 3-4 B) indicated that the parameter most significantly affecting liposome size and PDI was FRR (Table 3-5), followed by total lipid concentration. The effect of total lipid concentration, however, was not statistically significant. The R^2 value from the regression analysis was equal to 0.446 for liposome size after dialysis and equal to 0.2 for PDI, meaning that 44.6% and 20.0% of the variability of the output is explained by the independent factors of the respective models, which may suggest that the model is not a good fit for the data. In addition, the results of ANOVA and F-Test performed on the obtained data,

indicated that the fitted model can only predict liposomes size after dialysis, but not liposome PDI, with statistical significance (Table 3-6). Indeed, the regression model has a statistically significant F-statistic ($F(3,23)=6.177$, $p=0.003$), indicated by the p-value below 0.05, which suggests that the independent variables collectively explain a meaningful portion of the variability in liposome size. In contrast, the F-statistic for PDI ($F(3,23)=1.919$,$p=0.155$) is not statistically significant, as indicated by the p-value above 0.05. This non-significant p-value for PDI suggests that the model does not explain enough of the variation in PDI to be a reliable predictor.

In summary, while the model appears to be suitable for predicting liposome size after dialysis, further refinement or alternative approaches may be needed to improve the accuracy of predicting liposome PDI based on the experimental results. Furter improvements of the Taguchi model might consider refining the experimental design or exploring additional factors that might influence PDI as well as evaluate if there are interactions between the factors that were not considered in the initial model. Nevertheless, the Taguchi DoE analysis offered a valuable insight into the factors influencing liposome characteristics, as well as highlighting the need for refinement in predicting PDI. An independent T-test was run on liposome size, PDI and Z-Potential to determine if there was a mean difference in formulation physicochemical characteristics before and after dialysis. The T-test results showed that there was no significant difference in size and PDI before and after dialysis. In contrast, the mean Z-Potential of formulations F1, F3, F4 and F6 significantly increased magnitude after dialysis (Figure 3-3 C). It is worth noting that the Z-potential increased in magnitude after dialysis for all formulations, although this increase reached statistical significance only for specific formulations (F1, F3, F4, and F6). This suggests that while dialysis consistently enhances the surface charge by removing residual solvents or impurities, the extent of this effect is more pronounced in certain formulations.

Overall, in accordance with the mean plot of signal-to-noise for liposome size and PDI before and after dialysis (Figure 3-4) and the statistical analysis performed on F1-F9 formulations, process parameters for the manufacture of F7 were chosen to produce empty liposomes for further work. The Taguchi analysis identified an initial lipid concentration of 8 mg/mL and an FRR of 4:1 as the optimal parameters for achieving the

optimal liposome characteristics (Figure 3-4). These settings facilitated the production of liposomes with favorable size and low PDI, indicating a homogeneous population (Figure 3-3). Furthermore, the stability of physicochemical properties of F7, including size, PDI, and Z-potential, was maintained even after the purification process, underscoring its robustness and suitability for further studies (Figure 3-3).

As described above, the aim of the DoE study was to evaluate the impact of variations of initial lipid concentration, TFR and FRR on liposome size and PDI. The Taguchi analysis, using the “smaller-is-better” S/N ratio criterion, identified the optimal parameters for minimizing liposome particle size and PDI, as shown in Figure 3-4. The main parameter affecting liposome particle size and PDI was found to be FRR, which is the ratio between buffer and lipid solution, followed by lipid solution concentration and finally, with the lowest rank, the TFR. The most significant factor was the FRR, with an optimal value of 4:1 to manufacture small and monodisperse liposomes. Lipid concentration followed in significance, with a concentration of 8 mg/mL supporting particle uniformity without excess size. The TFR ranked last, and thus having a minimal impact on the output, showed an optimal setting at 5 mL/min. Thus, the optimal conditions for achieving minimal particle size and PDI are FRR of 4:1, lipid concentration of 8 mg/mL, and TFR of 5 mL/min. These settings provide a stable formulation for enhanced liposome performance. In particular, a 2:1 FRR was seen to form larger liposomes in comparison to higher FRRs (3:1, 4:1, $p<0.01$, Figure 3-4). These results corroborate findings extensively reported in literature [327, 587-589]. Liposome formation in the SHM spontaneously happens by rapid mixing between the organic and the aqueous phases which determines the nanoprecipitation and self-assembling of liposomes. As the lipids come into contact with the aqueous phase, they arrange themselves in a bilayer structure. The hydrophobic tails of the lipids tend to avoid contact with the aqueous phase, leading the planar lipid bilayer to bend. The planar lipid bilayer bends in order to reduce the interactions between the hydrophobic chains of the lipids and the hydrophilic buffer phase, and eventually closes into spherical vesicles. Thus, the exposure time of the two phases directly impacts the diameter of the formed lipid vesicles. With increasing FRR between the aqueous and the organic phase, the amount of lipid exposed at the interfaces is reduced, the alcohol concentration is decreased and

less time is required for the planar lipid bilayer to stabilize [327, 590]. Thus, as confirmed by the current study, at increased FRR, smaller lipid vesicles are expected [579, 588, 591]. In addition to this, the reduced solvent concentration when using higher FRRs decreases the Ostwald ripening phenomenon, which drives the formation of larger lipid vesicles via the insertion of phospholipid molecules into the lipid bilayer in order to lower the overall energy of the system [592, 593]. In contrast to the FRR, the TFR in the current study showed minimal to no impact on liposome particle size and PDI (Figure 3-4). These findings are in line with previous studies reported in literature where FRR showed an impact on particle size, but the total flow rate had no impact across all speeds tested [324, 589, 594].

However, despite the fact that these findings are broadly supported by literature, other studies have provided evidence of a correlation between the TFR employed and liposome size and PDI [595-597]. Maeki *et al.* showed that smaller liposomes can be manufactured using higher TFR; these results can be explained by the rapid mixing of both aqueous and organic phases within the micromixer enabling both phases to interact for a shorter period of time [595]. Interestingly, the same study showed the importance of lipid concentration on particle size, with an increase in initial lipid concentration across a range from 5 mg/mL to 20 mg/mL resulting in an increased lipid nanoparticle size [595], rather than liposomes. This finding contrasts with the results observed in the present study, where liposomal structures were developed rather than lipid nanoparticles. In this case, variations in lipid concentration did not yield a comparable increase in particle size, highlighting a key difference in the behavior of lipid nanoparticles and liposomes under similar experimental conditions. In accordance with the current results, where increasing initial lipid concentration is correlated with a trend in decreasing particle size (Figure 3-4), previous studies have demonstrated that mean diameter of the liposomes produced is directly related to lipid concentration [598-601] Forbes *et al*. showed that increasing initial lipid concentration from 0.3 mg/mL to 2 mg/mL resulted in a smaller particle size of neutral liposomes, and reached a plateau at concentrations higher than 4 mg/mL.

Results presented in this section help to identify critical parameters that need to be considered when developing a design space for liposome production via microfluidic mixing techniques. Significant correlations between FRR and liposome size, along with observed trends linking initial lipid concentration to size, align with findings from several previous studies and informed the selection of the empty optimum formulation F7 for subsequent studies.

3.4.1.2. Liposome Purification

Bacteriomimetic liposomes composed of POPE:POPG:CL were prepared using microfluidic mixing. The optimization of the dialysis procedure was first carried out using the DoE formulation candidate with the highest organic solvent content (F1) so that an optimized purification procedure could then be applied to all DoE formulations.

Organic volatile chemicals contained in pharmaceutical formulations for human use should be limited because of their inherent toxicity. In addition to this, residual solvent in formulation may contribute to the alteration of the physicochemical attributes of the product such as particle fusion. The residual solvent limit is dictated by the ICH Q3C guidelines [583]. DMF and 1-propanol, employed in the preparation of empty bacteriomimetic liposomes, belong to class 2 and class 3 as defined by these guidelines, respectively. The agreed limit for 1-propanol, classified as lower risk to human health, is 5000 ppm (or 0.5 % v/v), while the limit for DMF, which has a higher toxicity than class 3 solvents, is 880 ppm (or 0.088% v/v) [583]. The residual solvent in formulation was quantified by GC as described in 3.3.2.1.2.

A calibration curve was established (R^2=1, Figure 3-5) for both solvents and from this, the concentration of residual solvent in purified samples was calculated. For this purpose, F1 was dialyzed against 20 mL, 100 mL or 200 mL of PBS for 1, 2, 4, 6 and 24 hours to understand the minimum time and volume of outer media required to safely remove organic solvents.

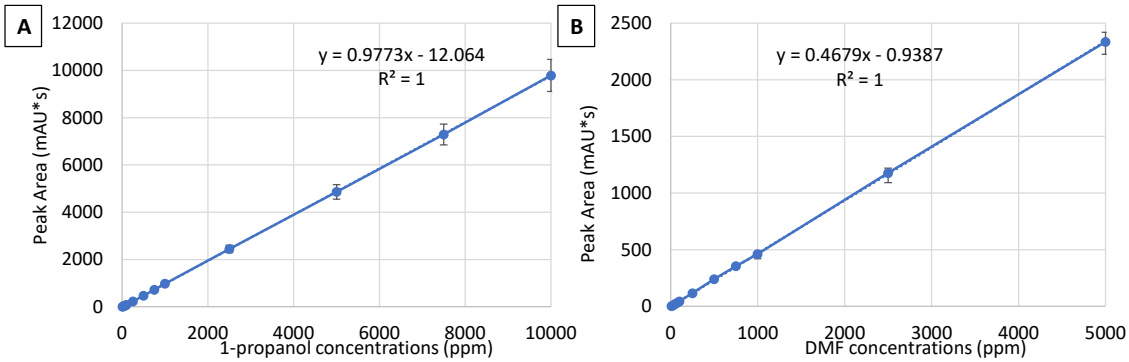

Figure 3-5: GC standard curve of peak area as a function of 1-propanol (A) and DMF (B) concentration, demonstrating a linear relationship for the investigated concentration range in both cases. Results show mean ± SD (n=3).

As shown in Figure 3-6 A, a 20 mL volume of PBS was not sufficient to safely reduce the level of volatile organic solvents even after 24 hours of dialysis. By increasing the volume of outer media to 100 mL or 200 mL (Figure 3-6 B and C), residual 1-propanol and DMF were reduced to values significantly below the allowable limit set by ICH guidelines after 6 hours of dialysis ($p<0.005$).

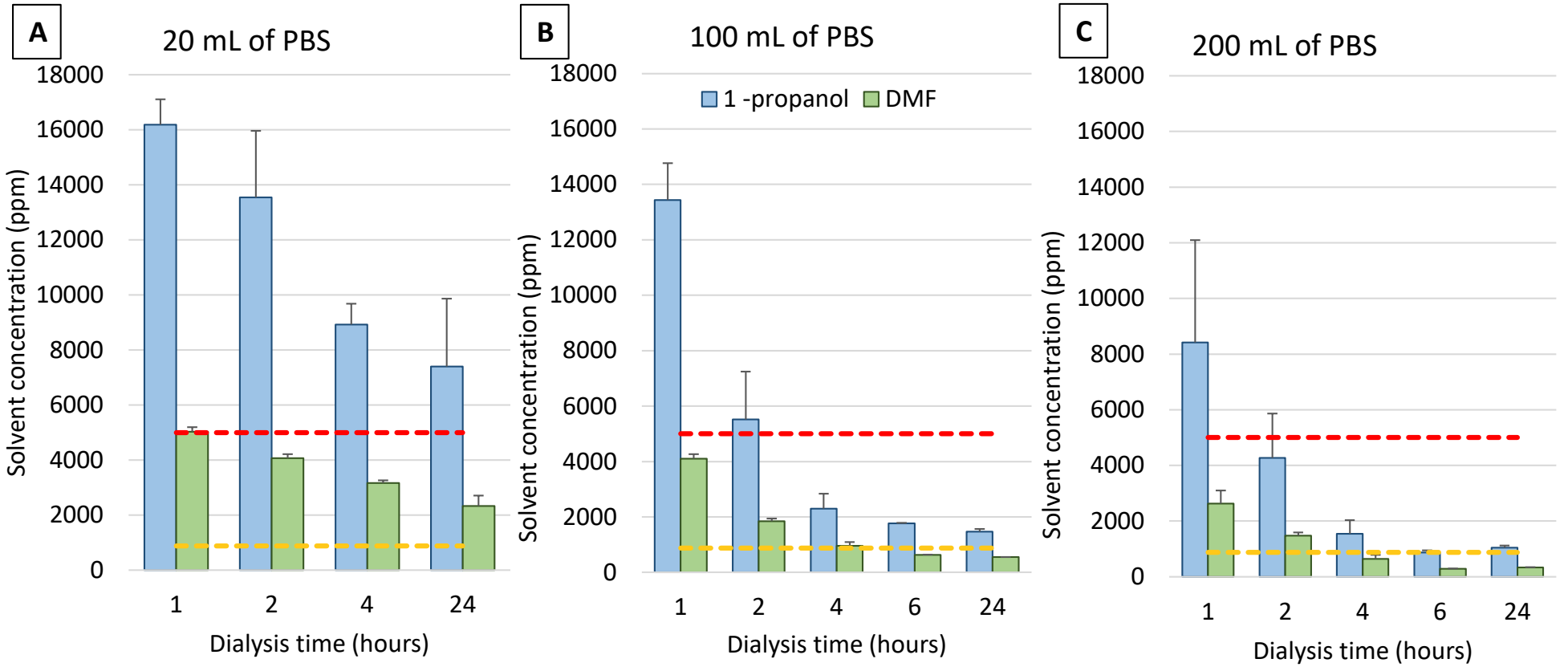

Figure 3-6: Concentration (ppm) of residual solvent in liposomal sample F1 produced using microfluidics after dialysis against 20 mL (A), 100 mL (B) or 200 mL (C) of PBS for up to 24 hours. Results represent the mean ± SD from at least 3 independent experiments. Yellow and red dotted lines represent residual solvent limits from ICH guidelines for 1-propanol and DMF, respectively.

While employing a 200 mL of PBS was the most efficient in removing 1-propanol and DMF than smaller volumes of PBS, a 100 mL volume of buffer was chosen as the outer media component for further dialysis studies, with dialysis conducted over a 6-hour time period. These conditions were selected as they resulted in acceptable removal of solvents with minimal wastage of PBS.

Given that dialysis with 100 mL of PBS for 6 hours resulted in acceptable solvent removal from F1, the formulation with the highest solvent content, it was hypothesized that using the same dialysis parameters would yield percentages of residual solvents within limits for the entire F1-F9 liposome panel. This was experimentally confirmed, as is demonstrated in Figure 3-7.

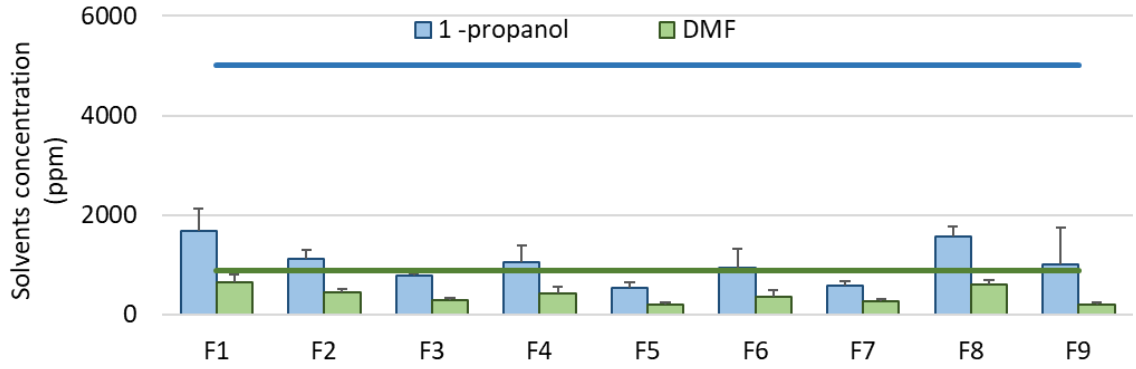

Figure 3-7: Concentrations (ppm) of residual solvent in the liposomal formulations F1-F9 produced using microfluidics after dialysis against 100 mL of PBS for 6 hours. Results represent the mean ± SD from at least 3 independent experiments. Green and blue lines represent residual solvent limit from ICH guidelines for 1-propanol and DMF, respectively.

The majority of techniques for liposomal preparation involve the use of organic solvents for dissolution of the lipids Chromatographic techniques are generally used for solvent quantification and several techniques exist for the purification of particles, the traditional methods including centrifugation, dialysis and gel filtration, and the newer techniques including diafiltration and tangential flow filtration (TFF) [602, 603]. For liposomal preparation, the use of centrifugation techniques may alter the final characteristics of the product. On the other hand, gel filtration and TFF risk the loss of lipids due to electrostatic interactions between the column membrane and the

liposomes. Thus, the use of dialysis was deemed the most appropriate method for the removal of solvent in this work. Dialysis is a commonly reported method for liposomal purification [578, 594], but it has certain limitations when scaled up for large-scale production. Dialysis is a relatively slow process, and as the volume of liposome dispersion increases, the time required for purification also increases. Moreover, the time required for purification is inversely proportional to the surface area available for diffusion [604]. As the scale increases, achieving efficient dialysis becomes challenging, leading to lower throughput [605] and potentially longer processing times. In addition to this, achieving uniform and complete buffer exchange across large volumes of liposomal dispersion can be challenging, leading to variability in liposome properties. However, due to the small production scale of liposomes employed in the current study, using dialysis for formulation purification was deemed suitable. Thus, here we present a rapid dialysis method for purification of bacteriomimetic liposomes resulting in residual levels of solvent below the ICH limits.

3.4.2. Nisin-adsorbed POPE:POPG:CL Liposomes

Following the initial optimization of empty liposomes, the selected F7 formulation (FRR 4:1, TFR 5 mL/min, lipid concentration 8 mg/mL) was employed as a platform for surface adsorption of the model peptide nisin in a two-step process (as described in 3.3.2.2.1). Nisin surface-adsorption was achieved by controlled mixing of pre-formed liposomes and nisin aqueous solution in the channels of the SHM by varying FRR, TFR and nisin solution concentration. While POPE:POPG:CL liposomes (as the 'shell' component of LPHNPs) are ultimately intended for RN7IN6 delivery, nisin was chosen in order to perform an initial screening of the design space for liposome surface-adsorption. While both peptides are amphiphilic in nature and carry the same net charge, nisin was not specifically selected in order to mimic RN7IN6 - and indeed, the two peptides differ in physicochemical characteristics such as peptide sequence length and molecular weight (Table 3-7). Nisin was rather chosen as a model peptide for initial surface adsorption studies due to its availability, cost-effectiveness, and ease of acquisition compared to RN7IN6. Indeed, nisin serves as a practical surrogate for preliminary screening within our study's constraints of time and budget. This approach allowed for efficient

exploration of the design space for bacteriomimetic liposome surface adsorption, facilitating subsequent investigations with RN7IN6.

Table 3-7:Comparison between main RN7IN6 and nisin physicochemical characteristics.

	RN7IN6	Nisin
Peptide sequence length	13 aa	34 aa
Molecular weight (g/mol)	1714.07	3354.09
Net charge*	+4	+4
Isoelectric point	14.0	8.8
Peptide nature	Amphiphilic	Amphiphilic
Peptide structure	linear	polycyclic

Loading studies aimed to identify and understand the parameters that influence AMP-adsorbed bacteriomimetic liposome size, PDI and AE% immediately after liposome loading as well as following purification, by performing a Taguchi DoE. Optimum conditions for nisin-adsorbed liposomes were determined as described in section 3.3.2.2.1. Optimization of the particle size and PDI was performed using the Taguchi's 'smaller-is-better' criterion to achieve a particle size and a PDI as small as possible. In contrast, optimization of the AE% was performed using the Taguchi's 'larger-is-better' criterion to achieve a high AE%.

Figure 3-8 A, B and C shows liposome size, PDI and Z-Potential results for the set of 9 experiments performed before and after purification using centrifugal ultrafiltration as detailed in section 3.3.2.2.2. Liposome size before purification ranged from 97.12 ± 1.77 nm to 241.05 ± 60.75 nm, with PDI values ranging from 0.16 ± 0.01 to 0.26 ± 0.02, while the Z-Potential ranged from -25.07 ± 1.57 mV to -22.57 ± 0.86 mV. Liposomes size after purification showed sizes ranging from 147.43 ± 38.02 nm to 250.67 ± 22.25 nm, PDI values from 0.24 ± 0.05 to 0.36 ± 0.06 and Z-Potential values ranging from -27.23 ± 0.68 mV to -23.00 ± 1.50 mV. These results indicate a small and monodisperse liposome population both immediately after preparation and loading as well as after purification, and a negative surface charge for all formulations manufactured.

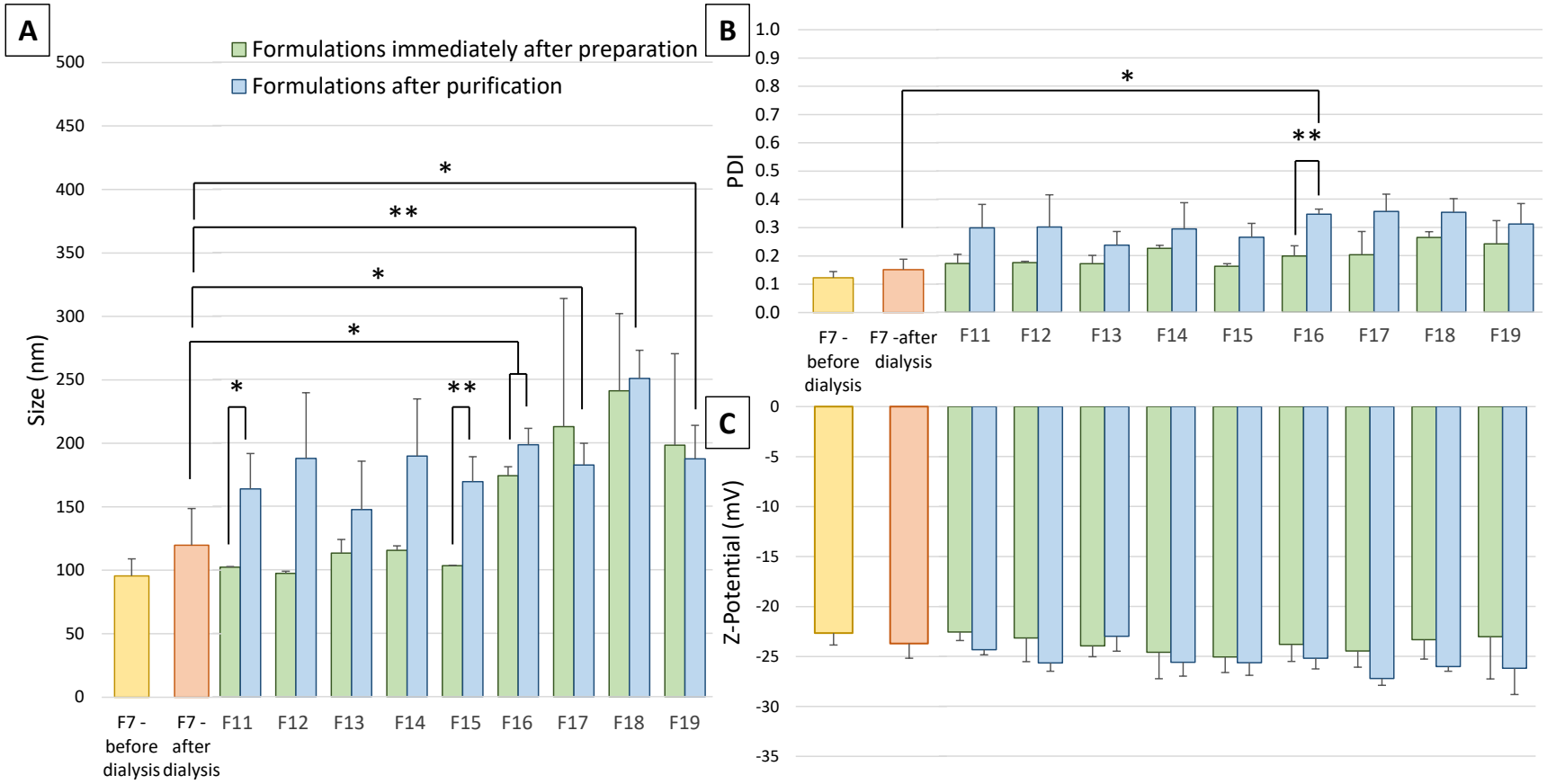

Figure 3-8: Size (A), PDI (B) and Z-Potential (C) of the 9 nisin-adsorbed liposome formulations prepared according to Taguchi L9 orthogonal array DoE. The results represent mean ± SD, n=3 independent batches. If the two-tailed p-value is less than 0.05, it is flagged with one star (*). If the two-tailed p-value is less than 0.01, it is flagged with 2 stars (**).

An independent T-test was run on liposome size, PDI and Z-Potential to determine if there was a mean difference in formulation physicochemical characteristics before and after purification. The T-test results showed that there was a significant difference in size for F11 and F15 (Figure 3-8 A) and in PDI for F16 (Figure 3-8 B) before and after liposome purification and resuspension in PBS ($p<0.05$) In contrast, the mean Z-Potential of all formulations was not affected by centrifugal ultrafiltration (Figure 3-8 C).

Upon association of nisin with POPE:POPG:CL liposomes and removal of non-adsorbed AMP through ultrafiltration, liposome size significantly increased for formulations F16 to F19 ($p<0.05$) in comparison to purified empty formulation (Figure 3-8). A trend can be outlined when considering that formulations loaded using higher effective nisin concentrations (calculated from the nisin loading concentration and the specific FRR used to manufacture each formulation, also referred to as "Final nisin concentration") were significantly affected in terms of liposome size by AMP surface adsorption (Table 3-8). This result is also in line with the analysis of the DoE results by Minitab 16 Statistical Software®, indicating that higher initial nisin concentrations (concentration of nisin in PBS introduced at the start of the formulation process, prior to any adjustments of the FRR used during manufacture) drives the formation of larger and more polydisperse particles (Figure 3-9 A and B). A significant increase in PDI was only observed for formulation F16, while the Z-potential of all formulations was not significantly affected by nisin adsorption to liposomal surfaces (Figure 3-8 C). This lack of change in Z-potential might potentially reflect the minimal amount of nisin adsorbed, which was insufficient to substantially alter the effective surface charge density.

Table 3-8: Formulations F11-F19 and the respective theoretical final nisin concentration in formulation before removal of non-adsorbed nisin. The final nisin concentration (mg/mL) represents the calculated concentration of nisin in formulation based on initial loading concentration and the specific FRR used during formulation. Formulations are ordered from lowest to highest final nisin concentration.

Formulation	Final nisin conc. mg/mL
F13	0.17
F12	0.25
F11	0.50
F15	0.50
F14	0.75
F17	0.83
F19	1.25
F16	1.50
F18	2.50

The collected data depicted in Figure 3-8 were analyzed by Minitab 16 Statistical Software® and results are shown in Figure 3-9 as a rank, where rank 1 shows the maximum influential factor on the output parameter (particle size and PDI) and rank 3 indicates the factor with the least influence. According to the ranking calculated by the software, the parameter that had the greatest influence on liposome size and PDI before or after purification was nisin loading concentration, followed by FRR, and finally TFR (Figure 3-9 A and B, respectively).

A

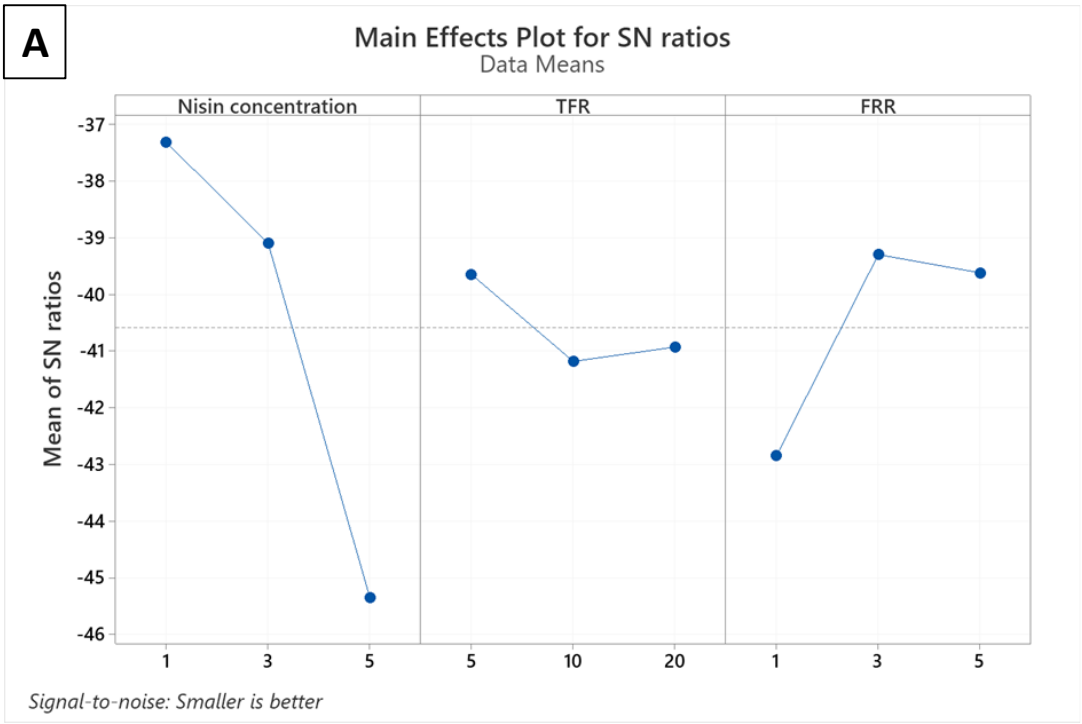

Rank:	1	3	2

B

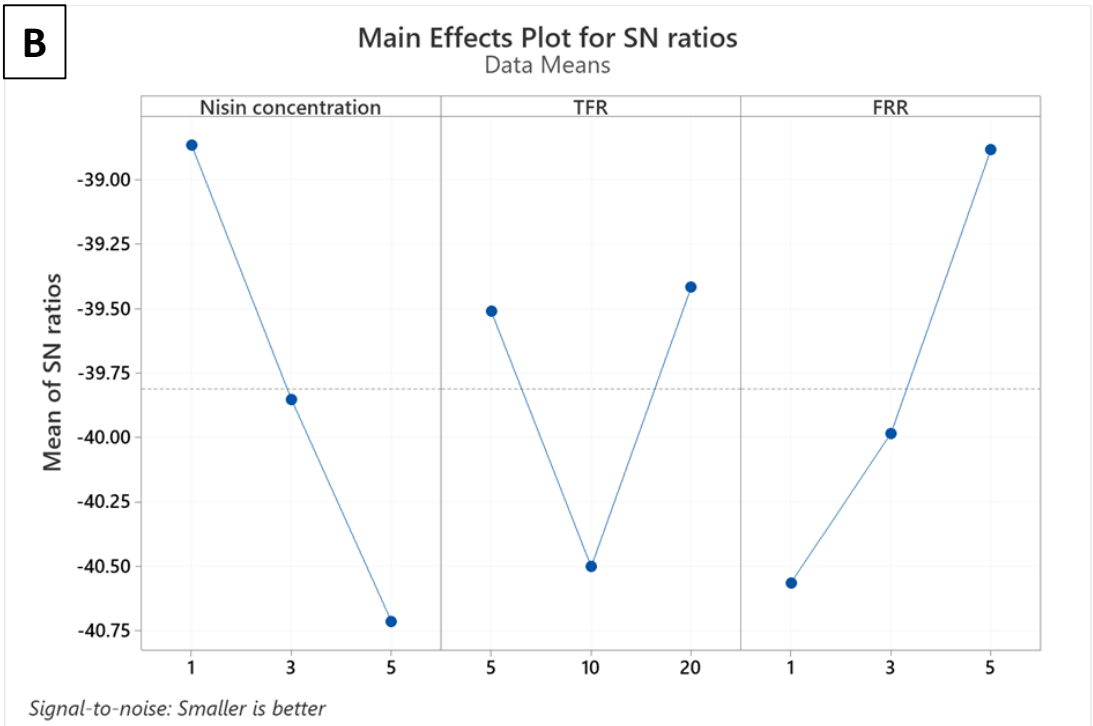

Rank:	1	3	2

Figure 3-9: Nisin-adsorbed liposome size and PDI before (A), and after purification (B) mean signal-to-noise (S/N) graph response. The nisin concentration has the most substantial impact (ranked 1), while FRR and TFR show lesser effects, ranked 2 and 3, respectively.

The performance of multiple linear regression analysis (Table 3-9) for nisin-adsorbed liposome size before purification indicated that only initial nisin concentration affected liposomes size with statistical significance, while the initial nisin concentration ($p = 0.032^*$) and FRR ($p = 0.045^*$) significantly affected liposome size after purification (Table 3-9). The R^2 value for the regression analysis was found to be 0.334 for liposome size before purification and 0.300 for liposome size after purification, indicating that 33.4% and 30.0%, respectively, of the variability of the dependent variable (output, liposome size in this case) is explained by the independent factors of the model, which may suggest that the model is not a good fit for the data.

Similarly, the linear regression analysis performed for liposome PDI before purification revealed that only initial nisin concentration affected this output with statistical significance (Table 3-9). On the other hand, the linear regression analysis performed for liposome PDI after purification revealed that none of the parameters employed in the study affected the output with statistical significance (Table 3-9). The very low value of calculated R^2 for PDI before and after purification (0.324 and 0.175, respectively) revealed that the model is not a good fit for the data. The low R^2 for PDI before and after purification could indicate the presence of additional variables or interactions not included in the model that may influence PDI. Additionally, the complexity of nisin's interaction with the lipid bilayer may lead to non-linear effects on PDI, which a simple linear model might not capture adequately. Consequently, a more complex model, potentially incorporating non-linear or interaction terms, might better describe the data.

Table 3-9: Regression analysis of nisin-adsorbed liposome size and PDI before and after purification versus liposomes preparation variables. Regression analysis of nisin-adsorbed liposome size and PDI before and after purification versus liposome preparation variables. The results of a regression analysis examinined the impact of nisin concentration (A), TFR (B), and FRR (C) on liposome particle size and PDI before and after the purification step detailed in section 3.3.2.1.1. Coefficients, standard errors, t-values, and p-values for each predictor variable are shown to assess the significance of each factor. The constant values reflect baseline measurements of size and PDI in liposome preparations without predictor adjustments, while the asterisks (*) highlight statistically significant values ($p < 0.05$).

		Particle size				PDI			
	Predictor (Symbol)	**Coefficients**	**Coefficients St. Err.**	**T**	**p**	**Coefficients**	**Coefficients St. Err.**	**T**	**p**
Liposomes before purification	**Constant**	103.867	79.304	1.310	0.203	0.184	0.038	4.832	0.000*
	Nisin concentration (A)	43.622	14.479	3.013	0.006*	0.02	0.007	2.828	0.01*
	Total Flow Rate (B)	0.383	3.791	0.101	0.92	158700	0.002	0.009	0.993
	Flow Rate Ratio (C)	-22.674	14.479	-1.566	0.131	-0.12	0.007	-1.736	0.096
Liposomes after purification	**Constant**	188.933	24.362	7.755	0.000*	0.309	0.049	6.303	0.000*
	Nisin concentration (A)	10.147	4.448	23281	0.032*	0.015	0.009	1.717	0.099
	Total Flow Rate (B)	-0.402	1.165	-0.345	0.733	-0.001	0.002	-0.488	0.630
	Flow Rate Ratio (C)	-9.453	4.448	-2.125	0.045*	-0.012	0.009	-1.302	0.206

The *F* value in the ANOVA table (Table 3-10) tests whether the overall regression model has any predictive power over the data, even if it may not account for all variances within the dataset. Table 3-10 shows that the independent variables predict liposome size (F(3, 23) = 3.846, *p* = 0.023*) and PDI (F(3,23) = 3.67, p = 0.027*) before purification with statistical significance. Although this suggests the model can predict trends within the data, it does not mean the model explains all of the variability in the output. However, the model can only predict nisin-adsorbed liposome size after purification with statistical significance (p = 0.039*, Table 3-10) and not PDI. Thus, the regression models offer a partial fit for predicting certain effects in the data rather than a comprehensive fit of all variables.

Table 3-10: ANOVA tables of fitted model for nisin-adsorbed liposome size and PDI before and after purification. ANOVA results for models assessing the influence of nisin concentration, TFR, and FRR on liposome size and PDI pre- and post-purification. Asterisks (*) indicate significance (p < 0.05).

		Source	Degree of Freedom	Sum of Squares	Mean square	F	p
Liposomes before purification	*Particle size*	Regression	3	174175.497	58058.499	3.846	0.023*
		Residual error	23	347159.756	15093.902		
		Total	6	521335.253			
	PDI	Regression	3	0.038	0.013	3.67	0.027*
		Residual error	23	0.08	0.003		
		Total	6	0.118			
Liposomes after purification	*Particle size*	Regression	3	14014.127	4672.376	3.280	0.039*
		Residual error	23	32760.500	1424.370		
		Total	6	46777.627			
	PDI	Regression	3	0.28	0.009	1.628	0.21
		Residual error	23	0.133	0.006		
		Total	6	0.161			

Regarding nisin AE%, Figure 3-10 displays nisin AE% (bars) and concentration of nisin adsorbed (dots) for the set of 9 experiments performed, indicating AE% ranging from 8.25 ± 3.81 to 74.08 ± 3.75%. Results showed that positively charged nisin was able to electrostatically bind to the surface of the highly negatively charged POPE:POPG:CL liposomes with different encapsulation efficiencies, dependent upon the selection of specific formulation parameters.

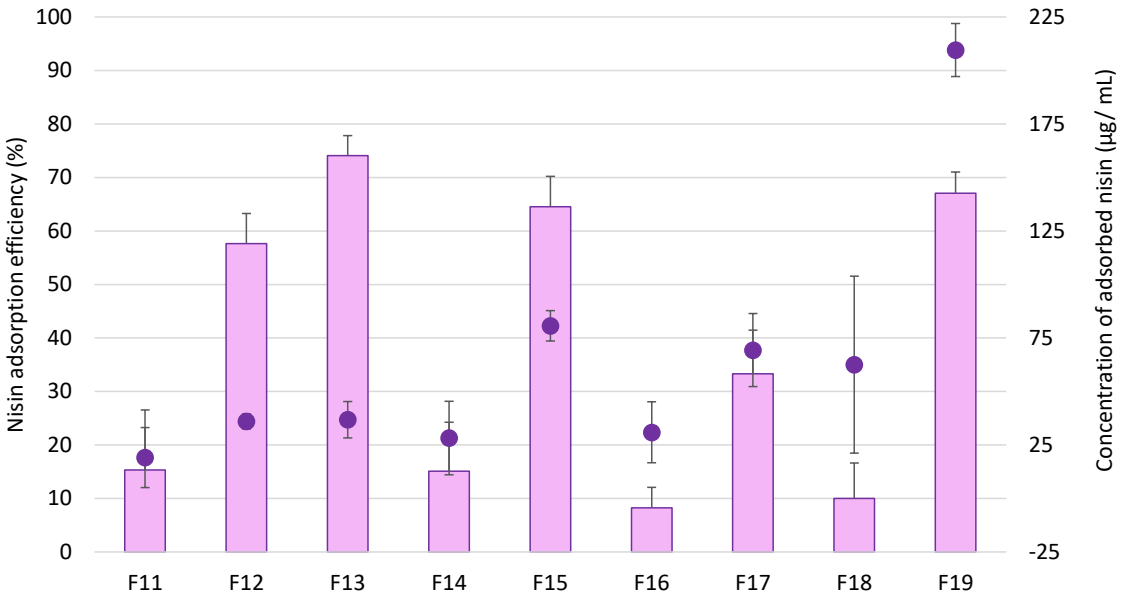

Figure 3-10: Nisin AE% (bars) and concentration of nisin adsorbed (dots) for each liposome formulation. Results represent mean ± SD, n=3 independent batches.

The analysis of the results by Minitab 16 Statistical Software® are shown in Figure 3-11. The parameter which affected AE% the most was FRR, followed by initial nisin concentration and TFR. On the other side, the ranking for parameters affecting adsorbed nisin concentration was TFR, initial nisin concentration and FRR (Figure 3-11). According to Taguchi DoE analysis with the 'larger-is-better' criterion, the best formulation in term of AE% can be manufactured employing the following parameters: nisin loading concentration 1 mg/mL, TFR 10 mL/min or 20 mL/min indistinctly, and FRR 5:1, which corresponds to formulation F13, while the formulation with the highest adsorbed nisin concentration can be manufactured with 5 mg/mL of nisin loading concentration, TFR 20 mL/min and a FRR of 5:1, which does not correspond to any of the formulations manufactured as part of the DoE. However, F17 includes a nisin concentration of 5 mg/mL, TFR of 5 mL/min, and FRR of 5:1, while F19 uses a nisin concentration of 5 mg/mL, TFR of 20 mL/min, and FRR of 3:1. Each of these formulations, therefore, shares two out of the three specified parameters with the optimum parameters derived from the DoE analysis.

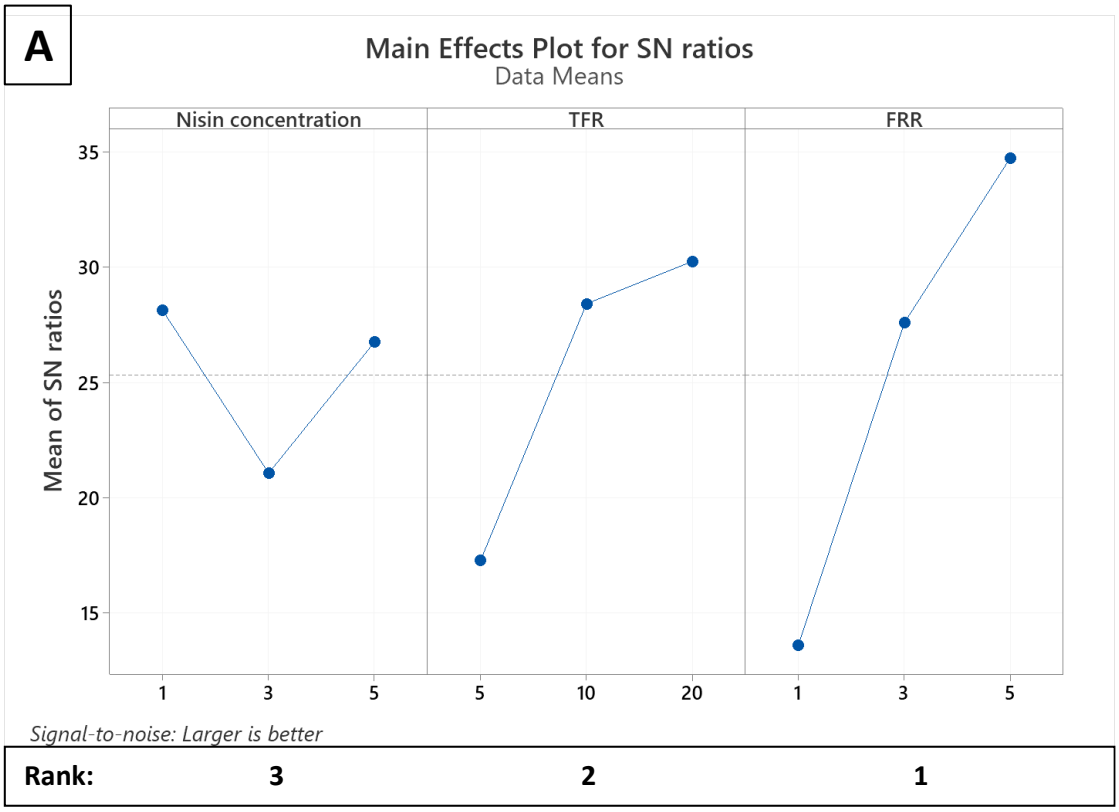

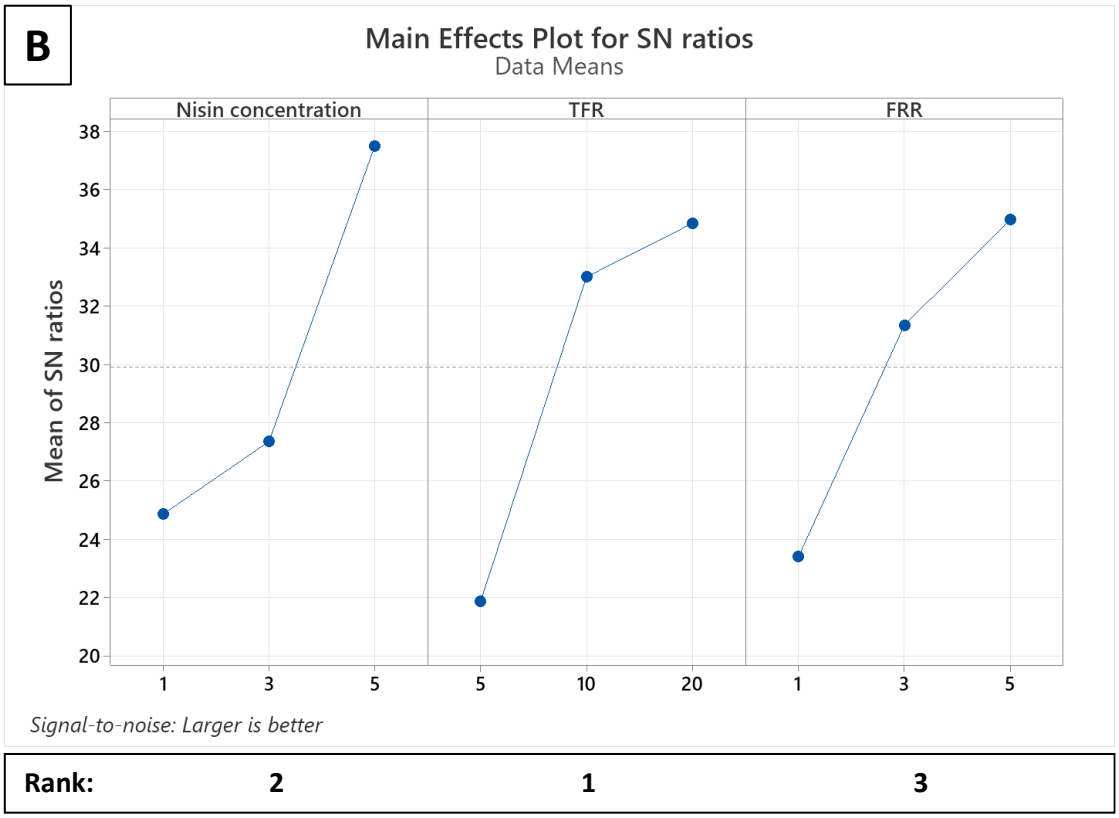

Figure 3-11: Nisin AE% (A) and adsorbed concentration (B) mean signal-to-noise (S/N) graph response. The TFR has the most substantial impact (ranked 1), while nisin concentration and FFR show lesser effects, ranked 2 and 3, respectively.

Multiple linear regression analysis was performed and indicated that all the parameters affected nisin AE% with statistical significance (Table 3-11, initial nisin concentration p=0.045*, TFR p=0.001*, FRR p=0.000*) while only initial nisin concentration (p=0.000*) and TFR (p=0.0168) significantly affected the adsorbed nisin concentration (Table 3-11).

Table 3-11: Regression analysis of nisin-adsorbed liposome AE% and adsorbed nisin concentration versus liposome preparation variables. Regression analysis of liposome AE% and adsorbed nisin concentration versus liposome preparation variables. The regression analysis examinined the impact of nisin concentration (A), TFR (B), and FRR (C) on liposome AE% and adsorbed nisin concentration. Coefficients, standard errors, t-values, and p-values for each predictor variable are shown to assess the significance of each factor. The constant values reflect baseline measurements of size and PDI in liposome preparations without predictor adjustments, while the asterisks (*) highlight statistically significant values (p < 0.05).

	Predictor (Symbol)	Coefficients	Coefficients St. Err.	T	p
AE% (%)	Constant	-9.467	10.961	-0.864	0.397
	Nisin concentration (A)	-4.245	2.001	-2.121	0.045*
	Total Flow Rate (B)	2.056	0.524	3.923	0.001*
	Flow Rate Ratio (C)	12.723	2.001	6.358	0.000*
Adsorbed nisin concentration (µg/mL)	Constant	-58.403	29.321	-2.062	0.51
	Nisin concentration (A)	20.797	5.171	4.022	0.000*
	Total Flow Rate (B)	3.527	1.354	2.605	0.016*
	Flow Rate Ratio (C)	6.190	5.171	1.197	0.243

The high R^2 value for the regression analysis for AE% (R^2 = 0.724) and adsorbed nisin concentration (R^2 = 0.515) indicated that 72.4% and 51.5%, respectively of the variability of the dependent variable is explained by the independent factors of the model, being initial nisin concentration, TFR and FRR. In addition, the results of ANOVA and F-Test performed on the obtained data, indicated that the fitted model can predict nisin AE% and adsorbed nisin concentration with statistical significance (p = 0.000*,Table 3-12) hence the regression models represent a good fit of the data.

Table 3-12: ANOVA tables of fitted model for nisin-adsorbed liposome AE% and adsorbed nisin concentration. ANOVA results for models assessing the influence of nisin concentration, TFR, and FRR on liposome AE% and adsorbed nisin concentration. Asterisks (*) indicate significance (p < 0.05).

	Source	Degree of Freedom	Sum of Squares	Mean square	F	p
Adsorption Efficiency (%)	Regression	3	17389.956	5796.652	20.102	0.000*
	Residual error	23	6632.301	288.361		
	Total	6	24022.257			
Adsorbed nisin concentration (µg/mL)	Regression	3	46962.475	15654.158	8.123	0.000*
	Residual error	23	44275.558	1925.024		
	Total	6	91238.033			

3.5. Conclusion

The present study aimed at optimizing the formulation of blank POPE:POPG:CL liposomes using microfluidic mixing technology and investigating the capacity of these liposomes to surface adsorption an AMP in the form of the model peptide nisin. Results revealed that microfluidic mixing technology is a promising approach to manufacture blank POPE:POPG:CL liposomes, and also a useful tool for the surface adsorption of an AMP while maintaining a small and uniform liposome size. This work serves as a foundation for the further development of liposomal formulations and will inform subsequent studies with the novel AMP, RN7IN6, in Chapter 4.

4. Bacteriomimetic Liposomes as a Platform for RN7IN6 Delivery

4.1.Introduction

4.1.1. RN7IN6 AMP

As previously discussed in Chapter 3, liposomes present an excellent platform for AMP delivery. In the context of Chapter 3 a POPE:POPG:CL liposomal formulation was developed, optimized and manufactured as a delivery system, with nisin being surface adsorbed to pre-formed liposomes. Nisin was employed as a readily available AMP model, allowing for the performance of initial screening to understand production parameters affecting liposome physiochemical characteristics prior to formulation with RN7IN6.

RN7IN6 is a novel synthetic AMP, derived from the naturally occurring indolicidin and ranalexin (Table 4-1). It was first synthesized by Jindal *et al.* and has shown potent antibacterial activity against *Streptococcus pneumoniae* in particular [606]. RN7IN6 showed faster killing time than antibiotics such as ceftriaxone and erythromycin against *S. pneumoniae*, which sets the basis for the usage of such a potent hybrid AMP. In addition, RN7IN6 demonstrated antimicrobial activity against other bacteria, such as *E. coli*, *S. aureus,* MRSA and *P. aeruginosa*. Jindal *et al* also investigated the mechanism of action of RN7IN6 against *S. pneumoniae,* and observed that the peptide was capable of disrupting the integrity of the bacterial membrane, resulting in bacterial death after 1 hour of incubation which was determined via the leakage of cytoplasmatic components [173].

Table 4-1: Amino acid sequence of RN7IN6 and parent peptides, ranalexin and indolicidin. The amino acids highlighted in bold within each peptide sequence represent the portions of the parent peptides, ranalexin and indolicidin, that make up the synthetic peptide RN7IN6.

Antimicrobial peptide	Amino acid sequence
Ranalexin	**FLGGLIK**IVPAMICAVTKKC-OH
Indolicidin	ILPWKWP**WWPWRR**-NH2
RN7IN6	**FLGGLIKWWPWRR**-NH2

RN7IN6 has a short amino acid (aa) sequence (13 aa) and is positively charged (+4 net charge) which is essential for its ability to selectively target and kill microbial pathogens [607]. In contrast to mammalian cell membranes, microbial membranes exhibit a higher abundance of anionic phospholipids. This characteristic facilitates the attraction of positively charged AMPs to bind specifically to microbial cell membranes rather than mammalian cell membranes [608]. The balance of hydrophobic (53% [606]) and hydrophilic residues optimizes its amphipathic nature, membrane disruption ability, and bacterial selectivity [609-611]. However, the strong hydrophobic character of AMPs has been significantly correlated with toxicity to mammalian cells and a reduction in antimicrobial specificity [608]. Indeed, excessive hydrophobicity can lead to increased selectivity for zwitterionic membranes, resulting in increased cytotoxicity in mammalian cells [608]. While there is not a universally defined threshold for what constitutes 'excessive' hydrophobicity, it generally refers to a level that significantly increases the peptide's affinity for mammalian cell membranes, leading to undesired cytotoxic effects. Therefore, it is crucial to introduce measures to reduce the cytotoxicity of AMPs while retaining their specificity for bacterial cells. In this context, RN7IN6 has not been observed to exhibit cytotoxicity against mammalian cells at its MIC concentration, which is likely due to its balanced hydrophobicity [173]. This balance enables RN7IN6 to effectively target bacterial cells without disrupting the integrity of mammalian cell membranes, thereby reducing cytotoxic effects. However, it is worth noting that RN7IN6, due to its amphipathic nature, exhibits low water solubility, which may pose challenges for its delivery. This solubility issue can vary depending on whether the peptide is in its crude or pure form, though an exact solubility value is not currently available.

The association of AMPs with liposomes has been shown to mitigate cytotoxicity and enhance therapeutic efficacy [612, 613]. Liposomes also enhance AMP stability and targeted delivery, increasing intracellular drug concentration and reducing degradation [615].

4.1.2. Strategies for Association of AMPs with Liposomes

With respect to surface adsorption, electrostatic interactions play a crucial role in the conjugation of peptides with liposomes [616]. When both the peptide and the liposome are charged, electrostatic interactions become the dominant force driving the conjugation process [393]. Thus, the electrostatic interaction between the peptide and the liposome surface allows for the attachment of the peptide to the liposome [617]. However, electrostatic binding primarily influences the adsorption of peptides onto the liposome surface, rather than facilitating their encapsulation within the liposome core [618]. The electrostatic interactions between peptides and liposomes can be influenced by the charge properties of both entities. For example, liposomes with a positive charge can bind with peptides that have a negative charge via electrostatic attraction [619]. Conversely, peptides with a positive charge can bind with negatively charged liposomes [619]. Other important parameters affecting peptide adsorption onto liposomes include peptide length, charge, and hydrophobicity, as well as the composition of the liposome membrane, which not only influences hydrophobic interactions but also determines the surface charge of the liposome [620]. For instance, the peptide length can influence the extent of interaction: longer peptides might exhibit stronger interactions due to the greater number of contact points with the liposome surface. The hydrophobicity of peptides can in fact lead to bilayer rather than surface localization, with more hydrophobic peptides potentially integrating more deeply into the liposome membrane. Additionally, the liposome membrane's composition, including its lipid constituents, can significantly impact the strength and specificity of the binding interactions.

The exposure of peptides on liposome surfaces may present some significant advantages. Surface adsorption of peptides onto liposomes can enhance the therapeutic effectiveness and specificity of liposomal drug delivery systems, allow for exclusive targeting of and interaction with specific cells (such as bacteria) or tissues, thus improving the targeting and delivery of the peptide [621, 622]. In contrast, loading of AMPs into liposomal bilayers (either as a result of incorporation during formulation, or AMP migration following surface adsorption) has the potential to offer protection against degradation as well as a reduction in AMP cytotoxicity. Optimizing AMP membrane loading efficiencies requires careful attention to formulation [567, 623, 624].

While bilayer loading can increase loading capacity, it also requires precise control to avoid potential issues, such as disruption of the bilayer structure, aggregation, or coalescence [625, 626].

Thus, in the current chapter RN7IN6 will be both surface-adsorbed onto and incorporated into the lipid bilayer of POPE:POPG:CL liposomes by taking advantage of the electrostatic disparity between the liposome surfaces and both the cationic and amphiphilic nature of the AMP.

4.2.Aim and Objectives

The aim of this chapter was to establish and optimize the production of RN7IN6-associated POPE:POPG:CL liposomes using a microfluidic mixing technique. The optimization of RN7IN6-associated POPE:POPG:CL liposomes in this chapter is a critical step towards developing the lipid component of the LPHNP system, supporting the thesis goal of creating an effective dual-delivery nanocarrier for CTX and RN7IN6.

This aim was achieved through the following objectives:

- Synthesis of RN7IN6 AMP using a Fmoc-SPPS method, followed by purification, characterization, and antimicrobial testing against clinically relevant bacteria (*S. aureus, P. aeruginosa, E. coli, and K. pneumoniae*) using resazurin and time-kill assays.
- Formulation and characterization of RN7IN6-association with POPE:POPG:CL liposomes, with microfluidic parameters optimized for production of nisin-adsorbed liposomes (Chapter 3) being employed as a starting point
- Antimicrobial testing of RN7IN6-loaded POPE:POPG:CL liposomes against *S. aureus* and *E. coli* using a time-kill assay, alongside evaluation of their physicochemical characteristics and release kinetics under varied initial peptide concentrations and FRR.

4.3. Materials and Methods

4.3.1. Materials

All Fmoc proteinogenic L-amino acids, Rink Amide ProTide resin (100-200 mesh, 0.56 mmol/g) and Oxyma Pure™ were purchased from CEM corporation (Matthews, USA). N,N'-diisopropylcarbodiimide (DIC), piperidine, trifluoroacetic acid (TFA), triisopropylsilane (TIPS), Mueller Hinton Broth 2 (MHB2), Mueller Hinton Agar (MHA), Nutrient agar (NA), resazurin and dialysis tubing (cellulose membrane, MWCO ~14kDa) were purchased from Sigma-Aldrich (Missouri, USA). POPE, POPG and CL were purchased from Avanti Polar Lipids (Merck, Ney Jersey, USA). Gentamicin discs (CN 10), ciprofloxacin discs (CIP 5) and PBS, pH 7.4, tablets were obtained from Oxoid Ltd (Basingstoke, UK). DMF was purchased from Acros Organics (New Jersey, USA). TrypLE solution was purchased from Thermo Fisher (Massachusetts, USA).

4.3.2. Methods

4.3.2.1. Antimicrobial Peptide RN7IN6

4.3.2.1.1. Fmoc Solid Phase peptide Synthesis

The Peptide Companion Excel spreadsheet was used to predict difficult couplings within the peptide sequence (http://www.spyderinstitute.com/software.htmL). RN7IN6 was examined with this tool to predict challenging coupling steps requiring double coupling to increase the likelihood of high synthesis yields.

RN7IN6 was prepared using an automated Fmoc-SPPS method on a Liberty Blue microwave-assisted Peptide Synthesizer (CEM, USA). RN7IN6 method was adapted from that of D'Aloisio *et al.* [449]. Solid phase synthesis was conducted on a 0.1 mmol scale using Rink Amide ProTide resin (179 mg, 0.56 mmol/g loading) employing the required Fmoc L-amino acids (0.2 M in DMF; 5eq.), and DIC (1 M in DMF; 10 eq.), Oxyma Pure (1 M in DMF; 5 eq.) and piperidine (20% *v/v* in DMF; 4 mL) as activator, racemization suppressor and deprotection reagent, respectively. The peptide synthesis was carried out using a standard coupling procedure employing double coupling of each amino acid (2.5 min, 90 ^{o}C) and Fmoc deprotection (2 min, 90 ^{o}C). Fmoc-Arg(Pbf)-OH was coupled with triple coupling under mild conditions (75 ^{o}C), while the subsequent Fmoc-Trp(Boc)-

OH was coupled with triple coupling (2.5 min, 90 ^{o}C). Upon completion of SPPS synthesis, the resin was washed with DIC and then shrunk with diethyl ether. Subsequently, the peptide was cleaved from the resin using 4 mL of cleavage solution (TFA, TIPS, water (8:1:1 v/v)) under regular shaking (Eppendorf Thermomixer comfort) at room temperature for 3 h. The crude peptide was precipitated dropwise in a cold mixture of diethyl and petroleum ether (1:1 v/v) and the obtained suspension was centrifuged (10 min, 3500 rpm, Eppendorf centrifuge 5804r, Germany). The pellet was then washed twice using a cold mixture of diethyl and petroleum ether (1:1 v/v) to remove the residual TFA. Finally, the crude peptide was dissolved in water, flash-frozen using liquid nitrogen, and lyophilized.

4.3.2.1.2. RN7IN6 Characterization: Liquid Chromatography-Mass Spectrometry (LC-MS) Analysis

Characterization of crude and purified RN7IN6 was performed with an orthogonal acceleration-time of flight (oa-TOF) mass spectrometer (Waters LCT) as described by D'Aloisio *et al.* [449]. The first system, constituting low-resolution LC-MS analysis, used an XBridge (Waters) C18 analytical column (5 µm particle size, 4.6 x 150 mm) with a binary eluent system comprising ACN/H_2O (20 min gradient: from 90% H_2O/10% ACN to 100% ACN with 0.1% FA in both phases) as mobile phase. Electrospray ionization mass spectrometry was conducted in positive ion mode (m/z range: 600–1700) using a cone voltage of 50 V, desolvation temperature of 300 °C and source temperature of 100 °C. Exact mass measurements of the products were based on the protonated molecules $[M^{+}H]^{+}$.

The second system employed high-resolution LC-MS analysis using an Agilent 85 ZORBAX Eclipse Plus C18 Rapid Resolution HD analytical column (1.8 µm particle size, 2.1 x 50 mm) with a binary eluent system comprising ACN/H_2O with 0.1% FA (from 1% to 99% ACN over 12 min gradient) as mobile phase as described by Killoran *et al.* [627]. Electrospray ionization mass spectrometry was conducted in positive ion mode (m/z range: 50 – 3200) using a fragmentor voltage of 150 V, gas temperature of 325 °C (flow 10 L/min) and sheath gas temperature of 400 °C (flow 11 L/min). In both cases, wavelengths detected were 214 nm and 280 nm and operating pressures were in the

range of 2000-3000 PSI and the exact mass measurements of the products were based on the protonated molecules $[M^+H]^+$.

4.3.2.1.3. RN7IN6 Characterization: HPLC Analysis

Analytical purity of produced AMP was determined by RP-HPLC using a method adapted from the one described by Polunin *et al.* [628]. The method used an Agilent 1200 series equipped with an Agilent Eclipse XDB-C18 column (4.6 × 150 mm, particle size 5 µm) by measuring the UV absorbance at 215 nm (HPLC system equipment is described in section 2.3.2.2.2). Samples were prepared by dissolving the compounds in water. The HPLC was used with a two-component system: mobile phase A (H_2O/ACN 95/5%, 0.1% TFA) and mobile phase B (H_2O/ACN 5/95%, 0.1% TFA). The run time was 34 min at a flow rate of 0.8 mL/min and column oven temperature was set at 25 ^oC (injection volume 10 µL). The elution method was set up as follows: from 0 to 20 min, a gradient was applied from 100% H_2O/ACN 95/5%, 0.1% TFA to 0% H_2O/ACN 95/5%, 0.1% TFA, after which the system was flushed with 100% H_2O/ACN 5/95%, 0.1% TFA for 3 min and, finally, equilibrated back to initial conditions for 11 min.

The purity percentage of the RN7IN6 was calculated comparing the peak of the main product with the side products as shown in Equation 4-1 using RP-HPLC analysis.

Equation 4-1

$$RN7IN6\ purity\ \% = \frac{Peptide\ area}{Sum\ of\ all\ areas}\ x\ 100$$

4.3.2.1.4. RN7IN6 Purification

Depending on the characterization and purity investigation performed on crude RN7IN6 as described in section 4.3.2.1.3, the peptide was purified using either preparative-HPLC or flash chromatography.

Preparative HPLC

For preparative-HPLC purification, crude samples (10 mg/mL in H_2O/ACN 80/20) were purified using an Agilent Infinity 1260 equipped with a Waters XBridge Peptide BEH C18 Prep 130 Å column (5 µm particle size, 10 x 150 mm) as described by D'Aloisio *et al.* [629]. A gradient elution method used H_2O/ACN (30 min: from 45 to 60% ACN, with 0.1% TFA, followed by a 100% ACN for 5 minutes) at a flow rate of 8 mL/min and 50-600 µL injection volumes. The column was kept at room temperature and signals were recorded at 215 nm. Isolated pure compound solutions were concentrated by evaporating residual organic solvents under an N_2 line. The resulting aqueous solutions were analyzed for purity by HPLC, flash frozen with liquid nitrogen, freeze-dried, and stored at -20 ^{o}C.

Flash Chromatography

Flash purification of RN7IN6 was performed using a Teledyne ISCO CombiFlash® NextGen 300+ instrument (California, US). The method was adapted from that described by D'Aloisio *et al.* [629]. Crude samples (8-16 mg/mL; 1 mL) were separated using RediSep Rf C18 Gold® 5.5 g cartridges (Teledyne ISCO) with a binary eluent system comprising water/0.1% TFA (A) and ACN/0.1% TFA (B) as mobile phase, from 10% to 100% B in 6 min. Flow rate was set at 18 mL/min and detection wavelengths were 215 nm and 280 nm. Solutions containing isolated pure compounds were concentrated by evaporating residual organic solvents under an N_2 line and the resulting aqueous solutions were analyzed for purity by HPLC, flash frozen with liquid nitrogen, lyophilized, and stored at -20 °C.

4.3.2.1.5. Free RN7IN6 in Vitro Antibacterial Activity

Free RN7IN6 was tested for antimicrobial activity against *P .aeruginosa* (NCTC 12903), *E. coli* (NCTC 2241), *S. aureus* (NCTC 12981) and *K. pneumoniae* (NCTC 9633) using the Resazurin Microtiter Plate assay (REMA) and the Time-kill assay.

REMA

The REMA method was adapted from that of Khalifa *et al.* [630]. MHA and MHB for microorganism sub-culturing and testing were prepared by dissolving 38 g or 21 g of base powder, respectively, in 1 L of distilled water into Duran bottles which were sterilized for 15 minutes at 121 °C. After autoclave-sterilization, MHB was stored in Duran bottles, while MHA was poured into 90 mm sterile agar plates, left to solidify overnight and subsequently stored at 4 °C.

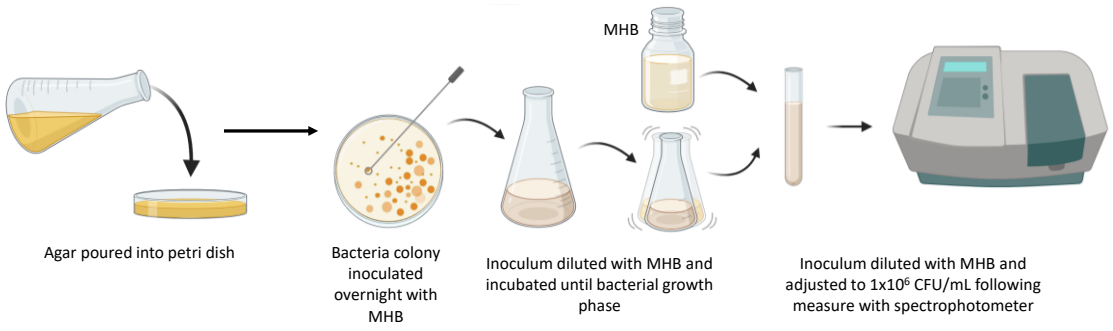

Figure 4-1: Schematic representation of the bacterial suspension preparation. Created with BioRender.com.

The preparation for the standardized bacterial suspension was achieved by the selection of a microorganism colony followed by its suspension in 50 mL of MHB, which was left to incubate in an orbital shaking incubator (250 rpm) set at 37 °C overnight (Figure 4-1). A 40 µL volume of the overnight culture was used to inoculate 150 mL of MHB, which was left in an orbital shacking incubator (250 rpm) set at 37 °C for 3 hours. Subsequently, bacterial suspensions were adjusted to OD_{600} 0.05-0.1, which corresponds to $1x10^6$ CFU/mL, after their OD_{600} measurement on a SpectroStar Nano microplate reader (BMG LABTECH). The OD_{600} that corresponds to $1x10^6$ CFU/mL was previously determined by bacterial growth curves

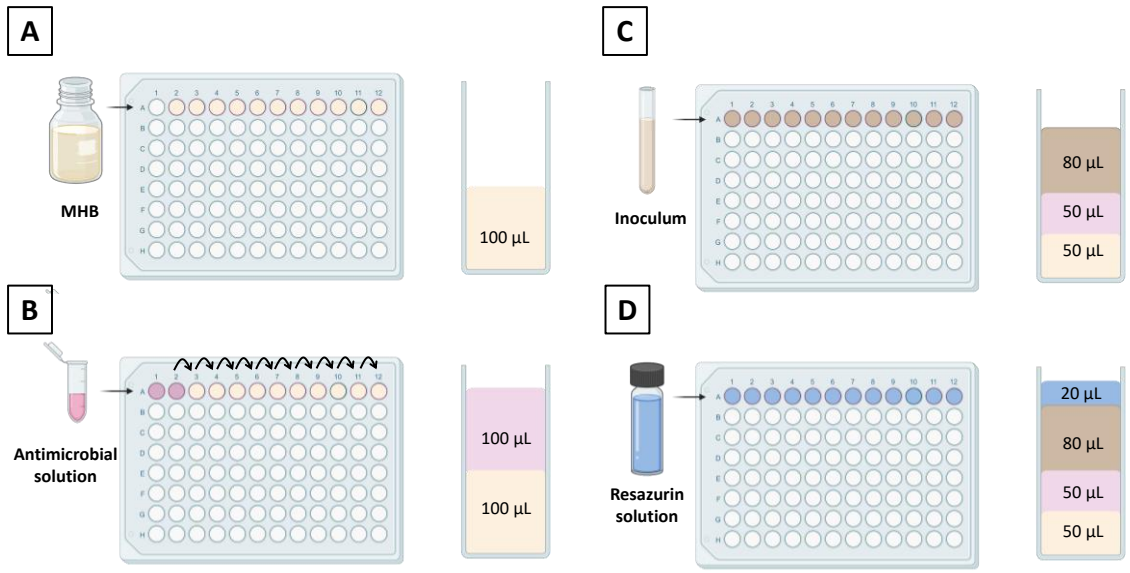

Figure 4-2: The process of determining the Minimum Inhibitory Concentration (MIC) using a 96-well microtitre plate, with vertical sections illustrating the contents of Well 2A at each step. (A) Addition of MHB to wells 1-12, (B) addition of RN7IN6 solution to wells 1 and 2 and two-fold dilutions from well 2 to well 12, (C) addition of bacteria inoculum suspension and (D) addition of resazurin solution. Created with BioRender.com.

A 100 µL volume of sterile MHB was added to 2-12 wells in a 96-well flat bottom microtitre plate (Figure 4-2 A), while 100 µL of RN7IN6 stock solution in sterile water was added to the wells 1 and 2 (Figure 4-2 B). A total of 10 successive 2-fold dilutions of the agent to test in broth were made from well 2 to 12, then 80 µL of adjusted bacterial suspension followed (Figure 4-2 C) by a 20 µL aliquot of sterile resazurin solution in MHB (0.2 mg/mL) were added to each well (Figure 4-2 D). The 96-well flat bottom microtitre plate was incubated overnight at 37 °C. The MIC endpoint was visually evaluated as the lowest nisin concentration which prevented a color change from blue to pink, following the adapted method from the standardized EUCAST guidelines (Figure 4-3). Controls were performed alongside each experiment: the negative control consisted of MHB + resazurin solution, the positive control consisted of MHB + resazurin solution + inoculum, and an additional control (MHB + resazurin + RN7IN6 solution) was included to verify that RN7IN6 did not affect the turbidity or color of the broth, ensuring accurate interpretation of the results.

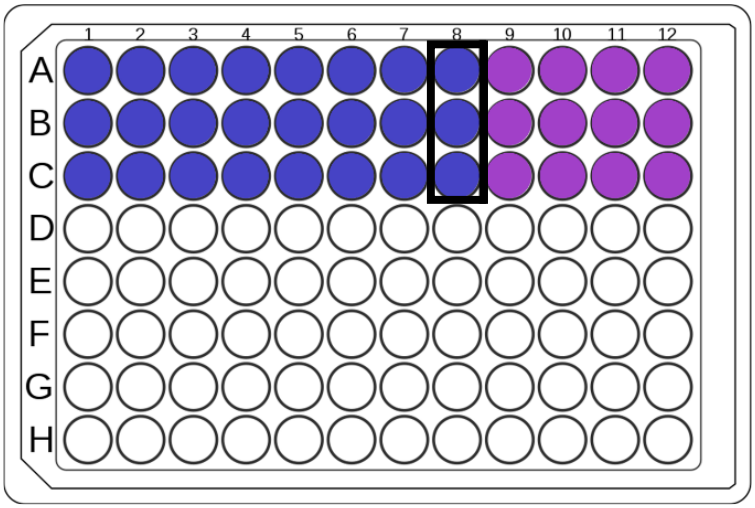

Figure 4-3: Schematic representation of the appearance of a 96-well plate after RN7IN6 incubation with bacterial inoculum and resazurin solution. Blue-colored wells indicate bacterial growth inhibition, while pink-colored wells represent viable bacterial cells. The black box indicates the MIC value, which corresponds to RN7IN6 concentration in column 8. Created with BioRender.com.

Time-kill Assay

The time-kill assay method was adapted from Montero *et al.* [631]. A standardized bacterial suspension was prepared as described above. Following overnight incubation, the inoculum was spectrophotometrically adjusted to $1x10^6$ CFU/mL. The inoculum (1 mL) was added to MHB (8.5 mL) and peptide solution (0.5 mL) to achieve a final inoculum concentration of $1x10^5$ CFU/mL. Peptide concentrations equal to MIC, 2xMIC, and 4xMIC were prepared and tested against *S. aureus* and *E. coli*. Each sample was incubated at 37 °C in an orbital shaking Incu-Shake MAXI incubator (SciQuip Ltd, Newtown, UK, 150 rpm). At pre-determined time points (1 hour, 2, 4, 24 hours, 5 days) an aliquot of 0.25 mL was withdrawn from each sample and serially 10-fold diluted with MHB. Colony counts were determined by plating three 10 µL aliquots of each dilution in MHA plates (Miles and Misra method) and incubating them at 37 °C overnight, with the average number of CFU per 10 µL drop used for calculation. Alongside peptide samples at different concentrations, a control (9 mL MHB + 1 mL inoculum) was performed. All time-kill experiments were repeated in duplicate (two independent experiments) and a graph of the log CFU/mL was plotted against time.

4.3.2.1.6. RN7IN6 Circular Dichroism

The secondary structure and conformational behavior of RN7IN6 was investigated at 20 °C using a CD spectropolarimeter (J-815, Jasco, UK), with studies conducted by Dr Sarah Rachel Dennison at University of Central Lancashire. The AMP was solubilized in either PBS (10 mM, pH 7.4 or a trifluoroethanol (TFE) and PBS (10 mM, pH 7.4) mixture (50%, v/v) to give a final concentration of 0.01 mg/mL in each case. In addition to this, the conformational behavior of RN7IN6 in the presence of large unilamellar vesicles (LUVs) prepared from the pure lipids, DMPC, DMPE, DMPG, and DMPS [632] (lipid to peptide ratio of 100:1) was assessed. For each lipid, LUVs were prepared by dissolving lipids in chloroform and drying under nitrogen gas before being placed under vacuum for 4 hours. The resulting lipid films were rehydrated using PBS (10 mM, pH 7.40), sonicated for an hour or until the solution was no longer turbid, and then subjected to 5 cycles of freeze-thawing. Four scans per sample (speed 50 nm/min) were completed applying a path-length cell (10 mm), far-UV wavelength (260–180 nm), data pitch (0.5 nm), and band width (2 nm). All spectra were baseline corrected, and the % α-helical content determined using the CDSSTR method (protein reference set 3) from the DichroWeb server [633-635].

4.3.2.2. POPE:POPG:CL Liposomes as Platform for RN7IN6 Delivery

Following their formulation and optimization in Chapter 3, and investigation of their ability to load the model peptide nisin, POPE:POPG:CL liposomes were investigated as a carrier for RN7IN6.

4.3.2.2.1. RN7IN6-adsorbed POPE:POPG:CL Liposomes: Manufacture and Characterization

Studies in Chapter 3 investigating formulation parameters for the manufacture of nisin-adsorbed liposomes, had identified optimum parameters for achieving a small size and PDI, and the highest nisin AE%. These optimum parameters, which resulted in formulations F13, F15 and F19 (Table 4-2), were employed to manufacture RN7IN6-adsorbed liposomes. The same manufacturing process described in section 3.3.2.2.1 was employed to manufacture RN7IN6-adsorbed liposomes with the only difference that a

RN7IN6 solution in PBS was prepared instead of a nisin solution. RN7IN6-adsored liposomes were characterized as described in section 2.3.2.1.2.

Table 4-2: Set of 3 formulations employed to manufacture RN7IN6-adsorbed liposomes.

Formulation	**Initial RN7IN6 concentration (mg/mL)**	**TFR (mL/min)**	**FRR (liposomes:RN7IN6 solution)**
F13	1	20	5:1
F15	3	10	5:1
F19	5	20	3:1

RN7IN6 AE%

A 1.5 mL volume of the RN7IN6-adsorbed liposomes was diluted with 3.5 mL of PBS and subjected to ultracentrifugation at 55000 rpm for 1 hour at 4 °C [581] (rotor type 70.1 Ti, Fixed angle Titanium Rotor, Beckman Coulter Inc., Brea, California, USA) to separate free RN7IN6 and liposomes with adsorbed peptide. Subsequently, RN7IN6 adsorption was indirectly calculated by HPLC quantification (as per section 4.3.2.1.3 below) of non-adsorbed peptide present in the supernatant after ultracentrifugation. RN7IN6 standard curves (10 µg/mL – 1 mg/mL) were constructed prior to each analysis, also using HPLC.

In Vitro Antibacterial Activity: Time-kill Assay

RN7IN6-adsorbed liposome dispersions collected via ultracentrifugation were diluted appropriately in sterile PBS to obtain a final peptide concentration equal to 1x, 2x and 4x the RN7IN6 MIC. Diluted samples were employed to assess the time-kill kinetics of peptide-adsorbed liposomes against *S. aureus* and *E. coli* as described in section 4.3.2.1.5.

4.3.2.2.2. Optimization and Characterization of RN7IN6 Loaded POPE:POPG:CL Liposomes

An alternative methodology to surface adsorption was further performed, investigating the possibility to load RN7IN6 within liposomal lipid bilayers.

Formulation Manufacture, Optimization and Characterization

A combined lipid and RN7IN6 solution was prepared in a mixture of 1-propanol:DMF (80:20 v/v) with additional FA (0.01%) to aid peptide solubilization [636]. The lipid concentration in solution was kept fixed at 8 mg/mL according to optimum parameters for empty liposomes found in the study described in 3.4.1, and the TFR at 5 mL/min, while 3 different RN7IN6 concentrations were employed (0.5, 0.75 and 1 mg/mL) as per Table 4-3. In order to investigate process parameters that affected particle size, PDI and Z-potential, different FRR of PBS : lipid/peptide mixture were investigated. RN7IN6-loaded liposomes were characterized as described in section 2.3.2.1.2.

Table 4-3: Parameters used to manufacture the set of 13 RN7IN6-loaded POPE:POPG:CL liposomes, with RN7IN6 being loaded within liposomal bilayers

Formulation	**RN7IN6 Conc.**	**Lipid Conc.**	**TFR**	**FRR**	
	mg/mL	**mg/mL**	**mL/min**	**Buffer**	**Lipid**
F 20	1	8	5	3	1
F 21	1	8	5	4	1
F 22	1	8	5	5	1
F23	1	8	5	6	1
F 24	1	8	5	8	1
F 25	1	8	5	10	1
F 30	0.5	8	5	2	1
F 31	0.5	8	5	3	1
F 32	0.5	8	5	4	1
F33	0.5	8	5	5	1
F 40	0.75	8	5	3	1
F 41	0.75	8	5	4	1
F 42	0.75	8	5	5	1

F41 stability

The stability of the F41 formulation, manufactured as per Table 4-3, was assessed over a 7-day period under controlled storage conditions. Liposomes were stored at 4°C, following the ICH guidelines for stability testing [637], which align with typical conditions for preserving formulation integrity and shelf life. The choice of 4°C as a storage temperature was based on known stability requirements for lipid-based formulations to prevent oxidation and hydrolysis of the lipid components [637]. At specific time points

(1, 2, 3, 4, 5, 6 and 7 days) an aliquot of the formulation was withdrawn, diluted in PSB and characterized in terms of size, PDI and Z-Potential as described in section 2.3.2.1.2.

RN7IN6 Encapsulation Efficiency

A 1.5 mL aliquot of RN7IN6-loaded liposomes was diluted with 3.5 mL of PBS. To separate the free RN7IN6 peptide from that incorporated into the liposomes, the dispersion was subjected to ultracentrifugation at 55,000 rpm for 1 hour at 4 °C [581] (Beckman Coulter Optima XPN-80, rotor type 70.1 Ti, Fixed angle Titanium Rotor, Beckman Coulter Inc., Brea, California, USA). Subsequently, RN7IN6 encapsulation efficiency was indirectly calculated by HPLC quantification as per section 4.3.2.1.3 of unentrapped peptide present in the supernatant after ultracentrifugation. EE% was calculated using Equation 2-4. RN7IN6 standard curves (10 µg/mL – 1 mg/mL) were constructed prior to each analysis.

In Vitro Antibacterial Activity: Time-kill Assay

The *in vitro* antibacterial activity of liposomes with bilayer-loaded RN7IN6 was evaluated against *S. aureus* and *E. coli* as described in section 4.3.2.1.5.

In Vitro Release Studies

The release kinetics of RN7IN6 from liposomal formulation F41 was investigated by determining the cumulative release of peptide at different time points (1 hour, 2, 4 hours, 1, 2, 3, 4, 5, 6, 7 and 14 days), and in two different release media: PBS (sodium chloride 137 mM, phosphate buffer 10 mM, potassium chloride 2.7 mM, pH 7.4) and acetate buffer (sodium acetate trihydrate 196 mM, glacial acetic acid 105 mM, pH 5).

The 'sample and separate' method was employed to assess the *in vitro* release as described by Solomon *et al.* [638]. Briefly, 10 mL of F41 were ultracentrifuged (55000 rpm, 1 hour, 4°C) [581], and following quantification of RN7IN6 content as described above, the supernatant was discarded, and the pellet was resuspended in 5 mL of either PBS or acetate buffer. Resuspended liposomes were incubated at 37 °C on a HulaMixer™ Sample Mixer (75 rpm). At various time points, the samples were ultracentrifuged at 55000 rpm for 1 hour at 4 °C and 0.5 mL of supernatant was collected for quantification,

replaced with fresh aliquot (0.5 mL) of release medium and incubation resumed. The supernatant was analyzed by HPLC as described in 4.3.2.1.3. Cumulative release (%) of RN7IN6 at each timepoint was calculated relative to the total amount of initially loaded RN7IN6.

4.3.2.3. Statistical Analysis

Data were analyzed using IBM SPSS statistical software (Version 26.0. Armonk, NY: IBM Corp). An independent T-test was run on formulation size, PDI and Z-Potential to determine if there was a mean difference in formulation physicochemical characteristics. If the output of Levene's test to assess equality of variance was $p>0.05$, the two-sided p value with equal variance assumed was considered; if the output of Levene's test was $p<0.05$, the two-sided p value with equal variance not assumed was considered.

4.4. Results and Discussion

4.4.1. Antimicrobial Peptide RN7IN6

4.4.1.1. RN7IN6 Synthesis and Purification

The antimicrobial peptide RN7IN6 was synthesized by automated microwave solid-phase peptide synthesis, recognized to significantly reduce coupling times and enhance product purity [639, 640]. RN7IN6 is a synthetic 13 aa hybrid AMP derived from indolicin and ranalexin [641, 642], originally designed by Jindal *et al.* as a first step towards development of alternative antimicrobial drugs against *S. pneumoniae* [606]. In addition to having a stronger activity against pneumococcus than the parent peptides indolicin and ranalexin, RN7IN6 showed a potent activity against a range of both Gram-positive and Gram-negative bacteria such as *P. aeruginosa, E. coli, S. aureus* and MRSA strains [606]. For these reasons, RN7IN6 was identified as a novel AMP with promising antimicrobial activity and was therefore selected here for further investigations and encapsulation studies which have never been conducted before according to published literature.

Following RN7IN6 peptide sequence examination, results showed that Trp 11, Arg 12 and Arg 13 were the most challenging aa to couple and therefore these three aa were triple-coupled during the synthesis. RN7IN6 was successfully synthesized and characterized with a 60.63% yield. Mass spectrometric analysis confirmed the molecular weight of the peptide (MW: 1714.01 g/mol) as shown in Figure 4-4, while the DAD1 spectrum was used to assess its purity (Figure 4-5).

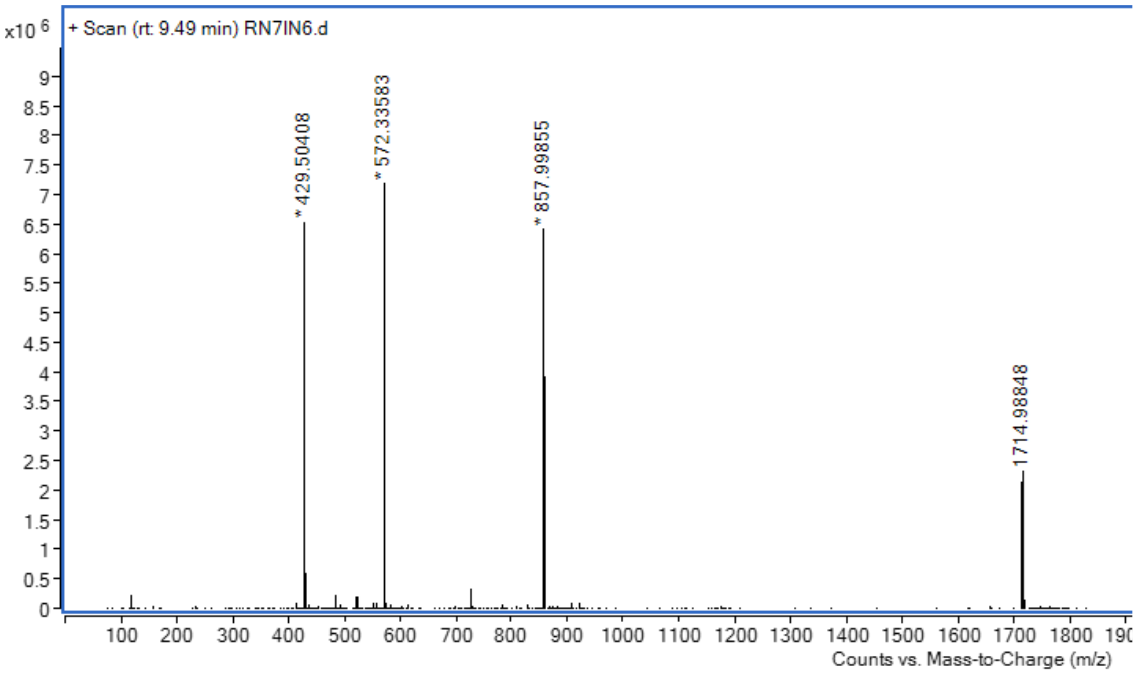

Figure 4-4: RN7IN6 mass spectrum expressed as a mass to charge ratio $[M^{+}H]^{+}$. Mass spectrum cropped to allow full spectrum visualization.

The Rt of RN7IN6 was found to be 9.45 min (Figure 4-5). RN7IN6 crude purity percentage was then calculated according to Equation 4-1 and was found to be approximately 70%. Solid-phase synthesis is an easy and fast procedure for small-size peptides, and it generally yields relatively pure products (~50 to 80%) [643]. However, purification is needed in most cases to yield higher purity percentages, removing large quantities of salts, impurities and contaminants that could affect the accuracy of e.g. microbiological assays.

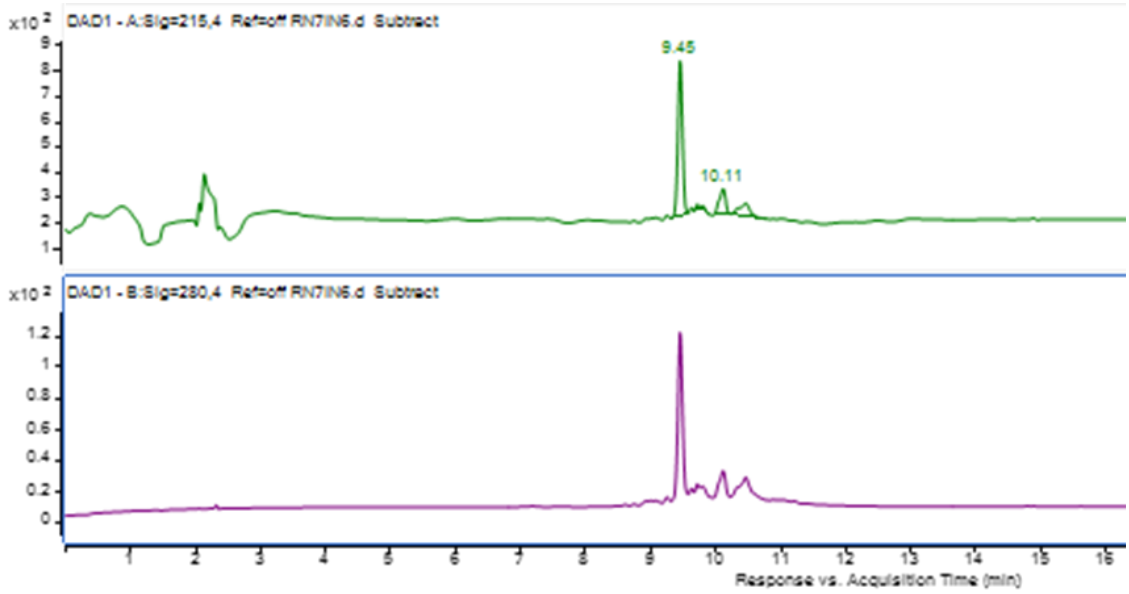

Figure 4-5: RN7IN6 DAD1 spectrum at two different wavelengths: 215 nm for the peptide bond and 280 nm for the Trp. Figure cropped to allow spectrum visualization.

Purification can be achieved through both preparative-HPLC and flash chromatography. The selection of the appropriate technique depends on the relative Rts of the impurities compared to the main compound peak. If the unwanted side product(s) is (are) eluting closely to the compound of interest, generally preparative HPLC is the technique of choice. However, if the two products are well separated, flash chromatography is the best option, as it can afford faster, easier, and cheaper purification on a larger scale [644]. RN7IN6 purification was attempted with both approaches, as shown in Figure 4-6.

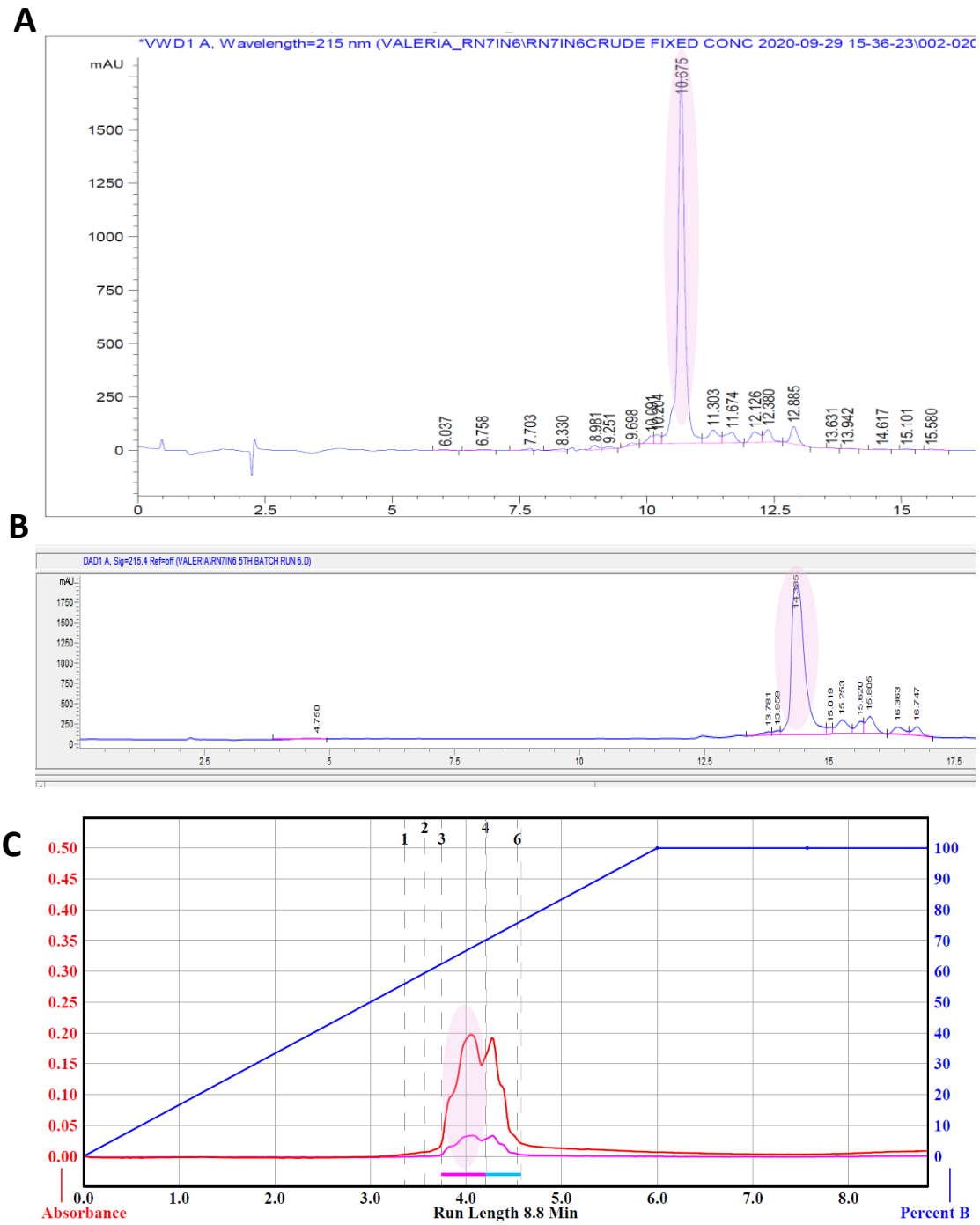

Figure 4-6: A. HPLC chromatogram of crude RN7IN6 after automated synthesis. B. HPLC chromatogram of crude RN7IN6 resulting from preparative-HPLC. C. HPLC chromatogram of crude RN7IN6 resulting from flash-chromatography. The peak of interest is highlighted in pink.

For this specific batch of RN7IN6, given as a representative example, chromatographic separation of RN7IN6 and impurities (the chromatogram of which is shown in Figure 4-6 A) was only achieved though preparative HPLC (Figure 4-6B) while flash chromatography

was not able to elute the compound of interest with a good resolution (Figure 4-6C). With preparative HPLC it was possible to obtain highly pure RN7IN6 (>95%, Figure 4-7) which was then employed for microbiological activity evaluation and structural investigations.

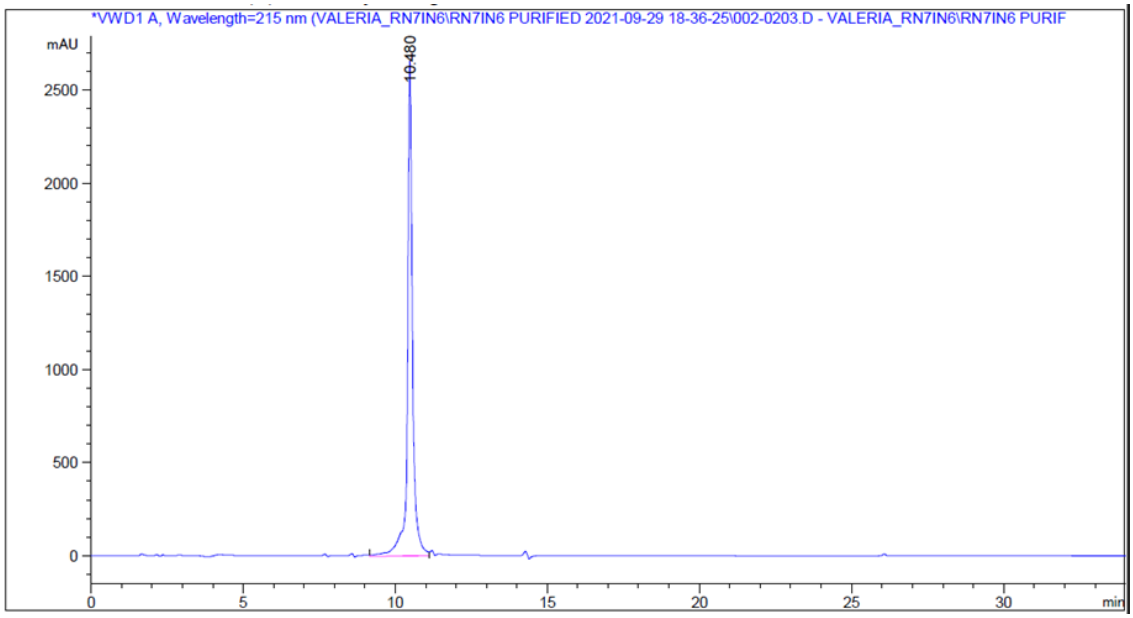

Figure 4-7: HPLC chromatogram of purified RN7IN6 after preparative-HPLC.

4.4.1.2. RN7IN6 Antimicrobial Activity

In a previous study, Jindal *et al.* designed a range of hybrid peptides derived from ranalexin and indolicidin [606], due to their short aa sequence and their positive net charge as well as their well-known activity against Gram-positive bacteria [641, 642]. From the hybrid peptides synthesized by Jindal *et al.*, RN7IN6 was chosen for the current study because, in addition to its cationic nature, it also showed a high percentage of hydrophobic residues within the aa sequence, which is a crucial parameter in determining effective membrane permeabilization [645]. Previous studies have shown that the positive net charge is one of the most important parameters that influence the antimicrobial activity of an AMP by playing a fundamental role in the electrostatic interaction between the AMP and negatively charged phospholipid membranes of bacteria [646]. The high content of phospholipids, LPS and teichoic acid in bacterial membranes confers an overall negative charge. The target bacterial cells possess a transmembrane potential which is up to 50% greater than mammalian cells [646], which

leads to a stronger affinity of AMPs to prokaryotic membranes over mammalian cells. However, a net charge above +6 and high levels of hydrophobicity are associated with hemolytic activity and increased mammalian cell toxicity, as well as loss of antimicrobial activity [646, 647]. It is therefore necessary to be careful when altering AMP crucial parameters such as the aa sequence which confers net charge or hydrophobicity to the peptide. For instance, RN7IN6 presents an aa sequence rich in tryptophan and arginine residues which have been reported to exhibit a strong membrane-disruptive activity by penetrating the interface layer of the membrane and creating strong hydrogen bonds with the bacterial membrane [648].

An initial objective of this study was to evaluate the antimicrobial activity of RN7IN6 against laboratory strains of clinically relevant Gram-positive and Gram-negative bacteria, in order to reinforce results reported in previous studies [173, 606]. Hence, the antimicrobial activity of RN7IN6 was assessed by the REMA assay and by evaluating the time course of killing of bacterial suspensions (time-kill assay). In the REMA assay, RN7IN6 showed the strongest antimicrobial activity against *S. aureus* with an MIC of 16 µg/mL followed by *E. coli* and *K. pneumoniae* (MIC = 32 µg/mL) as shown in Figure 4-8. *P. aeruginosa* was found to be the least susceptible bacterial strain to RN7IN6, with an MIC of 256 µg/mL obtained.

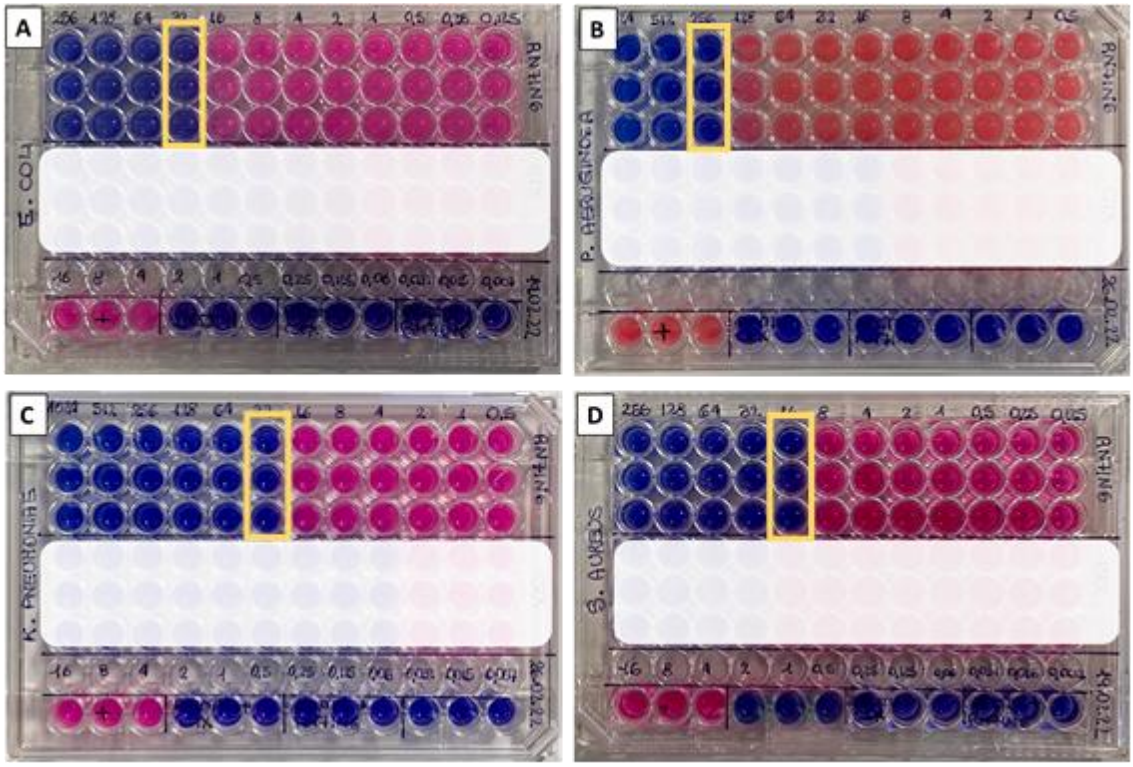

Figure 4-8: Antibacterial activity of pure antimicrobial peptide RN7IN6 against E. coli *(A),* P. aeruginosa *(B),* K. pneumoniae *(C) and* S. aureus *(D) assessed by the REMA assay. Yellow boxes indicate the MIC value. White boxes were used to obscure sections of the plate where another antimicrobial compound was tested, which is not relevant to the current analysis.*

Surprisingly, not all the results obtained in this study were in complete agreement with those of Jindal *et al.*, where RN7IN6 was described for the first time, and assessed for its antimicrobial activity against 30 *S. pneumoniae* clinical isolates and a panel of Gram-positive and Gram-negative bacteria [606]. A direct comparison of results presented in this study and in this previous literature can be made for *S. aureus* and *E. coli*, where the same strains were employed (NCTC 12241 and NCTC 12981, respectively); on the other hand, different strains of *P. aeruginosa* and *K. pneumoniae* were tested in the current study compared to previous literature. A comparison of bacterial strains tested and MIC values obtained in the current work with those of Jindal *et al. i*s shown in Table 4-4.

Table 4-4: Comparison between bacteria strain and reported RN7IN6 MIC in the current work and the study performed by Jindal et al. *(* not specified, resistant strain).*

	Bacterial strain employed		RN7IN6 MIC (µg/mL)	
	In the current study	In previous studies	In the current study	In previous studies
S. aureus	NCTC 12981 /ATCC 25923		16	7.81
E. coli	NCTC 12241/ATCC25922		32	7.81
P. aeruginosa	NCTC 12903/ATCC 27853	NCTC 13359/ATCC 15442	256	31.25
K. pneumoniae	NCTC 9633/ATCC 13883	*	32	>250

The study by Jindal *et al.* found that RN7IN6 has slightly higher antimicrobial activity against *S. aureus* and *E. coli*, specifically 2 and 4 times higher, compared to the results in this work. This difference is considered within an acceptable range given the variability that can occur in MIC determinations, especially when considering factors such as differences in experimental conditions or methodology used between studies. However, the slight discrepancies in the antimicrobial activity of RN7IN6 against *S. aureus* and *E. coli* between this study and that of Jindal *et al.* could be due to variations in experimental conditions, such as differences in methodology (REMA employed in this study and broth microdilution employed by Jindal *et al.),* growth media, incubation times, and inoculum concentration. Additionally, differences in the synthesis, purification, or storage of RN7IN6 might have resulted in minor structural or purity variations, potentially influencing its efficacy. Furthermore, the physiological state of the bacterial strains used in each study could also contribute to the observed variability in MIC values. These factors, either individually or collectively, likely account for the differences in antimicrobial activity reported.

The MIC of RN7IN6 presented in this study against *K. pneumoniae* cannot be correlated to the study carried out by Jindal *et al.* as, for testing, the current study employed a susceptible strain while the previous study used a resistant strain. For this reason, this study showed an RN7IN6 MIC of 32 µg/mL against *K. pneumoniae* while in the study carried out by Jindal *et al.* the AMP didn't show any activity at the concentrations tested (MIC > 250 µg/mL). On the other side, the opposite behavior for RN7IN6 against *P. aeruginosa* was observed; Jindal *et al.* showed an RN7IN6 antimicrobial activity of 31.25 µg/mL, while the current study revealed a higher MIC (256 µg/mL). These results may

be related to the different methodologies employed, as this study used the REMA assay, whereas Jindal *et al.* utilized the broth microdilution assay. Moreover, the discordant results are likely to be also related to the different *P. aeruginosa* strains employed in the current work and that of Jindal *et. al*, NCTC 12903 and NCTC 13359, respectively. According to EUCAST guidelines, *P. aeruginosa* NCTC 12903 is considered the recommended performance standard for antimicrobial susceptibility testing [649] and thus, was used in the current study. This particular *P. aeruginosa* strain is known to be a low inducible AmpC β-lactamase-producing strain [650]. β-lactamase enzymes in *P. aeruginosa* NCTC 12903 are usually kept at low levels, but their production might be induced when the bacteria is exposed to certain β-lactam agents leading to increased resistance to them. β-lactamase enzymes hydrolyze and open the β-lactam ring [651], a cyclic amide, which is part of the core structure of several antibiotic classes such as penicillins, cephalosporins and carbapenems. The β-lactam ring and the peptide structure of RN7IN6 have in common the presence of an amide bond, in the first case in a cyclic structure called lactam and in the latter case as a bond between each amino acid. Hence, it could conceivably be hypothesized that the β-lactamase inducible enzymes present in the strain NCTC 12903 might be potentially able to hydrolyze not only the amide bond of the β-lactam ring but also the amide bonds of the RN7IN6 backbone. Although this hypothesis is not explicitly addressed in the current literature by clear evidence to support this specific mechanism, it may provide a viable explanation for the higher MIC of RN7IN6 against *P. aeruginosa* NCTC 12903 compared to that reported by Jindal *et al.*

The antimicrobial potency of RN7IN6 was further studied by measuring its killing efficiency via bactericidal kinetics studies (also known as time-kill assays) to differentiate growth inhibition from cell death. *E coli* and *S. aureus* were employed in this study as representative Gram-positive and Gram-negative bacteria against which RN7IN6 was found to have appreciable activity (as discussed above and shown in Table 4-4). The time kill kinetics results for RN7IN6 against *S. aureus* and *E. coli* are shown in Figure 4-9 A and B, respectively. Of particular note, within 4 hours, RN7IN6 reduced 10^6 CFU/mL of *S. aureus* and *E. coli* to approximately 10^3 CFU/mL (a 3-log reduction) at MIC concentration.

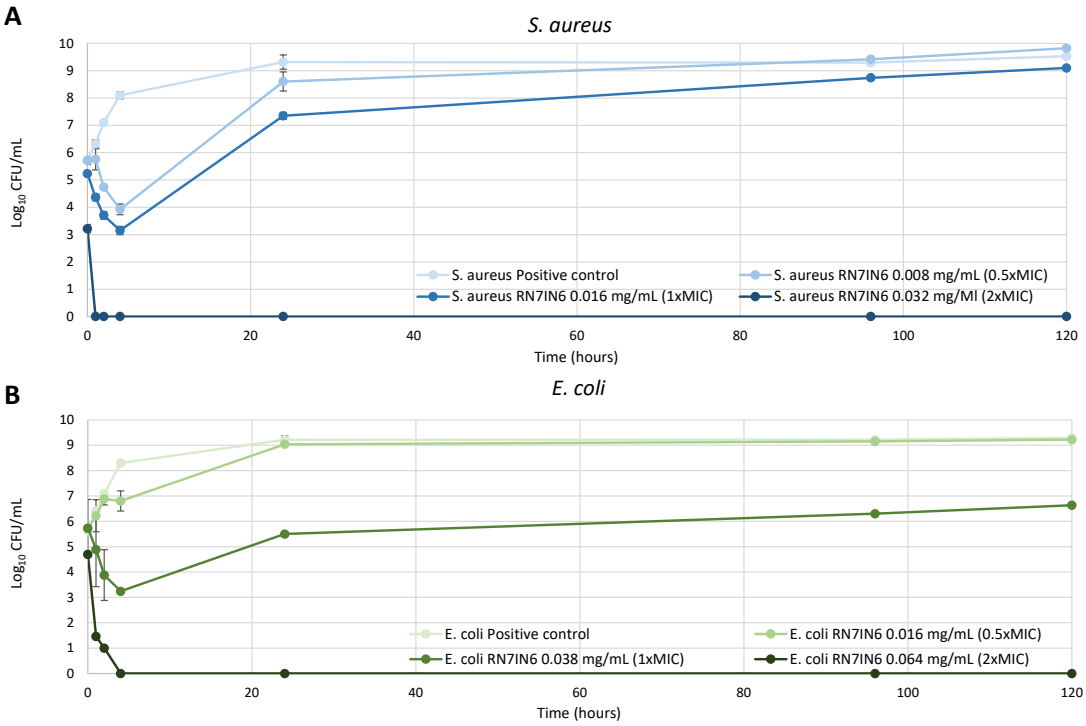

Figure 4-9: Time-killing kinetics of RN7IN6 against S. aureus *(A) and* E. coli *(B) at 0.5xMIC, 1xMIC and 2xMIC for 0, 1, 2, 4, 24, 96 and 120 h. Results show mean ± SD (n=2).*

Figure 4-9 also shows that RN7IN6 was lethal at 2xMIC concentration with a 5-log reduction of *S. aureus* and *E. coli* in less than 1 and 4 hours, respectively. The results clearly showed the ability of RN7IN6 to kill bacteria (bactericidal activity) not just inhibit growth (bacteriostatic activity). There are similarities between the results presented in this study and those described by Aleinein *et al*. [652], where the RN7IN6 parent peptide derived from frogs, ranalexin exhibited a rapid bactericidal effect at a concentration of 2 × MIC against *E. coli* and MRSA. This behavior is also in good agreement with the bactericidal kinetics of synthetically produced ranalexin and ranalexin analogues presented in previous studies [653-656]. These findings support the association of RN7IN6 bactericidal activity with the carboxyterminal amino acid sequences that contain a heptapeptide ring [657]. This structural feature is similar to the cyclic peptide core found in polymyxins, a class of antibiotics that includes colistin, which is widely known for its effectiveness against Gram-negative bacteria. The resemblance between the heptapeptide ring in RN7IN6 and the structure of polymyxins, particularly colistin,

suggests that RN7IN6 might share some of the membrane-targeting mechanisms that make these antibiotics potent, although further investigation is needed to confirm this.

In addition to the heptapeptide ring, specific Arg (12, 13) and Trp (9, 11) residues present in the RN7IN6 aa sequence and derived from the parent peptide indolicidin, are well known to play an important role in antimicrobial and hemolytic activities [658]. The Trp residue, followed by two consecutive Arg residues represents a repeated pattern that can be found in natural antimicrobial peptides which determines the selective attraction of the AMP to the interfacial region of the lipid bilayer [659], which is the amphiphilic boundary between the hydrophobic acyl chains and the hydrophilic head groups of the lipid bilayer. This region is critical for the activity of AMPs like RN7IN6, where Trp residues penetrate into the hydrophobic core while remaining associated with the hydrophilic head groups [659]. This dual interaction facilitates the disruption of membrane integrity. Moreover, the interactions between Arg residues and the indole rings of Trp residues further stabilize the peptide-membrane interaction, promoting membrane permeabilization and enhancing antimicrobial efficacy [659]. However, it has been extensively demonstrated that single substitutions of the two Trp residues in positions 9 and 11 are associated with a lower hemolytic activity compared to the parent peptide indolicidin. Therefore, further, future investigation is warranted to evaluate cytotoxicity of RN7IN6, particularly due to the critical presence of Trp residues in its structure.

4.4.1.3. RN7IN6 Circular Dichroism (CD)

The conformational behavior of RN71N6 in different environments was investigated using CD spectroscopy. In aqueous solution (PBS, 10 mM, pH 7.4), the peptide displayed spectra with two minima near 210 and 224 nm, respectively, and maxima at 193 nm, which is typical of α-helical peptides [660]. Analysis of these CD spectra showed that RN71N6 possessed 35.87 ± 0.98 % α-helical structure (Table 4-5Table 4-5). A key step in the membrane interaction of these peptides involves the adoption of secondary structures in the anisotropic environment of the interface [661] (the region where the directional-dependent physical properties of the membrane, such as polarity and hydrophobicity, interact with the surrounding aqueous environment), which is often

investigated using TFE, a membrane-mimicking solvent [662-664]. The choice of lipids in this study was made to model different types of membrane environments and to understand the interaction of RN71N6 with various membrane compositions. DMPC and DMPE are zwitterionic lipids representing the neutral charge environment of typical eukaryotic membranes, whereas DMPG and DMPS are anionic lipids that mimic the negatively charged bacterial membranes [665].

Table 4-5: % of secondary structure ± SD of RN71N6 in the presence of PBS pH 7.4, 50% TFE and pure lipid membranes.

Lipid	α-helical	ß-strands	Turns	Unordered
Solution	35.87 ± 0.98	18.07 ± 1.38	17.93 ± 0.86	27.67 ± 4.91
50% TFE	53.00 ± 3.46	21.33 ± 2.31	5.00 ± 3.46	20.67 ± 1.15
DMPC	52.00 ± 1.73	23.67 ± 2.88	5.67 ± 0.57	19.67 ± 1.15
DMPE	43.33 ± 1.52	26.33 ± 3.21	8.33 ± 1.15	21.67 ± 1.15
DMPG	48.00 ± 1.93	25.00 ± 1.60	7.67 ± 0.57	19.67 ± 1.52
DMPS	41.67 ± 1.52	28.66 ± 1.15	7.33 ± 0.58	22.33 ± 1.53

A variety of approaches have been employed in CD analysis to simulate the effect of membranes on the conformations of peptides, including the use of organic solvents, such as ethanol, acetonitrile, 1,1,1,3,3,3-hexafluoroisopropanol and TFE [666-669]. TFE is, by far, the most commonly used of these membrane-mimicking solvents and here, Figure 4-10 shows that in TFE / PBS (10 mM, pH 7.4) mixture (50 % v/v), RN71N6 displayed spectra characteristic of an α-helical structure.

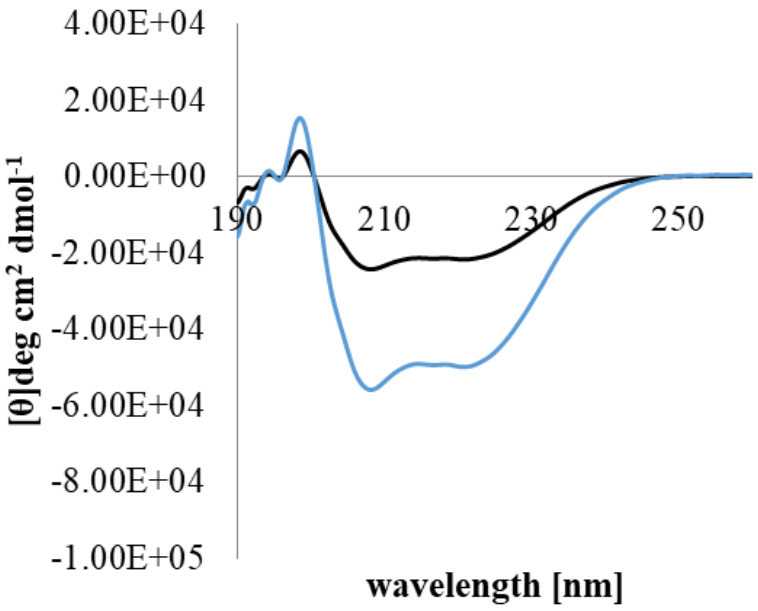

Figure 4-10: CD analysis of RN71N6 in aqueous solution (black) and a 50 % (v/v) mixture of TFE / PBS (10 mM, pH 7.4) (blue).

Further analysis of these CD spectra showed that RN71N6 was 53.00 ± 3.46 % α-helical with the remaining structural contributions to the peptide coming from random coil and β-type architectures (Table 4-5). One of the most commonly used strategies to form biologically relevant membranes in conformational studies on α-helix forming peptides is the use of large LUVs mimicking naturally occurring membranes [670]. [670]RN71N6 adopted a high degree of α-helicity in the presence of zwitterionic DMPC and DMPE LUVs (52 and 43 %). RN71N6 also showed predominantly α-helical structure in the presence of anionic DMPG and DMPS which were between 41% and 48 %. These CD results demonstrate RN71N6's structural adaptability, with an increase in α-helicity in membrane-like environments as compared to in solution, which is crucial for its antimicrobial function. The peptide's ability to maintain a high α-helical content across different membrane settings, along with reduced β-strands and unordered structures, underscores its potential for effective membrane disruption. This conformational stability across environments suggests that RN71N6 is a strong candidate for further development using liposomal delivery to further enhance its stability and efficacy.

4.4.2. RN7IN6-adsorbed POPE:POPG:CL Liposomes

4.4.2.1. RN7IN6-adsorbed Liposome Size, PDI and Z-Potential

Following the initial optimization of nisin-adsorbed liposomes described in the previous chapter, 3 formulations were chosen from the original 9 DoE formulations (Table 4-2). F13 was chosen according to the Minitab analysis of the DoE as the formulation manufactured with parameters predicted to give the highest peptide AE% while maintaining a uniformly sized liposome population. Formulation F19 was selected because the high initial nisin concentration used (5 mg/mL) led to a significantly higher amount of nisin adsorbed ($p<0.001$), although an increase in particle size was also observed. Finally, formulation F15 was chosen because it consistently demonstrated a high amount of nisin adsorbed to POPE:POPG:CL liposomes, with a low variability in AE%.

Informed by optimization work with nisin, work in this chapter aimed to identify and understand the parameters that influence RN7IN6-adsorbed liposome size, PDI and AE% immediately after manufacture and after liposome purification by applying the same parameters employed to manufacture nisin-adsorbed formulations. The process of surface-adsorption of RN7IN6 was achieved through the controlled mixing of pre-formed liposomes and an aqueous solution containing RN7IN6 in a microfluidic mixing chip.

Figure 4-11 A and B show RN7IN6-adsorbed liposome size and PDI results for the 3 formulations manufactured according to parameters shown in Table 4-2. Liposome size ranged from 171.17 ± 27.90 nm to 3418.50 ± 566.50 nm, while PDI values ranged from 0.280 ± 0.04 to 0.77 ± 0.13, indicating uniform and monodisperse populations. The collected data were analyzed using SPSS and an independent T-test was run on liposome size, PDI and Z-Potential to determine if there was a mean difference in formulation physicochemical characteristics.

The T-test was employed to compare empty liposomes (F7 after dialysis) with RN7IN6-adsorbed formulations immediately after manufacture and after purification. In

addition to this, the T-test was also employed to assess the statistical significance of differences in RN7IN6-adsorbed liposome formulations before and after purification via ultracentrifugation. The T-test indicated there was no significant difference in physiochemical characteristics of F13, F15 and F19 RN7IN6-adsorbed formulations immediately after preparation and then after purification, indicating that the method is able to successfully purify formulations from unbound peptide and organic solvent without altering size, PDI or surface charge.

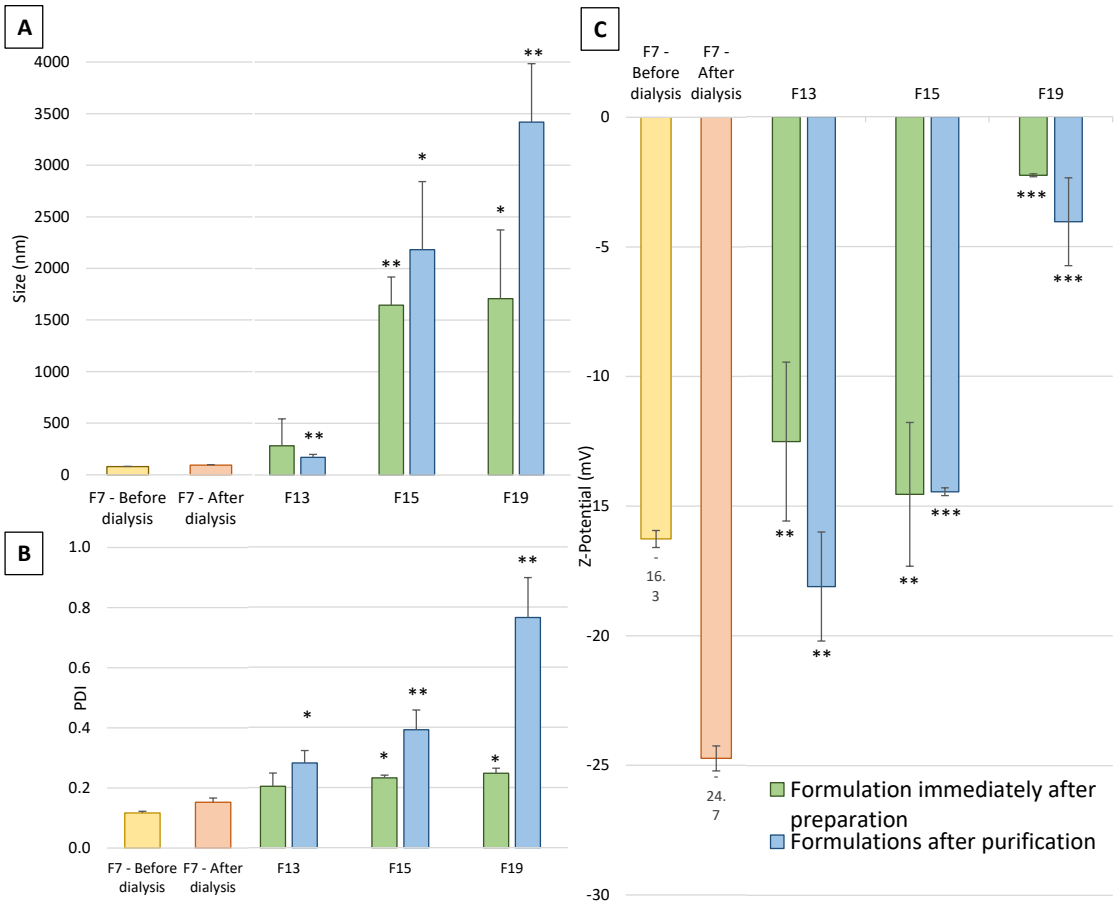

Figure 4-11: Size (A), PDI (B) and Z-Potential (C) of the 3 RN7IN6-adsorbed liposome formulations prepared. The results represent mean ± SD, n=3 independent batches. Statistical analysis shown represent differences between adsorbed formulations immediately after preparation or after purification compared to the empty liposome formulation (F7) after dialysis. If the two-tailed p-value is less than 0.05, it is flagged with one asterisk (*); less than 0.01, with two asterisks (**); and less than 0.001, with three asterisks (***). Green bars represent formulations immediately after preparation while blue bars represent formulations following purification (ultracentrifugation followed by pellet resuspension in PBS).

However, the T-test did highlight significant differences between adsorbed-formulation and empty purified POPE:POPG:CL liposome size, PDI and Z-potential, as shown in Figure 4-11 (green and blue bars in comparison to orange bar). Results for F15 and F19 immediately after purification, and for all adsorbed formulations after ultracentrifugation showed an increased size and PDI and a decreased Z-Potential in comparison to empty purified liposomes (p<0.05). This increase in size and PDI in particular suggests potential aggregation of the liposomes. Notably, F15 and F19 resuspended formulations also exhibited a statistically significant increase in particle size relative to the F13 resuspended formulation (T-test outcome not shown in Figure 4-11; F13-F15 p=0.027; F13-F19 p=0.005). Similar trends in increasing liposome size with surface loading have been discussed in literature. Chatzikleanthous *et al.* described an increased vesicle size of protein-conjugated liposomes in comparison with bare (cationic) liposomes [671]. Similar findings were also observed when producing lipoplexes, which are complexes of liposomes and DNA, where the colloidal properties were found to be correlated to the ratio of the cationic lipid to DNA. Indeed, charge ratios between 1:1 and 2:1 (lipid to DNA charge) resulted in the largest vesicles and subsequent precipitation of lipoplexes, while when lipoplexes were prepared at an excess of either DNA or liposomes the vesicle diameter was less than 100 nm, in comparison to empty DOTAP liposomes which typically showed diameters ranging from 30 nm to 60 nm [672]. In contrast to the electrostatic interaction-dependent formation of lipoplexes between cationic liposomes and plasmid DNA, liposome/protein complexes are additionally stabilized by van der Waals forces and hydrophobic interactions [673]. In addition, the overall electrical charge, lipid solubility, hydrophobic properties, and structural arrangement of the protein under investigation are factors that significantly influence liposome/protein complex formation and the resulting changes in liposome size, PDI, and Z-Potential [674]. These results demonstrate that liposomes to AMP mixing ratio is a critical process parameter, essential for designing homogenously-sized nanoscale systems.

Regarding the PDI, conclusions similar to those observed for liposome size can be inferred from the T-test comparing resuspended formulations – a trend for increasing PDI from F13 to F15 and further to F19 was noted, however this result was not

statistically significant (T-test outcome not shown in Figure 4-11; F13-F19 *p*=0.020; F15-19 *p*=0.049). In terms of Z-Potential, as the RN7IN6 loading concentration increased (F13 to F19), a steady decrease in surface charge can be observed from -18.10 mV (F13 after purification) to -4.05 mV (F19 after purification; T-test outcome not shown in Figure 4-11; F13-F19 *p*=0.006; F15-19 *p*=0.026). The reduction in the magnitude of the negative Z-Potential, influenced by increasing RN7IN6 concentrations, was expected due to the gradual neutralization of the anionic vesicles [675], as previously observed [671]. However, no plateau in Z-potential was observed as previously described for the surface adsorption of hydrophilic, non-conformational peptide epitopes to anionic liposomes [676]. The lack of a plateau in the current study might be due to the range of loading concentrations explored. It is possible that a greater range of loading concentrations would have led to observe a plateau in Z-potential, as the current concentrations may not have reached the threshold needed to fully neutralize the anionic vesicles or stabilize the system. Further investigation with an expanded concentration range could provide more insights into this phenomenon.

There are numerous examples in the literature of peptides either surface adsorbed or loaded causing aggregation of liposomes [677-680]. As an example, Ferreira *et al.* showed that, upon electrostatic binding of W-BP100 antimicrobial peptide to anionic vesicles, and after a certain threshold concentration (peptide-to-lipid-ratio), vesicle aggregation occurred. This observation could aid in explanation of the significant noted increases in RN7IN6-adsorbed formulation size and PDI and changes in zeta potential, as well as providing insight into why this was not observed to the same degree of aggregation in comparison with nisin-adsorbed formulations discussed in previous chapter. As was shown previously in Table 3-7, RN7IN6 has a lower molecular weight compared to nisin and thus, the final molarity of RN7IN6 adsorbed to formulations F13, F15 and F19 was (almost 2-fold) higher than that of nisin (Table 4-6).

Table 4-6: RN7IN6 and Nisin theoretical concentration in formulation (mg/mL and µM) for formulations F13, F15 and F19. Theoretical concentration refers to the final expected concentration of RN7IN6 / nisin in the formulation, which depends on both the initial concentration of RN7IN6 / nisin in one of the fluids and the specific FRR employed to manufacture formulations.

Formulation	Final RN7IN6 / nisin conc. (mg/mL)	Final RN7IN6 conc. (µM)	Final Nisin conc. (µM)
F13	0.17	99.2	51.0
F15	0.50	291.7	147.1
F19	1.25	729.3	372.7

4.4.2.2. RN7IN6-adsorbed Liposomes: AE%

The effect of different formulation manufacturing parameters and initial RN7IN6 concentrations on the AE% of formulations F13, F15 and F19 were investigated as described in section 4.3.2.2.1. Figure 4-12 shows RN7IN6 AE% as well as the amount of RN7IN6 successfully adsorbed on formulations F13, F15 and F19. The T-test employed to compare the three formulations did not reveal any significant difference in AE% (Figure 4-12, dots) despite the increasing amount of RN7IN6 used to manufacture F13, F15 and F19. However, the concentration of peptide adsorbed to liposomes significantly increased with increasing peptide loading concentrations, showing an adsorption of 31 mg, 93 mg, and 207 mg of RN7IN6 adsorbed per mL of F13, F15 and F19 liposomes respectively (Figure 4-12, bars). This is entirely in line with published literature, where the correlation between increasing initial drug loading and increasing amount of drug loaded/adsorbed has been previously observed [681].

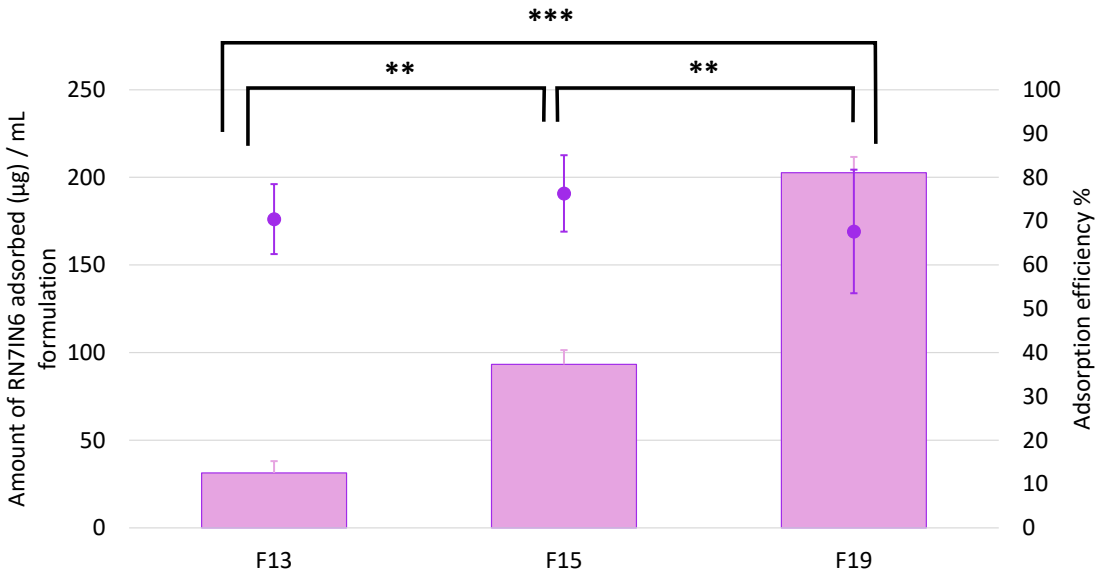

Figure 4-12: Amount of RN7IN6 adsorbed to pre-formed empty liposomes (bars) and RN7IN6 AE% (dots). The results represent mean ± SD, n=3 independent batches. Stars refer to amount of adsorbed RN7IN6 (bars). P-value less than 0.01, is flagged with two stars (**), while p-value less than 0.001, is flagged with 3 stars (***).

Suleiman *at al.* investigated the conditions to favor electrostatically-driven encapsulation of hydrophilic, non-conformational peptide epitopes into liposomes [676]. While the study primarily focused on encapsulation, it also provided insights into surface adsorption, as electrostatic interactions between the peptides and liposome surfaces were shown to play a crucial role in the initial binding process. Highly positively charged variants of OVA-323-339, a model peptide, were manufactured to study peptide-membrane interactions by employing anionic, neutral and positive liposomes with different lipid compositions. Suleiman *et al.* demonstrated a higher encapsulation efficiency of the OVA-323-339 into anionic liposomes, confirming the suggested electrostatically-driven encapsulation mechanism. Also, the same study showed that a similar encapsulation efficiency of around 50% was obtained when increasing peptide OVA-323-339 to anionic lipid ratios (1:6667; 1:667 and 1:67); however, with increasing peptide to lipid ratios, an increased peptide content/amount associated with liposomes was achieved, ranging from 0.8 to 73.9 µM, thus supporting the current work. On the other side, the absence of electrostatic interaction between peptide and liposome surfaces may cause poor adsorption efficiencies, as noted when a small hydrophobic and negatively charged peptide was loaded onto anionic liposomes as described by Shariat *et al.* [682]. Therefore, despite the importance of multiple factors such as pH and

buffer ionic strength, liposome composition and surface charge as well as peptide net charge and isoelectric point are crucial to control electrostatically-driven peptide adsorption to liposome surfaces. Also, when the above-mentioned conditions exist, the lipid-to-peptide ratio becomes fundamental to modulate the amount of peptide adsorbed to the formulation. This is particularly relevant to the current study, where the increased peptide-to-lipid ratio in formulations F13, F15, and F19 resulted in higher RN7IN6 adsorption, aligning with the findings in the literature and further emphasizing the critical role of the lipid-to-peptide ratio in determining AE% and liposome size.

In addition to lipids, buffer and peptide physiochemical characteristics, the loading or adsorption of peptides onto liposomes using microfluidics can be influenced by various microfluidic process parameters such as the geometry of the microfluidic device and the hydrodynamic flow [683], which cannot be controlled as precisely in conventional methods like simple benchtop mixing of liposomes and peptide. Microfluidic parameters such as FRR and TFR can be controlled to fine-tune liposome size, PDI and protein loading. Despite conflicting opinions in literature about the role of TFR in controlling drug surface AE%, there is a general consensus on the crucial role played by the FRR on surface AE%. Balbino *et al*. investigated the production of pDNA/cationic liposome complexes using microfluidic devices, specifically examining how variations in the FRR between the aqueous and lipid phases affected complex formation [684]. Their study found that altering the FRR from 3:1 (aqueous phase with plasmid DNA : liposome phase) to 5:1 had a significant impact on the binding efficiency of plasmid DNA to the liposome surfaces. Specifically, a lower FRR of 3:1 led to enhanced binding efficiency, resulting in a more stable complex, whereas increasing the FRR to 5:1 reduced the binding efficiency [684]. This highlights how adjusting the FRR can significantly influence loading efficiency, which aligns with our findings that a lower FRR in formulation F19 resulted in higher RN7IN6 adsorption compared to F15, where a higher FRR was used.

4.4.2.3. Empty and RN7IN6-adsorbed Liposomes: Antimicrobial Activity

Due to low availability, as well as time and financial costs associated with preparation of purified RN7IN6, formulation F13 alone was chosen for assessment of its antimicrobial activity. F13 was chosen from the three RN7IN6-adsorbed formulations due to having

the smallest size (in the nanometer size range) and most uniform size distribution. In addition to this, F13 was the formulation requiring the lowest initial RN7IN6 amount for liposome loading. The time-kill assay was employed to differentiate growth inhibition from bacterial cell death. As mentioned previously, the time-killing assay provides dynamic information about the antimicrobial activity of an agent over time, allowing for the assessment of the rate and extent of bacterial killing. It can also provide insights into the bactericidal or bacteriostatic nature of the antimicrobial agent. However, the assay requires frequent sampling and is more labor-intensive compared to the broth microdilution assay, as employed for an initial screening of free RN7IN6 antibacterial activity. To ensure consistency with previous antimicrobial susceptibility assessments and to allow for comparative analysis, the bacterial strains *S. aureus* and *E. coli* were selected for the RN7IN6 time-kill assay.

Formulation F13 was purified from unbound peptide and then diluted to obtain a peptide concentration corresponding to 1x, 2x and 4x free RN7IN6 MIC. The time kill kinetics results for RN7IN6 against *S. aureus* and *E. coli* are shown in Figure 4-13 A and B, respectively. The results of the time-kill kinetics clearly showed that formulation F13 was not able to kill *S. aureus* and *E. coli* at any concentration tested, while free RN7IN6 was previously determined to be bactericidal against both strains at 2xMIC (Figure 4-9). The RN7IN6-adsorbed liposome formulation (F13) was further unable to inhibit bacterial growth (bacteriostatic activity) as the time-kill kinetics obtained were seen to be comparable to those of the positive control ($p>0.05$).

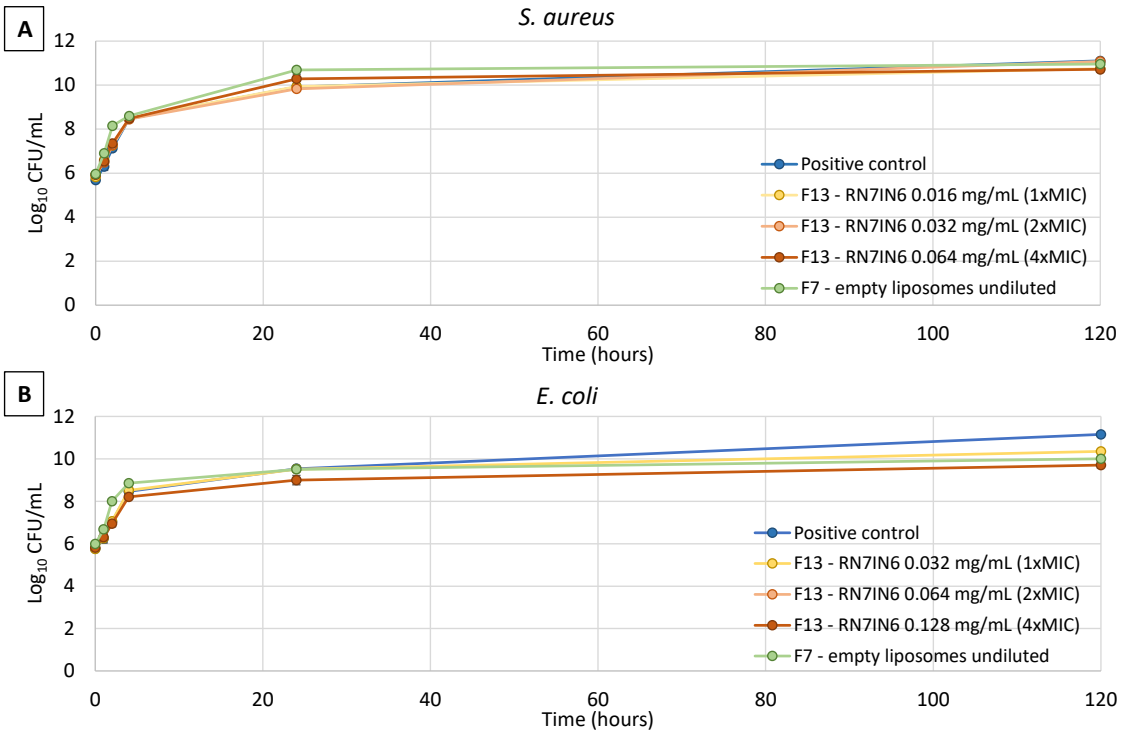

Figure 4-13: Time-killing kinetics of RN7IN6-adsorbed formulation F13 at 1xMIC, 2xMIC and 4xMIC and empty liposomal formulation F7 against S. aureus NCTC 12981 (A) and E. coli NCTC 12241 (B) assessed at 0, 1, 2, 4, 24, and 120 h. Data represents mean ± SD(n=2).

Prior to discussion of this finding, it is important to note that subsequent to optimization experiments, significant challenges were encountered with respect to reproducibly formulating RN7IN6-adsorbed liposomes, particularly formulation F13. Specifically, instances were observed where F13 exhibited significantly increased liposome sizes and elevated PDI values in comparison to those illustrated in Figure 4-11, indicative of potential aggregation. This aggregation likely compromised the antimicrobial efficacy of the formulation and may have considerably contributed to the absence of bactericidal or bacteriostatic activity against *S. aureus* or *E. coli* at any concentration tested.

Given this challenge in achieving consistent and effective formulations through surface-adsorption, a strategic decision was made to shift focus towards encapsulating RN7IN6 within the liposomal bilayer. This transition to encapsulation is anticipated to provide several advantages over surface adsorption. Encapsulation is expected to enhance the reproducibility and stability of the liposomal formulations by potentially mitigating the aggregation observed with surface adsorption, thereby maintaining consistent liposome

size and PDI values. Furthermore, encapsulation simplifies the liposome formulation process by eliminating the need for a separate surface adsorption step and will also allow for the simultaneous coating of the AMP and lipid onto polymeric cores when moving to the manufacture of lipid-polymer hybrid nanoparticles (as described in Chapter 5).

4.4.3. RN7IN6-loaded POPE:POPG:CL Liposomes

4.4.3.1. RN7IN6-encapsulated Liposome Size, PDI and Z-Potential

Following the production of RN7IN6-adsorbed liposomes discussed in the previous sections, RN7IN6-loaded liposomes were prepared as described in section 4.3.2.2.2. As a result of the change in peptide loading strategy further formulation work was carried out, which aimed to identify and understand the parameters that influence RN7IN6-loaded liposome size, PDI, Z-Potential and EE% straight after the manufacture and following purification via ultracentrifugation. The process of RN7IN6 loading was achieved through the controlled mixing of an RN7IN6 and lipid solution together with PBS in a SHM microfluidic chip. This approach was chosen to incorporate the peptide into the lipid bilayer rather than the aqueous core of the liposome due to the amphipathic nature and low water solubility of RN7IN6. Although the peptide has some degree of water solubility, its strong hydrophobic character suggests that it would preferentially interact with the lipid bilayer. This not only improves the stability and incorporation efficiency of the peptide within the liposomes but also ensures that RN7IN6 is readily available to interact with bacterial membranes, aligning with its membrane-disrupting mechanism of action. Moreover, the incorporation of RN7IN6 into the lipid bilayer instead of the aqueous core foreshadows the formulation strategy that will be utilized for the final LPHNPs. Since the LPHNPs lack an aqueous core, this approach is highly relevant in developing a cohesive strategy for RN7IN6 incorporation within the final formulation. By embedding the RN7IN6 into the lipid layer, we align the loading method with the structural design of the LPHNPs, which are progressively developed in subsequent chapters. This strategy ensures that the loading method remains adaptable as we transition towards the final LPHNP formulation in Chapter 5.

The TFR and the initial lipid concentration were kept fixed at 5 mL/min and 8 mg/mL respectively, as optimized for the empty liposome formulation F7. The FRR between the PBS and the lipid-peptide solution as well as the initial peptide concentration were varied in order to manufacture 13 different RN7IN6-loaded liposomal formulations as per Table 4-3. Figure 4-14 and Figure 4-15 show RN7IN6-loaded liposome size, PDI and Z-Potential results for the 13 formulations manufactured. As the purpose of this study was to perform a rapid initial screening to understand the impact of FRR and initial peptide concentration on the physiochemical characteristics of liposomes incorporating RN7IN6, and in consideration of the constraints around the time and expense associated with large-scale RN7IN6 production, all formulations were manufactured as n=1.

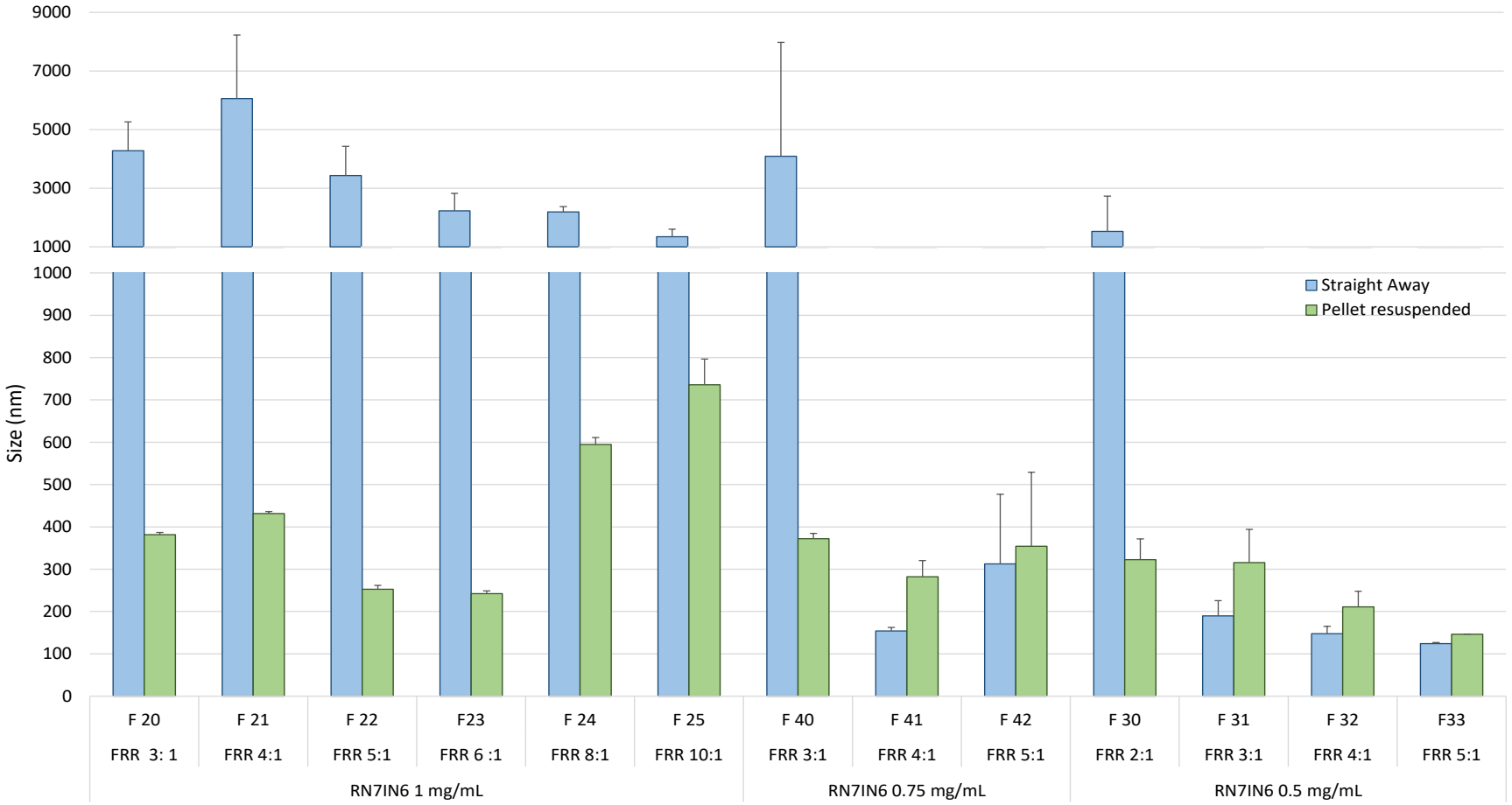

Figure 4-14: Size of the 13 RN7IN6-loaded POPE:POPG:CL liposome formulations prepared. Results for all formulations represent mean ± SD of 3 technical replicates .

While a statistical analysis was not feasible for the data displayed in Figure 4-14 and Figure 4-15, certain trends may be cautiously delineated. For all the formulations manufactured with RN7IN6 initial concentration of 1 mg/mL, the size of the formulation straight after manufacturing was larger than the size of the formulation after ultracentrifugation and pellet resuspension in PBS (Figure 4-14). The same behavior can be observed for formulations F40 and F30 that were manufactured with a smaller initial peptide concentration but a high FRR between the aqueous and the lipid phase (3:1 and 2:1, respectively). The high FRR employed in F40 and F30 actually determined a higher final peptide concentration, calculated from the RN7IN6 loading concentration and the specific FRR used to manufacture formulations, loaded into liposomes in comparison with formulations manufactured with a smaller FRR. Thus, F30 and F40, together with F20-F25 manufactured with the highest initial peptide concentration, were considered to be the formulations resulting in a high final RN7IN6 concentration. The high peptide concentration in formulation may have resulted in an excess of positive charges, leading to an imbalance between the positive charges of the peptide and the negatively charged liposomes. This excess or unincorporated peptide appears to associate with the liposomal surfaces, which leads to an increase in size and a decrease in the magnitude of the Z-potential, as shown in Figure 4-15. When this excess peptide is removed, the size of the liposomes is reduced, and the magnitude of the Z-potential increases (becomes more negative), which aligns with a more stable formulation. This observation is consistent with the findings reported in the study carried out by Dimov *et al.*, where the removal of non-entrapped compounds, such as proteins or hydrophobic drugs, through tangential flow filtration led to a decrease in liposome size and an increase in the magnitude of the Z-Potential [685]. This change indicates a more uniform particle distribution and a higher surface charge density, both of which contribute to the thermodynamic stability of the liposomes, minimizing the potential for aggregation and ensuring a more stable and effective drug delivery system [685]. This phenomenon could also be linked to the challenges observed with surface adsorption, where high peptide concentrations may have led to aggregation or inconsistent adsorption efficiencies.

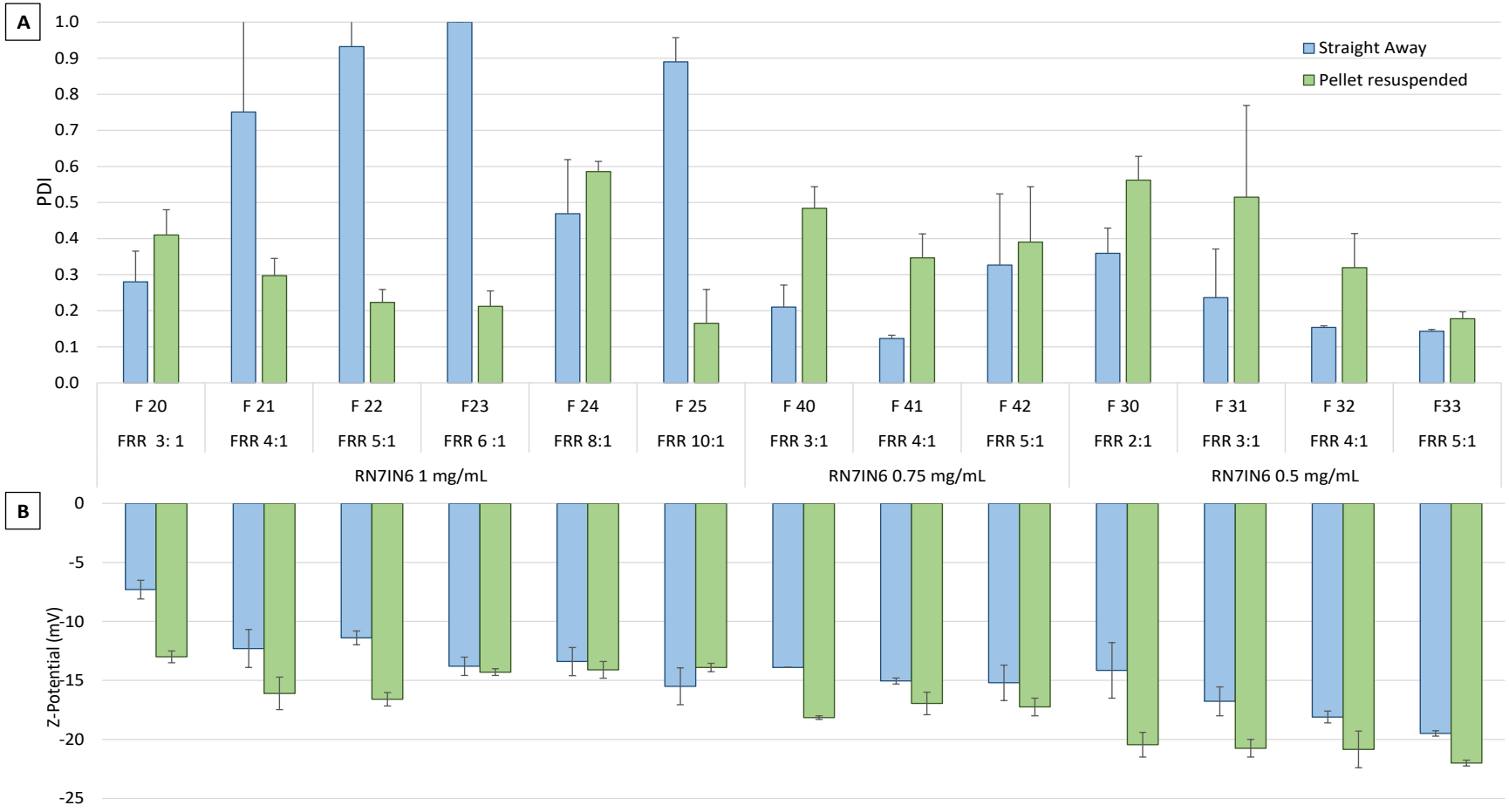

Figure 4-15: PDI (A) and Z-Potential (B) of the 13 RN7IN6-loaded POPE:POPG:CL liposome formulations prepared. Results for all formulations represent mean ± SD of 3 technical replicates.

4.4.3.2. RN7IN6-loaded Liposomes: Encapsulation efficiency

The encapsulation efficiency of single formulations shown in Figure 4-14 and Figure 4-15 was not determined because they were manufactured on a small scale (2 mL) for screening purposes and thus, upon dilution for ultracentrifugation, the theoretical final RN7IN6 concentration in formulation (which depends on both the initial concentration of RN7IN6 in one of the fluids and the specific mixing ratio of the two fluids) would have dropped below the limit of detection of the RN7IN6 HPLC method. Following initial screening therefore, three candidates were chosen from the initial set of 13 formulations and were manufactured to produce a higher final volume (5 mL) while keeping fixed all the other formulation parameters. One formulation for each initial peptide concentration used was chosen. Candidate formulations were selected in order to have a small and monodisperse population, as determined from the initial screening study, together with highest final theoretical peptide concentration incorporated into the formulation liposomal bilayers (theoretical final RN7IN6 concentration in formulation was calculated as per Table 4-7). Thus, formulations F22, F41 and F31 were selected to investigate the peptide encapsulation efficiency.

Table 4-7: Theoretical final RN7IN6 concentration in formulation for the set of 13 formulations manufactured. The theoretical final peptide concentration was calculated by taking into account the initial peptide concentration used to manufacture formulations and the FRR between the buffer and the lipid solution within which RN7IN6 was dissolved.

Formulation	Initial RN7IN6 Concentration in lipid solution	FRR		Theoretical final RN7IN6 Concentration in formulation
	mg/mL	Buffer	Lipid	µg/mL
F 20	1	3	1	250
F 21	1	4	1	200
F 22	**1**	**5**	**1**	**167**
F23	1	6	1	143
F 24	1	8	1	111
F 25	1	10	1	91
F 40	0.75	2	1	188
F 41	**0.75**	**3**	**1**	**150**
F 42	0.75	4	1	125
F 30	0.5	5	1	167
F 31	**0.5**	**3**	**1**	**125**
F 32	0.5	4	1	100
F33	0.5	5	1	83

Formulations F22, F41 and F31 were then manufactured in triplicate. The physiochemical characteristics of the three formulations manufactured using the original 2 mL or the higher 5 mL as final manufacturing volume were first compared in order to ensure no impact of changing this parameter - the size, PDI and Z-Potential of formulations manufactured in smaller or larger batches were comparable and no appreciable differences were noticed, and thus the results of all 4 independent replicates were pooled and reported together as n=4 in Figure 4-16.

The encapsulation efficiency and amount of peptide loaded per mL of formulation for RN7IN6-loaded POPE:POPG:CL liposome formulations F31, F41 and F22 are shown in Figure 4-16. As can be seen from the figure, the increasing initial RN7IN6 loading concentration did not result in aggregation and large particle sizes or increases in PDI as was noted for the previous, surface-adsorbed liposomes.

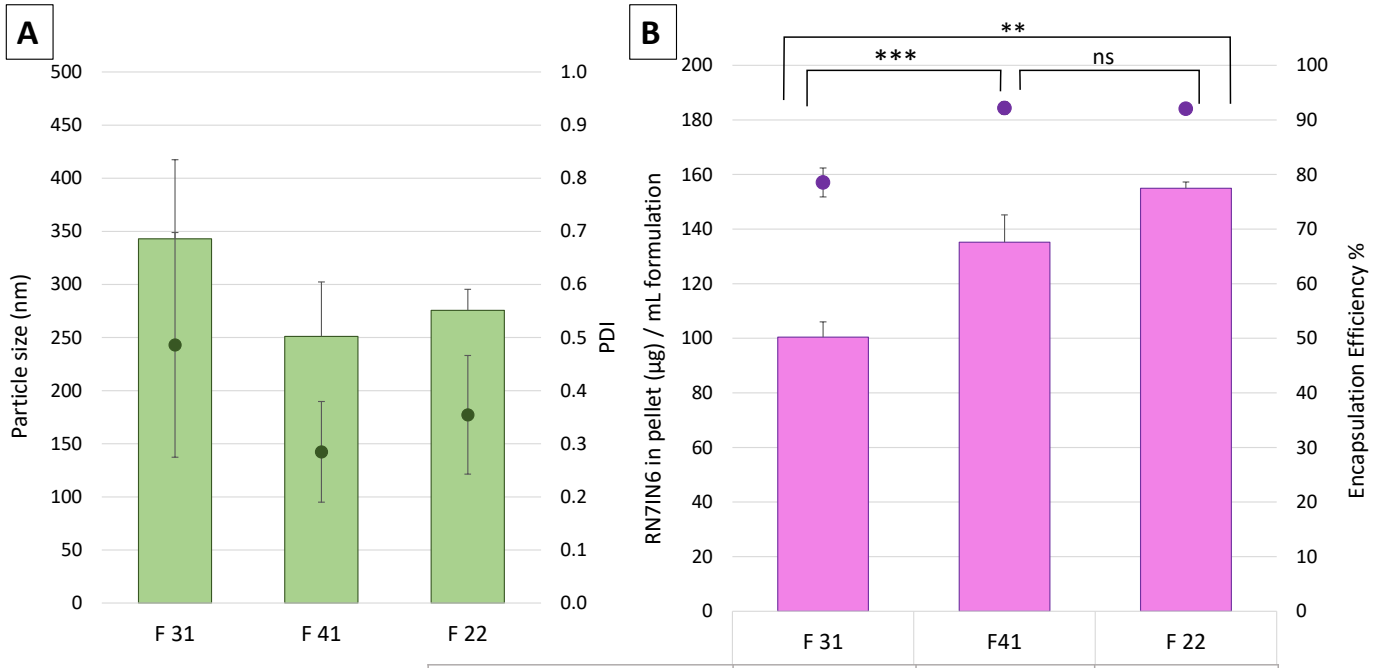

	F 31	F41	F 22
Initial RN7IN6 concentration (mg/mL)	0.50	0.75	1.00
Theoretical final RN7IN6 Concentration (mg/mL)	0.13	0.15	0.17

Figure 4-16: A. Size (bars) and PDI (dots) of RN7IN6-loaded POPE:POPG:CL liposome formulations F31, F41 and F22. The results represent mean ± SD, n=4 independent batches. Note: For size and PDI, results from both 5 mL (n=3) and 2 mL (n=1) batches were combined as n=4. Results represent mean ± SD (=4) B. RN7IN6 encapsulation efficiency (dots) and amount of peptide loaded per mL of formulation (bars) for RN7IN6-loaded POPE:POPG:CL liposome formulations. The results represent mean ± SD, n=3 independent 5 mL batches. p-value < 0.05 flagged with one star (*). p value < 0.001 flagged with 3 stars (***). Statistical analysis refers to bars.

While it appears that the lowest initial peptide concentration showed slightly larger and more polydisperse liposomes compared to those prepared with higher initial peptide concentrations, the T-test performed on F31, F41 and F22 particle size and PDI did not show any significant difference in these parameters. This trend is therefore cautiously suggested and should be interpreted with care given the lack of statistical significance. As observed for peptide-adsorbed liposome formulations, the small increase in the theoretical final peptide concentration did not result in an increase in encapsulation efficiency. Indeed, the independent T-test did not show any significant differences between the three formulations despite F41 and F22 showing a slightly higher mean encapsulation efficiency than F31. A significant increase in the amount of peptide encapsulated within liposomes with increasing initial peptide concentration was however observed, as shown in Figure 4-16 B. This is entirely in line with the linear correlation (R^2=0.88) observed between the initial CTX concentration employed to manufacture CS nanoparticles and the amount of drug loaded in formulation, with a similar encapsulation efficiency as reported in Chapter 2; it is also in agreement with the trend observed for surface-adsorbed formulations F13, F15, and F19, where a linear correlation (R^2 = 0.81) was found between the initial RN7IN6 concentration and the amount adsorbed, indicating that as the initial RN7IN6 concentration increased, the amount adsorbed to the liposomes also increased, although the AE% remained relatively constant as shown in section 4.4.2.2.

Hence, the three selected RN7IN6-loaded candidates F31, F41 and F22 did not show any appreciable differences apart from the amount of peptide loaded, which was significantly lower for F31 in comparison to F22 and F41. Hence, formulation F31 was excluded from further studies. When comparing F41 with F22, although both formulations showed similar physiochemical characteristics, similar encapsulation efficiency and amount of peptide encapsulated, F41 has a significant advantage: it is manufactured with a lower initial amount of peptide. This is particularly important given the high cost and time-consuming process involved in the synthesis and purification of the peptide. By requiring less peptide to achieve the same level of encapsulation, F41 offers a more cost-effective and resource-efficient option, making it the preferred choice. In contrast to surface-adsorbed formulations, F41 also stands out due to the lack

of aggregation, which was a notable issue in surface-adsorbed liposomes. Aggregation in RN7IN6 surface-adsorbed liposomes led to larger particle sizes and higher PDI values, compromising the stability, reproducibility and uniformity of the formulation. The lipid bilayer incorporation method used in F41 appears to avoid these problems and ensures a more controlled and predictable peptide loading, avoiding the variability and potential loss of efficacy seen with surface adsorption. Overall, F41 was selected for further studies not only because it outperformed F31 in terms of peptide loading but also because it is more cost-effective compared to F22, all while maintaining superior consistency compared to surface-adsorbed formulations.

4.4.3.3. F41 Stability

The preservation of liposome stability holds significant importance, particularly when incorporating AMPs, as alterations in liposome size resulting from aggregation or fusion, as well as the release of encapsulated substances due to leakage, can exert detrimental effects on the overall efficacy and performance of these formulations [686]. Chemical destabilization has been shown to have a significant impact on the storage and shelf life of liposomes [686]. Therefore, formulation F41 was tested for stability for up to 7 days at 4°C to reflect the storage conditions that may be required for these formulations. A temperature of 4°C was chosen in accordance with the International Conference on Harmonization (ICH) guidelines for stability testing [637].

The chemical destabilization of liposomes can be attributed to two main factors, oxidation of lipids and hydrolysis of ester bonds, and can be influenced by various factors, including the composition of the liposomal membrane itself. Murzyn *et al.* conducted a comprehensive examination of the characteristics exhibited by a bilayer composed of POPE and POPG, serving as a model for the inner bacterial membrane. The study showed that the mean surface area per molecule of POPG was comparatively greater than that of POPE, suggesting discernible dissimilarities in the arrangement and configuration of the lipids. Furthermore, it was observed that the alkyl chains of POPG exhibited a higher degree of ordering and a lower packing density compared to POPE [687]. Also, it was demonstrated that the inclusion of POPG within the liposomal membrane resulted in an increased fluidity when compared to membranes exclusively

composed of POPE [621], which suggests that the incorporation of POPG within liposomes may exert a positive influence on their fluidity and poses questions on its implications for the overall stability of liposomal structures. However, another study carried out by Tan *et al*., which investigated the effect of lipid composition on the stability of liposomes using small-angle neutron scattering, suggested that the addition of POPG to liposomes composed of POPE increased their stability, as evidenced by a decrease in vesicle size and reduced aggregation [688].

Similarly to POPE and POPG, conflicting results in literature were found about the influence of CL on liposomal membrane packing, fluidity and thus liposomal stability. Some studies showed that CL has the ability to reduce the surface area occupied by each molecule when it interacts with other phospholipids. This was determined by analyzing the percent condensation and elastic compressibility of monolayers at the air-water interface, which stabilizes the bilayer by reducing fluidity [689-691]. However, Unsay *et al.* suggested a concentration-dependent role of cardiolipin on membrane properties. Indeed the study showed that 20 mol % of cardiolipin determined the formation of stable bilayers, while the inclusion of a smaller amount of CL (5 mol %) increased the fluidity of lipid bilayer and decreased the mechanical stability by the formation of flowerlike domains [692]. In the current study, the formulation includes 10% w/w cardiolipin, which approximately corresponds to 5 mol%. This cardiolipin content may similarly enhance membrane fluidity and reduce bilayer mechanical stability, potentially influencing the structural integrity and functional performance of the liposomal formulations being investigated. This could lead to an increased likelihood of liposomal aggregation or fusion, which may reduce the homogeneity of the formulation, negatively impact particle size distribution, and alter the release kinetics of the encapsulated RN7IN6 peptide. This potential increase in membrane fluidity and reduction in mechanical stability, while presenting challenges for maintaining homogeneity and size distribution, could also be advantageous in promoting interactions or fusion with bacterial membranes, thereby enhancing the antimicrobial efficacy of the RN7IN6-loaded liposomal formulation. In addition to this, the stability of RN7IN6-loaded POPE:POPG:CL liposomes was assessed because several studies provide insights into the effects of tryptophan and arginine-rich antimicrobial peptides on

liposomes composed of POPE and POPG lipids, suggesting that AMPs can interact with the liposomal membrane, potentially leading to liposomal aggregation, peptide-lipid interactions, membrane disruption and leakage [693-695].

The results from Figure 4-17 A and B show that POPE:POPG:CL liposomes with membrane-incorporated RN7IN6 were stable. Liposome sizes ranged from approximately 230 to 260 nm and PDI remained low, below 0.3; no significant changes in size and PDI observed up to 7 days of storage. Despite some fluctuations in liposome Z-Potential, there were also no significant changes observed in this parameter.

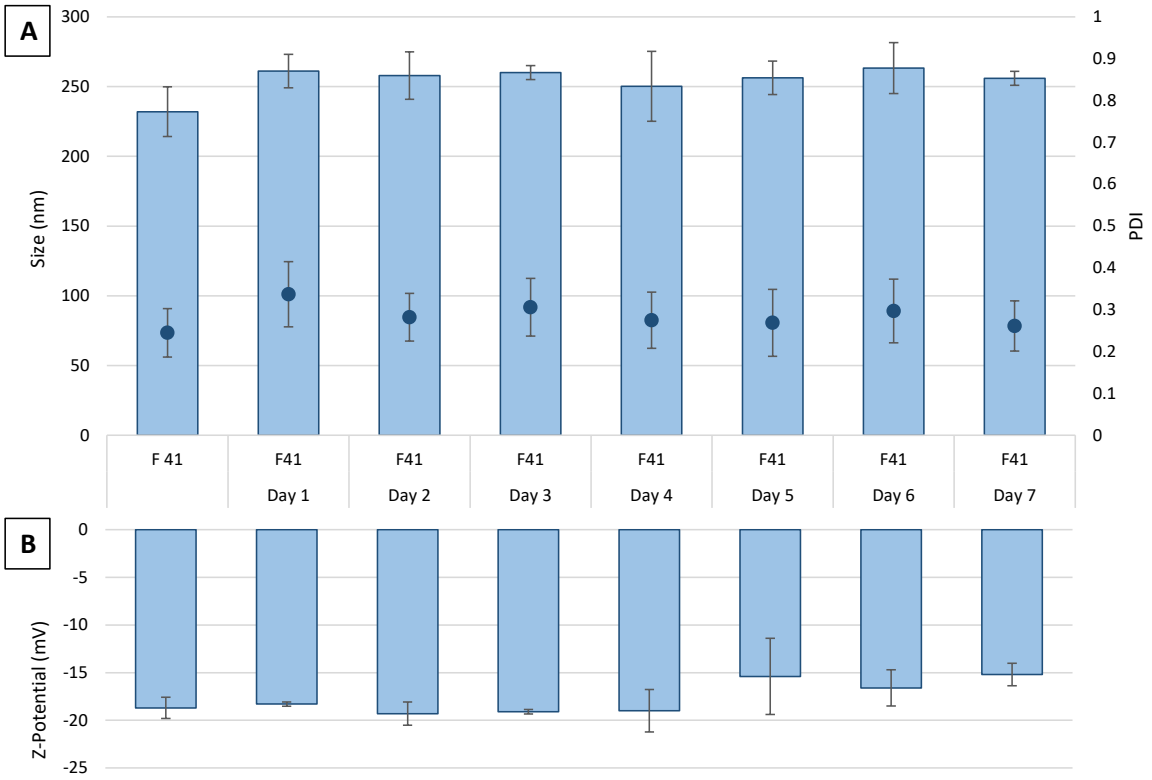

Figure 4-17: Stability of RN7IN6-loaded POPE:POPG:CL liposomes produced by microfluidics over 7 days, after ultracentrifugation and liposome resuspension in PBS. The formulation was kept at 4°C with changes to liposome size (bars), PDI (dots) (A) and Z-Potential (B) measured using dynamic light scattering. Results represent mean ± SD of n=3.

In addition to this, stability data demonstrated that, at the specific peptide concentration used to manufacture F41, liposomes did not aggregate upon storage. Indeed, previous studies highlighted that AMP containing sequences rich in arginine and

tryptophan tend to intrinsically self-associate and create aggregates and/or nanostructures of different morphologies over time [696]. Additionally, another study carried out by Bagheri *et al.* showed a time-dependent POPE/POPG (3/1) liposome aggregation upon exposure to a low concentration of tryptophan-rich peptide (25 µM) leading to a gradual increase in liposome dispersion turbidity [694]. However, it is important to note that these studies primarily investigated scenarios where peptides were either exposed to liposomes or surface-loaded, which closely mimics the surface adsorption approach rather than the membrane-entrapment approach as for this study. These conditions are prone to inducing aggregation, as seen both in the literature and in the previous sections investigating surface-adsorbed RN7IN6 formulations (see section 4.3.2.2.1). In contrast, the current study has demonstrated that when the peptide is loaded into the bilayer of liposomes, aggregation does not occur either during the formulation process or upon storage, suggesting a significant advantage of this method. This finding is particularly noteworthy because bilayer loading of AMPs into liposomes has been less frequently explored in existing literature. The ability to incorporate an AMP directly into the liposomal bilayer while maintaining a stable and uniform formulation suggests that bilayer loading may be an effective strategy for developing AMP-loaded liposomes. This method minimizes the risk of aggregation, which has been a common issue with surface adsorption, thereby offering a more consistent and stable formulation. The successful bilayer incorporation of RN7IN6 not only preserves the physicochemical properties of the liposomes but also ensures AMP structural integrity, which is crucial for its antimicrobial activity.

4.4.3.4. RN7IN6-loaded Liposomes: Antimicrobial Activity

The antimicrobial efficacy of F41 was further examined by conducting bactericidal kinetics studies. *E. coli* and *S. aureus* were again employed in this study as representative clinically relevant Gram-negative and Gram-positive bacteria respectively. The RN7IN6-loaded liposome formulation F41 was prepared and purified as described in section 4.3.2.2.2. According to the calculated peptide encapsulation efficiency, F41 was then resuspended in PBS buffer to achieve different encapsulated-peptide concentrations corresponding to 1xMIC, 2xMIC and 4xMIC of free RN7IN6. Alongside peptide-loaded

formulations, empty F7 liposomes were also assessed. Time-kill assay results for F41 and F7 against *S. aureus* and *E. coli* are shown in Figure 4-18 A and B, respectively.

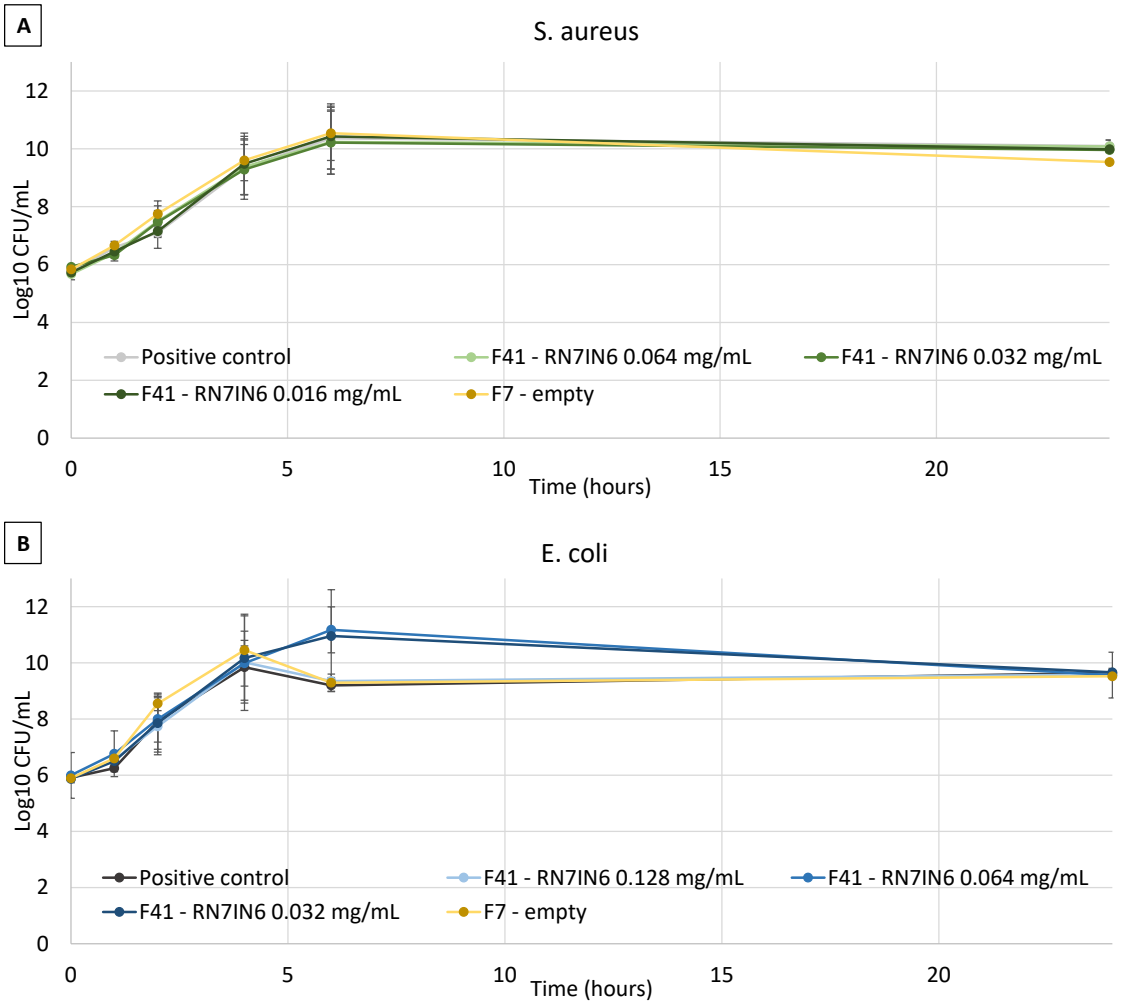

Figure 4-18: Time-killing kinetics of F7 and F41 against S. aureus *(A) and* E. coli *(B) at 0.5xMIC, 1xMIC and 2xMIC of free peptide for 0, 1, 2, 4, 6, and 24 hours. Data depicts mean ± SD (n=2).*

S. aureus and *E. coli* bacterial growth was unaffected by the presence of POPE:POPG:CL liposomes, as the empty F7 formulation showed the same kinetics as the positive control (PBS buffer + inoculum). This result illustrates consistency with findings shown in Figure 4-18, and are in accordance with a study carried out by Drost *et al.*, who manufactured a delivery system mimicking the lipid composition of *S. aureus* and *S. pneumoniae* membranes to deliver a novel energy-coupling factor transporter inhibitor. The study demonstrated that unloaded bacteriomimetic liposomes composed of DOPG, CL and

cholesterol did not significantly impair the viability and growth of *B. subtilis* colonies [305].

The RN7IN6-loaded formulation F41 also did not show any bactericidal or bacteriostatic effect against both Gram-positive and Gram-negative bacteria at any of the concentrations tested. While this was surprising, this is not the first time that it is observed that bacterial susceptibility to antibiotic-loaded liposomes is lower in comparison to the free drug, regardless of liposome composition and the liposome formulation charge [697-699]. The authors of the aforementioned references suggested that a possible explanation for the lack of antimicrobial activity of the encapsulated drug in comparison with free antibiotic, as was also observed in this study, might rely on the various antibiotics release profiles from liposomes and thus, a reduced concentration of drug molecules being available at any given time for interaction with bacterial cell receptors [697]. Indeed, Omri *et al.* showed that less than 16% of amikacin and tobramycin were released in serum from anionic (lecithin, dicetylphosphate, cholesterol) and cationic (egg lecithin, stearylamine, cholesterol) liposomes [698] while Antos *et al.* found that around 25% of aminoglycoside was released in bacterial growth media from multilamellar liposomes composed of phosphatidylcholine and cholesterol after 24 hours [697].

Thus, in order to confirm the abovementioned theory, a release study on formulation F41 was performed over 14 days at 37 °C in two different media: PBS (pH 7.4) and acetate buffer (pH 5.6) to simulate the acidic environment found at some infection sites [700]. The study was originally designed with a 48-hour release period to assess whether any appreciable peptide release from F41 would occur during the incubation time of the time-kill assay, as well as slightly beyond this standard timeframe. This initial setup aimed to capture any early release that might impact the antimicrobial activity observed. However, when the results indicated that no peptide was released within the initial 48 hours, the need for a more thorough investigation was recognized. Consequently, the study was extended to 14 days, allowing for a more comprehensive analysis of the peptide release kinetics over a significantly prolonged period. The release study performed showed that no peptide was released from formulation F41 after 14

days (data not shown). However, the HPLC method developed to quantify RN7IN6 showed a relatively high limit of detection (~26 µg/mL) for the specific peptide batch manufactured for the release study. Thus, according to the initial formulation F41 concentration used for the release study, the analytical method developed would only have been able to detect greater than ~10% of peptide released from the formulation per release timepoint. Thus, we can more accurately conclude that less than 10% of RN7IN6 was released from F41 over 14 days.

To ensure that the lack of detected release was not due to peptide instability, and to rule out the possibility that the peptide might have degraded in the release media, a stability study was conducted alongside the release study. Specifically, a peptide solution (0.5 mg/mL) was incubated at 37 °C with shaking (HulaMixer™ 75 rpm) for 7 days. The 0.5 mg/mL RN7IN6 concentration used for this investigation was slightly higher than that employed for the F41 release study, to ensure the detection of any potential degradation. This decision was based on the understanding that peptide degradation is concentration-dependent, with higher peptide concentrations leading to an increased rate of degradation. This is supported by findings of Witschi *et al.*, who have shown that the degradation of peptides encapsulated in PLA and PLGA microparticles was observed to be more pronounced at higher concentrations, indicating that the concentration of the peptide directly influences its stability and degradation profile [701]. Results of RN7IN6 stability study are shown in Figure 4-19.

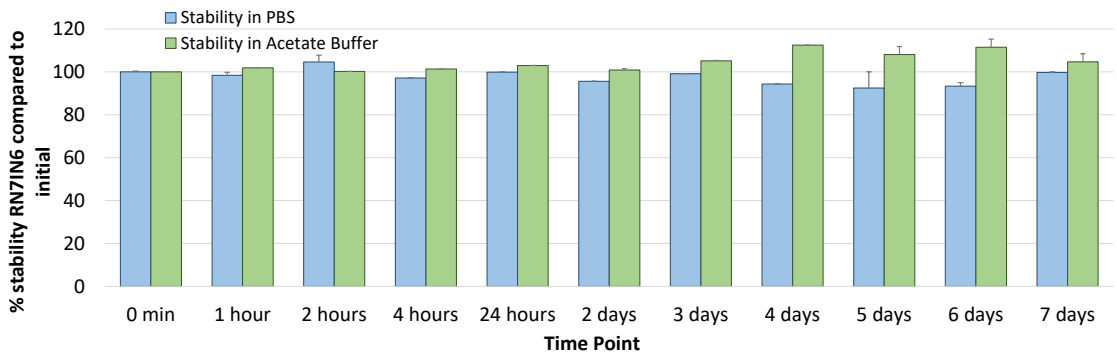

Figure 4-19: Thermal stability of RN7IN6 in PBS and acetate buffer over 7 days at 37 °C with shaking (HulaMixer™, 75 rpm), expressed as percentage of the initial RN7IN6 in solution (T=0 min). Results represent mean ± SD of 2 independent repetitions.

Although minor fluctuations were observed due to the sensitivity of the HPLC quantification method, the peptide was seen to be stable over 7 days and LC-MS analysis performed on day 7 confirmed that the peptide did not degrade (data not shown).

Thus, encouraging peptide stability results shown in Figure 4-19 would appear to confirm that RN7IN6 did not degrade over 7 days, even though it was not appreciably released from the formulation over 14 days. These data suggests that the lack of release, rather than peptide degradation, may potentially play a role in the observed inactivity of F41 in the time-kill study shown in Figure 4-18. Indeed, if it is not released from the liposomes, there may not be sufficient AMP available to interact with the bacteria to exert the desired antimicrobial effect.

As previously discussed in 4.4.2.3, it is possible to hypothesize a strong affinity of RN7IN6 for bacterial membranes. Indeed, indolicidin, a precursor of RN7IN6, has been found to share structural characteristics with bacterial membranes, given its amino acid composition, amphipathicity, cationic charge, and size, which allows it to attach to and insert into bacterial membrane bilayers [702]. Research findings have provided evidence that indolicidin exhibits interactions with bacterial cell membranes in a model system [703], and it is primarily localized at the lipid-water interface of the membranes composed of DOPG, with the distance between phosphate headgroups of each leaflet being reduced in the presence of indolicidin, which induced membranes thinning [704]. Also, indolicidin was proven to adsorb strongly to the model bacterial cell membrane in comparison to the eukaryotic membrane and the difference can be ascribed to different membrane compositions [703]. Thus, it could be inferred that that the lack of peptide release from POPE:POPG:CL liposomes can be ascribed to its strong affinity to the bacterial membrane-like nature of these liposomes. [705] However, this interaction potential must be considered together with the previously-discussed degree of fluidity of these liposomes [692], and the documented affinity of bacteriomimetic liposomes for bacterial cell membranes [305], [621] - which could also enable favorable interactions of these liposomes with bacterial membrane structures. Research has shown that antibiotic-loaded liposomes, upon adhering to or fusing with bacterial envelope structures, can facilitate direct transfer of the antibiotic into bacterial cells [706],

facilitating an effective antimicrobial action. As such an effective action was not observed with F41 in this study, future research should investigate and characterize the interaction between POPE:POPG:CL liposomes and bacterial cell envelopes to better elucidate the interaction dynamics (discussed further in Chapter 6). Moreover, cytotoxicity investigations on mammalian cells and comparisons between free RN7IN6 (see Appendix, Figure S-3 and Table S-2) and liposomal RN7IN6 formulations should be a priority in future work to ensure both the safety and efficacy of this bacteriomimetic system.

4.5.Conclusion

The present study aimed at synthesizing, purifying and characterizing RN7IN6 with a view to evaluating its potential for integration into LPHNPs. By exploring surface adsorption and direct bilayer incorporation within POPE:POPG:CL liposomes, this research sets a foundation for advancing RN7IN6 as a candidate for co-delivery within LPHNPs, with the bacteriomimetic lipid composition potentially enhancing interaction with bacterial cell envelopes and offering a protective environment for the peptide. Results revealed that the peptide was successfully synthesized and purified (purity >95%) using preparative-HPLC and showed a broad range of antimicrobial activity against both Gram-positive and Gram-negative bacteria. RN7IN6 was then surface-adsorbed to empty POPE:POPG:CL liposomes and high adsorption efficiencies were achieved, although physiochemical characteristics were not comparable to those of nisin-adsorbed liposomes prepared using the same parameters, with much larger particle sizes produced. The peptide-adsorbed formulation also did not show any antimicrobial activity against *S. aureus* and *E. coli.* RN7IN6 was subsequently incorporated directly within liposomal lipid bilayers. By altering the initial peptide concentration and the FRR, RN7IN6-loaded formulations with a small and uniform size as well as high encapsulation efficiencies were obtained. While loaded formulations did not show appreciable release of the peptide with a 14-day period and were not active against *S. aureus* and *E. coli,* the tested POPE:POPG:CL system may still offer key advantages for co-delivery as the 'shell' component of lipid-polymer hybrid nanoparticles, including the capability to enhance targeting and interaction with bacterial cells while providing a protective environment for RN7IN6. Furthermore, investigation of the impact of utilizing this bacteriomimetic lipid composition as a shell coating of CS NPs, rather than as standalone liposomal vesicles, is of considerable interest.

5. LPHNPs for CTX and RN7IN6 Co-delivery

5.1.Introduction

As discussed in Chapter 1 (see section 1.6.2.3), LPHNPs are an advanced nanocarrier system designed to optimize drug delivery by integrating the benefits of polymeric and lipid-based systems. These hybrid systems offer advantages over traditional single-material nanocarriers, such as liposomes, polymeric nanoparticles, dendrimers, and inorganic nanoparticles, which often suffer from rapid clearance, suboptimal drug loading, and premature release [707]. While LPHNPs have been explored in various biomedical applications, their use in antimicrobial therapy remains relatively underexplored [707]. However, due to their ability to encapsulate hydrophilic and hydrophobic drugs, improve drug stability, and enhance bacterial membrane interactions, they represent a promising platform for anti-infective delivery.

LPHNPs are composed of a polymeric core, which provides structural integrity and may enable sustained drug release, surrounded by a lipid shell that enhances biocompatibility and interaction with bacterial membranes [311, 708]. Previous studies have reported significant reductions in MIC values when antibiotics were encapsulated in LPHNPs compared to single-material carriers, demonstrating their potential for enhanced antibacterial efficacy [709].

5.1.1. Strategies to Synthesize LPHNPs

The synthesis of LPHNPs typically follows two main approaches: (i) a multi-step process, where the polymeric core and lipid shell are prepared separately before being combined [712-715], and (ii) co-assembly of polymers and lipids into core and shell structures in a single step [716-719]. In conventional multi-step fabrication, the polymeric core is first synthesized via methods such as solvent evaporation or nanoprecipitation, followed by the addition of a lipid layer using thin-film hydration [713, 720-722] or vesicle fusion[712, 723-727]. While effective, these methods often require multiple processing steps, making them time-consuming and less scalable [728].

To improve scalability and efficiency, single-step synthesis methods integrate polymer and lipid self-assembly into a streamlined process. In the emulsion-solvent-evaporation method, the polymer and lipid components are dissolved in an organic solvent and emulsified in an aqueous phase, forming core-shell structures upon solvent removal [729]. A variation of this is the nanoprecipitation method, where the polymer-lipid mixture is rapidly mixed with an anti-solvent, driving nanoparticle formation through controlled precipitation [730, 731].

While traditional LPHNP fabrication methods suffer from batch-to-batch variability, scalability issues, and poor control over nanoparticle characteristics, microfluidic mixing offers a precise, scalable alternative for LPHNP production (Section 1.6.4). Microfluidics enables continuous production, reducing synthesis time and enhancing reproducibility by maintaining strict control over flow rates, reagent mixing, and LPHNP formation parameters [737, 738]. In microfluidic-based fabrication, polymer and lipid precursors are introduced into microchannels, where controlled mixing leads to self-assembly into core-shell structures. The small reaction volumes facilitate rapid heat and mass transfer, improving size control, drug encapsulation efficiency, and uniformity. This method has been successfully implemented in the NanoAssemblr™ platform (Figure 1-10), which enables rapid and scalable LPHNP production. For instance, Rao *et al.* successfully produced Fe_3O_4 magnetic nanoparticles with red blood cell membrane coatings via microfluidics, demonstrating superior performance compared to extrusion-based methods [746]. Microfluidic-synthesized particles exhibited enhanced magnetic and photothermal properties, longer circulation times, uniform membrane coating, and improved colloidal stability, contributing to better bacterial interaction and antibacterial activity [746]. Despite these advantages, the adoption of microfluidics for LPHNP production in antimicrobial therapy remains an emerging area. Further research is needed to optimize process conditions for large-scale applications and ensure regulatory compliance. Nevertheless, microfluidics represents a promising approach to overcoming current challenges in LPHNP fabrication, offering a pathway toward clinical translation.

5.1.2. LPHNP Purification Methods

As for any NPs, purification of LPHNPs is a critical step to remove organic solvents used during preparation as well as unencapsulated/associated drug that may affect LPHNP performance or safety. Ensuring efficient purification is crucial for their biomedical applicability, as residual solvents and free drugs can alter stability and efficacy. Several purification techniques, such as dialysis, ultrafiltration, and ultracentrifugation

Dialysis is a commonly used method for purifying LPHNPs by removing small molecules while retaining nanoparticles [747, 748]. As utilized in section 3.4.1.2, this technique involves placing the nanoparticle dispersion in a dialysis bag with a specific molecular weight cutoff. While effective in solvent removal, dialysis is slow, labor-intensive, and impractical for large-scale purification [749]. Moreover, the long equilibration time between compartments [750] can cause significant drug leakage, affecting encapsulation efficiency. Additionally, solvent removal may alter LPHNP structure, increasing particle size due to changes in lipid packing [751]. Dialysis can also lead to aggregation, impacting LPHNP uniformity and stability [753].

Ultracentrifugation employs intense centrifugal forces to segregate particles according to their size, density, and shape and it offers high purity by efficiently separating particles from free drug [755]. Through ultracentrifugation, particles of varying sizes can be efficiently isolated, resulting in elevated purity levels; as a result, this technique is particularly beneficial for achieving high purity levels from the nanoparticle dispersion [755].However, the high centrifugal forces involved can disrupt drug-nanoparticle interactions, leading to aggregation or premature drug release [757]. Despite optimization in rotor design, ultracentrifugation remains labor-intensive, time-consuming, and difficult to scale up. High-speed conditions (up to 100,000 g) hinder large-scale processing due to rotor capacity limitations and uneven force distribution. Additionally, mechanical stress can alter LPHNP morphology and surface characteristics, increasing aggregation risk [754]. Thus, while ultracentrifugation achieves high purity, its scalability, high shear forces, and particle destabilization limit its practicality.

Ultrafiltration, as introduced in section 2.4.3, is a pressure-driven membrane separation process [761]. Unlike ultracentrifugation, ultrafiltration applies less mechanical stress, preserving particle integrity while efficiently removing free drug and solvents [762]. However, challenges such as membrane fouling and particle loss due to pore blockage remain significant drawbacks, which reduces filtration efficiency and retention of LPHNPs [764].

Ultimately, selecting the appropriate purification method for LPHNPs requires balancing efficiency, scalability, and nanoparticle integrity. While dialysis is effective for small-scale applications, it is slow and may cause aggregation. Ultracentrifugation provides high purity but induces mechanical stress and is not ideal for large-scale production. Ultrafiltration, although gentler, requires careful optimization to prevent membrane clogging and particle loss. Future research should focus on refining these purification techniques to improve scalability and reproducibility, ensuring optimized LPHNP formulation for biomedical applications.

5.1.3. LPHNPs as Therapeutic Delivery Systems Against Bacterial Infections

LPHNPs offer a promising delivery approach for bacterial infections, particularly those involving intracellular pathogens and biofilms. Intracellular bacteria such as *M. tuberculosis* [769, 770], *Salmonella enterica* [771] and *K. pneumoniae* [772] evade immune responses by surviving within host cells, making antibiotic penetration difficult. LPHNPs facilitate intracellular drug delivery by interacting with cell membranes and entering through endocytosis-like mechanisms [775]. In biofilm infections, LPHNPs enhance antibiotic penetration as the lipid shell of LPHNPs protects the drug from degradation and facilitates diffusion through the biofilm matrix, delivering antibiotics directly to embedded bacteria [213].

5.1.3.1. Bacterial Membrane–derived Coated Nanoparticles

Bacteria secrete vesicles containing antigens that can be leveraged for vaccine development, immune modulation, and drug delivery [777]. Gram-negative bacteria produce outer membrane vesicles, while Gram-positive bacteria release extracellular

vesicles and their potential in targeted drug delivery has been demonstrated. Wu *et al.* coated mesoporous silica NPs with E. coli outer membrane vesicles (OMVs) and loaded them with rifampicin, significantly enhancing bacterial uptake and eradication compared to free rifampicin [316]. Similarly, *S. aureus*-derived extracellular vesicles coated onto antibiotic-loaded NPs improved drug delivery to infected macrophages, enhancing bacterial clearance in metastatic infections [780]. In light of the numerous advantages of LPHNPs, particularly those coated with bacterial membrane components, and the further modifications and applications these systems enable, this chapter will focus on the manufacturing and characterization of LPHNPs for treating bacterial infections. Specifically, the LPHNPs developed in this chapter will be constructed by bringing together core and shell structures developed and characterized in previous chapters. LPHNPs will feature a CHCL core due to its ability to effectively encapsulate and deliver the conventional antibiotic CTX, as elaborated in Chapter 2. The shell of the LPHNPs will be composed of a mixture of the bacteria-relevant phospholipids POPE, POPG, and CL, forming a bacteriomimetic coating mimicking the composition of the Gram-negative bacterial inner membrane [312], as discussed in Chapters 3 and 4.

The LPHNPs will be manufactured using microfluidic techniques, leveraging the advantages of precise control over particle size and distribution. This method will build upon the optimized nanoparticle and liposome formulations discussed in Chapters 2, 3, and 4. The LPHNPs will be co-loaded with CTX, a conventional antibiotic, and RN7IN6, an AMP, to exploit the benefits of combination therapy for bacterial infections as detailed in Chapter 1. By combining the structural stability of the CS core with the bacteriomimetic capabilities of the lipid shell, these nanoparticles are anticipated to offer advantages for delivery to bacterial cells.

5.2.Aim and Objectives

This chapter represented the culmination of work conducted in Chapters 2-4, and aimed to establish and optimize a production process for LPHNPs as a co-delivery system for CTX and RN7IN6, using a microfluidic mixing technique. This was achieved through the following objectives:

- Optimizing the manufacture and purification of empty LPHNPs via a microfluidic mixing technique by varying parameters such as initial lipid concentration, TFR, FRR and solvent composition.
- Assessing the synergism activity of CTX and RN7IN6.
- Evaluating the physiochemical properties, release kinetics and antimicrobial activity of CTX and RN7IN6-loaded LPHNPs manufactured using microfluidic mixing.

5.3. Materials and Methods

5.3.1. Materials

Mueller Hinton Broth 2 (MHB2), Mueller Hinton Agar (MHA), Nutrient agar (NA), resazurin and dialysis tubing cellulose membrane (D9527, MWCO ~14kDa) were purchased from Sigma-Aldrich (Missouri, USA). Phosphate buffered saline (PBS, pH 7.4) tablets were obtained from Oxoid Ltd (Basingstoke, UK). POPE, POPG and CL were purchased from Avanti Polar Lipids (Merck, Ney Jersey, USA). HPLC grade acetonitrile, and HPLC grade methanol were purchased from Thermo Fisher Scientific (Massachusetts, USA). N,N-dimethylformamide (DMF) was bought from Acros Organics (New Jersey, USA). Propan-1-ol was purchased from VWR (Pennsylvania, USA).

5.3.2. Methods

5.3.2.1. Empty LPHNP Manufacture and Characterization

Empty LPHNPs were manufactured using a microfluidic mixing technique employing a NanoAssemblr® Benchtop from Precision Nanosystems (Vancouver, Canada) as described in section 1.6.4. Empty LPHNPs were formulated as a CHCL polymeric core, surrounded by a lipid shell composed of POPE, POPG and CL in a weight ratio of 70:20:10 (%wt) [312]. Empty LPHNPs were manufactured using a 2-step method, using a similar principle to the one described by Nie *et al.* [781].

CHCL was employed to manufacture the polymeric core of the LPHNPs due to its water solubility and ease of employability to manufacture NPs. Empty CHCL NPs were manufactured employing optimized process parameters detailed in Chapter 2 (Table 2-5). LPHNPs were then produced by loading CHCL NPs into one of the two channels of the NanoAssemblr™ platform and mixing with a 70:20:10 (%wt) POPE:POPG:CL lipid solution (detailed in Chapters 3 and 4) to facilitate NP coating and the production of LPHNPs.

An initial screening of LPHNP manufacturing parameters was performed in order to assess the influence of the initial lipid concentration, the TFR and the FRR between the

CHCL NP dispersion and the lipid solution (as shown in Table 5-1) on LPHNP size, PDI and Z-Potential. The initial screening was performed using a Taguchi L9 orthogonal array design with 3 variables set at 3 levels. CHCL NPs (produced as detailed in section 2.3.2.1) and without any additional purification were injected into the left inlet of the staggered herringbone micromixer (SHM) of the NanoAssemblr™ platform. Lipids dissolved in a mixture of 1-propanol and DMF (80:20 v/v) at the desired concentration were injected into the right inlet of the SHM. Following preparation, empty LPHNPs were diluted 1:10 with PBS (pH 7.4) and characterized in terms of size, Z-potential and PDI as detailed in 2.3.2.1.2.

Table 5-1: Set of 9 formulations employed to investigate the effect of initial lipid concentration, TFR and FRR on LPHNP size, PDI and Z-potential.

Formulation	Lipid Concentration	TFR	FRR
	mg/mL	mL/min	CHCL NPs : Lipid solution
F21	2	5	2:1
F22	2	10	3:1
F23	2	20	4:1
F24	4	5	3:1
F25	4	10	4:1
F26	4	20	2:1
F27	8	5	4:1
F28	8	10	2:1
F29	8	20	3:1

5.3.2.1.1. Additional Investigation of Lipid Concentration, TFR and FRR

Following the initial LPHNP screening as detailed above, the lipid concentration was lowered further and the impact of 3 additional initial lipid concentrations (2, 1 and 0.5 mg/mL) was assessed on empty LPHNP size, PDI and Z-potential. Similarly, 5 different FRR between CHCL NP dispersions and lipid solution (2:1, 3:1, 4:1, 5:1 and 6:1) and 2 levels of TFR (10 and 20 mL/min) were employed in the full factorial design in order to investigate one-variable-at-a-time (OVAT) changes on LPHNP physiochemical characteristics as described in section 2.3.2.1.2.

Table 5-2: Set of 30 formulations employed to further investigate the effect of the initial lipid concentration, TFR and FRR on LPHNP size, PDI and Z-potential.

Formulation	Lipid Concentration mg/mL	TFR	FRR	
		mL/min	CHCL NPs	Lipid solution
A.1	2	10 and 20	2	1
A.2	2	10 and 20	3	1
A.3	2	10 and 20	4	1
A.4	2	10 and 20	5	1
A.5	2	10 and 20	6	1
B.1	1	10 and 20	2	1
B.2	1	10 and 20	3	1
B.3	1	10 and 20	4	1
B.4	1	10 and 20	5	1
B.5	1	10 and 20	6	1
C.1	0.5	10 and 20	2	1
C.2	0.5	10 and 20	3	1
C.3	0.5	10 and 20	4	1
C.4	0.5	10 and 20	5	1
C.5	0.5	10 and 20	6	1

5.3.2.1.2. Addition of FA to Lipid Solution

Empty LPHNPs were optimized as an initial step towards the manufacture of CTX and RN7IN6 co-loaded LPHNPs. In order to develop the co-loaded formulation, the intention was to use crude RN7IN6 and thus, in order to improve the solubility of the crude peptide in the organic solvent composed of 1-propanol/DMF (80:20 v/v) used to dissolve lipids and RN7IN6, 0.1% of FA was added to the solvent mixture to aid solubility [636]. Hence, the impact of the addition of 0.1% FA on physiochemical characteristics of empty formulations C.1, C.2, C.3, C.4 and C.5 manufactured from Table 5-2 at TFR of 20 mL/min was investigated. These formulations are hereafter respectively called F.1, F.2, F.3, F.4 and F.5. Formulations were characterized as detailed in 2.3.2.1.2.

5.3.2.1.3. Formulation Purification via Dialysis

The optimum empty formulation (F.4) resulting from the study described under section 5.3.2.1.1 was purified firstly via dialysis. Dialysis tubing of MWCO ~ 14 kDa was employed for solvent removal as previously described by Roces *et al.* [326] from formed

LPHNPs as described in section 3.3.2.1.1. Formulation F.4 was dialyzed for 6 hours, as optimized and discussed for liposomes in section 3.4.1, against 100, 200 and 300 mL of PBS (pH 7.4) in order to safely remove organic solvents from the final formulation. Quantification of the residual 1-propanol and DMF within the LPHNP formulation after dialysis was performed by GC [582] as described in section 3.3.2.1.2. FA residual content was not assessed as its initial percentage in formulation was already below the safe limit established by ICH guidelines [583].

Following dialysis purification, LPHNP formulation F.4 was diluted 1:5 with PBS buffer and ultracentrifuged at 55000 rpm [581] (rotor type 70.1 Ti, Fixed angle Titanium Rotor, Beckman Coulter Inc., Brea, California, USA), at 4 °C for 1 hour (Optima XPN-80, Beckman Coulter Inc., Brea, California, USA). Formulations were characterized as detailed in 2.3.2.1.2.

5.3.2.1.4. Formulation Purification via Ultracentrifugation

Ultracentrifugation parameters were investigated in order to allow LPHNP resuspension in PBS with respect to maintaining a monodisperse formulation and avoiding increases in LPHNP size due to possible aggregation. The impact of several ultracentrifugation parameters on LPHNP size, PDI and Z-potential were investigated in a full factorial design. Th optimum empty LPHNP formulation F.4 was ultracentrifuged at different speeds (15000, 25000, 35000 and 55000 rpm, rotor type 70.1 Ti, Fixed angle Titanium Rotor, Beckman Coulter Inc., Brea, California, USA) at 4 ^{o}C or 25 ^{o}C for either 30 minutes or 1 hour. Following ultracentrifugation, 5 mL of PBS buffer were added to the pellet for redispersion and LPHNPs were sonicated in a sonicating water bath (GAH 209 Ultrawave Precision, UK) for 10 minutes. Formulations were characterized as detailed in 2.3.2.1.2.

5.3.2.2. CTX-loaded LPHNP Manufacture and Characterization

CTX loaded LPHNPs were formulated as a CTX-loaded CHCL NP core, surrounded by a lipid shell composed of POPE, POPG and CL in a weight ratio of 70:20:10 (%wt) [312].

As for production of empty CHCL NPs for preparation of unloaded LPHNPs, CTX-loaded CHCL NPs were manufactured employing optimized process parameters detailed in Table 2-5 and additionally using 3 mg/mL of CTX added to TPP solutions, as identified in Chapter 2. CTX-CHCL NPs without any additional purification were injected into the left inlet of the SHM of the Nanoassemblr™ platform. Lipids dissolved in a mixture of 1-propanol, DMF and FA (80:20:0.1 v/v) at the desired concentration were injected into the right inlet of the SHM. CTX-loaded LPHNPs were then manufactured using CTX-CHCL NPs, and process parameters detailed for formulation F.4 (as detailed in Table 5-2 for formulation C.4, manufactured at 20 mL/min).

Following preparation LPHNPs were diluted 1:10 with PBS buffer (pH 7.4) and characterized in terms of size, Z-potential and PDI (Zetasizer Nano ZS, Malvern Instruments Ltd., GB) as detailed in section 2.3.2.1.2.

5.3.2.2.1. CTX-loaded LPHNP Purification

CTX-loaded LPHNP purification from organic solvent and unentrapped CTX was investigated by assessing two different purification methods: ultracentrifugation and ultrafiltration. In the first case, 5 mL of CTX-loaded LPHNPs were collected via ultracentrifugation (Beckman Coulter Optima XPN-80) using a 70.1 Ti rotor at 55 000 rpm for 1 hour at 4 °C [581]. After ultracentrifugation, the pellet was resuspended in 5 mL of PBS and analyzed for purified LPHNP size, PDI and Z-potential.

In the latter case, 2 mL of CTX -loaded LPHNPs was loaded into centrifugal ultrafiltration units and centrifuged (Eppendorf centrifuge 5804r, Germany) at 1188 x *g* and 25 °C for 30 min. After centrifugation, the concentrated CTX-LPHNP dispersion was collected, diluted to 2 mL with PBS and analyzed for purified LPHNP size, PDI and Z-potential as detailed in 2.3.2.1.2.

5.3.2.2.2. CTX-loaded LPHNP EE% Evaluation

In the case of ultracentrifugation, the supernatant was analyzed, while for centrifugal ultrafiltration, the ultrafiltrate was analyzed using HPLC to determine CTX EE% as described in section 5.3.2.5.

5.3.2.3. CTX and RN7IN6 Loaded LPHNP Manufacturing and Characterization

The manufacturing process and parameters used to manufacture CTX (polymer core) and RN7IN6 (lipid shell) co-loaded LPHNPs wereas described in section 5.3.2.2. To investigate the additional, optimal loading of the AMP into LPHNP lipid shells, increasing loading concentrations of RN7IN6 ranging from 0.5 mg/mL to 2 mg/mL were dissolved in the organic phase, together with lipid, as summarized in Table 5-3.

Table 5-3: Microfluidic process parameters employed to manufacture CTX and RN7IN6 co-LPHNPs with varying RN7IN6 initial loading concentrations. The formulations have been named based on the initial loading concentrations of RN7IN6 in the lipid solution, as indicated in the table. Specifically, the "F.4" designation refers to a specific formulation code, while the numerical values following it represent the different RN7IN6 loading concentrations tested in the microfluidic process.

Formulation	Aqueous phase	Organic phase		TFR (mL/min)	FRR	
		RN7IN6 initial loading concentration (mg/mL)	Lipid concentration (mg/mL)		C TX CHCL NPs	Lipid and RN7IN6 solution
CTX F.4 0.5 R	CTX CHCL NPs	0.5	0.5	20	5	1
CTX F.4 0.75 R		0.75				
CTX F.4 1 R		1				
CTX F.4 1.5 R		1.5				
CTX F.4 2 R		2				

Following preparation co-loaded LPHNPs were diluted 1:10 with PBS buffer (pH 7.4) and characterized in terms of size, Z-potential and PDI (ZetaSizer Nano ZS, Malvern Instruments Ltd., GB) as detailed in section 2.3.2.1.2.

5.3.2.3.1. Co-loaded LPHNP Purification: Dialysis

A preliminary study to investigate the ability of CTX and RN7IN6 to pass through dialysis tubing of MWCO ~14kDa was assessed as described in section 3.3.2.1.1. Briefly, a 1 mL volume of CTX and RN7IN6 solutions, separately, each in PBS at 3 mg/mL, was dialyzed against 100 mL, 200 mL and 300 mL of PBS. After the allocated time (0, 30, 60, 90 minutes, 2, 3, 4, 5, 6, 7, 8 and 24 hours), 1 mL of outer media was withdrawn and replaced with an equal volume of fresh PBS. Samples were then analyzed via RP-HPLC for CTX and RN7IN6 quantification as detailed in section 5.3.2.5.

5.3.2.3.2. Co-loaded LPHNP Purification: Ultrafiltration

The ultrafiltration method (Centrisart® I centrifugal ultrafiltration units, MWCO of 300 kDa) was further investigated for co-loaded LPHNP purification and separation of unentrapped actives [782]. For particle purification, 2 mL of CTX and RN7IN6 co-loaded LPHNPs was loaded into centrifugal ultrafiltration units and centrifuged (Eppendorf centrifuge 5804r, Germany) at 1188 x *g* and 25 °C for 30 min. Ultrafiltrate samples were then analyzed as detailed in section 5.3.2.5.

5.3.2.4. RP-HPLC Method Validation

HPLC chromatographic system details are described in section 2.3.2.2.2. The HPLC analysis method employed to quantify both CTX and RN7IN6 was the same as used for RN7IN6 alone as described in section 4.3.2.1.3.

RP-HPLC chromatographic method validation was performed by assessing HPLC method linearity (as described in section 2.3.2.2.3), method precision, accuracy and sensitivity (as described in section 2.3.2.2.4).

5.3.2.5. Encapsulation Efficiency Evaluation

CTX and RN7IN6 encapsulation efficiency within CTX-loaded and CTX and RN7IN6 co-loaded LPHNPs was indirectly calculated by quantification of unentrapped CTX and/or RN7IN6 amounts using an optimized and validated HPLC method (see above), following centrifugal ultrafiltration in both cases. After centrifugation, the liquid present in the ultrafiltrate compartment was collected and analyzed via HPLC to quantify CTX and RN7IN6 EE% using Equation 2-4.

5.3.2.6. CTX and RN7IN6 Release from LPHNPs

The 'sample and separate' method was employed to assess the *in vitro* release as described by Solomon *et al.* [638]. The release profiles of CTX from loaded CHCL NPs (3 CTX CHCL NPs) and from loaded LPHNPs (3 CTX F.4) was determined. In addition to this, the release profile of CTX and RN7IN6 from co-loaded LPHNPs (CTX F.4 2R) was assessed. A 15 mL volume of loaded formulations were purified from unentrapped CTX, RN7IN6 or CTX and RN7IN6 via ultracentrifugation (55000 rpm, 1 hour, 4 °C, rotor type 70.1 Ti, Fixed angle, Beckman Coulter Inc., Brea, California, USA). The supernatant was employed to indirectly calculate the EE% of CTX/RN7IN6 by RP-HPLC as described in section 5.3.2.5. The pellet was resuspended in 9 mL of PBS (pH 7.4) by sonication (5 minutes) in a water bath (GAH 209 Ultrawave Precision, UK) followed by vortexing (SciQuip Vortex Mixer, SciQuip, UK).

The samples were then placed on a HulaMixer™ Sample Mixer (Thermo Fisher Scientific, US) at 75 rpm and incubated at 37 °C. At specific timepoints (0, 1, 2, 4, 6, 24 and 48 hours), 500 µL of supernatant was withdrawn and replaced with an equal volume of fresh PBS. The initial sample was taken immediately after the start of the experiment and was intended to represent the time zero measurement. Samples were analyzed via RP-HPLC for CTX/RN7IN6 quantification.

Alongside samples for release testing, aliquots of CTX and RN7IN6 solutions at 1 mg/mL in PBS (pH 7.4) were also incubated. At each release sampling time point a CTX and RN7IN6 solution aliquot was also withdrawn and employed to construct a calibration

curve used to quantify released CTX and RN7IN6. The cumulative percentage of CTX and RN7IN6 release (CCR%) from formulations was calculated in reference to the amount of CTX and RN7IN6 encapsulated within formulations after purification [783].

5.3.2.7. Antimicrobial Efficacy Assessment

5.3.2.7.1. Free CTX Antibacterial Activity

The antibacterial activity of CTX in solution was assessed using the REMA as detailed in section 4.3.2.1.5. CTX solutions were prepared in sterile water at desired concentrations. The REMA method was adapted from that described by Khalifa *et al.* [630].

5.3.2.7.2. CTX and RN7IN6 Synergism Assessment (Microdilution Checkerboard)

In order to determine whether co-administration of CTX and RN7IN6 can lead to an enhanced antibacterial effect, synergy analysis was carried out by a checkerboard titration method using 96-well microtiter plates. The checkerboard titration method was adapted from the one described by Bellio *et al.* [784].

Preparation of a standardized bacterial suspension was achieved by the selection of a microorganism colony followed by its suspension in 50 mL of MHB2, which was left to incubate in an orbital shaking incubator (250 rpm) set at 37 °C overnight. A 40 µL volume of the overnight culture was then used to inoculate 150 mL of MHB2, which was left in an orbital shaking incubator (250 rpm) set at 37 °C for 3 hours. The bacterial suspension ($1x10^6$ CFU/mL) was adjusted to OD_{600} 0.05-0.1 (corresponding to $1x10^6$ CFU/mL, as determined from bacterial growth curves) and a volume of 80 µL was added to each well along with 20 µL of sterile resazurin solution in MHB2 (0.2 mg/mL). The ranges of the antibiotic/AMP dilutions employed in the checkerboard assay were as per Table 5-4, decided according to free CTX and RN7IN6 MIC values.

Table 5-4: CTX and RN7IN6 concentration ranges (µg/mL) employed in the synergy analysis carried out by a checkerboard titration method using a 96-well microtiter plate for each bacteria tested.

	CTX concentration range (µg/mL)		RN7IN6 concentration range (µg/mL)	
	Upper	Lower	Upper	Lower
P. aeruginosa	256	4	1024	16
K. pneumoniae	1	0.016	512	8
S. aureus	16	0.25	128	2
E. coli	1	0.016	256	4

Briefly, RN7IN6 and CTX stock solutions were prepared in sterile water and diluted with MHB2 to give a concentration 4 times higher than the highest concentration to be tested in the microtiter plate. RN7IN6 was then plated in two-fold dilutions (MHB2) horizontally in rows, while CTX was diluted vertically in columns. Column 8 was set up to contain two-fold dilutions of CTX only, while row H contained two-fold dilutions of RN7IN6 only. An example of a microtitre plate setup can be found in Figure 5-1.

	1	2	3	4	5	6	7	8	9	10	11	12
A	128 16	64 16	32 16	16 16	8 16	4 16	2 16	0 16				
B	128 8	64 8	32 8	16 8	8 8	4 8	2 8	0 8	CTX concentration in well RN7IN6 concentration in well			
C	128 4	64 4	32 4	16 4	8 4	4 4	2 4	0 4				
D	128 2	64 2	32 2	16 2	8 2	4 2	2 2	0 2				
E	128 1	64 1	32 1	16 1	8 1	4 1	2 1	0 1				
F	128 0.5	64 0.5	32 0.5	16 0.5	8 0.5	4 0.5	2 0.5	0 0.5				
G	128 0.25	64 0.25	32 0.25	16 0.25	8 0.25	4 0.25	2 0.25	0 0.25				
H	128 0	64 0	32 0	16 0	8 0	4 0	2 0	0 0				

Figure 5-1: An example of a microtitre 96-well plate setup for broth microdilution checkerboard assay to assess CTX and RN7IN6 synergy.

Figure 5-1Following dilution of antimicrobial agents, 20 µL of sterile resazurin solution in MHB2 (0.2 mg/mL) was added to the plate. Negative controls (MHB2 + resazurin solution, MHB2 + resazurin + RN7IN6 solution or CTX solution) and positive controls (MHB2 + resazurin solution + inoculum) were performed alongside each experiment (a total of 200 µL each well). The MIC for the individual CTX and RN7IN6 was evaluated as the minimum concentration of antimicrobial that inhibited visible growth (blue/purple color), reflecting the absence of metabolic activity (see Figure 5-2).

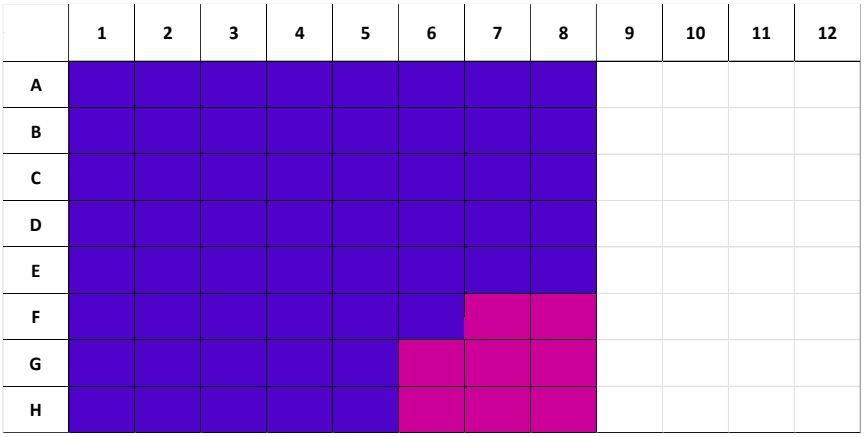

Figure 5-2: Example of checkerboard assay result. Blue/purple wells represent no bacterial growth while pink wells represent bacterial growth. In this specific example, wells E8 and H5 represent individual CTX and RN7IN6 MICs while well F6 indicates the combination resulting in a synergistic/partial synergistic effect.

These MICs were used in the equations below to calculate fractional inhibitory concentration indices (FICI), which is a measure used to assess the interaction between two antimicrobial agents. FICI indicates whether their combined effect is synergistic, additive, indifferent, or antagonistic by summing the fractional inhibitory concentrations (FICs) of each agent when used together. Several combination concentrations were tested as part of the checkerboard assay and the FICI was therefore calculated. FICs for RN7IN6 and CTX were first calculated by using Equation 5-1 and Equation 5-2, respectively as described by Orhan *et al.* [785].

Equation 5-1

$$FIC\ (RN7IN6) = \frac{MIC\ of\ RN7IN6\ in\ combination\ with\ CTX}{MIC\ of\ RN7IN6\ alone}$$

Equation 5-2

$$FIC\ (CTX) = \frac{MIC\ of\ CTX\ in\ combination\ with\ RN7IN6}{MIC\ of\ CTX\ alone}$$

The FICI was then calculated for each well where RN7IN6 and CTX combinations were tested as per Equation 5-3.

Equation 5-3

$$FICI = FIC\ (RN7IN6) + FIC\ (CTX)$$

FICIs were interpreted as follows [786]:

- FICI < 0.5: synergistic activity
- 0.5 < FICI < 1: partial synergism
- FICI = 1: addition
- 1 < FICI < 4: indifference
- FICI ≥ 4: antagonism

5.3.2.7.3. Antimicrobial Activity of Empty and Loaded LPHNPs

Empty and loaded formulation antibacterial activity was assessed by using the REMA. The procedure is detailed in section 4.3.2.1.5 and was adapted from the one described by Bellio *et al.* [784].

All the formulations used were purified using Centrisart® I centrifugal ultrafiltration units. Briefly, multiple batches of the same formulation were pooled together, and the final formulation was purified by loading 2 mL of pooled formulation into each centrifugal ultrafiltration unit. Formulations were centrifuged (Eppendorf centrifuge 5804r, Germany) at 1188 x *g* and 25 °C for 30 min. After centrifugation, the concentrated formulation dispersion was collected and diluted with sterile PBS to reach the desired CTX or RN7IN6 loaded concentration as follows:

- CTX-loaded CHCL NPs (3 CTX CHCL NPs) and CTX-loaded LPHNPs (CTX F.4) were diluted to reach a final CTX-loaded concentration of 512 µg/mL for *S. aureus* and 16 µg/mL for *E. coli.*
- Empty LPHNPs (F.4) was diluted using the same ratio between formulation and sterile PBS (depending on the encapsulation efficiency of the loaded formulation) used for 3 CTX CHCL NPs and CTX F.4
- CTX and RN7IN6 co-loaded LPHNPs (CTX F.4 2R) were diluted to obtain a RN7IN6-loaded concentration which was 32 times higher than the MIC of free RN7IN6 - this corresponds to 512 µg/mL for *S. aureus* and 1024 µg/mL for *E. coli.* As the formulation is co-loaded with CTX and the CTX and RN7IN6 loaded concentration ratio is fixed, the loaded concentration of CTX corresponded to 765 µg/mL for *S. aureus* and 1530 µg/mL for *E. coli.*

Thus, the final range of CTX and RN7IN6 loaded concentrations in formulations assessed is detailed in Table 5-5.

Table 5-5: Range of CTX and RN7IN6 loaded concentrations evaluated for antibacterial activity of various formulations S. aureus *and* E. coli *using the REMA. Concentrations listed represent the final concentrations tested in each well, which were achieved through serial dilution from stock formulations with higher initial concentrations.*

Formulation	Active	Concentration assessed (µg/mL)	
		S. aureus	*E. coli*
3 CTX CHCL NPs	**CTX**	256 – 0.125	8 – 0.0035
CTX F.4	**CTX**	256 – 0.125	8 – 0.0035
F.4	**N/A**	N/A	N/A
CTX F.4 2R	**RN7IN6**	256 – 0.125	512 – 0.25
	CTX	382.5 – 0.188	765 – 0.375

5.3.2.8. Statistical Analysis

Statistical analysis for formulations produced in sections 5.3.2.1.2, 5.3.2.1.3, 5.3.2.2 and 5.3.2.2.1 was performed using IBM SPSS statistic software (Version 28.0. Armonk, NY: IBM Corp). An independent T-test was run on LPHNP formulations to assess mean

differences in size, PDI and Z-potential. If the output of Levene's test to assess equality of variance was $p>0.05$, the two-sided p value with equal variance assumed (pooled T-test) was considered, while if the output of Levene's test was $p<0.05$, the two-sided p value with equal variance not assumed (unpooled T-test) was considered. A p value of <0.05 was taken as indicating statistical significance throughout the study.

Statistical analysis of formulations manufactured in section 5.3.2.3 was performed using JMP® 16.2.0 software (SAS Institute Inc., Cary, NC, US). An independent T-test was run on LPHNP size, PDI and Z-potential to determine if there was a mean difference in formulation physicochemical characteristics before and after purification via centrifugation ultrafiltration. If the output of Levene's test to assess equality of variance was $p>0.05$, the two-sided p value with equal variance assumed (pooled T-test) was considered, while if the output of Levene's test was $p<0.05$, the two-sided p value with equal variance not assumed (unpooled T-test) was considered. A p-value of <0.05 was taken as indicating statistical significance throughout the study.

Statistical analysis of formulations manufactured in section 5.4.3 was performed using JMP® 16.2.0 software (SAS Institute Inc., Cary, NC, US). One-way ANOVA with Tukey's post hoc test was employed to compare formulations produced as per section 5.3.2.3 and determine any significant difference in CTX or RN7IN6 EE%/concentration loaded. A p value of <0.05 was taken as indicating statistical significance throughout the studies.

5.4. Results and Discussion

5.4.1. Empty LPHNPs Manufacturing and Characterization

Following initial optimization, CHCL was chosen for the LPHNP core over CHT primarily due to its water solubility, which simplifies production by removing the need for acidic solubilization steps. While both CHT and CHCL NPs showed similar antimicrobial efficacy and physiochemical characteristics in terms of size, PDI and EE%, the higher Z-potential of CHCL NPs could enhance interactions with the lipid shell, making it suitable for further development into LPHNPs. This selection also addresses a notable literature gap in CHCL's application for nanoparticle manufacturing.

Given the novelty of this hybrid structure in utilizing CHCL as the polymeric core material combined with the specific lipid composition (POPE, POPG, CL), as well as the use of the microfluidic technology for the preparation of LPHNPs it was essential to investigate which parameters had the greatest degree of influence on the size, PDI and Z-potential of unloaded LPHNPs in the first instance.

An initial screening was performed to investigate critical microfluidic mixing parameters such as the initial lipid concentration, the TFR and the FRR between empty CHCL NPs and lipid solution as detailed in Table 5-1. An L9 orthogonal array mixed-design Taguchi DoE was constructed using Minitab 16 Statistical Software, which is more efficient in comparison to the traditional 'one factor at a time' to identify important process parameters required to more efficiently fine-tune desired outputs.

The characteristics of F21-29 LPHNPs (described in Table 5-1) manufactured using microfluidic mixing are displayed in Figure 5-3. The formulations demonstrated an average particle size ranging from 168.6 nm (F28) to 3501 nm (F24), with only 4 formulations (F22, F23, F26 and F28) having an average size smaller than 600 nm. Concerning the PDI, most of the formulations (F24 to F29) showed polydisperse particle populations with values ranging from 0.24 to 0.60. Formulations prepared using 2 mg/mL of initial lipid concentration (F21-F23) showed monodisperse and homogeneous populations with a PDI lower than 0.15. With respect to the Z-potential, all the

formulations showed a negative surface charge ranging from -3.53 mV to -19 mV, with only one formulation (F23) having a positive Z-potential.

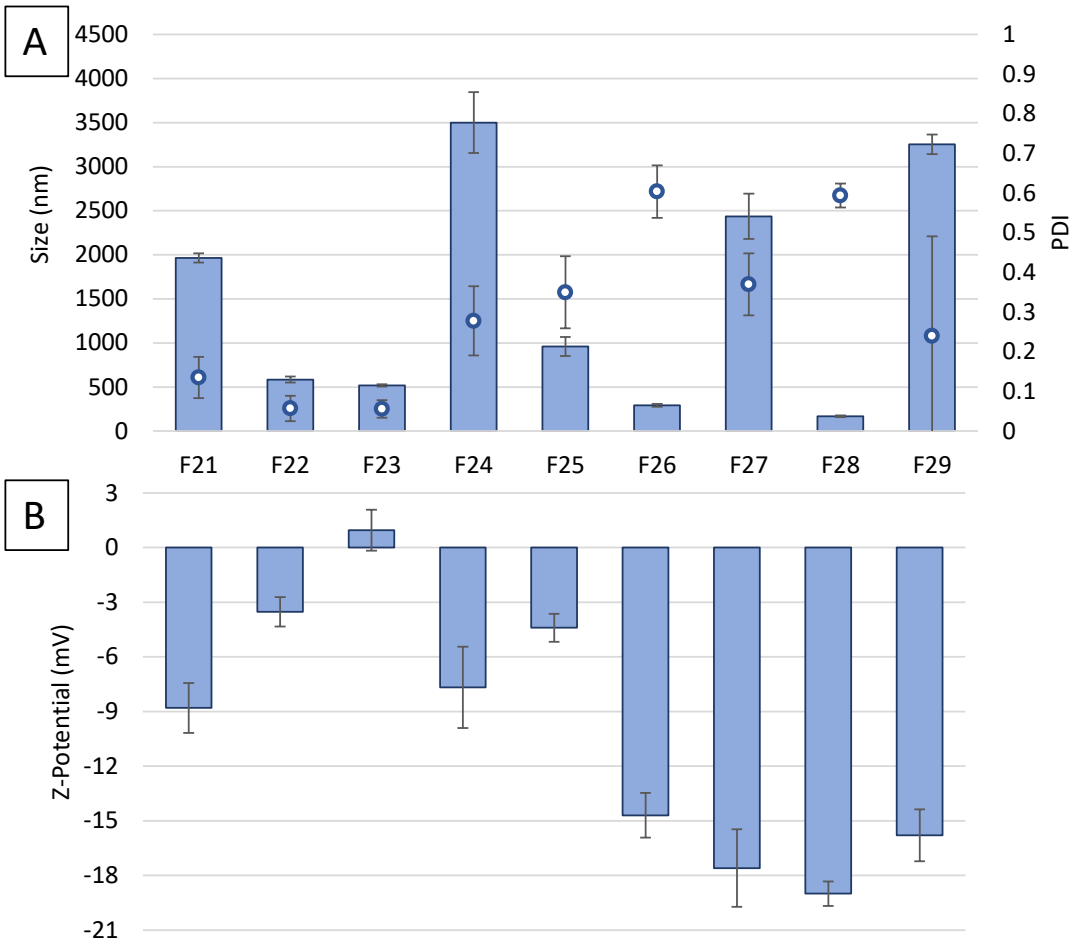

Figure 5-3: Size, PDI (A) and Z-potential (C) of the 9 empty LPHNP formulations prepared according to Taguchi L9 orthogonal array DoE (Table 5-1). The results represent mean ± SD, n=3 measurements of the same batch (3 technical replicates).

Only one biological replicate was performed for this study to serve as an initial screening, with three technical replicates measured from each prepared formulation. This approach provided a preliminary but essential basis for identifying trends and understanding the influence of process parameters on the characteristics of LPHNPs. Therefore, a multiple linear regression modelling was employed to understand the relationships between process parameters and the characteristics of LPHNPs (size, PDI, Z-potential) using JMP® 16.2.0 software (SAS Institute Inc., Cary, NC, US). This analysis helps to identify the significant parameters influencing the outcomes. The JMP

prediction profiler in Figure 5-4 shows the relationship between critical process parameters and the outputs being LPHNPs size, PDI and Z-potential.

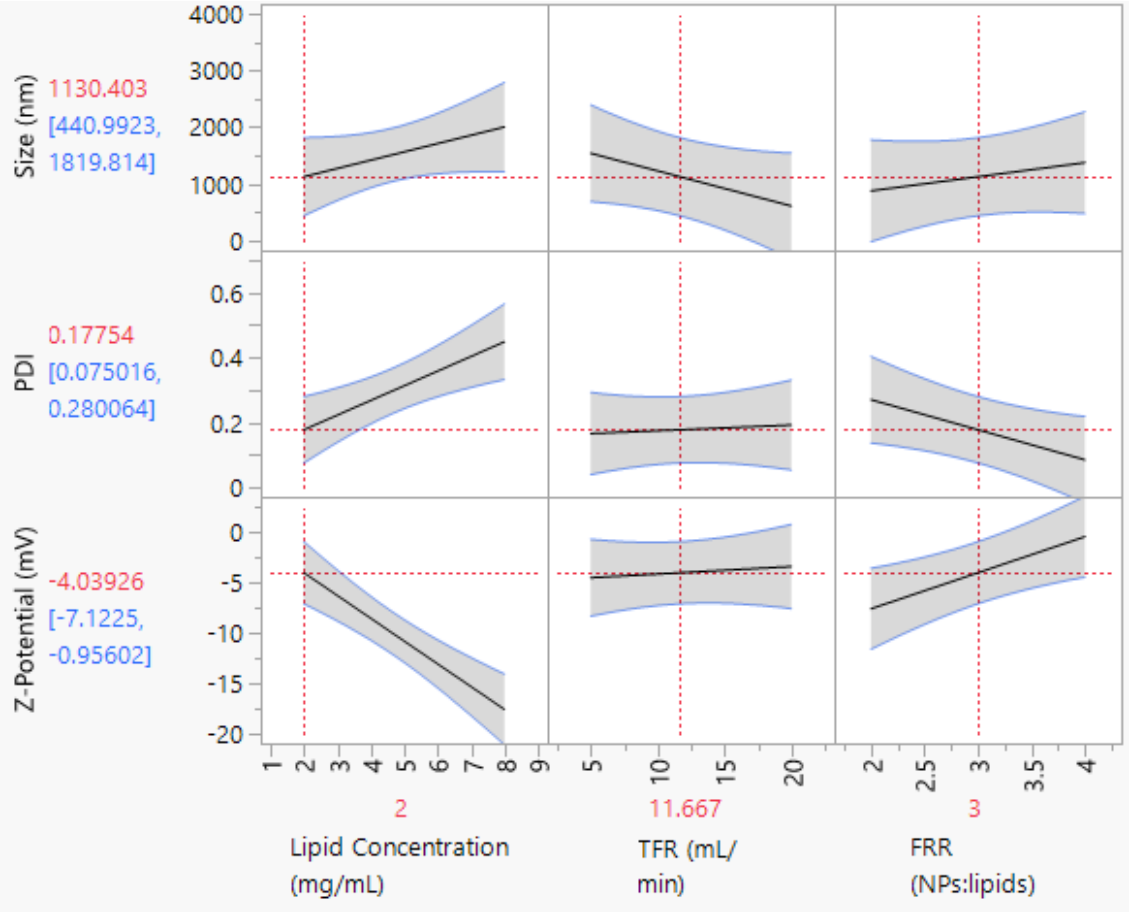

Figure 5-4: The model shown in the prediction profiler of the software (JMP) illustrates the relationship between critical process parameters (lipid concentration, TFR, and FRR) and the resulting characteristics of empty LPHNPs, specifically size, PDI, and Z-potential. The blue numbers given next to the response axes represent the minimum and maximum responses that can be obtained with the optimum parameter of each factor. The gray areas between the blue lines on each plot represent the confidence interval for each plot. The red numbers on the response axes represent the associated predicted values when the predictors are set to their corresponding red numbers. The black lines within the plots show how the predicted value changes when changing the value of the predictors - being lipid concentration, TFR and FRR.

The higher the slope in Figure 5-4, either positive or negative, the stronger the relationship between the predictor and the output. According to the multiple linear regression analysis, TFR and FRR did not significantly affect LPHNP size and PDI. However, lipid concentration affected all the outputs with statistical significance, and FRR affected LPHNP Z-potential with statistical significance, indicating that a change in the predictor value in each case determines a change in the output. Thus, by examining

the plots, it is possible to identify the optimal conditions of the process parameters that lead to desired characteristics of LPHNPs. These characteristics include a smaller particle size, which is generally preferred for better drug delivery and cellular uptake, and a lower PDI, which indicates a more monodisperse and homogeneous nanoparticle population. Additionally, the Z-potential should be sufficiently high (either positive or negative) to ensure stability and prevent aggregation of the nanoparticles in the formulation. According to the predictor profiler analysis, LPHNP size and PDI linearly increase with increasing lipid concentration from 2 mg/mL to 8 mg/mL. This is in line with experimental results shown in Figure 5-4, where formulations F21, F22 and F23, which were manufactured with 2 mg/mL of lipid, showed a smaller size and PDI compared to other formulations manufactured with higher initial lipid concentration.

As the preliminary study described here only aimed to screen important manufacturing parameters affecting critical quality attributes being LPHNP size, PDI and Z-potential, a more detailed and comprehensive study was subsequently performed in accordance with the initial screening output.

5.4.1.1. Additional Investigation of Lipid Concentration, TFR and FRR on Empty LPHNP Physiochemical Characteristics

According to the LPHNP prediction profiler (Figure 5-4), a reduction in initial lipid concentration is directly related to a decrease in LPHNP size and PDI and therefore additional initial lipid concentrations of 2 mg/mL, 1 mg/mL and 0.5 mg/mL were investigated in a follow up study. Moreover, the FRR vs. PDI plot had a negative slope indicating that an increase in FRR values (CHCL NPs : lipid solution) might represent a means to reduce spread of LPHNP particle size distribution (Figure 5-4). Hence, further to the initially screened FRR values of 2:1, 3:1 and 4:1, additional higher FRR values were investigated (5:1 and 6:1). Finally, the prediction profiler showed that there is no correlation between the TFR and LPHNP PDI and Z-potential (Figure 5-4). However, despite the fact that the relationship is not significant, increasing TFR might determine a reduction in LPHNP size indicated by the negative slope in the TFR vs LPHNP size plot in Figure 5-4. Therefore, only higher TFRs of 10 mL/min and 20 mL/min were

investigated in this second study. A full factorial design composed of 30 formulations detailed in Table 5-2 was performed.

The characteristics of A.1 to C.5 LPHNP formulations manufactured using the NanoAssemblr® Benchtop device using two different TFRs are displayed in Figure 5-5. Additional data on the characteristics of formulations A.1 to C.5 post-manufacture and after purification are available in Figure 1-S and Figure 2-S (see Appendix).

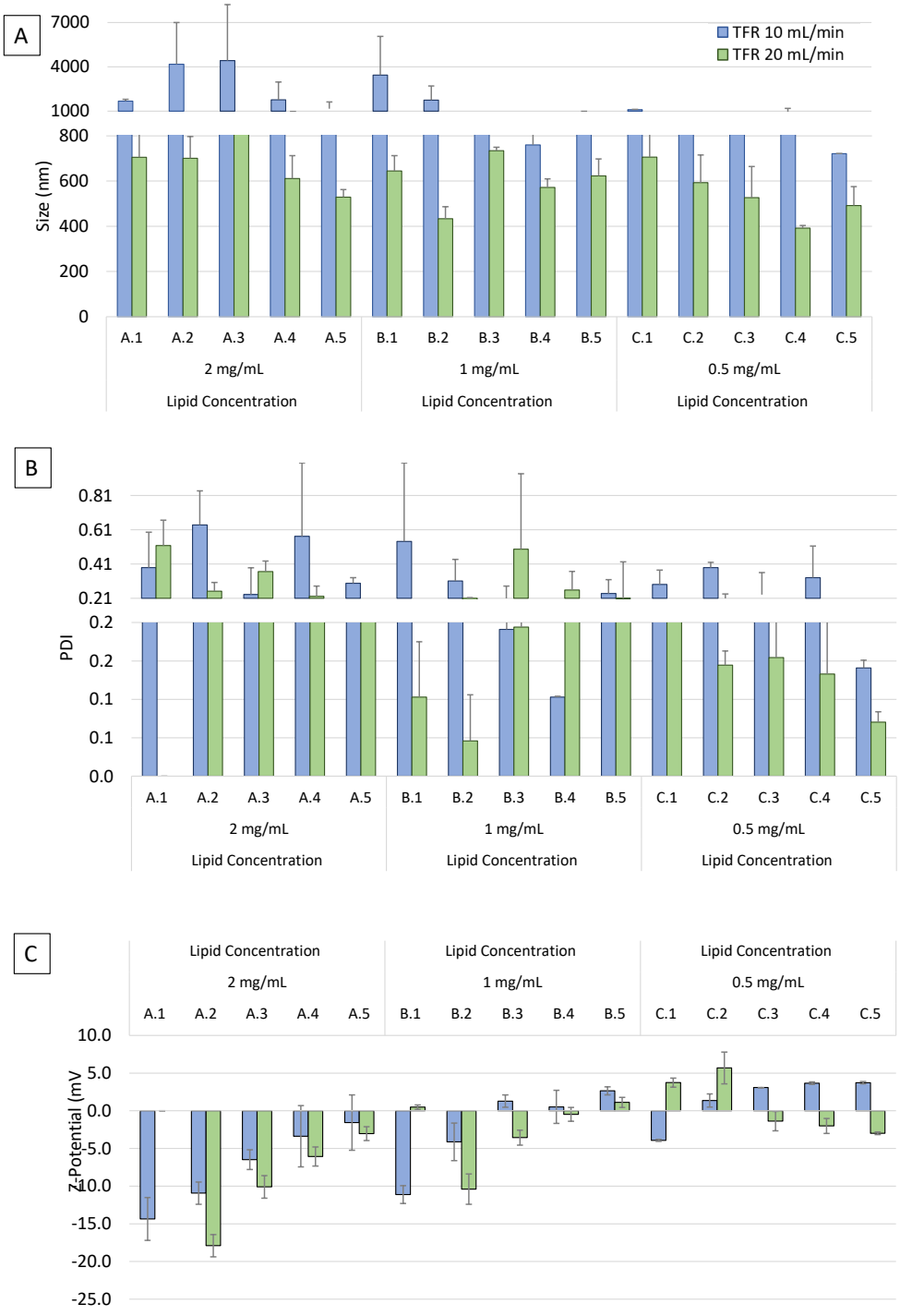

Figure 5-5: Size (A), PDI (B) and Z-potential (C) of the 15 LPHNP formulations prepared using the full factorial design detailed in Table 5-2 at a TFR of both 10 and 20 mL/min (a total of 30 LPHNP formulations). The results represent mean ± SD of 3 technical replicates.

The formulations demonstrated an average particle size ranging from 172.2 nm (C.5) to 4424.6 nm (A.3), with 5 formulations (A.1, A.2, A.4, B.1 and C.2) having a PDI higher than 0.3 indicating a more polydisperse formulation. Concerning the Z-potential, formulations showed a surface charge ranging from -14.4 mV to +3.7 mV.

The study was constructed by varying one factor at a time to fully investigate the impact of TFR, FRR, lipid concentration and all the two-way and three-way interactions between these factors on LPHNP size, PDI and Z-potential. Although the one-factor-at-a-time approach is not the most time-efficient compared to methods like Design of Experiments (DoE), it remains useful for thorough exploration of individual effects and interactions. This method allowed for an initial investigation of how each variable and their combinations influenced the critical characteristics of LPHNPs, despite the limited number of replicates. Despite the fact that the fitted model did not reveal any interaction between the factors, all the individual manufacturing parameters had a significant influence on the LPHNP size, PDI and Z-potential ($p<0.05$). However, this was not observed in the preliminary study, likely due to the limited range of values explored and the smaller number of experimental runs, which may have restricted the detection of significant effects from the individual parameters. Three-dimensional response surface response plots were generated by JMP® 16.2.0 software to help visualize the effect of FRR and lipid concentration of the 30 formulations manufactured on each response (Figure 5-6).

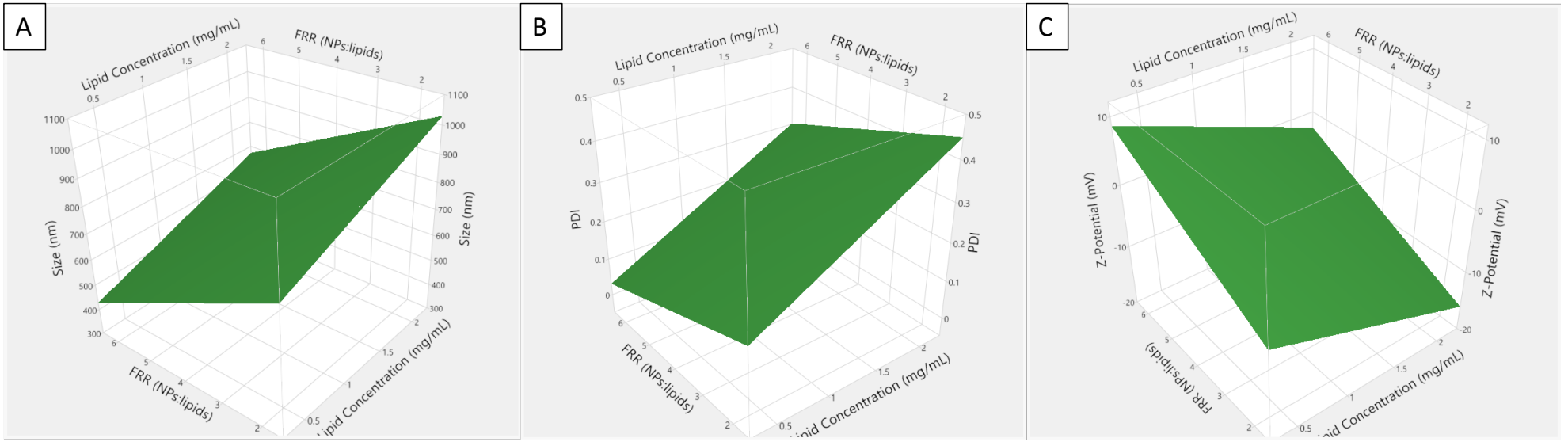

Figure 5-6: 3D response surface plots showing the effect of the independent variables lipid concentration and FRR (of CHCL NPs : lipid solution) on empty LPHNP size (A), PDI (B) and Z-potential (C).

Results in Figure 5-6 show that when lipid concentration was decreased from 2 mg/mL to 0.5 mg/mL and the FRR was increased from 2:1 to 6:1, LPHNP size and PDI decreased while Z-potential increased. Indeed, the reduction in lipid concentration within the formulation might lead to several interrelated mechanisms that result in the decrease of LPHNP size and PDI and increased Z-potential. Increasing the FRR between CHCL NPs and lipid solution from 2:1 to 6:1 contributes to a further reduction in the final lipid concentration in LPHNP shells. This determines a change in the charge balance between CHCL NPs which are positively charged, and POPE:POPG:CL organic phase which exhibit a negative charge due to the presence of anionic lipids. Thus, a reduction in lipid concentration alongside an increase in FRR determines a reduced amount of lipid, and thus a shift in Z-potential from negative to positive. Moreover, the reduced availability of lipids leads to a thinner lipid layer over the CS nanoparticle core. Secondly, the lower lipid concentration reduces the likelihood of lipid-lipid interactions, thereby decreasing the chances of LPHNP aggregation [787, 788]. This is crucial for maintaining the homogeneity of the nanoparticle dispersion, leading to the formation of smaller and more uniform LPHNPs by reducing excess lipid, which could otherwise form lipid-lipid aggregates, thereby facilitating more consistent coverage of the CS nanoparticle surface.

Studies by Cheow *et al*. and Zhang *et al.* demonstrated that adjusting the lipid-to-polymer ratio can lead to different outcomes in LPHNP characteristics [787, 789]. Cheow *et al.* observed that lowering the lipid content below a critical threshold resulted in larger particles and polydispersity, while increasing lipid concentration reduced the particle size until a saturation point, after which further lipid addition had no effect [787]. Similarly, Zhang *et al.* reported that lipid-to-polymer ratios play a key role in controlling LPHNP size and surface charge, showing that higher lipid content can lead to the formation of liposomes, which could contribute to increased particle sizes [789]. The data from this study suggest that further increasing the FRR and lowering the lipid concentration could optimize particle size reduction, though it is possible that beyond certain limits, further changes in FRR or lipid concentration could result in an increase in particle size. This pattern has been observed in other studies, and further investigation may help determine if an inflection point exists where this trend reverses.

Further to investigation of FRR and lipid concentration on LPHNPs size, PDI and Z-potential, the effect of TFR on LPHNPs was assessed. In this respect, a oneway analysis (pooled T-test) with Tukey post-hoc comparison was performed on formulations using JMP® 16.2.0 software (SAS Institute Inc., Cary, NC, US) to assess significant differences between the two TFR used (10 mL/min and 20 mL/min) on LPHNP size, PDI and Z-potential. Results are presented in Figure 5-7.

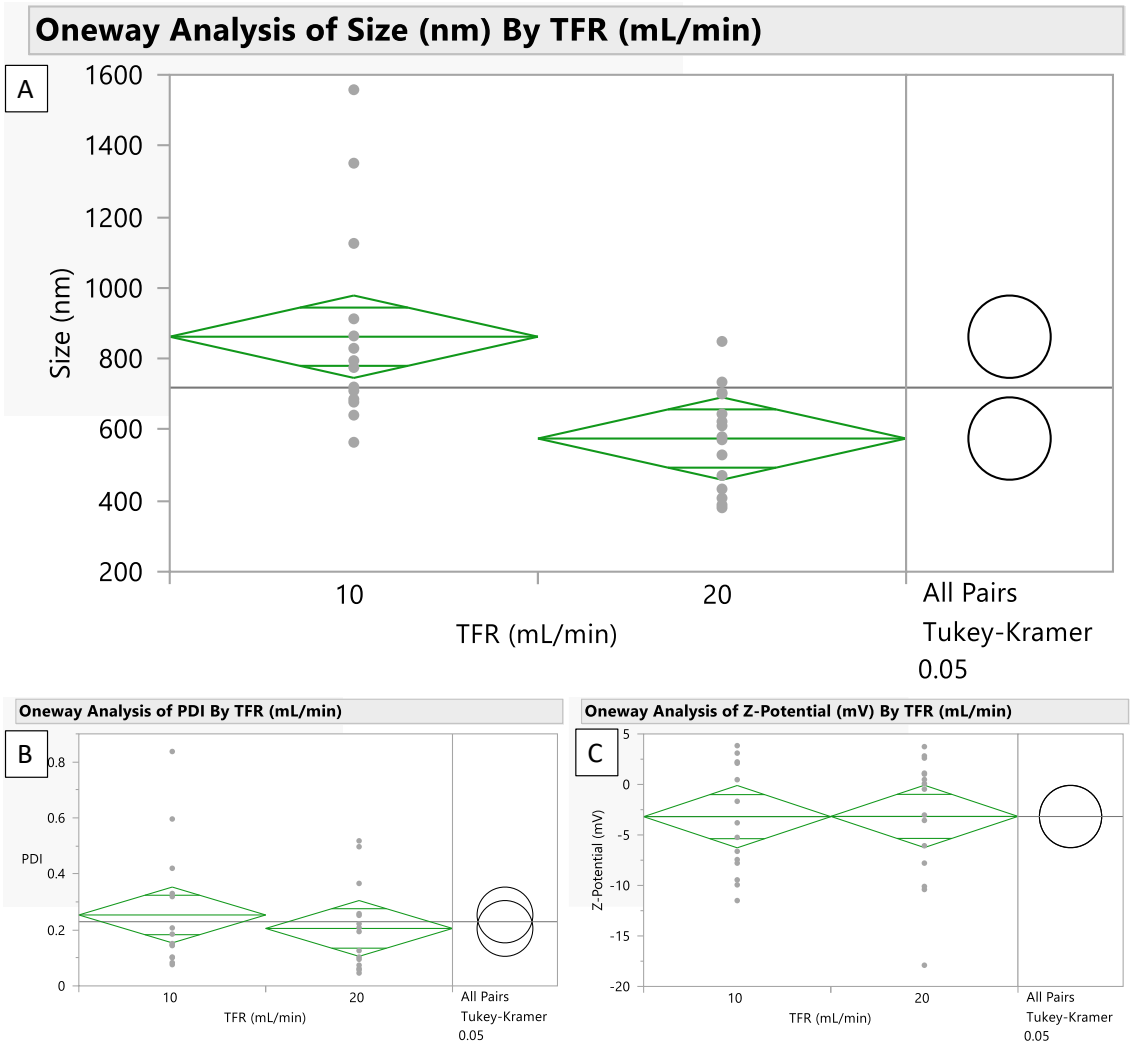

Figure 5-7: Oneway analysis (pooled T-test) with Tukey post-hoc comparison performed on formulations from Table 5-2 manufactured at different TFR (10 mL/min and 20 mL/min). The green diamonds represent the sample mean and the 95% confidence interval. The center line across each diamond corresponds to the group mean. The vertical span of each diamond represents the 95% confidence interval for each group. The width and height of the diamonds is proportional to the sample size at each time point with broad and short diamonds indicating many data points. The black dots represent individual data points. Each circle represents one group mean.

No differences were observed in LPHNP PDI and Z-potential between formulations manufactured at the two different TFR. Results presented in Figure 5-7 show that, regardless of variations in lipid concentration and FRR, the higher TFR employed to manufacture formulations (20 mL/min) resulted in a significantly lower LPHNP size in comparison with formulations manufactured at 10 mL/min (Figure 5-7 A). This is confirmed by the graphical representation of the pairwise comparisons made between group means, showed as circles in Figure 5-7 A. Circles which do not overlap represent means that are significantly different from one another, those that do overlap represent means that do not differ significantly. Thus, the size of LPHNPs manufactured at 20 mL/min is significantly smaller than the size of LPHNPs manufactured at 10 mL/min. In accordance with the present results, previous studies carried out by Feng *et al.* demonstrated the use of a two-stage microfluidic platform to control the size of core-shell lipid-PLGA NPs by regulating the total flow rate within the microfluidic channels [790]. Their study aimed to regulate the size of hybrid NPs by changing the total flow rate in the microfluidic channel between 41 mL/h and 246 mL/h. The study has demonstrated that increased mixing effect at high flow rates ultimately leads to the formation of hybrid nanoparticles that are both small and monodisperse [790].

A gradual decrease in hybrid NP size with increased flow rate was not observed, which could indeed be attributed to the sudden shift from diffusive to convective mixing, as reported in previous studies [790]. This transition to convective mixing at higher flow rates enhances the mixing efficiency, leading to smaller and more monodisperse nanoparticles. Although this phenomenon is relevant to the system described by Feng *et al.* [790], the flow rates used in this study were optimized to maintain laminar flow, ensuring controlled and predictable nanoparticle formation, minimizing aggregation, and promoting size uniformity. Indeed, higher flow rates can enhance the mixing of different components within the microfluidic channels. Improved mixing can lead to more uniform distribution of the lipid and polymer components, promoting the formation of smaller and more homogenous nanoparticles. Moreover, another key advantage of higher flow rates is the reduction in residence time of the materials within the microfluidic device. As the flow rate increases, the time that the components spend in the microfluidic channels decreases. This reduced residence time plays a crucial role

in preventing particle aggregation or coalescence, which can lead to the production of larger and less uniform nanoparticles [791].

Given the aforementioned considerations on manufacturing process parameters affecting LPHNP size, PDI and Z-potential, five final candidate formulations were chosen for subsequent studies. A TFR of 20 mL/min was chosen as optimum given the noticeably smaller LPHNP size obtained in comparison with TFR of 10 mL/min (Figure 5-7 A). Moreover, given the importance of the lipid concentration on hybrid NP size and PDI (Figure 5-5, Figure 5-6), a lipid concentration of 0.5 mg/mL was employed to manufacture formulations for subsequent studies. This led to selection of the 'C' series of formulations - C.1, C.2, C.3, C.4 and C.5 from Table 5-2, manufactured at TFR of 20 mL/min – for further investigation. These formulations, in the following studies will be respectively called F.1, F.2, F.3, F.4 and F.5. While an optimal TFR and lipid concentration were selected for further investigation, a single FRR condition was not fixed at this stage, as the size and PDI of all formulations were within acceptable ranges, and the Z-potential values were similar. Maintaining variation in FRR allowed for a more comprehensive analysis of its influence on LPHNP characteristics without significantly impacting the overall formulation quality.

5.4.1.2. Addition of FA to Lipid Solution

Following the initial optimization of LPHNP manufacturing process parameters described in previous sections, formulations F.1, F.2, F.3, F.4 and F.5 were selected for further process optimization. Given that the scope of the optimization of empty LPHNPs is ultimately to serve as a delivery system for CTX and RN7IN6, a preliminary study was conducted with the aim of assessing the feasibility of including CTX and RN7IN6 within empty LPHNP formulation candidates. As previously discussed, CTX was to be encapsulated within the CHCL NP core, and RN7IN6 loaded into the lipid shell. This approach was chosen due to the differing mechanisms of action of CTX and RN7IN6. Encapsulating CTX within the CHCL core ensures it remains protected until reaching its target, allowing it to effectively inhibit bacterial cell wall synthesis by binding to penicillin-binding proteins, while placing RN7IN6 in the lipid shell allows it to be readily available for interaction with bacterial membranes, as its mechanism involves disrupting

these membranes. This strategic configuration not only enables immediate RN7IN6-membrane interaction but may also facilitate improved intracellular delivery of the CTX-loaded CHCL NPs core by creating localized disruptions in the bacterial membrane. Such membrane perturbations could enhance the permeability of the bacterial cell envelope, potentially allowing for greater access of the LPHNPs to intracellular targets, thereby optimizing the antimicrobial efficacy of the co-delivered agents.

CTX and purified RN7IN6 were previously loaded within the core of CHCL NPs and within POPE:POPG:CL liposomes (as representative lipid shell structures) as detailed in section 2.4.3 and section 4.4.3 respectively. However, for initial screening purposes with respect to LPHNP loading, it was decided to employ crude RN7IN6 peptide due to the additional time and cost required for its purification, making it a more practical option for preliminary evaluations without compromising the overall investigative scope. Crude RN7IN6 has a different solubility compared to the purified peptide, being slightly soluble both in water and the organic lipid phase (1-propanol:DMF). Hence modification of the organic phase was necessary to aid crude RN7IN6 solubilization. Co-solvents are often used to increase the solubility of hydrophobic substances by acting on the extensive intermolecular and/or intramolecular H-bonds [792]. Several experiments were conducted to determine a co-solvent solution composition that would provide the greatest solubility of the crude RN7IN6 peptide into the organic lipid phase, without altering the final LPHNP characteristics. The addition of 0.01% of FA to the original 1-propanol and DMF solvent mixture resulted in a notable enhancement in the solubility of the crude peptide. This improvement can be attributed to the ability of FA to act as a protonating agent, specifically protonating amino and carboxyl groups present on the crude RN7IN6 peptide, enhancing solubility of the peptide in the organic solvent mixture through electrostatic interactions with solvent molecules [636]. FA was specifically chosen due to its compatibility with the lipid phase and its ability to improve peptide solubility without significantly altering the physicochemical properties of the final LPHNPs [793]. Once it was established that the addition of 0.01% FA is able to improve crude RN7IN6 solubility in 1-propanol and DMF, candidate empty LPHNPs formulations F.1, F.2, F.3, F.4 and F.5 were manufactured with the addition of 0.01% FA in the organic

phase. Characteristics of formulations manufactured with and without FA are shown in Figure 5-8.

The results of the independent T-test performed on empty LPHNP size and PDI showed no significant differences between sets of formulations manufactured with and without FA, indicating that FA does not impact these physiochemical characteristics. However, the T-test results showed a significant difference in the Z-potential of most of the formulations manufactured (with the exception of F.2, Figure 5-8).

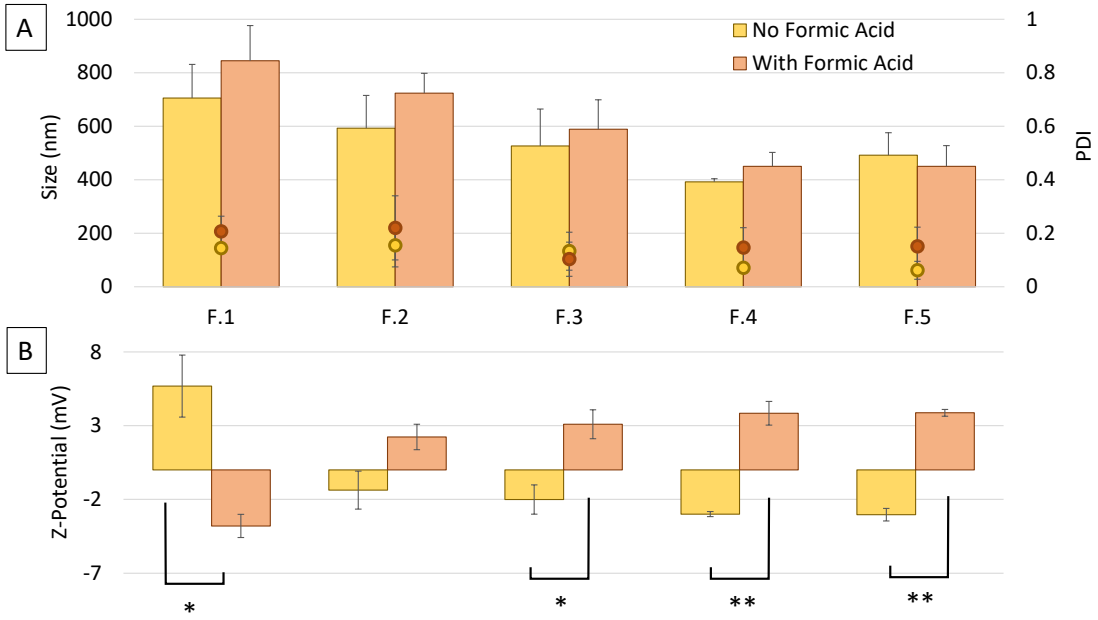

Figure 5-8: Size, PDI (bars and dots respectively - A) and Z-potential (B) of empty LPHNP formulations prepared using 1-propanol:DMF (80:20, yellow bars and dots) and 1-propanol:DMF:FA (80:20:0.1, orange bars and dots). Results represent the mean ± SD from 3 independent experiments/formulations. An independent T-test was run on formulations with and without FA. If the two-tailed p-value is less than 0.05, it is flagged with one star (*). If the two-tailed p-value is less than 0.01, it is flagged with 2 stars (**).

The change in Z-Potential upon the addition of FA can be explained by the protonation of carboxyl and phosphate groups on the lipidic surface of the LPHNPs. The surface charge is typically influenced by functional groups present on the surface of the nanocarriers. In the case of LPHNPs, the outer lipid components contain polar functional groups that contribute to the overall surface charge. Upon protonation by FA, these

functional groups undergo a chemical transformation where they acquire a positive charge by accepting a proton. This change in charge distribution on the nanoparticle surface can influence various properties such as surface charge, surface energy, and surface reactivity [794]. However, despite the Z-potential changes upon addition of FA, results for both sets of formulations manufactured with or without FA showed neutral LPHNPs with Z-potential ranging from +6 mV to -4 mV. Therefore, the addition of FA to the organic phase of the formulation was considered suitable as LPHNPs physiochemical characteristics were not strongly impacted. Although a statistically significant alteration in Z-potential was detected, the effect is negligible, given that the magnitude of change is insufficient to influence the physicochemical stability or performance of the nanoparticles.

While formulations manufactured with the addition of FA did not show any substantial differences in terms of size, PDI and Z-potential in comparison to their counterparts prepared without FA, resulting in no single 'best' candidate, formulation F.4 was chosen for further studies. Formulation F.4 was selected due to its optimal balance of size and PDI, both of which were among the smallest values observed across all formulations (F.1, F.2, F.3, and F.5). Given that smaller particle size and a low polydispersity index (PDI) are crucial for improving drug delivery and ensuring uniform nanoparticle populations, F.4 performed favorably in this regard. Although there was some variability in Z-potential among all formulations, the Z-potential of F.4 remained consistent with the others, providing sufficient surface charge to ensure stability. The combination of a small particle size, low PDI, and stable Z-potential made F.4 a strong candidate for further studies.

In order to move forward with subsequent applications, such as drug encapsulation and therapeutic delivery, it was then crucial to establish an appropriate purification method for formulation F.4. The selection of the purification method is crucial as it has a substantial impact on the physiochemical characteristics, effectiveness and safety of the end product. In light of the various benefits and limitations of different purification techniques discussed in section 5.1.2, next studies focused on investigating a range of purification methods including flash chromatography and preparative HPLC that could

efficiently eliminate organic solvents employed during the manufacturing process. In addition, it was crucial to verify that the chosen purification technique will be suitable not only for empty LPHNPs but also for the final product being CTX and RN7IN6 co-loaded LPHNPs.

5.4.1.3. Formulation Purification via Dialysis

Following the selection of an optimum empty LPHNP formulation, F.4, a thorough investigation into purification methods was necessary. Purification is essential because it ensures the removal of organic solvents such as 1-propanol, DMF and FA introduced during the formulation process but also unencapsulated drug, in the case of loaded LPHNPs. However, it is essential to consider the diverse advantages and drawbacks associated with different purification techniques as detailed in section 5.1.2. Initially, dialysis was investigated as a means to remove 1-propanol and DMF from F.4 because of its ability to provide gentle and gradual purification without subjecting the particles to excessive mechanical forces or shear stress. Formulation F.4 was dialyzed against 100, 200 and 300 mL of PBS, and the supernatant after subsequent ultracentrifugation was employed to evaluate the residual solvent content in formulation after purification. F.4 physiochemical characteristics being size, PDI and Z-potential were measured before and after the 6-hour dialysis process specifically against 200 mL of PBS, using the dialysis conditions optimized in section 3.3.2.1.1. This condition is presented because, while 100 mL of PBS was initially evaluated, it was insufficient to completely remove DMF, resulting in residual solvent levels approaching the safety limit. In contrast, both 200 mL and 300 mL of PBS were effective in reducing DMF concentrations to levels below the safety limit. However, 200 mL was selected as the optimal volume to balance efficient solvent removal while minimizing the consumption of PBS and reducing unnecessary resource expenditure during the dialysis process. Results are shown in Figure 5-9.

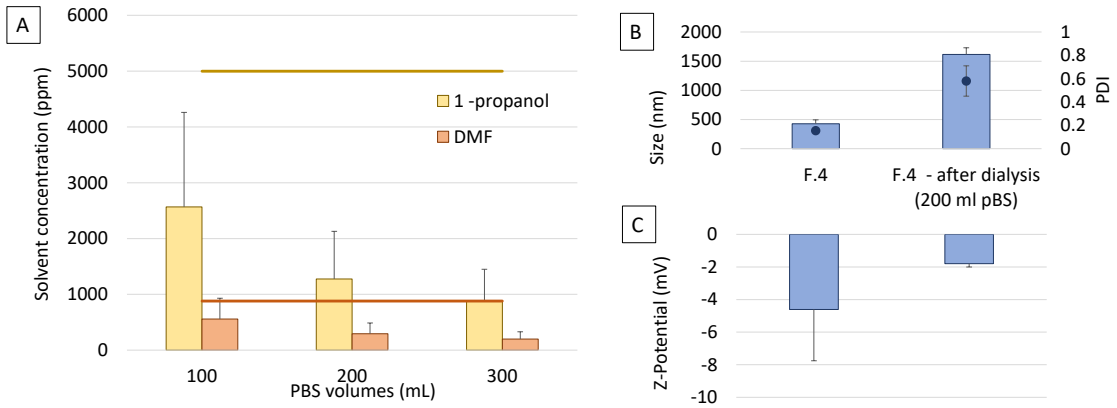

Figure 5-9: Concentration (ppm) of residual solvent (A), size (bars), PDI (dots) (B) and Z-potential (C) of LPHNP sample formulation F.4 following dialysis. Formulation F.4 was dialyzed against 100 mL, 200 mL or 300 mL of PBS for 6 hours. Results represent the mean ± SD from 3 independent experiments. Yellow and orange solid horizontal lines in (A) represent residual solvent limit from ICH guidelines for 1-propanol and DMF, respectively [583]. Independent t- test run on F.4 formulation size, PDI and Z-potential before and after dialysis: p=0.0092 for size and p=0.018 for PDI. No significant difference was found for LPHNP Z-potential. T-test run on residual solvent concentration: DMF residual concentration when dialyzing with 100 mL of PBS was not significantly different from the residual solvent limit (ICH guidelines).

The results revealed that dialysis effectively reduced the residual solvent content in formulation F.4 for both 1-propanol and DMF. Notably, despite residual 1-propanol levels being below the ICH guidelines limit when F.4 was dialyzed against 100 mL of PBS, the mean residual content of DMF approached the upper limit. This is of concern because the higher SD observed for DMF indicated that in at least one replicate, the residual DMF content exceeded the safety threshold [583]. However, this issue was overcome by using a larger volume of outer media such as 200 mL or 300 mL of PBS, which was able to safely remove the solvent in formulation to levels significantly below those specified by ICH guidelines. It is worth mentioning that the residual FA solvent content in formulation F.4 was not assessed due to its minimal percentage in the solvent mixture (0.01% FA), which is already below the residual solvent limit [583]. Evaluation of F.4 physicochemical characteristics, including size, polydispersity index (PDI), and Z potential, both before and after dialysis with 200 mL of PBS, indicated no changes in Z-potential but a significant increase in size and PDI. This outcome is contrary to that of

Ishak *et al.* where flavonoid rutin-loaded LPHNPs were prepared using a single-step nanoprecipitation technique. This study showed that non-significant alterations were recorded for LPHNP size and surface charge following dialysis in comparison with non-dialyzed ones [748]. However, LPHNPs were only dialyzed for 30 minutes, as this was deemed by the authors as sufficient to safely remove the surfactants being Tween-80, d-α-Tocopherol polyethylene glycol 1000 succinate (TPGS) and polyethylene glycol-15-hydroxy stearate (Solutol® HS 15), while in the current study LPHNPs were dialyzed for 6 hours. Longer dialysis times can indeed lead to more significant changes in particle size and PDI compared to shorter dialysis times [795]. The extended exposure of LPHNPs to the dialysis medium allows for increased interactions between particles, promoting aggregation and altering their size distribution [796].

Despite the limitations of dialysis, such as increased size and PDI for F.4, further investigation was performed to assess its suitability for CTX and RN7IN6-loaded LPHNPs. This study aimed to evaluate whether dialysis would effectively separate unencapsulated drug from LPHNPs. To achieve this, a solution containing CTX and RN7IN6 was subjected to dialysis, and the recovery of CTX and RN7IN6 in the outer media was quantified using an RP-HPLC method developed as discussed in the subsequent section (5.3.2.4). The study was carried out over 24 hours against 100, 200 and 300 mL of PBS, with sampling and analysis of outer compartment media at various timepoints as shown in Figure 5-10.

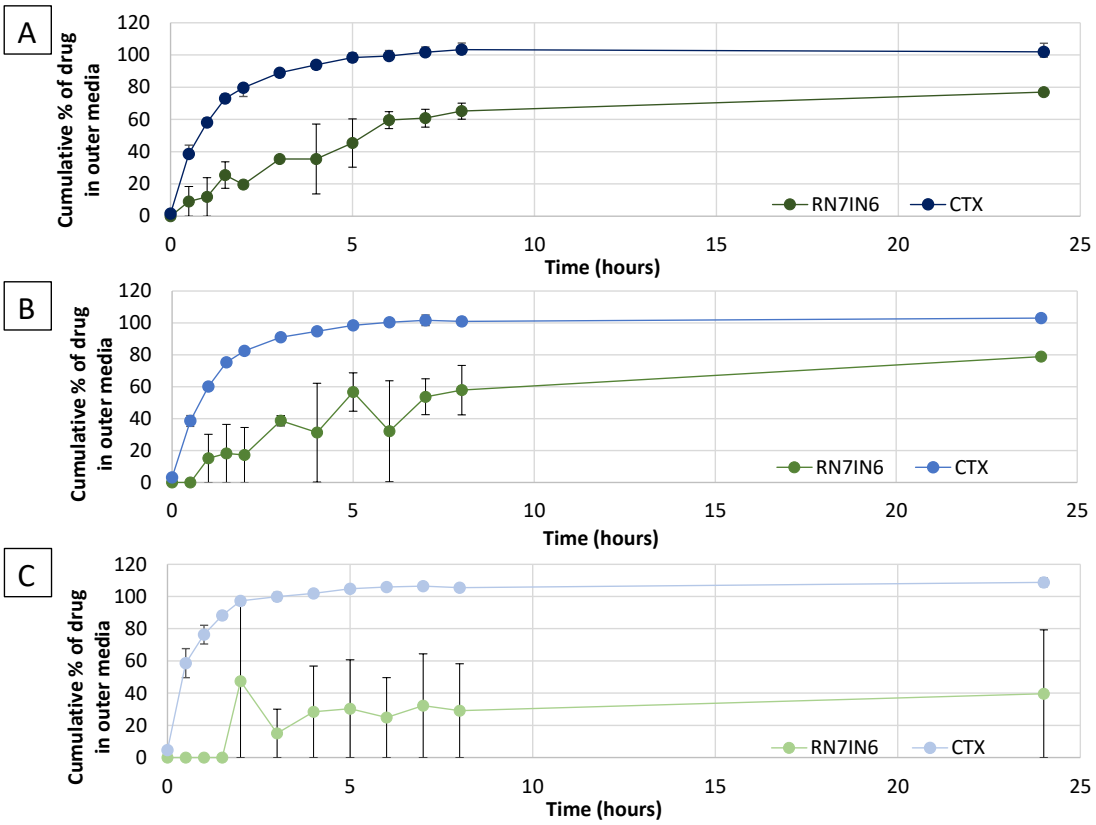

Figure 5-10: Percentage of CTX and RN7IN6 in outer dialysis media at pre-determined time points. CTX and RN7IN6 solutions in PBS (3 mg/mL) were dialyzed using dialysis tubing cellulose membrane against 100 mL (A), 200 mL (B) and 300 mL (C) of PBS for up to 24 hours. Results represent the mean ± SD of three independent studies.

As it can be seen from Figure 5-10, CTX was completely able to pass through the membrane into the outer media in 6, 5 and 4 hours when dialyzed against 100, 200 and 300 mL of PBS respectively. However, this extended dialysis time indicates that the passage of CTX from the donor to the acceptor PBS media is relatively slow, suggesting a potential limitation in diffusion across the membrane, particularly when dialyzed against smaller PBS volumes. This slow passage poses a concern, as such delays could inadvertently trigger the early release of CTX and RN7IN6 encapsulated within the formulation. This is particularly problematic, as early release during the purification stage could compromise formulation physiochemical characteristics. For RN7IN6, incomplete recovery in the acceptor compartment was noted. Variability was observed, particularly with larger PBS volumes (200 and 300 mL), which may be influenced by the analytical conditions, including the limit of detection of the HPLC method or specific interactions of RN7IN6 with the dialysis membrane.

Given the slow passage of CTX across dialysis membranes, the variability and incomplete passage of RN7IN6, and the increase in size and PDI of formulation F.4 following dialysis, an alternative purification method was sought. Ultracentrifugation, a well-established technique known for its efficiency in separating particles based on size and density, was selected for further investigation. This method offers a promising approach to achieve better separation and purification of the formulations while maintaining the integrity of the encapsulated CTX and RN7IN6.

5.4.1.4. LPHNP Purification via Ultracentrifugation

Ultracentrifugation emerged as a promising candidate for several reasons. Firstly, its ability to efficiently separate particles based on size, density, and shape offered the potential to achieve high purity levels and eliminate impurities from the nanoparticle dispersion as described in more detail in section 5.1.2. Therefore, a systematic investigation into various ultracentrifugation parameters was conducted. Ultracentrifugation temperatures of 4 °C and 25 °C, centrifugal speeds of 15000, 25000, 35000, and 55000 rpm and centrifugation durations of 30 minutes and 1 hour were tested. Following ultracentrifugation, the pelleted F.4 formulation was resuspended in PBS and LPHNP size, PDI and Z-potential were compared to unpurified formulation F.4 size, PDI and Z-potential in Figure 5-11.

When formulation F.4 was centrifuged for 30 minutes, at 15000, 25000 and 35000 rpm, regardless of the centrifugation temperature, the amount of pelleted particles was minimal compared to higher centrifugations speeds and times. However, after centrifugation at 55,000 rpm for 30 minutes and at all the tested speeds for 1 hour, a notable pellet was obtained, suggesting appreciable particle sedimentation.

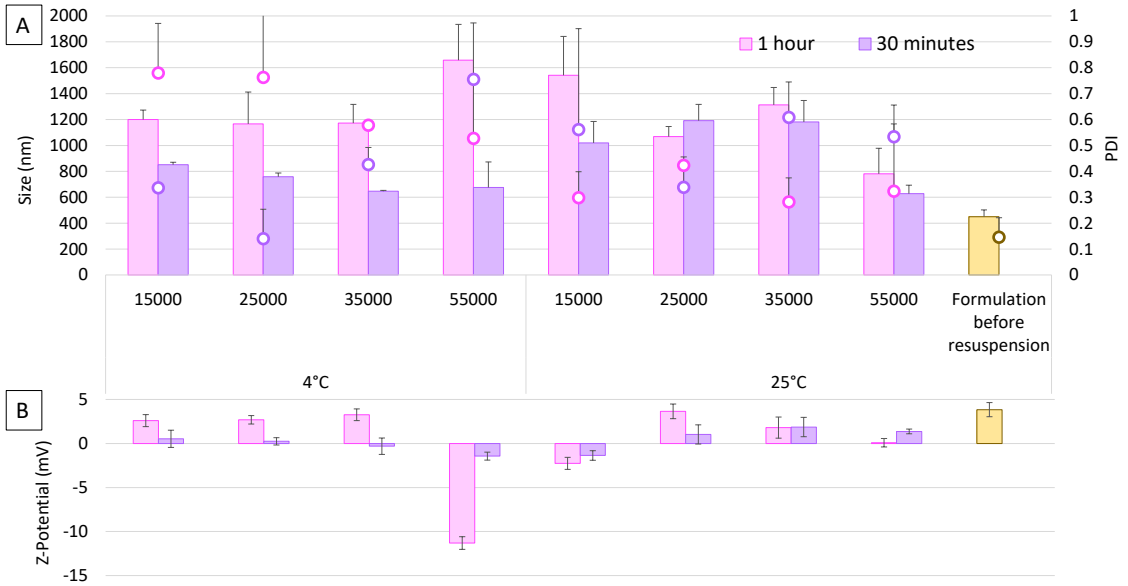

Figure 5-11: Size (bars, A), PDI (dots, A) and Z-potential (B) of empty LPHNP formulation F.4 before (yellow) and after ultracentrifugation and pellet resuspension in PBS (pink and purple). Formulation F.4 was ultracentrifuged at 4 ^{o}C and 25 ^{o}C for 30 minutes and 1 hour using different speeds ranging from 15000 to 55000 rpm. Results represent the mean ± SD of 3 technical replicates.

However, for all those combinations of centrifugation times, speeds and temperatures that were able to efficiently sediment particles, the size and PDI increased when F.4 was resuspended in PBS in comparison with the non-centrifuged formulation (Figure 5-11) indicating that the ultracentrifugation process also led to potential aggregation and altered size distribution of LPHNP formulations. The Z-Potential results were mostly stable, except for outliers observed at 55,000 rpm and 4 °C, where a noticeable shift in surface charge occurred, possibly due to nanoparticle destabilization or aggregation under these conditions.

The results presented in this section were in agreement with those of Santhanes *et al.* where LPHNPs formulated with high concentrations of surfactants (>2 mg/mL) showed aggregation upon ultracentrifugation [760]. Particle aggregation is a well-known issue associated with prolonged ultracentrifugation times, resulting in larger apparent particle sizes. This phenomenon occurs due to the increased likelihood of particles coming into contact with each other during ultracentrifugation, which is dependent on both centrifugation speed and duration. High speeds can increase the forces acting on the particles, while extended ultracentrifugation periods further enhance the probability of

aggregation. However, in the specific case of F.4, a reduction in ultracentrifugation speed and time resulted in LPHNPs not being pelleted.

In order to overcome the constraints associated with dialysis and ultracentrifugation in the purification of formulation F.4, the ultrafiltration purification technique (introduced in section 5.1.2) was investigated. The inquiry, detailed below in section 5.4.2.1, will focus specifically on CTX-loaded LPHNPs instead of empty ones, aligning with the primary objective of optimizing formulation F.4 for its dual role as a carrier for both CTX and RN7IN6. This approach is based on the need to assess the impact of encapsulating the active pharmaceutical ingredients within the lipid-polymer hybrid nanoparticles on their physicochemical characteristics, ensuring the formulation's suitability for drug delivery applications.

5.4.2. CTX-loaded LPHNPs: Manufacturing and Characterization

Briefly, CTX-loaded LPHNPs were manufactured using F.4 process parameters and employing CTX-loaded CHCL NPs as LPHNP core structures. As a first step, the physiochemical characteristics of CTX-loaded LPHNPs, named CTX F.4, were evaluated. In addition, a comparison between the CTX-loaded LPHNPs and the CTX-loaded CHCL NPs was conducted, with a specific focus on their relative size, PDI, and Z-Potential Figure 5-12.

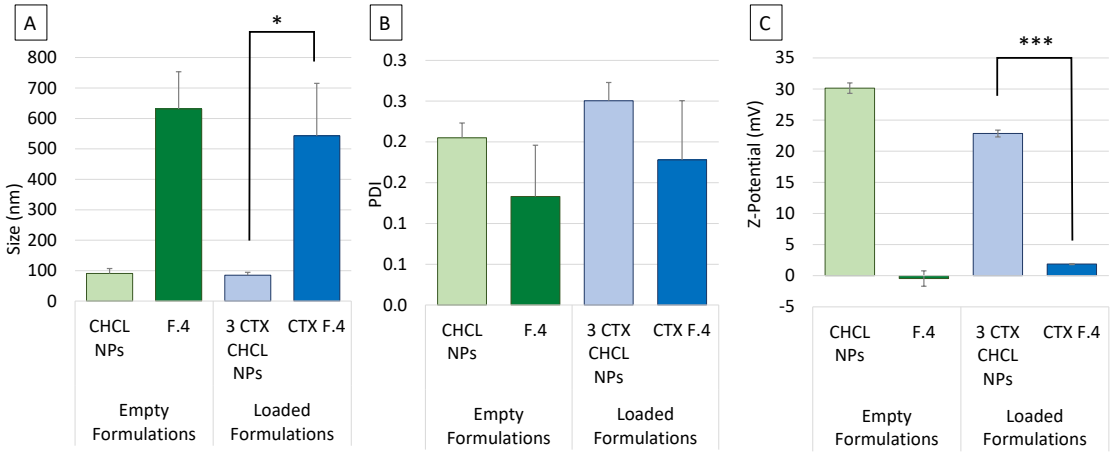

Figure 5-12: Size (A), PDI (B) and Z-potential (C) of empty and unpurified CTX-loaded NP and LPHNP formulations. Results represent the mean ± SD of three independent batches. If the two-tailed p-value is less than 0.05, it is flagged with one star (*). If the two-tailed p-value is less than 0.001, it is flagged with 3 stars (***).

Results showed that there was a significant difference between the size and Z-Potential of the CTX-loaded CHCL NPs and the CTX-loaded LPHNP formulations, indicating effective lipid coating. Specifically, the observed increase in particle size from CHCL NPs to LPHNPs is consistent with the addition of the lipid shell (consisting of POPE, POPG, and CL) around the polymeric core. This increase is a hallmark of lipid-coated nanoparticles and has been similarly observed in previous studies carried out by Answer *et al.* Their study demonstrated a similar size increase in Baricitinib-loaded LPHNPs, where the addition of the lipid layer (tristearin) around the PLGA polymeric core resulted in a significant particle size increase [797]. Moreover, the shift in Z-Potential from the highly positive charge of CHCL NPs to near-neutral or slightly negative values in LPHNPs further supports successful lipid coating. In uncoated CHCL NPs, the surface charge is dominated by the positively charged CS molecules, which provide a higher Z-Potential. Upon lipid coating, the surface charge shifts toward negative values due to the inclusion of anionic lipids such as POPG and CL in the lipid shell. Similarly, Answer *et al.* reported a change in Z-Potential from −21.1 mV of PLGA NPs to −36.5 mV of LPHNPs due to the negatively charged lipid layer [797].

In addition to differences in NP and LPHNP size and Z-potential, results in Figure 5-12 showed that there was no significant difference between the size, PDI and Z-Potential of F.4 and CTX F.4 LPHNPs where formulations were manufactured with an empty or CTX-loaded CHCL NP core respectively. This indicates that the incorporation of CTX into the polymeric core of LPHNPs did not significantly alter these physicochemical characteristics. A similar study was previously reported by Khan *et al.*, who manufactured norfloxacin-loaded LPHNPs. Their optimum unloaded LPHNP formulation showed similar particle size (115.25 nm) to the norfloxacin-loaded one (121.27 nm) and a PDI < 0.5 in both cases loaded LPHNPs in order to amplify the drug water solubility and its oral bioavailability [798].

A similar outcome showing comparable particle size, PDI and Z-potential for empty and core-loaded LPHNPs was also reported by Shafique *et al.*, who developed Doxorubicin-loaded LPHNPs composed of Eudragit RS-100 (polymer), stearic Acid (solid lipid), oleic acid (liquid lipid), and ethyl cellulose (Hepler polymer) [747]. Following optimization of LPHNP formulation parameters including surfactant concentration, magnetic stirring and sonication time, empty and Doxorubicin-loaded LPHNPs showed comparable particle size, PDI and Z-potential, in agreement with the current study, indicating that the physicochemical characteristics of LPHNPs remained consistent regardless of the incorporation of the drug into the polymeric core.

Subsequent studies focused on investigating purification methods to efficiently eliminate organic solvents used during manufacturing, ensuring the safety and efficacy of the final product. It was essential to verify the suitability of the chosen purification technique for CTX-loaded LPHNPs, as previous purification studies on empty LPHNPs were inconclusive (see sections 5.4.1.3 and 5.4.1.4). Therefore, ultrafiltration, which was introduced in section 5.1.2, was investigated as an alternative purification method.

5.4.2.1. Purification of CTX-loaded LPHNPs

Ultrafiltration has emerged as a promising method for purifying LPHNPs, with potential advantages over ultracentrifugation and dialysis [800]. Although there is a potential for loss of particles during the filtration process due to pore blocking [764], this issue can be mitigated by optimizing membrane pore size and operating conditions to minimize

fouling, thereby improving filtration efficiency. Ultrafiltration remains an efficient method for purifying LPHNPs with minimal detrimental effects on size and drug-loading capacity [782]. Therefore, ultrafiltration was assessed as a purification method for CTX-loaded LPHNPs (CTX F.4) and compared to ultracentrifugation. This study was deemed necessary given the limitations observed with dialysis and ultracentrifugation as purification methods for formulation F.4 (see sections 5.3.2.1.3 and 5.3.2.1.4, respectively).

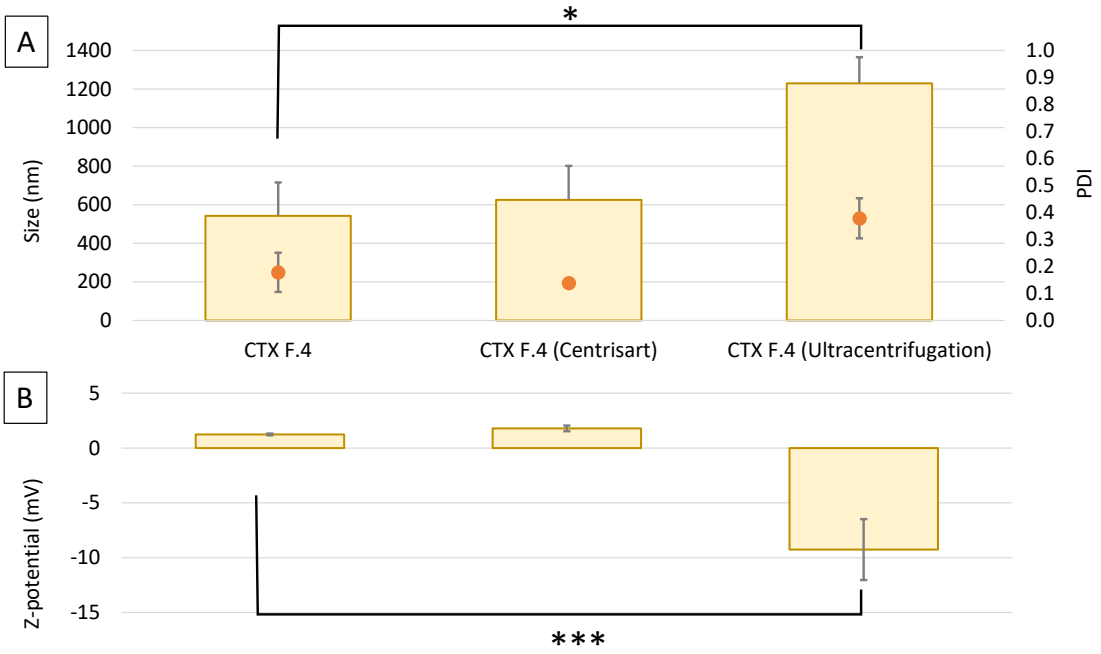

Figure 5-13: Size (bars), PDI (dots) (A) and Z-potential (B) of CTX-loaded LPHNP formulation purified using centrifugal ultrafiltration at 1188 x g and 25 °C for 30 min, or ultracentrifugation at 55000 rpm for 30 min. CTX F.4 unpurified formulation is shown for comparison. Results represent the mean ± SD of three independent replicates. If the two-tailed p-value is less than 0.05, it is flagged with one star (*). If the two-tailed p-value is less than 0.001, it is flagged with 3 stars (***).

Results shown in Figure 5-13 reveal that particle size, PDI and Z-potential of CTX-loaded LPHNPs (CTX F.4) remained unaffected upon ultrafiltration at 1188 x *g* and 25 °C for 30 min using Centrisart® I centrifugal ultrafiltration units ($p < 0.05$). Therefore, based on the comparative analysis of purification methods for LPHNPs, ultrafiltration emerged as the preferred purifying technique for maintaining LPHNPs physiochemical characteristics.

The current study highlights the lack of a universal protocol for LPHNP purification, and indeed, upon literature review a lack of agreement on optimal purification techniques was found. Various purification techniques have been explored in the literature, including centrifugation coupled with sonication or freeze-drying [801-803], ultrafiltration [711, 782], dialysis [804]. Another emerging LPHNP purification technique is tangential flow filtration, as it minimizes shear stress and aggregation by allowing the sample to pass tangentially across a filtration membrane, thus preserving the colloidal stability and structural integrity of nanoparticles while effectively removing impurities [763]. To the best of the author's knowledge, tangential flow filtration has not yet been employed for the purification of LPHNPs; however, it has been successfully utilized for purification of other core-shell nanoparticle systems, such as lauric acid-/albumin-coated particles, demonstrating its potential for efficient purification [763]. Moreover, it is important to note that the physicochemical characteristics reported in many studies often reflect the properties of LPHNPs immediately after preparation, without taking into account the potential alterations caused by the purification process [787, 805, 806]. This highlights the need for more comprehensive reporting of physicochemical properties post-purification to ensure the final product maintains its desired attributes.

5.4.3. CTX and RN7IN6 Co-loaded LPHNPs: Manufacturing and Characterization

Following successful evaluation of the manufacturing process and purification techniques for empty and CTX-loaded LPHNPs, the next critical step involved the incorporation of the peptide RN7IN6 within the lipid shell of LPHNPs. By integrating RN7IN6 into the lipid shell of LPHNPs, the goal is to establish a manufacturing method that efficiently loads both CTX and RN7IN6 into the LPHNP carrier system. Therefore, in the following sections the optimization of RN7IN6 loading and the release of CTX and RN7IN6 from LPHNPs are assessed.

5.4.3.1. Optimization of RN7IN6 Initial Loading Concentration

5.4.3.1.1. CTX and RN7IN6-loaded LPHNPs: Physiochemical Characterization

The encapsulation of the AMP RN7IN6 into the optimized LPHNP formulation was investigated to achieve co-loading with CTX. This incorporation aims to utilize the rapid bacterial-killing powers of RN7IN6 [606] to enhance the effectiveness of CTX [807], which acts by disrupting the bacterial cell wall synthesis [436]. Loading of RN7IN6 into the lipid shell of LPHNPs was chosen to maximize the potential for its direct interaction with the bacterial membrane upon contact, thus facilitating its mechanism of action which involves the disruption of bacterial cell membranes [173].

The LPHNP formulation was further optimized to achieve maximal RN7IN6 encapsulation within the lipid shell, while maintaining a small and uniform size distribution of the LPHNPs. The impact of increasing RN7IN6 loading concentrations on LPHNP size, PDI, Z-potential and CTX/RN7IN6 encapsulation efficiencies was investigated. Higher loading concentrations of RN7IN6 were hypothesized to potentially increase its encapsulation efficiency within the LPHNPs. By systematically increasing the initial RN7IN6 loading concentration from 0.5 mg/mL to 2 mg/mL (Table 5-3) while maintaining constant formulation parameters optimized in previous sections, the effects of varying peptide concentrations on the physicochemical properties of the LPHNPs were evaluated. Size, PDI and Z-potential of manufactured formulations shown in Figure 5-14 were analyzed using JMP® 16.2.0 software (SAS Institute Inc., Cary, NC, US). A one-way ANOVA with Tukey's post hoc test was employed to compare CTX-loaded LPHNP formulations with CTX and RN7IN6 co-loaded LPHNP formulations, to assess if there was a mean difference in size, PDI and Z-potential upon RN7IN6 loading (Figure 5-15). Also, an independent T-test was employed to assess any mean differences in formulation physicochemical characteristics before and after purification with Centrisart® I centrifugal ultrafiltration units (Figure 5-14). A p value of <0.05 was taken as indicating statistical significance throughout the studies.

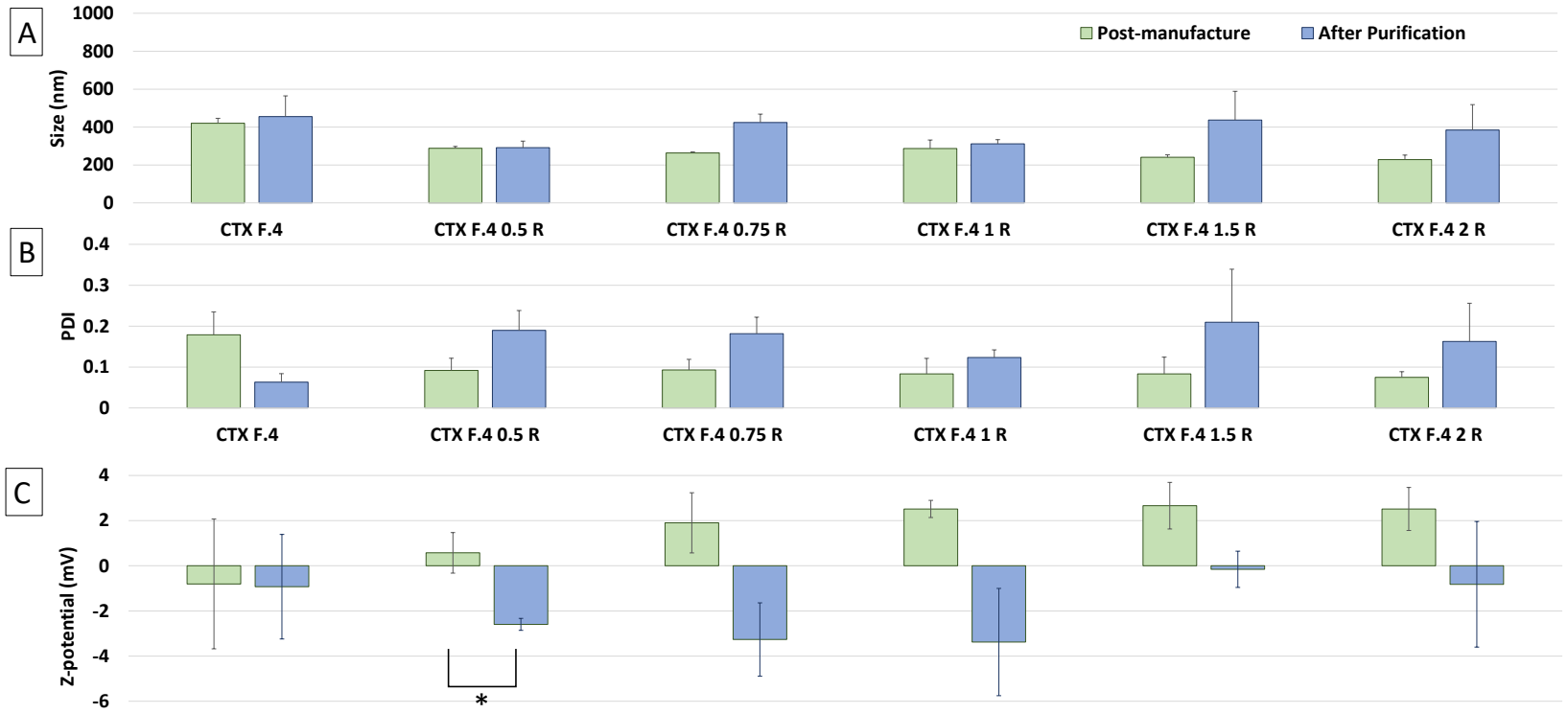

Figure 5-14: Size (A), PDI (B) and Z-potential (C) of CTX and RN7IN6 co-loaded LPHNP formulations prepared using increasing loading concentrations of RN7IN6 ranging from 0.5 mg/mL to 2 mg/mL according to Table 5-3, in comparison with CTX-loaded LPHNPs (CTX F.4). The formulations have been named based on the initial loading concentrations of RN7IN6 in the lipid solution. Specifically, the "F.4" designation refers to a specific formulation code, while the numeric values following it represent the different RN7IN6 loading concentrations tested in the microfluidic process. The results represent mean ± SD, n=3 independent batches. Independent sample T-test: a p-value of <0.05 was taken as indicating statistical significance throughout the study and indicated with a star (*)

The results shown in Figure 5-14 demonstrated that co-loaded LPHNP size and PDI were not significantly affected by purification by centrifugal ultrafiltration. These results further highlight that centrifugal ultrafiltration was deemed suitable not only for the purification of empty and CTX-loaded LPHNPs (see section 5.4.2.1) but also for the purification of CTX and RN7IN6 co-loaded LPHNPs. This chosen purification method ensures the maintenance of LPHNP physicochemical properties critical for their efficacy in delivering both CTX and RN7IN6 for enhanced antibacterial activity.

Regarding the Z-potential, formulation CTX F.4 0.5R showed a significant but slight decrease in surface charge upon ultrafiltration ($p<0.05$). All the other CTX and RN7IN6-loaded formulations showed the same trend, most notably those loaded with 0.75 and 1 mg/mL RN7IN6, but in the absence of statistical significance. While the trend was not statistically significant, it might potentially be explained by the fact that removing unencapsulated RN7IN6, which is positively charged, might affect the distribution of charged molecules on the surface of the formulation [808]. This change in surface charge density can lead to variations in the Z-Potential, and in this case can lead to a reduction in the Z-potential of the formulation.

The comparative analysis performed on LPHNP size, PDI and Z-potential showed in Figure 5-15 confirmed no differences in PDI and Z-potential of formulations upon RN7IN6 loading within the LPHNP formulations, in comparison to CTX-F.4. This indicates that the incorporation of RN7IN6 into the lipid shell of the LPHNPs did not significantly alter PDI and Z-potential at all the RN7IN6 loading concentrations assessed. It was unexpected not to observe significant changes in Z-potential, especially given prior findings for liposomes where a peptide concentration-dependent shift was observed (see section 4.3.2.2). This could be due to the use of crude (here) versus purified RN7IN6 peptide (for liposomal studies), or differences in loading concentrations between liposomes and LPHNPs, potentially affecting charge distribution. Although a trend of increasing Z-potential with RN7IN6 loading up to 1.5 mg/mL was visually observed (Figure 5-15 C), this was not statistically significant.

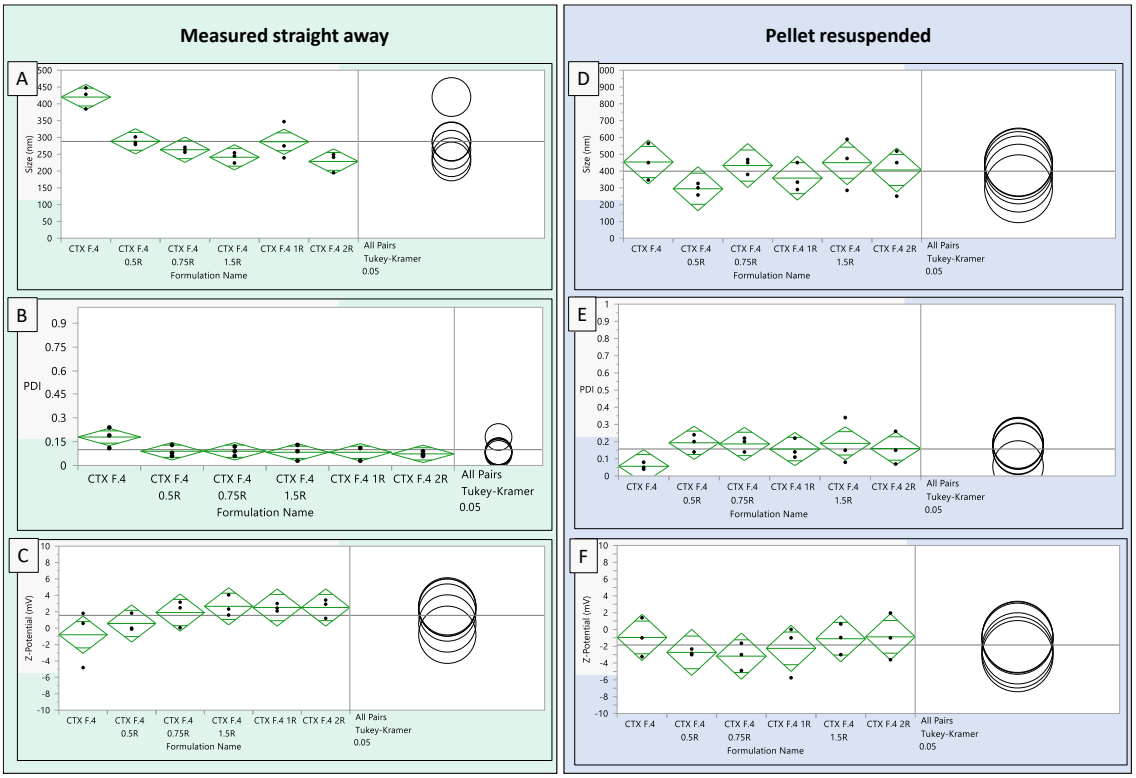

Figure 5-15: Oneway ANOVA analysis for size (A and D), PDI (B and E) and Z-potential (C and F) with Tukey's post-hoc comparison performed on CTX and RN7IN6 co-loaded LPHNPs measured straight away (A, B and C) and after centrifugal ultrafiltration (D, E and F). The green diamonds represent the sample mean and the 95% confidence interval. The center line across each diamond corresponds to the group mean. The vertical span of each diamond represents the 95% confidence interval for each group. The width and height of the diamonds is proportional to the sample size at each time point with broad and short diamonds indicating many data points. The black dots represent individual data points. Each circle represents one group's mean.

Regarding LPHNP size, the one-way ANOVA analysis revealed a reduction in LPHNP size upon encapsulation of RN7IN6 within the external layer of the LPHNPs (Figure 5-15 A). Indeed, all the CTX and RN7IN6 co-loaded LPHNP formulations showed a significantly lower size in comparison to CTX-loaded LPHNPs, when measure straight after formulation manufacture. The reduction in size of LPHNPs upon incorporation of the AMP RN7IN6 can be attributed to several factors influenced by the unique properties of both the peptide and the lipid components of the nanoparticles. The composition and structure of the lipid shell, that resembles the inner bacterial membrane [312], facilitates its interaction with RN7IN6. It is well documented that indolicidin, a precursor of RN7IN6, induces perturbation in the packing of membranes through its interactions with lipid bilayers [809, 810]. The study carried out by Nielsen *et al.* showed that

indolicidin migrates between the lipid headgroups and the lipid tail region in the outer leaflet of lipid vesicles resulting in a perturbation of the packing of the lipid tails in the membrane at highest assessed peptide to lipid ratio (1:5) , which allows for lipid bilayer structure rearrangements and re-organization [705]. Furthermore, indolicidin has been observed to induce continuous membrane shrinking and thinning in model membranes, further supporting its membrane-perturbing effects [811]. Therefore, it was hypothesized that the reduction in size of LPHNPs upon incorporation of RN7IN6 can be explained by peptide interaction with the lipid shell which induced a re-organization of the lipid layer in comparison with CTX-only loaded LPHNPs. However, as all the RN7IN6-loaded formulations showed comparable size despite the increasing RN7IN6 loading concentration, it is likely that a threshold peptide concentration was exceeded at all loading concentrations used, suggesting that once this threshold is reached, further increases in RN7IN6 do not induce additional lipid layer rearrangements.

5.4.3.2. CTX and RN7IN6 HPLC Method: Range and Linearity

An HPLC for the simultaneous quantification of CTX and RN7IN6 was optimized and validated. The peak area of standard solutions was directly related to CTX or RN7IN6 concentration over the concentration range of 1-1000 µg/mL (Figure 5-16A) or 5-750 µg/mL (Figure 5-16B) which covered the working concentration range of CTX-containing and RN7IN6-containing formulation samples, respectively. The calibration curve equation (displayed in Figure 5-16, where *y* represents the peak area and *x* the CTX or RN7IN6 concentration) resulting from the linear regression analysis (R^2 = 1 for CTX and R^2 = 0.9997 for RN7IN6) was further employed to determine the accuracy and relative SD of the analytical procedure.

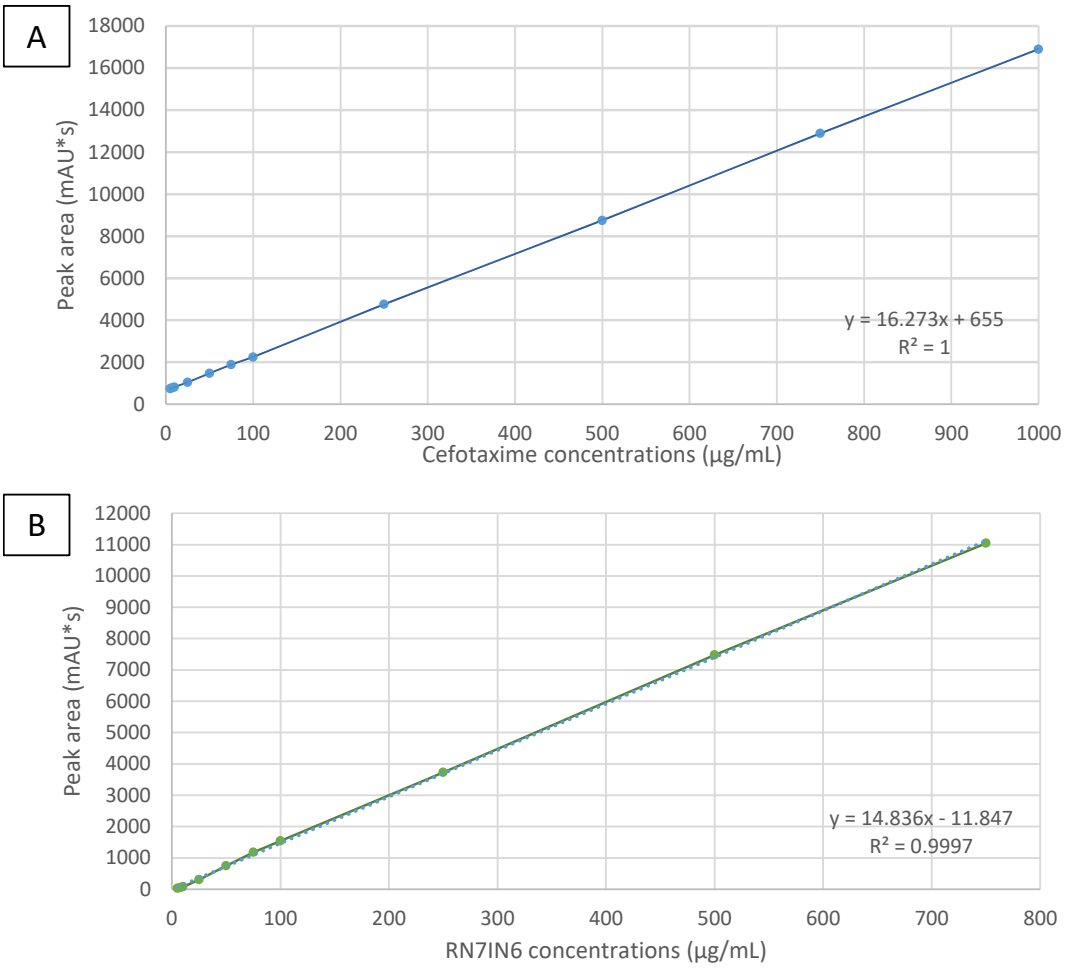

Figure 5-16: Standard curve of peak area as a function of CTX (A) or RN7IN6 concentration (B), demonstrating a linear relationship for the investigated concentration range in both cases (n=3). Results represent the mean ± SD of three independent sets of standards.

5.4.3.3. CTX and RN7IN6 HPLC Method: Precision, Accuracy and Limits

The employed gradient HPLC method was found to be precise for both intra-day and inter-day variability as indicated by RSD% values ≤5% (Table 5-6).

Table 5-6: Intraday and interday accuracy of the unweighted linear regression and RSD% applied to calibration standards in the range 75–750 µg/mL for CTX and RN7IN6. The results represent mean ± SD, n=3 independent samples.

	Spiked concentration (µg/mL)	**Calculated concentration (µg/mL) ± SD**	**Accuracy (%)**	**RSD (%)**
Cefotaxime	***Intraday repeatability***			
	75	74.3 ± 2.84	99.10	3.82
	250	274.8 ± 5.42	99.13	2.19
	750	727.8 ± 17.66	97.04	2.43
	Interday repeatability			
	75	75.5 ± 2.93	100.60	3.89
	250	252.7 ± 2.09	101.1	0.83
	750	760.3 ± 11.81	101.37	1.55
RN7IN6	***Intraday repeatability***			
	75	77.3 ± 3.27	103.02	4.23
	250	249.3 ± 5.69	99.73	2.28
	750	721.1 ± 13.38	96.15	1.86
	Interday repeatability			
	75	80.5 ± 3.00	107.27	3.73
	250	262.7 ± 7.72	105.10	2.94
	750	738.2 ± 15.92	98.42	2.16

There was no interference from formulation components at the Rt of either the CTX or the RN7IN6 analyte peak, and peak purity data revealed that there were no co-eluting peaks and no interference from impurities at the Rt of CTX (Rt = 7.634 min) and RN7IN6 (Rt = 10.608 min) as shown in Figure 5-17.

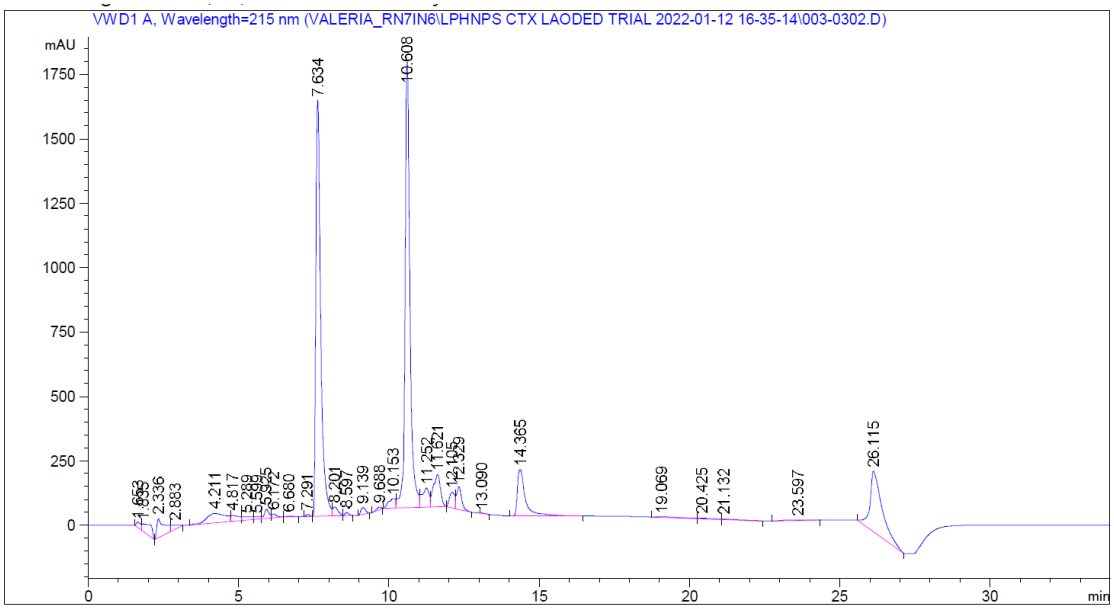

Figure 5-17: CTX (Rt =7.634) and RN7IN6 (Rt=10.608) HPLC chromatogram showing distinct analyte peaks with no interference from formulation components or impurities, confirming the specificity of the method for CTX and RN7IN6 detection.

For repeatability of injections (n=5), RSD was ≤2.0% and thus injections were repeatable for all concentrations tested (Table 5-7) further underpinning the precision of the assay.

Table 5-7: Injection repeatability for three different CTX and RN7IN6 concentrations. The results represent mean ± SD, n=5 independent samples

Drug	Spiked concentration (µg/mL)	Peak area ± SD	RSD (%)
CTX	75	170.3 ± 1.0	0.59
	250	442.2 ± 3.70	0.84
	750	1180.0 ± 19.7	1.67
RN7IN6	75	111.8 ± 1.40	1.23
	250	385.5 ± 2.60	0.66
	750	1074.6 ± 18.8	1.75

LLOD and LLOQ, which are particularly affected by small concentration changes and are thus variable, were calculated according to Equation 2-1 and Equation 2-2 and found to be lower for CTX than RN7IN6 (Table 5-8).

Table 5-8: RP-HPLC method sensitivity with respect to CTX and RN7IN6. Results represent the mean ± SD of three independent samples.

Drug	*Lower Limit of Detection (LLOD, µg/mL)*	*Lower Limit of Quantification (LLOQ, µg/mL)*
CTX	2.18	6.60
RN7IN6	5.61	17.01

5.4.3.3.1. CTX and RN7IN6-loaded LPHNP Encapsulation Efficiency Quantification

In contrast to the similar size, PDI and Z-potential shown by various CTX and RN7IN6 co-loaded formulations, the study on the encapsulation efficiency of both drugs showed a different trend. CTX and RN7IN6 co-loaded LPHNPs characterized in terms of size, PDI and Z-potential as detailed above, were purified using centrifugal ultrafiltration units and subsequent the ultrafiltrate analyzed via HPLC to quantify CTX and RN7IN6 EE%, as well as the concentration of CTX/RN7IN6 encapsulated within the formulations. Results of the study are shown in Figure 5-18. The results for CTX and RN7IN6 co-loaded formulations showed that the EE% and the concentration of CTX encapsulated were comparable across all the LPHNPs formulations manufactured according to Table 5-3. This outcome was logical as all the formulations were manufactured using the same CTX loading concentration as optimized in Chapter 2. Therefore, it was concluded that changes in RN7IN6 loading concentration, while keeping all the other formulation parameters fixed, did not impact the CTX EE%.

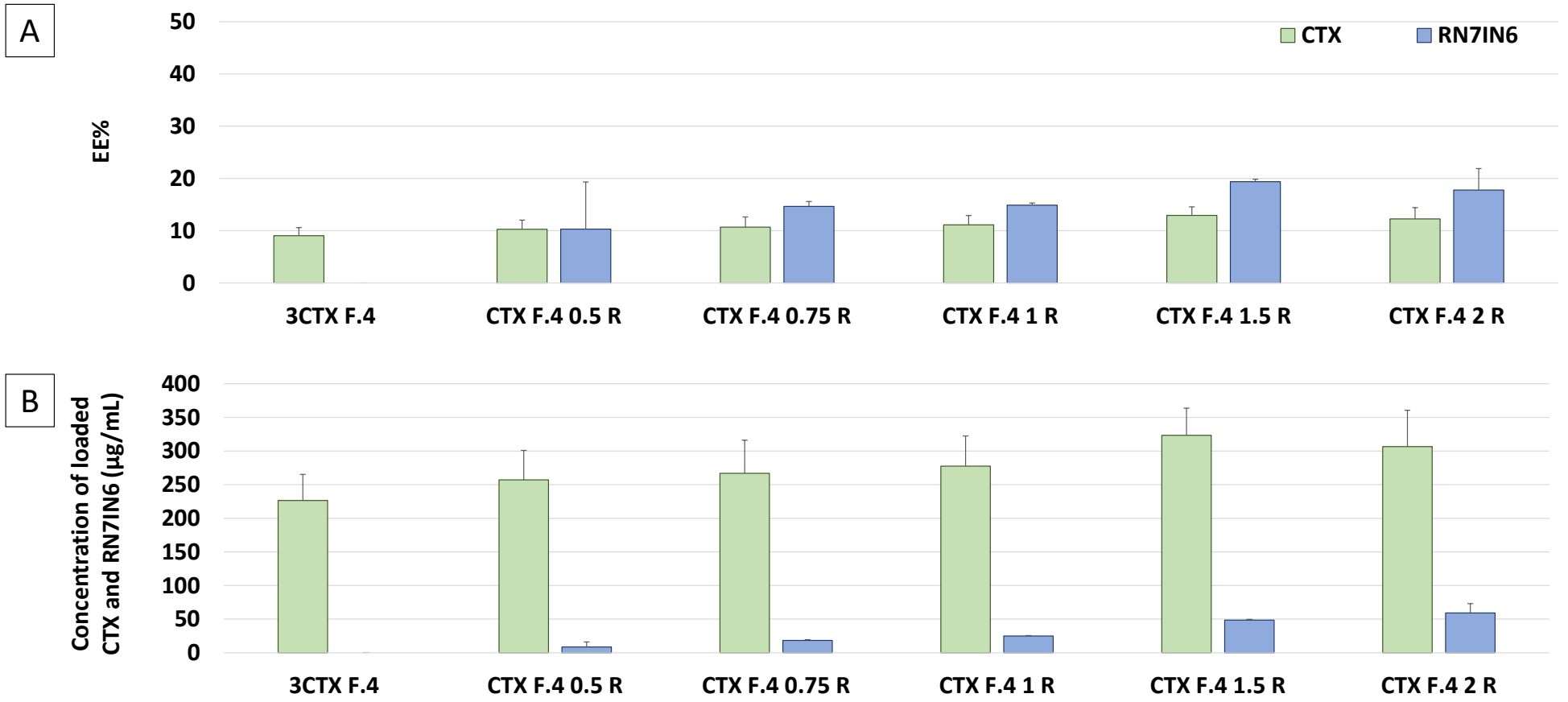

Figure 5-18: CTX and RN7IN6 Encapsulation Efficiency (EE%, A) and concentration of CTX and RN7IN6 (B) co-loaded into LPHNP formulations. LPHNP formulations were prepared using increasing loading concentrations of RN7IN6 ranging from 0.5 mg/mL to 2 mg/mL according to Table 5-3, in comparison with CTX-only loaded LPHNPs (CTX F.4). The results represent mean ± SD, n=3 independent batches.

This outcome was also confirmed by the statistical analysis performed on manufactured formulations and shown in Figure 5-19 A for CTX. The one-way ANOVA was employed to compare CTX EE% across different formulations and no differences were reported between CTX-only and CTX and RN7IN6 co-loaded formulations (Figure 5-19 A).

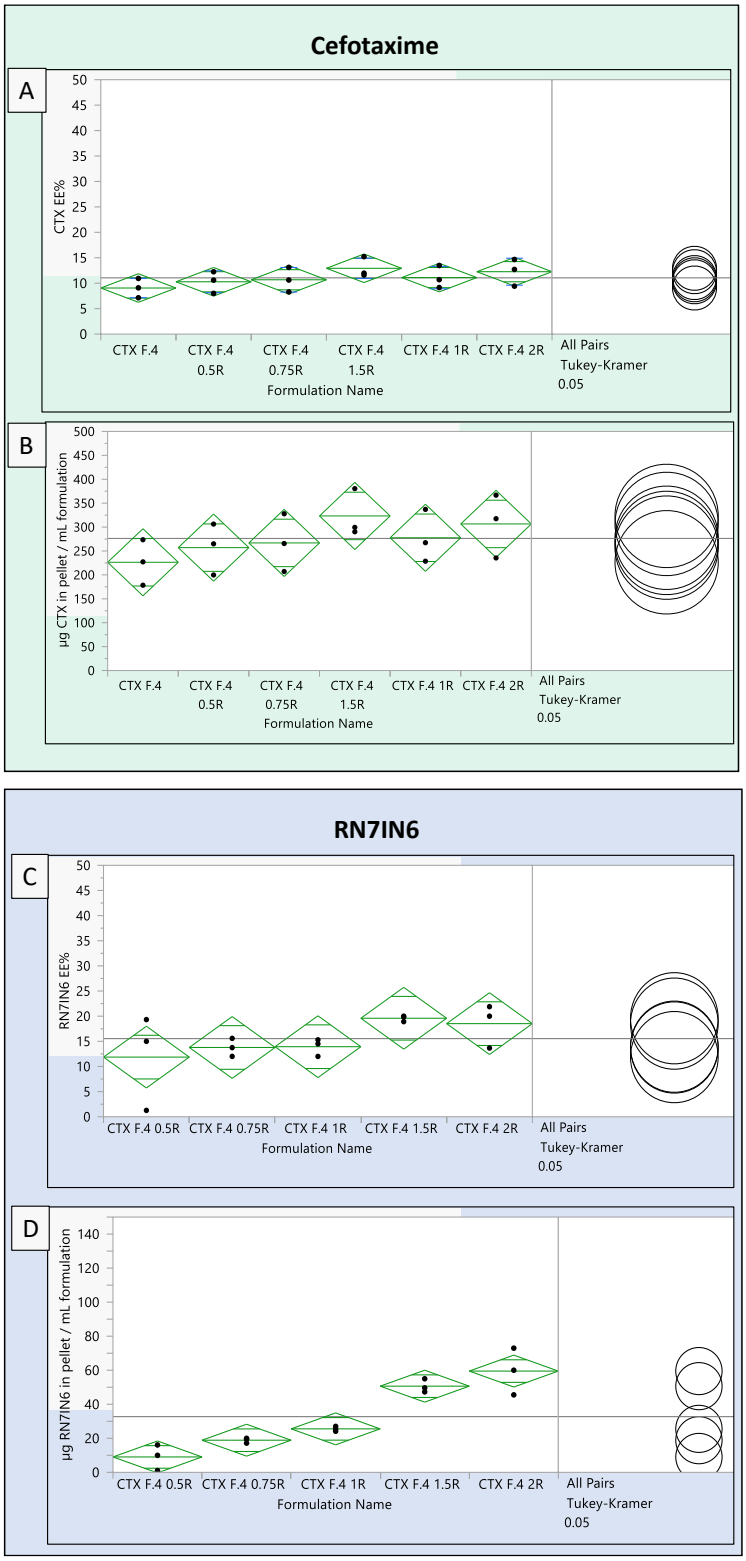

Figure 5-19: One-way ANOVA analysis for EE% (A and C) and drug loading concentration (B and D) with Tukey's post-hoc comparison performed on CTX (A and B) and RN7IN6 (C and D). The green diamonds represent the sample mean and the 95% confidence interval. The center line across each diamond corresponds to the group mean. The vertical span of each diamond represents the 95% confidence interval for each group. The width and height of the diamonds is proportional to the sample size at each time point with broad and short diamonds indicating many data points. The black dots represent individual data points. Each circle represents one group's mean.

Similarly to CTX, RN7IN6 showed a comparable %EE across all the formulations manufactured ranging from 10.3 % to 19.4% (Figure 5-18 A). No significant differences were observed ($p < 0.05$) in RN7IN6 EE% (Figure 5-19 C), despite the increasing RN7IN6 loading concentrations employed during the manufacturing process.

Figure 5-18 B and Figure 5-19 D show that despite a lack of significant increase in RN7IN6 EE% with increasing RN7IN6 loading concentrations, the final loaded concentration of peptide achieved in formulations did increase in a statistically significant manner over the entire loading concentration range. The concentration of RN7IN6 loaded within CTX F.4 1.5R and CTX F.4 2R was higher compared to other formulations manufactured with lower RN7IN6 loading concentrations (Figure 5-19 D), which is supported by the lack of overlap in the Tukey-Kramer circles on the right side of the plot. As the loading concentration of peptide increases, there is a proportional increase in the amount of peptide available for encapsulation leading to enhanced peptide incorporation into the formulation. However, it is reported that increasing the peptide loading concentration during encapsulation leads to a plateau in encapsulation efficiency once a certain threshold is reached. This occurs because higher concentrations can saturate the encapsulation capacity of the delivery system, limiting further encapsulation [812]. Beyond this point, adding more active does not significantly increase the active loaded concentration and may lead to a decrease due to saturation effects. This phenomenon was not observed in the current study as the trend indicates an increasing final peptide concentration in formulation with proportional increases in RN7IN6 loading concentrations (Figure 5-19 D). This indicates that the encapsulation capacity of delivery system was not saturated with the highest RN7IN6 loading concentration employed in the study, highlighting a potential avenue for future research to identify the maximum loading concentration that leads to saturation and the highest incorporated peptide concentration.

Further investigations could focus on optimizing the formulation by pinpointing this threshold to enhance peptide loading concentration. Given similarity in formulation physiochemical characteristics and CTX entrapment at all RN7IN6 loading

concentrations investigated, formulation CTX F.4 2R was employed in subsequent studies because it showed the highest final peptide concentration in formulation.

5.4.4. CTX and RN7IN6 Release from LPHNPs

Release studies were undertaken on CTX F.4 2R to understand drug release kinetics from LPHNPs, as a preliminary study ahead of antimicrobial efficacy assessment.

The release of CTX and RN7IN6 from CTX F.4 2R was assessed following the "sample and separate" method as described in 5.3.2.6. Alongside CTX and RN7IN6 co-loaded LPHNPs, CTX-only loaded LPHNPs and CTX-loaded CHCL NPs were also assessed. Therefore, this study aimed to assess whether changes in the formulation from liposomes to LPHNPs may impact on RN7IN6 release as previous findings from the RN7IN6-loaded liposomes (F41, see section 4.4.3.4) showed no peptide release up to 48 hours. Moreover, this comparative study was undertaken to understand the impact of the introduction of the lipid bilayer surrounding LPHNPs on CTX release kinetics, as well as any effect of introduction of RN7IN6 into the lipid shell on CTX release. Indeed, the lipid layer surrounding the hybrid nanoparticles and the presence of RN7IN6 has the potential to introduce distinct physicochemical properties which might modulate or alter CTX release kinetics. Therefore, by scrutinizing these different formulations, the study aimed to elucidate the individual and collective contributions of formulation components and RN7IN6 to the release of CTX, while also investigating the release behavior of RN7IN6.

In initial investigations, the CTX cumulative release from formulations showed an unusual behavior. After an initial burst release from CTX-loaded CHCL NPs and LPHNPs, after around 6 hours, the cumulative CTX release in PBS medium was seen to decrease with time (data not shown). However, given the nature of the "sample and separate method" employed to perform the release study, which involves periodic withdrawal of aliquots from the release medium and replacement with fresh medium and calculation of a cumulative percentage of drug released, the CTX concentration in release medium would be expected to either remain constant or increase over subsequent time points.

In cases where drug release is complete, repeated sampling could potentially result in dilution of the drug concentration in the release medium. However, this was ruled out by ensuring that release had not reached a plateau before subsequent sampling, and by accounting for potential dilution effects in the cumulative release calculations. Therefore, this reduction in cumulative release of CTX over time was investigated further.

The storage stability of CTX in water was previously evaluated when stored in the freezer (-18 °C), in the fridge (5 °C), and at room temperature (25 °C) for a period of up to 4 days, with results presented in section 2.4.2.5. The study undertaken and presented in Chapter 2 revealed that CTX was stable for up to 96 hours at all the conditions assessed. While previous findings indicated good drug stability at 4 °C and 25 °C, the initial release studies raised the question of CTX stability at 37 °C, which is crucial for release studies. Therefore, a solution of CTX was prepared in PBS at 0.5 mg/mL and placed on a HulaMixer™ Sample Mixer (Thermo Fisher Scientific, US) at 75 rpm and incubated at 37 °C for up to 4 days. The concentration of 0.5 mg/mL was selected as it aligns with the working concentration used in the release studies for CTX-loaded formulations, ensuring consistency in evaluating the stability of CTX under the same conditions as those employed during the drug release experiments. At each time point (0 min, 1, 2, 4, 6 hours, 1 and 2 days) an aliquot of the CTX solution was removed and analyzed. The HPLC analysis revealed that the area under the curve (AUC) of CTX (Rt: 7.9 min) was decreased considerably over the 4-day time period, with an additional peak emerging and increasing in intensity at an Rt of approximately 6 min (highlighted in light pink, Figure 5-20).

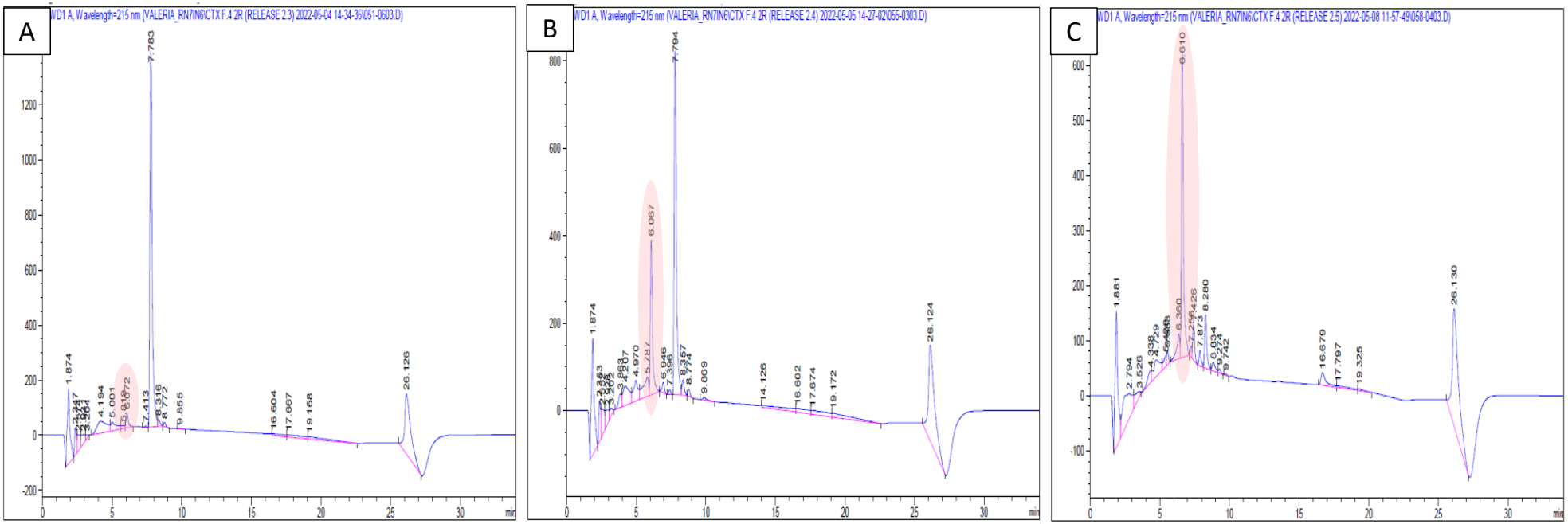

Figure 5-20: CTX RP-HPLC chromatogram of a 0.5 mg/mL CTX solution in PBS initially (A), and at 1 day (B) and 4 days (C) at 37 ^{o}C. CTX Rt=7.7 min. Circled in pink is a CTX degradation product (Rt around 6 minutes).

The concentration of CTX in solution was then calculated at each time point as a percentage of the initial concentration and plotted in Figure 5-21. The T-test statistical analysis was performed using IBM SPSS statistic software (Version 28.0. Armonk, NY: IBM Corp) revealed that CTX concentration significantly decreased at each time point when compared with the previous time point. The CTX concentration halved in 24 hours, surprisingly indicating that CTX is relatively unstable at 37 °C in solution in PBS.

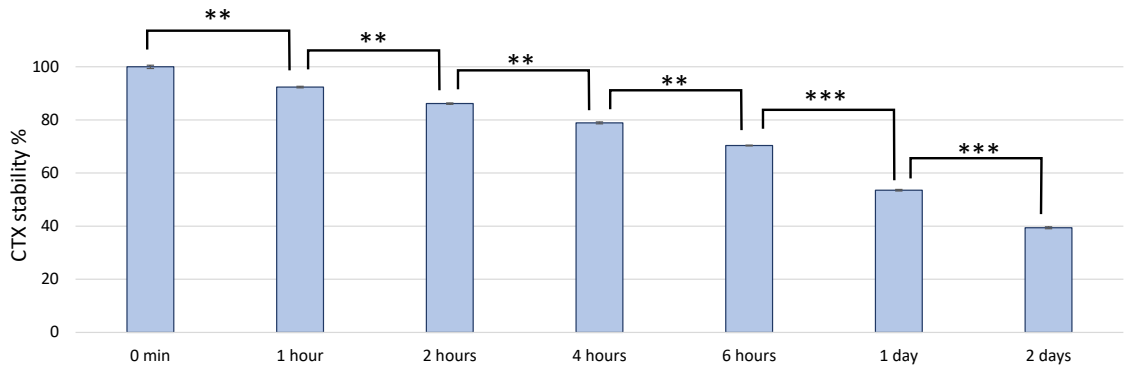

Figure 5-21: CTX stability, expressed as percentage of initial concentration, at 37 ± 2 °C for up to 2 days. Results represent the mean ± SD of three independent batches. An independent T-test was run on consecutive time points to determine if there was a mean difference in CTX concentration. If the two-tailed p-value is less than 0.01, it is flagged with 2 stars (**). If the two-tailed p-value is less than 0.001, it is flagged with 3 stars (***).

CTX has been shown to degrade in in aqueous solution by two parallel reactions being the de-esterification at the C-3 position and the β-lactam cleavage, despite observations that the presence of buffers including PBS did not accelerate CTX degradation [813]. Furthermore, Alsarra *et al.* demonstrated that CTX degradation was dependent on factors such as temperature, pH, and the presence of β-cyclodextrin derivatives with accelerated degradation rate upon increasing temperature from 25 °C to 37 °C and increasing pH from 3.5 to 7.5 [814]. Hence, in the absence of proof that could be obtained from LC-MS studies, it was theorized that the additional peak observed on CTX chromatograms (Figure 5-20) corresponded to a CTX degradation product caused the drug hydrolysis in solution at 37 °C. This degradation product is likely desacetyl CTX (des-CTX, [813]), which retains antibacterial activity, although its potency is circa 10 times lower compared to the parent drug, CTX [815]. Despite this reduction, des-CTX remains clinically relevant against *Pseudomonas* spp. and other bacterial species, including

Enterobacteriaceae, *S. aureus*, and *Streptococcus* spp [816]. Although the formation of des-CTX may lower the overall antibacterial efficacy during release studies, its residual activity could still contribute to therapeutic effect. Moreover, the potential for synergism between CTX and des-CTX should be considered, as the combination has demonstrated a high rate of synergistic antibacterial activity against various bacterial species, enhancing overall efficacy compared to each compound alone [816]. In the context of LPHNP formulations, while encapsulation may afford some degree of protection to CTX from degradation, the drug remains susceptible to hydrolysis upon release into the surrounding medium. This degradation behavior is critical to consider when interpreting both release kinetics and antimicrobial efficacy, especially over extended time periods where the formation of degradation products like des-CTX may influence overall therapeutic outcomes.

To address the issue related to CTX degradation in PBS at 37 °C in the context of obtaining information on release kinetics, the cumulative release of CTX from CTX-loaded formulations was calculated at each time point by constructing CTX standard curves at each time point [817] using CTX stock solutions that had been stored together with release samples at 37 °C, and using PBS as blank. The data presented in Figure 5-22 gives an indication of the cumulative release of CTX over 2 days from CTX-loaded CHCL NPs, CTX-loaded LPHNPs and CTX and RN7IN6 co-loaded LPHNPs using this approach. The cumulative release of CTX was measured over a 48-hour period to coincide with the duration of subsequent antimicrobial activity assays. This adjustment was implemented to ensure that the release kinetics are reflective of the experimental timeframe used for evaluating microbiological efficacy, thereby providing a more accurate correlation between drug release and bacterial inhibition.

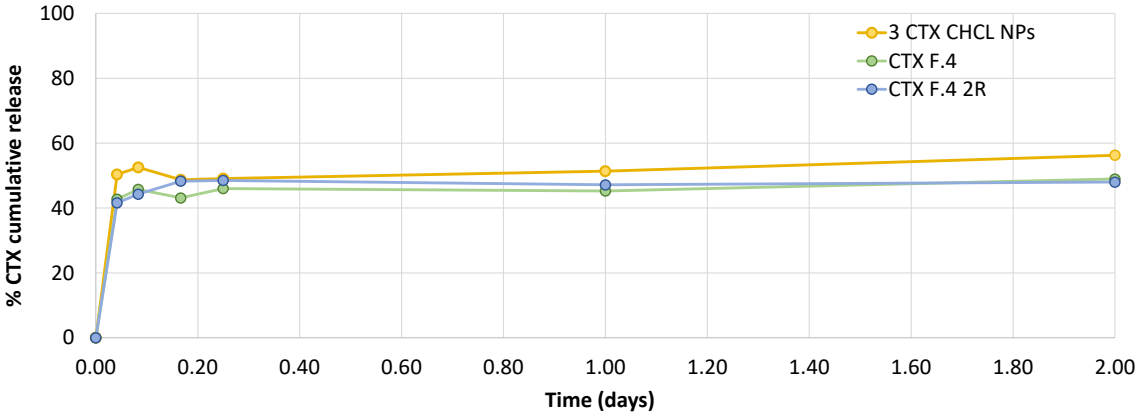

Figure 5-22: CTX cumulative release % of 3 CTX CHCL NPs, CTX-F.4 and CTX-F.4 2R formulation. The results represent mean ± SD, n=3 independent measurements of the same batch.

Observing the cumulative release profiles in Figure 5-22, all formulations appeared to exhibit similar CTX release kinetics over the assessed time frame, with a CTX burst release within the first hour and a plateau reached after 4 hours. The introduction of the lipid shell in CTX F.4 LPHNPs and the encapsulation of RN7IN6 in the lipid shell of CTX F.4 2R were potentially expected to influence CTX release dynamics. Upon closer examination of the 1-hour and 2-hour time points, a modest reduction in the initial burst release is observed for both CTX F.4 and CTX F.4 2R, which are lipid-coated formulations, compared to CTX-loaded CHCL NPs. This suggests that the lipid shell may introduce a diffusional barrier, slightly retarding the early release of CTX. While these findings are based on three technical replicates, the statistical analysis provides insights into trends within this set. However, due to the limited replication, these results should be interpreted with caution and are not necessarily representative of broader biological variability at this stage. Indeed, the outer lipid shell present in LPHNPs formulations likely introduces additional barriers to drug diffusion, potentially slowing drug release compared to that from uncoated polymeric NPs. Furthermore, the presence of RN7IN6 within the lipid shell might interact with the lipid bilayer or alter its properties, further modulating CTX release kinetics.

A study carried out by Lee *et al.,* showed that while the presence of a dioleoyl-3-trimethylammonium propane (DOTAP) lipid layer improved the EE% of vancomycin within PLGA NP cores, it also retarded and led to an incomplete release of vancomycin

from the lipid-coated nanoparticle formulation [313]. Similarly, Wang *et al.* demonstrated that folate-coated, PEGylated LPHNPs showed sustained release in comparison with uncoated PLGA nanoparticles, with only 25% of doxorubicin payload being released after 7 days in contrast to the 80% doxorubicin release for uncoated PLGA nanoparticles [818]. Indeed, the lipid shell not only serves to enhance the biocompatibility of the NP core [819] but also serves as a protective barrier preventing drug leakage and maintaining drug stability [820]. In contrast to these published findings, however, data presented in the current study suggest that the outer lipid shell and the presence of RN7IN6 do not alter the overall release behavior of CTX compared to CTX-loaded CHCL NPs to an appreciable extent. This discrepancy may be a result of the specific composition of the LPHNP formulations. Firstly, the composition and properties of the lipid coating play a crucial role. Factors such as lipid composition, thickness, and fluidity can significantly impact the permeability of the lipid shell, thus affecting drug release kinetics. Variations in lipids employed in the NP coating consequently influence drug diffusion rates within the bilayer as well as drug-lipid interactions. Secondly, the physicochemical properties of the drug itself are important determinants. Characteristics such as molecular weight, solubility, and lipophilicity influence drug interaction with the lipid bilayer and its diffusion through the nanoparticle matrix. Additionally, the presence of functional groups or chemical moieties, within the drug molecule, that can interact with the lipid membrane may further modulate drug release. Finally, physiochemical characteristics of the delivery system such as the particle size, which directly impacts their surface area-to-volume ratio affects the rate of drug release kinetics, and for instance smaller nanoparticles exhibit faster release due to their higher surface area-to-volume ratio, facilitating greater drug diffusion [821].

Overall, the release kinetics of drugs from lipid-coated nanoparticles are governed by a complex interplay of factors involving nanoparticle structure, drug properties, environmental conditions, and formulation parameters. Hence, even apparently negligible differences in delivery systems structure, composition or physiochemical characteristics might result in differences in drug release. Future investigations could focus on elucidating the lipid layer thickness of the LPHNPs to determine whether a

monolayer or bilayer structure is present, as this structural aspect could significantly influence drug release kinetics (and indeed, maximum drug loading capacity). Additionally, exploring the impact of maximizing RN7IN6 loading on CTX release could provide insights into potential interactions between the peptide and the drug release dynamics. Moreover, consideration should be given to whether a sustained or slow release of CTX is in fact desirable for therapeutic efficacy Investigating whether a slower release of CTX enhances or diminishes antibacterial activity could inform the optimal design of antibiotic-loaded LPHNPs.

Regarding RN7IN6 release, although no release from liposomal formulations was observed in Chapter 4, this lack of observed release was not considered prohibitive to further incorporation of both RN7IN6 and bacteriomimetic lipids into LPHNPs (see discussion in Chapter 4) because the change in formulation from liposomes to LPHNPs was hypothesized to potentially alter the release kinetics of RN7IN6. Indeed, although the lipid shell composition of LPHNPs is the same as those of the developed liposomes, the introduction of the polymeric core results in different LPHNP physiochemical characteristics to those of liposomes, possibly affecting RN7IN6 release. Additionally, the thickness and structure of the lipid layer in LPHNPs, which remains unknown, could differ from that of liposomes, potentially affecting the diffusion and release properties of RN7IN6.

Interestingly, no RN7IN6 release was also recorded from the CTX and RN7IN6-loaded CTX-F.4 2R formulation up to 48 hours (data not shown). The absence of quantifiable RN7IN6 release from LPHNPs over 48 hours could be attributed to several factors. Firstly, as similarly discussed in Chapter 4, the analytical method used to quantify RN7IN6 had a relatively high limit of detection (~26 µg/mL), potentially limiting the detection of released peptide. Thus, according to the initial formulation CTX-F.4 2R concentration used for the release study, the analytical method developed would have not been able to detect if less than ~10% of peptide was released from the formulation. Thus, we can conclude that a cumulative release less than 10% of the peptide was released from CTX F.4 2R over 48 hours, as the dilution of the media after sampling could have resulted in small amounts of peptide being released at each interval, but these amounts remained

below the LLOD of the analytical method. Moreover, the intrinsic affinity of RN7IN6 for the LPHNP membrane shell, mediated by its amphipathic nature, net positive charge, and specific amino acid sequence [705, 822] needs to be taken into account and might possibly explain why RN7IN6 is not released from LPHNPs. As previously discussed, AMPs like RN7IN6 interact with lipid headgroups via electrostatic interactions [823]. This is an important factor in determining peptide affinity for membranes. Previous studies, such as those by Nielsen *et al*., also demonstrated the migration of indolicidin, an RN7IN6 precursor, into lipid vesicle bilayers [705]. The strong affinity of RN7IN6 for the lipid bilayer, driven by its amphipathic nature, high tryptophan content, and bulky indole side group, may result in its retention within the lipid shell of the LPHNPs. This affinity likely leads to minimal release, as the peptide remains integrated within the bilayer, rather than diffusing out into the surrounding medium [822].

Despite the fact that an appreciable amount of RN7IN6 was not released from LPHNPs, the peptide encapsulated in the lipid shell of CTX F.4 2R could still have the potential to interact with bacterial cells. As discussed in detail in the context of Chapter 4, it is anticipated that the LPHNP lipid shell composition, which includes phospholipids commonly found and designed to mimic in bacterial membranes (POPE, POPG, and CL), can facilitate the initial contact and fusion with bacterial cell envelopes [824]. This interaction is critical as it may enable the peptide to exert its antimicrobial effects directly at the bacterial cell surface, potentially resulting in the introduction of the AMP into the bacterial cell membrane, facilitating membrane disruption. Thus, even without significant release, the formulation lipid shell with bacterial-derived lipids, along with the membrane-perturbing effects of RN7IN6, may lead to disruption of bacterial integrity, contributing to antimicrobial activity. Patel *et al.* demonstrated that bioinspired liposomes encapsulating colistin fused with *S. enterica* membranes, leading to drug exchange at the bacterial surface, which significantly increased intracellular antibiotic concentrations and enhanced bacterial killing [825]. These findings highlight the potential of the lipid shell in the LPHNP formulation to interact with bacterial membranes, facilitating the fusion and transfer of RN7IN6, contributing to antimicrobial efficacy even in the absence of notable peptide release.

The subsequent phase of the investigation aimed to evaluate the synergistic potential of CTX and RN7IN6, alongside assessing the antimicrobial efficacy of CTX F.42R to provide preliminary insights into the combined impact of CTX and RN7IN6 within the CTX F.42R formulation.

5.4.5. Antimicrobial Efficacy Assessment

5.4.5.1. CTX Antimicrobial Activity

Evaluating the activity of free CTX in a comparable assay before assessing the synergism between CTX and RN7IN6 is crucial for several reasons. Firstly, it establishes a baseline of CTX's inherent antimicrobial efficacy, enabling a clear comparison when RN7IN6 is introduced. Secondly, understanding CTX's standalone performance helps identify its antimicrobial properties and baseline activity against target bacterial strains, providing a clear reference point for evaluating the impact of combination therapy with RN7IN6. Since RN7IN6 and CTX have different modes of action – RN7IN6 disrupts bacterial membranes [173], while CTX inhibits bacterial cell wall synthesis [826] - knowing the individual contributions of each can clarify how they might work together to enhance overall antimicrobial activity. Furthermore, establishing the activity of free CTX is essential for optimizing concentration ranges when designing combination studies to test various ratios of CTX to RN7IN6.

CTX antimicrobial activity was already assessed in section 2.4.4. against *E. coli, K. pneumoniae, P. aeruginosa, and S. aureus,* using a well-diffusion assay. Results indicated significant inhibition across all CTX concentrations tested, with prominent zones of inhibition observed for *E. coli* and *K. pneumoniae*. However, inhibition of *P. aeruginosa* and *S. aureus* was less pronounced, indicating lower efficacy against these species. While the well-diffusion assay determines antimicrobial susceptibility, the broth microdilution assay provides specific MIC values, which are crucial for designing synergism studies.

Therefore, the MIC of CTX was assessed here against *E. coli*, *K. pneumoniae*, *P. aeruginosa* and *S. aureus* by employing the resazurin assay as detailed in section 4.3.2.1.5. The MIC values of CTX against various species were then compared to the EUCAST, [827] and the CLSI, [828] MIC breakpoints in Table 5-9. The MIC breakpoint refers to the threshold concentration of an antimicrobial agent at which a bacterial strain is classified as susceptible or resistant to the drug. It helps guide clinical decision-making by indicating the likelihood of effective treatment at specific concentrations.

Table 5-9: CTX MIC values and classification of antibiotic susceptibility according to EUCAST and CLSI clinical breakpoints against S. aureus*,* E. coli*,* P. aeruginosa *and* K. pneumoniae*. A "dash" indicates that the microbe can be reported resistant without further testing.*

	MIC reported in this study (µg/mL)	**MIC breakpoint by EUCAST (µg/mL) Susceptible ≤ / Resistant > [827]**	**MIC breakpoint by CLSI (µg/mL) Susceptible ≤ / Resistant ≥ [828]**
S. aureus	2	2/4*	-
E. coli	0.125	1/2	1/4
P. aeruginosa	16	-	-
K. pneumoniae	0.062	1/2	1/4

** Inferred from cefoxitin values [827] even though cefoxitin MIC is a poorer predictor of methicillin resistance than the disk diffusion test. This is due to the fact that the cefoxitin MIC, while effective at detecting mecA-mediated methicillin resistance, may miss borderline oxacillin-resistant S. aureus strains, which rely on enhanced β-lactamase production rather than the presence of mecA. The disk diffusion test is more sensitive in detecting these borderline-resistant strains, thereby providing a more comprehensive assessment of methicillin resistance [829].*

The MIC values obtained for each bacterial species were 2 µg/mL for *S. aureus*, 16 µg/mL for *P. aeruginosa*, 0.062 µg/mL for *K. pneumoniae* and 0.125 µg/mL for *E. coli* (Table 5-9).

According to EUCAST and CLSI guidelines, CTX MIC values for *P. aeruginosa* have not been provided, making interpretation of the observed antimicrobial activity challenging.

EUCAST guidance indicates that a "dash" signifies that the microbe can be reported resistant without further testing [830]. Moreover, EUCAST also discourages the use of CTX against *P. aeruginosa* when the MIC value exceeds 0.5 µg/mL [827, 830], supporting high MIC values reported in Table 5-9. Similarly, both EUCAST and CLSI have not explicitly mentioned the MIC breakpoint for CTX against *S. aureus*. However, EUCAST suggests that CTX MIC breakpoint, even though is considered to be a poor predictor of methicillin resistance, can be inferred from that of cefoxitin [827, 830]. This lack of specific breakpoints for cefotaxime is largely due to the variability in its effectiveness at standard doses, as high-dose regimens are required to ensure reliable efficacy against *S. aureus*. Consequently, cefotaxime is not routinely recommended as a primary agent for *S. aureus* infections, and its use is generally limited to cases where high dosing can be carefully managed [831].

Regarding *E. coli* and *K. pneumoniae*, the reported MIC values in this study (Table 5-9), were well within the susceptible range defined by EUCAST and CLSI, indicating susceptibility to the antimicrobial agent. However, as already seen for *S. aureus*, there is a discrepancy between EUCAST and CLSI established breakpoints for *E. coli* and *K. pneumoniae,* which can be linked to differences in the epidemiology of antimicrobial resistance, the availability of clinical outcome data, and the methods used for breakpoint determination [832]. EUCAST generally recommends lower MIC breakpoints defining resistance compared to CLSI, resulting in differences in the classification of resistant and susceptible isolates [833, 834].

5.4.5.2. CTX and RN7IN6 Synergism Assessment

To address the challenge of limited efficacy against resistant bacterial strains and the narrow spectrum of CTX when used alone, RN7IN6, which is known for its ability to disrupt bacterial membranes leading to cell lysis and death [173], was additionally employed. Therefore, the synergism of CTX and RN7IN6 was assessed, and results are shown in Table 5-10. This assessment was conducted using the free forms of CTX and RN7IN6 in combination in solution.

Table 5-10: FICI of combinations of RN7IN6 peptide with standard antibiotic CTX in solution, against P. aeruginosa*,* S. aureus*,* K. pneumoniae *and* E. coli*. Each entry in the table represents n=1.*

Bacteria	MIC alone µg/mL		MIC in combination µg/mL		FICI	Meaning
	RN7IN6	CTX	RN7IN6	CTX		
***S. aureus* NCTC 12241**	16	2	8	0.5	0.75	Partial synergism
			4	1	0.75	Partial synergism
***E. coli* NCTC 12241**	32	0.062	4	0.031	0.625	Partial synergism
	32	0.062	16	0.062	1.5	Indifference
	32	0.125	8	0.062	0.75	Partial synergism
	32	0.125	4	0.062	0.625	Partial synergism
***P. aeruginosa* NCTC 12903**	256	16	256	16	2	Indifference
***K. Pneumoniae* NCTC 9633**	32	0.062	32	0.062	2	Indifference

In the case of *S. aureus* and *E. coli*, initial tests indicated partial synergism, which prompted a re-test to confirm the results. For *E. soli*, the second replicate did not fully corroborate the findings from the first test, leading to two additional replicates being performed to further evaluate the consistency of the synergistic effect. Results revealed that combinations of RN7IN6 and CTX showed partial synergistic effect with FICI < 1 against *S. aureus* and *E. coli* (Table 5-10). Unlike complete synergism (FICI < 0.5), partial synergism reflects a moderate potentiation of antimicrobial activity when the two agents are combined. From a practical perspective, this implies that while co-loading RN7IN6 and CTX within LPHNPs could enhance the efficacy of this combination, the degree of improvement may potentially be less pronounced and more challenging to detect compared to combinations exhibiting full synergism. These results, however, interestingly indicate that RN7IN6 was able to enhance the antibacterial activity of CTX against both Gram-positive (*S. aureus*) and Gram-negative (*E. coli*) bacteria. In particular, regarding *S. aureus*, both replicates were in agreement while for *E. coli* not all the replicates determined the same outcome. Studies have demonstrated that conducting multiple replicated of the MIC testing can enhance the accuracy and validity of the obtained MIC values [835-837] and are usually reported as a mean of different replicates. Typically, acceptable reproducibility criteria involve a high percentage of MIC results being within one or two dilutions of the modal MIC, which is the most frequently observed MIC value in a set of replicates, indicating consistent agreement among

replicates [838]. However, challenges exist in achieving high reproducibility, especially in antimicrobial susceptibility testing. For instance, MIC values can inherently vary by up to three two-fold dilutions due to biological variability and technical factors, which can impact the FICI determination [839]. In the specific case of E. coli, despite some differences in FICI values, 3 of the 4 replicates were in agreement indicating partial synergism between CTX and RN7IN6. Regarding the second checkerboard assay performed on E. coli, it can be observed from Table 5-10 that the high value for RN7IN6 (16 µg/mL) in combination with CTX, only a two-fold dilution lower than the MIC of RN7IN6 alone (32 µg/mL) , is responsible for the high FICI value of CTX and RN7IN6. When observing slightly different MIC values while employing the same anti-infective concentration and experimental conditions, several factors can contribute to this variability. These can include the strength of the growth medium used during the testing process [840], the inoculum size and age, temperature, and incubation time [841]. Therefore, it can be concluded that an experimental error might have occurred during the analysis of the first checkerboard assay against E. coli and that CTX and RN7IN6 showed partial synergism.

A potential explanation for the synergistic effects of AMP-antibiotic combinations is that the AMPs might enhance permeability by interacting with the bacterial cell wall/membrane, so facilitating the action of conventional antibiotics on their targets. Previous studies have demonstrated that β-lactam antibiotics, such as CTX, exhibit increased antimicrobial efficacy when used in combination with membranolytic peptides like nisin. These AMPs alter the shape of cells by creating pores, which enables antibiotics to enhance their effectiveness and inflict more significant damage to the cell wall [842, 843].

Contrary to *S. aureus* and *E. coli,* RN7IN6 was not able to improve CTX antibacterial activity against *P. aeruginosa* and *K. pneumoniae* giving a FICI ≥ 1. Since the initial assay results for *P. aeruginosa* and *K. pneumoniae* showed clear indifference, no further replicates were conducted to avoid unnecessary use of RN7IN6, thereby minimizing resource utilization. This approach allowed us to focus on bacteria where partial synergism was observed and warranted further investigation. A result of FICI ≥ 1 means

that the interaction between the actives in the combination is neither synergistic nor antagonistic but rather falls within a range where the combined effect is considered neither significantly positive nor negative. The observed differences in synergistic effects against various bacteria in this study can be attributed to the complex interplay of several factors inherent to the bacteria and the antimicrobial agents used in combination. Firstly, the distinct structural and physiological characteristics of different bacterial species influence their susceptibility to antimicrobial agents and their interactions. Secondly, variations in the expression levels and mechanisms of resistance among different bacterial species play a crucial role. RN7IN6, while showing moderate antimicrobial activity against Gram-negative bacteria like *E. coli*, typically exhibits lower activity in Gram-negative bacteria compared to Gram-positive organisms such as *S. pneumoniae* and *S. aureus*. AMPs commonly show better efficacy against Gram-positive bacteria [173, 606] due to their thicker peptidoglycan layer that provides more access points for AMPs. In contrast, Gram-negative bacteria, particularly *P. aeruginosa*, have an additional outer membrane that acts as a significant barrier, limiting the activity of AMPs like RN7IN6. Indeed, bacteria like *P. aeruginosa* are notorious for their multidrug resistance mechanisms, including efflux pumps, enzymatic degradation of antibiotics, and impermeability barriers [844, 845]. Therefore, these resistance mechanisms can limit the synergistic potential of CTX and RN7IN6. Furthermore, the distinct mode of action of the CTX and RN7IN6 contributes to the observed differences in synergism. The complementary mechanisms of action of these agents in inhibiting the cell wall synthesis and in disrupting bacterial membranes may result in synergism particularly against certain bacterial species where both mechanisms effectively target vital bacterial functions. Indeed, RN7IN6 showed alone a high MIC (Table 5-10) against *P. aeruginosa* indicating the ineffectiveness of the peptide. Additionally, CTX displayed a comparatively higher MIC against P. aeruginosa than against other bacterial strains tested (see 5.4.5.1).

In the specific case of RN7IN6 and CTX, no direct comparison with previous studies can be performed due to the lack of published data on RN7IN6. Jindal et al. assessed the synergism of RN7IN6 and ceftriaxone against susceptible and resistant strains of Streptococcus pneumoniae, a Gram-positive bacterium. Despite bacteria employed by

Jindal et al. being different to those of the current study, CTX and ceftriaxone are both third-generation cephalosporin antibiotics that share similarities in their spectrum of activity and efficacy against a wide range of pathogenic organisms [846]. Jindal et al. showed that RN7IN6 and ceftriaxone had a synergistic effect against both susceptible and resistant strains of S. pneumoniae [173] further corroborating findings of the current study where the antibacterial activity of a conventional antibiotic was enhanced by the addition of RN7IN6. Furthermore, Jindal et al. assessed the in vivo therapeutic synergism of ceftriaxone with RN7IN6. Their results clearly showed that the survival rates of mice treated with this combination at different doses was significantly higher compared to the cumulative survival rates of individual treatments [173].

As the combined activity of CTX and RN7IN6 showed a promising effect against both the Gram-positive S. aureus and the Gram-negative E. coli, the antimicrobial activity of the formulation CTX F.4 2R (LPHNPs co-loaded with CTX and RN7IN6, as optimized in section 5.4.3.1) was assessed against these bacteria as a next step.

5.4.5.3. Antimicrobial Activity of CHCL NPs and LPHNP Formulations

In addition to assessing the antimicrobial activity of CTX F.4 2R - the CTX and RN7IN6 co-loaded LPHNP formulation - CTX-loaded NPs (3 CTX CHCL NPs), CTX-loaded LPHNPs (CTX F.4) and empty LPHNPs (F.4) were also assessed to allow for determination of the individual contributions of each component and formulation type to any noted efficacy. However, given constraints around time and the availability and cost of RN7IN6, it was not deemed feasible to assess the antimicrobial activity of RN7IN6-only loaded LPHNPs as part of this panel of formulation testing. For this reason, the following studies and the accompanying discussion will focus on the impact of RN7IN6 on CTX activity within co-loaded LPHNPs, rather than specifically examining and referring to synergism. Evaluating the antimicrobial efficacy of RN7IN6-only LPHNPs is identified as a clear direction for future work.

The MIC results for all the formulations tested against S. aureus and E. coli are shown in Table 5-11.

Table 5-11: Antibacterial activity (MIC values) of various empty and CTX/RN7IN6 loaded formulations as well as CTX-loaded CHCL NPs for comparison, against S. aureus *and* E. coli *assessed using the REMA assay (n=3 technical replicates). Note: Empty LPHNPs were diluted using the same dilution factor as the loaded LPHNPs to achieve equivalent particle concentrations in the formulations.*

Bacteria	MIC (µg/mL)				
	CTX-loaded CHCL NPs	CTX-loaded LPHNPs	Empty LPHNPs	CTX/RN7IN6-loaded LPHNPs	
				CTX F.4 2R	
	3 CTX CHCL NPs	CTX F.4	F.4	CTX	RN7IN6
S. aureus NCTC 12981	4	8	64	6	4
E. coli NCTC 12241	0.25	0.25	2	<0.375	<0.25

5.4.5.3.1. Antimicrobial Activity of CTX-loaded CHCL NPs – 3 CTX CHCL NPs

Results from this study showed that the MIC of CTX-loaded CHCL NPs was 2-fold higher (Table 5-11) than the MIC of free CTX (Table 5-9). When CTX is encapsulated within NPs, its release is somewhat sustained rather than being immediately available to interact with bacteria, as is the case for antibiotic in solution. These results can be considered to be in agreement with the results obtained from the release study for CTX-loaded CHCL NPs (Figure 5-22). Within the first 24 hours, which is the incubation time for the 96-well plates, only 51% of CTX was seen to be released from the CHCL NP formulation. The sustained release of CTX can lead to a slower onset of its effects, meaning that a higher encapsulated concentration is needed to achieve the same inhibitory effect as the freely available substance, which can immediately interact with bacterial targets. However, this assumption does not fully account for the potential contribution to antibacterial activity mediated by the interaction of the cationic CHCL NPs with the negatively charged bacterial cell envelopes. This interaction may facilitate increased uptake and association of the LPHNPs with bacterial cells, thereby enhancing the local concentration of the antibiotic at the bacterial site and potentially bypassing the need for full release before exerting an effect. A study conducted by Jiang *et al.* showed that gentamicin-

loaded PLGA NPs exhibited reduced antimicrobial effects in comparison to equivalent concentrations of the free drug [847]. It was hypothesized that this was a consequence of the delayed exposure of the antibiotic to the bacteria which is also in accordance with the gentamicin release kinetics observed [847]. However, Jiang *et al.* were also able to prove that the encapsulation of gentamicin within a nanocarrier enhanced the survival rate of *Galleria* larvae infected with *K. pneumoniae* from 24 hours with free gentamicin, to 72 hours [847]. Similarly, the study carried out by Cheow *et al.* demonstrated a biphasic release profile of levofloxacin from PLGA or PCL nanoparticles where a fast initial release is followed by a sustained slow release, allowing prolonged exposure of bacteria to the drug over several days as being crucial for eradicating biofilm-forming bacteria. This extended release helps maintain therapeutic concentrations of the antibiotic, facilitating effective bacterial suppression even after the initial burst of drug release [848].

5.4.5.3.2. Antimicrobial Activity of CTX-loaded LPHNPs - CTX-F.4

Similarly to CTX-loaded CHCL NPs, CTX F.4 formulations showed a 4-fold higher MIC against *S. aureus* and a 2-fold higher MIC against *E. coli* in comparison to free CTX. In comparison with CTX-loaded NPs, the introduction of a lipid shell led to a reduced antimicrobial activity against the Gram-positive *S. aureus* and a comparable activity against the Gram-negative *E. coli*, indicating the potential influence of the lipid shell composition on the antimicrobial efficacy (Table 5-11). The POPE:POPG:CL lipid shell in CTX F.4 LPHNPs showed a slight reduction in the initial burst release compared to CTX-loaded CHCL NPs (Figure 5-22). Although this alteration in release kinetics was modest and derived from limited replicates, it may nonetheless contribute to variations in antimicrobial efficacy, particularly in preserving activity against *E. coli*. This observation suggests that even minor modifications in early release profiles could impact the antibacterial activity of the formulation. These findings underscore the importance of determining an optimal release profile for CTX, balancing early and sustained drug availability to enhance antibacterial activity across target pathogens. Further investigation is warranted to assess how variations in release kinetics may modulate

antibacterial efficacy, given that these nuanced differences could be critical to maximizing therapeutic outcomes.

5.4.5.3.3. Antimicrobial Activity of Empty LPHNPs – F.4

To further investigate any input of the formulation itself in the antimicrobial activity of loaded LPHNPs, the empty LPHNP formulation F.4, with the same dilution factor as used for CTX-loaded NPs and CTX-loaded LPHNPs, was tested against *S. aureus* and *E. coli*. Interestingly, the results showed that empty LPHNPs had an antimicrobial activity against both bacteria, with the MIC being considerably lower for the Gram-negative *E. coli* as compared to the Gram-positive *S. aureus* (Table 5-11). This result is of some interest, particularly given that empty CHCL NPs and more specifically, bacteriomimetic liposomes, similar to the surface-exposed shell structure of LPHNPs (see sections 2.4.4.2 and 4.3.2.2.2, respectively), revealed no activity against either Gram-positive or Gram-negative bacteria. Table 5-11[849-852] Therefore, the observation of antimicrobial activity for LPHNPs, but not for empty liposomes in particular, raises an important question. This discrepancy could potentially be attributed to differences in lipid layer structure, thickness, or fluidity between liposomes and LPHNPs. These factors might influence the interaction between the nanoparticles and bacterial membranes, and therefore warrant further investigation. Future studies could explore this hypothesis using advanced imaging and analytical techniques to provide a detailed view of nanoparticle-bacteria interactions. Scanning electron microscopy and transmission electron microscopy could help visualize the binding affinity and morphological effects of CS NPs, liposomes, and LPHNPs on bacterial surfaces. Langmuir studies, by examining lipid monolayer behavior under various conditions, could offer insights into lipid shell dynamics, specifically in terms of molecular packing within the monolayer, mimicking interactions at the bacterial membrane level. Moreover, techniques such as small-angle X-ray scattering or atomic force microscopy could help determine lipid shell thickness, structure (monolayer versus bilayer), and fluidity. This structural data would be valuable in understanding how lipid shell composition and organization influence both drug release kinetics and the nanoparticle's efficacy in disrupting bacterial membranes.

5.4.5.3.4. Antimicrobial Activity of CTX and RN7IN6-loaded LPHNPs – CTX F.4 2R

Antimicrobial activity assessment was also performed on CTX and RN7IN6 co-loaded LPHNPs (CTX F.4 2R formulation optimized in Section 5.4.3.1) alongside the other formulations discussed above. However, some limitations and constraints of the testing should be acknowledged here as already alluded to in part in section 5.4.5.3.

Firstly, the co-loaded formulation was developed before the results from the CTX and RN7IN6 synergism assessment were available, and ahead of empty and CTX-loaded formulation antimicrobial activity assessment. Therefore, CTX and RN7IN6 co-loaded LPHNPs were purely optimized at this stage with a view to obtaining the highest CTX and RN7IN6 loading efficiency possible, in order to maximize the potential antimicrobial effect and minimize the dose required. Subsequent to this formulation optimization, it was determined that CTX showed a higher antimicrobial efficacy than RN7IN6 against *E. coli* and *S. aureus* with lower MIC values (see Table 4-4 and Table 5-9). Given that the amount of CTX encapsulated within CTX F.4 2R is considerably higher than that of RN7IN6 (see Figure 5-18 B) and considering the higher intrinsic antimicrobial activity of CTX, results obtained for the co-loaded formulation must be interpreted carefully. The conscious decision not to formulate RN7IN6-loaded LPHNPs as a standalone control, necessitates further caution, particularly with regard to evaluation of any potential synergistic effects.

The MIC results for CTX F.4 2R against *E. coli* and *S. aureus* are shown in Table 5-11. CTX and RN7IN6 co-loaded LPHNPs showed antimicrobial activity against both the Gram-positive and Gram-negative bacteria assessed. Specifically, CTX F.4 2R showed an MIC corresponding to 6 µg/mL for CTX and 4 µg/mL for RN7IN6 against *S. aureus,* while the formulation showed an MIC below the lowest concentrations tested for both CTX and RN7IN6 (<0.375 µg/mL and <0.25 µg/mL, respectively) against *E. coli*. When focusing on the CTX contribution, it can be observed that the MIC against *S. aureus* was lower for the co-loaded formulation compared to the CTX-only formulation. This result suggests an advantage of incorporating RN7IN6 into CTX-loaded LPHNPs, as the reduction in MIC demonstrates that the combination of CTX and RN7IN6 is more effective at inhibiting bacterial growth than CTX alone. However, this improvement is not observed in

comparison to CTX CHCL NPs. Specifically, as previously discussed, the MIC for *S. aureus* in CTX-loaded LPHNPs was 8 µg/mL compared to 4 µg/mL for CTX CHCL NPs. These findings highlight the potential modulation of antimicrobial activity due to the lipid coating as well as then inclusion of RN7IN6 within the lipid shell as compared to CTX-loaded CHCL NPs.

Regarding findings for *E. coli,* exact MIC values for CTX and RN7IN6 could not be determined for the co-loaded LPHNP as these values were lower than the lowest concentrations contained in formulations assessed. This outcome is encouraging however, suggesting that the antimicrobial activity of the co-loaded formulation was so potent that even at the highest dilution employed, complete inhibition of *E. coli* growth was observed, indicated by a blue color in the resazurin assay across all wells. This highlights the strong bactericidal effect of CTX F.4 2R, but also suggests that future studies should explore lower concentration ranges to accurately determine the MIC.

The considerations from sections 5.4.5.3.2 and 5.4.5.3.3, highlighting the antimicrobial activity observed with empty and CTX-loaded LPHNPs, indicate that this hybrid structure may enhance bacterial membrane interactions, particularly with Gram-negative bacteria like *E. coli*. Given that the MIC for CTX in the co-loaded LPHNPs is <0.375 µg/mL, closely aligned with (and likely, even lower than) the 0.25 µg/mL MIC observed for CTX-loaded NPs and CTX-alone LPHNPs, it is reasonable to assume that the antimicrobial activity of the co-loaded formulation is at least comparable, if not superior, to these formulations.

While the above hypothesis can be postulated, it is not possible to speculate on whether the co-loading of CTX and RN7IN6 within LPHNPs provides a synergistic effect or not. When looking, cautiously, at the RN7IN6 contribution, it is possible to observe that the MIC against both bacteria was much lower than the MIC of free RN7IN6 (see section 4.4.1.2 and Table 5-11). However, this is likely an artefact attributed to the high concentration of CTX within the formulation. Consequently, the antimicrobial effect observed in the co-loaded formulation is likely predominantly due to CTX rather than RN7IN6. This underscores the challenge in isolating the specific contribution of RN7IN6

to the antimicrobial activity of CTX F.4 2R. Future studies prioritizing the formulation and investigation of RN7IN6-only loaded LPHNPs would be of considerable interest and would allow for the precise assessment of the individual antimicrobial properties of RN7IN6 and its potential role in enhancing therapeutic efficacy of CTX within the LPHNP delivery system. Additionally, reducing the CTX loading within co-loaded LPHNPs to achieve a fixed-dose combination where both CTX and RN7IN6 are present at their respective MIC levels could provide critical insights into the synergistic effects or independent action of the two agents. This approach would not only help delineate their respective contributions but also optimize the co-delivery system for potential clinical applications.

Previous studies revealed that use of LPHNPs that simultaneously deliver multiple medications have shown an improvement in therapeutic efficacy due to the enhanced bioavailability, sustained release, and targeted delivery provided by the LPHNP delivery system. Indeed, Jaglal *et al.* demonstrated that co-loading vancomycin and 18β-glycyrrhetinic acid, a natural triterpenoid with antimicrobial properties, into pH-responsive LPHNPs resulted in an 8-fold higher antibacterial activity against MRSA at pH 6, compared to singly-loaded vancomycin LPHNPs, with 75% bacterial elimination achieved in less than 12 hours [853]. In contrast, while our study observed enhanced antimicrobial efficacy of the CTX and RN7IN6 co-loaded formulation against *S. aureus* compared to the CTX-only loaded formulation, no definitive conclusions about synergism can be drawn due to limitations in the available data and the lack of consistent evidence for a synergistic effect. Similarly, Mohammadi *et al.* showed that the co-loading of curcumin and gentamicin into LPHNPs led to a potent antibacterial and antibiofilm activity against *P. aeruginosa* compared to when either compound was loaded individually into LPHNPs [854]. They attributed the enhanced antimicrobial activity to the synergistic effect of the dual-drug delivery system, wherein curcumin enhances the bactericidal properties of gentamicin, leading to effective eradication of bacterial biofilm [854], corroborating findings of other similar studies [855]. LPHNP delivery systems have therefore demonstrated efficient cellular uptake by bacterial cells, facilitating targeted drug delivery and intracellular action [854], thus highlighting

the potential of LPHNPs as a promising therapeutic strategy for co-delivering drugs and combating infections.

Despite challenges in delineating the specific contribution of RN7IN6 due to the predominance of CTX effects in the co-loaded LPHNPs, and challenges in identifying MIC value for CTX F.4 2R against *E. coli* due to the MIC being lower than the tested range of concentrations, this study demonstrates that co-delivery of CTX and RN7IN6 within LPHNPs enhances antimicrobial efficacy against Gram-positive bacteria in comparison to CTX-only loaded LPHNPs. Moreover, these results suggest that the co-loaded CTX and RN7IN6 LPHNPs demonstrate particularly strong activity against *E. coli*, with MIC values below the lowest concentration tested, and likely also lower than the MIC observed for CTX-loaded NPs and CTX-alone LPHNPs. This observation underscores the potential of this co-delivery system for achieving potent and broad-spectrum antibacterial effects, against both Gram-positive and Gram-negative bacteria.

5.5.Conclusion

The co-loaded LPHNP formulation developed and optimized in this study, CTX F.4 2R, demonstrated promising characteristics for drug delivery applications with respect to size, PDI and Z-potential. The introduction of a lipid shell composed of POPE, POPG and CL surrounding the CHCL NP core and the encapsulation of RN7IN6 within the external shell showed a small, but noteworthy impact on CTX release behavior in comparison to CTX-loaded CHCL nanoparticles, while RN7IN6 was hypothesized to largely be retained within the lipid shell of co-loaded LPHNPs. While the specific contributions of RN7IN6 and the lipid shell to the overall antimicrobial activity of co-loaded LPHNPs remain to be elucidated due to the predominant influence of CTX , the antimicrobial activity of co-loaded LPHNPs observed against Gram-positive *S. aureus* and particularly, the Gram-negative bacterium *E. coli* (as well as the intrinsic Gram-negative activity of empty LPHNPs) underscores the considerable potential of LPHNPs as a versatile platform for antimicrobial drug delivery. The synergistic effect observed for free CTX and free RN7IN6 against *S. aureus* and *E. coli* highlights their complementary mechanism of action and sets the basis for further exploration of their combined efficacy within the LPHNP formulation. Further investigation into the mechanisms underlying the observed effects is warranted to fully harness the therapeutic potential of LPHNPs. Specific investigations following on from the work described in this Chapter could include elucidating the lipid layer thickness and structure (monolayer vs. bilayer) of LPHNPs, assessing the potential interactions between RN7IN6 and the lipid bilayer of bacteria, and importantly, exploring the mechanisms and extent of interaction of LPHNPs with bacterial membrane structures .

6. Summary Overview of the Project and Future Work

6.1. Summary Overview of the Project

The overarching aim of this project was to develop and optimize LPHNPs as an advanced nanocarrier delivery system for the co-delivery of the antibiotic CTX and the AMP RN7IN6. This work is situated within the broader scientific context of the global AMR crisis, which has severely limited the efficacy of many conventional antibiotics, particularly against Gram-negative bacteria. In response to this challenge, novel drug delivery platforms capable of enhancing the therapeutic potential of both conventional antibiotics and alternatives such as AMPs are urgently needed. The project focused on the formulation of two primary types of drug delivery systems — CS NPs and POPE:POPG:CL liposomes — as key LPHNP components, ultimately progressing toward LPHNPs to co-deliver CTX and RN7IN6.

6.1.1. Scientific Background and Rationale

AMR represents one of the most significant global health threats of our time [4]. The WHO has consistently emphasized the critical need for novel antimicrobial agents and innovative drug delivery systems to combat multidrug-resistant bacterial strains, which are responsible for significant morbidity and mortality worldwide [26]. Current estimates suggest that by 2050, AMR could lead to 10 million deaths annually, surpassing even cancer as a leading cause of death [4].

The rise of resistant strains is largely due to the overuse and misuse of antibiotics [54], resulting in resistance mechanisms such as β-lactamase production and the upregulation of efflux pumps, which expel drugs from bacterial cells. These mechanisms significantly reduce the efficacy of standard treatments like β-lactams [65], including CTX, a broad-spectrum cephalosporin widely used in clinical settings. One critical challenge is the increasing prevalence of ESBLs and carbapenemases produced by Gram-negative bacteria like *E. coli* and *K. pneumoniae*, which render β-lactam antibiotics ineffective. In addition, pathogens like *P. aeruginosa* and *A. baumannii* exhibit intrinsic

resistance due to their impermeable outer membranes and highly efficient efflux systems, further complicating treatment efforts. Addressing AMR requires innovative drug development and delivery strategies that can bypass traditional resistance pathways while enhancing the efficacy and specificity of existing treatments [4].

As mentioned, one of the primary issues facing the treatment of bacterial infections is the development of resistance to standard antibiotic regimens, such as CTX. To address this, researchers are investigating nanocarrier systems that can deliver antimicrobial agents in a controlled, targeted manner, thus enhancing drug efficacy while reducing systemic side effects. Nanotechnology offers a promising solution by enabling the encapsulation of antimicrobial agents, protecting them from degradation and allowing for their gradual release in targeted sites of infection [198]. Polymeric NPs and liposomes, two well-studied drug delivery platforms, offer the potential for improving the pharmacokinetic and pharmacodynamic profiles of antimicrobial agents. By exploring both platforms individually at first, and then in combination as components of LPHNPs, this project sought to leverage the individual strengths of these nanocarrier systems and understand how they could be optimized for enhanced, dual-drug delivery of a conventional, water-soluble antibiotic and a novel, amphiphilic AMP.

The choice of co-loading a conventional antibiotic, CTX, with a novel AMP, RN7IN6, was driven by the need to combat bacterial infections via multiple mechanisms of action. CTX inhibits bacterial cell wall synthesis by targeting penicillin-binding proteins [436], which are essential for the cross-linking of peptidoglycans in the bacterial cell wall. This action predominantly targets Gram-negative bacteria, which possess a thinner peptidoglycan layer but are protected by an additional, outer membrane (Figure 1-2), making them particularly susceptible to β-lactams. However, many bacterial strains, such as *E. coli* and *K. pneumoniae*, have developed resistance to CTX through the production of β-lactamases, which hydrolyze the β-lactam ring and render the antibiotic ineffective [74]. RN7IN6 offers a complementary mechanism of action by disrupting bacterial membranes through electrostatic interactions between its positively charged residues and the negatively charged components of bacterial membranes [173, 606], such as LPS in Gram-negative bacteria and teichoic acids in Gram-positive bacteria. This

mechanism, characteristic of AMPs, may allow RN7IN6 to bypass β-lactamase-mediated resistance, as it does not rely on targeting penicillin binding proteins but rather induces bacterial membrane destabilization, leading to pore formation, leakage of intracellular contents, and eventual cell death [173, 606].

Together, these two drugs were hypothesized to act synergistically, potentially overcoming bacterial resistance by attacking bacterial cells through different pathways. This hypothesis was further supported by studies from Jindal *et al.* demonstrating synergism between RN7IN6 and ceftriaxone, a β-lactam antibiotic similar to CTX, which strengthens the rationale for co-loading a nanocarrier with CTX and RN7IN6 in this project [173, 606]. The ultimate aim was to create a versatile nanocarrier platform that could co-deliver CTX and RN7IN6, providing dual-action antimicrobial therapy capable of addressing bacterial infections. The development process was guided by the need to ensure stable encapsulation and optimized particle size for effective bacterial interaction.

6.1.1.1. Optimizing Antimicrobial Delivery: CS Nanoparticles and Bacteriomimetic Liposomes

The selection of materials and delivery systems is critical for optimizing the therapeutic efficacy of antimicrobial agents. This project focused on NPs (composed of CS) and liposomes (composed of a POPE:POPG:CL mixture), two well-studied drug delivery platforms, due to their unique properties that make them highly suitable for delivering conventional antibiotics as well as novel AMPs. These systems were chosen for their potential ability to enhance the stability and release of CTX and RN7IN6, ultimately with the aim of merging them into LPHNPs for combination drug delivery.

The advantages of nanoparticle-based drug delivery systems, particularly CS NPs, make them an attractive option for antimicrobial delivery. CS, a natural polymer derived from chitin, is widely used in pharmaceutical applications due to its biocompatibility, biodegradability, and inherent antimicrobial properties [379, 466, 468, 469]. The positive charge of CS allows it to interact electrostatically with negatively charged bacterial membranes, which can enhance its ability to target and disrupt bacterial cells

[418, 423]. These characteristics make CS an ideal material for nanoparticles, as it not only serves as a carrier for antibiotics like CTX but may also contribute to the overall antimicrobial effect. In addition to this, CS is known for its mucoadhesive capabilities, which allow nanoparticles to adhere to mucosal surfaces in the body, enhancing localized delivery [465]. This is particularly useful for targeting infections in the respiratory and gastrointestinal tracts, where biofilms and mucosal barriers can limit the efficacy of traditional drug delivery methods.

The process of forming CS nanoparticles typically involves ionic gelation with a crosslinking agent like TPP, which helps stabilize the particles and control their size [393]. In this project, the formation of CS NPs was optimized to achieve highly monodispersed particles while maintaining high encapsulation efficiency for CTX. A high positive surface charge of the NPs was also noted[856]. The versatility of CS NPs, particularly their ability to encapsulate hydrophilic drugs like CTX with high efficiency, makes them a strong candidate for nanoparticle-based antimicrobial delivery systems.

Liposomes, which are vesicles composed of one or more phospholipid bilayers, are well-known for their ability to encapsulate both hydrophilic and hydrophobic drugs [335], making them particularly suitable for incorporation and delivery of amphiphilic molecules like AMPs. Liposomes used in this project were composed of POPE, POPG, and CL, carefully selected in order to design liposomes with bacteriomimetic properties, as highlighted in the work of Graef *et al.* [312]. These lipids closely resemble the composition of bacterial membranes, particularly those of Gram-negative bacteria [312], making them ideal to improve liposome interaction with the notoriously hard to treat Gram-negative bacteria themselves [312].

POPE is a neutral phospholipid commonly found in bacterial membranes [687]. Its inclusion in the liposome formulation helps promote liposome membrane fusion and flexibility, potentially enhancing the ability of the liposomes to merge with bacterial cell membranes [555]. POPG and cardiolipin are negatively charged phospholipids that are abundant in the membranes of Gram-negative bacteria [312] - as such, they play key roles in the bacteriomimetic properties of formed liposomes. By mimicking the composition of bacterial membranes, these liposomes were designed to improve the

interaction with and uptake of RN7IN6 by bacterial cells, potentially enhancing its antimicrobial activity. Moreover, AMPs like RN7IN6 are prone to enzymatic degradation in the bloodstream, which limits their therapeutic potential when administered systemically [179]. By encapsulating RN7IN6 within liposomes, the peptide is protected from degradation, allowing it to reach the site of infection in higher concentrations. Hence, the selection of CS NPs and POPE:POPG:CL liposomes was driven not only by their individual advantages but also by their complementary properties, which together were hypothesized to create an even more effective drug delivery system. While CS NPs might potentially offer antimicrobial properties as well as stability and robustness, POPE:POPG:CL liposomes are capable of providing a degree of fluidity and bacteriomimetic properties for more specific bacterial envelope interactions. This complementary functionality is critical for addressing the limitations of traditional antibiotic therapy, particularly in cases of multidrug-resistant bacterial infections where a combination of drugs with different mechanisms of action is required.

The manufacture of both CS NPs and POPE:POPG:CL liposomes in this project was achieved using microfluidic mixing, which offers advantages over conventional NP or liposome preparation methods such as solvent evaporation or thin film hydration by providing precise control over particle size, polydispersity, and encapsulation efficiency [327]. Microfluidics allows for rapid mixing at the microscale, reducing batch-to-batch variability and ensuring consistent production of nanocarrier systems, making it ideal for scalable manufacturing [327].

The initial development of these two systems, CS NPs and POPE:POPG:CL liposomes, served as the foundation for their eventual combination into LPHNPs. By developing them separately, the aim was to understand their individual characteristics, such as the ability of CS NPs to encapsulate hydrophilic drugs like CTX and the capacity of bacteriomimetic liposomes to serve as carriers for AMPs associated with their lipid bilayer. This work laid the groundwork for the later merging of these two platforms into a hybrid system.

6.1.2. Design and Optimization of CS NPs for CTX delivery

The thesis began with the development and optimization of empty CS NPs. Two types of CS were considered for this formulation: CHT, which is soluble in slightly acidic solutions, and CHCL, which provides the advantage of water solubility over CHT. Initial studies focused on the preparation and optimization of empty NPs to understand their physicochemical properties, including particle size, PDI, and Z-Potential, which are critical for both stability and interaction with bacterial cells. The goal was to create particles with a small size and narrow PDI, and a sufficiently positive Z-Potential to allow for coating with POPE:POPG:CL lipid mixture in the second step of the project.

Optimization of empty NPs involved examining multiple factors, including CS and TPP concentration as well as flow parameters in the microfluidic mixing process (Table 2-2). Using a DoE approach, the formulations were fine-tuned to achieve the desired particle characteristics. Subsequently, the FRR was systematically varied to study its effects on CS NP size and PDI (Figure 2-6 and Figure 2-7). It was observed that formulations manufactured using FRR ranging from 1.75:1 to 7:1 for CHT NPs and between 1.25:1 and 7:1 for CHCL NPs showed a considerably smaller size and more monodisperse size distribution compared to formulations manufactured with smaller FFR values (Figure 2-6 and Figure 2-7). Therefore, optimum manufacturing parameters for empty CHT and CHCL NPs were selected within this range as shown in Table 2-5.

Once the empty formulations were optimized, the focus shifted to loading CTX into the CS NPs. Encapsulation efficiency was a key parameter during this phase, as the goal was to maximize the amount of CTX encapsulated while maintaining favorable particle characteristics. Increasing CTX loading concentrations ranging from 0.3 mg/mL to 3 mg/mL were added either to the CS solution or the TPP solution – a novel step, as the addition of the antibiotic to either CS or TPP solutions to understand the impact on NP physiochemical characteristics has not been systematically investigated and documented in literature to-date. The results showed that, when CTX was added to the CHT or CHCL solution, NP size and PDI , was increased in comparison to the empty formulations and to formulations manufactured with CTX added to the TPP solution (Figure 2-12 and Figure 2-13). Moreover, despite no significant changes being observed

in the Z-Potential with increasing CTX loading concentrations, a significantly higher surface charge was noted for CHCL-based formulations (~ 30 mV) in comparison to CHT-based formulations (~ 10 mV, Figure 2-14). This was particularly important when considering the subsequent coating of these NPs with lipids in the LPHNP system, where a higher Z-Potential would likely result in more efficient lipid coating and particle stability.

Increasing CTX loading concentrations from 0.3 mg/mL to 3 mg/mL led to an increase in EE% for both CHT and CHCL NPs, with EE% rising from ~15 % to ~ 38 % in CHT NPs and showing a similar trend for CHCL NPs (Figure 2-15). The amount of CTX encapsulated per mL of formulation also increased significantly across all loading concentrations, with higher encapsulation observed with 3 mg/mL of CTX loading concentration when CTX was added to TPP rather than CS solution (Figure 2-16). Notably, the encapsulation efficiency did not plateau at any point across the loading concentration range, which might indicate that the saturation capacity of NPs was not reached using a 3 mg/mL CTX loading concentration.

The purification of CTX-loaded NPs was also a critical step in the development process, and therefore ultracentrifugation and ultrafiltration were assessed as potential purification methods. Results obtained showed a different impact of both purification techniques on the NP size, PDI, Z-Potential and EE%. Despite ultrafiltration demonstrated the ability to better preserve formulation physicochemical characteristics upon purification (Figure 2-18), it also resulted in a higher calculated CTX EE% in comparison to ultracentrifugation (Figure 2-17). This may potentially occur as a result of filter clogging and interactions with free CTX, leading to an overestimation of EE%, especially at higher loading concentrations. On the other hand, ultracentrifugation, while yielding lower EE% values, was thought to provide a more reliable measure of drug encapsulation – despite it resulting in some particle aggregation, particularly with CHCL NPs (Figure 2-18). However, neither method was entirely optimal. Ultrafiltration preserved particle characteristics but overestimated EE%, while ultracentrifugation, though more accurate for EE%, caused particle aggregation. Future work should

therefore involve optimizing or finding alternative purification methods to balance particle integrity with accurate EE% estimation.

In conclusion, after evaluating multiple production parameters, the 3 mg/mL CTX loading concentration in the TPP solution was identified as optimal for encapsulating CTX in CS NPs, as it achieved the highest CTX loading concentration without significantly affecting particle size or PDI as discussed in section 2.3.2.3. CTX-loaded CHCL NPs were selected over CHT NPs for further development into LPHNPs, as CHCL offers simplified production due to its water solubility, which enhances process efficiency by eliminating the need for specific solubilizing conditions. Moreover, CHCL-based NPs demonstrated a higher Z-potential (~30 mV) compared to CHT NPs (~10 mV), facilitating stronger electrostatic interactions with negatively charged lipid components in the hybrid nanoparticle system. Consequently, CTX-loaded CHCL NPs at the 3 mg/mL loading concentration of CTX were identified as the optimal formulation for further development in this project.

6.1.3. Development and Optimization of RN7IN6-Loaded Liposomal Formulations

The development of POPE:POPG:CL liposomes for the delivery of AMPs followed a similar systematic approach as for CS NPs, beginning with the formulation and optimization of empty liposomes in terms of their particle size, PDI, and Z-Potential, which are critical for stability, drug loading, and cellular interactions.

A DoE approach was employed to optimize formulation parameters, including lipid concentration, FRR between PBS buffer and lipid mixture solutions, and TFR during the microfluidic mixing process. FRR was found to have the greatest impact on liposome size (Figure 3-4). The optimum formulation, identified as F7 (see section 3.4.1), showed a size of 89 nm, a PDI of 0.14 and a negative Z-Potential (-22 mV). The formulation (1 mL) was then dialyzed against 100 mL of PBS for 6 hours. No significant changes in formulation physiochemical characteristics were observed (see section 3.4.1.2), and the formulation was therefore deemed to remain stable without signs of aggregation.

After the optimization of empty liposomes, RN7IN6 was intended to be adsorbed onto liposome surfaces to enable rapid interaction with bacterial membranes, maximizing antimicrobial activity through immediate contact and electrostatic interactions. This approach aimed to enhance efficacy by ensuring faster action compared to AMP encapsulation within the lipid bilayer, which could slow its release. To achieve this goal, nisin, a well-studied AMP, was first used as a model to guide the development of the RN7IN6-adsorbed liposomes. Indeed, using a model AMP like nisin provided a well-characterized framework to understand the general behavior of AMPs in the liposomal formulations. Moreover, as RN7IN6 was synthesized and purified in-house, employing a model peptide in the first instance allowed the optimization process to proceed more efficiently, minimizing the risk of material loss and reducing the time and cost associated with considerable RN7IN6 production, purification and subsequent use in formulation trials.

Using an initial DoE approach investigating nisin concentration, TFR and FRR, nisin was successfully surface-adsorbed onto bacteriomimetic liposomes, showing no aggregation upon purification with dialysis (Figure 3-8). The AE% for nisin-adsorbed formulations (F13, F15 and F19) exceeded 60%, with the concentration of loaded nisin increasing with increasing initial loading concentration (Figure 3-10), making it an ideal starting point for the RN7IN6-adorbed formulations. However, when the same surface adsorption parameters employed to manufacture F13, F15 and F19 were applied to RN7IN6, the results were less promising.

The adsorption of RN7IN6 to the liposomes resulted in increased particle sizes and PDI values compared to nisin-adsorbed formulations, indicating less reproducible formulations and the potential aggregation of liposomes. This was particularly evident in formulations where higher concentrations of RN7IN6 were used (F19, Figure 4-11). The Z-Potential also showed a notable decrease with increasing RN7NI6 loading concentrations, indicating that the adsorbed peptide (~75%, Figure 4-12) was neutralizing the negative charge of the POPE:POPG:CL liposomes. This drop in Z-Potential could potentially compromise the stability of the formulation, as a higher Z-

Potential is typically required to maintain colloidal stability and prevent aggregation [675].

Moreover, despite the strong antimicrobial activity of free RN7IN6 (Table 4-4), the adsorbed liposomes showed no significant antimicrobial effect against *S. aureus* or *E. coli* (Figure 4-13). The adsorption of RN7IN6 onto POPE:POPG:CL liposomes increased particle size and PDI. Notably, this aggregation appeared more pronounced with higher RN7IN6 loading, such as in F19, where increased peptide adsorption correlated with greater size and PDI values (see Figure 4-11). Therefore, in response to this unexpected outcome, the formulation strategy was adjusted, and RN7IN6 was encapsulated within the liposome bilayer rather than adsorbed onto the surface. It was hypothesized that lipid bilayer encapsulation of RN7IN6 could lead to improved formulation reproducibility and less aggregation. Therefore, RN7IN6 was dissolved in the lipid mixture to allow for its encapsulation within the liposomal layer using a systematic approach which investigated increasing initial RN7IN6 concentration, as well as different FRRs between PBS buffer and lipid/RN7IN6 solutions (Table 4-3).

The screening of 13 RN7IN6-loaded formulations revealed key trends in liposome size, PDI (Figure 4-14), and Z-potential. Higher initial RN7IN6 concentrations and FRRs generally resulted in larger particle sizes and less negative Z-potentials (Figure 4-15). Following purification with ultracentrifugation, most formulations showed a reduction in both size, PDI and Z-Potential, likely due to the removal of excess, unencapsulated peptide, which reduced the likelihood of aggregation [685] and resulted in more homogeneous liposome populations.

The most promising candidates from each RN7IN6 loading concentration – F22, F31, and F41 – were further investigated for their EE%. All three formulations showed high EE% (> 80%), with an increase in peptide loading as the initial RN7IN6 loading concentration increased (Figure 4-16). From these three formulations, F41 was ultimately selected for continuation due to its high EE%, as well as the lower peptide requirement as compared to F22, which was comparable in RN7N6 loaded concentration to F41 but was manufactured with a higher RN7IN6 loading concentration. This minimized the

consumption of RN7IN6, a crucial factor given the high cost and complexity of peptide synthesis and purification. Formulation F41 was assessed for its physiochemical stability over 7 days at 4 °C, and the formulation did not show any evidence of aggregation. This suggested an advantage of AMP bilayer incorporation in maintaining the physicochemical properties of the liposomes, and avoidance of the instability issues previously encountered for RN7IN6-adsorbed liposomes. However, despite these promising findings, F41 did not show any antimicrobial activity against *S. aureus* and *E. coli* (Figure 4-18). A subsequent release study confirmed that a cumulative release less than 10% of the encapsulated RN7IN6 was released over 14 days, potentially explaining the lack of activity; however, the lack of antimicrobial activity was still surprising, given the anticipated ability of bacteriomimetic liposomes to interact with bacterial cell envelopes and mediate direct transfer of AMP into these structures.

To address these challenges and questions future work could focus on optimizing the formulation to promote a more controlled release of RN7IN6, as well as investigating the interaction between the liposomal formulation and bacterial membrane structures to better understand how to enhance the delivery and efficacy of the encapsulated peptide.

6.1.4. Development and Optimization of LPHNPs

6.1.4.1. Formulation Development of Empty LPHNPs

Building on the findings from the optimization of CS NPs and POPE:POPG:CL liposomes, the focus of the thesis shifted towards the development and optimization of LPHNPs. The rationale behind the development of LPHNPs in this work lies in their ability to combine the developed polymeric CS NPs with a bacteriomimetic POPE, POPE and CL lipid coating. This hybrid structure makes LPHNPs a versatile platform for antimicrobial therapy. As such, the goal of this work was to develop LPHNPs capable of co-delivering both CTX and RN7IN6, exploiting the complementary properties of these two therapeutic agents to combat bacterial infections.

The formulation strategy involved using a core of CHCL NPs, which had previously shown a higher Z-Potential than CHT NPs, making it the ideal candidate for coating with anionic lipids. The initial optimization of empty LPHNPs was carried out using a DoE approach to evaluate the influence of various formulation parameters, such as lipid concentration, TFR and the FRR between NPs and lipid mixture during microfluidic mixing.

Initially, an L9 orthogonal array mixed-design Taguchi DoE was employed to systematically evaluate initial lipid concentration, TFR and FRR, allowing for more efficient identification of their effects compared to traditional 'one factor at a time' approaches. The results showed that the lipid concentration and the FRR were the most significant factors affecting LPHNP size, PDI, and Z-potential (Figure 5-3). The particle sizes of the different LPHNP formulations ranged from 168.6 nm to 3501 nm, with formulations prepared at lower lipid concentrations (2 mg/mL) exhibiting smaller particle sizes and more monodisperse populations (PDI < 0.15, Figure 5-3). These formulations also displayed more uniform characteristics compared to those prepared at higher lipid concentrations (8 mg/mL), which resulted in larger, more polydisperse particles. The Z-potential values of the LPHNPs ranged from -3.53 mV to -19 mV, with most formulations exhibiting a negative charge (Figure 5-3).

Further refinement of the process parameters, particularly lipid concentration and FRR, was carried out to achieve more optimal nanoparticle characteristics. A lower lipid concentration (0.5 mg/mL) and higher FRR (up to 6:1) were explored in follow-up studies, resulting in even smaller particle sizes and lower PDI values, confirming that reducing lipid concentration leads to more homogenous LPHNP formulations (Figure 5-5). Additionally, higher FRR values led to reduced lipid content in the LPHNP shell, shifting the Z-potential from slightly negative to slightly positive due to the relatively higher positive charge from the CHCL core. This adjustment minimized the likelihood of lipid-lipid interactions [787], thereby reducing aggregation and yielding more stable, smaller particles. However, this increase in Z-potential pushed the overall surface charge closer to zero, which is problematic for colloidal stability, as a Z-potential near zero can lead to reduced repulsive forces between particles and increased aggregation [857]. This

delicate balance of maintaining sufficient surface charge to prevent aggregation is crucial for ensuring the long-term stability of the formulation.

In addition to FRR and lipid concentration, TFR was investigated for its influence on LPHNP size and PDI. Results indicated that a higher TFR (20 mL/min) resulted in significantly smaller particle sizes compared to formulations prepared at a lower TFR (10 mL/min, Figure 5-7), further confirming that increased mixing efficiency at higher flow rates enhances the homogeneity and size uniformity of LPHNPs [790].

The optimization of these parameters culminated in the selection of the optimum parameters to manufacture LPHNPs (F.4, Figure 5-5) for further studies. Formulation F.4 was chosen based on its optimal size, PDI, and Z-potential, with TFR of 20 mL/min and lipid concentration of 0.5 mg/mL being identified as the best conditions for producing small, stable, and monodisperse LPHNPs. These findings highlight that microfluidic platforms allow for fine-tuning of parameters based on desired outcomes, ensuring adaptability and optimization for drug delivery applications. The flexibility in adjusting particle characteristics highlights LPHNPs as a versatile and efficient nanocarrier system, well placed for overcoming the limitations of traditional delivery methods.

6.1.4.2. Development of CTX- and RN7IN6-Loaded LPHNPs for Dual Drug Delivery

Following the development of empty and CTX-loaded LPHNPs, the next step was to optimize the co-loading of CTX and RN7IN6 into the LPHNP system. The goal was to incorporate both agents while maintaining the desirable physicochemical properties established in earlier stages, such as size, PDI, and Z-potential.

CTX-loaded LPHNPs were first manufactured by using optimum parameters to manufacture the CTX-loaded CHCL NPs, followed by lipid coating with POPE:POPG:CL, using optimum parameters identified for F.4. The CTX-loaded LPHNPs demonstrated an increase in particle size compared to CHCL NPs, indicating successful lipid coating (Figure 5-12). The Z-potential shifted from highly positive for CHCL NPs to near-neutral values after lipid coating, reflecting the incorporation of a negatively charged lipid shell. These

results are consistent with previous studies on lipid-coated nanoparticles and suggest effective coating with minimal aggregation [797].

The co-loading of CTX and RN7IN6 into LPHNPs was then optimized by systematically varying the RN7IN6 loading concentration ranging from 0.5 mg/mL to 2 mg/mL, while maintaining the same CTX concentration. The size and PDI of the co-loaded formulations remained similar to those of CTX-only LPHNPs, suggesting that RN7IN6 loading did not significantly alter the particle size or distribution (Figure 5-14). However, a slight reduction in Z-potential was observed with increasing RN7IN6 concentration, reflecting the neutralization effect of the positively charged peptide on the negatively charged lipid shell (Figure 5-14). While this reduction in Z-potential did not significantly affect colloidal stability, future optimization may be required to prevent potential aggregation over time. The EE% for CTX remained consistent across all formulations, with values around 10%, however, RN7IN6 EE% proportionally increased with the initial RN7IN6 loading concentration (Figure 5-18). This suggests that the system was not saturated at the RN7IN6 concentrations tested [812], leaving room for further optimization to maximize peptide loading.

Purification methods played a crucial role in maintaining the integrity of the co-loaded LPHNPs. Ultrafiltration proved to be the superior method, preserving particle size, PDI, and Z-potential (as summarized in Figure 6-1), unlike ultracentrifugation, which caused a significant particle aggregation and slightly increased PDI due to the high centrifugal forces (Figure 5-13). Ultrafiltration efficiently removed free drug and solvents while maintaining EE%, making it the preferred method for purifying LPHNPs in this work.

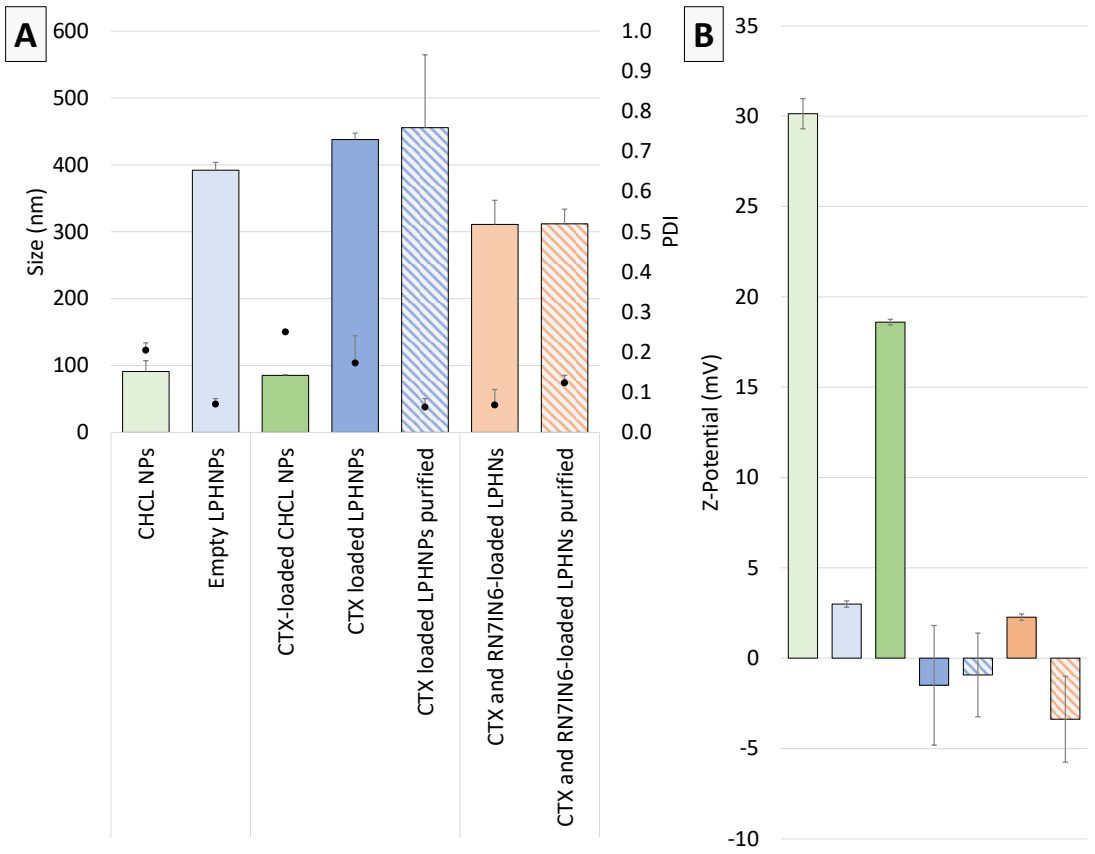

Figure 6-1: Summary of particle size, PDI (A) and Z-Potential (B) for the final optimized formulation panel, measured post manufacturing and following purification with centrifugal ultrafiltration.

In conclusion, the co-loading of CTX and RN7IN6 into LPHNPs demonstrated promising results, with both drugs encapsulated effectively without compromising the stability or physicochemical properties of the formulations. Further optimization of RN7IN6 EE% and investigation of scalable purification techniques, such as tangential flow filtration, will be essential for advancing this dual-drug delivery system.

6.1.5. Kinetics of Drug Release and Evaluation of Nanocarrier Antimicrobial Efficacy

The release kinetics and antimicrobial activity of both CTX and RN7IN6 were systematically evaluated when encapsulated within various nanocarrier systems, including CHCL NPs, POPE:POPG:CL liposomes, and LPHNPs. These investigations aimed to evaluate the equilibrium between free and encapsulated active agents over time and

to examine the potential synergistic effects when co-encapsulated within the same nanocarrier system. The findings from these studies offer critical insights into formulation efficacy and highlight key areas for further optimization.

6.1.5.1. CTX Release Kinetics and its Antimicrobial Performance in Nanocarrier Systems

CTX demonstrated similar release profiles across various nanocarrier formulations, including CHCL NPs, CTX-loaded LPHNPs, and co-loaded CTX/RN7IN6 LPHNPs (Figure 5-22). The release of CTX from CHCL NPs and LPHNPs followed a biphasic pattern, with an initial burst release occurring within the first 2 hours, followed by a much slower, sustained release. This profile facilitated immediate antimicrobial effects of CTX-loaded CHCL NPs and CTX-loaded LHNPs (Figure 5-10). While CHCL NPs provided stable encapsulation, further optimization is required to investigate the therapeutic action of the formulation over time, particularly for infections where prolonged drug release is essential to prevent bacterial regrowth.

In terms of antimicrobial activity, free CTX exhibited potent efficacy against both Gram-positive and Gram-negative bacteria, with pronounced activity against *S. aureus* and *E. coli*. Encapsulation of CTX in CHCL NPs demonstrated antimicrobial activity comparable to the free drug. The biphasic release pattern—an initial burst release followed by sustained release—was observed across formulations, though the impact of this release profile on bacterial inhibition warrants further studies. Notably, CTX degradation observed at 37 °C suggests that stability over the experimental period may influence antimicrobial efficacy, underscoring the need to consider degradation kinetics in interpreting release profiles.

6.1.5.2. Synergistic Potential of CTX and RN7IN6 Against Pathogenic Bacteria

The potential synergism of free CTX and RN7IN6 was assessed against various Gram-positive and Gram-negative bacterial strains to evaluate their combined efficacy and potential for enhanced antimicrobial activity, to set the basis for their co-loading in LPHNPs. Partial synergism was observed, particularly against *S. aureus* and *E. coli*, where even minimal concentrations of RN7IN6 enhanced the antimicrobial effects of CTX

(Table 5-10). This suggests that RN7IN6,holds potential for augmenting the efficacy of CTX. However, this synergistic effect was not pronounced against *P. aeruginosa* and *K. pneumoniae,* and therefore further refinement and understanding of RN7IN6's interaction with Gram-negative bacteria are needed to fully exploit this synergistic potential in a wider range of Gram-negative organisms. This limited effect may also be partly attributed to the poor activity of CTX against *P. aeruginosa*, rather than solely reflecting limitations in RN7IN6's efficacy.

6.1.5.3. Challenges in RN7IN6 Release from Liposomal and Hybrid Systems

RN7IN6 was delivered via two main systems: POPE:POPG:CL liposomes (both adsorbed and encapsulated) and LPHNPs (encapsulated within the lipid shell). In the case of both systems, RN7IN6 displayed negligible release, which may contribute to explanation of the limited antimicrobial activity observed in particular for RN7IN6-loaded liposomes (sections 4.4.2.3. and 4.4.3.4 and 5.4.5.3). In the case of both liposomes and LPHNPs, the strong affinity of RN7IN6 to the lipid components, particularly to the negatively charged phospholipids POPG and CL, could explain the lack of its release. As mentioned, this limitation translated into poor antimicrobial performance in the case of RN7IN6-loaded bacteriomimetic liposomes (Figure 4-13and Figure 4-18), an interesting observation as it was hypothesized that the bacteriomimetic nature of the liposomes might enhance interactions with bacterial membranes and facilitate direct transfer of RN7IN6 into these structures.

6.1.5.4. Analysis of Drug Release Dynamics and Antimicrobial Effects

The evaluation of antimicrobial activity across the different optimized formulations provided important insights into the performance of CTX and RN7IN6, both individually and in combination. By assessing their release profiles and efficacy, several key observations were made regarding the potential of each drug delivery system. The following summarizes the main findings:

- Free CTX and RN7IN6: Free CTX exhibited potent antimicrobial activity against *E. coli* and *S. aureus*, with reduced effectiveness against *P. aeruginosa* and *K. pneumoniae*. Free RN7IN6 demonstrated strong activity against all bacteria assessed except *P. aeruginosa.* When tested together, CTX and RN7IN6 exhibited partial synergism, particularly against *S. aureus* and *E. coli*, where the combined effect was greater than the sum of their individual activities.

- CHCL NPs: Encapsulating CTX into CHCL NPs resulted in a lower antimicrobial efficacy compared to free CTX, which may be reflective of the immediate availability of CTX in solution as compared to a slower release and availability of free CTX from CHCL NPs. This may potentially point to an improved efficacy of CHCL NPs over an extended time period, highlighting the need for investigation of long-term efficacy of formulations.

- CTX-loaded LPHNPs: Lipid coating of CTX-loaded CHCL NPs to produce CTX-loaded LPHNPs resulted in an antimicrobial activity similar to that of CTX-CHCL NPs, with slight improvements against *E. coli*. Against *S. aureus*, the MIC was lower compared to CTX-only formulations, suggesting an enhanced effect, likely due to CTX's higher concentration in the formulation. While RN7IN6's contribution remains unclear, future studies are needed to assess any synergistic or additive effects, and to optimize co-loading ratios.

Co-loaded CTX/RN7IN6 LPHNPs: The co-loading of CTX and RN7IN6 into LPHNPs resulted in a complete inhibition of *E. coli* growth at all concentrations tested, and a CTX-specific MIC value similar to (and most likely actually lower than) that of both CTX-loaded CHCL NPs and CTX-LPHNPs . However, due to the predominance of CTX in the formulation, only the antimicrobial effect of CTX was clearly observable, while the contribution of RN7IN6 to the overall activity of the co-loaded LPHNP system remains uncertain. Consequently, further research is required to evaluate RN7IN6-loaded LPHNPs as a standalone system to determine the precise antimicrobial contribution of RN7IN6. Additionally, reducing CTX concentrations in the co-loaded system would allow for a more balanced evaluation of the roles of both agents in the overall efficacy of the formulation. In summary, the release profiles of CTX across different nanocarriers were relatively consistent with an initial burst release followed by a sustained phase. A slight

reduction in burst release was noted for LPHNP formulations as compared to CHCL NPs. RN7IN6, however, faced significant challenges in terms of release, raising questions central to future work regarding the relative contributions of released, free RN7IN6 and direct-to-membrane transferred RN7IN6 on antimicrobial efficacy.

6.2. Future Work

6.2.1. Tuning Drug Delivery Systems for Enhanced Activity

In the current co-loaded LPHNP formulation CTX likely dominated the observed antimicrobial activity. This could have potentially occurred for several reasons; the main reason however can likely be attributed to the CTX/RN7IN6 ratio loaded into the formulation. In the current system, CTX dominates the antimicrobial response due to its much higher loading as compared to RN7IN6. This imbalance might overshadow the potential effects of RN7IN6. To address this, future work should focus on optimizing the loading ratio of CTX and RN7IN6 to ensure both drugs contribute more evenly to the overall antimicrobial effect. This could involve reducing the CTX loading or increasing RN7IN6 loading in the LPHNPs. Notably, as seen in section 5.4.3.3.1 no plateau was reached for RN7IN6 EE%, suggesting that there is room to further increase RN7IN6 loading without saturating the system, which may help balance the therapeutic activities of both agents.

6.2.1.1. Achieving Stability: Tuning Lipid-CS Ratios to Preserve Surface Charge

Maintaining a stable surface charge is essential for preventing nanoparticle aggregation, particularly in LPHNPs. The Z-potential is a critical parameter that indicates the electrostatic repulsion between particles; when it approaches neutrality as seen for CTX and RN7IN6-loaded LPHNPs (Figure 5-14) where the positive charge of the CS core and the RN7IN6 was neutralized by negatively charged lipids, the risk of aggregation increases due to insufficient repulsive forces [858]. Therefore, future research should focus on optimizing the lipid-to-CS ratios or increasing the RN7IN6 loading, as discussed above, to maintain a more favorable Z-potential, ideally away from neutrality. Additionally, techniques such as lyophilization can be explored to enhance formulation stability during storage by removing water content and preserving LPHNP structures [859]. However, the effects of lyophilization on reconstitution and physicochemical properties must be carefully evaluated to ensure long-term formulation viability.

6.2.2. Comprehensive Assessment of Antimicrobial Activity and Cytotoxicity

The current study on the antimicrobial efficacy of various CNP, liposomal and LPHNP formulations showed some notable assay-based limitations, with one significant limitation being the reliance on MIC assays to assess antimicrobial efficacy. While MIC assays are valuable for determining the lowest concentration of an antimicrobial agent required to inhibit bacterial growth, they do not provide insights into the bactericidal dynamics over time [363]. Therefore, this limitation can be addressed by incorporating time-kill assays in future studies, particularly for further testing of the co-loaded LPHNP formulation and relevant comparators. As employed in the context of Chapter 4, time-kill assays offer a more comprehensive understanding of bacterial killing kinetics by evaluating the reduction of bacterial populations over time [363]. This would allow for a better assessment of the sustained bactericidal efficacy of CTX and RN7IN6 when co-loaded in LPHNPs, particularly against resistant bacterial strains. Furthermore, it would be beneficial to evaluate the inhibition kinetics of LPHNPs under multiple exposure conditions [860].

One approach to achieving this could involve a modified time-kill assay, similar to the method used in the study carried out by Chad *et al*. In this approach, bacterial cultures were exposed to repeated doses of CTX and RN7IN6 to mimic real-world treatment scenarios. The assay can be modified by centrifuging the bacterial cultures at 1–2 hour intervals, removing the supernatant, and resuspending the bacteria in fresh media containing steady-state concentrations and thus emphasizing the adaptability of the method to various antibacterial treatments [860]. This method more closely simulates *in vivo* and repeated administration conditions, allowing for an evaluation of how sustained or repeated exposure to the antimicrobial agents impacts bacterial growth and potential resistance development. Repeated exposure of bacteria to the co-loaded LPHNP formulation could reveal how sustained or repeated doses of CTX and RN7IN6 affect antimicrobial efficacy and the potential development of resistance.

Another limitation of the current study is the omission of antimicrobial efficacy assessments for LPHNPs loaded solely with RN7IN6. This omission was a conscious decision made primarily due to time and budget constraints, but evaluating RN7IN6-only

LPHNPs as a control would provide a baseline to isolate and quantify the specific contribution of RN7IN6 in the co-loaded CTX/RN7IN6 LPHNP formulation. Including RN7IN6-only LPHNPs in future work, along with the already investigated CTX-alone LPHNPs, will enhance the understanding of the independent and combined effects of each agent, particularly with respect to any synergism between CTX and RN7IN6 in the LPHNP formulation.

Additionally, assessing the cytotoxicity of RN7IN6-loaded formulations is crucial. Although encapsulation of RN7IN6 within liposomes or LPHNPs is expected to reduce peptide cytotoxicity compared to its free form [612, 613], this hypothesis requires empirical validation. In the current study, cytotoxicity tests on free RN7IN6 were performed (see Appendix, Figure S-3 and Table S-2), which provided a baseline for understanding its potential toxicity in unencapsulated form. Therefore, cytotoxicity assays using mammalian cell lines should be conducted to evaluate the safety of encapsulated RN7IN6 compared to its free form, ensuring that the delivery system is capable of minimizing toxicity to host cells.

6.2.3. Unlocking the Mechanisms: LPHNP-Bacteria Interactions

Future investigation of the interactions between LPHNPs and bacterial membranes are pivotal for clarifying and further optimizing their antimicrobial efficacy. The lipid composition of the investigated liposomes as well as the lipid shell of LPHNPs, which mimics bacterial membranes [312], suggests a potential for significant interaction with bacterial cells. However, the lack of RN7IN6 activity observed when encapsulated within liposomes in particular (RN7IN6 activity in LPHNPs is currently unclear, for reasons detailed above) raises questions regarding the interaction of liposome bilayers/LPHNP lipid shells with bacterial cell [26]. To add to this already complex challenge, the precise mechanisms of interactions of particular nanocarriers with bacterial envelope structures (whether through adhesion, fusion, or penetration), remain inadequately understood. Advanced microscopy techniques such as structured illumination microscopy [861], transmission electron microscopy [299], and confocal microscopy [862] can provide real-time visualization of these interactions, in some cases elucidating whether LPHNPs

adhere to the bacterial membrane or penetrate into/through the structure. Such imaging studies are essential for understanding the dynamics of particle-membrane interactions and could shed light on the observed lack of antimicrobial activity of RN7IN6 when encapsulated within liposomes, as well as providing valuable complementary information to further RN7IN6-LPHNP efficacy assessment. The ability of liposomes to promote adhesion and fusion with Gram-negative bacterial membranes has been demonstrated for several lipid compositions, such as those containing DPPC, DOTAP, and DOPE [849, 850, 852]. However, this has not yet been fully explored for the bacteriomimetic lipid composition used in this study [706, 824]. Langmuir monolayers, which simulate the fluidity and packing density of lipid membranes, are especially valuable here, as they allow precise control of surface pressure, which directly impacts particle interaction and membrane penetration [863]. Investigating the lipid composition of LPHNPs in more detail, particularly their fusogenic properties, could elucidate how they interact with bacterial membranes and potentially enhance RN7IN6 delivery. By employing more advanced models such as bacteria-relevant Langmuir monolayers [863] or giant unilamellar vesicles, the interaction of LPHNPs with bacterial membranes can be studied at a molecular level [864-868]. These controlled monolayer systems also facilitate detailed mechanistic analysis through complementary techniques enabling further insights into interaction dynamics [863]. This approach would enable a better understanding of how modifications in lipid composition or peptide loading can optimize the performance of these nanocarriers.

If such future work was to demonstrate considerable interactions between bacteriomimetic liposomes/LPHNPs and bacterial membranes, but these were not seen to result in significant antimicrobial activity, several factors may explain this discrepancy. While a primary consideration in this case is the release kinetics and activity of free RN7IN6, as discussed at length in Chapters 4 and 0, a further consideration is RN7IN6 release by means of direct transfer from the delivery system to the bacterial envelope While bacteriomimetic liposomes/LPHNPs may effectively interact with bacterial surfaces, the insufficient or delayed transfer of RN7IN6 from bacteriomimetic systems (for which the AMP has a high affinity) could hinder its antimicrobial efficacy. Increasing the loading of RN7IN6 within LPHNPs may enhance the antimicrobial effect by delivering

a higher concentration of the peptide directly to the bacterial cells; moreover, exploring alternative AMPs, with different amino acid structures that reduce interactions with and affinity for the bacteriomimetic liposome/LPHNP lipid layer could be of interest. Additionally, optimizing the lipid composition of LPHNPs could improve both the release (of free AMP and/or of AMP by direct transfer) and activity of AMPs. Such approaches could provide valuable insights into how lipid-based delivery system design and AMP selection influence antimicrobial efficacy.

6.2.4. The Lipid Shell: A Key Factor in LPHNP Drug Delivery Systems

The lipid shell structure of LPHNPs is crucial for optimizing their performance against bacterial infections. The integrity and characteristics of the lipid coating, such as its thickness, fluidity, and structural organization, significantly influence drug release kinetics and the overall stability of the nanoparticles. Incomplete or inadequate lipid coatings can hinder for instance the interaction of the delivery system with the bacterial envelope and thereby limiting their antimicrobial efficacy.

Characterization techniques such as transmission electron microscopy could prove useful tools for future work, providing valuable insights into the structural integrity of the LPHNP lipid shell, and confirming whether the CS core is fully encapsulated [869]. This is vital for understanding the interactions between the lipid shell and bacterial membranes, which may be compromised by poorly structured coatings. Furthermore, the fluidity of the lipid layer is a critical factor affecting drug release behavior (as well as bacterial cell interaction). Lipid layers with higher fluidity, typically achieved with unsaturated phospholipids, facilitate faster release of encapsulated agents [870]. Conversely, more rigid lipid compositions can slow down drug release, necessitating a careful balance in lipid selection to optimize therapeutic outcomes [871]. Therefore, the choice of lipid composition, including the ratio of saturated to unsaturated lipids and the incorporation of cholesterol, can modulate membrane fluidity and, consequently, the release kinetics of the therapeutic agents [872]. Moreover, the thickness of the lipid shell also plays a pivotal role in determining the stability and release behavior of CTX and RN7IN6 from LPHNPs. A thicker lipid layer may enhance nanoparticle stability but

could impede the release/transfer of encapsulated drugs, while a thinner layer may promote faster release/transfer at the cost of stability [873]. Therefore, characterizing and optimizing the lipid layer thickness is crucial for balancing stability and drug release profiles in nanoparticle formulations. To investigate the fluidity of the lipid layer, techniques such as fluorescence recovery after photobleaching (FRAP) [874] and differential scanning calorimetry [875] can be employed. [874]

6.2.5. Expanding the Therapeutic Potential of LPHNPs

LPHNPs represent a versatile platform for drug delivery, particularly in the context of antimicrobial therapy (including for the treatment of biofilm-associated infections) and cancer therapy. The unique properties of LPHNPs, which combine the beneficial characteristics of liposomes and polymeric nanoparticles, enable them to encapsulate both hydrophilic and hydrophobic therapeutic agents effectively [315]. This capability is crucial for the co-delivery of multiple drugs, in different compartments of the LPHNP delivery system, enhancing therapeutic efficacy.

In cancer therapy, LPHNPs have shown promise in delivering chemotherapeutic agents such as doxorubicin, paclitaxel, and cisplatin [53]. These nanoparticles can improve drug accumulation at tumor sites while providing controlled release profiles, which are essential for maximizing therapeutic effects and minimizing systemic toxicity [876]. For instance, studies have demonstrated that LPHNPs can co-encapsulate chemotherapeutics such as curcumin and cisplatin, to inhibit tumor growth more effectively [315]. This dual delivery approach not only enhances the cytotoxicity of the drugs against tumor cells but also addresses the issue of drug resistance, a significant hurdle in oncology [315]. Dual-drug delivery systems utilizing LPHNPs can simultaneously deliver chemotherapeutics and adjuvant therapies, such as antiangiogenic agents or radiotherapeutic agents, to achieve synergistic effects [53]. This strategy has already shown promise, where LPHNPs co-loaded with chemotherapeutic agents such as Paclitaxel and Gemtacibine hydrochloride, have demonstrated enhanced tumor targeting and efficacy compared to single-drug formulations [53]. While LPHNPs show great promise in cancer therapy, this application

represents only one facet of their therapeutic potential and future work is necessary to optimize their clinical utility. For instance, targeted functionalization of LPHNPs could enhance specificity and reduce off-target effects, a significant hurdle in cancer treatments. Furthermore, although LPHNPs have demonstrated effective dual-drug delivery, research into advanced combinatorial loading with immunotherapies could provide greater synergistic effects, combat drug resistance, and enhance patient outcomes. Additionally, theranostic-grafted LPHNPs could allow real-time imaging and drug tracking, crucial for personalized treatment strategies. Hence, future work on these fronts will be essential to translate promising in vitro and preclinical findings into reliable, scalable, and effective treatments for complex cancer systems.

In addition to their applications in oncology, LPHNPs are also being explored for their potential in treating biofilm-associated infections [877]. Biofilms pose a significant challenge in chronic infection management due to their resistance to conventional antibiotics. In particular, studies on LPHNPs have shown enhanced antibiofilm efficacy due to their ability to fuse with and penetrate the biofilm matrix [313]. The ability of LPHNPs to deliver both antibiotics and AMPs like RN7IN6 could be exploited to disrupt biofilm structures more effectively and enhance bacterial clearance. Therefore, future studies could focus on optimizing LPHNPs for biofilm penetration and investigating the release kinetics within biofilm environments to improve their therapeutic performance.

Additionally, LPHNPs could be explored for gene therapy [803], as well as drug delivery platforms for vascular disorders [53] and inflammatory diseases [878], given their ability to co-deliver therapeutic agents (such as nucleic acids or anti-inflammatory drugs) to specific tissue targets. The potential for controlled release, coupled with targeted delivery, makes LPHNPs an attractive candidate for a wide range of disease treatments. Therefore, longer-term future work could continue optimizing their composition for specific therapeutic areas, leveraging their versatility for more personalized and efficient medical treatments. Indeed, expanding the application of LPHNPs beyond antimicrobial peptides and antibiotics could significantly broaden their clinical utility, making them a valuable platform in various therapeutic domains.

6.2.6. Streamlining Nanoparticle Production: One-Step Microfluidic Mixing and In-Line TFF

The current microfluidic processes for nanocarrier production, particularly in the context of LPHNPs and liposomal formulations, face significant challenges. More traditional microfluidic methods often involve multiple purification steps, such as ultracentrifugation and dialysis as discussed in section 5.1.2, which can introduce variability and complexity, ultimately affecting the reproducibility of the formulations. These purification techniques are not only time-consuming but also inconsistent in effectively removing unencapsulated drugs and residual solvents, which can compromise the stability and efficacy of the LPHNPs. Therefore, the need for more streamlined and reliable methods is becoming increasingly critical.

Transitioning to a continuous process that incorporates microfluidic mixing and in-line TFF represents a promising solution to these challenges. This integrated approach would allow for the purification of LPHNPs directly during their production, enhancing the consistency and quality of the formulations while significantly reducing processing time [879]. The continuous solvent and unencapsulated drug removal as well as product concentration facilitated by in-line TFF would simplify the workflow and help maintain critical physicochemical properties such as particle size and PDI [880]. Studies have shown that TFF is particularly effective in removing residual solvents and unencapsulated drugs, outperforming traditional methods like dialysis and ultracentrifugation in terms of efficiency and thoroughness [881]. Moreover, the adoption of a true one-step microfluidic process (together with in-line TFF purification) could lead to improved scalability and efficiency in nanoparticle production. For instance, microfluidic systems with chips that have more than two inlet channels and multiple mixing stages could facilitate even more complex co-formulation strategies. For example, a multiple-inlet, multiple-mixing stage system would allow for the simultaneous mixing of CS and TPP/CTX mixture in an initial mixing stage to form CS NP, followed by the introduction of lipid and AMP solution into a second mixing stage to achieve LPHNP formation as a result of controlled mixing with formed CS NPs. Coupling such a system with in-line TFF purification would streamline LPHNP production, enabling

precise control over the encapsulation process and further reducing the need for separate steps for drug loading and purification. By allowing real-time control over critical parameters such as FRR and TFR, this method could produce more homogeneous formulations with consistently low PDI values and optimal encapsulation efficiency [879].

6.3. Overall conclusion

The scientific rationale behind this thesis stems from the urgent need to develop advanced drug delivery systems to combat the growing threat of AMR. The aim of this work was to develop, optimize, and evaluate LPHNPs as a co-delivery platform for CTX and the antimicrobial peptide RN7IN6, assessing their antibacterial efficacy against clinically relevant Gram-positive and Gram-negative pathogens. To achieve this, a variety of methodologies were employed, including microfluidic mixing technology to produce and optimize LPHNPs as well as component nanoparticle and liposomal formulations, HPLC for drug quantification, and antimicrobial activity assays to evaluate efficacy.

CS NPs loaded with CTX were successfully manufactured with tunable characteristics such as size, PDI, and Z-potential. The optimization of liposomal systems revealed that POPE:POPG:CL liposomes, that mimic the composition of the inner membrane of Gram-negative bacteria, were effective at achieving small, monodisperse particles, and showed potential for antimicrobial peptide delivery. RN7IN6, when synthesized and incorporated into these liposomes, encountered significant challenges in achieving effective release and demonstrating antimicrobial efficacy. However, the liposomal system still offered key advantages in terms of stability and encapsulation efficiency.

A co-loaded LPHNP formulation with favorable physicochemical characteristics (namely, size and PDI) was successfully developed. A synergistic effect of free CTX and RN7IN6 was observed, and while further antimicrobial testing is required, a promising indication of co-loaded LPHNP efficacy against the Gram-negative bacterium *E. coli* was noted.

Priorities for future LPHNP development include optimizing release/transfer kinetics and further exploring interactions between the LPHNP lipid layer and bacterial membranes, as well as expanding the applications of the platform beyond antimicrobial therapy.

References

1. Kennedy, D.A. and A.F. Read, *Why does drug resistance readily evolve but vaccine resistance does not?* Proc Biol Sci, 2017. **284**(1851).
2. Lewis, K., *New approaches to antimicrobial discovery.* Biochem Pharmacol, 2017. **134**: p. 87-98.
3. Organization, W.H., *Antimicrobial resistance: global report on surveillance 2014. Geneva: WHO; 2014*. 2015.
4. O'Neill, J., *Review on antimicrobial resistance: tackling drug-resistant infections globally: final report and recommendations.* Review on antimicrobial resistance: tackling drug-resistant infections globally: final report and recommendations., 2016.
5. Worthington, R.J. and C. Melander, *Overcoming Resistance to β-Lactam Antibiotics.* The Journal of Organic Chemistry, 2013. **78**(9): p. 4207-4213.
6. Labriola, L., *Antibiotic Locks for the Treatment of Catheter-related Blood Stream Infection: Still More Hope Than Data.* Seminars in Dialysis, 2019. **32**(5): p. 402-405.
7. Uruén, C., et al., *Biofilms as Promoters of Bacterial Antibiotic Resistance and Tolerance.* Antibiotics, 2020. **10**(1): p. 3.
8. Barber, M. and J.E. Whitehead, *Bacteriophage types in penicillin-resistant staphylococcal infection.* Br Med J, 1949. **2**(4627): p. 565-9.
9. Katayama, Y., T. Ito, and K. Hiramatsu, *A new class of genetic element, staphylococcus cassette chromosome mec, encodes methicillin resistance in Staphylococcus aureus.* Antimicrob Agents Chemother, 2000. **44**(6): p. 1549-55.
10. Ugwuanyi, F.C., et al., *Evaluation of Efflux Pump Activity and Biofilm Formation in Multidrug Resistant Clinical Isolates of Pseudomonas Aeruginosa Isolated From a Federal Medical Center in Nigeria.* Annals of Clinical Microbiology and Antimicrobials, 2021. **20**(1).
11. Dahal, R.H. and D.K. Chaudhary, *Microbial Infections and Antimicrobial Resistance in Nepal: Current Trends and Recommendations.* Open Microbiol J, 2018. **12**: p. 230-242.
12. Högberg, L.D., A. Heddini, and O. Cars, *The global need for effective antibiotics: challenges and recent advances.* Trends Pharmacol Sci, 2010. **31**(11): p. 509-15.
13. Zaman, S.B., et al., *A Review on Antibiotic Resistance: Alarm Bells are Ringing.* Cureus, 2017. **9**(6): p. e1403.
14. Clatworthy, A.E., E. Pierson, and D.T. Hung, *Targeting virulence: a new paradigm for antimicrobial therapy.* Nat Chem Biol, 2007. **3**(9): p. 541-8.
15. Ventola, C.L., *The antibiotic resistance crisis: part 1: causes and threats.* P t, 2015. **40**(4): p. 277-83.
16. Rutherford, S.T. and B.L. Bassler, *Bacterial quorum sensing: its role in virulence and possibilities for its control.* Cold Spring Harb Perspect Med, 2012. **2**(11).
17. Laxminarayan, R., T.V. Boeckel, and A. Teillant, *The Economic Costs of Withdrawing Antimicrobial Growth Promoters from the Livestock Sector.* 2015.
18. Naylor, N.R., et al., *Estimating the burden of antimicrobial resistance: a systematic literature review.* Antimicrob Resist Infect Control, 2018. **7**: p. 58.
19. Control, C.f.D. and Prevention, *Antibiotic resistance threats in the United States, 2019*. 2019: US Department of Health and Human Services, Centres for Disease Control and ….
20. Agency, U.H.S., *English surveillance programme for antimicrobial utilisation and resistance (ESPAUR) report.* GOV.UK, 2024.

21. Kitagawa, Y., et al., *≪p>Safety and Efficacy of Amrubicin Monotherapy in Patients With Platinum-Refractory Metastatic Neuroendocrine Carcinoma of the Gastrointestinal Tract: A Single Cancer Center Retrospective Study</P&gt.* Cancer Management and Research, 2019. **Volume 11**: p. 5757-5764.
22. Kim, Y.H., et al., *Retrospective Analysis of Japanese Patients With Relapse or Refractory Small-Cell Lung Cancer Treated With Amrubicin Hydrochloride.* Oncology Letters, 2010. **1**(3): p. 569-572.
23. Roux, A., et al., *Antibody-Mediated Rejection in Lung Transplantation: Clinical Outcomes and Donor-Specific Antibody Characteristics.* American Journal of Transplantation, 2016. **16**(4): p. 1216-1228.
24. Wilkins, M.D., et al., *New Approaches to the Treatment of Biofilm-Related Infections.* Journal of Infection, 2014. **69**: p. S47-S52.
25. Wingender, J. and H.-C. Flemming, *Biofilms in drinking water and their role as reservoir for pathogens.* International journal of hygiene and environmental health, 2011. **214**(6): p. 417-423.
26. Organization, W.H., *WHO bacterial priority pathogens list, 2024. Bacterial pathogens of public health importance to guide research, development and strategies to prevent and control antimicrobial resistance.* 2024.
27. WHO, *WHO publishes list of bacteria for which new antibiotics are urgently needed.* Media Centre, 2017. **New release**.
28. Andre, A., L. Debande, and B. Marteyn, *The Selective Advantage of Facultative Anaerobes Relies on Their Unique Ability to Cope With Changing Oxygen Levels During Infection.* Cellular Microbiology, 2021. **23**(8).
29. Rice, L.B., *Federal funding for the study of antimicrobial resistance in nosocomial pathogens: no ESKAPE*. 2008, The University of Chicago Press. p. 1079-1081.
30. Tacconelli, E., et al., *Discovery, research, and development of new antibiotics: the WHO priority list of antibiotic-resistant bacteria and tuberculosis.* The Lancet Infectious Diseases, 2018. **18**(3): p. 318-327.
31. Hall-Stoodley, L., et al., *Characterization of Biofilm Matrix, Degradation by DNase Treatment and Evidence of Capsule Downregulation in Streptococcus Pneumoniae Clinical Isolates.* BMC Microbiology, 2008. **8**(1): p. 173.
32. Terra, L., et al., *A Novel Alkaliphilic Streptomyces Inhibits ESKAPE Pathogens.* Frontiers in Microbiology, 2018. **9**.
33. Drieux, L., et al., *Phenotypic Detection of Extended-Spectrum B-Lactamase Production in Enterobacteriaceae: Review and Bench Guide.* Clinical Microbiology and Infection, 2008. **14**: p. 90-103.
34. Sader, H.S., et al., *Antimicrobial Activity of CXA-101, a Novel Cephalosporin Tested in Combination With Tazobactam Against Enterobacteriaceae, Pseudomonas Aeruginosa, and Bacteroides Fragilis Strains Having Various Resistance Phenotypes.* Antimicrobial Agents and Chemotherapy, 2011. **55**(5): p. 2390-2394.
35. Elton, L., et al., *Antimicrobial Resistance Preparedness in Sub-Saharan African Countries.* Antimicrobial Resistance and Infection Control, 2020. **9**(1).
36. Nisa, T.T., et al., *Antimicrobial Resistance Patterns of WHO Priority Pathogens Isolated in Hospitalized Patients in Japan: A Tertiary Center Observational Study.* Plos One, 2024. **19**(1): p. e0294229.
37. Baraka, M., et al., *The Healthcare Professionals' Perspectives on Antimicrobial Resistance (AMR) Associated Factors and Their Consequences: A Cross Sectional Study in Eastern Province of Saudi Arabia.* 2021.
38. Organization, W.H., *Report of the 6th meeting of the WHO advisory group on integrated surveillance of antimicrobial resistance with AGISAR 5-year strategic framework to*

support implementation of the global action plan on antimicrobial resistance (2015-2019), 10-12 June 2015, Seoul, Republic of Korea. 2015: World Health Organization.

39. GOV.UK, *Confronting antimicrobial resistance 2024 to 2029.* GOV.UK, 2024.
40. Vedadhir, A.A., C.F. Rodrigues, and H. Lambert, *Social Science Research Contributions to Antimicrobial Resistance: Protocol for a Scoping Review.* Systematic Reviews, 2020. **9**(1).
41. Hossain, M.J., et al., *Zoonotic Significance and Antimicrobial Resistance in Salmonella in Poultry in Bangladesh for the Period of 2011–2021.* Zoonotic Diseases, 2021. **1**(1): p. 3-24.
42. Svet, L., et al., *Competitive Interactions Facilitate Resistance Development Against Antimicrobials.* Applied and Environmental Microbiology, 2023. **89**(10).
43. Huang, M., et al., *Evolutionary Dynamics of Candida Albicans During <i>In Vitro</I> Evolution.* Eukaryotic Cell, 2011. **10**(11): p. 1413-1421.
44. Lerminiaux, N.A. and A.D.S. Cameron, *Horizontal transfer of antibiotic resistance genes in clinical environments.* Can J Microbiol, 2019. **65**(1): p. 34-44.
45. Michael, C.A., D. Dominey-Howes, and M. Labbate, *The Antimicrobial Resistance Crisis: Causes, Consequences, and Management.* Frontiers in Public Health, 2014. **2**.
46. Principi, N., E. Silvestri, and S. Esposito, *Advantages and Limitations of Bacteriophages for the Treatment of Bacterial Infections.* Frontiers in Pharmacology, 2019. **10**.
47. Ronson, C., et al., *Brenner's Encyclopedia of Genetics (Second Edition)*. 2013. p. 598–600.
48. Sun, D., *Pull in and Push Out: Mechanisms of Horizontal Gene Transfer in Bacteria.* Frontiers in Microbiology, 2018. **9**.
49. Torres-Barceló, C., *The disparate effects of bacteriophages on antibiotic-resistant bacteria.* Emerg Microbes Infect, 2018. **7**(1): p. 168.
50. Tsaneva, K., *Modelling Within-Host Evolutionary Dynamics of Antimicrobial Resistance.* Peer Community in Mathematical and Computational Biology, 2021.
51. Novais, Â., et al., *Evolutionary Trajectories of Beta-Lactamase CTX-M-1 Cluster Enzymes: Predicting Antibiotic Resistance.* Plos Pathogens, 2010. **6**(1): p. e1000735.
52. Pál, C., B. Papp, and V. Lázár, *Collateral Sensitivity of Antibiotic-Resistant Microbes.* Trends in Microbiology, 2015. **23**(7): p. 401-407.
53. Sivadasan, D., et al., *Polymeric Lipid Hybrid Nanoparticles (PLNs) as Emerging Drug Delivery Platform-A Comprehensive Review of Their Properties, Preparation Methods, and Therapeutic Applications.* Pharmaceutics, 2021. **13**(8).
54. Collignon, P. and S.A. McEwen, *One Health—Its Importance in Helping to Better Control Antimicrobial Resistance.* Tropical Medicine and Infectious Disease, 2019. **4**(1): p. 22.
55. Manaia, C.M., et al., *The Complex Interplay Between Antibiotic Resistance and Pharmaceutical and Personal Care Products in the Environment.* Environmental Toxicology and Chemistry, 2023. **43**(3): p. 637-652.
56. Siddiqui, K., N. Khatoon, and P.C. Roy, *Untreated Liquid Hospital Waste: Potential Source of Multidrug Resistant Bacteria.* Bangladesh Journal of Microbiology, 2016: p. 21-24.
57. Wooldridge, M., *Evidence for the Circulation of Antimicrobialresistant Strains and Genes in Nature and Especially Between Humans and Animals.* Revue Scientifique Et Technique De L Oie, 2012. **31**(1): p. 231-247.
58. Ma, F., et al., *Use of antimicrobials in food animals and impact of transmission of antimicrobial resistance on humans.* Biosafety and Health, 2021. **3**(1): p. 32-38.
59. Lien, L.T.Q., et al., *Antibiotics in Wastewater of a Rural and an Urban Hospital Before and After Wastewater Treatment, and the Relationship With Antibiotic Use—A One Year Study From Vietnam.* International Journal of Environmental Research and Public Health, 2016. **13**(6): p. 588.

60. Nastiti, A., et al., *Self-Reported Pharmaceutical Storage, Use, and Improper Disposal to the Environment Among Urban Parents in Indonesia.* Iop Conference Series Earth and Environmental Science, 2022. **1111**(1): p. 012045.
61. Cheng, V.C.-C., et al., *Strategic Measures for the Control of Surging Antimicrobial Resistance in Hong Kong and Mainland of China.* Emerging Microbes & Infections, 2015. **4**(1): p. 1-13.
62. Nicolle, L.E. and W.H. Organization, *Infection control programmes to control antimicrobial resistance (AMR).* 2001.
63. D'Atri, F., et al., *Targets for the reduction of antibiotic use in humans in the Transatlantic Taskforce on Antimicrobial Resistance (TATFAR) partner countries.* Euro Surveill, 2019. **24**(28).
64. Shelke, Y.P., et al., *An Overview of Preventive Strategies and the Role of Various Organizations in Combating Antimicrobial Resistance.* Cureus, 2023. **15**(9): p. e44666.
65. Gauba, A. and K.M. Rahman, *Evaluation of Antibiotic Resistance Mechanisms in Gram-Negative Bacteria.* Antibiotics, 2023. **12**(11): p. 1590.
66. Videau, P., et al., *Mutation of The <i>murC</I> And <i>murB</I> Genes Impairs Heterocyst Differentiation in Anabaena Sp. Strain PCC 7120.* Journal of Bacteriology, 2016. **198**(8): p. 1196-1206.
67. Jin, H.J., J.H. Jeong, and Y.-G. Kim, *Crystallization and Preliminary X-Ray Crystallographic Analysis of PBPD2 From<i>Listeria Monocytogenes</I>.* Acta Crystallographica Section F Structural Biology Communications, 2014. **70**(4): p. 535-537.
68. Baumgartner, J., et al., *Structure of The<i>Bacillus Anthracis</I>dTDP-<scp>L</Scp>-Rhamnose-Biosynthetic Enzyme Glucose-1-Phosphate Thymidylyltransferase (RfbA).* Acta Crystallographica Section F Structural Biology Communications, 2017. **73**(11): p. 621-628.
69. Sohlenkamp, C. and O. Geiger, *Bacterial Membrane Lipids: Diversity in Structures and Pathways.* Fems Microbiology Reviews, 2015. **40**(1): p. 133-159.
70. Epand, R.M. and R.F. Epand, *Domains in Bacterial Membranes and the Action of Antimicrobial Agents.* Molecular Biosystems, 2009. **5**(6): p. 580.
71. Hospenthal, M.K., T. Costa, and G. Waksman, *A Comprehensive Guide to Pilus Biogenesis in Gram-Negative Bacteria.* Nature Reviews Microbiology, 2017. **15**(6): p. 365-379.
72. Silhavy, T.J., D. Kahne, and S. Walker, *The bacterial cell envelope.* Cold Spring Harb Perspect Biol, 2010. **2**(5): p. a000414.
73. Piddock, L.J., *Clinically relevant chromosomally encoded multidrug resistance efflux pumps in bacteria.* Clin Microbiol Rev, 2006. **19**(2): p. 382-402.
74. Evans, L., et al., *Exploitation of Antibiotic Resistance as a Novel Drug Target: Development of a B-Lactamase-Activated Antibacterial Prodrug.* Journal of Medicinal Chemistry, 2019. **62**(9): p. 4411-4425.
75. Leiris, S., et al., *SAR Studies Leading to the Identification of a Novel Series of Metallo-B-Lactamase Inhibitors for the Treatment of Carbapenem-Resistant Enterobacteriaceae Infections That Display Efficacy in an Animal Infection Model.* Acs Infectious Diseases, 2018. **5**(1): p. 131-140.
76. Stoesser, N., et al., *Genomic Epidemiology of Global Klebsiella Pneumoniae Carbapenemase (KPC)-producing Escherichia Coli.* Scientific Reports, 2017. **7**(1).
77. Khan, H., A. Ahmad, and R. Mehboob, *Nosocomial Infections and Their Control Strategies.* Asian Pacific Journal of Tropical Biomedicine, 2015. **5**(7): p. 509-514.
78. Heinz, U. and H.-W. Adolph, *Metallo-?-Lactamases: Two Binding Sites for One Catalytic Metal Ion?* Cellular and Molecular Life Sciences, 2004. **61**(22): p. 2827-2839.
79. Tooke, C.L., et al., *B-Lactamases and B-Lactamase Inhibitors in the 21st Century.* Journal of Molecular Biology, 2019. **431**(18): p. 3472-3500.

80. Harting, J., *Carbapenem-Resistant Enterobacteriaceae Infections: A Review of Epidemiology and Treatment Options.* Journal of Respiratory Infections, 2019. **3**(1).
81. Ahmadian, L., et al., *Role of Aminoglycoside-Modifying Enzymes (AMEs) in Resistance to Aminoglycosides Among Clinical Isolates of Pseudomonas Aeruginosa in the North of Iran.* Biomed Research International, 2021. **2021**: p. 1-10.
82. Blair, J.M., G.E. Richmond, and L.J. Piddock, *Multidrug efflux pumps in Gram-negative bacteria and their role in antibiotic resistance.* Future microbiology, 2014. **9**(10): p. 1165-1177.
83. Jana, S. and J.K. Deb, *Molecular Understanding of Aminoglycoside Action and Resistance.* Applied Microbiology and Biotechnology, 2006. **70**(2): p. 140-150.
84. Lorusso, A.B., et al., *Role of efflux pumps on antimicrobial resistance in Pseudomonas aeruginosa.* International journal of molecular sciences, 2022. **23**(24): p. 15779.
85. Auda, I.G., I.M.A. Salman, and J.G. Odah, *Efflux pumps of Gram-negative bacteria in brief.* Gene Reports, 2020. **20**: p. 100666.
86. Acosta-Gutiérrez, S., et al., *Getting Drugs Into Gram-Negative Bacteria: Rational Rules for Permeation Through General Porins.* Acs Infectious Diseases, 2018. **4**(10): p. 1487-1498.
87. Liao, J., M.J. Schurr, and K. Sauer, *The MerR-Like Regulator BrlR Confers Biofilm Tolerance by Activating Multidrug Efflux Pumps in Pseudomonas Aeruginosa Biofilms.* Journal of Bacteriology, 2013. **195**(15): p. 3352-3363.
88. Horna, G., et al., *Interplay Between MexAB-OprM and MexEF-OprN in Clinical Isolates of Pseudomonas Aeruginosa.* Scientific Reports, 2018. **8**(1).
89. Kenney, L.J. and G.S. Anand, *EnvZ/OmpR Two-Component Signaling: An Archetype System That Can Function Noncanonically.* EcoSal Plus, 2020. **9**(1).
90. MacDermott-Opeskin, H.I., V. Gupta, and M.L. O'Mara, *Lipid-mediated antimicrobial resistance: a phantom menace or a new hope?* Biophys Rev, 2022. **14**(1): p. 145-162.
91. Yang, H., et al., *Lipid a Structural Determination From a Single Colony.* Analytical Chemistry, 2022. **94**(21): p. 7460-7465.
92. Anandan, A. and A. Vrielink, *Structure and function of lipid A–modifying enzymes.* Annals of the New York Academy of Sciences, 2020. **1459**(1): p. 19-37.
93. Qureshi, Z.A., et al., *Colistin-Resistant Acinetobacter Baumannii: Beyond Carbapenem Resistance.* Clinical Infectious Diseases, 2015. **60**(9): p. 1295-1303.
94. Doi, Y. and Y. Arakawa, *16S Ribosomal RNA Methylation: Emerging Resistance Mechanism against Aminoglycosides.* Clinical Infectious Diseases, 2007. **45**(1): p. 88-94.
95. Hainrichson, M., I. Nudelman, and T. Baasov, *Designer Aminoglycosides: The Race to Develop Improved Antibiotics and Compounds for the Treatment of Human Genetic Diseases.* Organic & Biomolecular Chemistry, 2008. **6**(2): p. 227-239.
96. Sarkar, T., et al., *Mechanism of Protease Resistance of <scp>D</Scp>-Amino Acid Residue Containing Cationic Antimicrobial Heptapeptides.* Acs Infectious Diseases, 2024. **10**(2): p. 562-581.
97. Jasovský, D., et al., *Antimicrobial resistance—a threat to the world's sustainable development.* Upsala journal of medical sciences, 2016. **121**(3): p. 159-164.
98. Kim, S.-K., et al., *Antibiotic Resistance in Bacteria: Novel Metalloenzyme Inhibitors.* Chemical Biology & Drug Design, 2009. **74**(4): p. 343-348.
99. Aslam, M.Z., et al., *Detecting the Mechanism of Action of Antimicrobial Peptides by Using Microscopic Detection Techniques.* Foods, 2022. **11**(18): p. 2809.
100. Getahun, Y.A., et al., *Multidrug-Resistant Microbial Therapy Using Antimicrobial Peptides and the CRISPR/Cas9 System.* Veterinary Medicine Research and Reports, 2022. **Volume 13**: p. 173-190.

101. Neidig, A., et al., *Knock-out of Multidrug Efflux Pump MexXY-OprM Results in Increased Susceptibility to Antimicrobial Peptides in <i>Pseudomonas Aeruginosa</I>.* Microbiology and Immunology, 2023.
102. Ito, T., et al., *Enhancing Chemical Stability Through Structural Modification of Antimicrobial Peptides With Non-Proteinogenic Amino Acids.* Antibiotics, 2023. **12**(8): p. 1326.
103. Ji, S., et al., *Antimicrobial peptides: An alternative to traditional antibiotics.* European Journal of Medicinal Chemistry, 2024. **265**: p. 116072.
104. Lee, T.-H., K. N Hall, and M.-I. Aguilar, *Antimicrobial peptide structure and mechanism of action: a focus on the role of membrane structure.* Current topics in medicinal chemistry, 2016. **16**(1): p. 25-39.
105. Lü, Y., et al., *Synergistic Antimicrobial Effect of Antimicrobial Peptides CATH-1, CATH-3, and PMAP-36 With Erythromycin Against Bacterial Pathogens.* Frontiers in Microbiology, 2022. **13**.
106. Silva, L.V.d., et al., *Evaluation of the synergistic potential of vancomycin combined with other antimicrobial agents against methicillin-resistant Staphylococcus aureus and coagulase-negative Staphylococcus spp strains.* Memorias do Instituto Oswaldo Cruz, 2011. **106**: p. 44-50.
107. Meader, E., et al., *Evaluation of bacteriophage therapy to control Clostridium difficile and toxin production in an in vitro human colon model system.* Anaerobe, 2013. **22**: p. 25-30.
108. Watanabe, R., et al., *Efficacy of bacteriophage therapy against gut-derived sepsis caused by Pseudomonas aeruginosa in mice.* Antimicrobial agents and chemotherapy, 2007. **51**(2): p. 446-452.
109. Shree, P., et al., *Biofilms: Understanding the structure and contribution towards bacterial resistance in antibiotics.* Medicine in Microecology, 2023. **16**: p. 100084.
110. Alaoui Mdarhri, H., et al., *Alternatives Therapeutic Approaches to Conventional Antibiotics: Advantages, Limitations and Potential Application in Medicine.* Antibiotics (Basel), 2022. **11**(12).
111. Kalia, V.C., *Quorum Sensing Inhibitors: An Overview.* Biotechnology Advances, 2013. **31**(2): p. 224-245.
112. Stokes, J.M., et al., *A deep learning approach to antibiotic discovery.* Cell, 2020. **180**(4): p. 688-702. e13.
113. Piddock, L.J., *Teixobactin, the first of a new class of antibiotics discovered by iChip technology?* Journal of Antimicrobial Chemotherapy, 2015. **70**(10): p. 2679-2680.
114. Aslam, B., et al., *CRISPR-Cas system: a potential alternative tool to cope antibiotic resistance.* Antimicrobial Resistance & Infection Control, 2020. **9**: p. 1-3.
115. Araya, D.P., K.L. Palmer, and B.A. Duerkop, *Correction: CRISPR-based antimicrobials to obstruct antibiotic-resistant and pathogenic bacteria.* PLoS Pathogens, 2021. **17**(12): p. e1010153.
116. Briner, A.E. and R. Barrangou, *Deciphering and shaping bacterial diversity through CRISPR.* Current Opinion in Microbiology, 2016. **31**: p. 101-108.
117. Duan, C., et al., *Harnessing the CRISPR-Cas systems to combat antimicrobial resistance.* Frontiers in Microbiology, 2021. **12**: p. 716064.
118. Gholizadeh, P., et al., *How CRISPR-Cas system could be used to combat antimicrobial resistance.* Infection and drug resistance, 2020: p. 1111-1121.
119. Halawa, E.M., et al., *Antibiotic action and resistance: updated review of mechanisms, spread, influencing factors, and alternative approaches for combating resistance.* Frontiers in Pharmacology, 2024. **14**.

120. Rajamanickam, K., J. Yang, and M.K. Sakharkar, *A Novel Antimicrobial–Phytochemical Conjugate With Antimicrobial Activity Against Streptococcus Uberis, Enterococcus Faecium, and Enterococcus Faecalis.* Frontiers in Pharmacology, 2019. **10**.
121. Hadiya, S., et al., *Nanoparticles Based Combined Antimicrobial Drug Delivery System as a Solution for Bacterial Resistance.* Bulletin of Pharmaceutical Sciences Assiut, 2022. **45**(2): p. 1121-1141.
122. Sun, H.Y., et al., *A Novel Combination Regimen for the Treatment of Refractory Bacteremia Due to Multidrug-Resistant Pseudomonas Aeruginosa in a Liver Transplant Recipient.* Transplant Infectious Disease, 2010. **12**(6): p. 555-560.
123. Ünlü, Ö. and K. Yılancıoğlu, *Exploration of Synergistic Antibiotic Interactions in Klebsiella Pneumoniae.* Romanian Biotechnological Letters, 2020. **25**(1): p. 1246-1252.
124. Murugaiyan, J., et al., *Progress in Alternative Strategies to Combat Antimicrobial Resistance: Focus on Antibiotics.* Antibiotics (Basel), 2022. **11**(2).
125. Coates, A.R.M., et al., *Antibiotic combination therapy against resistant bacterial infections: synergy, rejuvenation and resistance reduction.* Expert Rev Anti Infect Ther, 2020. **18**(1): p. 5-15.
126. Yu, X.-B., et al., *Population Pharmacokinetics of Colistin Sulfate in Critically Ill Patients: Exposure and Clinical Efficacy.* Frontiers in Pharmacology, 2022. **13**.
127. Gandhi, L., et al., *Pembrolizumab plus chemotherapy in metastatic non–small-cell lung cancer.* New England journal of medicine, 2018. **378**(22): p. 2078-2092.
128. Toews, M.L. and D.B. Bylund, *Pharmacologic principles for combination therapy.* Proceedings of the American Thoracic Society, 2005. **2**(4): p. 282-289.
129. Tamma, P.D., S.E. Cosgrove, and L.L. Maragakis, *Combination therapy for treatment of infections with gram-negative bacteria.* Clinical microbiology reviews, 2012. **25**(3): p. 450-470.
130. LaPlante, K.L. and S. Woodmansee, *Activities of Daptomycin and Vancomycin Alone and in Combination with Rifampin and Gentamicin against Biofilm-Forming Methicillin-Resistant Staphylococcus aureus Isolates in an Experimental Model of Endocarditis.* Antimicrobial Agents and Chemotherapy, 2009. **53**(9): p. 3880-3886.
131. Cheesman, M.J., et al., *Developing New Antimicrobial Therapies: Are Synergistic Combinations of Plant Extracts/Compounds With Conventional Antibiotics the Solution?* Pharmacognosy Reviews, 2017. **11**(22): p. 57.
132. Lázár, V., et al., *Antibiotic-Resistant Bacteria Show Widespread Collateral Sensitivity to Antimicrobial Peptides.* Nature Microbiology, 2018. **3**(6): p. 718-731.
133. Takahashi, D., et al., *Structural determinants of host defense peptides for antimicrobial activity and target cell selectivity.* Biochimie, 2010. **92**(9): p. 1236-1241.
134. Zasloff, M., *Magainins, a class of antimicrobial peptides from Xenopus skin: isolation, characterization of two active forms, and partial cDNA sequence of a precursor.* Proceedings of the National Academy of Sciences, 1987. **84**(15): p. 5449-5453.
135. Nguyen, L.T., E.F. Haney, and H.J. Vogel, *The expanding scope of antimicrobial peptide structures and their modes of action.* Trends in biotechnology, 2011. **29**(9): p. 464-472.
136. Deshayes, C., et al., *Drug delivery systems for the oral administration of antimicrobial peptides: Promising tools to treat infectious diseases.* Frontiers in Medical Technology, 2022. **3**: p. 778645.
137. Wang, G., *Human antimicrobial peptides and proteins.* Pharmaceuticals, 2014. **7**(5): p. 545-594.
138. Koehbach, J. and D.J. Craik, *The vast structural diversity of antimicrobial peptides.* Trends in pharmacological sciences, 2019. **40**(7): p. 517-528.
139. Shafee, T.M., et al., *Convergent evolution of defensin sequence, structure and function.* Cellular and Molecular Life Sciences, 2017. **74**: p. 663-682.

140. Jackson, M., H.H. Mantsch, and J.H. Spencer, *Conformation of Magainin-2 and Related Peptides in Aqueous Solution and Membrane Environments Probed by Fourier Transform Infrared Spectroscopy.* Biochemistry, 1992. **31**(32): p. 7289-7293.

141. Bhopale, G.M., *Antimicrobial peptides: a promising avenue for human healthcare.* Current pharmaceutical biotechnology, 2020. **21**(2): p. 90-96.

142. Yang, L., et al., *Barrel-Stave Model or Toroidal Model? A Case Study on Melittin Pores.* Biophysical Journal, 2001. **81**(3): p. 1475-1485.

143. Su, Y., S. Li, and M. Hong, *Cationic Membrane Peptides: Atomic-Level Insight of Structure–activity Relationships From Solid-State NMR.* Amino Acids, 2012. **44**(3): p. 821-833.

144. Mihajlovic, M. and T. Lazaridis, *Antimicrobial Peptides in Toroidal and Cylindrical Pores.* Biochimica Et Biophysica Acta (Bba) - Biomembranes, 2010. **1798**(8): p. 1485-1493.

145. Matsuzaki, K., K.-i. Sugishita, and K. Miyajima, *Interactions of an Antimicrobial Peptide, Magainin 2, With Lipopolysaccharide-containing Liposomes as a Model for Outer Membranes of Gram-negative Bacteria.* Febs Letters, 1999. **449**(2-3): p. 221-224.

146. Yi, T., Y. Huang, and Y. Chen, *Production of an Antimicrobial Peptide <scp>AN</Scp>5-1 in <i>Escherichia Coli</I> and Its Dual Mechanisms Against Bacteria.* Chemical Biology & Drug Design, 2014. **85**(5): p. 598-607.

147. Parker, J., et al., *Derivatisation of buforin IIb, a cationic henicosapeptide, to afford its complexation to platinum (ii) resulting in a novel platinum (ii)–buforin IIb conjugate with anti-cancer activity.* Dalton Transactions, 2016. **45**(33): p. 13038-13041.

148. Mardirossian, M., et al., *Fragments of the nonlytic proline-rich antimicrobial peptide Bac5 kill Escherichia coli cells by inhibiting protein synthesis.* Antimicrobial agents and chemotherapy, 2018. **62**(8): p. 10.1128/aac. 00534-18.

149. Kim, S., J.S. Hwang, and D.G. Lee, *Lactoferricin B like peptide triggers mitochondrial disruption-mediated apoptosis by inhibiting respiration under nitric oxide accumulation in Candida albicans.* IUBMB life, 2020. **72**(7): p. 1515-1527.

150. Liu, Z., et al., *Gene-trait matching analysis reveals putative genes involved in Bifidobacterium spp. biofilm formation.* Gene, 2022. **826**: p. 146449.

151. Memariani, H. and M. Memariani, *Antibiofilm properties of cathelicidin LL-37: an in-depth review.* World Journal of Microbiology and Biotechnology, 2023. **39**(4): p. 99.

152. Mishra, B. and G. Wang, *Individual and combined effects of engineered peptides and antibiotics on Pseudomonas aeruginosa biofilms.* Pharmaceuticals, 2017. **10**(3): p. 58.

153. Roy, N., et al., *Outcomes After Implant-Based Breast Reconstruction Following the National Institution of a Ban on Bacitracin Irrigation.* Annals of Plastic Surgery, 2024. **92**(4S): p. S191-S195.

154. Tran, T.B., et al., *Pharmacokinetics/pharmacodynamics of colistin and polymyxin B: are we there yet?* International journal of antimicrobial agents, 2016. **48**(6): p. 592-597.

155. Zhanel, G.G., et al., *New lipoglycopeptides: a comparative review of dalbavancin, oritavancin and telavancin.* Drugs, 2010. **70**: p. 859-886.

156. Tally, F.P. and M.F. DeBruin, *Development of daptomycin for gram-positive infections.* Journal of Antimicrobial Chemotherapy, 2000. **46**(4): p. 523-526.

157. Elbehiry, A., et al., *The development of technology to prevent, diagnose, and manage antimicrobial resistance in healthcare-associated infections.* Vaccines, 2022. **10**(12): p. 2100.

158. Mahlapuu, M., C. Björn, and J. Ekblom, *Antimicrobial Peptides as Therapeutic Agents: Opportunities and Challenges.* Critical Reviews in Biotechnology, 2020. **40**(7): p. 978-992.

159. Lipsky, B.A., K.J. Holroyd, and M. Zasloff, *Topical versus systemic antimicrobial therapy for treating mildly infected diabetic foot ulcers: a randomized, controlled, double-*

blinded, multicenter trial of pexiganan cream. Clinical infectious diseases, 2008. **47**(12): p. 1537-1545.

160. Mahlapuu, M., et al., *Antimicrobial peptides: an emerging category of therapeutic agents. Front Cell Infect Microbiol. 2016; 6: 194*. 2016, Epub 2017/01/14. https://doi. org/10.3389/fcimb. 2016.00194 PMID: 28083516.
161. Rizzetto, G., et al., *Our Experience over 20 years: antimicrobial peptides against gram positives, gram negatives, and fungi.* Pharmaceutics, 2022. **15**(1): p. 40.
162. Zhu, Y., et al., *Antimicrobial peptides, conventional antibiotics, and their synergistic utility for the treatment of drug-resistant infections.* Medicinal Research Reviews, 2022. **42**(4): p. 1377-1422.
163. Gottler, L.M. and A. Ramamoorthy, *Structure, Membrane Orientation, Mechanism, and Function of Pexiganan — A Highly Potent Antimicrobial Peptide Designed From Magainin.* Biochimica Et Biophysica Acta (Bba) - Biomembranes, 2009. **1788**(8): p. 1680-1686.
164. Jaśkiewicz, M., et al., *The Study of Antistaphylococcal Potential of Omiganan and Retro-Omiganan Under Flow Conditions.* Probiotics and Antimicrobial Proteins, 2024.
165. Boullet, H., et al., *Small AntiMicrobial Peptide With in Vivo Activity Against Sepsis.* Molecules, 2019. **24**(9): p. 1702.
166. Zharkova, M.S., et al., *Application of antimicrobial peptides of the innate immune system in combination with conventional antibiotics—a novel way to combat antibiotic resistance?* Frontiers in cellular and infection microbiology, 2019. **9**: p. 128.
167. Yamauchi, R., et al., *Development of Antimicrobial Peptide–Antibiotic Conjugates to Improve the Outer Membrane Permeability of Antibiotics Against Gram-Negative Bacteria.* Acs Infectious Diseases, 2022. **8**(11): p. 2339-2347.
168. Xia, Y., et al., *Elucidating the mechanism by which synthetic helper peptides sensitize Pseudomonas aeruginosa to multiple antibiotics.* PLoS Pathog, 2021. **17**(9): p. e1009909.
169. Choi, H. and D.G. Lee, *Synergistic effect of antimicrobial peptide arenicin-1 in combination with antibiotics against pathogenic bacteria.* Research in microbiology, 2012. **163**(6-7): p. 479-486.
170. Liu, Y., et al., *Antagonizing vancomycin resistance in Enterococcus by surface localized antimicrobial display-derived peptides.* ACS Infectious Diseases, 2019. **6**(5): p. 761-767.
171. Chen, C., et al., *Antimicrobial peptides as promising antibiotic adjuvants to combat drug-resistant pathogens.* Critical Reviews in Microbiology, 2024. **50**(3): p. 267-284.
172. Otvos Jr, L., et al., *Synergy between proline-rich antimicrobial peptides and small molecule antibiotics against selected gram-negative pathogens in vitro and in vivo.* Frontiers in chemistry, 2018. **6**: p. 309.
173. Jindal, H.M., et al., *Mechanisms of action and in vivo antibacterial efficacy assessment of five novel hybrid peptides derived from Indolicidin and Ranalexin against Streptococcus pneumoniae.* PeerJ, 2017. **5**: p. e3887.
174. Vries, R.d., et al., *Next-Generation Nanoantibacterial Tools Developed From Peptides.* Nanomedicine, 2015. **10**(10): p. 1643-1661.
175. Kumar, P., J.N. Kizhakkedathu, and S.K. Straus, *Antimicrobial Peptides: Diversity, Mechanism of Action and Strategies to Improve the Activity and Biocompatibility in Vivo.* Biomolecules, 2018. **8**(1): p. 4.
176. Ting, D.S.J., et al., *Strategies in translating the therapeutic potentials of host defense peptides.* Frontiers in Immunology, 2020. **11**: p. 983.
177. Blondelle, S.E., et al., *Influence of tryptophan residues on melittin's hemolytic activity.* Biochimica et Biophysica Acta (BBA)-Protein Structure and Molecular Enzymology, 1993. **1202**(2): p. 331-336.

178. Dong, B., et al., *Tolerance Assessment of Atractylodes Macrocephala Polysaccharide in the Diet of Largemouth Bass (Micropterus Salmoides).* Antioxidants, 2022. **11**(8): p. 1581.
179. Lu, J., et al., *D- And Unnatural Amino Acid Substituted Antimicrobial Peptides With Improved Proteolytic Resistance and Their Proteolytic Degradation Characteristics.* Frontiers in Microbiology, 2020. **11**.
180. Tsikourkitoudi, V., et al., *Flame-Made Calcium Phosphate Nanoparticles With High Drug Loading for Delivery of Biologics.* Molecules, 2020. **25**(7): p. 1747.
181. Ki, M.-R., et al., *Self-Entrapment of Antimicrobial Peptides in Silica Nanoparticles for Stable and Effective Antimicrobial Peptide Delivery System.* 2023.
182. Wang, T., et al., *The Effect of Structural Modification of Antimicrobial Peptides on Their Antimicrobial Activity, Hemolytic Activity, and Plasma Stability.* Journal of Peptide Science, 2021. **27**(5).
183. Qvit, N., et al., *Peptidomimetic therapeutics: scientific approaches and opportunities.* Drug discovery today, 2017. **22**(2): p. 454-462.
184. Torres, M.D., et al., *Peptide design principles for antimicrobial applications.* Journal of molecular biology, 2019. **431**(18): p. 3547-3567.
185. Kang, S.-J., S.H. Nam, and B.-J. Lee, *Engineering approaches for the development of antimicrobial peptide-based antibiotics.* Antibiotics, 2022. **11**(10): p. 1338.
186. Han, Y., et al., *Chemical modifications to increase the therapeutic potential of antimicrobial peptides.* Peptides, 2021. **146**: p. 170666.
187. Petrou, C. and Y. Sarigiannis, *Peptide synthesis: Methods, trends, and challenges.* Peptide applications in biomedicine, biotechnology and bioengineering, 2018: p. 1-21.
188. Lee, A.C.-L., et al., *A comprehensive review on current advances in peptide drug development and design.* International journal of molecular sciences, 2019. **20**(10): p. 2383.
189. Mwangi, J., et al., *The antimicrobial peptide ZY4 combats multidrug-resistant Pseudomonas aeruginosa and Acinetobacter baumannii infection.* Proceedings of the National Academy of Sciences, 2019. **116**(52): p. 26516-26522.
190. Agrawal, P. and G.P.S. Raghava, *Prediction of Antimicrobial Potential of a Chemically Modified Peptide From Its Tertiary Structure.* Frontiers in Microbiology, 2018. **9**.
191. Vejzovic, D., et al., *Where Electrostatics Matter: Bacterial Surface Neutralization and Membrane Disruption by Antimicrobial Peptides SAAP-148 and OP-145.* Biomolecules, 2022. **12**(9): p. 1252.
192. Li, H., et al., *Novel Stapling by Lysine Tethering Provides Stable and Low Hemolytic Cationic Antimicrobial Peptides.* Journal of Medicinal Chemistry, 2020. **63**(8): p. 4081-4089.
193. Boge, L., et al., *Lipid-Based Liquid Crystals as Carriers for Antimicrobial Peptides: Phase Behavior and Antimicrobial Effect.* Langmuir, 2016. **32**(17): p. 4217-4228.
194. Sowers, A., et al., *Advances in Antimicrobial Peptide Discovery via Machine Learning and Delivery via Nanotechnology.* Microorganisms, 2023. **11**(5): p. 1129.
195. Lindquist, E., K.N. Mosher-Howe, and X. Liu, *Nanotechnology . . . What Is It Good For? (Absolutely Everything): A Problem Definition Approach.* Review of Policy Research, 2010. **27**(3): p. 255-271.
196. Mehmood, A. and N. None, *Nano-Warriors Against Cancer: Who Won?* Austin Journal of Nanomedicine & Nanotechnology, 2023. **11**(1).
197. Anisuzzaman, A.S.M. and A. Alim, *Nanomedicines and Its Applications in the Healthcare.* Biomedical Sciences, 2019. **5**(4): p. 57.

198. Sachithanandan, J.S., et al., *Revolutionizing Antimicrobial Solutions Nanotechnology, CRISPR-Cas9 and Innovative Approaches to Combat Drug Resistance in ESKAPE Pathogens.* Journal of Pure and Applied Microbiology, 2024. **18**(2): p. 808-822.
199. Chu, L., et al., *A Charge-Adaptive Nanosystem for Prolonged and Enhanced in Vivo Antibiotic Delivery.* Chemical Communications, 2016. **52**(37): p. 6265-6268.
200. Dubald, M., et al., *Ophthalmic Drug Delivery Systems for Antibiotherapy—A Review.* Pharmaceutics, 2018. **10**(1): p. 10.
201. Jackson, J.E., Z. Kopecki, and A.J. Cowin, *Nanotechnological Advances in Cutaneous Medicine.* Journal of Nanomaterials, 2013. **2013**: p. 1-8.
202. Scicluna, M.C. and L. Vella-Żarb, *Evolution of Nanocarrier Drug-Delivery Systems and Recent Advancements in Covalent Organic Framework–Drug Systems.* Acs Applied Nano Materials, 2020. **3**(4): p. 3097-3115.
203. Dizaj, S.M., et al., *Nanosizing of drugs: Effect on dissolution rate.* Res Pharm Sci, 2015. **10**(2): p. 95-108.
204. Xie, B., et al., *Solubilization techniques used for poorly water-soluble drugs.* Acta Pharmaceutica Sinica B, 2024.
205. Saleem, K., et al., *Applications of Nanomaterials in Leishmaniasis: A Focus on Recent Advances and Challenges.* Nanomaterials, 2019. **9**(12): p. 1749.
206. Dai, X., et al., *Intracellular Infection-Responsive Macrophage-Targeted Nanoparticles for Synergistic Antibiotic Immunotherapy of Bacterial Infection.* Journal of Materials Chemistry B, 2024. **12**(21): p. 5248-5260.
207. Zhang, W., et al., *Emerging Antibacterial Strategies With Application of Targeting Drug Delivery System and Combined Treatment.* International Journal of Nanomedicine, 2021. **Volume 16**: p. 6141-6156.
208. Radovic-Moreno, A.F., et al., *Surface charge-switching polymeric nanoparticles for bacterial cell wall-targeted delivery of antibiotics.* ACS nano, 2012. **6**(5): p. 4279-4287.
209. Si, Y., et al., *Rapid and accurate detection of Escherichia coli growth by fluorescent pH-sensitive organic nanoparticles for high-throughput screening applications.* Biosensors and Bioelectronics, 2016. **75**: p. 320-327.
210. Wang, B., et al., *A self-defensive antibacterial coating acting through the bacteria-triggered release of a hydrophobic antibiotic from layer-by-layer films.* Journal of Materials Chemistry B, 2017. **5**(7): p. 1498-1506.
211. Thamphiwatana, S., et al., *Phospholipase A2-responsive antibiotic delivery via nanoparticle-stabilized liposomes for the treatment of bacterial infection.* Journal of Materials Chemistry B, 2014. **2**(46): p. 8201-8207.
212. Pornpattananangkul, D., et al., *Bacterial toxin-triggered drug release from gold nanoparticle-stabilized liposomes for the treatment of bacterial infection.* Journal of the American Chemical Society, 2011. **133**(11): p. 4132-4139.
213. Yang, S., et al., *Bacteria-Targeting Nanoparticles with Microenvironment-Responsive Antibiotic Release To Eliminate Intracellular Staphylococcus aureus and Associated Infection.* ACS Applied Materials & Interfaces, 2018. **10**(17): p. 14299-14311.
214. Long, Y., et al., *Novel polymeric nanoparticles targeting the lipopolysaccharides of Pseudomonas aeruginosa.* International journal of pharmaceutics, 2016. **502**(1-2): p. 232-241.
215. Alvarez-Lorenzo, C., et al., *Stimuli-responsive polymers for antimicrobial therapy: drug targeting, contact-killing surfaces and competitive release.* Expert opinion on drug delivery, 2016. **13**(8): p. 1109-1119.
216. Yu, H.S., et al., *Facile Fabrication of Hyaluronated Starch Nanogels for Efficient Docetaxel Delivery.* Journal of Bioactive and Compatible Polymers, 2019. **34**(4-5): p. 321-330.

217. Deepika, M., et al., *Co-Delivery of Diverse Therapeutic Compounds Using PEG–PLGA Nanoparticle Cargo Against Drug-Resistant Bacteria: An Improved Anti-Biofilm Strategy.* Acs Applied Bio Materials, 2019. **3**(1): p. 385-399.

218. Yang, M., et al., *Advances in Research on Cellulose-Based Drug Carriers.* Paper and Biomaterials, 2023. **8**(4): p. 55-68.

219. Karbalaeiheidar, H. and F. Ashrafi, *Vancomycin-Gingerol Encapsulated Niosomal Formulation Against Carbapenem-Resistant Klebsiella Pneumoniae.* Biomedical Materials, 2023. **18**(4): p. 045015.

220. Geng, M., et al., *Efficacious Analogs of the Lantibiotic Mutacin 1140 Against a Systemic Methicillin-Resistant Staphylococcus Aureus Infection.* Antimicrobial Agents and Chemotherapy, 2018. **62**(12).

221. Zhang, Y., et al., *A Bioadhesive Nanoparticle–Hydrogel Hybrid System for Localized Antimicrobial Drug Delivery.* Acs Applied Materials & Interfaces, 2016. **8**(28): p. 18367-18374.

222. Dhanalakshmi, V., et al., *Skin and Muscle Permeating Antibacterial Nanoparticles for Treating <i>Staphylococcus Aureus</I> Infected Wounds.* Journal of Biomedical Materials Research Part B Applied Biomaterials, 2016. **104**(4): p. 797-807.

223. Bose, S., A. Kaur, and S. Sharma, *A Review on Advances of Sustained Release Drug Delivery System.* International Research Journal of Pharmacy, 2013. **4**(6): p. 1-5.

224. Hsu, Y.H., et al., *Sustained Release of Antifungal and Antibacterial Agents From Novel Hybrid Degradable Nanofibers for the Treatment of Polymicrobial Osteomyelitis.* International Journal of Molecular Sciences, 2023. **24**(4): p. 3254.

225. Lai, W.-F., et al., *Cross-Linked Chitosan/Lysozyme Hydrogels With Inherent Antibacterial Activity and Tuneable Drug Release Properties for Cutaneous Drug Administration.* Science and Technology of Advanced Materials, 2023. **24**(1).

226. Osman, N., et al., *Surface Modification of Nano-drug Delivery Systems for Enhancing Antibiotic Delivery and Activity.* Wiley Interdisciplinary Reviews Nanomedicine and Nanobiotechnology, 2021. **14**(1).

227. Jia, Z., *Application of Degradable Polymers for the Treatment of Wounds and Tumors.* Highlights in Science Engineering and Technology, 2022. **26**: p. 288-295.

228. Pan, K., et al., *Development of Intelligent Redox-Responsive Biopolymer-Based Antibacterial Coating for Controlled Drug Release.* Journal of Physics Conference Series, 2024. **2789**(1): p. 012004.

229. Leslie, J.L., et al., *Persistence and Toxin Production by Clostridium Difficile Within Human Intestinal Organoids Result in Disruption of Epithelial Paracellular Barrier Function.* Infection and Immunity, 2015. **83**(1): p. 138-145.

230. von Roemeling, C., et al., *Breaking down the barriers to precision cancer nanomedicine.* Trends in biotechnology, 2017. **35**(2): p. 159-171.

231. Schwartz Jr, S., *Unmet needs in developing nanoparticles for precision medicine*. 2017, Taylor & Francis. p. 271-274.

232. Xin, L., et al., *Ultrasound-Activatable Phase-Shift Nanoparticle as a Targeting Antibacterial Agent for Efficient Eradication Of<i>Pseudomonas Aeruginosa</I>Biofilms.* Acs Applied Materials & Interfaces, 2022. **14**(42): p. 47420-47431.

233. Cao, J., et al., *Phosphorylcholine-Based Polymer Encapsulated Chitosan Nanoparticles Enhance the Penetration of Antimicrobials in a Staphylococcal Biofilm.* Acs Macro Letters, 2019. **8**(6): p. 651-657.

234. Dyett, B., et al., *Uptake Dynamics of Cubosome Nanocarriers at Bacterial Surfaces and the Routes for Cargo Internalization.* Acs Applied Materials & Interfaces, 2021. **13**(45): p. 53530-53540.

235. Li, L., et al., *Surface Charge Generation in Nanogels for Activated Cellular Uptake at Tumor-Relevant pH.* Chemical Science, 2013. **4**(9): p. 3654.
236. Liu, Y., et al., *Surface-Adaptive, Antimicrobially Loaded, Micellar Nanocarriers With Enhanced Penetration and Killing Efficiency in Staphylococcal Biofilms.* Acs Nano, 2016. **10**(4): p. 4779-4789.
237. Phakatkar, A.H., et al., *In-Situ TEM Studies on Nanoparticle Interactions With Bacterial Cells.* Microscopy and Microanalysis, 2022. **28**(S1): p. 1104-1106.
238. Zhang, Q., et al., *In Vivo Bioluminescence Imaging of Natural Bacteria Within Deep Tissues via ATP-binding Cassette Sugar Transporter.* Nature Communications, 2023. **14**(1).
239. Brandelli, A., *The interaction of nanostructured antimicrobials with biological systems: Cellular uptake, trafficking and potential toxicity.* Food Science and Human Wellness, 2020. **9**(1): p. 8-20.
240. *The Effect of Silver Nanoparticles and Thioacetamide on Blood Urea Nitrogen and Creatinine in Male Laboratory Mice.* International Journal of Biosciences (Ijb), 2014. **4**(1): p. 139-142.
241. Burga, R.A., et al., *Designing Magnetically Responsive Biohybrids Composed of Cord Blood-Derived Natural Killer Cells and Iron Oxide Nanoparticles.* Bioconjugate Chemistry, 2019. **30**(3): p. 552-560.
242. Qu, X., et al., *Anti-Cd30-Targeted Gold Nanoparticles for Photothermal Therapy of L-428 Hodgkin's Cell.* International Journal of Nanomedicine, 2012: p. 6095.
243. Zheng, P., et al., *Formation of Gold@Polymer Core–Shell Particles and Gold Particle Clusters on a Template of Thermoresponsive and pH-Responsive Coordination Triblock Copolymer.* Langmuir, 2006. **22**(22): p. 9393-9396.
244. Shaker, M.A. and M.I. Shaaban, *Synthesis of Silver Nanoparticles With Antimicrobial and Anti-Adherence Activities Against Multidrug-Resistant Isolates From Acinetobacter Baumannii.* Journal of Taibah University Medical Sciences, 2017. **12**(4): p. 291-297.
245. Alizadeh, H., M. Salouti, and R. Shapouri, *Bactericidal Effect of Silver Nanoparticles on Intramacrophage Brucella Abortus 544.* Jundishapur Journal of Microbiology, 2014. **7**(3).
246. Ilkov, O., et al., *Antibacterial and Cytotoxic Activity of Metronidazole and Levofloxacin Composites With Silver Nanoparticle.* Current Issues in Pharmacy and Medical Sciences, 2021. **34**(4): p. 224-228.
247. Uzair, M., et al., *Review: Biomedical Applications of Carbon Nanotubes.* Nano Biomedicine and Engineering, 2021. **13**(1).
248. Zhao, S., et al., *Synthesis of Carbon Nitride Hollow Microspheres With Highly Hierarchical Porosity Templated by Poly (Ionic Liquid) for Photocatalytic Hydrogen Evolution.* Applied Organometallic Chemistry, 2020. **34**(4).
249. Kong, X., et al., *Graphitic carbon nitride-based materials for photocatalytic antibacterial application.* Materials Science and Engineering: R: Reports, 2021. **145**: p. 100610.
250. Lu, M., et al., *Synergistic Bactericidal Activity of Chlorhexidine-Loaded, Silver-Decorated Mesoporous Silica Nanoparticles.* International Journal of Nanomedicine, 2017. **Volume 12**: p. 3577-3589.
251. Zhang, J., et al., *Nanotechnology-driven Strategies to Enhance the Treatment of Drug-resistant Bacterial Infections.* Wiley Interdisciplinary Reviews Nanomedicine and Nanobiotechnology, 2024. **16**(3).
252. Dhingra, K., et al., *Therapeutics Potential of Polysaccharide Based Nanocarriers: A Review.* Plant Archives, 2023. **23**(2).
253. Mazayen, Z.M., et al., *Pharmaceutical Nanotechnology: From the Bench to the Market.* Future Journal of Pharmaceutical Sciences, 2022. **8**(1).

254. Simpson, E., et al., *Evaluation of the Potential of Chitosan Nanoparticles as a Delivery Vehicle for Gentamicin for the Treatment of Osteomyelitis.* Antibiotics, 2024. **13**(3): p. 208.

255. Arana, L., L. Gallego, and I. Alkorta, *Incorporation of Antibiotics Into Solid Lipid Nanoparticles: A Promising Approach to Reduce Antibiotic Resistance Emergence.* Nanomaterials, 2021. **11**(5): p. 1251.

256. Esposito, E., et al., *Lipid Nanostructures for Antioxidant Delivery: A Comparative Preformulation Study.* Beilstein Journal of Nanotechnology, 2019. **10**: p. 1789-1801.

257. Kiymaci, M.E., et al., *Evaluation of Bacterial Uptake, Antibacterial Efficacy Against <i>Escherichia Coli</I>, and Cytotoxic Effects of Moxifloxacin-Loaded Solid Lipid Nanoparticles.* Archives of Industrial Hygiene and Toxicology, 2022. **73**(4): p. 260-269.

258. Piazzini, V., et al., *Nanostructured Lipid Carriers as Promising Delivery Systems for Plant Extracts: The Case of Silymarin.* Applied Sciences, 2018. **8**(7): p. 1163.

259. Ryan, A., et al., *The Development of a Solid Lipid Nanoparticle (SLN)-based Lacticin 3147 Hydrogel for the Treatment of Wound Infections.* Drug Delivery and Translational Research, 2023. **13**(9): p. 2407-2423.

260. Yang, K., et al., *Wheat Germ Agglutinin Modified Liposomes for the Photodynamic Inactivation of Bacteria[†].* Photochemistry and Photobiology, 2011. **88**(3): p. 548-556.

261. Zhang, K., et al., *Preparation, Characterization, and in Vivo Pharmacokinetics of Nanostructured Lipid Carriers Loaded With Oleanolic Acid and Gentiopicrin.* International Journal of Nanomedicine, 2013: p. 3227.

262. You, J., G. Zhang, and C. Li, *Exceptionally High Payload of Doxorubicin in Hollow Gold Nanospheres for Near-Infrared Light-Triggered Drug Release.* Acs Nano, 2010. **4**(2): p. 1033-1041.

263. Hamdi, M., et al., *An Integrated Vitamin E-Coated Polymer Hybrid Nanoplatform: A Lucrative Option for an Enhanced in Vitro Macrophage Retention for an Anti-Hepatitis B Therapeutic Prospect.* Plos One, 2020. **15**(1): p. e0227231.

264. Huang, B., et al., *IR780 Based Sonotherapeutic Nanoparticles to Combat Multidrug-Resistant Bacterial Infections.* Frontiers in Chemistry, 2022. **10**.

265. Lee, H.W., S. Kharel, and S.C.J. Loo, *Lipid-Coated Hybrid Nanoparticles for Enhanced Bacterial Biofilm Penetration and Antibiofilm Efficacy.* 2022.

266. Arafa, M.G., H. Mousa, and N.N. Afifi, *Preparation of PLGA-chitosan Based Nanocarriers for Enhancing Antibacterial Effect of Ciprofloxacin in Root Canal Infection.* Drug Delivery, 2019. **27**(1): p. 26-39.

267. Tan, S., et al., *Lipid-Enveloped Hybrid Nanoparticles for Drug Delivery.* Nanoscale, 2013. **5**(3): p. 860.

268. Effah, C.Y., et al., *Bacteria-derived extracellular vesicles: endogenous roles, therapeutic potentials and their biomimetics for the treatment and prevention of sepsis.* Frontiers in Immunology, 2024. **15**.

269. Jafari, N., et al., *Mesenchymal Stromal/Stem Cells-Derived Exosomes as an Antimicrobial Weapon for Orodental Infections.* Frontiers in Microbiology, 2022. **12**.

270. Mawad, D., et al., *Synthesis and Characterization of Novel Radiopaque Poly(allyl Amine) Nanoparticles.* Nanotechnology, 2010. **21**(33): p. 335603.

271. Malek-Khatabi, A., et al., *Long-Term Vaccine Delivery and Immunological Responses Using Biodegradable Polymer-Based Carriers.* Acs Applied Bio Materials, 2022. **5**(11): p. 5015-5040.

272. Da Costa, D., et al., *Surface charge modulation of rifampicin-loaded PLA nanoparticles to improve antibiotic delivery in Staphylococcus aureus biofilms.* Journal of nanobiotechnology, 2021. **19**: p. 1-17.

273. Deepika, M.S., et al., *Co-delivery of diverse therapeutic compounds using PEG–PLGA nanoparticle cargo against drug-resistant bacteria: an improved anti-biofilm strategy.* ACS Applied Bio Materials, 2019. **3**(1): p. 385-399.

274. Srisang, S. and N. Nasongkla, *Spray coating of foley urinary catheter by chlorhexidine-loadedpoly (ε-caprolactone) nanospheres: effect of lyoprotectants, characteristics, and antibacterial activity evaluation.* Pharmaceutical development and technology, 2019. **24**(4): p. 402-409.

275. Zamani, N., et al., *The New Probiotic Lactobacillus Plantarum Strain Isolated From Traditional Dairy Showed the Synergistic Effect on Aflatoxin B1 Detoxification Along With Nanochitosan Particles.* 2021.

276. Barzegar, F., et al., *Preparation and Evaluation of Chitosan Nanoparticles Containing Iranian Eschium Amoenum Extract and Its Antimicrobial Effects on Common Oral Microorganisms.* The Open Dentistry Journal, 2023. **17**(1).

277. Aioub, M. and M.A. El-Sayed, *A Real-Time Surface Enhanced Raman Spectroscopy Study of Plasmonic Photothermal Cell Death Using Targeted Gold Nanoparticles.* Journal of the American Chemical Society, 2016. **138**(4): p. 1258-1264.

278. Bernal-Mercado, A.T., et al., *Hydrophobic Chitosan Nanoparticles Loaded With Carvacrol Against Pseudomonas Aeruginosa Biofilms.* Molecules, 2022. **27**(3): p. 699.

279. Choudhary, D.K. and S. Parveen, *Nanoparticles as Surrogates of Antibiotics: A Comprehensive Review.* International Journal of Research Publication and Reviews, 2024. **5**(3): p. 6952-6960.

280. Ucak, S., et al., *Inhibitory effects of aptamer targeted teicoplanin encapsulated PLGA nanoparticles for Staphylococcus aureus strains.* World Journal of Microbiology and Biotechnology, 2020. **36**: p. 1-9.

281. Engevik, M.A., et al., *Microbial Metabolic Capacity for Intestinal Folate Production and Modulation of Host Folate Receptors.* Frontiers in Microbiology, 2019. **10**.

282. Wolff, K. and L. Nguyen, *Strategies for Potentiation of Ethionamide and Folate Antagonists Against<i>Mycobacterium Tuberculosis</I>.* Expert Review of Anti-Infective Therapy, 2012. **10**(9): p. 971-981.

283. Pan, L., et al., *ICAM-1-targeted and Antibacterial Peptide Modified Polymeric Nanoparticles for Specific Combating Sepsis.* Materials & Design, 2022. **222**: p. 111007.

284. Aruguete, D.M. and M.F. Hochella, *Bacteria–nanoparticle interactions and their environmental implications.* Environmental Chemistry, 2010. **7**(1): p. 3-9.

285. Applerot, G., et al., *Understanding the antibacterial mechanism of CuO nanoparticles: revealing the route of induced oxidative stress.* Small, 2012. **8**(21): p. 3326-3337.

286. Sohm, B., et al., *Insight into the primary mode of action of TiO2 nanoparticles on Escherichia coli in the dark.* Proteomics, 2015. **15**(1): p. 98-113.

287. Yang, H., et al., *Comparative study of cytotoxicity, oxidative stress and genotoxicity induced by four typical nanomaterials: the role of particle size, shape and composition.* Journal of applied Toxicology, 2009. **29**(1): p. 69-78.

288. Wang, L., et al., *Morphology-dependent bactericidal activities of Ag/CeO2 catalysts against Escherichia coli.* Journal of inorganic biochemistry, 2014. **135**: p. 45-53.

289. Pal, S., Y.K. Tak, and J.M. Song, *Does the antibacterial activity of silver nanoparticles depend on the shape of the nanoparticle? A study of the gram-negative bacterium Escherichia coli.* Applied and environmental microbiology, 2007. **73**(6): p. 1712-1720.

290. Talebian, N., S.M. Amininezhad, and M. Doudi, *Controllable synthesis of ZnO nanoparticles and their morphology-dependent antibacterial and optical properties.* Journal of Photochemistry and Photobiology B: Biology, 2013. **120**: p. 66-73.

291. Dzuvor, C.K.O., et al., *Coassembled Multicomponent Protein Nanoparticles Elicit Enhanced Antibacterial Activity.* Acs Nano, 2024. **18**(5): p. 4478-4494.

292. Ivask, A., et al., *Toxicity mechanisms in Escherichia coli vary for silver nanoparticles and differ from ionic silver.* ACS nano, 2014. **8**(1): p. 374-386.
293. Cao, B., et al., *Polyprodrug antimicrobials: remarkable membrane damage and concurrent drug release to combat antibiotic resistance of methicillin-resistant staphylococcus aureus.* Small, 2018. **14**(41): p. 1802008.
294. Sercombe, L., et al., *Advances and Challenges of Liposome Assisted Drug Delivery.* Frontiers in Pharmacology, 2015. **6**.
295. Nsairat, H., et al., *Liposomes: structure, composition, types, and clinical applications.* Heliyon, 2022. **8**(5): p. e09394.
296. Webb, M.S., et al., *Antibacterial Efficacy Against an in Vivo <i>Salmonella Typhimurium</I> Infection Model and Pharmacokinetics of a Liposomal Ciprofloxacin Formulation.* Antimicrobial Agents and Chemotherapy, 1998. **42**(1): p. 45-52.
297. Zhang, H., G. Wang, and H. Yang, *Drug delivery systems for differential release in combination therapy.* Expert Opinion on Drug Delivery, 2011. **8**(2): p. 171-190.
298. Zamboni, W.C., et al., *Phase I and Pharmacokinetic Study of Pegylated Liposomal CKD-602 in Patients with Advanced Malignancies.* Clinical Cancer Research, 2009. **15**(4): p. 1466-1472.
299. Nicolosi, D., et al., *Encapsulation in fusogenic liposomes broadens the spectrum of action of vancomycin against Gram-negative bacteria.* International journal of antimicrobial agents, 2010. **35**(6): p. 553-558.
300. Chen, F., et al., *Fusogenic Liposome-Enhanced Cytosolic Delivery of Magnetic Nanoparticles.* RSC Advances, 2021. **11**(57): p. 35796-35805.
301. Cavalcanti, R.R.M., R.B. Lira, and K.A. Riske, *Membrane Fusion Biophysical Analysis of Fusogenic Liposomes.* Langmuir, 2022. **38**(34): p. 10430-10441.
302. Scheeder, A., et al., *Molecular Mechanisms of Cationic Fusogenic Liposome Interactions with Bacterial Envelopes.* Journal of the American Chemical Society, 2023. **145**(51): p. 28240-28250.
303. Fazal, S. and R. Lee, *Biomimetic Bacterial Membrane Vesicles for Drug Delivery Applications.* Pharmaceutics, 2021. **13**(9): p. 1430.
304. Spinozzi, F., et al., *Small-Angle Neutron Scattering Reveals the Nanostructure of Liposomes With Embedded OprF Porins of <i>Pseudomonas Aeruginosa</I>.* Langmuir, 2022. **38**(49): p. 15026-15037.
305. Drost, M., et al. *Bacteriomimetic Liposomes Improve Antibiotic Activity of a Novel Energy-Coupling Factor Transporter Inhibitor*. Pharmaceutics, 2022. **14**, DOI: 10.3390/pharmaceutics14010004.
306. Xu, J., et al., *Encapsulation of Oyster Protein Hydrolysates in Nanoliposomes: Vesicle Characteristics, Storage Stability, <i>in Vitro</I> Release, and Gastrointestinal Digestion.* Journal of Food Science, 2021. **86**(3): p. 960-968.
307. Panthi, V.K., K.E. Fairfull-Smith, and N. Islam, *Liposomal drug delivery strategies to eradicate bacterial biofilms: Challenges, recent advances, and future perspectives.* International Journal of Pharmaceutics, 2024. **655**: p. 124046.
308. Oku, N. and Y. Namba, *Long-circulating liposomes.* Critical reviews in therapeutic drug carrier systems, 1994. **11**(4): p. 231-270.
309. Du, Y., et al., *Thioether Phosphatidylcholine Liposomes: A Novel ROS-Responsive Platform for Drug Delivery.* Acs Applied Materials & Interfaces, 2019. **11**(41): p. 37411-37420.
310. Yanar, F., et al., *Continuous-Flow Production of Liposomes With a Millireactor Under Varying Fluidic Conditions.* Pharmaceutics, 2020. **12**(11): p. 1001.
311. Jiang, L., H.W. Lee, and S.C.J. Loo, *Therapeutic lipid-coated hybrid nanoparticles against bacterial infections.* RSC advances, 2020. **10**(14): p. 8497-8517.

312. Graef, F., et al., *The bacterial cell envelope as delimiter of anti-infective bioavailability – An in vitro permeation model of the Gram-negative bacterial inner membrane.* Journal of Controlled Release, 2016. **243**: p. 214-224.
313. Lee, H.W., S. Kharel, and S.C.J. Loo, *Lipid-Coated Hybrid Nanoparticles for Enhanced Bacterial Biofilm Penetration and Antibiofilm Efficacy.* ACS Omega, 2022. **7**(40): p. 35814-35824.
314. Fernández-Borbolla, A., L. García-Hevia, and M.L. Fanarraga, *Cell Membrane-Coated Nanoparticles for Precision Medicine: A Comprehensive Review of Coating Techniques for Tissue-Specific Therapeutics.* International Journal of Molecular Sciences, 2024. **25**(4): p. 2071.
315. Khan, M.M., et al., *Co-Delivery of Curcumin and Cisplatin to Enhance Cytotoxicity of Cisplatin Using Lipid-Chitosan Hybrid Nanoparticles.* International Journal of Nanomedicine, 2020. **Volume 15**: p. 2207-2217.
316. Wu, S., et al., *Bacterial Outer Membrane-Coated Mesoporous Silica Nanoparticles for Targeted Delivery of Antibiotic Rifampicin against Gram-Negative Bacterial Infection In Vivo.* Advanced Functional Materials, 2021. **31**(35): p. 2103442.
317. Weers, J., et al., *A gamma scintigraphy study to investigate lung deposition and clearance of inhaled amikacin-loaded liposomes in healthy male volunteers.* Journal of aerosol medicine and pulmonary drug delivery, 2009. **22**(2): p. 131-138.
318. FDA, U., *Arikayce®(amikacin liposome inhalation suspension): US prescribing information.* 2018.
319. Miller, C.B., et al., *Lipid Formulations of Amphotericin B Preserve and Stabilize Renal Function in HSCT Recipients.* Bone Marrow Transplantation, 2004. **33**(5): p. 543-548.
320. Yardley, V. and S.L. Croft, *In Vitro and in Vivo Activity of Amphotericin B-Lipid Formulations Against Experimental Trypanosoma Cruzi Infections.* American Journal of Tropical Medicine and Hygiene, 1999. **61**(2): p. 193-197.
321. Quilitz, R., *The Use of LIPID Formulations of Amphotericin B in Cancer Patients.* Cancer Control, 1998. **5**(5): p. 439-449.
322. Colilla, M. and M. Vallet-Regí, *Organically Modified Mesoporous Silica Nanoparticles Against Bacterial Resistance.* Chemistry of Materials, 2023. **35**(21): p. 8788-8805.
323. Campos, M.D., et al., *The Activity of Antimicrobial Surfaces Varies by Testing Protocol Utilized.* Plos One, 2016. **11**(8): p. e0160728.
324. Forbes, N., et al., *Rapid and scale-independent microfluidic manufacture of liposomes entrapping protein incorporating in-line purification and at-line size monitoring.* Int J Pharm, 2019. **556**: p. 68-81.
325. Chiesa, E., et al., *Staggered Herringbone Microfluid Device for the Manufacturing of Chitosan/TPP Nanoparticles: Systematic Optimization and Preliminary Biological Evaluation.* International journal of molecular sciences, 2019. **20**(24): p. 6212.
326. Roces, C.B., et al., *Scale-Independent Microfluidic Production of Cationic Liposomal Adjuvants and Development of Enhanced Lymphatic Targeting Strategies.* Molecular Pharmaceutics, 2019. **16**(10): p. 4372-4386.
327. Forbes, N., et al., *Rapid and scale-independent microfluidic manufacture of liposomes entrapping protein incorporating in-line purification and at-line size monitoring.* International journal of pharmaceutics, 2019. **556**: p. 68-81.
328. Stroock, A.D., et al., *Chaotic mixer for microchannels.* Science, 2002. **295**(5555): p. 647-651.
329. Tsai, H.-F., S. Podder, and P.-Y. Chen, *Microsystem Advances Through Integration With Artificial Intelligence.* Micromachines, 2023. **14**(4): p. 826.
330. Tresset, G., et al., *Fine Control Over the Size of Surfactant–Polyelectrolyte Nanoparticles by Hydrodynamic Flow Focusing.* Analytical Chemistry, 2013. **85**(12): p. 5850-5856.

331. Bezelya, A., B. Küçüktürkmen, and A. Bozkır, *Microfluidic Devices for Precision Nanoparticle Production.* Micro, 2023. **3**(4): p. 822-866.
332. Prakash, G., et al., *Microfluidic fabrication of lipid nanoparticles for the delivery of nucleic acids.* Adv Drug Deliv Rev, 2022. **184**: p. 114197.
333. Lou, G., et al., *Delivery of self-amplifying mRNA vaccines by cationic lipid nanoparticles: The impact of cationic lipid selection.* J Control Release, 2020. **325**: p. 370-379.
334. Hussain, M.T., et al., *Microfluidic production of protein loaded chimeric stealth liposomes.* Int J Pharm, 2020. **590**: p. 119955.
335. Roces, C.B., et al., *Investigating Prime-Pull Vaccination through a Combination of Parenteral Vaccination and Intranasal Boosting.* Vaccines, 2020. **8**(1): p. 10.
336. Liu, Y., et al., *Microfluidic Nanoparticles for Drug Delivery.* Small, 2022. **18**(36): p. 2106580.
337. Wu, J., et al., *Preparation, Characterization, and Antibacterial Effects of Chitosan Nanoparticles Embedded With Essential Oils Synthesized in an Ionic Liquid Containing System.* Journal of Agricultural and Food Chemistry, 2018. **66**(27): p. 7006-7014.
338. Feng, Q., et al., *Microfluidic Based High Throughput Synthesis of Lipid-Polymer Hybrid Nanoparticles With Tunable Diameters.* Biomicrofluidics, 2015. **9**(5).
339. Chen, C., et al., *Rapid Fabrication of Composite Hydrogel Microfibers for Weavable and Sustainable Antibacterial Applications.* Acs Sustainable Chemistry & Engineering, 2016. **4**(12): p. 6534-6542.
340. Liu, J., et al., *Biocompatible Sodium Alginate–silk Fibroin Antibacterial Microspheres From a Microfluidic Platform for Infected Wound Repair.* Journal of Bioactive and Compatible Polymers, 2024. **39**(3): p. 197-213.
341. Yang, C.H., et al., *Microfluidic assisted synthesis of silver nanoparticle-chitosan composite microparticles for antibacterial applications.* Int J Pharm, 2016. **510**(2): p. 493-500.
342. Gaur, P., et al., *Interpretation of Antimicrobial Susceptibility Testing Using European Committee on Antimicrobial Susceptibility Testing (EUCAST) and Clinical and Laboratory Standards Institute (CLSI) Breakpoints: Analysis of Agreement.* Cureus, 2023. **15**(3): p. e36977.
343. Montagna, M.T., et al., *Susceptibility to Echinocandins of Candida Spp. Strains Isolated in Italy Assessed by European Committee for Antimicrobial Susceptibility Testing and Clinical Laboratory Standards Institute Broth Microdilution Methods.* BMC Microbiology, 2015. **15**(1).
344. Meletiadis, J., et al., *Intra- And Interlaboratory Agreement in Assessing The <i>In Vitro</I> Activity of Micafungin Against Common and Rare Candida Species With the EUCAST, CLSI, and Etest Methods.* Antimicrobial Agents and Chemotherapy, 2016. **60**(10): p. 6173-6178.
345. Jang, M.W., et al., *<i>In Vitro</I> Fluconazole and Voriconazole Susceptibilities of Candida Bloodstream Isolates in Korea: Use of the CLSI and EUCAST Epidemiological Cutoff Values.* Annals of Laboratory Medicine, 2013. **33**(3): p. 167-173.
346. Rodríguez-Tudela, J.L., et al., *Comparison of Caspofungin MICs by Means of EUCAST Method EDef 7.1 Using Two Different Concentrations of Glucose.* Antimicrobial Agents and Chemotherapy, 2010. **54**(7): p. 3056-3057.
347. Pujol, I., et al., *Effects of Incubation Temperature, Inoculum Size, and Time of Reading on Broth Microdilution Susceptibility Test Results for Amphotericin B Fgainst Fusarium.* Antimicrobial Agents and Chemotherapy, 1997. **41**(4): p. 808-811.
348. Ming, X., et al., *Efficacy of Oxy-Ionic Solutions With Varying pH Levels Against Streptococcus Mutans in Vitro.* Cureus, 2024.

349. Guidotti-Takeuchi, M., et al., *Essential Oil-Based Nanoparticles as Antimicrobial Agents in the Food Industry.* Microorganisms, 2022. **10**(8): p. 1504.
350. Fazly Bazzaz, B.S., et al., *Solid Lipid Nanoparticles (SLN) carrying Eugenia caryophyllata essential oil: The novel nanoparticulate systems with broad-spectrum antimicrobial activity.* Letters in Applied Microbiology, 2018. **66**.
351. Hossain, T.J., *Methods for Screening and Evaluation of Antimicrobial Activity: A Review of Protocols, Advantages, and Limitations.* European Journal of Microbiology and Immunology, 2024. **14**(2): p. 97-115.
352. Jalil, M.T.M., N.H.B.M. Hairudin, and İ. Demirtaş, *<b>Muscodor Sp. IBRL OS-94, a Promising Endophytic Fungus of <i>Ocimum Sanctum</I> With Antimicrobial Activity</B>.* Pharmaceutical Sciences, 2020. **27**(2): p. 268-280.
353. Chiavini, M.S., et al., *In Vitro Inhibition of Escherichia Coli From Women With Urinary Tract Infection by Cranberry Hydroalcoholic Extract.* Revista Fitos, 2019. **13**(4): p. 278-288.
354. Hoseinzadeh, E., et al., *A review of available techniques for determination of nano-antimicrobials activity.* Toxin Reviews, 2017. **36**(1): p. 18-32.
355. Kadiyala, U., N.A. Kotov, and J.S. VanEpps, *Antibacterial Metal Oxide Nanoparticles: Challenges in Interpreting the Literature.* Curr Pharm Des, 2018. **24**(8): p. 896-903.
356. Schacht, V.J., et al., *Effects of Silver Nanoparticles on Microbial Growth Dynamics.* Journal of Applied Microbiology, 2012. **114**(1): p. 25-35.
357. Chung, E., et al., *Applied Methods to Assess the Antimicrobial Activity of Metallic-Based Nanoparticles.* Bioengineering (Basel), 2023. **10**(11).
358. Xia, Y., et al., *Self-assembly of self-limiting monodisperse supraparticles from polydisperse nanoparticles.* Nature nanotechnology, 2011. **6**(9): p. 580-587.
359. Teethaisong, Y., et al., *A combined disc method with resazurin agar plate assay for early phenotypic screening of KPC, MBL and OXA-48 carbapenemases among Enterobacteriaceae.* Journal of Applied Microbiology, 2016. **121**(2): p. 408-414.
360. Ong, K.J., et al., *Widespread nanoparticle-assay interference: implications for nanotoxicity testing.* PloS one, 2014. **9**(3): p. e90650.
361. Juliano, C.C.A., C. Demurtas, and L. Piu, *<i>In Vitro</I> Study on the Anticandidal Activity of <i>Melaleuca Alternifolia</I> (Tea Tree) Essential Oil Combined With Chitosan.* Flavour and Fragrance Journal, 2008. **23**(4): p. 227-231.
362. Sales, G.W.P., et al., *Antifungal and Modulatory Activity of Lemon Balm (Lippia Alba (MILL.) N. E. BROWN) Essential Oil.* Scientia Pharmaceutica, 2022. **90**(2): p. 31.
363. Wang, Y., et al., *Heteroresistance Is Associated With in Vitro Regrowth During Colistin Treatment in Carbapenem-Resistant Klebsiella Pneumoniae.* Frontiers in Microbiology, 2022. **13**.
364. Moore, T.L., et al., *Nanoparticle colloidal stability in cell culture media and impact on cellular interactions.* Chemical Society Reviews, 2015. **44**(17): p. 6287-6305.
365. Llor, C. and L. Bjerrum, *Antimicrobial resistance: risk associated with antibiotic overuse and initiatives to reduce the problem.* Ther Adv Drug Saf, 2014. **5**(6): p. 229-41.
366. Shallcross, L., et al., *Tackling the Threat of Antimicrobial Resistance: From Policy to Sustainable Action.* Philosophical Transactions of the Royal Society B Biological Sciences, 2015.
367. Butler, M.S., M.A.T. Blaskovich, and M.A. Cooper, *Antibiotics in the Clinical Pipeline in 2013.* The Journal of Antibiotics, 2013.
368. Fair, R.J. and Y. Tor, *Antibiotics and Bacterial Resistance in the 21st Century.* Perspectives in Medicinal Chemistry, 2014.
369. Nepal, G. and S. Bhatta, *Self-Medication With Antibiotics in WHO Southeast Asian Region: A Systematic Review.* Cureus, 2018.

370. Poudel, A.N., et al., *The Economic Burden of Antibiotic Resistance: A Systematic Review and Meta-Analysis.* Plos One, 2023. **18**(5): p. e0285170.
371. Wang, L., C. Hu, and L. Shao, *The Antimicrobial Activity of Nanoparticles: Present Situation and Prospects for the Future.* International Journal of Nanomedicine, 2017.
372. Liao, W., et al., *Nanoencapsulation of Essential Oils as Natural Food Antimicrobial Agents: An Overview.* Applied Sciences, 2021.
373. Thaher, Y.A., S. Perni, and P. Prokopovich, *Nano-Carrier Based Drug Delivery Systems for Sustained Antimicrobial Agent Release From Orthopaedic Cementous Material.* Advances in Colloid and Interface Science, 2017.
374. Zhang, W., et al., *Emerging Antibacterial Strategies With Application of Targeting Drug Delivery System and Combined Treatment.* International Journal of Nanomedicine, 2021.
375. Farjadian, F., et al., *Nanopharmaceuticals and nanomedicines currently on the market: challenges and opportunities.* Nanomedicine (Lond), 2019. **14**(1): p. 93-126.
376. Devnarain, N., et al., *Intrinsic <scp>stimuli-responsive</Scp> Nanocarriers for Smart Drug Delivery of Antibacterial Agents—An <scp>in-depth</Scp> Review of the Last Two Decades.* Wiley Interdisciplinary Reviews Nanomedicine and Nanobiotechnology, 2020.
377. Hosseini, S.H., S. Alipour, and N. Zohreh, *Delivery of Doxorubicin Using Double-Layered Core–Shell Nanocarrier Based on Magnetic Fe₃O₄ Core and Salep Shells.* Langmuir, 2018.
378. Jawahar, N. and S.N. Meyyanathan, *Polymeric Nanoparticles for Drug Delivery and Targeting: A Comprehensive Review.* International Journal of Health & Allied Sciences, 2012.
379. Duceac, L.D., et al., *Third-Generation Cephalosporin-Loaded Chitosan Used to Limit Microorganisms Resistance.* Materials, 2020.
380. Harugade, A., A.P. Sherje, and A. Pethe, *Chitosan: A review on properties, biological activities and recent progress in biomedical applications.* Reactive and Functional Polymers, 2023. **191**: p. 105634.
381. Dai, T., et al., *Chitosan preparations for wounds and burns: antimicrobial and wound-healing effects.* Expert Rev Anti Infect Ther, 2011. **9**(7): p. 857-79.
382. Aziz, M.A., et al., *Antimicrobial properties of a chitosan dextran-based hydrogel for surgical use.* Antimicrob Agents Chemother, 2012. **56**(1): p. 280-7.
383. Kong, M., et al., *Antimicrobial properties of chitosan and mode of action: a state of the art review.* Int J Food Microbiol, 2010. **144**(1): p. 51-63.
384. Aider, M., *Chitosan application for active bio-based films production and potential in the food industry: Review.* LWT - Food Science and Technology, 2010. **43**(6): p. 837-842.
385. Ta, Q., et al., *Chitosan nanoparticles for enhancing drugs and cosmetic components penetration through the skin.* European Journal of Pharmaceutical Sciences, 2021. **160**: p. 105765.
386. Dash, M., et al., *Chitosan—A versatile semi-synthetic polymer in biomedical applications.* Progress in Polymer Science, 2011. **36**(8): p. 981-1014.
387. Bellich, B., et al., *"The Good, the Bad and the Ugly" of Chitosans.* Mar Drugs, 2016. **14**(5).
388. Negm, N.A., et al., *Advancement on modification of chitosan biopolymer and its potential applications.* Int J Biol Macromol, 2020. **152**: p. 681-702.
389. Minh, N.C., et al., *Preparation of water soluble hydrochloric chitosan from low molecular weight chitosan in the solid state.* International Journal of Biological Macromolecules, 2019. **121**: p. 718-726.
390. Mohammed, M., et al., *An Overview of Chitosan Nanoparticles and Its Application in Non-Parenteral Drug Delivery.* Pharmaceutics, 2017.

391. Ing, L.Y., et al., *Antifungal Activity of Chitosan Nanoparticles and Correlation With Their Physical Properties.* International Journal of Biomaterials, 2012.
392. Shu, X.Z. and K.J. Zhu, *Controlled drug release properties of ionically cross-linked chitosan beads: the influence of anion structure.* Int J Pharm, 2002. **233**(1-2): p. 217-25.
393. Calvo, P., et al., *Novel hydrophilic chitosan-polyethylene oxide nanoparticles as protein carriers.* Journal of Applied Polymer Science, 1997. **63**(1): p. 125-132.
394. Mohanraj, V. and Y. Chen, *Nanoparticles-a review.* Tropical journal of pharmaceutical research, 2006. **5**(1): p. 561-573.
395. Koukaras, E.N., et al., *Insight on the Formation of Chitosan Nanoparticles Through Ionotropic Gelation With Tripolyphosphate.* Molecular Pharmaceutics, 2012.
396. Budi, S., et al., *Size-Controlled Chitosan Nanoparticles Prepared Using Ionotropic Gelation.* Scienceasia, 2020.
397. Rinaldi, I., et al., *Primaquine-Chitosan Nanoparticle Improves Drug Delivery to Liver Tissue in Rats.* Open Access Macedonian Journal of Medical Sciences, 2022.
398. Pedroso-Santana, S. and N. Fleitas-Salazar, *Ionotropic Gelation Method in the Synthesis of Nanoparticles/Microparticles for Biomedical Purposes.* Polymer International, 2020.
399. Zou, P., et al., *Advances in characterisation and biological activities of chitosan and chitosan oligosaccharides.* Food chemistry, 2016. **190**: p. 1174-1181.
400. Ngo, D.-H., et al., *Biological effects of chitosan and its derivatives.* Food Hydrocolloids, 2015. **51**: p. 200-216.
401. Giftania, W., Mahmiah, and S. Sri Agus, *In vitro Antibacterial Activity of Chitosan Nanoparticles against Mycobacterium tuberculosis.* Pharmacognosy Journal, 2018. **10**(1).
402. Divya, K., et al., *Antimicrobial properties of chitosan nanoparticles: Mode of action and factors affecting activity.* Fibers and Polymers, 2017. **18**(2): p. 221-230.
403. de Campos, A.M., et al., *Chitosan nanoparticles as new ocular drug delivery systems: in vitro stability, in vivo fate, and cellular toxicity.* Pharm Res, 2004. **21**(5): p. 803-10.
404. Qi, L., et al., *Preparation and antibacterial activity of chitosan nanoparticles.* Carbohydrate Research, 2004. **339**(16): p. 2693-2700.
405. Ibrahim, H., et al., *Chitosan nanoparticles loaded antibiotics as drug delivery biomaterial.* Journal of Applied Pharmaceutical Science, 2015. **5**: p. 085-090.
406. Chung, Y.C., et al., *Relationship between antibacterial activity of chitosan and surface characteristics of cell wall.* Acta Pharmacol Sin, 2004. **25**(7): p. 932-6.
407. Wang, X., Y. Du, and H. Liu, *Preparation, characterization and antimicrobial activity of chitosan–Zn complex.* Carbohydrate Polymers, 2004. **56**(1): p. 21-26.
408. Bretado Aragón, L., et al., *Composites of silver-chitosan nanoparticles: a potential source for new antimicrobial therapies.* Revista Mexicana de Ciencias Farmaceuticas, 2018. **47**: p. 7-25.
409. Sahariah, P. and M. Másson, *Antimicrobial Chitosan and Chitosan Derivatives: A Review of the Structure-Activity Relationship.* Biomacromolecules, 2017. **18**(11): p. 3846-3868.
410. Matica, M.A., et al., *Chitosan as a Wound Dressing Starting Material: Antimicrobial Properties and Mode of Action.* Int J Mol Sci, 2019. **20**(23).
411. Indumathi, M.P., K. Saral Sarojini, and G.R. Rajarajeswari, *Antimicrobial and biodegradable chitosan/cellulose acetate phthalate/ZnO nano composite films with optimal oxygen permeability and hydrophobicity for extending the shelf life of black grape fruits.* International Journal of Biological Macromolecules, 2019. **132**: p. 1112-1120.
412. Montaser, A.S., A.R. Wassel, and O.N. Al-Shaye'a, *Synthesis, characterization and antimicrobial activity of Schiff bases from chitosan and salicylaldehyde/TiO2*

nanocomposite membrane. International Journal of Biological Macromolecules, 2019. **124**: p. 802-809.

413. Kumar-Krishnan, S., et al., *Chitosan/silver nanocomposites: Synergistic antibacterial action of silver nanoparticles and silver ions.* European Polymer Journal, 2015. **67**: p. 242-251.
414. Feng, P., et al., *Chitosan-based functional materials for skin wound repair: Mechanisms and applications.* Frontiers in Bioengineering and Biotechnology, 2021. **9**: p. 650598.
415. Packirisamy, R.G., et al., *Synthesis and Antibacterial Properties of Novel ZnMn2O4–Chitosan Nanocomposites.* Nanomaterials, 2019. **9**(11).
416. Packirisamy, R.G., et al., *Synthesis of novel Sn1-xZnxO-chitosan nanocomposites: Structural, morphological and luminescence properties and investigation of antibacterial properties.* International Journal of Biological Macromolecules, 2019. **138**: p. 546-555.
417. Li, X.-f., et al., *Chitosan kills Escherichia coli through damage to be of cell membrane mechanism.* Carbohydrate Polymers, 2010. **79**(3): p. 493-499.
418. Liu, H., et al., *Chitosan kills bacteria through cell membrane damage.* International Journal of Food Microbiology, 2004. **95**(2): p. 147-155.
419. Rabea, E.I., et al., *Chitosan as Antimicrobial Agent: Applications and Mode of Action.* Biomacromolecules, 2003. **4**(6): p. 1457-1465.
420. Hosseinnejad, M. and S.M. Jafari, *Evaluation of different factors affecting antimicrobial properties of chitosan.* Int J Biol Macromol, 2016. **85**: p. 467-75.
421. Sobhani, Z., et al., *Nanoparticles of Chitosan Loaded Ciprofloxacin: Fabrication and Antimicrobial Activity.* Adv Pharm Bull, 2017. **7**(3): p. 427-432.
422. Xing, K., et al., *Oleoyl-chitosan nanoparticles inhibits Escherichia coli and Staphylococcus aureus by damaging the cell membrane and putative binding to extracellular or intracellular targets.* Int J Food Microbiol, 2009. **132**(2-3): p. 127-33.
423. Ke, C.L., et al., *Antimicrobial Actions and Applications of Chitosan.* Polymers (Basel), 2021. **13**(6).
424. Feng, P., et al., *Chitosan-Based Functional Materials for Skin Wound Repair: Mechanisms and Applications.* Front Bioeng Biotechnol, 2021. **9**: p. 650598.
425. Khalid, S., T.J. Piggot, and F. Samsudin, *Atomistic and Coarse Grain Simulations of the Cell Envelope of Gram-Negative Bacteria: What Have We Learned?* Acc Chem Res, 2019. **52**(1): p. 180-188.
426. Van Giau, V., S.S.A. An, and J. Hulme, *Recent advances in the treatment of pathogenic infections using antibiotics and nano-drug delivery vehicles.* Drug Des Devel Ther, 2019. **13**: p. 327-343.
427. Koo, H., et al., *Targeting Microbial Biofilms: Current and Prospective Therapeutic Strategies.* Nature Reviews Microbiology, 2017.
428. Gao, Y., et al., *Size and Charge Adaptive Clustered Nanoparticles Targeting the Biofilm Microenvironment for Chronic Lung Infection Management.* Acs Nano, 2020.
429. Faridi, F., et al., *Antibacterial Activity of Chitosan and PAβN on MexAB Expression in Clinical Isolates of Ciprofloxacin Resistant Pseudomonas aeruginosa.* 2021. **14**(5): p. e115652.
430. Chandrasekaran, M., K.D. Kim, and S.C. Chun, *Antibacterial Activity of Chitosan Nanoparticles: A Review.* Processes, 2020. **8**(9).
431. Hsieh, Y.-H., et al., *The synergistic effect of nisin and garlic shoot juice against Listeria spp. in soymilk.* Journal of the Taiwan Institute of Chemical Engineers, 2011. **42**(4): p. 576-579.
432. Brasil, M.S.L., et al., *Synergism in the Antibacterial Action of Ternary Mixtures Involving Silver Nanoparticles, Chitosan and Antibiotics.* Journal of the Brazilian Chemical Society, 2018.

433. Paap, C.M., et al., *Pharmacokinetics of Cefotaxime and Its Active Metabolite in Children With Renal Dysfunction.* Antimicrobial Agents and Chemotherapy, 1991. **35**(9): p. 1879-1883.
434. Asmar, B.I., et al., *Cefotaxime Diffusion Into Cerebrospinal Fluid of Children With Meningitis.* Antimicrobial Agents and Chemotherapy, 1985. **28**(1): p. 138-140.
435. Arreaza, L., L.d.l. Fuente, and J. Vázquez, *Antibiotic Susceptibility Patterns Of <i>Neisseria Meningitidis</I> Isolates From Patients and Asymptomatic Carriers.* Antimicrobial Agents and Chemotherapy, 2000. **44**(6): p. 1705-1707.
436. Carmine, A.A., et al., *Cefotaxime. A review of its antibacterial activity, pharmacological properties and therapeutic use.* Drugs, 1983. **25**(3): p. 223-89.
437. Jones, R.N. and C. Thornsberry, *Cefotaxime: A Review of in Vitro Antimicrobial Properties and Spectrum of Activity.* Reviews of Infectious Diseases, 1982. **4**(Supplement_2): p. S300-S315.
438. Thapa, T.B., et al., *Detection of Hypermucoviscous Klebsiella Pneumoniae and Phenotypic Comparison of Their Virulence Factors With Classical Strains Among Patients Visiting Tertiary Care Hospital.* 2020.
439. Mushtaq, S., et al., *Biocompatible biodegradable polymeric antibacterial nanoparticles for enhancing the effects of a third-generation cephalosporin against resistant bacteria.* Journal of Medical Microbiology, 2017. **66**(3): p. 318-327.
440. Sobhani, Z., et al., *Nanoparticles of Chitosan Loaded Ciprofloxacin: Fabrication and Antimicrobial Activity.* Advanced pharmaceutical bulletin, 2017. **7**(3): p. 427-432.
441. Sreekumar, S., et al., *Parameters influencing the size of chitosan-TPP nano- and microparticles.* Scientific Reports, 2018. **8**(1): p. 4695.
442. Benamer Oudih, S., et al., *Chitosan nanoparticles with controlled size and zeta potential.* Polymer Engineering & Science, 2023. **63**(3): p. 1011-1021.
443. Kim, K.D., S.H. Kim, and H.T. Kim, *Applying the Taguchi method to the optimization for the synthesis of TiO2 nanoparticles by hydrolysis of TEOT in micelles.* Colloids and Surfaces A: Physicochemical and Engineering Aspects, 2005. **254**: p. 99-105.
444. Alfagih, I., et al., *Pulmonary Delivery of Proteins Using Nanocomposite Microcarriers.* Journal of Pharmaceutical Sciences, 2015. **104**(12): p. 4386-4398.
445. Thamilarasan, V., et al., *Single Step Fabrication of Chitosan Nanocrystals Using Penaeus semisulcatus: Potential as New Insecticides, Antimicrobials and Plant Growth Promoters.* Journal of Cluster Science, 2018. **29**.
446. Meynaud, S., et al., *Impact of UV Irradiation on the Chitosan Bioactivity for Biopesticide Applications.* Molecules, 2023. **28**(13): p. 4954.
447. González-Martínez, J., et al., *Improved mechanical, optical, and electrical properties of chitosan films with the synergistic reinforcing effect of carbon nanotubes and reduced graphene oxide for potential optoelectronic applications*. 2023.
448. Borman, P. and D. Elder, *Q2(R1) Validation of Analytical Procedures*, in *ICH Quality Guidelines*. 2017. p. 127-166.
449. D'Aloisio, V., et al., *The development and optimisation of an HPLC-based in vitro serum stability assay for a calcitonin gene-related peptide receptor antagonist peptide.* Journal of peptide science : an official publication of the European Peptide Society, 2023. **30**: p. e3539.
450. Rawal, T., et al., *Rifampicin loaded chitosan nanoparticle dry powder presents an improved therapeutic approach for alveolar tuberculosis.* Colloids and Surfaces B: Biointerfaces, 2017. **154**: p. 321-330.
451. Jafarinejad, S., et al., *Development of chitosan-based nanoparticles for pulmonary delivery of itraconazole as dry powder formulation.* Powder Technology, 2012. **222**: p. 65-70.

452. Soares, P.I.P., et al., *Chitosan-based nanoparticles as drug delivery systems for doxorubicin: Optimization and modelling.* Carbohydrate Polymers, 2016. **147**: p. 304-312.
453. Al-Kassas, R., et al., *Transdermal delivery of propranolol hydrochloride through chitosan nanoparticles dispersed in mucoadhesive gel.* Carbohydrate Polymers, 2016. **153**: p. 176-186.
454. Guan, J., et al., *Optimized Preparation of Levofloxacin-loaded Chitosan Nanoparticles by Ionotropic Gelation.* Physics Procedia, 2011. **22**: p. 163-169.
455. Binesh, N., N. Farhadian, and A. Mohammadzadeh, *Enhanced stability of salt-assisted sodium ceftriaxone-loaded chitosan nanoparticles: Formulation and optimization by 32-full factorial design and antibacterial effect study against aerobic and anaerobic bacteria.* Colloids and Surfaces A: Physicochemical and Engineering Aspects, 2021. **618**: p. 126429.
456. Hasan, M., et al., *Preparation, Characterization, and Release Kinetics of Chitosan-Coated Nanoliposomes Encapsulating Curcumin in Simulated Environments.* Molecules, 2019. **24**(10): p. 2023.
457. Katas, H. and H.O. Alpar, *Development and characterisation of chitosan nanoparticles for siRNA delivery.* Journal of Controlled Release, 2006. **115**(2): p. 216-225.
458. Coico, R., *Gram Staining.* Current Protocols in Microbiology, 2006. **00**(1): p. A.3C.1-A.3C.2.
459. Katz, D.S., *Coagulase test protocol.* American Society for Microbiology Laboratory Protocols. Available online: https://www. asmscience. org/content/education/protocol/protocol, 2010. **3220**.
460. Shields, P. and L. Cathcart, *Oxidase test protocol.* American Society for Microbiology, 2010: p. 1-9.
461. Reiner, K., *Catalase test protocol.* American society for microbiology, 2010. **1**(1): p. 1-9.
462. Valizadeh, H., et al., *Antibacterial activity of clarithromycin loaded PLGA nanoparticles.* Die Pharmazie-An International Journal of Pharmaceutical Sciences, 2012. **67**(1): p. 63-68.
463. Magaldi, S., et al., *Well diffusion for antifungal susceptibility testing.* International Journal of Infectious Diseases, 2004. **8**(1): p. 39-45.
464. Yan, T., et al., *Chitosan capped pH-responsive hollow mesoporous silica nanoparticles for targeted chemo-photo combination therapy.* Carbohydrate Polymers, 2020. **231**: p. 115706.
465. Liang, Y., et al., *pH-responsive injectable hydrogels with mucosal adhesiveness based on chitosan-grafted-dihydrocaffeic acid and oxidized pullulan for localized drug delivery.* Journal of Colloid and Interface Science, 2019. **536**: p. 224-234.
466. Piras, A.M., et al., *Chitosan nanoparticles loaded with the antimicrobial peptide temporin B exert a long-term antibacterial activity in vitro against clinical isolates of Staphylococcus epidermidis.* Frontiers in Microbiology, 2015. **6**(372).
467. Duceac, L.D., et al., *Third-Generation Cephalosporin-Loaded Chitosan Used to Limit Microorganisms Resistance.* Materials (Basel, Switzerland), 2020. **13**(21): p. 4792.
468. Ibrahim, H.M., et al., *Chitosan nanoparticles loaded antibiotics as drug delivery biomaterial.* journal of applied pharmaceutical science, 2015. **5**: p. 085-090.
469. Nur Amiera Syuhada, R., et al., *Potential Antimicrobial Applications of Chitosan Nanoparticles (ChNP).* Journal of Microbiology and Biotechnology, 2019. **29**(7): p. 1009-1013.
470. Greco, A., et al., *Microfluidic mixing as platform technology for production of chitosan nanoparticles loaded with different macromolecules.* Eur J Pharm Biopharm, 2023. **188**: p. 170-181.

471. Fonseca, D.R., et al., *One-Pot Microfluidics to Engineer Chitosan Nanoparticles Conjugated with Antimicrobial Peptides Using "Photoclick" Chemistry: Validation Using the Gastric Bacterium Helicobacter pylori.* ACS Applied Materials & Interfaces, 2024. **16**(12): p. 14533-14547.
472. Huanbutta, K., et al., *Key Fabrications of Chitosan Nanoparticles for Effective Drug Delivery Using Flow Chemistry Reactors.* Int J Nanomedicine, 2023. **18**: p. 7889-7900.
473. Xu, Y., et al., *Nanoparticles based on chitosan hydrochloride/hyaluronic acid/PEG containing curcumin: In vitro evaluation and pharmacokinetics in rats.* International Journal of Biological Macromolecules, 2017. **102**.
474. Yan, L., et al., *Formulation and characterization of chitosan hydrochloride and carboxymethyl chitosan encapsulated quercetin nanoparticles for controlled applications in foods system and simulated gastrointestinal condition.* Food Hydrocolloids, 2018. **84**: p. 450-457.
475. Pant, A. and J.S. Negi, *Novel controlled ionic gelation strategy for chitosan nanoparticles preparation using TPP-β-CD inclusion complex.* European Journal of Pharmaceutical Sciences, 2018. **112**: p. 180-185.
476. Dashtimoghadam, E., et al., *Microfluidic self-assembly of polymeric nanoparticles with tunable compactness for controlled drug delivery.* Polymer, 2013. **54**(18): p. 4972-4979.
477. Koukaras, E.N., et al., *Insight on the Formation of Chitosan Nanoparticles through Ionotropic Gelation with Tripolyphosphate.* Molecular Pharmaceutics, 2012. **9**(10): p. 2856-2862.
478. Kumar, V. and R.K. Prud'Homme, *Thermodynamic limits on drug loading in nanoparticle cores.* Journal of Pharmaceutical Sciences, 2008. **97**(11): p. 4904-4914.
479. Dong, Y. and P. Liu, *Amphiphilic Triblock Copolymer Prodrug for Tumor-Specific pH/Reduction Dual-Triggered Drug Delivery: Effect of Self-Assembly Behaviors.* Langmuir, 2021.
480. Caldera-Villalobos, M., et al., *Polyelectrolytes With Tetrazole Pendant Groups Useful in the Stabilization of Au and Ag Nanoparticles.* Journal of Applied Polymer Science, 2016.
481. Aggarwal, P., et al., *Nanoparticle Interaction With Plasma Proteins as It Relates to Particle Biodistribution, Biocompatibility and Therapeutic Efficacy.* Advanced Drug Delivery Reviews, 2009.
482. Lazaridou, M., et al., *Formulation and In-Vitro Characterization of Chitosan-Nanoparticles Loaded with the Iron Chelator Deferoxamine Mesylate (DFO).* Pharmaceutics, 2020. **12**(3).
483. Halawani, E.M., A.M. Hassan, and S.M.F. Gad El-Rab, *Nanoformulation of Biogenic Cefotaxime-Conjugated-Silver Nanoparticles for Enhanced Antibacterial Efficacy Against Multidrug-Resistant Bacteria and Anticancer Studies.* Int J Nanomedicine, 2020. **15**: p. 1889-1901.
484. Yi, H., et al., *Chitosan Scaffolds for Biomolecular Assembly: Coupling Nucleic Acid Probes for Detecting Hybridization.* Biotechnology and Bioengineering, 2003.
485. Raval, N., et al., *Importance of Physicochemical Characterization of Nanoparticles in Pharmaceutical Product Development*. 2019. p. 369-400.
486. Oliveira Lima, K., et al., *Characterization, Bioactivity and Application of Chitosan-Based Nanoparticles in a Food Emulsion Model.* Polymers, 2021. **13**(19).
487. Gianak, O., et al., *Silk Fibroin Nanoparticles for Drug Delivery: Effect of Bovine Serum Albumin and Magnetic Nanoparticles Addition on Drug Encapsulation and Release.* Separations, 2018.
488. Liu, Y., et al., *Tetrahedral Framework Nucleic Acids Deliver Antimicrobial Peptides with Improved Effects and Less Susceptibility to Bacterial Degradation.* Nano Letters, 2020. **20**(5): p. 3602-3610.

489. Ahmad, R.M., et al., *Preparation and Characterization of Blank and Nerolidol-Loaded Chitosan–Alginate Nanoparticles.* Nanomaterials, 2022.
490. Wallace, S.J., et al., *Drug release from nanomedicines: selection of appropriate encapsulation and release methodology.* Drug Delivery and Translational Research, 2012. **2**(4): p. 284-292.
491. Salafi, T., K.K. Zeming, and Y. Zhang, *Advancements in Microfluidics for Nanoparticle Separation.* Lab on a Chip, 2017.
492. Marques, S.S., et al., *Insights on Ultrafiltration-Based Separation for the Purification and Quantification of Methotrexate in Nanocarriers.* Molecules (Basel, Switzerland), 2020. **25**(8): p. 1879.
493. Lv, Y., et al., *Visual validation of the measurement of entrapment efficiency of drug nanocarriers.* Int J Pharm, 2018. **547**(1-2): p. 395-403.
494. Wang, F. and V.V. Tarabara, *Pore blocking mechanisms during early stages of membrane fouling by colloids.* J Colloid Interface Sci, 2008. **328**(2): p. 464-9.
495. Xie, Y., X. Liu, and Q. Chen, *Synthesis and characterization of water-soluble chitosan derivate and its antibacterial activity.* Carbohydrate polymers, 2007. **69**(1): p. 142-147.
496. Ke, C.-L., et al., *Antimicrobial Actions and Applications of Chitosan.* Polymers, 2021.
497. Signini, R. and S.P. Campana Filho, *On the preparation and characterization of chitosan hydrochloride.* Polymer Bulletin, 1999. **42**(2): p. 159-166.
498. Shaikh, S., et al., *Synthesis and Characterization of Cefotaxime Conjugated Gold Nanoparticles and Their Use to Target Drug-Resistant CTX-M-Producing Bacterial Pathogens.* Journal of Cellular Biochemistry, 2017. **118**(9): p. 2802-2808.
499. Cavassin, E.D., et al., *Comparison of methods to detect the in vitro activity of silver nanoparticles (AgNP) against multidrug resistant bacteria.* Journal of Nanobiotechnology, 2015. **13**(1): p. 64.
500. Aswapokee, N., et al., *Diffusion disk susceptibility testing with cefotaxime.* Antimicrob Agents Chemother, 1979. **16**(2): p. 164-6.
501. Clyde, T., et al., *Antimicrobial Susceptibility Tests with Cefotaxime and Correlation with Clinical Bacteriologic Response.* Reviews of Infectious Diseases, 1982. **4**: p. S316-S324.
502. Javaid, S., et al., *Cefotaxime Loaded Polycaprolactone Based Polymeric Nanoparticles with Antifouling Properties for In-Vitro Drug Release Applications.* Polymers, 2021. **13**(13).
503. Carmine, A.A., et al., *Cefotaxime.* Drugs, 1983. **25**(3): p. 223-289.
504. Jones, R.N., *The antimicrobial activity of cefotaxime: Comparative multinational hospital isolate surveys covering 15 years.* Infection, 1994. **22**(3): p. S152-S160.
505. Jamil, B., et al., *Development of Cefotaxime Impregnated Chitosan as Nano-antibiotics: De Novo Strategy to Combat Biofilm Forming Multi-drug Resistant Pathogens.* Frontiers in Microbiology, 2016. **7**.
506. Al Hagbani, T., et al., *Cefotaxime Mediated Synthesis of Gold Nanoparticles: Characterization and Antibacterial Activity.* Polymers, 2022. **14**(4).
507. Pradeepa, et al., *Preparation of gold nanoparticles by novel bacterial exopolysaccharide for antibiotic delivery.* Life Sciences, 2016. **153**: p. 171-179.
508. Raafat, D., et al., *Insights into the mode of action of chitosan as an antibacterial compound.* Applied and environmental microbiology, 2008. **74**(12): p. 3764-3773.
509. Hosseinnejad, M. and S.M. Jafari, *Evaluation of different factors affecting antimicrobial properties of chitosan.* International Journal of Biological Macromolecules, 2016. **85**: p. 467-475.
510. Yilmaz Atay, H., *Antibacterial Activity of Chitosan-Based Systems.* Functional Chitosan: Drug Delivery and Biomedical Applications, 2020: p. 457-489.

511. Tolaimate, A., et al., *Contribution to the preparation of chitins and chitosans with controlled physico-chemical properties.* Polymer, 2003. **44**(26): p. 7939-7952.
512. Kravanja, G., et al., *Chitosan-Based (Nano)Materials for Novel Biomedical Applications.* Molecules, 2019.
513. Vivek, R., et al., *pH-responsive drug delivery of chitosan nanoparticles as Tamoxifen carriers for effective anti-tumor activity in breast cancer cells.* Colloids and Surfaces B: Biointerfaces, 2013. **111**: p. 117-123.
514. Huang, L., et al., *Preparation, characterization, and antibacterial activity of oleic acid-grafted chitosan oligosaccharide nanoparticles.* Frontiers of Biology in China, 2009. **4**(3): p. 321-327.
515. Shahidi, F., J.K.V. Arachchi, and Y.-J. Jeon, *Food applications of chitin and chitosans.* Trends in food science & technology, 1999. **10**(2): p. 37-51.
516. Xing, K., et al., *Antibacterial activity of oleoyl-chitosan nanoparticles: A novel antibacterial dispersion system.* Carbohydrate Polymers, 2008. **74**(1): p. 114-120.
517. Aydın, R.S.T. and M. Pulat, *5-Fluorouracil Encapsulated Chitosan Nanoparticles for pH-Stimulated Drug Delivery: Evaluation of Controlled Release Kinetics.* Journal of Nanomaterials, 2012.
518. Ibañez-Peinado, D., et al., *Antimicrobial Effect of Insect Chitosan on Salmonella Typhimurium, Escherichia Coli O157:H7 and Listeria Monocytogenes Survival.* Plos One, 2020.
519. Wang, X., et al., *Microenvironment-Responsive Magnetic Nanocomposites Based on Silver Nanoparticles/Gentamicin for Enhanced Biofilm Disruption by Magnetic Field.* Acs Applied Materials & Interfaces, 2018.
520. Arasoğlu, T., S. Derman, and B. Mansuroğlu, *Comparative Evaluation of Antibacterial Activity of Caffeic Acid Phenethyl Ester and PLGA Nanoparticle Formulation by Different Methods.* Nanotechnology, 2015. **27**(2): p. 025103.
521. Singhal, S.K., et al., *Synthesis of Cu/CNTs nanocomposites for antimicrobial activity.* Advances in Natural Sciences: Nanoscience and Nanotechnology, 2012. **3**(4): p. 045011.
522. Martins, A.F., et al., *Antimicrobial Activity of Chitosan Derivatives Containing N-Quaternized Moieties in Its Backbone: A Review.* International Journal of Molecular Sciences, 2014.
523. Rúnarsson, Ö.V., et al., *Antibacterial activity of methylated chitosan and chitooligomer derivatives: Synthesis and structure activity relationships.* European Polymer Journal, 2007. **43**(6): p. 2660-2671.
524. Xiao, B., et al., *Preparation and characterization of antimicrobial chitosan-N-arginine with different degrees of substitution.* Carbohydrate Polymers, 2011. **83**(1): p. 144-150.
525. Li, P., et al., *A polycationic antimicrobial and biocompatible hydrogel with microbe membrane suctioning ability.* Nature Materials, 2011. **10**(2): p. 149-156.
526. Szczepański, R., et al., *Chitosan-Derivatives in Combinations With Selected Porphyrinoids as Novel Hybrid Materials for Medicine and Pharmacy.* Progress on Chemistry and Application of Chitin and Its Derivatives, 2020.
527. Geçer, A., et al., *Trimethyl Chitosan Nanoparticles Enhances Dissolution of the Poorly Water Soluble Drug Candesartan-Cilexetil.* Macromolecular Research, 2010.
528. Kwon, J.H. and W.G. Powderly, *The post-antibiotic era is here.* Science, 2021. **373**(6554): p. 471-471.
529. Park, S.-C., Y. Park, and K.-S. Hahm, *The role of antimicrobial peptides in preventing multidrug-resistant bacterial infections and biofilm formation.* International journal of molecular sciences, 2011. **12**(9): p. 5971-5992.
530. Diamond, G., et al., *The roles of antimicrobial peptides in innate host defense.* Curr Pharm Des, 2009. **15**(21): p. 2377-92.

531. Zhang, Q.-Y., et al., *Antimicrobial peptides: mechanism of action, activity and clinical potential.* Military Medical Research, 2021. **8**(1): p. 48.
532. Li, B. and T.J. Webster, *Bacteria Antibiotic Resistance: New Challenges and Opportunities for Implant-associated Orthopedic Infections.* Journal of Orthopaedic Research®, 2017. **36**(1): p. 22-32.
533. Rodríguez, V., J.A. Asenjo, and B.A. Andrews, *Design and Implementation of a High Yield Production System for Recombinant Expression of Peptides.* Microbial Cell Factories, 2014.
534. Mardirossian, M., et al., *D-BMAP18 antimicrobial peptide is active in vitro, resists to pulmonary proteases but loses its activity in a murine model of Pseudomonas aeruginosa lung infection.* Frontiers in chemistry, 2017. **5**: p. 40.
535. Crommelin, D.J., et al., *Shifting paradigms: biopharmaceuticals versus low molecular weight drugs.* International journal of pharmaceutics, 2003. **266**(1-2): p. 3-16.
536. Saw, P.E., et al., *Biomedical Applications of a Novel Class of High-Affinity Peptides.* Accounts of Chemical Research, 2021.
537. Lei, J., et al., *The antimicrobial peptides and their potential clinical applications.* Am J Transl Res, 2019. **11**(7): p. 3919-3931.
538. Porras-Luque, J.I., *[Topical antimicrobial agents in dermatology].* Actas Dermosifiliogr, 2007. **98 Suppl 1**: p. 29-39.
539. Higgins, D.L., et al., *Telavancin, a multifunctional lipoglycopeptide, disrupts both cell wall synthesis and cell membrane integrity in methicillin-resistant Staphylococcus aureus.* Antimicrob Agents Chemother, 2005. **49**(3): p. 1127-34.
540. McNamara, D.R. and J.M. Steckelberg, *Vancomycin.* JAAOS-Journal of the American Academy of Orthopaedic Surgeons, 2005. **13**(2): p. 89-92.
541. Audrain, B., et al., *Induction of the CPX Envelope Stress Pathway Contributes to Escherichia Coli Tolerance to Antimicrobial Peptides.* Applied and Environmental Microbiology, 2013. **79**(24): p. 7770-7779.
542. Yeaman, M.R. and N.Y. Yount, *Mechanisms of Antimicrobial Peptide Action and Resistance.* Pharmacological Reviews, 2003. **55**(1): p. 27-55.
543. Bachrach, G., et al., *Resistance Of <i>Porphyromonas Gingivalis</I> ATCC 33277 to Direct Killing by Antimicrobial Peptides Is Protease Independent.* Antimicrobial Agents and Chemotherapy, 2008. **52**(2): p. 638-642.
544. Rangel, K., et al., *An Update on the Therapeutic Potential of Antimicrobial Peptides Against Acinetobacter Baumannii Infections.* Pharmaceuticals, 2023. **16**(9): p. 1281.
545. Tang, Z., et al., *Recent Advances and Challenges in Nanodelivery Systems for Antimicrobial Peptides (AMPs).* Antibiotics, 2021.
546. Morales-Ávila, E., et al., *Antibacterial Efficacy of Gold and Silver Nanoparticles Functionalized With the Ubiquicidin (29–41) Antimicrobial Peptide.* Journal of Nanomaterials, 2017.
547. Cruz, J., et al., *Antimicrobial activity of a new synthetic peptide loaded in polylactic acid or poly (lactic-co-glycolic) acid nanoparticles against Pseudomonas aeruginosa, Escherichia coli O157: H7 and methicillin resistant Staphylococcus aureus (MRSA).* Nanotechnology, 2017. **28**(13): p. 135102.
548. Sun, L., C. Zheng, and T.J. Webster, *Self-assembled peptide nanomaterials for biomedical applications: promises and pitfalls.* International journal of nanomedicine, 2017. **12**: p. 73.
549. Zhang, X.-L., et al., *The synthetic antimicrobial peptide pexiganan and its nanoparticles (PNPs) exhibit the anti-Helicobacter pylori activity in vitro and in vivo.* Molecules, 2015. **20**(3): p. 3972-3985.

550. Ferreira, M., et al., *Liposomes as Antibiotic Delivery Systems: A Promising Nanotechnological Strategy Against Antimicrobial Resistance.* Molecules, 2021.
551. Mugabe, C., et al., *Mechanism of Enhanced Activity of Liposome-Entrapped Aminoglycosides Against Resistant Strains Of <i>Pseudomonas Aeruginosa</I>.* Antimicrobial Agents and Chemotherapy, 2006.
552. Alipour, M., et al., *Antimicrobial effectiveness of liposomal polymyxin B against resistant Gram-negative bacterial strains.* International Journal of Pharmaceutics, 2008. **355**(1-2): p. 293-298.
553. Nicolosi, D., et al., *Nanotechnology approaches for antibacterial drug delivery: preparation and microbiological evaluation of fusogenic liposomes carrying fusidic acid.* International journal of antimicrobial agents, 2015. **45**(6): p. 622-626.
554. Yoo, J.-W., et al., *Bio-inspired, bioengineered and biomimetic drug delivery carriers.* Nature reviews Drug discovery, 2011. **10**(7): p. 521-535.
555. Dowhan, W. and M. Bogdanov, *Functional roles of lipids in membranes*, in *New comprehensive biochemistry*. 2002, Elsevier. p. 1-35.
556. Murzyn, K., T. Róg, and M. Pasenkiewicz-Gierula, *Phosphatidylethanolamine-phosphatidylglycerol bilayer as a model of the inner bacterial membrane.* Biophys J, 2005. **88**(2): p. 1091-103.
557. Kolašinac, R., et al., *Deciphering the Functional Composition of Fusogenic Liposomes.* Int J Mol Sci, 2018. **19**(2).
558. Were, L.M., et al., *Encapsulation of nisin and lysozyme in liposomes enhances efficacy against Listeria monocytogenes.* Journal of food protection, 2004. **67**(5): p. 922-927.
559. Agadi, N., et al., *Distinct mode of membrane interaction and disintegration by diverse class of antimicrobial peptides.* Biochimica et Biophysica Acta (BBA) - Biomembranes, 2022. **1864**(12): p. 184047.
560. Pozo Navas, B., et al., *Composition dependence of vesicle morphology and mixing properties in a bacterial model membrane system.* Biochimica et Biophysica Acta (BBA) - Biomembranes, 2005. **1716**(1): p. 40-48.
561. Nishijima, S., et al., *Disruption of the Escherichia Coli CLS Gene Responsible for Cardiolipin Synthesis.* Journal of Bacteriology, 1988.
562. Dalebroux, Z.D., et al., *Delivery of Cardiolipins to the Salmonella Outer Membrane Is Necessary for Survival Within Host Tissues and Virulence.* Cell Host & Microbe, 2015.
563. Rocha-Roa, C., et al., *Cardiolipin prevents pore formation in phosphatidylglycerol bacterial membrane models.* FEBS Letters, 2021. **595**(21): p. 2701-2714.
564. Ikon, N. and R.O. Ryan, *Cardiolipin and Mitochondrial Cristae Organization.* Biochimica Et Biophysica Acta (Bba) - Biomembranes, 2017.
565. Mironova, G.D. and E. Pavlov, *Mitochondrial Cyclosporine a-Independent Palmitate/Ca2+-Induced Permeability Transition Pore (PA-mPT Pore) and Its Role in Mitochondrial Function and Protection Against Calcium Overload and Glutamate Toxicity.* Cells, 2021.
566. Goes, A., et al., *Myxobacteria-Derived Outer Membrane Vesicles: Potential Applicability Against Intracellular Infections.* Cells, 2020. **9**(1): p. 194.
567. Gubernator, J., *Active methods of drug loading into liposomes: recent strategies for stable drug entrapment and increased in vivo activity.* Expert opinion on drug delivery, 2011. **8**(5): p. 565-580.
568. Deng, Y., J. Ling, and M.-H. Li, *Physical stimuli-responsive liposomes and polymersomes as drug delivery vehicles based on phase transitions in the membrane.* Nanoscale, 2018. **10**(15): p. 6781-6800.
569. Ascenso, A., et al., *Novel tretinoin formulations: a drug-in-cyclodextrin-in-liposome approach.* Journal of liposome research, 2013. **23**(3): p. 211-219.

570. Hwang, S., et al., *Remote loading of diclofenac, insulin and fluorescein isothiocyanate labeled insulin into liposomes by pH and acetate gradient methods.* International journal of pharmaceutics, 1999. **179**(1): p. 85-95.
571. Heuts, J., et al., *Cationic Liposomes: A Flexible Vaccine Delivery System for Physicochemically Diverse Antigenic Peptides.* Pharm Res, 2018. **35**(11): p. 207.
572. Milicic, A., et al., *Small cationic DDA:TDB liposomes as protein vaccine adjuvants obviate the need for TLR agonists in inducing cellular and humoral responses.* PLoS One, 2012. **7**(3): p. e34255.
573. Varypataki, E.M., et al., *Efficient Eradication of Established Tumors in Mice with Cationic Liposome-Based Synthetic Long-Peptide Vaccines.* Cancer Immunol Res, 2017. **5**(3): p. 222-233.
574. Chatin, B., et al., *Liposome-based Formulation for Intracellular Delivery of Functional Proteins.* Molecular Therapy - Nucleic Acids, 2015. **4**.
575. Biswaro, L.S., et al., *Antimicrobial peptides and nanotechnology, recent advances and challenges.* Frontiers in microbiology, 2018. **9**: p. 855.
576. Carmona-Ribeiro, A.M. and L.D.d.M. Carrasco, *Novel formulations for antimicrobial peptides.* International journal of molecular sciences, 2014. **15**(10): p. 18040-18083.
577. Adler-Moore, J. and R.T. Proffitt, *AmBisome: liposomal formulation, structure, mechanism of action and pre-clinical experience.* J Antimicrob Chemother, 2002. **49 Suppl 1**: p. 21-30.
578. Kastner, E., et al., *Microfluidic-controlled manufacture of liposomes for the solubilisation of a poorly water soluble drug.* Int J Pharm, 2015. **485**(1-2): p. 122-30.
579. Jahn, A., et al., *Microfluidic directed formation of liposomes of controlled size.* Langmuir, 2007. **23**(11): p. 6289-6293.
580. Adamala, K., et al., *Construction of a liposome dialyzer for the preparation of high-value, small-volume liposome formulations.* Nat Protoc, 2015. **10**(6): p. 927-38.
581. Yanagihara, S., et al., *Preparing Size-Controlled Liposomes Modified with Polysaccharide Derivatives for pH-Responsive Drug Delivery Applications.* Life, 2023. **13**(11): p. 2158.
582. Dikpati, A., et al., *Residual Solvents in Nanomedicine and Lipid-Based Drug Delivery Systems: a Case Study to Better Understand Processes.* Pharm Res, 2020. **37**(8): p. 149.
583. Agency, E.M., *ICH guideline Q3C (R8) on impurities: guideline for residual solvents* in *Step 5*. 2022.
584. Balbino, T.A., et al., *Microfluidic Assembly of pDNA/Cationic Liposome Lipoplexes with High pDNA Loading for Gene Delivery.* Langmuir, 2016. **32**(7): p. 1799-1807.
585. Abts, A., et al., *Easy and rapid purification of highly active nisin.* Int J Pept, 2011. **2011**: p. 175145.
586. Danaei, M., et al., *Impact of Particle Size and Polydispersity Index on the Clinical Applications of Lipidic Nanocarrier Systems.* Pharmaceutics, 2018.
587. Zook, J.M. and W.N. Vreeland, *Effects of temperature, acyl chain length, and flow-rate ratio on liposome formation and size in a microfluidic hydrodynamic focusing device.* Soft Matter, 2010. **6**(6): p. 1352-1360.
588. Jahn, A., et al., *Microfluidic mixing and the formation of nanoscale lipid vesicles.* ACS nano, 2010. **4**(4): p. 2077-2087.
589. Kastner, E., et al., *High-throughput manufacturing of size-tuned liposomes by a new microfluidics method using enhanced statistical tools for characterization.* International Journal of Pharmaceutics, 2014. **477**(1): p. 361-368.
590. Lou, G., et al., *A novel microfluidic-based approach to formulate size-tuneable large unilamellar cationic liposomes: Formulation, cellular uptake and biodistribution investigations.* European Journal of Pharmaceutics and Biopharmaceutics, 2019. **143**: p. 51-60.

591. Zizzari, A., et al., *Continuous-Flow Production of Injectable Liposomes via a Microfluidic Approach.* Materials (Basel), 2017. **10**(12).
592. Reiss, H., *The growth of uniform colloidal dispersions.* The Journal of Chemical Physics, 1951. **19**(4): p. 482-487.
593. Lifshitz, I.M. and V.V. Slyozov, *The kinetics of precipitation from supersaturated solid solutions.* Journal of Physics and Chemistry of Solids, 1961. **19**(1): p. 35-50.
594. Joshi, S., et al., *Microfluidics based manufacture of liposomes simultaneously entrapping hydrophilic and lipophilic drugs.* Int J Pharm, 2016. **514**(1): p. 160-168.
595. Maeki, M., et al., *Understanding the formation mechanism of lipid nanoparticles in microfluidic devices with chaotic micromixers.* PLOS ONE, 2017. **12**(11): p. e0187962.
596. López, R.R., et al., *Surface Response Based Modeling of Liposome Characteristics in a Periodic Disturbance Mixer.* Micromachines (Basel), 2020. **11**(3).
597. Yanar, F., et al., *Continuous-Flow Production of Liposomes with a Millireactor under Varying Fluidic Conditions.* Pharmaceutics, 2020. **12**: p. 1001.
598. Carugo, D., et al., *Liposome production by microfluidics: potential and limiting factors.* Scientific Reports, 2016. **6**(1): p. 25876.
599. Mijajlovic, M., et al., *Microfluidic hydrodynamic focusing based synthesis of POPC liposomes for model biological systems.* Colloids and Surfaces B: Biointerfaces, 2013. **104**: p. 276-281.
600. Balbino, T.A., et al., *Continuous flow production of cationic liposomes at high lipid concentration in microfluidic devices for gene delivery applications.* Chemical Engineering Journal, 2013. **226**: p. 423-433.
601. Hood, R.R., et al., *Microfluidic synthesis of PEG- and folate-conjugated liposomes for one-step formation of targeted stealth nanocarriers.* Pharm Res, 2013. **30**(6): p. 1597-607.
602. Veeken, J. *Purification of nanoparticles by hollow fiber diafiltration*. in *IOP Conference Series: Materials Science and Engineering*. 2012. IOP Publishing.
603. Dalwadi, G., H.A. Benson, and Y. Chen, *Comparison of diafiltration and tangential flow filtration for purification of nanoparticle suspensions.* Pharmaceutical research, 2005. **22**: p. 2152-2162.
604. Kato, A. and H. Ohashi, *Quick Refolding of High-Concentration Proteins via Microchannel Dialysis.* Industrial & Engineering Chemistry Research, 2021.
605. Lohse, S.E., et al., *A Simple Millifluidic Benchtop Reactor System for the High-Throughput Synthesis and Functionalization of Gold Nanoparticles With Different Sizes and Shapes.* Acs Nano, 2013.
606. Jindal, H.M., et al., *Antimicrobial Activity of Novel Synthetic Peptides Derived from Indolicidin and Ranalexin against Streptococcus pneumoniae.* PLoS One, 2015. **10**(6): p. e0128532.
607. Glukhov, E., et al., *Basis for Selectivity of Cationic Antimicrobial Peptides for Bacterial Versus Mammalian Membranes.* Journal of Biological Chemistry, 2005.
608. Michael, R.Y. and Y.Y. Nannette, *Mechanisms of Antimicrobial Peptide Action and Resistance.* Pharmacological Reviews, 2003. **55**(1): p. 27.
609. Chen, Y., et al., *Role of Peptide Hydrophobicity in the Mechanism of Action of A-Helical Antimicrobial Peptides.* Antimicrobial Agents and Chemotherapy, 2007.
610. Yin, L.M., et al., *Roles of Hydrophobicity and Charge Distribution of Cationic Antimicrobial Peptides in Peptide-Membrane Interactions.* Journal of Biological Chemistry, 2012.
611. Deslouches, B., et al., *De Novo Generation of Cationic Antimicrobial Peptides: Influence of Length and Tryptophan Substitution on Antimicrobial Activity.* Antimicrobial Agents and Chemotherapy, 2005.

612. Makowski, M., et al., *Advances in Lipid and Metal Nanoparticles for Antimicrobial Peptide Delivery.* Pharmaceutics, 2019.
613. Pinilla, C.M.B., N.A. Lopes, and A. Brandelli, *Lipid-Based Nanostructures for the Delivery of Natural Antimicrobials.* Molecules, 2021.
614. Furneri, P.M., et al., *Ofloxacin-Loaded Liposomes: In Vitro Activity and Drug Accumulation in Bacteria.* Antimicrobial Agents and Chemotherapy, 2000.
615. Paoli, E., et al., *Accumulation, Internalization and Therapeutic Efficacy of Neuropilin-1-Targeted Liposomes.* Journal of Controlled Release, 2014.
616. Seelig, J., *Thermodynamics of Lipid–peptide Interactions.* Biochimica Et Biophysica Acta (Bba) - Biomembranes, 2004.
617. Sun, Y., et al., *Cell Permeable NBD Peptide-Modified Liposomes by Hyaluronic Acid Coating for the Synergistic Targeted Therapy of Metastatic Inflammatory Breast Cancer.* Molecular Pharmaceutics, 2019.
618. Suleiman, E., et al., *Electrostatically Driven Encapsulation of Hydrophilic, Non-Conformational Peptide Epitopes Into Liposomes.* Pharmaceutics, 2019.
619. Peng, J., et al., *Carboxymethyl Chitosan Modified Oxymatrine Liposomes for the Alleviation of Emphysema in Mice via Pulmonary Administration.* Molecules, 2022.
620. Papareddy, P., et al., *Antimicrobial Activity of Peptides Derived From Human <i>ß</I>-amyloid Precursor Protein.* Journal of Peptide Science, 2012.
621. Al-Ahmady, Z.S., et al., *Lipid–Peptide Vesicle Nanoscale Hybrids for Triggered Drug Release by Mild Hyperthermia <i>in Vitro</I> and <i>in Vivo</I>.* Acs Nano, 2012.
622. Lü, Y., et al., *Development and Adsorption Characterization of Metal Affinity-Immobilized Magnetic Liposome.* Journal of Nanomaterials, 2020.
623. Torchilin, V.P., et al., *Immunomicelles: Targeted Pharmaceutical Carriers for Poorly Soluble Drugs.* Proceedings of the National Academy of Sciences, 2003.
624. Roberts, S.A., et al., *Versatile Encapsulation and Synthesis of Potent Liposomes by Thermal Equilibration.* Membranes, 2022.
625. Lapenda, T.L.S., et al., *Encapsulation of ≪I>Trans</I>-Dehydrocrotonin in Liposomes: An Enhancement of the Antitumor Activity.* Journal of Biomedical Nanotechnology, 2013.
626. Piel, G., et al., *Betamethasone-in-cyclodextrin-in-liposome: the effect of cyclodextrins on encapsulation efficiency and release kinetics.* Int J Pharm, 2006. **312**(1-2): p. 75-82.
627. Killoran, P.M., et al., *Novel peptide calcitonin gene-related peptide antagonists for migraine therapy.* Journal of Pharmacy and Pharmacology, 2023. **75**(12): p. 1581-1589.
628. Polunin, K.E., et al., *Optimizing the Chromatographic Separation of Antibacterial Peptides of Galleria mellonella.* Russian Journal of Physical Chemistry A, 2022. **96**(8): p. 1773-1781.
629. D'Aloisio, V., *Design, synthesis, and evaluation of serum-stable peptide antagonists of the CGRP receptor as a novel treatment for migraine*. 2022: Liverpool John Moores University (United Kingdom).
630. Khalifa, R.A., et al., *Resazurin Microtiter Assay Plate method for detection of susceptibility of multidrug resistant Mycobacterium tuberculosis to second-line anti-tuberculous drugs.* Egyptian Journal of Chest Diseases and Tuberculosis, 2013. **62**(2): p. 241-247.
631. Montero, M.M., et al., *Time-Kill Evaluation of Antibiotic Combinations Containing Ceftazidime-Avibactam against Extensively Drug-Resistant Pseudomonas aeruginosa and Their Potential Role against Ceftazidime-Avibactam-Resistant Isolates.* Microbiol Spectr, 2021. **9**(1): p. e0058521.
632. Lohner, K. and E.J. Prenner, *Differential scanning calorimetry and X-ray diffraction studies of the specificity of the interaction of antimicrobial peptides with membrane-*

mimetic systems. Biochimica et Biophysica Acta (BBA) - Biomembranes, 1999. **1462**(1): p. 141-156.

633. Whitmore, L. and B.A. Wallace, *DICHROWEB, an online server for protein secondary structure analyses from circular dichroism spectroscopic data.* Nucleic Acids Res, 2004. **32**(Web Server issue): p. W668-73.
634. Whitmore, L. and B.A. Wallace, *Protein secondary structure analyses from circular dichroism spectroscopy: methods and reference databases.* Biopolymers: Original Research on Biomolecules, 2008. **89**(5): p. 392-400.
635. Whitmore, L., et al., *The protein circular dichroism data bank, a Web-based site for access to circular dichroism spectroscopic data.* Structure, 2010. **18**(10): p. 1267-9.
636. Henzel, W.J. and J.T. Stults, *Reversed-Phase Isolation of Peptides.* Current Protocols in Molecular Biology, 2001.
637. Muthu, M.S. and S.-S. Feng, *Pharmaceutical Stability Aspects of Nanomedicines.* Nanomedicine, 2009. **4**(8): p. 857-860.
638. Solomon, D., et al., *Role of In Vitro Release Methods in Liposomal Formulation Development: Challenges and Regulatory Perspective.* The AAPS Journal, 2017. **19**(6): p. 1669-1681.
639. Olivos, H.J., et al., *Microwave-assisted solid-phase synthesis of peptoids.* Organic letters, 2002. **4**(23): p. 4057-4059.
640. Gorske, B.C., et al., *Expedient synthesis and design strategies for new peptoid construction.* Organic letters, 2005. **7**(8): p. 1521-1524.
641. Selsted, M.E., et al., *Indolicidin, a novel bactericidal tridecapeptide amide from neutrophils.* Journal of Biological Chemistry, 1992. **267**(7): p. 4292-4295.
642. Clark, D.P., et al., *Ranalexin. A novel antimicrobial peptide from bullfrog (Rana catesbeiana) skin, structurally related to the bacterial antibiotic, polymyxin.* Journal of Biological Chemistry, 1994. **269**(14): p. 10849-10855.
643. Merrifield, R.B., *Automated Synthesis of Peptides.* Science, 1965. **150**(3693): p. 178-185.
644. Jokela, J. and M. Leisola, *Chromatographic Separation of Nucleosides Using a Cross-linked Xylose Isomerase Crystal Stationary Phase.* Journal of Separation Science, 2004. **27**(17-18): p. 1491-1497.
645. Tachi, T., et al., *Position-dependent hydrophobicity of the antimicrobial magainin peptide affects the mode of peptide− lipid interactions and selective toxicity.* Biochemistry, 2002. **41**(34): p. 10723-10731.
646. Yeaman, M.R. and N.Y. Yount, *Mechanisms of Antimicrobial Peptide Action and Resistance.* Pharmacological Reviews, 2003. **55**(1): p. 27.
647. Dathe, M., et al., *Optimization of the antimicrobial activity of magainin peptides by modification of charge.* FEBS Lett, 2001. **501**(2-3): p. 146-50.
648. Chan, D.I., E.J. Prenner, and H.J. Vogel, *Tryptophan- and arginine-rich antimicrobial peptides: Structures and mechanisms of action.* Biochimica et Biophysica Acta (BBA) - Biomembranes, 2006. **1758**(9): p. 1184-1202.
649. Testing, E.C.o.A.S., *Routine and extended internal quality control for MIC determination and disk diffusion as recommended by EUCAST.* 2022.
650. Lahiri, S.D., et al., *Selection and molecular characterization of ceftazidime/avibactam-resistant mutants in Pseudomonas aeruginosa strains containing derepressed AmpC.* Journal of Antimicrobial Chemotherapy, 2015. **70**(6): p. 1650-1658.
651. Waley, S.G., *ß-Lactamase: mechanism of action*, in *The Chemistry of β-Lactams*, M.I. Page, Editor. 1992, Springer Netherlands: Dordrecht. p. 198-228.
652. Aleinein, R.A., H. Schäfer, and M. Wink, *Secretory ranalexin produced in recombinant Pichia pastoris exhibits additive or synergistic bactericidal activity when used in*

combination with polymyxin B or linezolid against multi-drug resistant bacteria. Biotechnology Journal, 2014. **9**(1): p. 110-119.

653. Giacometti, A., et al., *In-vitro activity and killing effect of polycationic peptides on methicillin-resistant Staphylococcus aureus and interactions with clinically used antibiotics.* Diagnostic Microbiology and Infectious Disease, 2000. **38**(2): p. 115-118.
654. Giacometti, A., et al., *In vitro activities of polycationic peptides alone and in combination with clinically used antimicrobial agents against Rhodococcus equi.* Antimicrob Agents Chemother, 1999. **43**(8): p. 2093-6.
655. Domhan, C., et al., *Replacement of l-Amino Acids by d-Amino Acids in the Antimicrobial Peptide Ranalexin and Its Consequences for Antimicrobial Activity and Biodistribution.* Molecules, 2019. **24**(16).
656. Domhan, C., et al., *A novel tool against multiresistant bacterial pathogens: lipopeptide modification of the natural antimicrobial peptide ranalexin for enhanced antimicrobial activity and improved pharmacokinetics.* International Journal of Antimicrobial Agents, 2018. **52**(1): p. 52-62.
657. Clark, D.P., et al., *Ranalexin. A novel antimicrobial peptide from bullfrog (Rana catesbeiana) skin, structurally related to the bacterial antibiotic, polymyxin.* J Biol Chem, 1994. **269**(14): p. 10849-55.
658. Ando, S., et al., *Structure-activity relationship of indolicidin, a Trp-rich antibacterial peptide.* Journal of Peptide Science, 2010. **16**(4): p. 171-177.
659. Khandelia, H. and Y.N. Kaznessis, *Cation-pi interactions stabilize the structure of the antimicrobial peptide indolicidin near membranes: molecular dynamics simulations.* J Phys Chem B, 2007. **111**(1): p. 242-50.
660. Greenfield, N.J., *Using circular dichroism spectra to estimate protein secondary structure.* Nature Protocols, 2006. **1**(6): p. 2876-2890.
661. Seelig, J., *Thermodynamics of lipid–peptide interactions.* Biochimica et Biophysica Acta (BBA)-Biomembranes, 2004. **1666**(1-2): p. 40-50.
662. Luo, P. and R.L. Baldwin, *Mechanism of helix induction by trifluoroethanol: a framework for extrapolating the helix-forming properties of peptides from trifluoroethanol/water mixtures back to water.* Biochemistry, 1997. **36**(27): p. 8413-8421.
663. Buck, M., *Trifluoroethanol and colleagues: cosolvents come of age. Recent studies with peptides and proteins.* Quarterly reviews of biophysics, 1998. **31**(3): p. 297-355.
664. Hong, D.-P., et al., *Clustering of fluorine-substituted alcohols as a factor responsible for their marked effects on proteins and peptides.* Journal of the American Chemical Society, 1999. **121**(37): p. 8427-8433.
665. Witschas, K., et al., *Interaction of a peptide derived from C-terminus of human TRPA1 channel with model membranes mimicking the inner leaflet of the plasma membrane.* Biochim Biophys Acta, 2015. **1848**(5): p. 1147-56.
666. Blondelle, S.E., K. Lohner, and M.-I. Aguilar, *Lipid-induced conformation and lipid-binding properties of cytolytic and antimicrobial peptides: determination and biological specificity.* Biochimica et Biophysica Acta (BBA)-Biomembranes, 1999. **1462**(1-2): p. 89-108.
667. Miles, A.J. and B.A. Wallace, *Circular dichroism spectroscopy of membrane proteins.* Chemical Society Reviews, 2016. **45**(18): p. 4859-4872.
668. Avitabile, C., L.D. D'Andrea, and A. Romanelli, *Circular Dichroism studies on the interactions of antimicrobial peptides with bacterial cells.* Scientific reports, 2014. **4**(1): p. 4293.
669. Fasman, G.D., *Circular dichroism and the conformational analysis of biomolecules*. 2013: Springer Science & Business Media.

670. Jelinek, R. and S. Kolusheva, *Membrane interactions of host-defense peptides studied in model systems.* Current Protein and Peptide Science, 2005. **6**(1): p. 103-114.
671. Chatzikleanthous, D., et al., *Synthesis of protein conjugates adsorbed on cationic liposomes surface.* MethodsX, 2020. **7**: p. 100942.
672. Xu, Y., et al., *Physicochemical characterization and purification of cationic lipoplexes.* Biophys J, 1999. **77**(1): p. 341-53.
673. Dalkara, D., G. Zuber, and J.-P. Behr, *Intracytoplasmic delivery of anionic proteins.* Molecular Therapy, 2004. **9**(6): p. 964-969.
674. Zelphati, O., et al., *Intracellular Delivery of Proteins with a New Lipid-mediated Delivery System *.* Journal of Biological Chemistry, 2001. **276**(37): p. 35103-35110.
675. Sarker, S.R., R. Hokama, and S. Takeoka, *Intracellular Delivery of Universal Proteins Using a Lysine Headgroup Containing Cationic Liposomes: Deciphering the Uptake Mechanism.* Molecular Pharmaceutics, 2014. **11**(1): p. 164-174.
676. Suleiman, E., et al., *Electrostatically Driven Encapsulation of Hydrophilic, Non-Conformational Peptide Epitopes into Liposomes.* Pharmaceutics, 2019. **11**(11).
677. Persson, D., P.E. Thorén, and B. Nordén, *Penetratin-induced aggregation and subsequent dissociation of negatively charged phospholipid vesicles.* FEBS Lett, 2001. **505**(2): p. 307-12.
678. Durell, S.R., et al., *What studies of fusion peptides tell us about viral envelope glycoprotein-mediated membrane fusion (review).* Mol Membr Biol, 1997. **14**(3): p. 97-112.
679. Martin, I. and J.M. Ruysschaert, *Common properties of fusion peptides from diverse systems.* Biosci Rep, 2000. **20**(6): p. 483-500.
680. Nir, S. and J.L. Nieva, *Interactions of peptides with liposomes: pore formation and fusion.* Prog Lipid Res, 2000. **39**(2): p. 181-206.
681. Jeong, Y.I., et al., *Preparation of poly (dl-lactide-co-glycolide) Nanoparticles Without Surfactant.* Journal of Applied Polymer Science, 2001. **80**(12): p. 2228-2236.
682. Shariat, S., et al., *Optimization of a Method to Prepare Liposomes Containing HER2/Neu-Derived Peptide as a Vaccine Delivery System for Breast Cancer.* Iran J Pharm Res, 2014. **13**(Suppl): p. 15-25.
683. Jahn, A., et al., *Microfluidic Mixing and the Formation of Nanoscale Lipid Vesicles.* Acs Nano, 2010.
684. Balbino, T.A., A.R. Azzoni, and L.G. de la Torre, *Microfluidic devices for continuous production of pDNA/cationic liposome complexes for gene delivery and vaccine therapy.* Colloids and Surfaces B: Biointerfaces, 2013. **111**: p. 203-210.
685. Dimov, N., et al., *Formation and purification of tailored liposomes for drug delivery using a module-based micro continuous-flow system.* Scientific Reports, 2017. **7**(1): p. 12045.
686. Crommelin, D.J.A., et al., *Liposomes as Carriers for Drugs and Antigens: Approaches to Preserve Their Long Term Stability.* Drug Development and Industrial Pharmacy, 1994. **20**(4): p. 547-556.
687. Murzyn, K., T. Róg, and M. Pasenkiewicz-Gierula, *Phosphatidylethanolamine-Phosphatidylglycerol Bilayer as a Model of the Inner Bacterial Membrane.* Biophysical Journal, 2005.
688. Tan, C., et al., *Dual Effects of Chitosan Decoration on the Liposomal Membrane Physicochemical Properties as Affected by Chitosan Concentration and Molecular Conformation.* Journal of Agricultural and Food Chemistry, 2013.
689. Nichols-Smith, S., S.-Y. Teh, and T.L. Kuhl, *Thermodynamic and mechanical properties of model mitochondrial membranes.* Biochimica et Biophysica Acta (BBA)-Biomembranes, 2004. **1663**(1-2): p. 82-88.

690. Domènech, Ò., et al., *Thermodynamic and structural study of the main phospholipid components comprising the mitochondrial inner membrane.* Biochimica et Biophysica Acta (BBA)-Biomembranes, 2006. **1758**(2): p. 213-221.

691. Yamauchi, T., et al., *Thermal adaptation of Tetrahymena membranes with special reference to mitochondria Role of cardiolipin in fluidity of mitochondrial membranes.* Biochimica et Biophysica Acta (BBA)-Biomembranes, 1981. **649**(2): p. 385-392.

692. Unsay, J.D., et al., *Cardiolipin Effects on Membrane Structure and Dynamics.* Langmuir, 2013. **29**(51): p. 15878-15887.

693. Castelletto, V., et al., *Restructuring of Lipid Membranes by an Arginine-Capped Peptide Bolaamphiphile.* Langmuir, 2018.

694. Bagheri, M., et al., *Bacterial Aggregation Triggered by Fibril Forming Tryptophan-Rich Sequences: Effects of Peptide Side Chain and Membrane Phospholipids.* Acs Applied Materials & Interfaces, 2020.

695. Rydberg, H., et al., *Peptide-Membrane Interactions of Arginine-Tryptophan Peptides Probed Using Quartz Crystal Microbalance With Dissipation Monitoring.* European Biophysics Journal, 2014.

696. Chan, D.I., E.J. Prenner, and H.J. Vogel, *Tryptophan- and arginine-rich antimicrobial peptides: structures and mechanisms of action.* Biochim Biophys Acta, 2006. **1758**(9): p. 1184-202.

697. Antos, M., E.A. Trafny, and J. Grzybowski, *Antibacterial activity of liposomal amikacin against Pseudomonas aeruginosa in vitro.* Pharmacological Research, 1995. **32**(1): p. 85-87.

698. Omri, A., M. Ravaoarinoro, and M. Poisson, *Incorporation, release and in-vitro antibacterial activity of liposomal aminoglycosides against Pseudomonas aeruginosa.* J Antimicrob Chemother, 1995. **36**(4): p. 631-9.

699. Omri, A. and M. Ravaoarinoro, *Comparison of the Bactericidal Action of Amikacin, Netilmicin and Tobramycin in Free and Liposomal Formulation against Pseudomonas aeruginosa.* Chemotherapy, 2009. **42**(3): p. 170-176.

700. Lewenza, S., et al., *Extracellular DNA Controls Expression of Pseudomonas Aeruginosa Genes Involved in Nutrient Utilization, Metal Homeostasis, Acid pH Tolerance and Virulence.* Journal of Medical Microbiology, 2020. **69**(6): p. 895-905.

701. Witschi, C. and E. Doelker, *Peptide degradation during preparation and in vitro release testing of poly(l-lactic acid) and poly(dl-lactic-co-glycolic acid) microparticles.* International Journal of Pharmaceutics, 1998. **171**(1): p. 1-18.

702. Brogden, K.A., *Antimicrobial Peptides: Pore Formers or Metabolic Inhibitors in Bacteria?* Nature Reviews Microbiology, 2005.

703. Yeh, I.C., D.R. Ripoll, and A. Wallqvist, *Free Energy Difference in Indolicidin Attraction to Eukaryotic and Prokaryotic Model Cell Membranes.* The Journal of Physical Chemistry B, 2012.

704. Hsu, J.C. and C.M. Yip, *Molecular dynamics simulations of indolicidin association with model lipid bilayers.* Biophys J, 2007. **92**(12): p. L100-2.

705. Nielsen, J.E., V.A. Bjørnestad, and D. Danino, *Resolving the Structural Interactions Between Antimicrobial Peptides and Lipid Membranes Using Small-Angle Scattering Methods: The Case of Indolicidin.* Soft Matter, 2018.

706. Tomlinson, S., P.W. Taylor, and J.P. Luzio, *Transfer of phospholipid and protein into the envelope of gram-negative bacteria by liposome fusion.* Biochemistry, 1989. **28**(21): p. 8303-11.

707. Tan, C.H., et al., *Lipid-polymer hybrid nanoparticles enhance the potency of ampicillin against Enterococcus faecalis in a protozoa infection model.* ACS Infectious Diseases, 2021. **7**(6): p. 1607-1618.

708. Yeh, Y.-C., et al., *Nano-based drug delivery or targeting to eradicate bacteria for infection mitigation: a review of recent advances.* Frontiers in chemistry, 2020. **8**: p. 286.
709. Baek, J.-S., et al., *A programmable lipid-polymer hybrid nanoparticle system for localized, sustained antibiotic delivery to Gram-positive and Gram-negative bacterial biofilms.* Nanoscale Horizons, 2018. **3**(3): p. 305-311.
710. Bose, R.J.C., et al., *Combating Intracellular Pathogens with Nanohybrid-Facilitated Antibiotic Delivery.* International Journal of Nanomedicine, 2020. **15**(null): p. 8437-8449.
711. Tahir, N., et al., *Development and optimization of methotrexate-loaded lipid-polymer hybrid nanoparticles for controlled drug delivery applications.* International Journal of Pharmaceutics, 2017. **533**(1): p. 156-168.
712. Mandal, B., et al., *Core–shell-type lipid–polymer hybrid nanoparticles as a drug delivery platform.* Nanomedicine: Nanotechnology, Biology and Medicine, 2013. **9**(4): p. 474-491.
713. Liu, D., et al., *Hyaluronic-acid-modified lipid-polymer hybrid nanoparticles as an efficient ocular delivery platform for moxifloxacin hydrochloride.* International Journal of Biological Macromolecules, 2018. **116**: p. 1026-1036.
714. Gao, L.-Y., et al., *Core-Shell type lipid/rPAA-Chol polymer hybrid nanoparticles for in vivo siRNA delivery.* Biomaterials, 2014. **35**(6): p. 2066-2078.
715. Chan, J.M., et al., *PLGA–lecithin–PEG core–shell nanoparticles for controlled drug delivery.* Biomaterials, 2009. **30**(8): p. 1627-1634.
716. Zhang, M., et al., *Fabrication of TPGS-Stabilized Liposome-PLGA Hybrid Nanoparticle Via a New Modified Nanoprecipitation Approach: In Vitro and In Vivo Evaluation.* Pharmaceutical Research, 2018. **35**(11): p. 199.
717. Yang, X.-Z., et al., *Single-Step Assembly of Cationic Lipid–Polymer Hybrid Nanoparticles for Systemic Delivery of siRNA.* ACS Nano, 2012. **6**(6): p. 4955-4965.
718. Wang, C., et al., *RGD peptide targeted lipid-coated nanoparticles for combinatorial delivery of sorafenib and quercetin against hepatocellular carcinoma.* Drug Development and Industrial Pharmacy, 2016. **42**(12): p. 1938-1944.
719. Dave, V., et al., *Lipid-polymer hybrid nanoparticles: Development & statistical optimization of norfloxacin for topical drug delivery system.* Bioactive Materials, 2017. **2**(4): p. 269-280.
720. Lin, J., et al., *PEGylated Lipid bilayer coated mesoporous silica nanoparticles for co-delivery of paclitaxel and curcumin: Design, characterization and its cytotoxic effect.* International Journal of Pharmaceutics, 2018. **536**(1): p. 272-282.
721. Gui, K., et al., *Lipid-polymer nanoparticles with CD133 aptamers for targeted delivery of all-trans retinoic acid to osteosarcoma initiating cells.* Biomedicine & Pharmacotherapy, 2019. **111**: p. 751-764.
722. Li, P., et al., *Mucus penetration enhanced lipid polymer nanoparticles improve the eradication rate of Helicobacter pylori biofilm.* Journal of Controlled Release, 2019. **300**: p. 52-63.
723. Wan, F., et al., *Lipid Shell-Enveloped Polymeric Nanoparticles with High Integrity of Lipid Shells Improve Mucus Penetration and Interaction with Cystic Fibrosis-Related Bacterial Biofilms.* ACS Applied Materials & Interfaces, 2018. **10**(13): p. 10678-10687.
724. Fang, Y., et al., *Lipid-Coated, pH-Sensitive Magnesium Phosphate Particles for Intracellular Protein Delivery.* Pharmaceutical Research, 2019. **36**(6): p. 81.
725. Hamilton, D.J., et al., *Lipid-Coated Gold Nanoparticles and FRET Allow Sensitive Monitoring of Liposome Clustering Mediated by the Synaptotagmin-7 C2A Domain.* Langmuir, 2017. **33**(36): p. 9222-9230.

726. Taheri, S., et al., *Antibacterial Plasma Polymer Films Conjugated with Phospholipid Encapsulated Silver Nanoparticles.* ACS Biomaterials Science & Engineering, 2015. **1**(12): p. 1278-1286.
727. Hu, Y., et al., *Engineering the lipid layer of lipid–PLGA hybrid nanoparticles for enhanced in vitro cellular uptake and improved stability.* Acta Biomaterialia, 2015. **28**: p. 149-159.
728. Jain, S., et al., *Lipid–Polymer Hybrid Nanosystems: A Rational Fusion for Advanced Therapeutic Delivery.* Journal of Functional Biomaterials, 2023. **14**(9): p. 437.
729. Wang, Y., et al., *Manufacturing Techniques and Surface Engineering of Polymer Based Nanoparticles for Targeted Drug Delivery to Cancer.* Nanomaterials, 2016. **6**(2): p. 26.
730. Zhuang, J., R.H. Fang, and L. Zhang, *Preparation of Particulate Polymeric Therapeutics for Medical Applications.* Small Methods, 2017. **1**(9): p. 1700147.
731. Bilati, U., E. Allémann, and E. Doelker, *Development of a nanoprecipitation method intended for the entrapment of hydrophilic drugs into nanoparticles.* European Journal of Pharmaceutical Sciences, 2005. **24**(1): p. 67-75.
732. Gao, W. and L. Zhang, *Coating nanoparticles with cell membranes for targeted drug delivery.* Journal of Drug Targeting, 2015. **23**(7-8): p. 619-626.
733. Chai, Z., X. Hu, and W. Lu, *Cell membrane-coated nanoparticles for tumor-targeted drug delivery.* Science China Materials, 2017. **60**(6): p. 504-510.
734. Fang, R.H., et al., *Cell Membrane Coating Nanotechnology.* Advanced Materials, 2018. **30**(23): p. 1706759.
735. Jc Bose, R., S.-H. Lee, and H. Park, *Lipid polymer hybrid nanospheres encapsulating antiproliferative agents for stent applications.* Journal of Industrial and Engineering Chemistry, 2016. **36**: p. 284-292.
736. Dave, V., et al., *Lipid-polymer hybrid nanoparticles: Synthesis strategies and biomedical applications.* Journal of Microbiological Methods, 2019. **160**: p. 130-142.
737. Solorzano, I.O.d., et al., *Microfluidic Synthesis and Biological Evaluation of Photothermal Biodegradable Copper Sulfide Nanoparticles.* Acs Applied Materials & Interfaces, 2016. **8**(33): p. 21545-21554.
738. Khizar, S., et al., *Microfluidic-based Nanoparticle Synthesis and Their Potential Applications.* Electrophoresis, 2021. **43**(7-8): p. 819-838.
739. Jain, R.A., *The manufacturing techniques of various drug loaded biodegradable poly(lactide-co-glycolide) (PLGA) devices.* Biomaterials, 2000. **21**(23): p. 2475-2490.
740. Karnik, R., et al., *Microfluidic Platform for Controlled Synthesis of Polymeric Nanoparticles.* Nano Letters, 2008. **8**(9): p. 2906-2912.
741. Städler, B., et al., *A Microreactor with Thousands of Subcompartments: Enzyme-Loaded Liposomes within Polymer Capsules.* Angewandte Chemie International Edition, 2009. **48**(24): p. 4359-4362.
742. Gdowski, A., et al., *Optimization and Scale Up of Microfluidic Nanolipomer Production Method for Preclinical and Potential Clinical Trials.* Journal of Nanobiotechnology, 2018. **16**(1).
743. Jahn, A., et al., *Preparation of nanoparticles by continuous-flow microfluidics.* Journal of Nanoparticle Research, 2008. **10**(6): p. 925-934.
744. Liu, D., et al., *A Versatile and Robust Microfluidic Platform Toward High Throughput Synthesis of Homogeneous Nanoparticles with Tunable Properties.* Advanced Materials, 2015. **27**(14): p. 2298-2304.
745. Jahn, A., et al., *Controlled Vesicle Self-Assembly in Microfluidic Channels with Hydrodynamic Focusing.* Journal of the American Chemical Society, 2004. **126**(9): p. 2674-2675.

746. Rao, L., et al., *Microfluidic Electroporation-Facilitated Synthesis of Erythrocyte Membrane-Coated Magnetic Nanoparticles for Enhanced Imaging-Guided Cancer Therapy.* ACS Nano, 2017. **11**(4): p. 3496-3505.

747. Shafique, M., et al., *Formulation development of lipid polymer hybrid nanoparticles of doxorubicin and its in-vitro, in-vivo and computational evaluation.* Front Pharmacol, 2023. **14**: p. 1025013.

748. Ishak, R.A.H., N.M. Mostafa, and A.O. Kamel, *Stealth lipid polymer hybrid nanoparticles loaded with rutin for effective brain delivery - comparative study with the gold standard (Tween 80): optimization, characterization and biodistribution.* Drug Deliv, 2017. **24**(1): p. 1874-1890.

749. Gao, Y., et al., *Small Extracellular Vesicles: A Novel Avenue for Cancer Management.* Frontiers in Oncology, 2021.

750. Wallace, S.J., et al., *Drug release from nanomedicines: selection of appropriate encapsulation and release methodology.* Drug delivery and translational research, 2012. **2**: p. 284-292.

751. Hart, K.R., et al., *Liposomes to Augment Dialysis in Preclinical Models: A Structured Review.* Pharmaceutics, 2021.

752. Leng, J., S.U. Egelhaaf, and M.E. Cates, *Kinetics of the Micelle-to-Vesicle Transition: Aqueous Lecithin-Bile Salt Mixtures.* Biophysical Journal, 2003.

753. Lee, A.L.Z., et al., *Efficient intracellular delivery of functional proteins using cationic polymer core/shell nanoparticles.* Biomaterials, 2008. **29**(9): p. 1224-1232.

754. Mukherjee, A., et al., *Lipid Polymer Hybrid Nanoparticles as a Next-Generation Drug Delivery Platform: State of the Art, Emerging Technologies, and Perspectives.* International Journal of Nanomedicine, 2019.

755. Rauber, G.S., D.F. Argenta, and T. Caon, *Emerging Technologies to Target Drug Delivery to the Skin – The Role of Crystals and Carrier-Based Systems in the Case Study of Dapsone.* Pharmaceutical Research, 2020.

756. Dave, V., et al., *Lipid-polymer hybrid nanoparticles: Development & statistical optimization of norfloxacin for topical drug delivery system.* Bioact Mater, 2017. **2**(4): p. 269-280.

757. Wallace, S.J., et al., *Drug Release From Nanomedicines: Selection of Appropriate Encapsulation and Release Methodology.* Drug Delivery and Translational Research, 2012.

758. Deregibus, M.C., et al., *Charge-Based Precipitation of Extracellular Vesicles.* International Journal of Molecular Medicine, 2016.

759. Ohnishi, N., et al., *Rapid determination of the encapsulation efficiency of a liposome formulation using column-switching HPLC.* Int J Pharm, 2013. **441**(1-2): p. 67-74.

760. Santhanes, D., et al., *Microfluidic formulation of lipid/polymer hybrid nanoparticles for plasmid DNA (pDNA) delivery.* International Journal of Pharmaceutics, 2022. **627**: p. 122223.

761. Beicha, A., R. Zaamouch, and N.M.N. Sulaiman, *Permeate Flux in Ultrafiltration Membrane: A Review.* Journal of Applied Membrane Science & Technology, 2017. **14**(1).

762. Vauthier, C. and K. Bouchemal, *Methods for the Preparation and Manufacture of Polymeric Nanoparticles.* Pharmaceutical Research, 2008.

763. Zaloga, J., et al., *Tangential Flow Ultrafiltration Allows Purification and Concentration of Lauric Acid-/Albumin-Coated Particles for Improved Magnetic Treatment.* International Journal of Molecular Sciences, 2015.

764. Ma, B., et al., *Effect of Low Dosage of Coagulant on the Ultrafiltration Membrane Performance in Feedwater Treatment.* Water Research, 2014.

765. Sun, Y. and A. Geng, *Study on the Mechanism of Humic Acid on Ultrafiltration Membrane.* American Journal of Basic and Applied Sciences, 2019.

766. Fateev, N., et al., *Influence of Additives of Amphiphilic Block Copolymers on the Porosity of Hollow Ultrafiltration Membranes Based on Polyethersulfone.* E3s Web of Conferences, 2023.

767. Brauner, A., et al., *Distinguishing between resistance, tolerance and persistence to antibiotic treatment.* Nature Reviews Microbiology, 2016. **14**(5): p. 320-330.

768. Balaban, N.Q., et al., *Bacterial Persistence as a Phenotypic Switch.* Science, 2004. **305**(5690): p. 1622-1625.

769. Mahamed, D., et al., *Intracellular growth of Mycobacterium tuberculosis after macrophage cell death leads to serial killing of host cells.* Elife, 2017. **6**.

770. Zhai, W., et al., *The Immune Escape Mechanisms of Mycobacterium Tuberculosis.* International Journal of Molecular Sciences, 2019. **20**(2): p. 340.

771. Diacovich, L., et al., *The infectious intracellular lifestyle of Salmonella enterica relies on the adaptation to nutritional conditions within the Salmonella-containing vacuole.* Virulence, 2017. **8**(6): p. 975-992.

772. Bengoechea, J.A. and J. Sa Pessoa, *Klebsiella pneumoniae infection biology: living to counteract host defences.* FEMS Microbiology Reviews, 2018. **43**(2): p. 123-144.

773. Lebeaux, D., et al., *pH-Mediated Potentiation of Aminoglycosides Kills Bacterial Persisters and Eradicates In Vivo Biofilms.* The Journal of Infectious Diseases, 2014. **210**(9): p. 1357-1366.

774. Zazo, H., C.I. Colino, and J.M. Lanao, *Current applications of nanoparticles in infectious diseases.* Journal of Controlled Release, 2016. **224**: p. 86-102.

775. Kim, B., et al., *Immunogene therapy with fusogenic nanoparticles modulates macrophage response to Staphylococcus aureus.* Nature Communications, 2018. **9**(1): p. 1969.

776. Nazir, R., M.R. Zaffar, and I. Amin, *Chapter 8 - Bacterial biofilms: the remarkable heterogeneous biological communities and nitrogen fixing microorganisms in lakes*, in *Freshwater Microbiology*, S.A. Bandh, S. Shafi, and N. Shameem, Editors. 2019, Academic Press. p. 307-340.

777. Sartorio, M.G., et al., *Bacterial Outer Membrane Vesicles: From Discovery to Applications.* Annual Review of Microbiology, 2021. **75**(Volume 75, 2021): p. 609-630.

778. Behrens, F., et al., *Bacterial Membrane Vesicles in Pneumonia: From Mediators of Virulence to Innovative Vaccine Candidates.* International Journal of Molecular Sciences, 2021. **22**(8): p. 3858.

779. Gao, W., et al., *Modulating Antibacterial Immunity via Bacterial Membrane-Coated Nanoparticles.* Nano Letters, 2015. **15**(2): p. 1403-1409.

780. Gao, F., et al., *Kill the Real with the Fake: Eliminate Intracellular Staphylococcus aureus Using Nanoparticle Coated with Its Extracellular Vesicle Membrane as Active-Targeting Drug Carrier.* ACS Infectious Diseases, 2019. **5**(2): p. 218-227.

781. Nie, T., et al., *Surface Coating Approach to Overcome Mucosal Entrapment of DNA Nanoparticles for Oral Gene Delivery of Glucagon-like Peptide 1.* ACS Applied Materials & Interfaces, 2019. **11**(33): p. 29593-29603.

782. Wilhelm Romero, K., et al., *Design of Hybrid Polymeric-Lipid Nanoparticles Using Curcumin as a Model: Preparation, Characterization, and In Vitro Evaluation of Demethoxycurcumin and Bisdemethoxycurcumin-Loaded Nanoparticles.* Polymers (Basel), 2021. **13**(23).

783. Chandrasekaran, A.R., et al., *Invitro studies and evaluation of metformin marketed tablets-Malaysia.* Journal of Applied Pharmaceutical Science, 2011. **1**: p. 214-217.

784. Bellio, P., et al., *New and simplified method for drug combination studies by checkerboard assay.* MethodsX, 2021. **8**: p. 101543.

785. Orhan, G., et al., *Synergy tests by E test and checkerboard methods of antimicrobial combinations against Brucella melitensis.* J Clin Microbiol, 2005. **43**(1): p. 140-3.

786. Odds, F.C., *Synergy, antagonism, and what the chequerboard puts between them*. 2003, Oxford University Press. p. 1-1.

787. Cheow, W.S. and K. Hadinoto, *Factors affecting drug encapsulation and stability of lipid–polymer hybrid nanoparticles.* Colloids and Surfaces B: Biointerfaces, 2011. **85**(2): p. 214-220.

788. Kim, Y., et al., *Mass production and size control of lipid–polymer hybrid nanoparticles through controlled microvortices.* Nano letters, 2012. **12**(7): p. 3587-3591.

789. Zhang, L., et al., *Self-assembled lipid− polymer hybrid nanoparticles: a robust drug delivery platform.* ACS nano, 2008. **2**(8): p. 1696-1702.

790. Feng, Q., et al., *Microfluidic based high throughput synthesis of lipid-polymer hybrid nanoparticles with tunable diameters.* Biomicrofluidics, 2015. **9**(5): p. 052604.

791. Gimondi, S., et al., *Microfluidic Devices: A Tool for Nanoparticle Synthesis and Performance Evaluation.* ACS Nano, 2023. **17**(15): p. 14205-14228.

792. Burra, G. and A.K. Thakur, *Insights Into the Molecular Mechanism Behind Solubilization of Amyloidogenic Polyglutamine-containing Peptides.* Peptide Science, 2018.

793. Cox, H.D., et al., *Efficient digestion and mass spectral analysis of vesicular glutamate transporter 1: a recombinant membrane protein expressed in yeast.* J Proteome Res, 2008. **7**(2): p. 570-8.

794. Mohanta, V. and S. Patil, *Enhancing Surface Coverage and Growth in Layer-by-Layer Assembly of Protein Nanoparticles.* Langmuir, 2013.

795. Bosworth, M.E., C. Anthony Hunt, and D. Pratt, *Liposome Dialysis for Improved Size Distributions.* Journal of Pharmaceutical Sciences, 1982. **71**(7): p. 806-812.

796. Vargas, R., et al., *Dialysis is a key factor modulating interactions between critical process parameters during the microfluidic preparation of lipid nanoparticles.* Colloid and Interface Science Communications, 2023. **54**: p. 100709.

797. Anwer, M.K., et al., *Development of Sustained Release Baricitinib Loaded Lipid-Polymer Hybrid Nanoparticles With Improved Oral Bioavailability.* Molecules, 2021. **27**(1): p. 168.

798. Khan, M.A., et al., *Norfloxacin Loaded Lipid Polymer Hybrid Nanoparticles for Oral Administration: Fabrication, Characterization, In Silico Modelling and Toxicity Evaluation.* Pharmaceutics, 2021. **13**(10): p. 1632.

799. Inam, W., et al., *Interactions Between Polymeric Nanoparticles and Different Buffers as Investigated by Zeta Potential Measurements and Molecular Dynamics Simulations.* View, 2022.

800. Tang, B., Y. Qian, and G. Fang, *Development of Lipid-Polymer Hybrid Nanoparticles for Improving Oral Absorption of Enoxaparin.* Pharmaceutics, 2020. **12**(7).

801. Awadeen, R.H., et al., *Formulation of lipid polymer hybrid nanoparticles of the phytochemical Fisetin and its in vivo assessment against severe acute pancreatitis.* Scientific Reports, 2023. **13**(1): p. 19110.

802. Mukherjee, A., et al., *Lipid-polymer hybrid nanoparticles as a next-generation drug delivery platform: state of the art, emerging technologies, and perspectives.* Int J Nanomedicine, 2019. **14**: p. 1937-1952.

803. Gajbhiye, K.R., et al., *Lipid polymer hybrid nanoparticles: a custom-tailored next-generation approach for cancer therapeutics.* Molecular Cancer, 2023. **22**(1): p. 160.

804. Kliesch, L., et al. *Lipid–Polymer Hybrid Nanoparticles for mRNA Delivery to Dendritic Cells: Impact of Lipid Composition on Performance in Different Media*. Pharmaceutics, 2022. **14**, DOI: 10.3390/pharmaceutics14122675.

805. Wang, T., et al., *Solid lipid-polymer hybrid nanoparticles prepared with natural biomaterials: A new platform for oral delivery of lipophilic bioactives.* Food Hydrocolloids, 2018. **84**: p. 581-592.
806. Rouco, H., et al., *Screening strategies for surface modification of lipid-polymer hybrid nanoparticles.* International Journal of Pharmaceutics, 2022. **624**: p. 121973.
807. Pletzer, D., S.C. Mansour, and R.E.W. Hancock, *Synergy between conventional antibiotics and anti-biofilm peptides in a murine, sub-cutaneous abscess model caused by recalcitrant ESKAPE pathogens.* PLoS Pathog, 2018. **14**(6): p. e1007084.
808. Aibani, N., T.N. Khan, and B. Callan, *Liposome mimicking polymersomes; A comparative study of the merits of polymersomes in terms of formulation and stability.* Int J Pharm X, 2020. **2**: p. 100040.
809. Tsai, C.-W., et al., *Development of an indolicidin-derived peptide by reducing membrane perturbation to decrease cytotoxicity and maintain gene delivery ability.* Colloids and Surfaces B: Biointerfaces, 2018. **165**: p. 18-27.
810. Neale, C., et al., *Indolicidin binding induces thinning of a lipid bilayer.* Biophys J, 2014. **106**(8): p. L29-31.
811. Fojan, P., *In Situ Atomic Force Microscopy Studies of the Effect of Indolicidin on E.coli Cells.* Journal of Self-Assembly and Molecular Electronics (Same), 2023.
812. Nie, C., et al., *Peptides as carriers of active ingredients: A review.* Curr Res Food Sci, 2023. **7**: p. 100592.
813. Berge, S.M., N.L. Henderson, and M.J. Frank, *Kinetics and Mechanism of Degradation of Cefotaxime Sodium in Aqueous Solution.* Journal of Pharmaceutical Sciences, 1983. **72**(1): p. 59-63.
814. Alsarra, I.A., et al., *Effect of β-cyclodextrin derivatives on the kinetics of degradation of cefotaxime sodium in solution state.* Journal of Drug Delivery Science and Technology, 2007. **17**(5): p. 353-357.
815. Wise, R., et al., *Activity of the cefotaxime (HR756) desacetyl metabolite compared with those of cefotaxime and other cephalosporins.* Antimicrob Agents Chemother, 1980. **17**(1): p. 84-6.
816. Jones, R.N., A.L. Barry, and C. Thornsberry, *Antimicrobial activity of desacetylcefotaxime alone and in combination with cefotaxime: evidence of synergy.* Rev Infect Dis, 1982. **4 Suppl**: p. S366-73.
817. Korte, C. and J. Quodbach, *3D-printed network structures as controlled-release drug delivery systems: dose adjustment, API release analysis and prediction.* AAPS PharmSciTech, 2018. **19**: p. 3333-3342.
818. Wang, H., et al., *PLGA/polymeric liposome for targeted drug and gene co-delivery.* Biomaterials, 2010. **31**(33): p. 8741-8748.
819. Bi, H., Z. Chen, and J. Qiu, *Drug Release and Magneto-Calorific Analysis of Magnetic Lipid Microcapsules for Potential Cancer Therapeutics.* Designed Monomers & Polymers, 2021. **24**(1): p. 158-163.
820. Ghaghelestani, T.N., N. Farhadian, and N. Binesh, *Preparation a <scp>core-shell</Scp> Lipid/Polymer Nanoparticle Containing Isotretinoin Drug With <scp>pH</Scp> Sensitive Property: A Response Surface Methodology Study.* Journal of Applied Polymer Science, 2021. **138**(30).
821. Azhar Shekoufeh Bahari, L. and H. Hamishehkar, *The Impact of Variables on Particle Size of Solid Lipid Nanoparticles and Nanostructured Lipid Carriers; A Comparative Literature Review.* Adv Pharm Bull, 2016. **6**(2): p. 143-51.
822. Yau, W.-M., et al., *The Preference of Tryptophan for Membrane Interfaces.* Biochemistry, 1998. **37**(42): p. 14713-14718.

823. Henriques, S.T., M.N. Melo, and M.A.R.B. Castanho, *Cell-Penetrating Peptides and Antimicrobial Peptides: How Different Are They?* Biochemical Journal, 2006. **399**(1): p. 1-7.
824. Kadurugamuwa, J.L. and T.J. Beveridge, *Bacteriolytic effect of membrane vesicles from Pseudomonas aeruginosa on other bacteria including pathogens: conceptually new antibiotics.* J Bacteriol, 1996. **178**(10): p. 2767-74.
825. Patel, A., et al., *Sulfonium-based liposome-encapsulated antibiotics deliver a synergistic antibacterial activity.* RSC Medicinal Chemistry, 2021. **12**(6): p. 1005-1015.
826. LeFrock, J.L., R.A. Prince, and R.D. Left, *Mechanism of Action, Antimicrobial Activity, Pharmacology, Adverse Effects, and Clinical Efficacy of Cefotaxime.* Pharmacotherapy: The Journal of Human Pharmacology and Drug Therapy, 1982. **2**(4): p. 174-184.
827. Testing, T.E.C.o.A.S., *Breakpoint tables for interpretation of MICs and zone diameters. Version 9.0*. 2019.
828. Institute, C.A.L.S., *Performance Standards for Antimicrobial Susceptibility Testing*. 2019.
829. Peacock, S.J. and G.K. Paterson, *Mechanisms of Methicillin Resistance in Staphylococcus aureus.* Annu Rev Biochem, 2015. **84**: p. 577-601.
830. (EUCAST), T.E.C.o.A.S.T., *EUCAST guidance on When there are no breakpoints in breakpoint tables?* 2024.
831. Testing, T.E.C.O.A.S., *Guidance Document on Cefotaxime and Ceftriaxone for Staphylococcus aureus infection*. 2023.
832. Rodríguez-Baño, J., et al., *Impact of changes in CLSI and EUCAST breakpoints for susceptibility in bloodstream infections due to extended-spectrum β-lactamase-producing Escherichia coli.* Clinical Microbiology and Infection, 2012. **18**(9): p. 894-900.
833. Sharma, T., et al., *Galaxy ASIST: A Web-Based Platform for Mapping and Assessment of Global Standards of Antimicrobial Susceptibility: A Case Study in Acinetobacter Baumannii Genomes.* Frontiers in Microbiology, 2023. **13**.
834. Bij, A.K.v.d., et al., *Clinical Breakpoint Changes and Their Impact on Surveillance of Antimicrobial Resistance in Escherichia Coli Causing Bacteraemia.* Clinical Microbiology and Infection, 2012. **18**(11): p. E466-E472.
835. Okoliegbe, I., et al., *Antimicrobial Synergy Testing: Comparing the Tobramycin and Ceftazidime Gradient Diffusion Methodology Used in Assessing Synergy in Cystic Fibrosis-Derived Multidrug-Resistant Pseudomonas Aeruginosa.* Antibiotics, 2021. **10**(8): p. 967.
836. Bowler, S.L., et al., *Evaluation of the Accelerate Pheno System for Identification Of <i>Acinetobacter</I> Clinical Isolates and Minocycline Susceptibility Testing.* Journal of Clinical Microbiology, 2019. **57**(3).
837. Podnecky, N.L., et al., *Mechanisms of Resistance to Folate Pathway Inhibitors In <i>Burkholderia Pseudomallei</I> : Deviation From the Norm.* Mbio, 2017. **8**(5).
838. Rand, K.H., et al., *Reproducibility of the Microdilution Checkerboard Method for Antibiotic Synergy.* Antimicrobial Agents and Chemotherapy, 1993. **37**(3): p. 613-615.
839. Gómara-Lomero, M. and S. Ramón-García, *The FICI Paradigm: Correcting Flaws in Antimicrobial in Vitro Synergy Screens at Their Inception.* Biochemical Pharmacology, 2019. **163**: p. 299-307.
840. Štumpf, S., et al., *The Influence of Chestnut Extract and Its Components on Antibacterial Activity Against Staphylococcus Aureus.* Plants, 2023. **12**(10): p. 2043.
841. Lundov, M.D., et al., *Low-level Efficacy of Cosmetic Preservatives.* International Journal of Cosmetic Science, 2011. **33**(2): p. 190-196.
842. Singh, A.P., V. Prabha, and P. Rishi, *Value addition in the efficacy of conventional antibiotics by nisin against Salmonella.* PLoS One, 2013. **8**(10): p. e76844.
843. Tong, Z., et al., *An in vitro study on the effects of nisin on the antibacterial activities of 18 antibiotics against Enterococcus faecalis.* PloS one, 2014. **9**(2): p. e89209.

844. Carvalho, R.H.d. and P.P.G. Filho, *Epidemiologically Relevant Antimicrobial Resistance Phenotypes in Pathogens Isolated From Critically Ill Patients in a Brazilian Universitary Hospital.* Brazilian Journal of Microbiology, 2008. **39**(4): p. 623-630.

845. Masoud, S., et al., *Extent and Resistance Patterns of ESKAPE Pathogens Isolated in Pus Swabs From Hospitalized Patients.* Canadian Journal of Infectious Diseases and Medical Microbiology, 2022. **2022**: p. 1-7.

846. Woodfield, J.C., et al., *Using Cost of Infection as a Tool to Demonstrate a Difference in Prophylactic Antibiotic Efficacy: A Prospective Randomized Comparison of the Pharmacoecomonic Effectiveness of Ceftriaxone and Cefotaxime Prophylaxis in Abdominal Surgery.* World Journal of Surgery, 2004. **29**(1): p. 18-24.

847. Jiang, L., et al., *Clearance of intracellular Klebsiella pneumoniae infection using gentamicin-loaded nanoparticles.* Journal of Controlled Release, 2018. **279**: p. 316-325.

848. Cheow, W.S., M.W. Chang, and K. Hadinoto, *Antibacterial efficacy of inhalable levofloxacin-loaded polymeric nanoparticles against E. coli biofilm cells: the effect of antibiotic release profile.* Pharmaceutical research, 2010. **27**: p. 1597-1609.

849. Mugabe, C., et al., *Mechanism of enhanced activity of liposome-entrapped aminoglycosides against resistant strains of Pseudomonas aeruginosa.* Antimicrob Agents Chemother, 2006. **50**(6): p. 2016-22.

850. Drulis-Kawa, Z., et al., *The interaction between Pseudomonas aeruginosa cells and cationic PC:Chol:DOTAP liposomal vesicles versus outer-membrane structure and envelope properties of bacterial cell.* Int J Pharm, 2009. **367**(1-2): p. 211-9.

851. Sachetelli, S., et al., *Demonstration of a fusion mechanism between a fluid bactericidal liposomal formulation and bacterial cells.* Biochim Biophys Acta, 2000. **1463**(2): p. 254-66.

852. Nicolosi, D., et al., *Encapsulation in fusogenic liposomes broadens the spectrum of action of vancomycin against Gram-negative bacteria.* Int J Antimicrob Agents, 2010. **35**(6): p. 553-8.

853. Jaglal, Y., et al., *Formulation of pH-responsive lipid-polymer hybrid nanoparticles for co-delivery and enhancement of the antibacterial activity of vancomycin and 18β-glycyrrhetinic acid.* Journal of Drug Delivery Science and Technology, 2021. **64**: p. 102607.

854. Sadeghi Mohammadi, S., Z. Vaezi, and H. Naderi-Manesh, *Improvement of anti-biofilm activities via co-delivery of curcumin and gentamicin in lipid-polymer hybrid nanoparticle.* Journal of Biomaterials Science, Polymer Edition, 2022. **33**(2): p. 174-196.

855. Ben Khalifa, R., et al., *Multiple lipid nanoparticles as antimicrobial drug delivery systems.* Journal of Drug Delivery Science and Technology, 2022. **67**: p. 102887.

856. alsaady, w.n., *The Synergistic Effect of Chitosan-Alginate Nanoparticle Loaded With Doxycycline Antibiotic Against Multidrug Resist Enterobacteriaceae.* Iraqi Journal of Science, 2020.

857. Firouzeh, N., et al., *Lethal in Vitro Effects of Optimized Chitosan Nanoparticles Against Protoscoleces of <i>Echinococcus Granulosus</I>.* Journal of Bioactive and Compatible Polymers, 2021. **36**(3): p. 237-248.

858. Paun, R.A., et al., *One-Step Synthesis of Nanoliposomal Copper Diethyldithiocarbamate and Its Assessment for Cancer Therapy.* Pharmaceutics, 2022. **14**(3): p. 640.

859. Muramatsu, H., et al., *Lyophilization Provides Long-Term Stability for a Lipid Nanoparticle-Formulated, Nucleoside-Modified mRNA Vaccine.* Molecular Therapy, 2022. **30**(5): p. 1941-1951.

860. Messick, C.R., K.A. Rodvold, and S.L. Pendland, *Modified time–kill assay against multidrug-resistant Enterococcus faecium with novel antimicrobial combinations.* Journal of Antimicrobial Chemotherapy, 1999. **44**(6): p. 831-834.

861. Scheeder, A., et al., *Molecular Mechanisms of Cationic Fusogenic Liposome Interactions with Bacterial Envelopes.* J Am Chem Soc, 2023. **145**(51): p. 28240-28250.
862. Ahmed, K., P.N. Gribbon, and M.N. Jones, *The application of confocal microscopy to the study of liposome adsorption onto bacterial biofilms.* J Liposome Res, 2002. **12**(4): p. 285-300.
863. Spadea, A., et al., *Nucleic Acid-Loaded Lipid Nanoparticle Interactions with Model Endosomal Membranes.* ACS Applied Materials & Interfaces, 2022. **14**(26): p. 30371-30384.
864. Perczyk, P. and M. Broniatowski, *Simultaneous action of microbial phospholipase C and lipase on model bacterial membranes – Modeling the processes crucial for bioaugmentation.* Biochimica et Biophysica Acta (BBA) - Biomembranes, 2021. **1863**(7): p. 183620.
865. Micciulla, S., Y. Gerelli, and E. Schneck, *Structure and Conformation of Wild-Type Bacterial Lipopolysaccharide Layers at Air-Water Interfaces.* Biophys J, 2019. **116**(7): p. 1259-1269.
866. Mach, M., et al., *The studies on the membrane activity of triester of phosphatidylcholine in artificial membrane systems.* Biochim Biophys Acta Biomembr, 2021. **1863**(11): p. 183711.
867. Krajewska, B., P. Wydro, and A. Jańczyk, *Probing the Modes of Antibacterial Activity of Chitosan. Effects of pH and Molecular Weight on Chitosan Interactions with Membrane Lipids in Langmuir Films.* Biomacromolecules, 2011. **12**(11): p. 4144-4152.
868. Guo, X. and W.H. Briscoe, *Molecular interactions, elastic properties, and nanostructure of Langmuir bacterial-lipid monolayers: Towards solving the mystery in bacterial membrane asymmetry.* Current Opinion in Colloid & Interface Science, 2023. **67**: p. 101731.
869. Roffo, F., et al., *coupled Hydrodynamic Flow Focusing (cHFF) to Engineer Lipid–Polymer Nanoparticles (LiPoNs) for Multimodal Imaging and Theranostic Applications.* Biomedicines, 2022. **10**(2): p. 438.
870. Kawano, K., et al., *Higher Liposomal Membrane Fluidity Enhances the in Vitro Antitumor Activity of Folate-Targeted Liposomal Mitoxantrone.* Molecular Pharmaceutics, 2008. **6**(1): p. 98-104.
871. Das, M.K., *Lipid-polycaprolactone Core-shell Hybrid Nanoparticles for Controlled Delivery of Nateglinide.* Asian Journal of Pharmaceutics, 2021.
872. Stonebraker, A.R., et al., *Cholesterol Impacts the Formation of Huntingtin/Lipid Complexes and Subsequent Aggregation.* Protein Science, 2023. **32**(5).
873. Amin, M., et al., *Ultrasound-Responsive Smart Drug Delivery System of Lipid Coated Mesoporous Silica Nanoparticles.* Pharmaceutics, 2021. **13**(9): p. 1396.
874. Bruzas, I., et al., *Surface-Enhanced Raman Spectroscopy of Fluid-Supported Lipid Bilayers.* Acs Applied Materials & Interfaces, 2019. **11**(36): p. 33442-33451.
875. Banigan, J.R., A. Gayen, and N.J. Traaseth, *Correlating lipid bilayer fluidity with sensitivity and resolution of polytopic membrane protein spectra by solid-state NMR spectroscopy.* Biochim Biophys Acta, 2015. **1848**(1 Pt B): p. 334-41.
876. Zhou, Z., et al., *Calcium Phosphate-Polymer Hybrid Nanoparticles for Enhanced Triple Negative Breast Cancer Treatment via Co-Delivery of Paclitaxel and miR-221/222 Inhibitors.* Nanomedicine Nanotechnology Biology and Medicine, 2017. **13**(2): p. 403-410.
877. Cheow, W.S. and K. Hadinoto, *Lipid-polymer hybrid nanoparticles with rhamnolipid-triggered release capabilities as anti-biofilm drug delivery vehicles.* Particuology, 2012. **10**(3): p. 327-333.

878. Alsaidan, O.A., et al., *Hydrocortisone-Loaded Lipid–Polymer Hybrid Nanoparticles for Controlled Topical Delivery: Formulation Design Optimization and In Vitro and In Vivo Appraisal.* ACS Omega, 2023. **8**(21): p. 18714-18725.

879. Anderluzzi, G. and Y. Perrie, *Microfluidic Manufacture of Solid Lipid Nanoparticles: A Case Study on Tristearin-Based Systems.* Drug Delivery Letters, 2020. **10**(3): p. 197-208.

880. Anderluzzi, G., et al., *Scalable Manufacturing Processes for Solid Lipid Nanoparticles.* Pharmaceutical Nanotechnology, 2019. **7**(6): p. 444-459.

881. Liu, H.W., et al., *Scalable Purification of Plasmid DNA Nanoparticles by Tangential Flow Filtration for Systemic Delivery.* Acs Applied Materials & Interfaces, 2021. **13**(26): p. 30326-30336.

Appendix

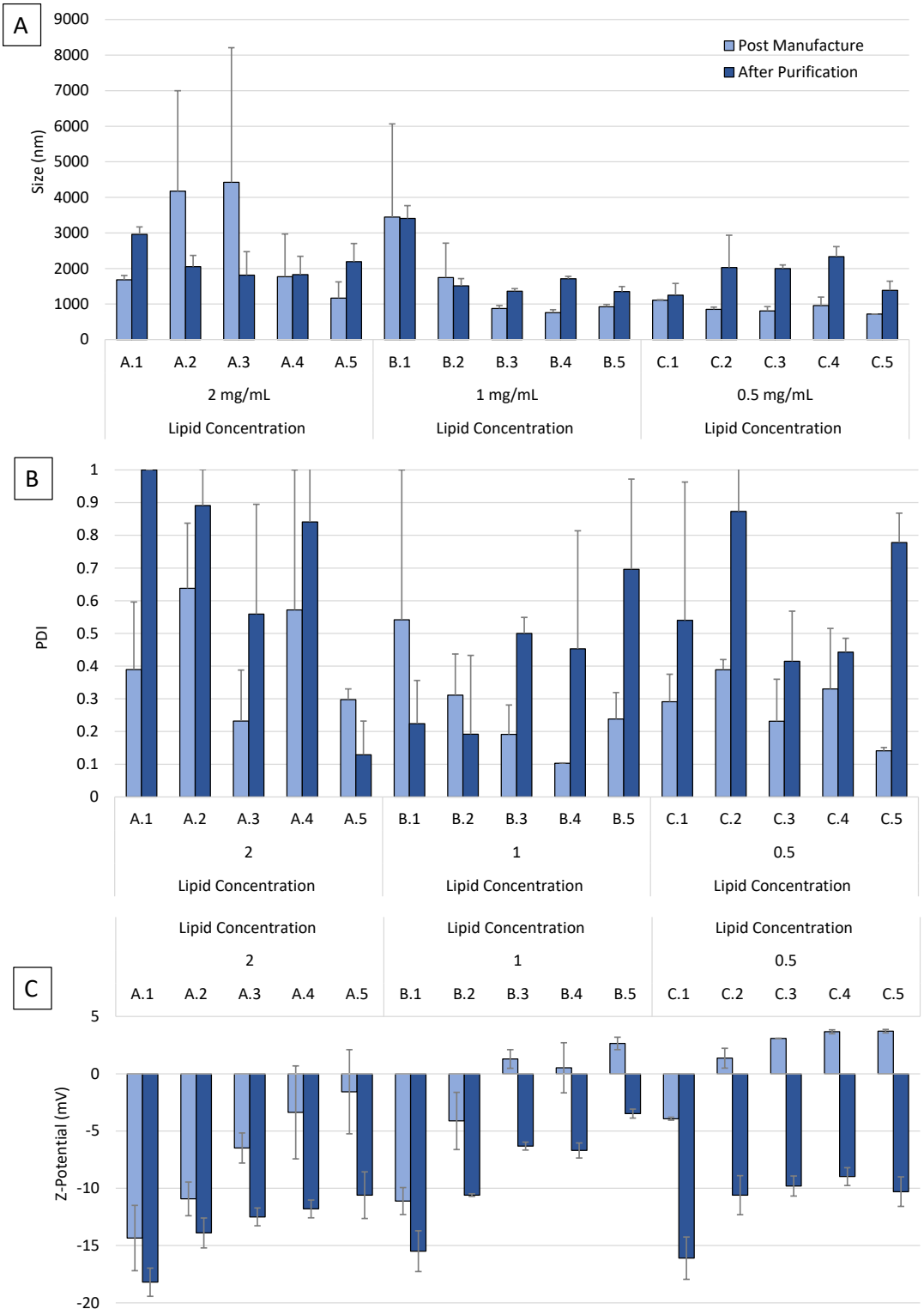

Figure S-1: Size (A), PDI (B) and Z-potential (C) of the 15 LPHNP formulations prepared using the full factorial design detailed in Table 5-2 at a TFR of both 10 mL/min (a total of 15 LPHNP formulations). Formulations were measured post manufacture and after purification performed using centrifugal ultrafiltration and resuspension in PBS. The results represent mean ± SD of 3 technical replicates.

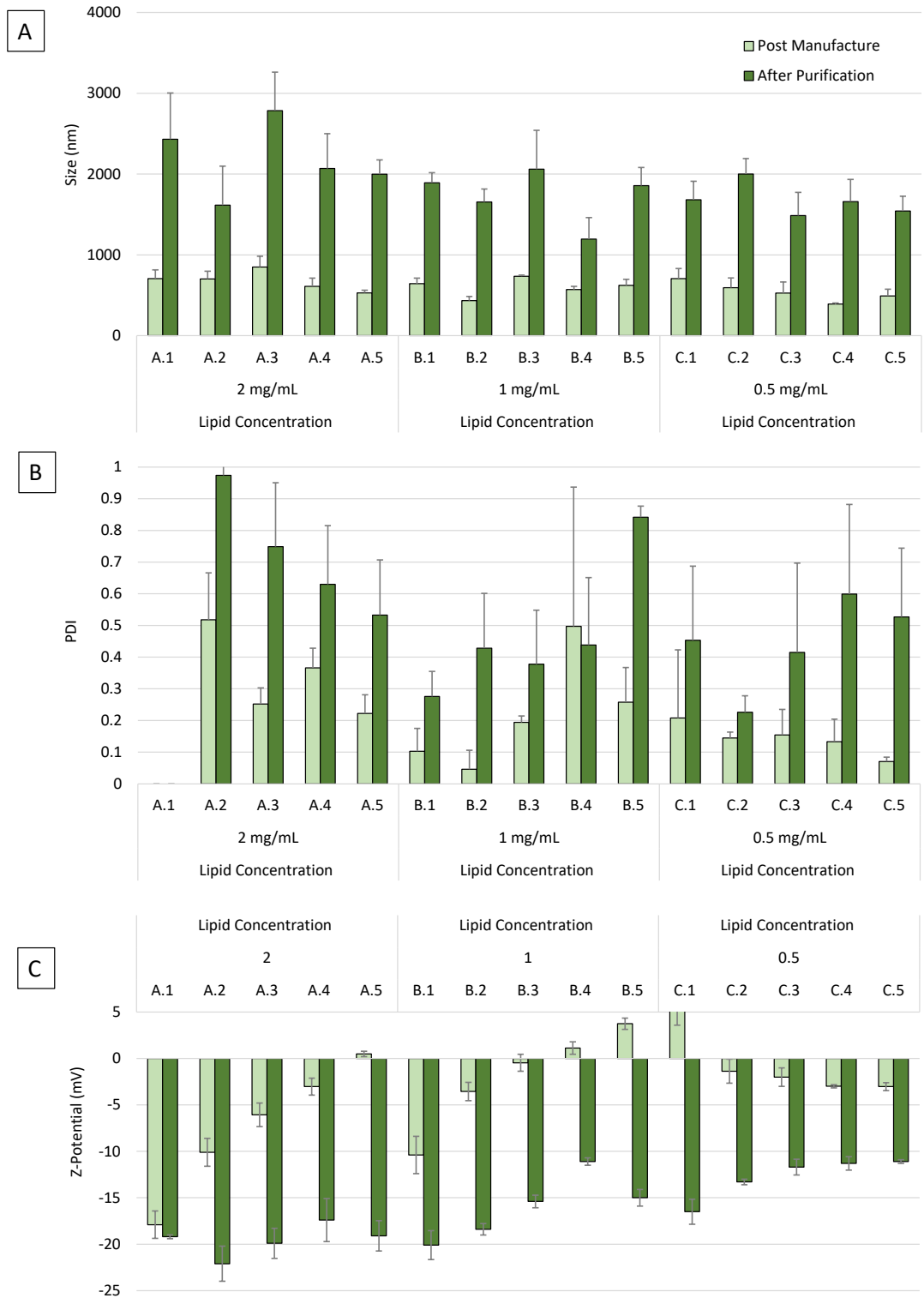

Figure S-2: Size (A), PDI (B) and Z-potential (C) of the 15 LPHNP formulations prepared using the full factorial design detailed in Table 5-2 at a TFR of both 20 mL/min (a total of 15 LPHNP formulations). Formulations were measured post manufacture and after purification performed using centrifugal ultrafiltration and resuspension in PBS. The results represent mean ± SD of 3 technical replicates.

Table S- 1: Comparison of liposome attributes produced by either thin film lipid hydration followed by extrusion or microfluidics. The physicochemical properties for liposomal formulations were investigated using dynamic light scattering. The results represent mean ± SD of 3 technical replicates. Fo the thin film hydration method followed by extrusion, POPE, POPG, and CL in (70:20:10 w/w%, 52.4 mg total lipid) were dissolved in a chloroform and methanol mixture (3:1 v/v, 5 mL). The organic solvent was removed by rotary vacuum evaporation (Heidolph Laborota 4000 Efficient, Austria) at 45 °C and 200 rpm to form a thin, homogeneous lipid film. After one hour, 5 mL of pre-warmed PBS buffer (pH 7.4) was added, and rotation continued for liposome formation. The rehydrated mixture was sonicated for one hour in a water bath (GAH 209 Ultrawave Precision, UK) and subsequently extruded through 200 nm membrane filters (Liposofast LF 50, Avestin, Mannheim, Germany) at 45 °C for 10 cycles to obtain small unilamellar liposomes.

	Temperature (°C)	Size (nm)	PDI	Z-Potential (mV)
Microfluidics (F7)		89.25 ± 7.87	0.135 ± 0.03	-22.23 ± 1.92
Thin film hydration followed by extrusion	70 °C	97.9 ± 1.56	0.171 ± 0.01	-20.1 ± 0.55
	45 °C	143.2 ± 0.46	0.185 ± 0.00	-30.9 ± 0.36

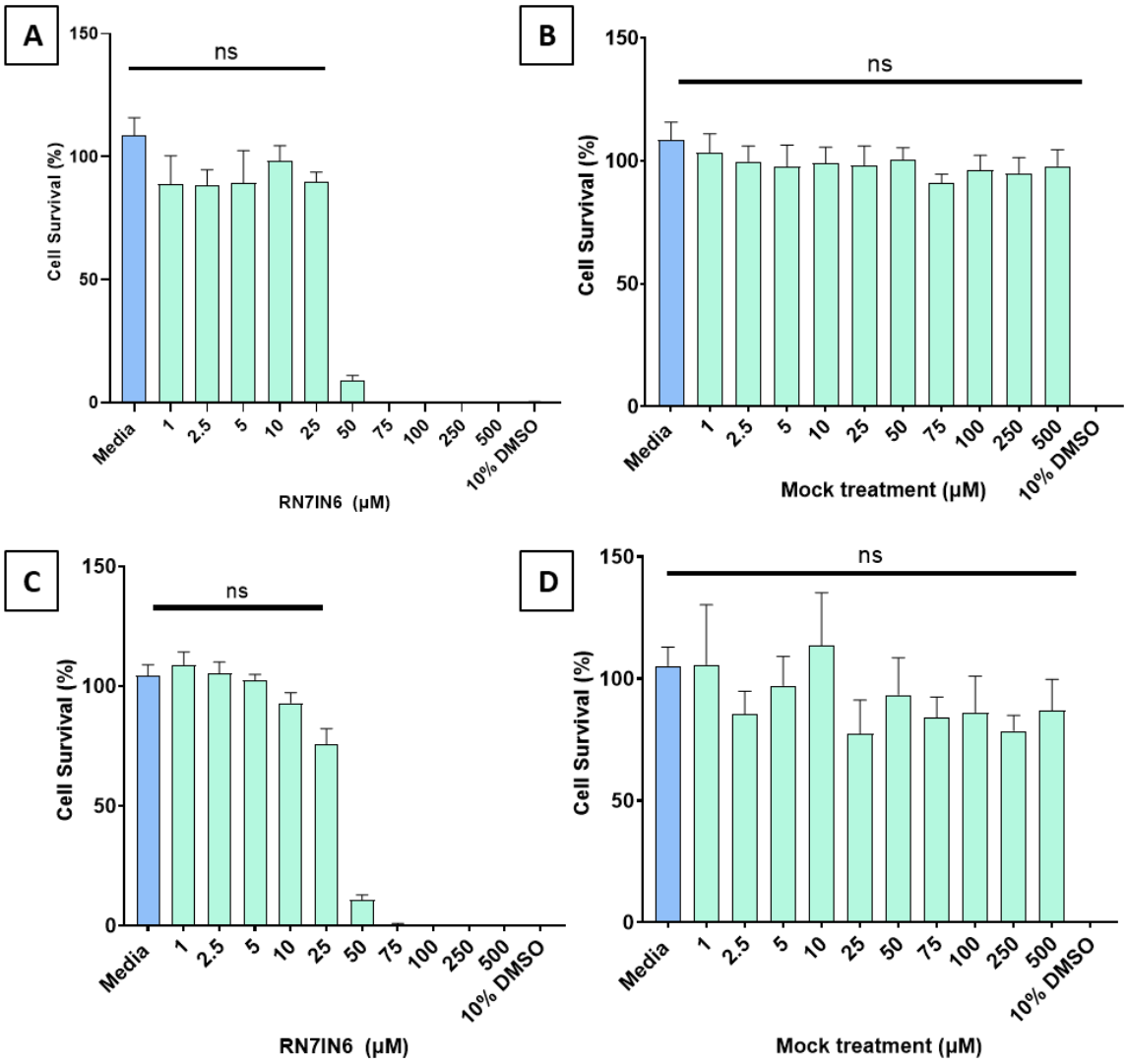

Figure S-3: Calu-3 treatment with RN7IN6. Cytotoxic effect of RN7IN6 incubated at different concentrations ranging from 1 µM to 500 µM with Calu-3 cells for 24h (A) and 48h (C) in comparison with mock treatment at 24h (B) and 48h (D). Alamar Blue was used as a cell viability assay, relying on the reduction of resazurin (non-fluorescent, blue) to resorufin (fluorescent, pink) by metabolically active cells. Calu-3 cells, cultured in MEM supplemented with 10% FBS and 1% penicillin/streptomycin, were seeded at a density of 5x10^4 cells/mL in a 96-well plate and incubated overnight for attachment. RN7IN6 solutions at varying concentrations were added, with complete media as the negative control (100% viability) and 10% DMSO as the positive control (0% viability). After 24 or 48 h treatment, cells were washed, 100 µL of resazurin solution was added, and the plate was incubated at 37 °C for 4 h. Fluorescence was measured (excitation: 530 nm, emission: 590 nm) as a proxy for cell viability. One-way ANOVA analysis of the results with Dunnet post-test revealed that concentrations ranging from 50 µM to 500 µM at 24 h and concentrations ranging from 25 µM to 500 µM at 48 h were statistically significantly different from the control (media-treated control cells) (n=3, mean ± SEM; $p < 0.0001$).

TableS-2: (A) Conversion table between RN7IN6 molarity concentration, employed in cytotoxicity studies, and weight per volume (µg/mL) concentration employed in MIC/time-kill assay studies. (B) Reported RN7IN6 MIC in the current study. Over 20% cytotoxicity was observed when epithelial adenocarcinoma cells were treated with RN7IN6 at 25 µM after 48 hours, while treatment with 50 µM RN7IN6 led to over 80% cytotoxicity at both 24 and 48 hours compared to untreated controls. This indicates that RN7IN6 exhibits strong cytotoxic effects (>80%) after 48-hour exposure at concentrations equivalent to 2.5 and 5 times the MIC values against S. aureus and E. coli/K. pneumoniae, respectively, which suggests that the peptide is safe at MIC concentrations.

A

Conc (µM)	1	2.5	5	10	25	50	75	100	250	500
Conc (µg/mL)	1.7	4.3	8.6	17.1	42.9	85.7	128.6	171.4	428.5	857.0

B

	MIC reported in this study (µg/mL)
S. aureus NCTC 12981	16
E. coli NCTC 12241	32
P. aeruginosa NCTC 12903	256
K. pneumoniae NCTC 9633	32